Numerical simulation of spark ignition engines with special emphasis on radiative heat transfer

Numerical Simulation of Spark Ignition Engines

with special emphasis on

Radiative Heat Transfer

Jonathan Charles Henson

A Doctoral Thesis

Submitted in partial fulfilment of the requirements for the award of
Doctor of Philosophy of the Loughborough University

October 1998

To my parents, brother

and

Στη Μαρία

με αγάπη

Abstract

The in-cylinder combustion dynamics of spark-ignition (SI) engines involves a complex interaction of physical and chemical processes. Despite significant progress in the numerical simulation of these phenomena with computational fluid dynamics (CFD), there is a need for generalised models to describe the emission, absorption and scattering of thermal radiation within the 'participating' combustion gases. Therefore, the present work advances the predictive capability of numerical methods for radiation transport in participating media for inclusion into an established finite-volume CFD code.

The research focuses on three radiation methods: discrete transfer, YIX and a pathlength-based Monte Carlo algorithm. The three-dimensional formulation and coding of each method combines the best available knowledge from heat transfer, statistical and graphics literature. In particular, the tracing and searching of complex arbitrary geometries utilises an efficient ray-triangle intersection algorithm in a novel way to handle cell face distortion and edge intersections with minimum computation. A new general weighted-sum-of-gray-gases model (WSGG) is implemented in order to first resolve the spectral (nongray) dependence of high-temperature gas radiative properties prior to solution by one of the three radiation methods.

The present methods are first verified against published benchmark solutions for radiating media in the absence of other modes of heat transfer. Subsequently, the discrete transfer-WSGG model is coupled with the engine-specific CFD code KIVA-II for studies of the flow field, flame propagation and infrared emission in pancake and pentroof SI engines. Here, the Favre-averaged Navier-Stokes, energy and radiation conservation equations are solved over a nonorthogonal, curvilinear mesh of arbitrary hexahedrons, body-fitted to the combustion chamber geometry. Flexible algebraic and elliptic mesh generation tools are developed for this purpose. Additional $k-\varepsilon$ turbulence terms for variable density flows, the EDC model for mixing-controlled combustion, the Shell model for auto-ignition and the capability to simulate ports and valves with wave action are new features added to KIVA-II to ensure a good description of the turbulent, chemically reacting flow field as a basis for the radiation studies. Comparisons with experimental measurements from optical engine studies are presented.

Acknowledgements

I am deeply grateful to my mentor and supervisor Dr. Malalasekera who provided the motivation and opportunity for me to pursue this research and further my education. I also thank Dr. Colin Garner, Mr. Henk Versteeg, Mr. Alan Baggott, and all others in the Department of Mechanical Engineering for making my years there educational and enjoyable.

I am very grateful to Professor N. Halliwell for acting as my Director of Research.

I would like also to acknowledge Professor J. C. Dent for supporting this work by providing access to experimental facilities and the KIVA-II CFD software.

I especially wish to thank Mr. Graham Gerrard at Computing Services who in addition to managing numerous facilities on campus found the time to teach me the intricacies of UNIX.

Thank you to Shaheed, Saul, Sara, Adel, Miles, Richard, Pali, John, Eli, Mamdud and not forgetting Ann, who have all been very supportive and helpful. Moreover to the many old friends elsewhere, especially Spiros, Nikos, Euripides, Elmer, Tien, Kaweh, Ming and Maria who have shared with me many happy memories.

Finally, I would like to acknowledge Professor John R. Howell (The University of Texas at Austin), Dr. Shawn P. Burns (Sandia National Laboratories), Dr. Jeff T. Farmer (NASA Marshall Space Flight Centre) and Professor Pei-feng Hsu (Florida Institute of Technology) for their helpful discussions and information on radiation methods.

This work was funded with a research studentship from the Department of Mechanical Engineering, Loughborough University and is gratefully acknowledged.

Contents

Abstract iii

Acknowledgements iv

Contents v

1 Introduction 1

1.1 Motivation for this Research 1
1.2 A 'Grand Challenge' Problem 2
1.3 Objectives of this Research 2
1.4 Outline of the Thesis 5

2 Numerical Mesh Generation 7

2.1 Mapping Techniques 8
2.2 Algebraic Mesh Generation 9
2.2.1 One-Dimensional Interpolation and Stretching Functions 9
2.2.2 Transfinite Interpolation 12
2.3 Elliptic Mesh Generation 14
2.3.1 General Equation 15
2.3.2 Finite-difference Form 16
2.3.3 Solution of Discretised Equation with TDMA–ADI Procedure 20
2.3.4 Control Functions 24
2.4 Meshing Application: Pentroof Combustion Chamber Geometry 27
2.4.1 Physical Geometry 28
2.4.2 Selection of Mapping Type 29
2.4.3 Surface Definition 31
2.4.4 Generation of the Interior Mesh 34
2.4.5 Rezoning and Chopping: Piston and Valve Simulation 37
2.5 Summary 40

3 Turbulent Combustion 41

3.1 Averaged Transport Equations 42
3.1.1 Averaging Procedures 42
3.1.2 Species Mass Conservation 44
3.1.3 Total Mass Continuity 45
3.1.4 Momentum Conservation 45
3.1.5 Internal Energy Conservation 46
3.1.6 State Relations 47
3.2 Turbulence Model 48
3.2.1 Second-Moment Closure (Reynolds Stress Model) 49
3.2.2 Algebraic Stress Model 50
3.2.3 Standard $k-\varepsilon$ Turbulence Model 51
3.2.4 Model Selection 54
3.2.5 Modification for Variable Density Flow 55
3.2.6 Turbulence Closure 57
3.3 Combustion and Ignition Models 60
3.3.1 Equilibrium Reactions 62
3.3.2 Kinetic Reactions 62
3.3.3 KIVA-II Kinetic Model 63
3.3.4 Eddy Break-Up Models: The Eddy Dissipation Concept 64
3.3.5 Hybrid Kinetic/EDC Model 67
3.3.6 Spark Ignition 68
3.3.7 Autoignition & Knock 69
3.4 Boundary Conditions 76
3.4.1 Turbulent Wall Functions 76
3.4.2 Open Boundaries: Intake and Exhaust Ports 78
3.4.3 Moving Boundaries: Piston and Poppet Valve Simulation 80
3.4.4 Periodic Boundaries 83
3.5 KIVA-II Numerical Scheme 83
3.5.1 Temporal and Spatial Differencing 84
3.5.2 Solution Procedure 84
3.5.3 Methodology Changes 86
3.5.4 Program Structure 88
3.5.5 Troubleshooting 90
3.6 Summary 91

4 Development Of Radiative Heat Transfer Methods 92

4.1 Equations for Radiation Transport in Participating Media 92
4.1.1 Integro-Differential Formulation 93
4.1.2 Integral Formulation 97
4.1.3 Closure Conditions: Surface Flux & Divergence of Radiative Flux 99
4.2 Numerical Methods for Participating Media: A Review 100
4.3 Geometric Modelling and Ray Tracing 108
4.3.1 Spatial Discretisation and Element Properties 108
4.3.2 Ray Tracing and Search Strategies 110
4.3.3 Finite Element Parametric Mapping: Nonhomogeneous Properties 117
4.4 Pathlength-Based Monte Carlo 120
4.4.1 Probability Distributions 120
4.4.2 Simulation Procedure 125
4.4.3 Solution Values and Statistical Uncertainty 129
4.4.4 Hybrid Monte Carlo/Zonal Solution 131
4.5 YIX Method 133
4.5.1 Angular-Distance Form of the Integral Radiation Equations 133
4.5.2 Angular and Distance Integration: YIX Quadrature 134
4.5.3 Solution Procedure 141
4.6 Discrete Transfer Method 144
4.6.1 Original Formulation 144
4.6.2 Modifications/Extensions 149
4.7 Summary 153

5 Generalised WSGG Model for Nonhomogeneous, Nongray Media 154

5.1 Gas Property Models: A Review 154
5.2 Nongray Model Selection 157
5.3 Computation of the Spectral Absorption Coefficient 158
5.4 Weighted-Sum-of-Gray-Gases (WSGG) Model 160
5.4.1 Bandwise Solution 160
5.4.2 Banded Solution using Absorption Cross-Sections 165
5.5 Combined Mode Heat Transfer: Radiation Coupling 171
5.6 Summary 174

6 Results and Discussion

Part A: Pure Radiative Heat Transfer Studies 175

6.1 Nonhomogeneous Scattering Gray Media 177
6.1.1 Case A: Axially Fired Furnace of Rectangular Cross-Section 177
6.1.2 Case B: Nonorthogonal Cylindrical Geometry. 179
6.1.3 Case C: Cubic Benchmarking Media with Nonhomogeneous Extinction, a Hot Emitting Wall and Anisotropic Scattering. 183
6.1.4 Case D: Nonorthogonal, Nonhomogeneous L-shaped Geometry 185
6.1.5 Run Times and Memory Requirements 186
6.2 Homogeneous Scattering NonGray Media 208
Part A: Summary 227

Part B: SI Engine Simulations 228

6.3 Parametric Studies and Comparisons: Ricardo E6 Engine 228
6.3.1 Experimental Observations 228
6.3.2 Present Predictions 229
6.4 Full Cycle Simulation of a Four Valve Pentroof Combustion Chamber: Ricardo Hydra Engine 248
6.4.1 Engine Test Conditions and Cylinder Pressure Measurement 248
6.4.2 Computational Model: Mesh Definition and Boundary Conditions 249
6.4.3 Flow Characteristics over a Full Cycle 251
6.4.4 Flame Development and Radiative Heat Flux 253
Part B: Summary 267

7 Conclusions and Recommendations 268

7.1 Present Contribution 268
7.2 Concluding Remarks 269
7.2.1 Spatial Discretisation 269
7.2.2 Description of Turbulence and Combustion 270
7.2.3 Radiation Model 272
7.3 Recommendations for Further Work 275

Appendices

A Transformation Relations 276

A.1 Basic Relations 276
A.2 Covariant and Contravariant Base Vectors 277
A.3 Covariant and Contravariant Metric Tensors 278
A.4 Tensor Relations for the Jacobian 278
A.5 The Laplacian 279

B FORTRAN Mesh Generation Routines 281

B.1 Subroutine *Trans* 282
B.2 Subroutine *Metric* 283
B.3 Subroutine *Lisolv* 285

C Differencing of Pressure-density Term in KIVA-II Numerical Scheme 287

D Discrete Ordinate Sets 289

Nomenclature 290

References 297

Chapter 1 Introduction

1.1 Motivation for this Research

Numerical models of engine combustion have improved dramatically in recent years from the combined efforts of the fluid dynamics and combustion modelling communities. This has resulted in the development of simulation software for the calculation of transient turbulent chemically reacting flows in complex port/cylinder geometries. Three notable examples are the engine-specific codes FIRE (Tatschl *et al.* 1996), VECTIS (Bensler and Oppermann 1996) and, to be used in the present study, KIVA (see Chapter 3), although more general-purpose computational fluid dynamics (CFD) packages such as STAR-CD, CFX and FLUENT amongst others also offer this capability. These can all describe key phenomena such as turbulence, mixing, ignition, chemical reaction and heat transfer (by conduction and convection). Often a well-established selection of models are available with different orders of computation and accuracy providing the analyst with multiple solver choices.

However, one important exception is the lack of generalised models to describe emission, absorption and scattering of thermal radiation within the 'participating' combustion gases. To date calculations have largely relied on empirical relations (Heywood 1988, Sec. 12.5), but this situation is no longer acceptable: as overall modelling fidelity improves new work is showing that turbulence, chemistry and radiation are all intimately related (Chan 1998).

It is the aim of this study to thoroughly address this problem with an end to developing contemporary techniques for radiatively participating media which lead themselves to a coupled solution with the equations for turbulent flow and the other heat transfer modes. Attention is to be given to important difficulties namely, complex geometries, anisotropy, nonuniform properties and spectrally dependent effects. A novel study will then be made of how the detailed geometry and gas composition influence flame radiation in spark-ignition engines.

1.2 A 'Grand Challenge' Problem

The simulation of thermal radiation in complex participating media with other modes of heat transfer was deemed as a 'grand challenge' problem and stimulated the most interest of attendees at a 1994 U.S. National Science Foundation (NSF) workshop (Gritzo *et al.* 1995). This provided a forum for experts in radiative heat transfer and high-performance computing to identify highly challenging, nationally important problems (i.e. research thrusts) of mutual interest. Several key difficulties are identified for complex/combined-mode problems (Gritzo *et al.* 1995, p.16):

> *'The ability to address 3D complex geometries was cited as being imperative to applying this capacity to practical applications. Inhomogeneous (both spatially and temporally) media, anisotropic scattering, and spectral dependence should also be included. The ability to address the interaction of radiative heat transfer with chemically reacting flows, turbulent flows, conditions which include phase change and mass transfer, and environments which include the production and destruction of species were also presented as essential features of this capability.'*

Relevant applications included modelling gas turbines, coal furnaces, fuel fires and with particular relevance here – internal combustion engines. It is also noteworthy that these comments were reiterated in more recent open forum sessions at the ASME 31st National Heat Transfer Conference (Houston, Texas, 1996) and at the ICHMT 2nd International Symposium on Radiative Transfer (Kusadasi, Turkey, 1997).

1.3 Objectives of this Research

This section defines key objectives in order to form a framework from which a complete numerical solution to the posed problem can be developed. It was decided early on that any radiation software arising from this research should have the dual capability to be used as a stand-alone code or to be interfaced with a finite-volume-based computational fluid dynamics (CFD) solver. The CFD solver KIVA-II (Amsden *et al.* 1989) was chosen to demonstrate coupled mode operation. Other codes were considered but either their source versions were unavailable, or they were too large to execute, e.g. the smallest version of FIRE was for problem sizes up to 50,000 elements: twice the capacity of the modest machines available for this work at that time.

It was also intended that the flow-radiation solver should be suitable for simulations of two Ricardo spark-ignition research engines within the institute (to enable validation of numerical results by experimental methods in later studies). The relevance of this was that the more complex (geometrically speaking) of these engines – a Ricardo Hydra – has a modern four-valve pentroof head, well beyond the basic axisymmetric meshing capabilities of KIVA-II. Moreover, the rather general boundary options in KIVA-II did not provide for a description of the valves and open ports. Finally, some aspects of the physical submodels fell short of the state-of-the-art. Consequently, improving the CFD solver was also a significant requirement of this work, in addition to the development of radiation software. This is reflected the objectives set out below.

1.3.1 Objective 1: To develop a suite of numerical mesh generation tools for the body-fitted description of complex combustion chambers.

Finite element (FE) preprocessors were well developed at the start of this research and the possibility of using these for meshing complex engine geometries was considered. Trials were made with the preprocessor in the FE software FEMSYS. It was found that the meshing constraints imposed for the FE solver were too relaxed and failed to meet the criteria of the KIVA-II finite volume solver. Others have been more successful: Taghavi and Dupont (1989) used the preprocessors GIBI and SUPERTAB to describe a port/ cylinder assembly for KIVA solution. However, even here intermediate re-numbering of the cells and vertices was necessary. Furthermore, new grid handling procedures had to be written to smooth the mesh as it distorted in a concertina-like manner with the piston and valve movement. Consequently, Buchou (1994) chose to eliminate this redundancy with dedicated KIVA-II routines for both mesh generation and smoothing. Likewise, this is the approach preferred here.

1.3.2 Objective 2: To improve and extend the physical models for flow and combustion in KIVA-II.

Modelling technology in thermofluids has moved on somewhat since the public release of KIVA-II in 1989. Since the physical processes governing flow, combustion and radiative heat transfer are all intimately linked, these developments can not be ignored. Advantage should be taken of recent improvements to the KIVA-II numerical schemes and physical models; and of new submodels for mixing-controlled combustion, autoignition and wave action developed in-house.

1.3.3 Objective 3: To develop radiation solvers for gray participating media.

Reference to recent texts or review papers (see Sec. 4.2 refs.) on the numerical solution of radiative heat transfer reveals a bewildering variety of methods but very little comment as to their comparative performance. Until recently researchers have tended to separately investigate a single method, compartmentalising the research, and making criticism of other techniques difficult (and possibly unpopular). While this may protect new methods from being abandoned prematurely, it also hinders a natural selection of the best methods and is certainly an inhibiting factor in the transfer of technology to industry – a problem noted at the ICHMT 2nd International Symposium on Radiative Transfer (Turkey, 1997).

Benchmarking is seen as the best way to address this issue: a well-defined problem is posed for which a verified 'benchmark' solution can be found by either analytical means or massive computation (e.g. Monte Carlo solution). This is then used for the verification of other methods. To date most benchmarking studies have involved the collaboration of research groups running their own codes on their own machines, e.g. Tong and Skocypec (1992). Consequently, a fair assessment of methods is still difficult. Therefore, there is a clear need to identify, implement and compare some of the most promising techniques under conditions without bias, (i.e. using state-of-the-art algorithms, similarities in coding, identical compiler options and the same platform).

1.3.4 Objective 4: To find efficient means of modelling spectral dependence.

Modelling nongray, or spectral dependent, behaviour in gaseous media is one of the most challenging aspects of participating radiation and an essential requirement if models are to be applicable to problems of technical interest. Severe difficulties are encountered in combusting systems where there rapid, even discontinuous, spectral and spatial variations in properties, e.g. sudden transitions from opaque-to-transparent transfer characteristics across flame fronts.

A sliding scale of gas property models has evolved for various trade-offs between accuracy and economy. Their diversity is so great that the treatment of nongray media may be considered as a distinct research field in its own right. The object here is to find and/or develop a generalised model for gas mixtures (of combustion products) with high accuracy but a low-to-moderate computational requirement. This method should also be compatible with the radiation solvers developed under objective 3.

1.3.5 Objective 5: To verify and validate the present numerical models and identify areas requiring further work.

Here, 'verification' is used to mean a check on the numerical aspects of a model by, for example, comparison with analytical or benchmark solutions of contrived, often idealised problems, whereas 'validation' is a check against actual experimental data. The former process enables coding errors to be systematically eliminated, and distinguishing strengths and weaknesses to be identified. Then, validation is concerned with how well a verified code simulates reality and indicates where theoretical improvements should be made.

1.4 Outline of the Thesis

Chapters 2–5 are largely theoretical and respond respectively to objectives 1–4. Each focuses on a different research area, namely, mesh generation, turbulent combustion, gray radiation and nongray radiation. A substantial portion of this work is either new or not well documented elsewhere. Chapters 6 and 7 respond to objective 5.

Chapter 2 summarises algebraic and elliptic mesh generation techniques used herein to mesh a 4-valve pentroof combustion chamber. Emphasis is placed on the approach used to transform the mesh generation equations into forms suitable for numerical solution.

Chapter 3 deals with all aspects of the turbulent combustion model with the exception of radiation. The governing equations are presented in Cartesian tensor notation. Stress is placed on the assumptions, limitations and aspects less often documented. Both gradient transport and second-order closure assumptions for the Reynolds stresses are discussed. A hybrid kinetic/mixing-controlled (EDC) combustion model is developed. Models for ignition, autoignition (knock) and the boundary layer are also described. Finally, the numerical solution scheme is summarised together with advice on troubleshooting.

Chapter 4 introduces the fundamental equations for radiative transport in participating media and then reviews contemporary solution techniques. These are for the solution of *gray* systems. A detailed formulation of the Monte Carlo, YIX and discrete transfer models is then given based on the best available knowledge from heat transfer, statistical and graphics literature. Consequently, several aspects of the theory and/or coding of each models implemented here are completely novel.

Chapter 5 is concerned with treatment of *non*gray media. Various gas property models are reviewed leading to the implementation of a generalised WSGG model. Treatment of nonisothermal and/or nonhomogeneous media is also considered. Finally, it is explained how the turbulent combustion and radiation models are coupled together for a combined mode analysis. (N.B. The overall solution procedure is summarised in Fig. 5.7 (p. 173) and the reader is encouraged to refer to this figure regularly while reading theory chapters 3, 4 and 5.)

All numerical solutions are collected together in **Chapter 6**. It is divided into two parts: **Part A** is concerned with verification of the radiation model. Calculations with the present Monte Carlo, YIX and discrete transfer models are made for a series of benchmark problems of increasing complexity. This study is unique in that virtually bias-free comparisons are made of both their accuracy *and* computational efficiency. **Part B** demonstrates calculations of radiative heat transfer in two spark-ignition engines.

Chapter 7 presents the conclusions and limitations of this research, and suggestions for further work.

Also note:

Figures and tables are included within the text, except in Chapter 6, where they have been collected together at the end of each main section. A short summary is provided at the end of Chapters 2–5 and at the end of Part A and Part B in Chapter 6.

Chapter 2

Numerical Mesh Generation

A key issue in the numerical simulation of fluid dynamics and heat transfer is the approach used to discretise the problem geometry into a collection of elemental volumes termed *cells*. These cells constitute a *mesh* of the physical region. The governing transport equations are then approximated over this mesh as a system of algebraic equations and solved to determine the temporal and spatial variation of the physical properties within the region. The quality of this solution is related to how accurately the computational mesh conforms to the physical boundaries of the problem geometry. In particular, the study of the turbulent reacting flow field in spark-ignition engines requires meshing tools able to represent the highly contoured interior surfaces of the combustion chamber. Furthermore, these should efficiently control the vertex spacing and mesh deformation due to piston and valve movement to provide the necessary fidelity in results.

To obtain this flexibility, several techniques have been employed to mesh an arbitrary geometry using a curvilinear coordinate system with coordinate lines coincident with the physical boundaries (i.e. body-fitted). These are discussed in detail in the sections below. Emphasis has been placed on the approach used to transform the mesh generation equations into forms suitable for numerical solution in three-dimensions, because this area is not well documented in the mesh generation literature. Procedures for controlling the distribution of coordinate lines such they can be concentrated as desired are also described.

Finally, to demonstrate how the techniques are applied to a real problem, the stages in meshing a 4-valve pentroof combustion chamber are described. (This is the problem geometry simulated later in Sec. 6.4.)

2.1 Mapping Techniques

To describe an arbitrary problem geometry its physical Cartesian coordinates (x, y, z) are transformed to curvilinear coordinates (ξ, η, ζ) in a regular computational domain. A unique correspondence between the Cartesian and curvilinear coordinates must be found, such that every point in the physical region maps on to one, and only one, point in the computational (or transformed) region. The simplest three-dimensional mappings require that a region bounded by six generally curved sides is transformed to a cubic domain, where one of the curvilinear coordinates is constant, and the others vary monotonically, over each surface of the cube. (N. B. More sophisticated multi-block structures are not considered here, since these are not appropriate for the numerical scheme in Chapter 3.) The problem geometry is then defined with a cubic array of position vectors:

$$\mathbf{x}_{ijk} \quad (i = 1,2,\ldots,I; \quad j = 1,2,\ldots,J; \quad k = 1,2,\ldots,K) \tag{2.1}$$

such that the computational mesh is composed of a single block of cells, indexed by the integers (i, j, k) corresponding to the three curvilinear coordinate directions (ξ, η, ζ) respectively. The vector $\mathbf{x}$ is a three-vector giving the values of the x, y and z Cartesian coordinates of a mesh point.

Following the almost universally adopted practice of Thompson *et al.* (1985), the generation of a computational mesh can then expressed, with respect to the *computational* region, as the following boundary value problem. Given all $\mathbf{x}$ on boundary $\partial\Re$ (Fig. 2.1) determine x, y and z as functions of ξ, η and ζ in the interior $\Re$.

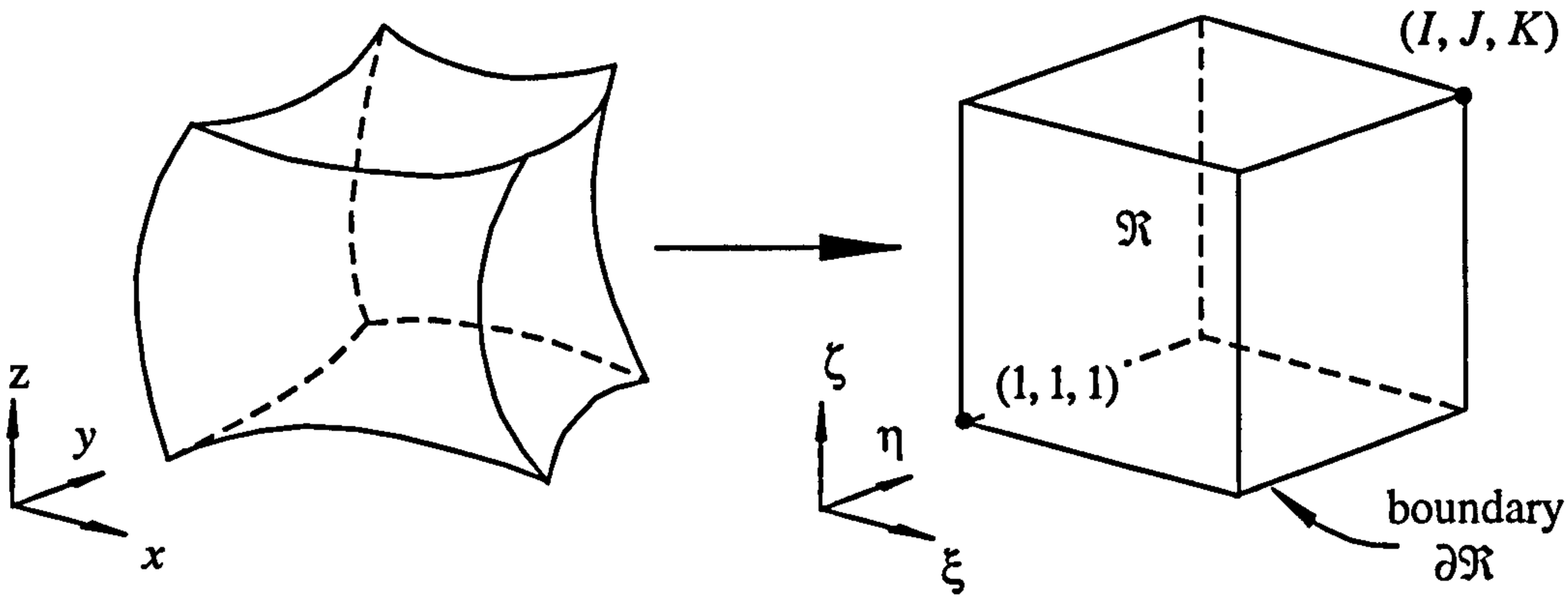

Figure 2.1 Mesh generation as a boundary value problem in the computational domain.

Numerically this problem is implemented in three stages: first (1) point distributions are specified along appropriate boundary contours of the problem geometry, then (2) the entire boundary point distribution is defined by generating surface meshes between these contours, and finally (3), the interior mesh is generated from the Cartesian coordinates of these boundary points. Each of these tasks are accomplished with algebraic mapping techniques and/or by the solution of suitable partial differential equations as described in the following sections. A key requirement is that the generated mesh is well-conditioned: smoothly varying, close to orthogonal and with local grid aspect ratios close to unity.

2.2 Algebraic Mesh Generation

Algebraic mapping techniques interpolate between boundaries to generate the interior mesh. The placement of mesh points along these boundaries is by one-dimensional interpolation, with stretching functions to provide concentrations of points at one or both ends, or in the centre, as desired. This control is very important since the distribution of mesh points in the interior is mainly governed by the boundary description, irrespective of whether an algebraic mapping technique (Sec. 2.2.2) *or* solution of a system of partial differential equations (Sec. 2.3) is used to generate the mesh.

2.2.1 One-Dimensional Interpolation and Stretching Functions

Several types of one-dimensional interpolation are available: Lagrangian, Hermite, Bezier, splines (Thompson *et al.* 1985, pp. 279-294). These are used to interpolate in one curvilinear direction only between points lying on a boundary (and perhaps interior) curve or surface. The shape of the interpolating curve, its slope continuity, and the degree of local refinement possible, depend on the interpolation method. Lagrangian and Hermite interpolation functions fit a single polynomial between boundary end points, matching specified interior control points (or coordinates) and perhaps derivatives of the point spacing. Attempting to match more interior points and/or higher-order derivatives, requires that the order of the interpolating polynomial is increased, such that it becomes susceptible to oscillations. Therefore, an alternative approach is to fit low-order polynomials between each of the specified interior points, at which the continuity of the slope, and higher derivatives, is enforced. The interpolation function is then a piecewise-continuous polynomial called a spline. There are several types of spline function, but by far the most popular are B-splines which have the important feature of being non-zero

only over four intervals and yet have continuous second derivatives everywhere (see Dierckx 1993; Rogers & Adams 1990). This allows highly localised adjustments to the interpolation without affecting other parts of the spline. In particular, a development of these, called nonuniform rational B-splines (NURBS), are now used as a standard descriptor in several commercial mesh generation packages.

At present single polynomials are used for interpolations in a Lagrangian form. A NURBS definition would be preferred for its increased flexibility, but considerable work is required to enable these to be generated on a three-dimensional surface, and subsequently implemented in the interior mesh generation procedures. Consider an $\xi-$coordinate line from ξ_1 to ξ_I as shown in Fig. 2.2. A normalised coordinate s may be defined as:

$$s=\frac{\xi-\xi_1}{\xi_I-\xi_1} \qquad \text{so} \qquad 0\le s\le 1 \qquad \text{as} \qquad \xi_1\le\xi\le\xi_I \tag{2.2}$$

Then Lagrangian interpolation along a physical boundary is given by the general formula:

$$\mathbf{x}(\xi)=\sum_n \phi_n(s)\mathbf{x}_n \tag{2.3}$$

where ϕ_n are polynomials defined over the entire interval $\xi_1\le\xi\le\xi_I$ such that they are zero everywhere except at the corresponding control points (or coordinates) $\mathbf{x}_n$. The simplest application of Eq. (2.3) is with *no* interior control points, such that the interpolation is just between the end points $\mathbf{x}_1$ and $\mathbf{x}_2$ (i.e. $n=2$). i.e. Specifying the functions, $\phi_1(s)=1-s$ and $\phi_2(s)=s$, then:

$$\mathbf{x}(\xi)=(1-s)\mathbf{x}_1+s\mathbf{x}_2 \tag{2.4}$$

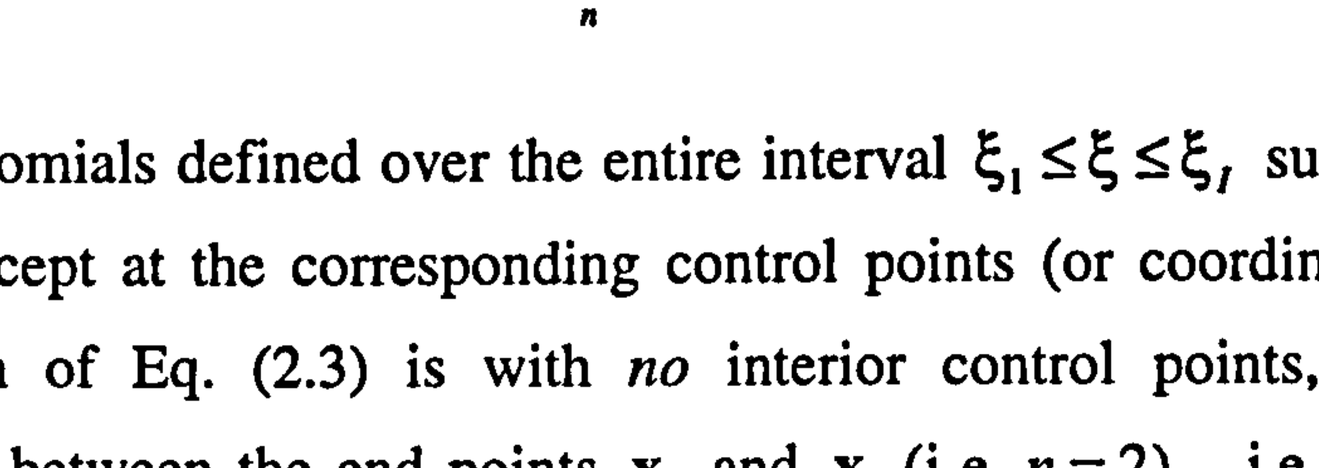

Figure 2.2 Interpolation along an $\xi-$coordinate line with n control coordinates.

To define a nonlinear spacing of the mesh points the normalised coordinate s is replaced by an appropriate stretching (or blending) function, $f(s)$. A simple form for $f(s)$ suggested by Thompson (1988, p. 918) is:

$$f(s) = (e^{\alpha s} - 1)/(e^{\alpha} - 1) \tag{2.5}$$

where α is a parameter to control the point spacing. However, the following hyperbolic tangent stretching function from Fletcher (1991, p. 105) is preferred in the present study:

$$f(s) = \alpha s + (1-\alpha)\left(1 - \frac{\tanh[\beta(1-s)]}{\tanh\beta}\right) \tag{2.6}$$

where *two* parameters, α and β, are used to control the point spacing. α effectively provides the slope of the distribution, i.e. $f(s) \sim \alpha s$, close to $s = 0$. β is a damping factor since it controls the departure from a linear $f(s)$ versus s behaviour. Large values of β result in large departures from linearity, e.g. see typical distributions in Fig. 2.3. For $\alpha > 1.0$ it is possible to cluster points close to the right-hand end, but this requirement is better handled by using a reverse mapping over the interval and keeping $\alpha < 1.0$.

Alternative hyperbolic tangent forms to Eq. (2.6) are given by Vinokur (1983). The two parameters α and β are defined in terms of the spacing, Δs, at each end of interval $s = 0$ and $s = 1$, enabling multiple contiguous stretching functions to be used along a boundary with continuity in the point spacing at the function interfaces. Other expressions use only one spacing increment, Δs, at any position on the interval to define the point distribution. In all cases a nonlinear equation must be solved prior to calculating the point distribution $f(s)$ from an expression similar to Eq. (2.6).

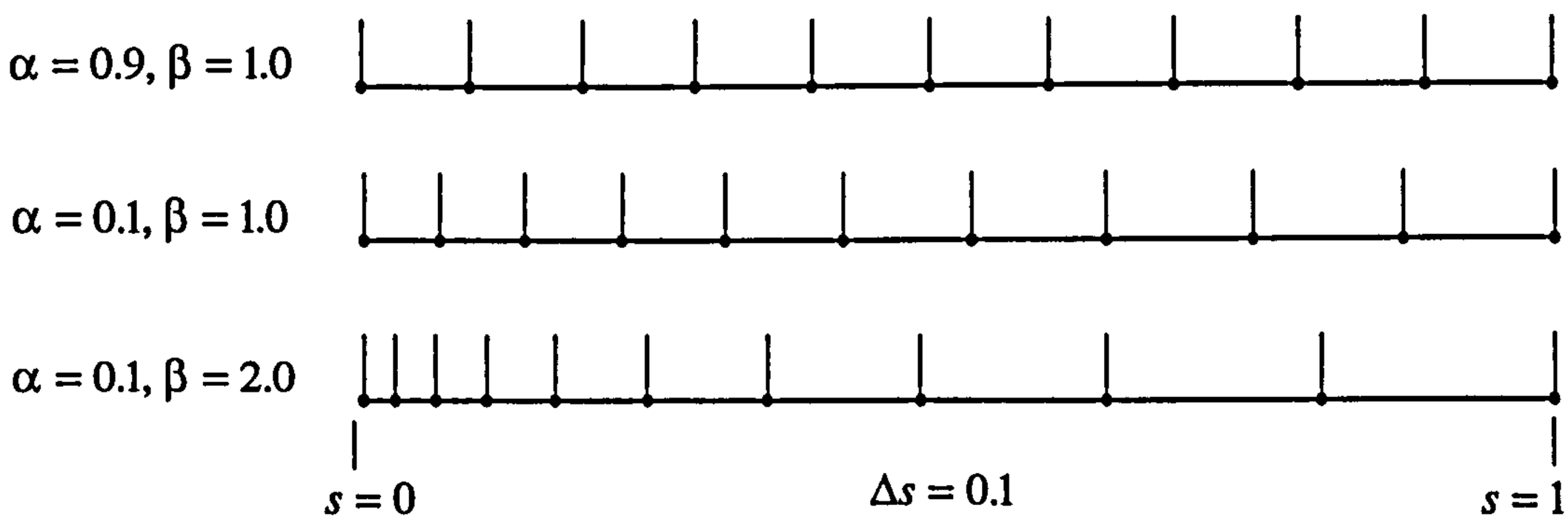

Figure 2.3 Example point distributions $f(s)$ for various parameter values in Eq. (2.6).

2.2.2 Transfinite Interpolation

Transfinite interpolation is a procedure for interpolating in multi-dimensions such that the interior coordinate lines follow the contours of the boundaries. A three-dimensional scheme can be built up from a combination of one-dimensional interpolation steps or *projections* in each curvilinear coordinate direction as follows. For convenience the (i, j, k) indexing notation described in Sec. 2.1 will be used to define mesh points in terms of the position vector, $\mathbf{x}_{ijk}$. Therefore, the six logical surfaces bounding a three-dimensional physical region are defined by the vectors, $\mathbf{x}_{1jk}, \mathbf{x}_{Ijk}, \mathbf{x}_{i1k}, \mathbf{x}_{iJk}, \mathbf{x}_{ij1}$ and $\mathbf{x}_{ijK}$.

Consider first a one-dimensional Lagrangian interpolation between two physical boundaries on which the coordinate i is constant. Eq. (2.4) is re-expressed as:

$$\mathbf{x}_{ijk} = (1 - f_i)\mathbf{x}_{1jk} + f_i \mathbf{x}_{Ijk} \tag{2.7}$$

where the generalised blending function f_i has been substituted for s, such that it varies monotonically from $f_1 = 0$ to $f_I = 1$ for $i = 1, 2, \cdots, I$. Analogous forms apply for interpolations in the j and k directions. These interpolation operations are defined as the projectors, $P^{(i)}$, $P^{(j)}$ and $P^{(k)}$. i.e.

$$\mathbf{x}_{ijk} = P^{(i)} = (1 - f_i)\mathbf{x}_{1jk} + f_i \mathbf{x}_{Ijk} \tag{2.8}$$

Then two- and three-dimensional transfinite interpolation schemes are generated by combining these projectors using Boolean sums. A detailed discussion of the theory, with additional references, is provided by Thompson *et al.* (1985, pp. 310-326). Therefore, only the final forms will be stated here. Two-dimensional transfinite interpolation over a surface on which k is constant is given by the projector:

$$\mathbf{x}_{ijk} = P^{(i)} + P^{(j)} - P^{(i)}P^{(j)} \tag{2.9}$$

where

$$P^{(i)}P^{(j)} = (1 - f_i)(1 - g_j)\mathbf{x}_{11k} + (1 - f_i)g_j\mathbf{x}_{1Jk} + f_i(1 - g_j)\mathbf{x}_{I1k} + f_i g_j \mathbf{x}_{IJk} \tag{2.10}$$

and g_j varies monotonically from $g_1 = 0$ to $g_J = 1$ for $j = 1, 2, \cdots, J$. Analogous forms apply over surfaces on which i or j are constant. These interpolations are called 'transfinite' since *all* the possible infinity of points are matched on the boundary curves,

as compared to other forms which interpolate to a *finite* number of points, e.g. the product projector, $P^{(i)}P^{(j)}$, matches at only the four corners of the boundary given by the vectors $\mathbf{x}_{11k}, \mathbf{x}_{1Jk}, \mathbf{x}_{I1k}$ and $\mathbf{x}_{IJk}$. Transfinite interpolation in three-dimensions is accomplished by the projector:

$$\mathbf{x}_{ijk} = P^{(i)} + P^{(j)} + P^{(k)} - P^{(i)}P^{(j)} - P^{(j)}P^{(j)} - P^{(k)}P^{(i)} + P^{(i)}P^{(j)}P^{(k)} \tag{2.11}$$

where

$$\begin{aligned} P^{(i)}P^{(j)}P^{(k)} = {} & (1-f_i)(1-g_j)(1-h_k)\mathbf{x}_{111} + (1-f_i)(1-g_j)h_k\mathbf{x}_{11K} \\ & + (1-f_i)g_j(1-h_k)\mathbf{x}_{1J1} + f_i(1-g_j)(1-h_k)\mathbf{x}_{I11} \\ & + (1-f_i)g_jh_k\mathbf{x}_{1JK} + f_i(1-g_j)h_k\mathbf{x}_{I1K} + f_ig_j(1-h_k)\mathbf{x}_{IJ1} \\ & + f_ig_jh_k\mathbf{x}_{IJK} \end{aligned} \tag{2.12}$$

and the function h_k varies monotonically from $h_k = 0$ to $h_K = 1$ for $k = 1, 2, \cdots, K$.

Numerically, Eqs. (2.11) and (2.12) are implemented such that the each successive step in the i, j and k (when appropriate) sequence of one-dimensional interpolations utilises the result of interpolations from the preceding i or j-step. Therefore a two-dimensional transfinite interpolation proceeds by: (1) interpolating in the i-direction, (2) calculating the discrepancy between the boundary and this result on the j-coordinate lines that are to be used in the j-interpolation, (3) interpolating this discrepancy in the j-direction, and (4) adding the result of this j-interpolation to that of the i-interpolation. An additional step is incorporated in an analogous manner to interpolate in the k-direction for three-dimensional problems (see Thompson *et al.* 1985, p.326). This substitution procedure considerably reduces the amount of calculation such that a full mesh is generated extremely quickly.

The complete three-dimensional scheme was coded in the short FORTRAN routine *Trans* (Appendix B.1), using the linear Lagrangian blending functions `f`, `g` and `h` synonymous with f_i, g_j and h_k in Eq. (2.12). Transfinite interpolation in two-dimensions is given by zeroing the *x3* array in the final summation, and in one-dimensional by taking solely the mesh coordinate positions given by the *x1* array (i.e. zeroing the *x2* and *x3* arrays in summation). Therefore, a more versatile version of this routine was written to interpolate from either a one, two or three-dimensional boundary depending on the value of the calling arguments.

Although a Lagrangian interpolation was used in each curvilinear coordinate direction, it is noteworthy that another type (or a mixture of types) of one-directional interpolation can be used to define the projectors, Eq. (2.8). For example a transfinite mesh can be generated using Hermite interpolation polynomials or splines (see Sec. 2.2.1). In fact, spline-blended forms give the smoothest mesh with continuous second derivatives (Thompson *et al.* 1985, p. 315). These alternate forms might help to mitigate a weakness of algebraic mesh generation systems in that they tend to propagate boundary slope discontinuities into the interior (Thompson 1984). (Multi-surface interpolation methods may also be used to alleviate this problem – see Thompson 1988, p. 920.) However, in the present study, all transfinite structures were subsequently smoothed using an elliptic mesh generator. Hence, simple functions were adequate for the transfinite interpolation.

2.3 Elliptic Mesh Generation

The field values of a function may be obtained for a given set of boundary values by solving a suitable system of partial differential equations. This is the principle of all elliptic mesh generators whereby all the interior mesh points are obtained for a specified point distribution on the boundary. Alternatively, the slope of coordinate lines intersecting the boundary can be specified, and it is even possible to devise generation systems with the capability to achieve both: i.e. Dirichlet, von Neumann or mixed (Robin) boundary conditions are all possible. Moreover, elliptic operators can generate smoother meshes, without the overlapping problems that often occur with algebraic meshing techniques (see Sec. 2.2) when the boundary has a complex shape. In fact, it can be shown by the calculus of variations that a mesh generated as the solution of Laplace equations is the smoothest possible (Thompson *et al.* 1985, p. 191). i.e.

$$\nabla^2 \xi^i = 0, \qquad i = 1, 2, 3 \tag{2.13}$$

where ∇ is the Laplacian operator and ξ^i represents the three coordinates (ξ, η, ζ) of an arbitrary coordinate system. A one-to-one mapping is guaranteed by this generation system because it satisfies the extremum principles: i.e. the maximum and minimum values of ξ, η and ζ must occur on the region boundary (Thompson *et al.* 1985, p. 189). The interior coordinate lines will tend to be equally spaced in the absence of boundary curvature because of the inherent smoothing effect of the Laplacian, but more closely spaced over convex boundaries, and less so over concave boundaries.

Explicit control over the coordinate line spacing and orientation in the generated mesh is obtained by generalising Eq. (2.13) to the following system of Poisson equations:

$$\nabla^2 \xi^i = P^i, \qquad i = 1, 2, 3 \tag{2.14}$$

in which P^i are appropriate functions fashioned to achieve the desired effect. These control functions may be either specified externally or determined automatically from the boundary-point distribution. The later approach is particularly useful when orthogonality of the mesh lines at the boundaries is required (see Thompson *et al.* 1985, pp. 226-237). However, in the present study, non-zero values for these control functions were specified directly in specific regions of the mesh to remove unacceptable cell distortions (Sec. 2.4).

2.3.1 General Equation

Computations are performed with respect to a cubic transformed region, as discussed in Sec. 2.1, where the curvilinear coordinates (ξ, η, ζ) are the independent variables, with the Cartesian coordinates (x, y, z) as the dependent variables. The Cartesian coordinate system is taken to satisfy a Laplace system (i.e. $\nabla^2 \mathbf{x} = 0$) in the physical region. The transformation relation, Eq. (A.20) in Appendix A, is then used to express this system with respect to the computational region. i.e. Replacing the tensor **A** with **x** gives:

$$\nabla^2 \mathbf{x} = \sum_{i=1}^{3} \sum_{j=1}^{3} g^{ij} \mathbf{x}_{\xi^i \xi^j} + \sum_{k=1}^{3} (\nabla^2 \xi^k) \mathbf{x}_{\xi^k} = 0 \tag{2.15}$$

where the subscripts of position vector **x** indicate partial differentiation with respect to the curvilinear coordinates, ξ^i, and g^{ij} are the elements of the contravariant metric tensor (Table A.1, Appendix A). Note that the summation indices i, j and k used here should not be confused with the indices (i, j, k) associated with the curvilinear coordinates (ξ, η, ζ) in Sec. 2.1.

When the Laplace system is transformed to the computational region, it is found that the new coordinate system is the solution of a Poisson system, Eq. (2.14). An exact form can be derived for the control functions, P^i (see Thompson *et al.* 1985, Eq. (5), p. 197), but a simplification involving only three functions is used presently given by:

$$\nabla^2 \xi^i = g^{ii} P_i, \qquad i = 1, 2, 3 \tag{2.16}$$

Suitable expressions for the control functions P_i are given in Sec. 2.3.4. Each represents a one-dimensional stretching in the ξ^i curvilinear coordinate direction. Thus, substituting for $\nabla^2\xi^i$ in Eq. (2.15) gives:

$$\sum_{i=1}^{3}\sum_{j=1}^{3} g^{ij}\mathbf{x}_{\xi^i\xi^j} + \sum_{k=1}^{3} g^{ii}P_i\,\mathbf{x}_{\xi^k} = 0 \tag{2.17}$$

This system of partial differential equations must be solved to generate the interior mesh for a specified boundary point distribution. In order to construct a finite-difference approximation to Eq. (2.17), it is first expanded for ϕ equal to either x, y or z as follows:

$$\begin{aligned} g^{11}\left(\frac{\partial^2\phi}{\partial\xi^2}+P_1\frac{\partial\phi}{\partial\xi}\right)+g^{12}\frac{\partial^2\phi}{\partial\xi\partial\eta}+g^{13}\frac{\partial^2\phi}{\partial\xi\partial\zeta} \\ +g^{21}\frac{\partial^2\phi}{\partial\eta\partial\xi}+g^{22}\left(\frac{\partial^2\phi}{\partial\eta^2}+P_2\frac{\partial\phi}{\partial\eta}\right)+g^{23}\frac{\partial^2\phi}{\partial\eta\partial\zeta} \\ +g^{31}\frac{\partial^2\phi}{\partial\zeta\partial\xi}+g^{32}\frac{\partial^2\phi}{\partial\zeta\partial\eta}+g^{33}\left(\frac{\partial^2\phi}{\partial\zeta^2}+P_3\frac{\partial\phi}{\partial\zeta}\right)=0 \end{aligned} \tag{2.18}$$

where elements of the contravariant metric tensor are calculated from those of the covariant metric tensor using Eqs. (A.15) and (A.19) in Appendix A. i.e.

$$\begin{bmatrix} g^{11} & g^{21} & g^{31} \\ g^{12} & g^{22} & g^{32} \\ g^{13} & g^{23} & g^{33} \end{bmatrix} = \frac{1}{g}\begin{bmatrix} g_{22}g_{33}-g_{23}^2 & g_{32}g_{13}-g_{33}g_{12} & g_{12}g_{23}-g_{13}g_{22} \\ g_{23}g_{31}-g_{21}g_{33} & g_{33}g_{11}-g_{13}^2 & g_{13}g_{21}-g_{11}g_{23} \\ g_{21}g_{32}-g_{22}g_{31} & g_{31}g_{12}-g_{32}g_{11} & g_{11}g_{22}-g_{12}^2 \end{bmatrix} \tag{2.19}$$

$$g=\det\left|\,g_{ij}\,\right| = g_{11}(g_{22}g_{33}-g_{23}^2)+g_{12}(g_{23}g_{31}-g_{21}g_{33})+g_{13}(g_{21}g_{32}-g_{31}g_{22}) \tag{2.20}$$

2.3.2 Finite-difference Form

The coordinate system described by Eq. (2.18) is discretised over the regular mesh of the computational region using Taylor series expansions to approximate the derivative terms (see Pletcher *et al.* 1988, Sec. 1.7.2, p.55). Difference expressions are written in terms of the general mesh point P and its neighbouring points W, E, N, S, T and B arranged as shown in Fig. 2.4.

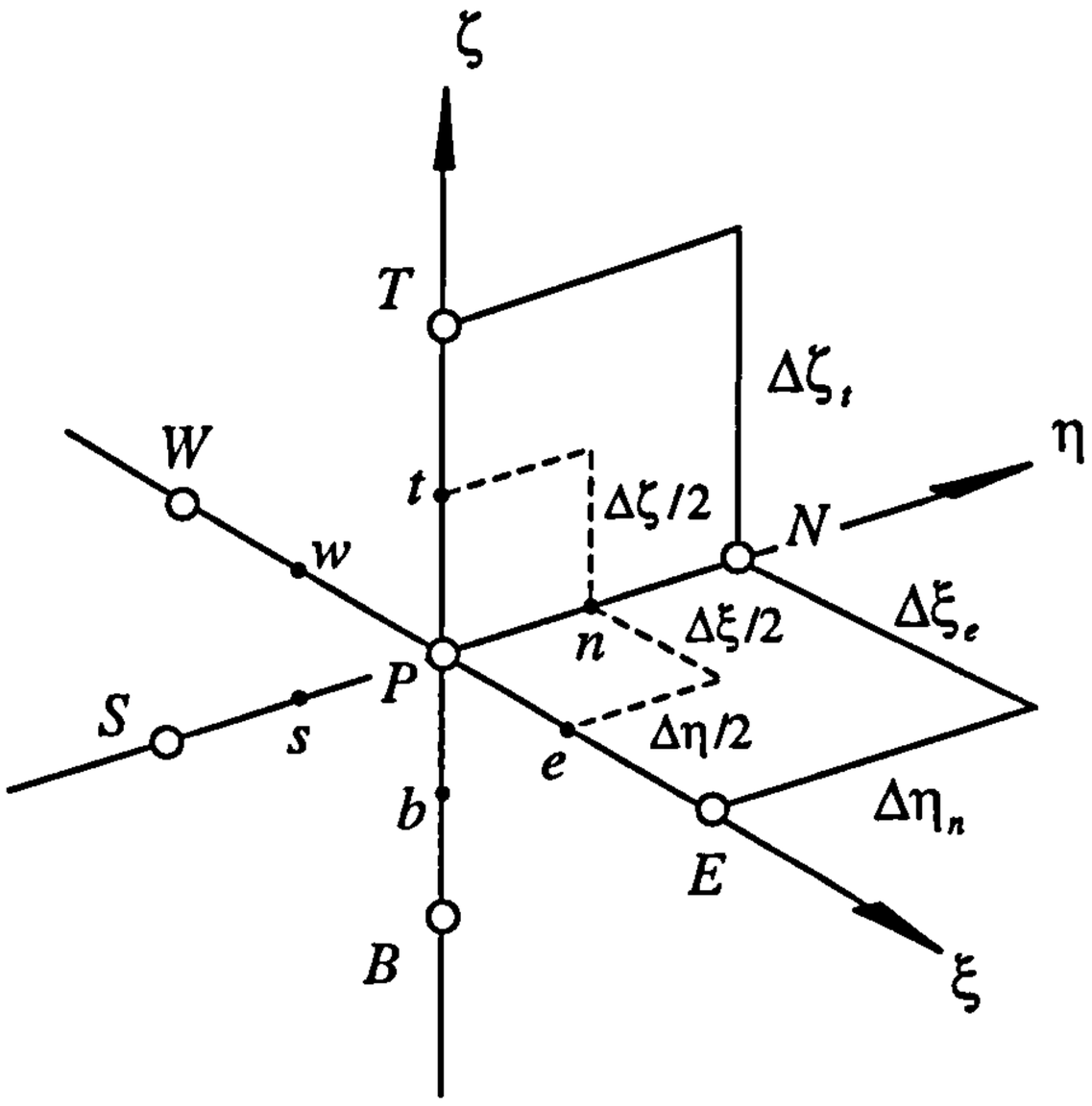

Symbol	Curvilinear indices
P	i, j, k
E	$i+1, j, k$
W	$i-1, j, k$
N	$i, j+1, k$
S	$i, j-1, k$
T	$i, j, k+1$
B	$i, j, k-1$

Figure 2.4 Differencing notation used to discretise Eq. (2.18) about a mesh point P in the three-dimensional computational region.

The spacing between successive mesh planes is then defined as:

$$\begin{aligned} \Delta\xi_w &= \xi_P - \xi_W, \qquad \Delta\eta_s = \eta_P - \eta_S, \qquad \Delta\zeta_b = \zeta_P - \zeta_B \\ \Delta\xi_e &= \xi_E - \xi_P, \qquad \Delta\eta_n = \eta_N - \eta_P, \qquad \Delta\zeta_t = \zeta_T - \zeta_P \end{aligned} \tag{2.21}$$

These intervals are often identical. However, to obtain more control over the spacing of mesh planes in the physical region, it is advantageous to develop finite difference expressions for nonuniformly spaced coordinate planes in the computational domain. This flexibility proved extremely useful for the pentroof combustion chamber meshing problem described in Sec. 2.4.

Consider a control volume enclosing point P with distances between opposite faces of:

$$\Delta\xi = \tfrac{1}{2}(\xi_E - \xi_W), \qquad \Delta\eta = \tfrac{1}{2}(\eta_N - \eta_S), \qquad \Delta\zeta = \tfrac{1}{2}(\zeta_T - \zeta_B) \tag{2.22}$$

Then the difference representation of Eq. (2.18) at P is taken as:

$$g^{11}\frac{\left(\frac{\phi_E-\phi_P}{\Delta\xi_e}\right)-\left(\frac{\phi_P-\phi_W}{\Delta\xi_w}\right)}{\Delta\xi}+g^{22}\frac{\left(\frac{\phi_N-\phi_P}{\Delta\eta_n}\right)-\left(\frac{\phi_P-\phi_S}{\Delta\eta_s}\right)}{\Delta\eta}+g^{33}\frac{\left(\frac{\phi_T-\phi_P}{\Delta\zeta_t}\right)-\left(\frac{\phi_P-\phi_B}{\Delta\zeta_b}\right)}{\Delta\zeta}+S=0 \tag{2.23}$$

where the source term S is defined as:

$$\begin{aligned} S = {} & g^{11}P_1\frac{\partial\phi}{\partial\xi}+g^{12}\frac{\partial^2\phi}{\partial\xi\partial\eta}+g^{13}\frac{\partial^2\phi}{\partial\xi\partial\zeta} \\ & +g^{21}\frac{\partial^2\phi}{\partial\eta\partial\xi}+g^{22}P_2\frac{\partial\phi}{\partial\eta}+g^{23}\frac{\partial^2\phi}{\partial\eta\partial\zeta} \\ & +g^{31}\frac{\partial^2\phi}{\partial\zeta\partial\xi}+g^{32}\frac{\partial^2\phi}{\partial\zeta\partial\eta}+g^{22}P_3\frac{\partial\phi}{\partial\zeta} \end{aligned} \tag{2.24}$$

Central difference approximations are used to calculate the derivative terms in S. First-order partial derivatives are differenced at P as:

$$\frac{\partial\phi}{\partial\xi}=\frac{\Delta\xi_w\left(\frac{\phi_E-\phi_P}{\Delta\xi_e}\right)-\Delta\xi_e\left(\frac{\phi_W-\phi_P}{\Delta\xi_w}\right)}{2\Delta\xi} \tag{2.25}$$

$$\frac{\partial\phi}{\partial\eta}=\frac{\Delta\eta_s\left(\frac{\phi_N-\phi_P}{\Delta\eta_n}\right)-\Delta\eta_n\left(\frac{\phi_S-\phi_P}{\Delta\eta_s}\right)}{2\Delta\eta} \tag{2.26}$$

$$\frac{\partial\phi}{\partial\zeta}=\frac{\Delta\zeta_b\left(\frac{\phi_T-\phi_P}{\Delta\zeta_t}\right)-\Delta\zeta_t\left(\frac{\phi_B-\phi_P}{\Delta\zeta_b}\right)}{2\Delta\zeta} \tag{2.27}$$

These expressions are then used to obtain approximations for the mixed derivatives by replacing ϕ in each equation with its first-order derivatives.

For example $\frac{\partial^2\phi}{\partial\xi\partial\eta}$ is found by substituting Eq. (2.26) into Eq. (2.25) as follows:

$$
\begin{aligned}
\frac{\partial^2\phi}{\partial\xi\partial\eta} &= \frac{\partial}{\partial\xi}\left[\frac{\partial\phi}{\partial\eta}\right] \\
&= \frac{1}{2\Delta\xi}\left\{\Delta\xi_w\left(\frac{\phi_{\eta,E}-\phi_{\eta,P}}{\Delta\xi_e}\right)-\Delta\xi_e\left(\frac{\phi_{\eta,W}-\phi_{\eta,P}}{\Delta\xi_w}\right)\right\} \\
&= \frac{1}{4\Delta\xi\Delta\eta}\left\{\frac{\Delta\xi_w}{\Delta\xi_e}\left[\frac{\Delta\eta_s}{\Delta\eta_n}(\phi_{NE}-\phi_E)-\frac{\Delta\eta_n}{\Delta\eta_s}(\phi_{SE}-\phi_E)-2\Delta\eta\frac{\partial\phi}{\partial\eta}_P\right]\right. \\
&\qquad \left.-\frac{\Delta\xi_e}{\Delta\xi_w}\left[\frac{\Delta\eta_s}{\Delta\eta_n}(\phi_{NW}-\phi_W)-\frac{\Delta\eta_n}{\Delta\eta_s}(\phi_{SW}-\phi_W)-2\Delta\eta\frac{\partial\phi}{\partial\eta}_P\right]\right\}
\end{aligned}
\tag{2.28}
$$

where $\phi_{\eta,P}=\partial\phi/\partial\eta$ at P, etc. Analogous forms apply for the other five mixed derivatives in Eq. (2.24).

Multiplying throughout Eq. (2.23) by the volume, $\Delta V=\Delta\xi\Delta\eta\Delta\zeta$, of the control volume about point P and rearranging gives the final discretised form:

$$a_P\phi_P=a_E\phi_E+a_W\phi_W+a_N\phi_N+a_S\phi_S+a_T\phi_T+a_B\phi_B+S\cdot\Delta V \tag{2.29}$$

where the coefficient:

$$a_P=\sum_n a_n \tag{2.30}$$

and the summation is taken over all n neighbours of the mesh point P with coefficients:

$$
\begin{aligned}
a_E &= g^{11}\frac{\Delta\eta\Delta\zeta}{\Delta\xi_e}, & a_W &= g^{11}\frac{\Delta\eta\Delta\zeta}{\Delta\xi_w} \\
a_N &= g^{22}\frac{\Delta\xi\Delta\zeta}{\Delta\eta_n}, & a_S &= g^{22}\frac{\Delta\xi\Delta\zeta}{\Delta\eta_s} \\
a_T &= g^{33}\frac{\Delta\xi\Delta\eta}{\Delta\zeta_t}, & a_B &= g^{33}\frac{\Delta\xi\Delta\eta}{\Delta\zeta_b}
\end{aligned}
\tag{2.31}
$$

The source term S is as defined previously in Eq. (2.24).

The FORTRAN computer code *Metric* (Appendix B.2) implements Eqs. (2.24) – (2.31) to determine the coefficients a_n and source term S.

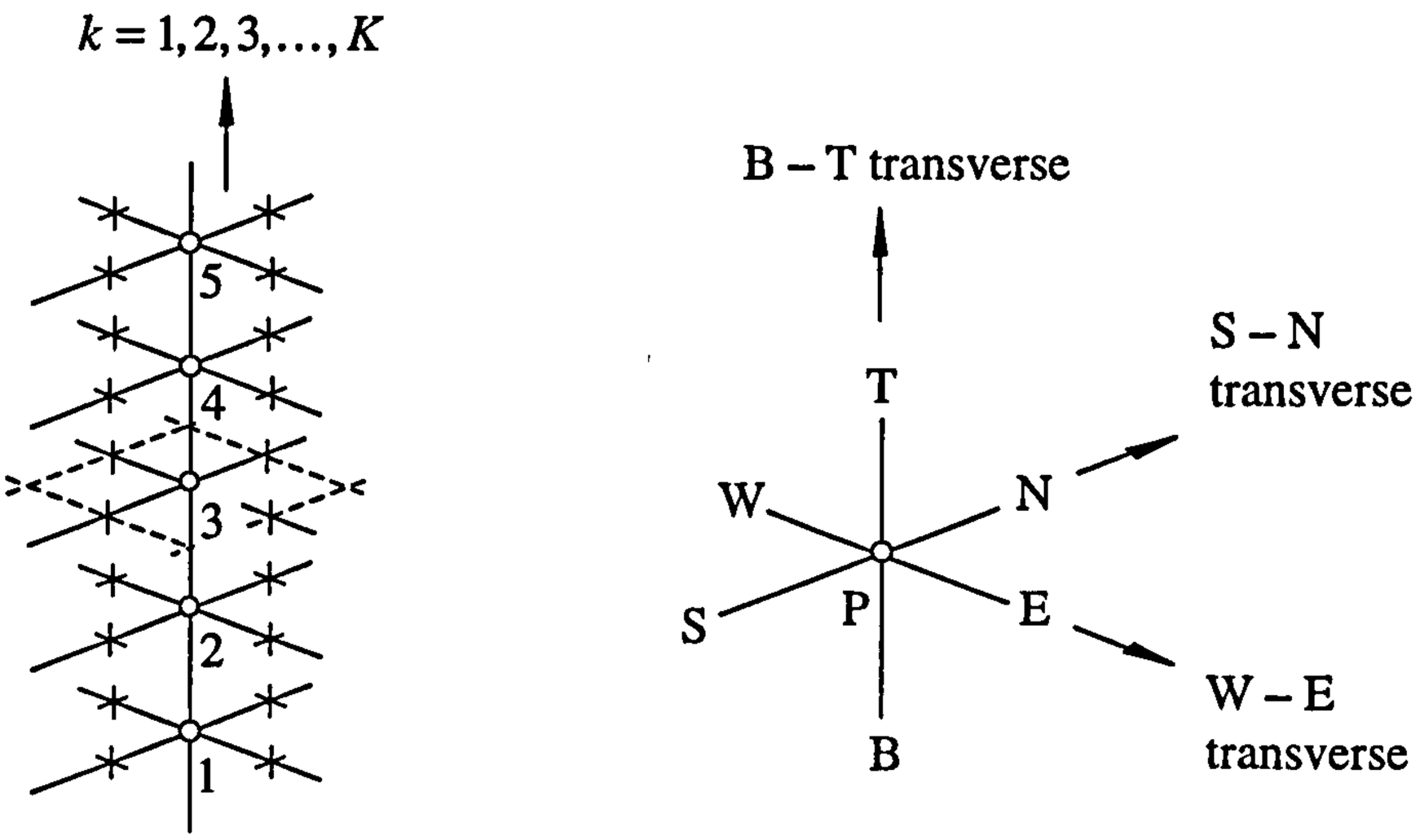

Figure 2.5 ζ – coordinate line in a three-dimensional mesh together with the traverse directions in the line-by-line iterative solver.

2.3.3 Solution of Discretised Equation with TDMA–ADI Procedure

The discretised equation, Eq. (2.29), for the Cartesian coordinates ϕ (i.e. x, y or z) is solved with the boundary point values using a line-by-line iterative procedure to obtain the distribution of ϕ. First consider the ζ –coordinate line shown in Fig. 2.5 on which the mesh points have a curvilinear index $k = 1, 2, 3, \ldots, K$. Then Eq. (2.29) is written as:

$$A_k\phi_k = B_k\phi_{k+1} + C_k\phi_{k-1} + D_k\,, \qquad k = 2, 3, \ldots, K-1 \tag{2.32}$$

with the translations that ϕ_k stands for ϕ_P, $A_k = a_P$, $\phi_{k+1} = \phi_T$, $B_k = a_T$, etc. The remaining terms are collected in D_k given by:

$$D_k = a_E\phi_E + a_W\phi_W + a_N\phi_N + a_S\phi_S + S\cdot\Delta V \tag{2.33}$$

Rearranging Eq. (2.32) gives a set of equations with a tridiagonal matrix of coefficients as follows:

$$\begin{aligned}
-C_2\phi_1 + A_2\phi_2 - B_2\phi_3 &= D_2 && \text{(a)}\\
-C_3\phi_2 + A_3\phi_3 - B_3\phi_4 &= D_3 && \text{(b)}\\
-C_4\phi_3 + A_4\phi_4 - B_4\phi_5 &= D_4 && \text{(c)}\\
\cdots \quad \cdots \quad \cdots &\quad \cdots && \\
-C_k\phi_{k-1} + A_k\phi_k - B_k\phi_{k+1} &= D_k && (2.34)
\end{aligned}$$

These equations are now in a suitable form for solution by an efficient procedure known as the Thomas algorithm or the tridiagonal matrix algorithm (TDMA). The values of ϕ_1 and ϕ_K are the known boundary coordinates. Therefore, by eliminating ϕ_2 from (b), ϕ_3 from (c) and so on, a general formula for ϕ_k is:

$$\phi_k = \alpha_k \phi_{k+1} + \beta_k \tag{2.35}$$

where:

$$\alpha_k = \frac{B_k}{A_k - \alpha_{k-1} C_k}, \qquad \beta_k = \frac{\beta_{k-1} C_k + D_k}{A_k - \alpha_{k-1} C_k} \tag{2.36}$$

At the $k = 1$ boundary: $\alpha_1 = 0$ and $\beta_1 = \phi_1$. Given the values of the coefficients A_k, B_k, C_k and D_k in Eq. (2.32), the full TDMA procedure is then as follows:

1. Calculate α_k and β_k for $k = 2, 3, \ldots, K-1$ from the recurrence relations in Eq. (2.36).
2. Obtain new $\phi_{K-1}, \phi_{K-2}, \ldots, \phi_2$ by successive back-substitution in Eq. (2.35) from ϕ_K.

An analogous procedure is used to solve along ξ and η –coordinate lines. After TDMA is used to solve Eq. (2.35) for each coordinate line, the newly calculated values can be relaxed before the calculation is advanced to the next line. i.e.

$$\phi_P^{relaxed} = \phi_P^{old} + \omega (\phi_P^{new} - \phi_P^{old}) \tag{2.37}$$

where $0 < \omega < 1$ for under-relaxation and $1 < \omega < 2$ for over-relaxation. When the latter is employed the complete scheme is known as successive line over-relaxation (SLOR) for which relations can be derived to enable optimal values of ω to be selected (e.g. see Hirsch 1988, pp. 471-478). It was found that the convergence time was reduced by 75% with optimal over-relaxation compared with an unrelaxed solution for the meshing problem described in Sec. 2.4. In this trial TDMA was applied along successive ξ–coordinate lines *only*.

To enable the boundary values to exert a greater influence on the solution in each iterative pass, and thus improve convergence rates, TDMA is applied to all families of coordinate lines (i.e. ξ, η and ζ) in an alternating direction implicit (ADI) procedure as follows:

1. Traverse W–E along successive ξ –coordinate lines, sweeping first S–N and then B–T.
2. Traverse S–N along successive η –coordinate lines, sweeping first W–E and then B–T.
3. Traverse B–T along successive ζ –coordinate lines, sweeping first W–E and then S–N.

The ADI scheme with over-relaxation was found to be susceptible to oscillatory behaviour such that it was generally better to use values of $\omega \leq 1$, particularly as the control functions increase in magnitude. However, despite this limitation, convergence rates where comparable or better to those obtained with optimal relaxation in only one coordinate direction (i.e. without ADI). Furthermore, the convergence rates in trial studies using ADI and over-relaxation (i.e. $\omega > 1$) showed little improvement as ω was increased (also see comparison in Table 6.3 by Fletcher 1991, p. 195).

The FORTRAN computer code *Lisolv* (Appendix B.3) implements this line-by-line TDMA solver using ADI. Note that Eq. (2.37) is not solved as a separate step but as part of the TDMA solution by introducing the relaxation parameter ω into the coefficients A and D of Eq. (2.32) prior to calling *Lisolv*. Their new form is obtained by substituting Eq. (2.37) into Eq. (2.32) as:

$$A \leftarrow \frac{A}{\omega}, \qquad D \leftarrow D + \frac{A(1-\omega)}{\omega}\phi_P^{old} \tag{2.38}$$

where '$\leftarrow$' means 'is replaced by' and the subscript k has been omitted to emphasise that Eq. (2.32) is applied in all three coordinate directions (i, j, k) in the ADI procedure.

The value of the coefficient D is calculated using guessed values for ϕ (x, y or z) initially and the most recently computed values thereafter. Since the original Poisson generation system of Eq. (2.17) is quasi-linear, convergence depends on the quality of the initial guess. A reliable initial field for ϕ may be efficiently generated from the boundary point distribution using transfinite interpolation (Sec. 2.2.2). Thompson *et al.* (1985, p. 252) notes this method is better than say a field generated by one-dimensional interpolation (Sec. 2.2.1) because of the reduced skewness in the former. Smoothing of the mesh with the elliptic solver then progresses until the movement of any mesh point between successive iterations is several orders of magnitude smaller than a characteristic dimension of the geometry.

This corresponds to a total residual $\Re$, equal to the sum of the R residuals from Eq. (2.29) for x, y and z at all mesh points, i.e.,

$$\Re = \sum_{R} (a_P \phi_P - \sum_{n} a_n \phi_n - S \cdot \Delta V) \tag{2.39}$$

being less than a specified tolerance. For example, $\Re < 10^{-3}$ in the meshing problem described in Sec. 2.4.

The solution may be converged with fixed interior mesh points or coordinate lines if required. All stationary vertices are flagged on input to the solver and on each iteration the values a_P and source term in Eq. (2.29) are reset at each of these as follows:

$$a_P = \alpha, \qquad S \cdot \Delta V = \alpha \phi_P^{fixed} \tag{2.40}$$

where α is a very large number (e.g. 10^{30}) and ϕ_P^{fixed} is the x, y or z–coordinate of the fixed vertex.

Finally, the following procedure was used to smooth *two*-dimensional algebraic meshes with the *three*-dimensional elliptic solver, thus avoiding the need for coding a separate routine. A three-plane sandwich is defined with the two-dimensional geometry positioned between two auxiliary plane, parallel boundaries in the physical region. These planes are arranged to be perpendicular to one of the coordinate directions x, y or z. Assuming that the z–coordinate direction is chosen, then the x and y coordinate positions of each mesh point on the two outer boundary planes are updated, after each complete iteration of the solver, equal to the x and y coordinates of their corresponding interior mesh point. All three planes then have an identical mesh point distribution. The solution is then effectively two-dimensional in nature, even though a three-dimensional solver is being employed.

Allowing points to 'float' over the geometry surfaces is also useful in three-dimensional problems as a simple method of generating meshes which are orthogonal at boundaries where there is freedom to vary the boundary point spacing (see Sec. 2.4.4). Alternatively, suitable control functions can be iteratively determined at boundaries in the solution procedure to achieve local orthogonality with a specified point distribution. (See discussion at the end of the next section.)

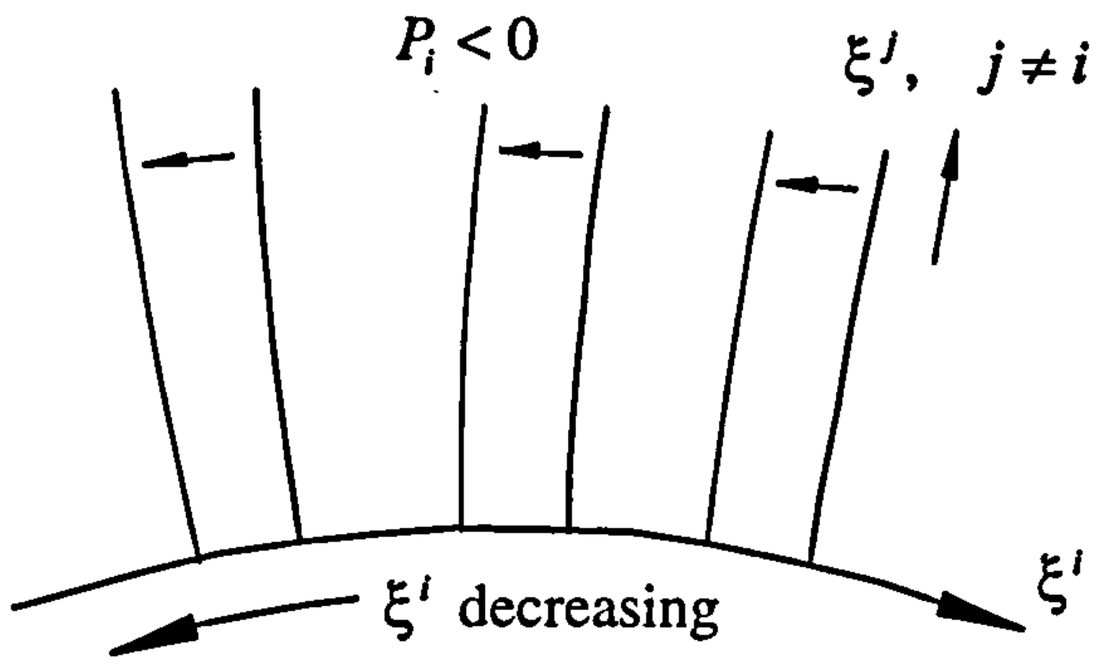

Figure 2.6

The influence of the control functions P_i on mesh line spacing. If ξ^i is a boundary coordinate line on which the point spacing is fixed, then the control functions affect the intersection angle of the mesh lines with the boundary.

2.3.4 Control Functions

The control functions P^i in the elliptic system given by Eq. (2.14) are used to increase or decrease the mesh line density in specific areas of the physical region. This enables improved resolution and the numerical accuracy in the subsequent flow and combustion analysis. As a general rule, *negative* values of the control functions P^i cause the mesh lines on which the coordinate ξ^i is constant to move in the direction in which the coordinate *decreases* (Fig. 2.6). Positive values of the control functions result in an opposite effect. This behaviour is also followed by the functions P_i in the present elliptic system, after the substitution $P^i = g^{ii} P_i$, since the diagonal contravariant metric tensor elements $g^{ii} > 0$.

The functions P_i are free to be constructed in any manner in order to obtain the desired mesh line spacing. Popular forms use a summation of several exponential or hyperbolic terms. For example, attraction of ξ–coordinate lines to other lines ξ_i (Fig. 2.7) can be achieved with the following expression for P_1:

$$P_1(\xi) = -\sum_{i=1}^{n} a_i \, \text{sign}(\xi - \xi_i) \cdot \left[1 - e^{-b_i |\xi - \xi_i|} \right] \tag{2.41}$$

where a_i and b_i are appropriate amplitude and decay factors.

Notes:

- The subscript i on ξ identifies particular ξ–lines and should not be confused with the superscript i used to refer to curvilinear coordinates in general.
- A negative amplitude, a_i, results in a repulsive (rather than attractive) effect.

- The sign changing function ensures attraction occurs on both sides of ξ_i–lines, otherwise attraction occurs only on the side towards increasing ξ, with repulsion occurring on the other side.
- In three-dimensions these ξ_i 'lines' correspond to $\eta\zeta$–planes.
- Analogous expressions can be formed for the control functions P_2 and P_3 to cause the attraction (or repulsion) of η and ζ–coordinate lines, respectively.

Equation (2.41) may be extended to achieve attraction to a point (ξ_i,η_i) in two-dimensions or to an ζ–coordinate line in a three-dimensions by modifying the decay term to include a η–distance as follows:

$$P_1(\xi,\eta)=-\sum_{i=1}^{m} c_i \cdot \text{sign}(\xi-\xi_i)\cdot\left[1-e^{-d_i\sqrt{(\xi-\xi_i)^2+(\eta-\eta_i)^2}}\right] \tag{2.42}$$

where c_i and d_i are appropriate amplitude and decay factors. The attraction is now limited to short portions of the ξ–lines, rather than the entire coordinate line as before. Again, analogous expressions can be formed for the control functions P_2 and P_3.

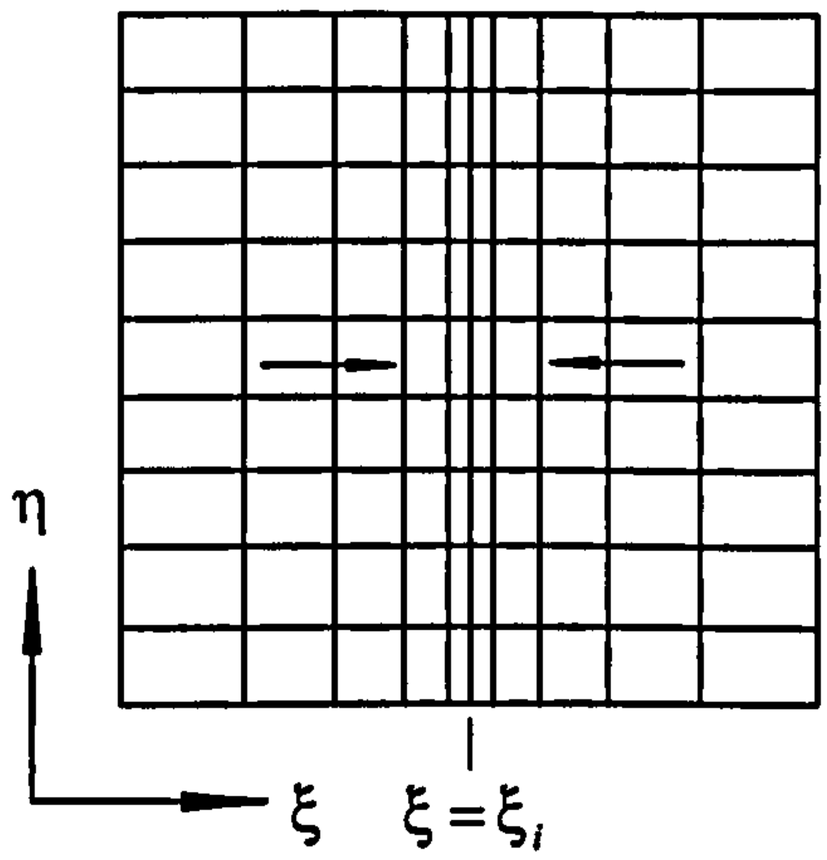

Figure 2.7

Attraction of ξ–coordinate lines to other lines ξ_i (in this example just the centre line).

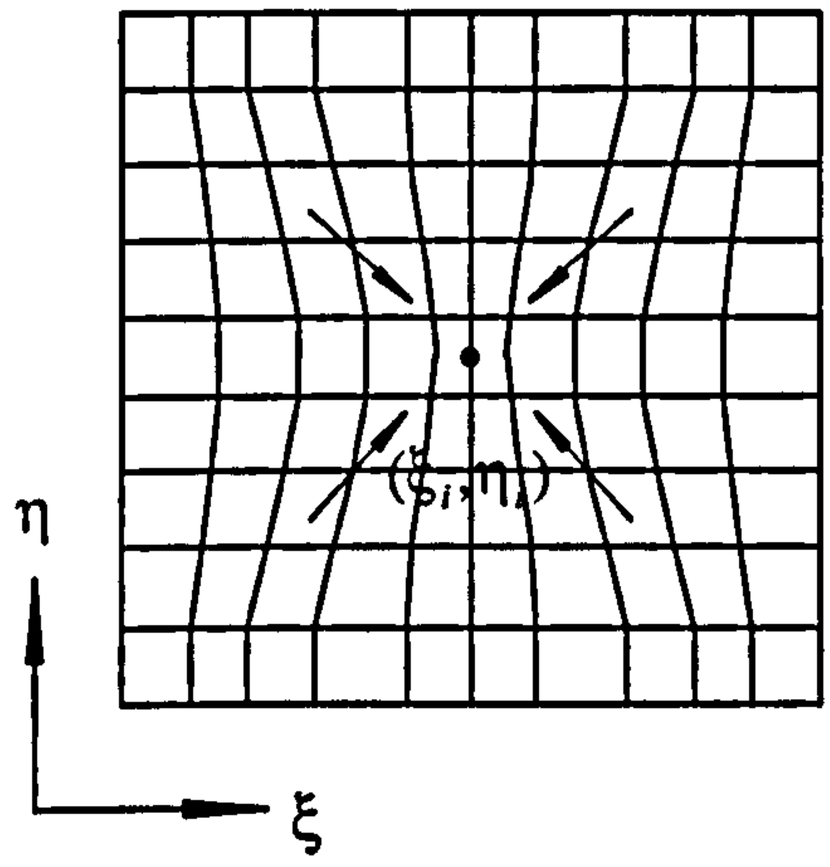

Figure 2.8

Attraction of ξ–coordinate lines to the point (ξ_i,η_i), or corresponding line in three dimensions.

Combining Eqs. (2.41) and (2.42) results in a control function capable of generating highly localised attraction (or repulsion) about a point in two-dimensions, or a coordinate line in three-dimensions. Separately the values for the amplitude (a_i or c_i) in each equation must be limited, otherwise overlapping mesh lines result in the physical region, i.e. the extremum principles of the Laplacian having been completely lost in the Poisson system. However, these limits can be increased by combining two opposing effects, such that one equation causes repulsion of the grid lines, and the other attraction. This is achieved by setting a negative value for the amplitude a_i and a positive value for the other amplitude c_i, or vice versa. The strong distortion of ξ–coordinate lines with such a control function is shown in Fig. 2.8.

For a three-dimensional mesh, an ζ–distance can also be included in the decay term of Eq. (2.42) to achieve attraction about a point (ξ_i,η_i,ζ_i). However, in actual application this has not been very practical and the control function given by Eq. (2.41) was adequate for the meshing problems encountered in the present study.

It is also noteworthy that the attraction lines and/or points can be arbitrarily specified in the computational region. Thus they can be independent of the curvilinear generation system. Moreover, it is also possible to take the control functions to be functions of the Cartesian coordinates (x, y, z) instead of the logical coordinates (ξ, η, ζ), to achieve attraction to fixed lines and/or points in the physical region. However, this case is much more complex since the control functions contain derivatives of the dependent variables in the transformation. Care also has to be taken to ensure that the coordinate lines from different families are not attracted parallel to themselves, thus collapsing the physical coordinate system in the transformation. However, control functions evaluated from the boundary point distribution in the physical region can provide a large degree of automatic control over the interior mesh line spacing, and are worthy of the extra computational effort. First, from the given surface coordinates of a three-dimensional geometry, control functions are constructed for all the logical boundary points. These functions are then interpolated to obtain the control functions at every interior point using transfinite interpolation (see Sec. 2.2.2). Finally, Eq. (2.18) is solved to generate the mesh in the physical region. If necessary the control functions on the boundary can then be adjusted and the procedure repeated in an iterative fashion until the desired coordinate system is generated (e.g. Shieh 1984). It is possible to specify both the coordinate line slope at the

boundary, together with the spacing of the first interior coordinate surface from the boundary using this procedure (Fig. 2.9). The ability to iteratively determine control functions is not available in the present elliptic mesh generator, since it was not essential for the present study. However, suitable expressions and details are given by Thompson *et al.* (1985, pp. 228-237). Taghavi and Dupont (1989) also present a interesting grid preconditioning scheme as an alternative to solving an elliptic system.

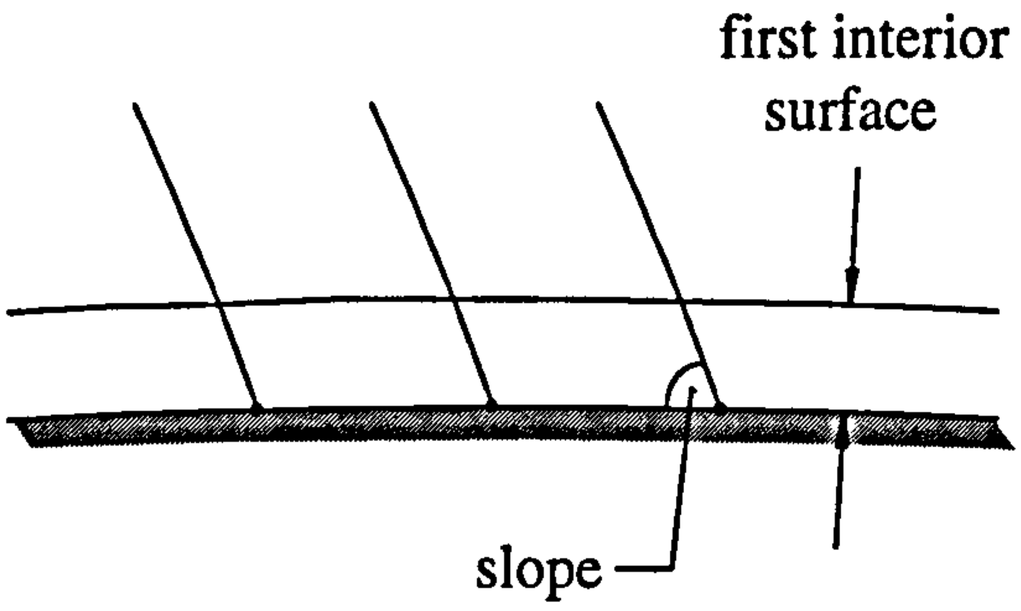

Figure 2.9

A specified boundary point distribution, line slope and spacing of the first interior surface can be obtained with iterative adjustment of the control functions in the general system of Eq. (2.18).

2.4 Meshing Application: Pentroof Combustion Chamber Geometry

This section details the stages in generating a mesh of the pentroof combustion chamber studied later in Sec. 6.4. Algebraic and elliptic techniques are combined to generate a smoothly varying mesh of the geometry with direct control over the interior line spacing. The computational mesh is required to satisfy the following criteria. These are imposed by the numerical scheme in Chapter 3 for the calculation of turbulent, reacting flow.

- The mesh must be a single block of cells encompassing the entire physical region. These are organised in a structured arrangement such that each interior mesh vertex is surrounded by eight cells and the cell faces always coincide between neighbouring cells (i.e. there are no partial cell faces or sliding interfaces). Each cell is indexed by its three curvilinear indices (i, j, k) as described in Sec. 2.1. To define a smaller structure projecting from the main region of interest, it is embedded in additional layers of cells in which most cells lie outside of the computational domain and are deactivated. Minimising the number of these 'dead cells' is a priority, since their indexing, checking and storage imposes a significant performance penalty.

- All mesh cells must be hexahedral, but their vertex positions may be arbitrarily specified in order to fit the boundaries, as long as reasonable aspect ratios are maintained (i.e. typically < 10) and the cell face distortion is minimal (i.e. typically a few degrees).

- The included angle between coordinate lines should be in the range 45°–135°. Local excessive mesh skewness can be tolerated by the numerical scheme, but trials have shown that an included angle of 33° is a absolute minimum for converged, accurate simulations. Below this limit large cross-derivative terms in the discretised flow equations destabilise the solution and the boundary layer treatment deteriorates unacceptably.

- Mesh lines should smoothly vary around abrupt geometries, with local refinement in regions of large flow gradients, and the coordinate lines closely aligned with the streamlines to reduce numerical diffusion.

Generally a compromise is made between meeting these requirements and including all of the detail in a complex geometry.

2.4.1 Physical Geometry

Figure 2.10 shows a wireframe drawing of the engine combustion chamber with the piston near top dead centre. The profiled interior surface of the cylinder head may be subdivided into several smaller patches. Two of these are planar and inclined at 20° to the horizontal about an axis of rotation slightly offset from the cylinder axis. These form the pentroof while the sides of the cylinder head are patched together from several smooth concave surfaces. Four small areas of squish are created where these side walls meet the top of the cylinder body. Small cylinders have been drawn to represent the position and lift of the inlet and exhaust poppet valves in the cylinder head. These are seated in pairs perpendicular to the planar surfaces of the pentroof with the two larger inlet valves shown on the near-side in Fig. 2.10. Finally, a single spark plug is positioned on the cylinder axis between the four valve ports (not shown). The entire chamber geometry has half-symmetry about the vertical plane through A – A.

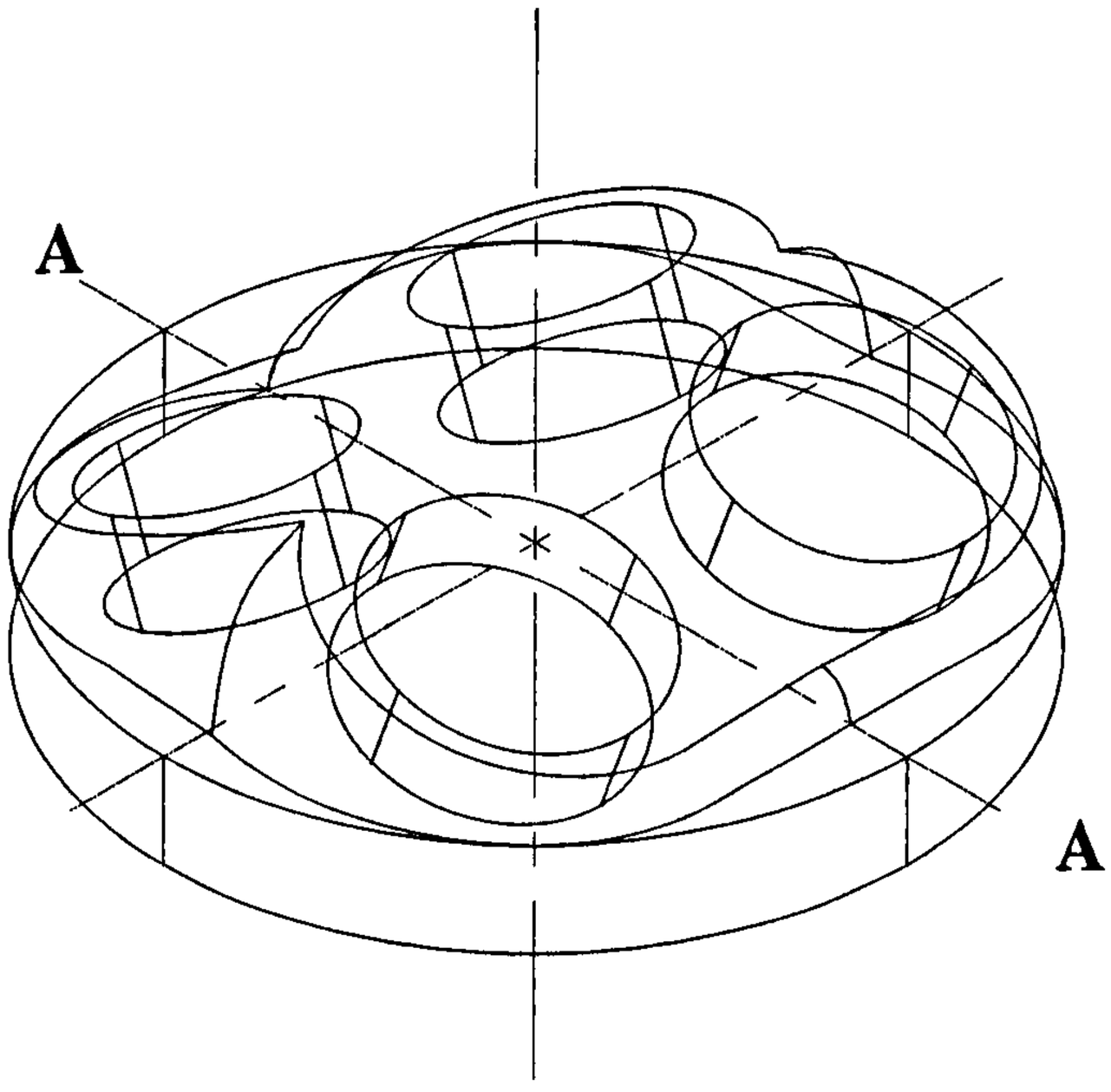

Figure 2.10 Scaled wireframe model of 4-valve pentroof combustion chamber geometry for Ricardo Hydra engine studied in Sec. 6.4. Bore diameter is 80.065 mm.

2.4.2 Selection of Mapping Type

It is necessary to first decide on the type of mapping which will be used to transform between the regular computational domain and the physical region for this geometry. The complex shape of the combustion chamber may be characterised by a cylindrical form for which two possible mappings are depicted in Fig. 2.11. In mapping *A* the computational domain is wrapped around its left boundary such that the front and derriere plane faces become coincident re-entrant boundaries. Each horizontal k–plane is effectively a O-type grid in standard mapping terminology. The left boundary is then shrunk onto the cylinder axis to complete the transformation. Therefore, special treatment is required in the numerical scheme at the left boundary, and also for the conditions on the front and derriere boundaries (see Sec. 3.4.4). This type of mapping is a natural choice for axisymmetric (engine) geometries, or ones that can be treated as such, e.g. see generation of offset piston bowl and domed head configurations by Amsden *et al.* (1989, pp. 69-76). Usually the mesh can be easily generated by rotation of a suitable two-dimensional radial plane about a central axis. However, representation of the valve ports and surface detail of the pentroof head in the present engine geometry is not practical with this type of mapping.

Conceptually mapping *B* is much simpler in that the six faces of the computational domain are stretched to fit six surface patches enclosing the physical region. Thus with respect to the generalised combustion chamber form in Fig. 2.11, the left, right, front and derriere logical faces each cover a 90° sector of the cylinder wall. No special numerical treatment is required at boundaries in contrast to the pseudo-polar meshes generated by mapping *A*. Moreover, it is possible to define the four valve ports and more accurately represent the cylinder head shape since the distribution of mesh points is better. Therefore, mapping *B* is the most appropriate choice for the pentroof combustion chamber geometry.

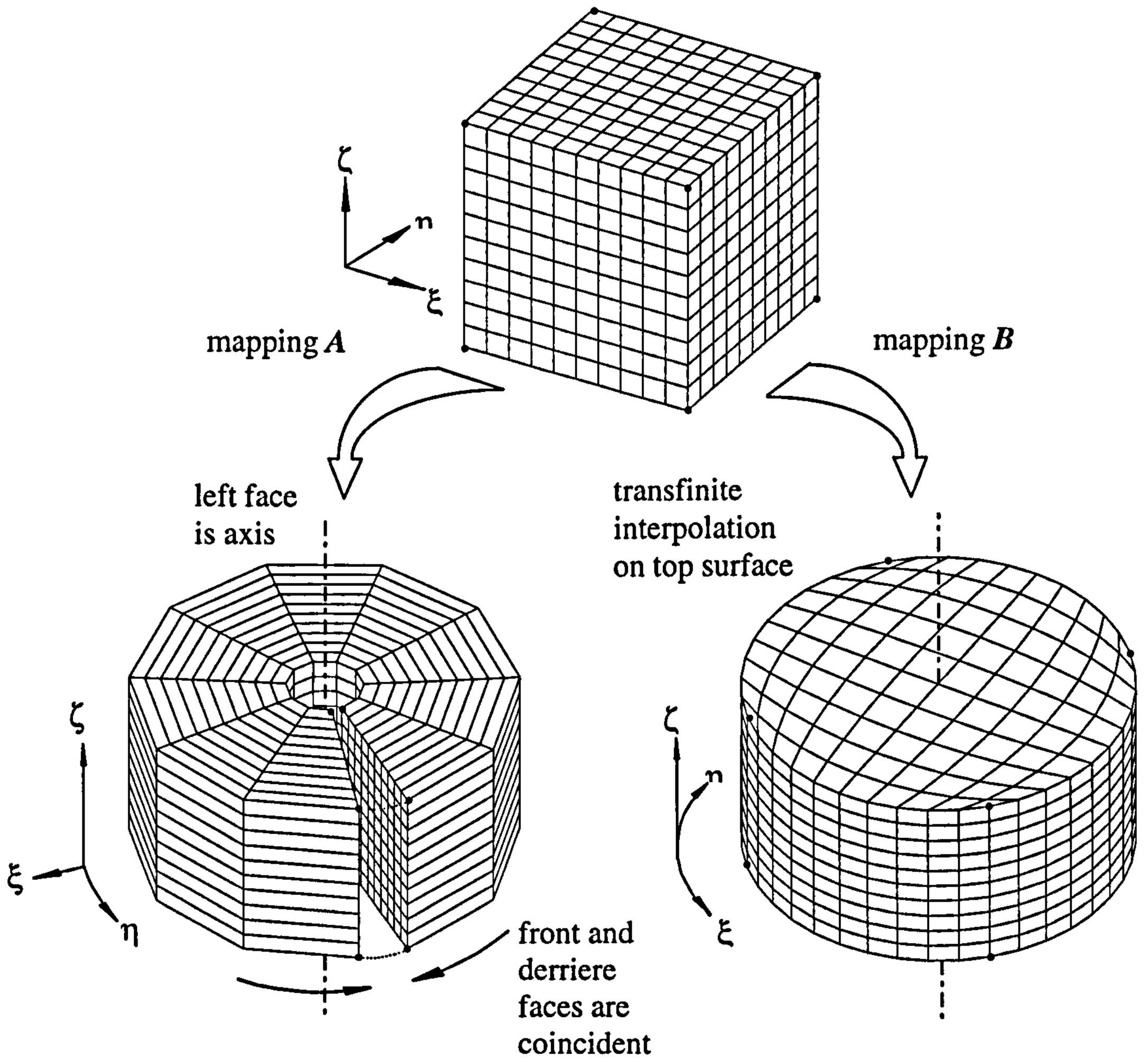

Figure 2.11 Mapping types between the regular computational region and a generalised cylindrical form in the physical region.

2.4.3 Surface Definition

To set up the configuration in mapping *B*, a correspondence must be established between the eight logical corners of the computational region and eight arbitrary points on the physical boundary. Point distributions are then specified as desired along boundary curves connecting these corner vertices to generate a wireframe description of the problem geometry. Subsequently, extra line segments are added or interpolated, to define the point distribution over the entire boundary surface.

At least two configurations were initially considered for the present combustion chamber geometry. However, it was found that the mapping is best accomplished by representing the entire pentroof cylinder head by the top face of the computational region, the piston surface by its bottom face and the cylinder walls by its four side faces. The physical geometry is orientated with respect to the computational region such that the valve ports lie on the corner diagonals of the logical mesh. Computation limitations restrict the mesh size to 34×34 cells in the *i* and *j* logical directions, and 7 cells in the *k*–direction when the piston is at or very near top dead centre. Additional *k*–planes are inserted or removed according to the piston movement as discussed in Sec. 2.4.4. The surface topology is generated in two stages as shown by Figs. 2.12 and 2.13.

Stage 1: The main boundary segments (including the valve port outlines) are constructed from straight lines and circular arcs on an *xy*–plane in physical space. These lines and arcs are read from an ASCII input data file into the mesh generator, thus providing some degree of generality if modifications to the mesh size or geometry are required. Mirroring about the axis of symmetry, transfinite interpolation and elliptic smoothing operations complete the two-dimensional point distribution.

Stage 2: Rotation and translation of mesh points is used to create the three-dimensional form. The concave boundary surfaces are generated by interpolation along parabolic arcs constructed between upper and lower boundary curves on the cylinder head. Stretching functions (Sec. 2.2.1) are used to control the point spacing along these arcs and thereby the distribution of coordinate lines over the concave surfaces. Ensuring acceptable included angles between the surface mesh lines (i.e.>33°) in the corner regions is particularly problematic. After optimisation of the spacing parameters in both the circumferencial and diagonal directions, the minimum angle is 33.5°.

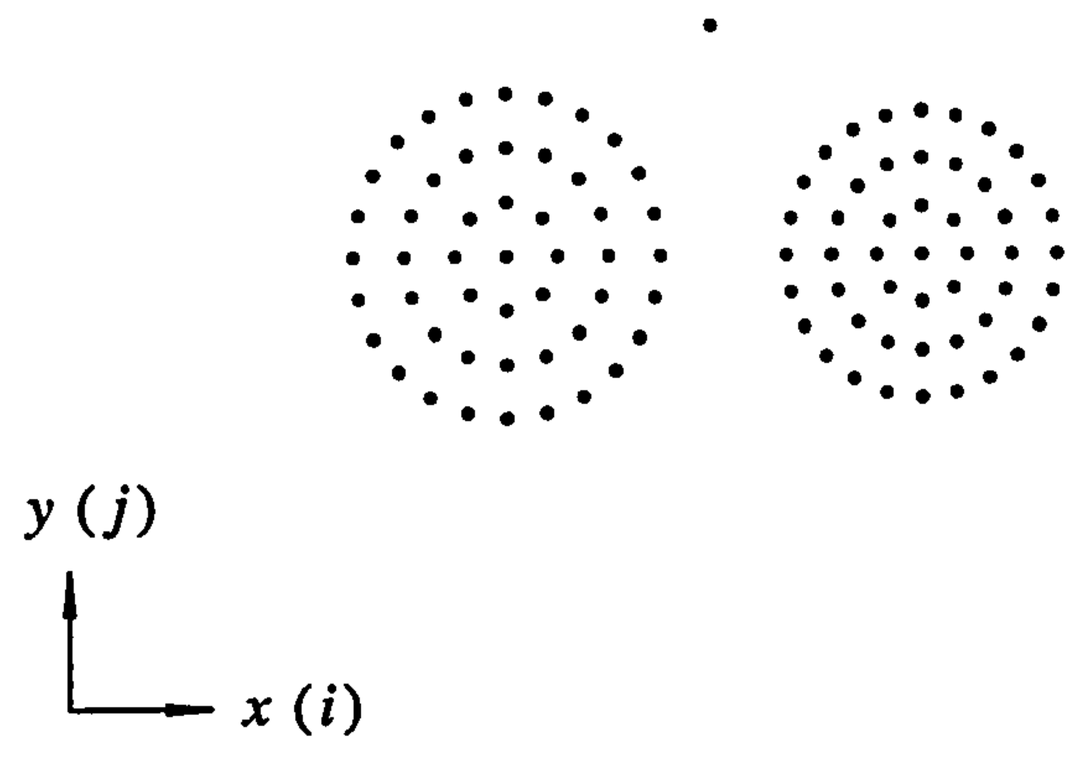

1. Inlet (left) & exhaust (right) poppet valve ports. Vertices are uniformly spaced on concentric circles about the centres.

ASCII data file input:

Logical and physical coordinates of port centres, their radii & cell width.

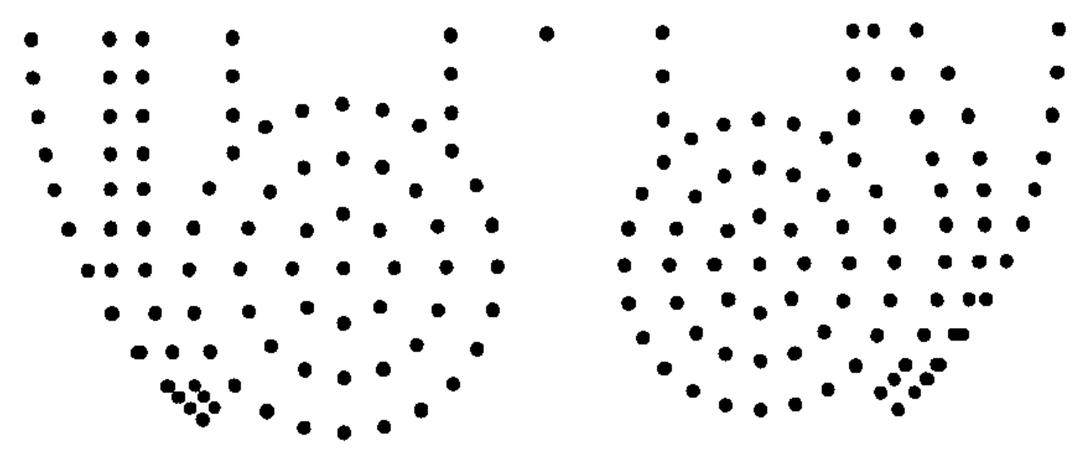

2. Lines and circular arcs with constant *i*–index. Points are positioned with linear interpolation and adjusted such that vertices with the same *j*–index are aligned horizontally.

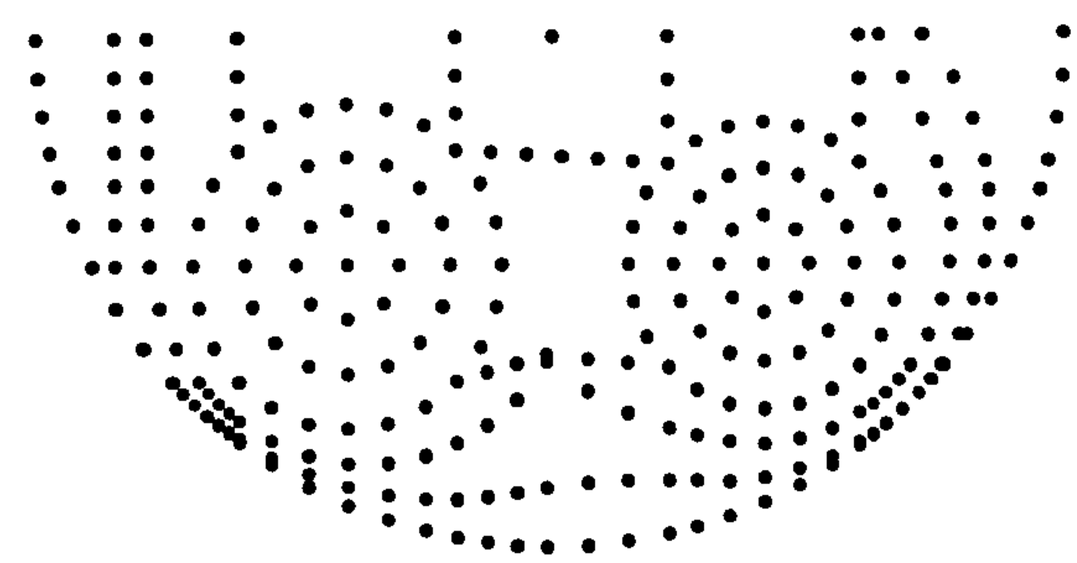

3. Lines and arcs with constant *j*–index.

ASCII data file input (steps 2 & 3):

Logical & physical coordinates of end points, arc radii (set equal to zero for straight lines).

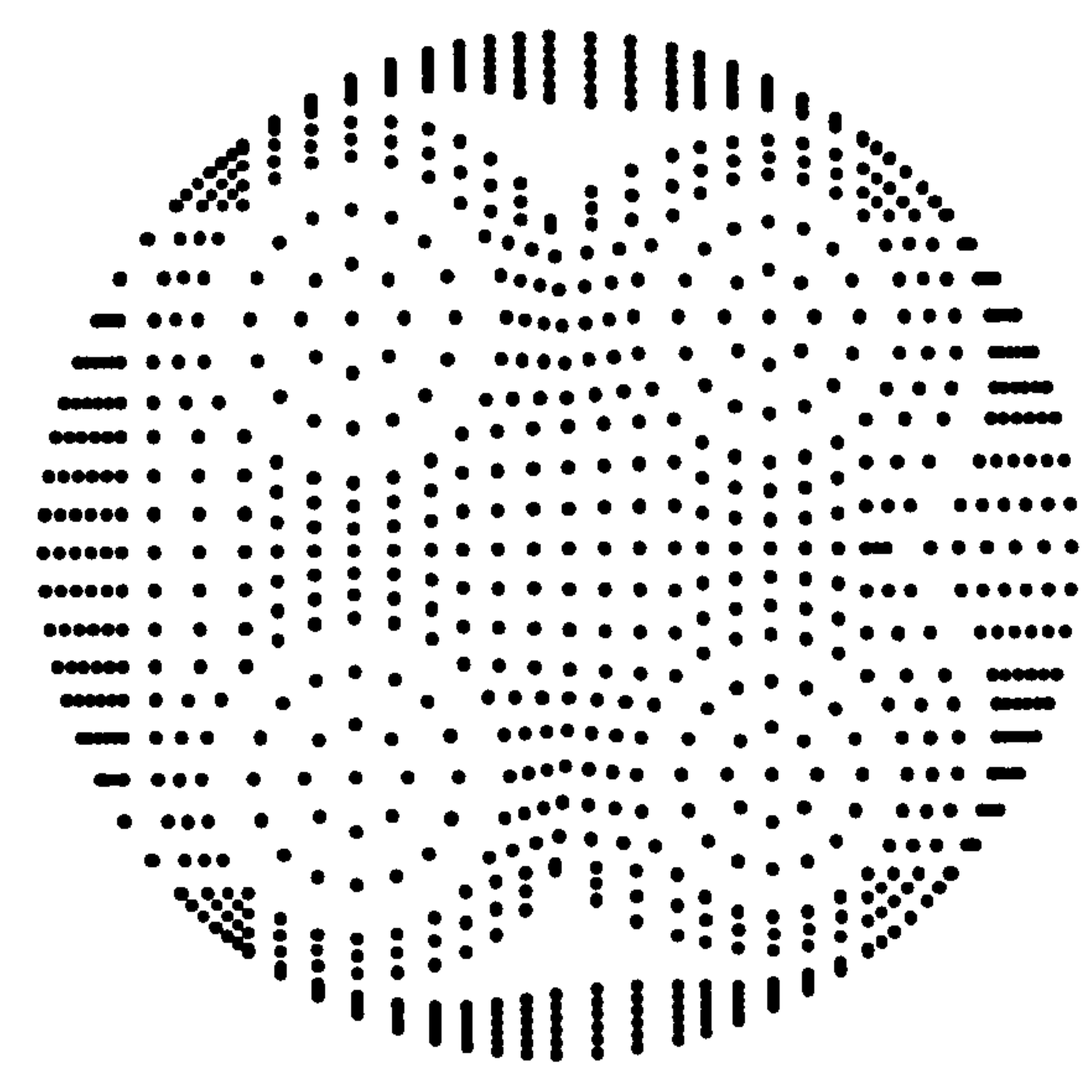

4. Mirroring of vertex positions about the axis of symmetry at $i=18$, transfinite interpolation and elliptic smoothing operations complete the definition of the top surface point distribution.

ASCII data file input:

Logical *i*, *j*–coordinates defining regions for transfinite interpolation and the coordinates of fixed points during the subsequent smoothing operation.

Figure 2.12 Stage 1: Initial two-dimensional definition of pentroof surface.

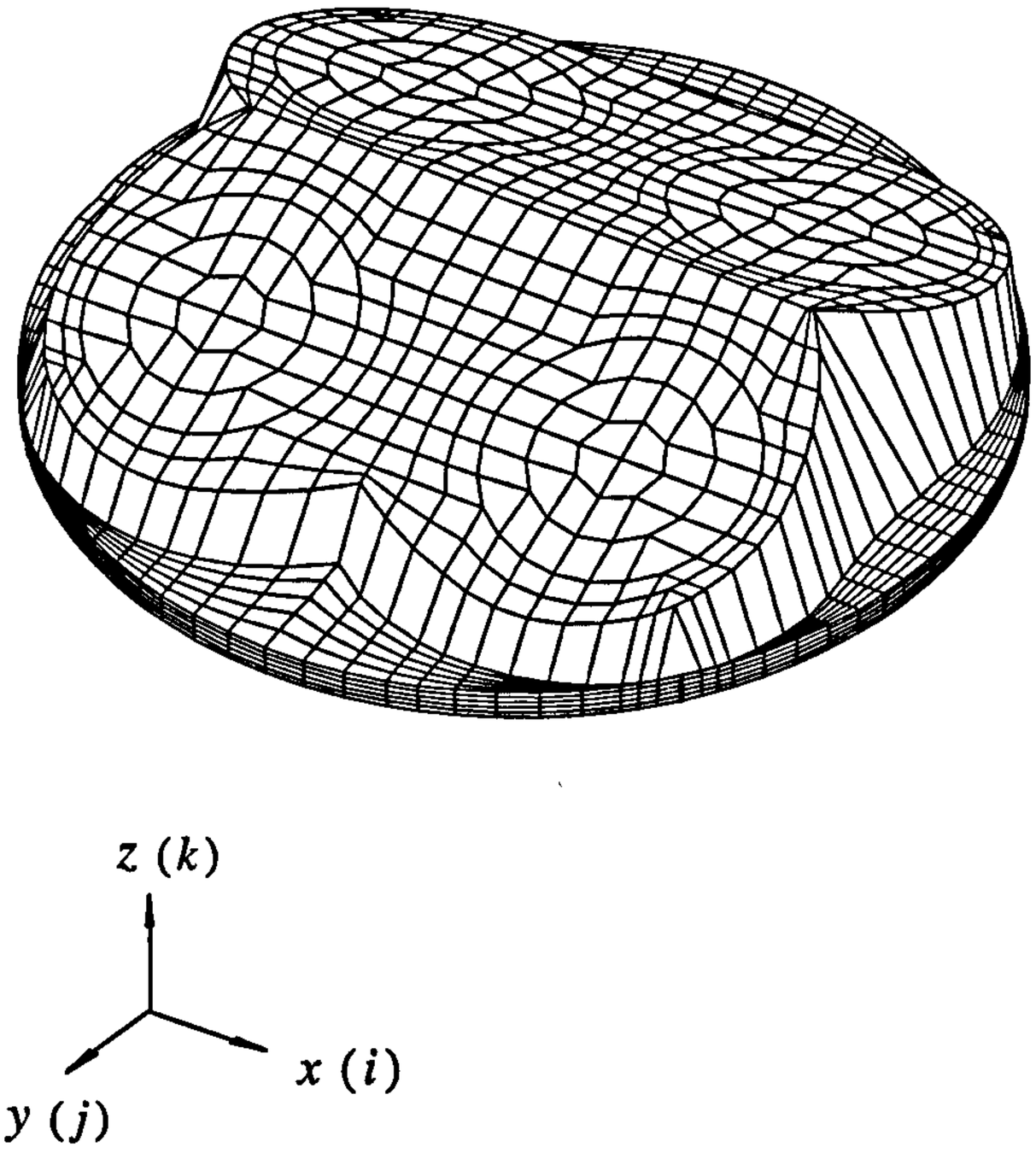

5. Mesh points enclosed by the boundary segments defining the planar surfaces of the pentroof are elevated and rotated by 20° about the logical plane $i = 18$.

The squish region is defined by translating the original two-dimensional boundary point x and y–coordinates to planes normal to the cylinder axis at successive locations along the axis.

6. The smooth concave interior surfaces of the cylinder head are generated by placing vertices along parabolic arcs constructed between boundary segments on the squish and planar pentroof surfaces.

7. Definition of corner regions with several interpolation steps. The region boundaries are first defined using one-dimensional interpolation with stretching.

Transfinite interpolation is then used to generate the interior.

Figure 2.13 Stage 2 – Transformation to three-dimensional surface.

Finally, the squish region below the cylinder head is generated by projecting the x and y coordinates from the top surface onto successive xy–planes evenly spaced along the cylinder axis. It should be noted that only the point distributions generated on the cylinder walls is of importance in this last operation, since other vertices (i.e. those in the interior and on the bottom boundary) are to be repositioned later.

2.4.4 Generation of the Interior Mesh

The complex boundary shape of the present geometry is almost certain to result in a poorly conditioned mesh if its interior is generated with an algebraic system. Nevertheless, all the interior coordinates are first found by transfinite interpolation of the boundaries (Sec. 2.2.2). This can save considerable work in cases were the mesh is found to be acceptable, otherwise as noted earlier, the transfinite solution serves as a reliable initial guess for an elliptic generation system.

In the present case, elliptic smoothing of the transfinite solution is required to improve the mesh orthogonality and spacing, particularly in the concave corner regions of the combustion chamber where the surface curvature is large. Therefore, the interior mesh coordinates are regenerated to optimise these properties by solving a system of elliptic partial differential equations as described in Sec. 2.3. Strict orthogonality is desired at the bottom boundary to allow rezoning and chopping operations (see Sec. 2.4.5). As the coordinate system on this surface is planar, its point distribution can be released from the fixed condition imposed at other boundaries. Then, after each iteration of the elliptic solver, the x and y coordinates of points on the bottom surface are replaced with the x and y coordinates of their neighbours generated on the first interior plane (i.e. at $k = 2$). Thus, all ζ – coordinate lines intersect the bottom boundary orthogonally.

Suitable values must be found for the control functions (Sec. 2.3.4) at each mesh point but as a first solution these are all set to zero, i.e. a Laplacian generation system. Figure 2.14 shows the edge of a j–plane from the mesh obtained by solving such a system. Although the degree of orthogonality and smoothness is good at points in the interior, the line slope and cell aspect ratios are unacceptable near the concave boundary. Control functions can be assigned to attract ζ –coordinate lines towards the cylinder axis as shown.

However, this problem is also observed on all the other vertical coordinate planes (including *i*-planes), since the concave surface extends around all sides of the pentroof cylinder head. Hence, the job of allocating appropriate spacing parameters for the control functions on each plane is lengthy, unless an automatic procedure is adopted.

By noting that the line spacing in the physical mesh is a function of the spacings $\Delta\xi$, $\Delta\eta$ and $\Delta\zeta$ in computational domain, a more novel remedy is possible. Prescribing $\Delta\xi$ and $\Delta\eta$ with the nonuniform spacing shown in Fig. 2.15 achieves the desired correction to the line slopes near the concave boundaries without the need to use control functions. The logical spacing is made larger near the side boundaries, such that transformation to the physical region results in the ζ–coordinate lines being attracted towards the cylinder axis as required. A few non-zero control functions are then selectively applied to individual mesh points until the entire mesh is well-conditioned.

Figure 2.16 shows an interior $\xi\eta$–plane demonstrating the characteristic smoothness obtained from an elliptic generation system. The solver required 16 iterations to converge taking only 15 seconds on a Hewlett Packard HP9000/750 machine (see Table 2.1).

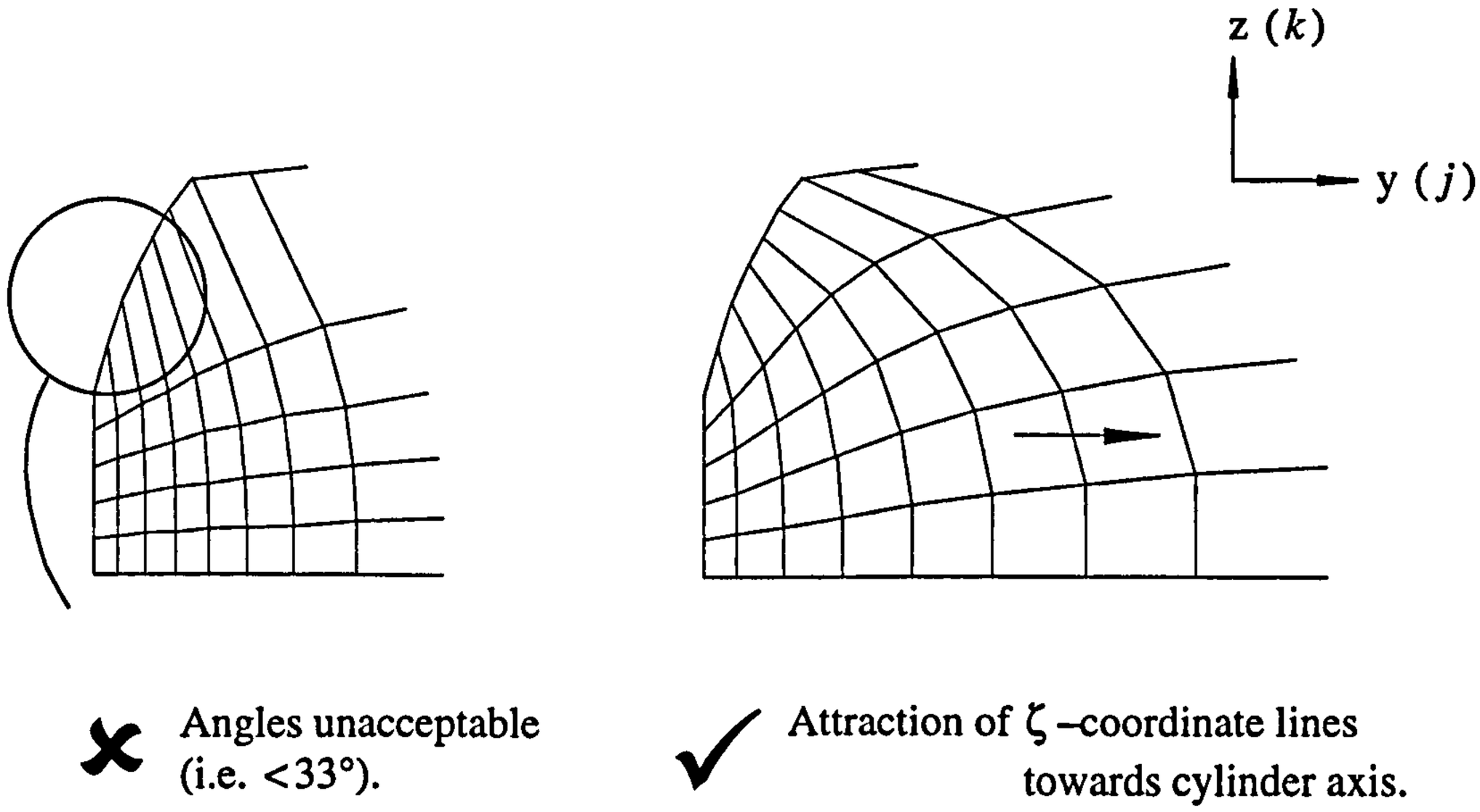

Figure 2.14 Effect of applying control functions to adjust the *y*–spacing of coordinate lines on the $j = 11$ plane in the mesh.

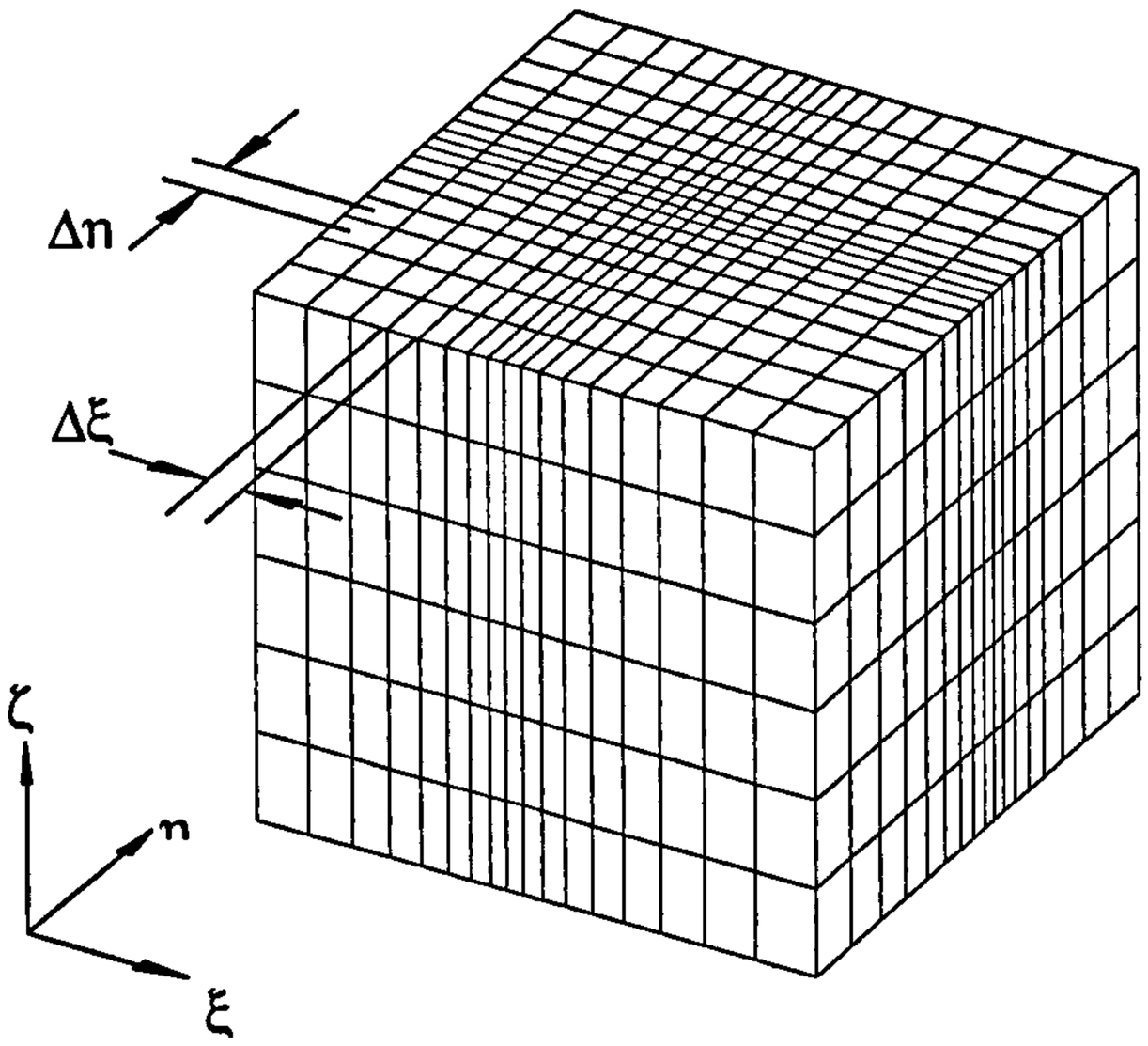

Figure 2.15 Computational region with nonuniform spacing for $\Delta\xi$ and $\Delta\eta$. A 17×17×6 mesh has been shown for clarity.

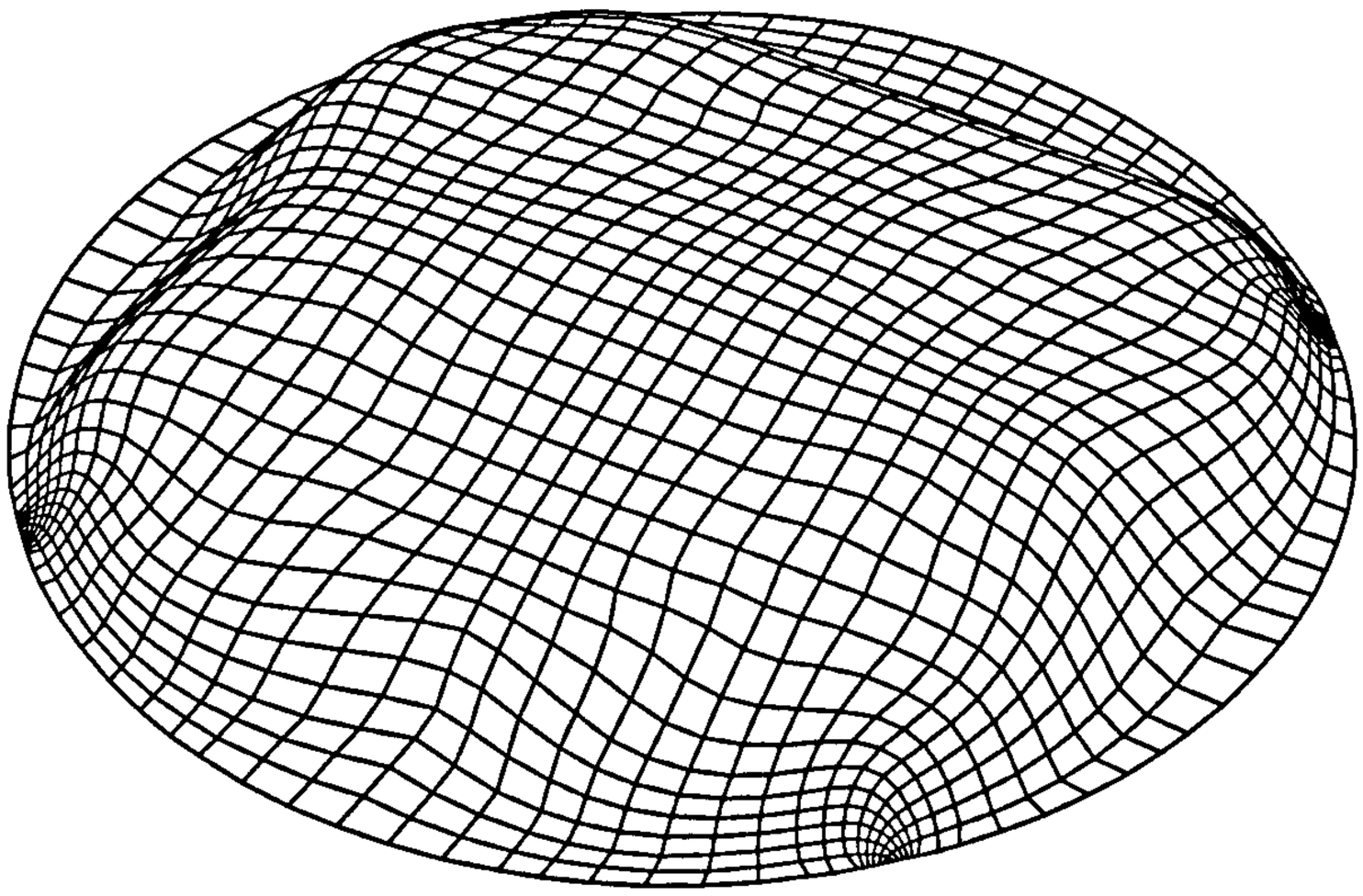

Figure 2.16 Pentroof combustion chamber: first interior $\xi\eta$–plane below the top boundary surface generated with a Poisson system. A 34×34×7 mesh with nonunifrom spacing similar to that in Fig. 2.15 was specified in the computational region. The minimum included angle between coordinate lines is 51.5°.

Ricardo Hydra 4-Valve Pentroof Geometry

Calculation Monitoring Information

Monitored location is at 5, 5, 4

Iter No.	Global Absolute Residual X	Y	Z	Values At Monitored Location X	Y	Z
1	1.029E-01	1.253E-01	9.587E-02	-2.649E+01	-2.905E+01	4.788E+01
2	9.944E-02	1.247E-01	1.173E-01	-2.621E+01	-2.862E+01	4.769E+01
3	5.177E-02	4.868E-02	3.849E-02	-2.601E+01	-2.834E+01	4.754E+01
4	2.821E-02	2.359E-02	1.468E-02	-2.583E+01	-2.814E+01	4.747E+01
5	1.772E-02	1.460E-02	5.645E-03	-2.570E+01	-2.803E+01	4.747E+01
6	1.214E-02	9.996E-03	3.485E-03	-2.563E+01	-2.796E+01	4.749E+01
7	8.521E-03	7.176E-03	2.710E-03	-2.559E+01	-2.793E+01	4.752E+01
8	6.139E-03	5.349E-03	2.146E-03	-2.557E+01	-2.791E+01	4.756E+01
9	4.559E-03	4.111E-03	1.671E-03	-2.556E+01	-2.789E+01	4.759E+01
10	3.472E-03	3.241E-03	1.282E-03	-2.555E+01	-2.788E+01	4.761E+01
11	2.710E-03	2.604E-03	9.785E-04	-2.554E+01	-2.787E+01	4.763E+01
12	2.154E-03	2.112E-03	7.488E-04	-2.554E+01	-2.786E+01	4.764E+01
13	1.730E-03	1.725E-03	5.767E-04	-2.554E+01	-2.786E+01	4.765E+01
14	1.403E-03	1.421E-03	4.480E-04	-2.553E+01	-2.785E+01	4.766E+01
15	1.148E-03	1.178E-03	3.522E-04	-2.553E+01	-2.785E+01	4.767E+01
16	9.429E-04	9.815E-04	2.794E-04	-2.553E+01	-2.785E+01	4.767E+01

Convergence: maximum residual source < 1.000E-03 Time: 15 s

Table 2.1 Residual history during convergence of the solution.

2.4.5 Rezoning and Chopping: Piston and Valve Simulation

Simulation of the piston and valve motions requires that the mesh is adaptive in the sense of following a boundary or some internal demarcation. One option is to regenerate the entire mesh for each new crank position; almost certainly requiring a fully automated solver. However, a much similar and more economical approach has been adopted in the present study. Consider the mesh developed in preceding sections in which the bottom boundary represents the piston surface at or near top dead centre. As the piston descends, the bottom cell layer becomes extended in the z–direction. Therefore, to prevent large aspect ratios plane layers of cells are inserted above the piston on the intake or expansion

strokes and stripped out on the exhaust and compression strokes. An auxiliary routine referred to as the 'chopper' (see Amsden *et al.* 1989, p. 94) is called by the numerical solution scheme to rezone the flow field each time a plane is added or removed. Thus, piston motion is accommodated by only rezoning in the squish region between the piston surface and base of the cylinder head. At bottom dead centre 16 logical k–planes are used corresponding to a mesh of (34×34×15 =) 17340 cells.

The poppet valves move in a direction perpendicular to the planar pentroof surfaces, crossing several interior k–planes in the cylinder head. Aligning these planes parallel to the top surface in the vicinity of the valve ports, enables each valve head to be defined by 'snapping' mesh vertices from successive k–planes on to its surface as it passes (see Fig. 2.17). Conditions at these vertices are set as those of a solid boundary in the numerical scheme (Sec. 3.4.3). A similar technique is also used to define valve stems by deactivating the vertices along an appropriate z–coordinate lines between each valve head and port. Then, in theory, an elliptic system can be solved with fixed interior values (i.e. the valve bodies) to regenerate the mesh at each new valve position.

However, in practice a serious problem arises. It is found that the vertices defining the valve bodies severely restrict the coordinate line spacing in the densely packed corner regions of the pentroof geometry. Convergence of the elliptic solver ends prematurely and the mesh is not well-conditioned. A review of the situation indicates that it is impossible to define both the valve motion and the complex pentroof boundary surface of the combustion chamber, given the limitations of a structured mesh and a restricted number of cells. Hence, a simpler mesh design is used for the cylinder head during the valve open period, which only approximates the concave surface shape of the pentroof. This mesh is rapidly regenerated at each crank position using transfinite interpolation. Subsequently, at inlet valve closure, the flow field is rezoned on to a 'firing' mesh which accurate models the surface detail. Since the valve description is not of interest during the closed period, the port outlines are removed from the surface definition. However, a concentric region is added in order to better define the spark-ignition. Both meshes are identical in the squish region and it is only the head description that is modified as shown in Fig. 2.18. This unconventional approach proved extremely effective and was easy to incorporate into the numerical scheme.

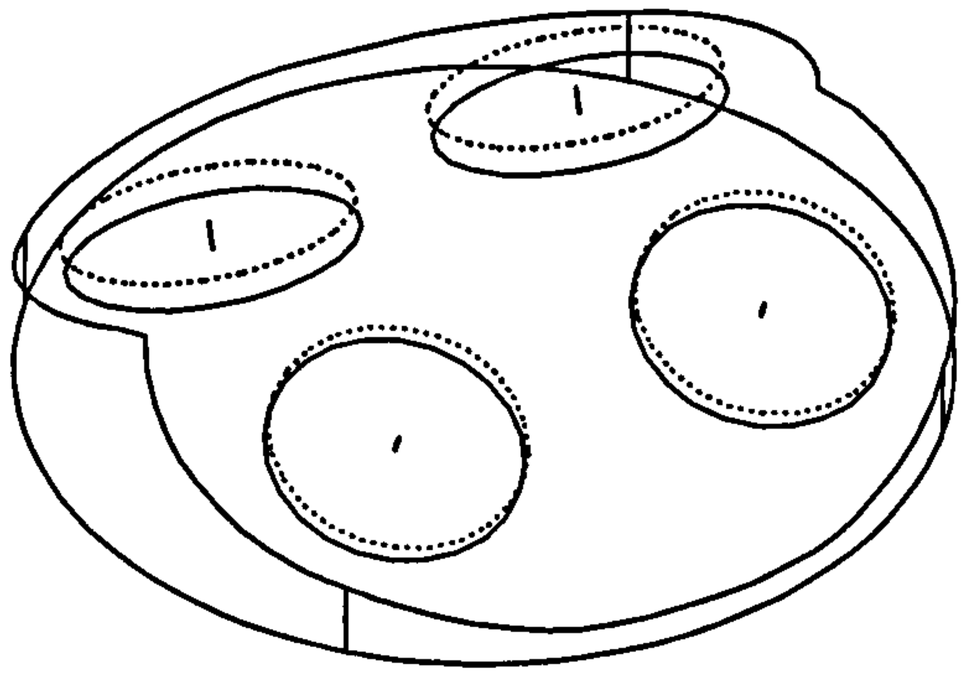

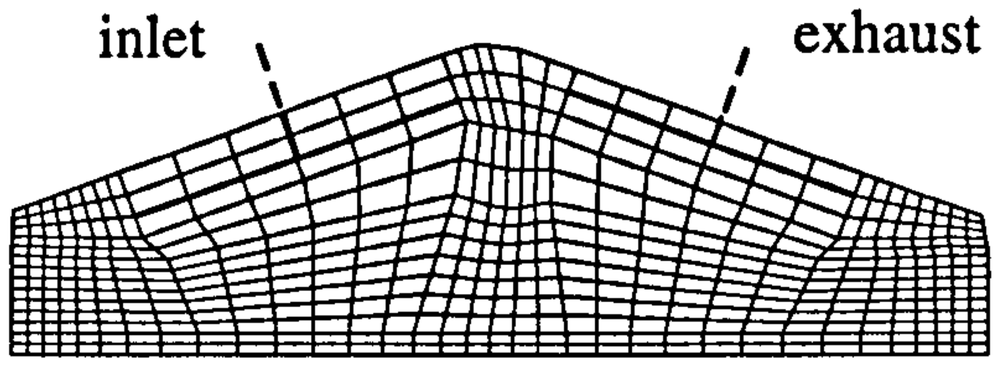

Figure 2.17 Description of open poppet valves (solid outline) and ports (dashed outline) by deactivating specific vertices on appropriate $\xi\eta$ –planes and along ζ – coordinate lines. Shown during valve overlap period.

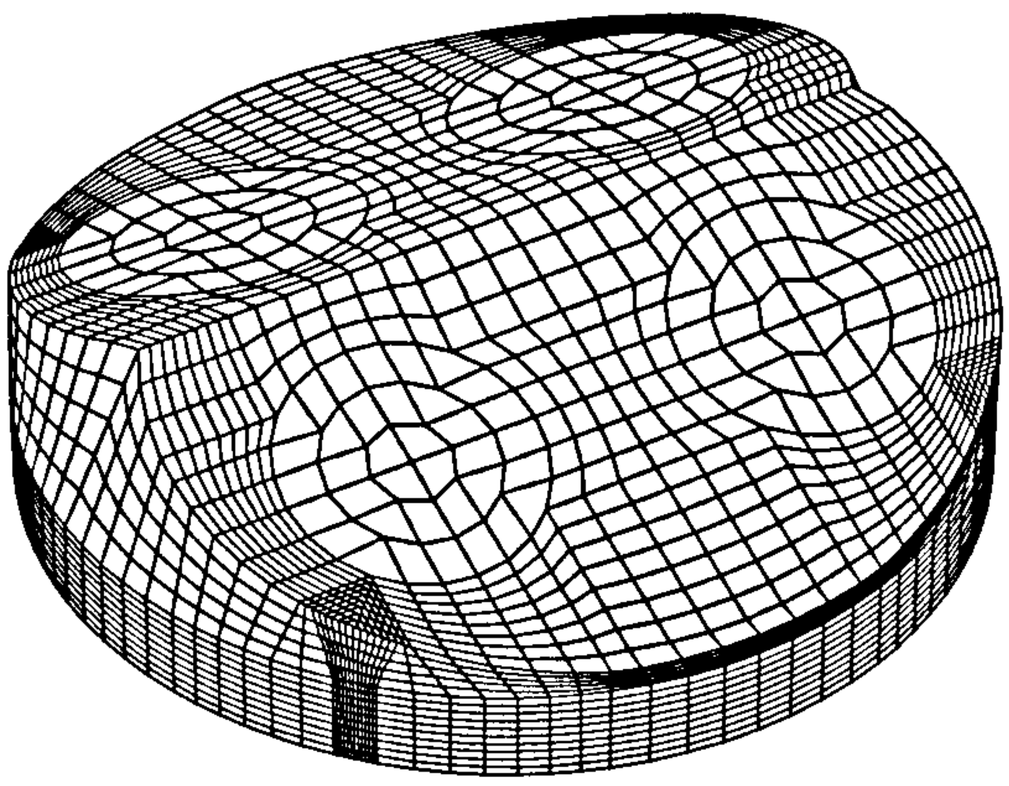

Transfinite mesh:

Valve open period

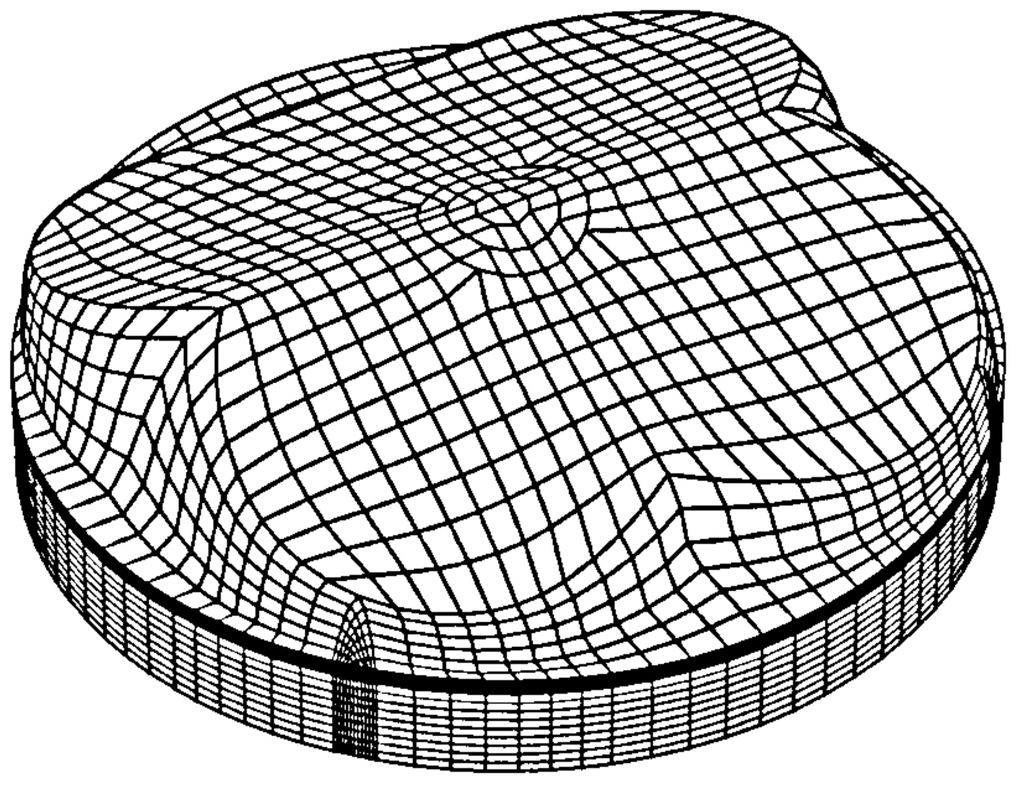

Elliptic mesh:

Combustion period

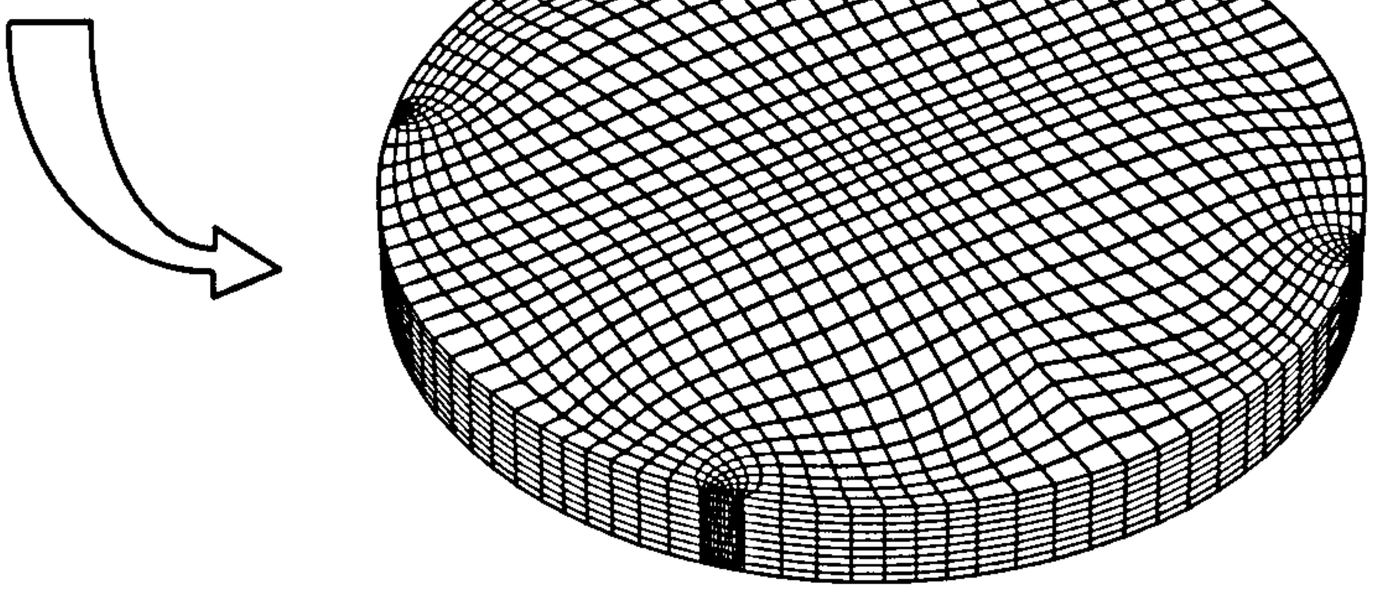

Squish region

(common to both).

Figure 2.18 Two mesh solution: the squish region between the piston face and the base of the cylinder head (i.e. at the gasket plane) is identical in both meshes during the rezoning period at inlet valve closure.

2.5 Summary

1. Techniques for numerical mesh generation enable an arbitrary-shaped geometry to be described by using transformation relations to map its physical coordinates (x, y, z) on to corresponding curvilinear coordinates (ξ, η, ζ) in a regular computational domain.

2. Algebraic mapping techniques are relatively easy to code and computationally efficient. A transfinite solver for interpolation in one, two and three-dimensions is detailed. This is the preferred choice for meshing a geometry with moderate boundary curvature.

3. Elliptic mesh generators are superior for complex boundary shapes: discontinuities on the boundary are not transmitted into the interior and explicit control of the coordinate line spacing and orientation may be achieved with appropriate control functions. An elliptic solver employing line-by-line TDMA with ADI is fully described.

4. Application of the algebraic and elliptic mesh generation techniques is demonstrated for a pentroof combustion chamber geometry. This example features the use of control functions, nonuniform spacing in the computational domain, fixed interior vertices and enforced orthogonality of grid lines at a specified boundary.

Chapter 3

Turbulent Combustion

The in-cylinder dynamics of advanced spark-ignition combustion engines involves a complex interaction of physical and chemical processes. The turbulent flow field is characterised by continuous fluctuations in velocity that arise from three-dimensional vortex elements (eddies) generated by shear within the fluid. This vorticity then leads to fluctuations in the scalar properties such as density, temperature and mixture composition. Consequently, the complexity of chemically reacting turbulent flow is such that it is a specialised research area (see review by Jones and Whitelaw, 1982). The sections below present the salient features of the turbulent combustion model developed in the present study. Alternative mathematical models are discussed where these might provide a more accurate description of the reacting flow, but usually with a significant increase in the computational requirement.

The present approach is implemented within the CFD code KIVA-II, developed primarily for modelling chemically reactive flows and sprays in internal combustion engines (Amsden *et al.* 1989). KIVA-II evolved from a series of multidimensional codes developed over a twelve year period at Los Alamos National Laboratory in New Mexico, under the sponsorship of the US Department of Energy. It is noteworthy that this code has undergone two upgrades during the present research period: KIVA-3 (Amsden 1993) and KIVA-3V (Amsden 1997). Distribution of KIVA-3 was restricted after its release for some years. It principally extends the single-block meshing methodology of KIVA-II (Sec. 2.1) to support a multi-block structured mesh. KIVA-3V further includes a valve model and several other new features. Importantly, numerous methodology changes and additions to KIVA-II *made here* parallel those from Los Alamos, with the exception of the multi-block structured analysis. Consequently, the present study is not seriously disadvantaged though transfer of the novel technology developed here to a newer KIVA version is suggested for a future work.

3.1 Averaged Transport Equations

The state of a turbulent reacting flow is completely specified when its velocity u_i, temperature T, pressure p, density ρ and mass fraction Y_s, for each chemical species s, are known at all points in both space and time. The spatial and temporal variation of these properties can be modelled from a mathematical description of the governing physical processes: convection, molecular transport, chemical reaction and radiation. The conservation laws of mass, momentum and energy are applied to these processes to derive a coupled system of partial differential equations. The complete set of equations are now commonly referred to as the Navier-Stokes equations for Newtonian fluids and may be represented in Cartesian form for each conserved quantity $\phi(x_j,t)$ by the general transport equation:

$$\frac{\partial \phi}{\partial t}+\frac{\partial}{\partial x_j}(\rho u_i \phi)=\frac{\partial}{\partial x_j}\left(\Gamma_\phi \frac{\partial \phi}{\partial x_j}\right)+S_\phi, \qquad \phi = 1,\ u_i,\ I,\ Y_s \tag{3.1}$$

where t is time, x_j is the spatial coordinate, $u_i(x_j,t)$ is the velocity vector field and the other quantities are as defined above. The four terms from left-to-right represent, respectively, the time rate of change of ϕ, the convective transport of ϕ by the flow, the diffusion of ϕ due to molecular transport and the net generation of ϕ within the reacting flow. Γ_ϕ denote the diffusivities and S_ϕ the volumetric sources of each conserved quantity. A detailed derivation of Navier-Stokes equations can be found in any basic text on fluid or continuum mechanics (see books by Anderson *et al.* 1984; Kuo 1986; Fletcher 1991). For now it is only important to know that they are represented by Eqs. (3.1). The following sections will demonstrate how the averaged equation set for a turbulent reacting flow can be developed from Eqs. (3.1) and specify in full all their constituent terms.

3.1.1 Averaging Procedures

The random, chaotic nature of turbulent flow involves a wide spectrum of length and time scales. This spectrum is so wide that direct numerical simulation (DNS) of turbulence, where all the relevant scales are resolved with extremely fine spatial and temporal discretisation, and large eddy simulation (LES), where the smallest length scales are modelled, has only been achieved in a few limited cases with supercomputing capability. Therefore, for the practical engineering analysis of turbulence it is natural to seek equations describing the mean flow properties. These may be developed from the Navier-

Stokes equations (3.1) using a statistical analysis. The vector and scalar properties of a fluid are represented by a normalised probability density function (PDF), P, given at a spatial location, x_i, by the expression:

$$P(\rho, u, v, w, Y_1, \ldots, Y_N, p, T; x_i)\, d\rho\, du\, dv\, dw\, dY_1 \ldots dY_N\, dp\, dT \tag{3.2}$$

If this PDF is known at a position, x_i, then the mean value of a flow property ϕ is given by multiplying its instantaneous value by the PDF and integrating for all the properties. i.e.

$$\overline{\phi}(x_i) = \int \phi\, P(\rho, \ldots, T; x_i)\, d\rho \ldots dT \tag{3.3}$$

This is ensemble-averaging. However, the large dimensionality of the PDF inhibits this approach and two alternative averaging techniques are adopted: classical Reynolds-averaging and density-weighted (or Favre) averaging. In the former procedure, a time-averaged mean quantity is defined as:

$$\overline{\phi}(x_i) = \lim_{\Delta t \to \infty} \frac{1}{\Delta t} \int_{t}^{t+\Delta t} \phi(x_i, t)\, dt \tag{3.4}$$

It is assumed that the time Δt is larger than the characteristic turbulence time but smaller than the characteristic time of the mean flow. The average quantities are then statistically stationary and equal to their ensemble average. However, these conditions may not be satisfied in internal combustion engines where the time scales of the energy-containing eddies are of the same order of magnitude as the time scales of the mean flow, and cycle times are short compared to relaxation times for important flow-adjustment phenomena (Ramos 1989, p. 37). Nevertheless, Eq. (3.4) is used to split the instantaneous flow variables into mean and fluctuating components as:

$$\phi(x_i, t) = \overline{\phi}(x_i) + \phi'(x_i, t) \tag{3.5}$$

where ϕ' is the turbulent fluctuation such that $\overline{\phi'} = 0$. Expression (3.5) may be substituted for all the state variables in Eqs. (3.1) then each term time-averaged, to obtain the Reynolds-averaged Navier-Stokes equations for turbulent flow. However, large density variations are typical for chemically reacting mixtures and it is convenient to define a density-weighted mean value, namely the Favre-average, as follows:

$$\tilde{\phi} = \frac{\overline{\rho\phi}}{\overline{\rho}} \qquad \text{where} \qquad \overline{\rho\phi}(x_i) = \lim_{\Delta t \to \infty} \frac{1}{\Delta t} \int_{t}^{t+\Delta t} \rho\,\phi(x_i, t)\, dt \tag{3.6}$$

All the instantaneous flow properties, except density and pressure, are then split by Favre-averaging according to the relation:

$$\phi(x_i, t) = \tilde{\phi}(x_i) + \phi''(x_i, t) \tag{3.7}$$

where the time-average of the density × Favre fluctuation $\overline{\rho\phi''} = 0$ but $\overline{\phi''} \neq 0$. Substituting into Eqs. (3.1) and time-averaging then gives the Favre-averaged Navier-Stokes equations. These have a simpler and more compact form, with fewer turbulent correlations than the corresponding Reynolds-averaged equations (see comparison by Warnatz *et al.* 1996, p.163) and for incompressible flow, the two formulations become identical. Furthermore, experimentally measured values from sample problems more closely approximate density-weighted concentrations rather than time-averaged concentrations (Kuo 1986, p.419).

The Favre-averaged Navier-Stokes equations solved in the present study are stated below in their conservative form using Cartesian vector and tensor notation. These govern the transport of chemical species, mass, momentum and internal energy in a three-dimensional turbulent reacting flow. Important assumptions and special terms have been highlighted were relevant.

3.1.2 Species Mass Conservation

If Y_s denotes the mass fraction of the chemical species s in a reacting mixture, then the turbulent species conservation equation has the following form:

$$\frac{\partial}{\partial t}(\overline{\rho}\tilde{Y}_s) + \frac{\partial}{\partial x_i}(\overline{\rho}\tilde{u}_i\tilde{Y}_s) = \frac{\partial}{\partial x_i}\left(D\overline{\rho}\frac{\partial \tilde{Y}_s}{\partial x_i} - \overline{\rho u_i'' Y_s''} \right) + D\overline{\rho\frac{\partial Y_s''}{\partial x_i}} + \overline{\dot{\rho}}_s, \qquad s = 1,2, \ldots, N \tag{3.8}$$

where Fick's law diffusion is assumed, with a single diffusion coefficient, D, for all species. This law expresses the tendency of each species to diffuse in the direction of decreasing mass fraction, thus smoothing out concentration gradients in the flow. Three other diffusion mechanisms are neglected in the combustion process. These describe the species transport arising from thermal diffusion (the Soret effect), pressure-gradients and body forces per unit mass on molecules of different species (Kuo 1986, pp. 206-209).

Fluctuations in species diffusivity are also neglected. The two turbulence correlations in Eq. (3.8) are introduced from Favre-averaging the convection and diffusion terms. Gradients in mass fraction fluctuation are expected to be small, such that the diffusive fluctuating term can be neglected. Closure of Eq. (3.8) then requires expressions for the convective turbulence correlation $\overline{\rho u_i'' Y_s''}$ and the chemical source term, $\dot{\rho}_s$.

3.1.3 Total Mass Continuity

The continuity equation is obtained by summing Eq. (3.8) over all species, since mass is conserved in the chemical reactions, as:

$$\frac{\partial \overline{\rho}}{\partial t} + \frac{\partial}{\partial x_i}(\overline{\rho}\tilde{u}_i) = 0 \tag{3.9}$$

3.1.4 Momentum Conservation

The vector equation for momentum transport is given by:

$$\frac{\partial}{\partial t}(\overline{\rho}\tilde{u}_i) + \frac{\partial}{\partial x_j}(\overline{\rho}\tilde{u}_i\tilde{u}_j) = -\frac{\partial \overline{p}}{\partial x_i} + \frac{\partial}{\partial x_j}(\overline{\sigma}_{ij} - \overline{\rho}\widetilde{u_i'' u_j''}) + \overline{\rho}\,\overline{g}_{ij} \tag{3.10}$$

where p is the fluid pressure, σ_{ij} is the viscous stress tensor, and g_{ij} represents a constant specific body force (e.g. gravitational force). The fluid is assumed Newtonian such that the Favre-averaged viscous stress tensor, $\overline{\sigma}_{ij}$, neglecting viscosity fluctuations, is given by:

$$\overline{\sigma}_{ij} = \mu\left(\frac{\partial \tilde{u}_i}{\partial x_j} + \frac{\partial \tilde{u}_j}{\partial x_i}\right) + \lambda\delta_{ij}\frac{\partial \tilde{u}_k}{\partial x_k} + \mu\left(\frac{\partial u_i''}{\partial x_j} + \frac{\partial u_j''}{\partial x_i}\right) + \lambda\delta_{ij}\frac{\partial u_k''}{\partial x_k} \tag{3.11}$$

where μ and λ are the first and second coefficients of dynamic viscosity, respectively, and δ_{ij} is the Kronecker delta function. The two coefficients of viscosity are related to the coefficient of bulk viscosity, κ, by the expression (Anderson *et al.* 1984, Eq. 5-13):

$$\kappa = \tfrac{2}{3}\mu + \lambda \tag{3.12}$$

In combustion processes, it is a common practice to adopt Stokes hypothesis and assume that $\kappa = 0$, since it is only significant in shock waves or in the absorption and attenuation of acoustic waves (Anderson *et al.* 1984, p.185). The second coefficient of viscosity can

then be replaced by $-\frac{2}{3}\mu$. Furthermore, the viscous terms involving the Favre-fluctuations are assumed to be small and neglected on the basis of order of magnitude arguments, such that $\overline{\sigma}_{ij}$ becomes:

$$\overline{\sigma}_{ij} = \mu\left[\left(\frac{\partial \tilde{u}_i}{\partial x_j}+\frac{\partial \tilde{u}_j}{\partial x_i}\right)-\tfrac{2}{3}\delta_{ij}\frac{\partial \tilde{u}_k}{\partial x_k}\right] \tag{3.13}$$

If body forces are neglected (i.e. $g_{ij}=0$), then closure of equation (3.10) only requires an expression for the turbulence correlations $\overline{\rho u_i'' u_j''}$ arising from Favre-averaging the non-linear convection term. These are known as the Reynolds stresses.

3.1.5 Internal Energy Conservation

From the first law of thermodynamics, the conservation equation for specific internal energy, I, is given by:

$$\underbrace{\frac{\partial}{\partial t}(\overline{\rho}\tilde{I})+\frac{\partial}{\partial x_i}(\overline{\rho}\tilde{u}_i\tilde{I})}_{\text{mean increase in internal energy}}=\underbrace{-\overline{p}\frac{\partial \tilde{u}_i}{\partial x_i}}_{\text{flow work}}\underbrace{-\overline{p\frac{\partial u_i''}{\partial x_i}}}_{}+\underbrace{\overline{\sigma}_{ij}\frac{\partial \tilde{u}_i}{\partial x_j}}_{\text{dissipation by viscous stress}}+\underbrace{\overline{\sigma_{ij}\frac{\partial u_i''}{\partial x_j}}}_{}+\underbrace{\frac{\partial}{\partial x_i}(-\overline{q}_i}_{\text{heat influx}}\underbrace{-\widetilde{\overline{\rho}u_i''I''})}_{\text{turbulent convection}}+\underbrace{\overline{\dot{Q}}_{chem}}_{\text{chemical heat}} \tag{3.14}$$

where q_i is the heat flux vector and $\dot{Q}_{chem}$ is the rate of chemical heat release. The heat flux is composed of four contributions: heat conduction, enthalpy diffusion, the Dufour effect and, radiative heat flux, q_r due to radiatively participating gases within the reacting flow. The Dufour effect (Warnatz *et al.* 1996, p.152) is a process where concentration gradients in the reacting mixture produce a heat flux in a reciprocal action to the Soret effect (see Sec. 3.1.2). Its contribution can be assumed negligible in combustion processes, such that the Favre-averaged heat flux vector, $\overline{q}_i$, is be taken as:

$$\overline{q}_i = -K\frac{\partial \tilde{T}}{\partial x_i}-\overline{\rho}D\sum_s h_s(\tilde{T})\frac{\partial \tilde{Y}_s}{\partial x_i}+\overline{q}_{r,i} \tag{3.15}$$

where K and D represent the thermal conductivity and mass diffusivity of the reacting mixture, respectively, and h_s is specific enthalpy of species s. Fluctuations in these quantities are neglected. Furthermore, time-averaged terms involving gradients of fluctuating quantities in Eq. (3.15) have been neglected, since these are assumed small in

comparison to the other terms. Extending this argument to Eq. (3.14) also removes the two pressure and viscous terms involving Favre-fluctuations. Therefore, substituting for $\overline{\sigma}_{ij}$ from Eq. (3.13), the Favre-averaged viscous dissipation term can be represented by the following function:

$$\overline{\Phi} = \overline{\sigma}_{ij}\frac{\partial \tilde{u}_i}{\partial x_j} = \mu\left[2\left(\frac{\partial \tilde{u}}{\partial x}\right)^2 + 2\left(\frac{\partial \tilde{v}}{\partial y}\right)^2 + 2\left(\frac{\partial \tilde{w}}{\partial z}\right)^2 + \left(\frac{\partial \tilde{u}}{\partial y} + \frac{\partial \tilde{v}}{\partial x}\right)^2 + \left(\frac{\partial \tilde{v}}{\partial z} + \frac{\partial \tilde{w}}{\partial y}\right)^2 + \left(\frac{\partial \tilde{w}}{\partial x} + \frac{\partial \tilde{u}}{\partial z}\right)^2 - \tfrac{2}{3}\left(\frac{\partial \tilde{u}}{\partial x} + \frac{\partial \tilde{v}}{\partial y} + \frac{\partial \tilde{w}}{\partial z}\right)^2\right] \tag{3.16}$$

Closure of Eq. (3.14) then requires suitable expressions for the turbulence correlation $\overline{\rho u_i'' I''}$, the chemical source term $\dot{Q}_{chem}$, and the radiative heat flux q_r.

Note: In addition to q_r, the conservation equations should strictly include terms for radiation pressure and radiative energy storage due to transients, but these effects are so small that they have been ignored (Modest 1993, p.316).

3.1.6 State Relations

The state relationships between the thermodynamic variables are assumed to be those of an ideal gas mixture. The partial specific enthalpies, h_s, for each species s in the reacting mixture are taken from JANAF tables (Stull and Prophet 1974) at 100K temperature intervals from absolute zero to 5000K. These tabulated enthalpies are then converted to values of specific internal energy, I_s, at the temperature datum points with the relationship:

$$I_s(\tilde{T}) = h_s(\tilde{T}) - R_u\tilde{T}/W_s \tag{3.17}$$

where R_u is the universal gas constant and W_s is the molecular weight of species s. The total specific internal energy, I, for a specific mixture composition is then given by the summation:

$$I(\tilde{T}) = \sum_s \tilde{Y}_s I_s(\tilde{T}) \tag{3.18}$$

Values of total internal energy satisfying the energy conservation equation (3.14) are then used to interpolate the mixture temperature field, $\tilde{T}(x_i)$, from the datum internal energies.

Furthermore, these datum values are used to determine the constant volume specific heat, c_v, over the 100K temperature intervals from the approximation:

$$c_v(\tilde{T}) = dI/d\tilde{T} = 0.01\ (I_2 - I_1) \tag{3.19}$$

where I_2 and I_1 are the upper and lower tabulated internal energies for the interval. The mixture pressure, $\bar{p}$, and ratio of specific heats, $\bar{\gamma}$, are then obtained from the relationships:

$$\bar{p} = \bar{\rho} R_u \tilde{T} \sum_s \frac{\tilde{Y}_s}{W_s} \tag{3.20}$$

$$\bar{\gamma} = \frac{c_P}{c_V} = 1 + \frac{\bar{p}}{\bar{\rho} c_V \tilde{T}} \tag{3.21}$$

where c_P is the specific heat at constant pressure.

3.2 Turbulence Model

A turbulence model is required to evaluate the three second-moment statistical correlations arising in the Favre-averaged Navier-Stokes equations above, namely the Reynolds stresses, $\overline{\rho u_i'' u_j''}$ together with the two turbulent scalar fluxes: $\overline{\rho u_i'' Y_s''}$ and $\overline{\rho u_i'' I''}$.

The KIVA-II code incorporates a standard version of the k–ε turbulence model, modified to include volumetric expansion effects. For the present combustion studies in variable density flows, this model was further modified to incorporate pressure-density-interaction effects. In this its final form, the model then arguably gives a reasonable approximation of the turbulence behaviour. To justify this statement and appreciate how the k–ε model fits into the overall framework of turbulence modelling, this section will present the exact transport equations for the turbulent correlations, and demonstrate how these are reduced to the form of the present model. In addition to highlighting the underlying assumptions and limitations of the present approach, the following discussion also forms a basis for any further work requiring the introduction of more sophisticated turbulence models.

3.2.1 Second-Moment Closure (Reynolds Stress Model)

An exact Favre-averaged transport equation for the Reynolds stresses can be derived from Eqs. (3.9) and (3.10) as follows (cf. panel 11/21, Jones 1982):

$$\underbrace{\frac{\partial}{\partial t}(\overline{\rho}\widetilde{u_i''u_j''}) + \frac{\partial}{\partial x_k}(\overline{\rho}\widetilde{u_i''u_j''}\,\widetilde{u}_k)}_{\text{mean increase in Reynolds stresses}} = \underbrace{-\overline{\rho}\widetilde{u_i''u_k''}\frac{\partial \widetilde{u}_j}{\partial x_k} - \overline{\rho}\widetilde{u_j''u_k''}\frac{\partial \widetilde{u}_i}{\partial x_k}}_{\text{production}} - \underbrace{\frac{\partial}{\partial x_k}(\overline{\rho}\widetilde{u_i''u_j''u_k''} + \tfrac{2}{3}\delta_{ij}\overline{p'u_k''})}_{\text{diffusion}}$$

$$\underbrace{-\overline{u_j''\frac{\partial p'}{\partial x_i}} - \overline{u_i''\frac{\partial p'}{\partial x_j}} + \tfrac{2}{3}\delta_{ij}\overline{u_k''\frac{\partial p'}{\partial x_k}}}_{\text{pressure redistribution}} - \underbrace{\overline{u_i''}\frac{\partial \overline{p}}{\partial x_j} - \overline{u_j''}\frac{\partial \overline{p}}{\partial x_i}}_{\substack{\text{production/destruction by} \\ \text{mean pressure gradient}}}$$

$$\underbrace{-\overline{\sigma'_{ki}\frac{\partial u_j''}{\partial x_k}} - \overline{\sigma'_{kj}\frac{\partial u_i''}{\partial x_k}}}_{\substack{\text{viscous} \\ \text{dissipation}}} + \underbrace{\tfrac{2}{3}\delta_{ij}\overline{p'\frac{\partial u_k''}{\partial x_k}}}_{\substack{\text{fluctuation pressure} \\ \times \text{ velocity dilation}}} \tag{3.22}$$

Equation (3.22) represents a highly nonlinear system of six partial differential equations: one for each of the six independent Reynolds stresses. The left-hand side expresses the total rate of increase of the Reynolds stresses which arises from an imbalance of the terms on the right. Here the terms have been grouped, following well established practice, to allow a physical interpretation of the processes. Evaluation of these terms, containing even higher-order unknown correlations, requires numerous modelling assumptions. Second-moment closure or Reynolds stress turbulence models thus solve a modelled form of Eq. (3.22). The first pair of terms on the right-hand side describes the production of the Reynolds stresses from the effects of mean strain. These terms are exactly representable since they involve only second-moment correlations and mean velocity gradients. Terms in the second grouping are diffusive in character and describe the spatial redistribution of the Reynolds stresses by (a) velocity and (b) pressure fluctuations. Additional terms can also be included to describe represent transport due to molecular action, but over all or nearly all the flow their effect is negligible (Launder 1983, p.6). Correlations between fluctuating velocity and derivatives of fluctuating pressure in the third grouping physically represent the redistribution of energy amongst the normal Reynolds stresses ($i = j$) so as to make them more isotropic and to reduce the Reynolds shear stresses ($i \neq j$). Pressure terms in fourth and sixth groupings are only present where density variations are significant. Finally, terms with viscous stress fluctuation

(fifth grouping) describe the rate of dissipation of the Reynolds stresses due to viscous action. Molecular viscosity converts their energy into internal heat by the acting on the small-scale, high-frequency motions. Launder (1983, Sec. 1.5) demonstrates that if these motions are assumed to be isotropic (in high Reynolds number flows) then these terms can be modelled by a scalar quantity, ε, representing the rate of viscous dissipation of turbulent kinetic energy (see definition in Sec. 3.2.3) as follows:

$$\overline{\sigma'_{ki}\frac{\partial u''_j}{\partial x_k}}+\overline{\sigma'_{kj}\frac{\partial u''_i}{\partial x_k}} \approx \tfrac{2}{3}\delta_{ij}\bar{\rho}\tilde{\varepsilon} \tag{3.23}$$

e.g. Jones and Whitelaw (1982) states a reduced form of Eq. (3.22) which includes this approximation for the viscous dissipation terms. An additional scalar transport equation is then solved for ε or an associated scalar quantity (see Sec. 3.2.3). Therefore, to approximate the Reynolds stresses, a system of seven partial differential equations must be solved, representing a considerable computational effort. The production of the Reynolds stresses is the only term obtained directly, and closure approximations for the other terms introduces a number (eight) of empirical coefficients. A present, a unique set of coefficients that are generally applicable to a wide range of flow has not been established. Furthermore, to complete the second-moment closure, additional transport equations are required for the turbulent energy flux and species fluxes. These have a similar structure to the Reynolds stress equation, Eq. (3.22) and their solution necessitates fitting additional model constants. Hence, lack of sufficient validation and the large computational costs necessitate rejecting a second-moment closure model for the present study, in favour of a more economic and more widely tested simplified form.

3.2.2 Algebraic Stress Model

An order-of-magnitude analysis of the transport processes in the Reynolds stress and scalar flux equations indicates that the broad characteristics of the turbulence arise from the production terms. However, the main computational effort in second-moment closure methods is caused by the Reynolds stress or scalar flux gradients that appear in the convective and diffusive terms of the modelled form of Eq. (3.22). An algebraic stress model (ASM) is a simplification in which the convective and diffusive processes are removed or modelled without these gradients, thereby reducing the system of partial differential equations to a set of algebraic equations (Launder 1983). The Reynolds stresses and scalar fluxes can then be obtained by simultaneous solutions using matrix

inversion or iterative techniques. The loss in accuracy associated with this approximation is mitigated to some extent by the fact that the production terms are still retained in their exact form, while the task of numerical solution is greatly simplified. However, for multidimensional in-cylinder engine flows, the benefits of adopting an algebraic stress model, compared to models at the next level of simplification, have not been clearly established. This is an area for further work.

3.2.3 Standard k–ε Turbulence Model

The k–ε model is the most widely applied and validated turbulence model. It represents the highest level of sophistication in a hierarchy of methods in which a first-order closure is used to evaluate the Reynolds stresses as a function of the flow velocity gradients and geometry alone. The numerical advantages arising from this approximation are considerable, since there is now no need to store the stress field or, indeed, to evaluate it explicitly. The simplest case is to assume a linear relationship between the turbulent stresses and mean rates of strain (Jones and Launder 1972):

$$-\overline{\rho}\widetilde{u_i''u_j''} = \mu_t\left(\frac{\partial\tilde{u}_i}{\partial x_j}+\frac{\partial\tilde{u}_j}{\partial x_i}\right)-\tfrac{2}{3}\delta_{ij}\left(\overline{\rho}k+\mu_t\frac{\partial\tilde{u}_k}{\partial x_k}\right) \tag{3.24}$$

where the coefficient of proportionally, μ_t, defines the turbulent (or eddy) viscosity and k is the turbulent kinetic energy (as defined later). In parallel with the turbulent viscosity concept for momentum transport, a gradient-diffusion model is adopted for the scalar fluxes:

$$-\overline{\rho}\widetilde{u_i''\phi''} = \frac{\mu_t}{\sigma_t}\frac{\partial\tilde{\phi}}{\partial x_i}, \qquad \phi = \{I, Y_s\} \tag{3.25}$$

where the turbulent Prandtl/Schmidt number, σ_t, is an appropriate scaling function for ϕ, usually taken as a constant near unity. The turbulent viscosity is then defined at each point in the flow field by the relation:

$$\mu_t = c_\mu \overline{\rho} k^2/\varepsilon \tag{3.26}$$

where k and ε, are extra variables introduced to represent the velocity and length scales of the turbulence motions, respectively, and c_μ is a model constant. An additional partial differential equation is solved for each of these new variables. The turbulent kinetic energy, k, measures the fluctuation intensity according to $k = \frac{1}{2}u_i''u_i''$.

Therefore, contraction of Eq. (3.22) by setting $i = j$ produces an equation for the transport of (twice) the turbulent kinetic energy. Substituting the ε-approximation in Eq. (3.23) for the viscous dissipation terms, dividing throughout by two and rearranging then gives:

$$\underbrace{\frac{\partial}{\partial t}(\bar{\rho}k)}_{\text{increase in turbulent k.e.}} + \underbrace{\frac{\partial}{\partial x_j}(\bar{\rho}\tilde{u}_j k)}_{\text{increase in turbulent k.e.}} = \underbrace{-\frac{\partial}{\partial x_j}(\tfrac{1}{2}\bar{\rho}\widetilde{u_i'' u_i'' u_j''})}_{\text{diffusion of fluctuation energy}} \underbrace{-\overline{u_i''\frac{\partial p}{\partial x_i}}}_{\text{work due to turbulence}} \underbrace{-\bar{\rho}\widetilde{u_i'' u_j''}\frac{\partial \tilde{u}_i}{\partial x_j}}_{\text{production of turbulent k.e.}} \underbrace{-\bar{\rho}\varepsilon}_{\text{viscous dissipation}} \tag{3.27}$$

It should be noted that the pressure redistribution and pressure fluctuation terms of Eq. (3.22) vanish during the contraction process. Hence, the transport equation for k has discarded much of the information concerning pressure-flow interactions, resulting in a loss in accuracy where these effects are important. Closure of Eq. (3.27) then requires modelled approximations for the diffusion, work and production terms. The diffusion of fluctuation energy described by the triple correlation term, is modelled with the following gradient transport approximation:

$$-\frac{\partial}{\partial x_j}(\tfrac{1}{2}\bar{\rho}\widetilde{u_i'' u_i'' u_j''}) = \frac{\partial}{\partial x_j}\left(\frac{\mu_{eff}}{\sigma_k}\frac{\partial k}{\partial x_j}\right) \tag{3.28}$$

where σ_k is an equivalent turbulent Prandtl/Schmidt number for k and μ_{eff} is the effective viscosity defined as the sum of the laminar and turbulent viscosities:

$$\mu_{eff} = \mu + \mu_t \tag{3.29}$$

The production term P_k is obtained by substituting Eq. (3.24) for the Reynolds stresses in:

$$P_k = -\bar{\rho}\widetilde{u_i'' u_j''}\frac{\partial \tilde{u}_i}{\partial x_j} \tag{3.30}$$

Finally, the pressure-work term is usually neglected, giving the following closed form for the turbulent kinetic energy equation:

$$\frac{\partial}{\partial t}(\bar{\rho}k) + \frac{\partial}{\partial x_j}(\bar{\rho}\tilde{u}_j k) = \frac{\partial}{\partial x_j}\left(\frac{\mu_{eff}}{\sigma_k}\frac{\partial k}{\partial x_j}\right) + P_k - \bar{\rho}\varepsilon \tag{3.31}$$

An exact transport equation for the rate of dissipation of turbulent kinetic energy, ε, may also be obtained from the averaged Navier-Stokes equations. However, the derivation of this equation for compressible flow is forbiddingly complex and involves many unknown terms, none of which are amenable to direct measurement (Launder 1983, p. 60). Therefore, as a basis for developing a modelled equation for ε it is of little practical value and thus omitted here. Rather, a model form of the ε-equation has been devised more from dimensional analysis, intuition and analogy such that it is expected to contain similar terms to the k-equation, Eq. (3.31). Thus, the turbulent dissipation rate is found from the following transport equation for ε in the standard $k-\varepsilon$ model:

$$\frac{\partial}{\partial t}(\bar{\rho}\varepsilon)+\frac{\partial}{\partial x_j}(\bar{\rho}\tilde{u}_j\varepsilon)=\frac{\partial}{\partial x_j}\left(\frac{\mu_{eff}}{\sigma_\varepsilon}\frac{\partial \varepsilon}{\partial x_j}\right)+\frac{\varepsilon}{k}(c_{\varepsilon 1}P_k-c_{\varepsilon 2}\bar{\rho}\varepsilon) \tag{3.32}$$

where σ_ε is an equivalent turbulent Prandtl/Schmidt number for ε and $c_{\varepsilon 1}$ and $c_{\varepsilon 2}$ are additional model constants in the production and dissipation terms, respectively. In terms of physical processes, Eq. (3.32) represents a balance between the rate of transport of ε by the mean flow and the rates of its diffusion by the turbulence fluctuations, its generation by vortex stretching and, finally, its destruction by the action of viscosity. Extensive computations reported in the literature with this standard $k-\varepsilon$ turbulence model have mainly used a single set of coefficients given in Table 3.1 (p. 59). A wide variety of thin shear layer and recirculating flows have been successfully simulated with these values. Furthermore, recent interest in developing statistical mechanical descriptions of turbulence using Renormalisation Group (RNG) theory have been able to obtain all of their values independently and also provided a more theoretical basis for the modelled ε-equation (Smirnoff, 1995).

However, despite notable successes the standard $k-\varepsilon$ model has serious limitations. These can largely be attributed to two major weakness in the model:

1. Inadequacy of Eq. (3.24) to describe the complex, non-linear, stress-strain interactions in flows driven by large anisotropy in the stress field, or in swirling flows, with large, rapid, extra strains.

2. Failure of the ε-equation to provide a universally valid description for the way ε evolves in some experimentally measured flows (Launder 1983, Sec. 3).

Since swirl and tumbling motion are prevalent in modern in-cylinder engine flows, the first shortcoming is of particular concern in the present study. Several modifications have been proposed in the literature to account for these effects in the k–ε model, usually by introducing corrections to the eddy viscosity (Eq. 3.26) or additions to the source term of the ε-equation. However, the success of these modifications is debatable and difficult to ascertain for a general problem. A better solution might be to adopt one of the more sophisticated models discussed in the previous sections. Unfortunately, this does not remove the second problem, since the ε-equation (Eq. 3.32), albeit with a modified diffusive term, is usually also adopted within the framework of a full second-moment closure (Sec. 3.2.1) or an algebraic stress model (Sec. 3.2.2). Therefore, errors arising from using an approximate form for the scale-determining equation are common to all three types of turbulence model discussed here. In this respect, the more sophisticated turbulence models gain no advantage over the standard k–ε approach.

3.2.4 Model Selection

The k–ε turbulence model has been selected for the present study for the following main reasons:

1. Numerous multi-dimensional studies of turbulent in-cylinder engine flows have shown good agreement with experimental observations, and where deficiencies occur, these have been well documented.

2. The existing k–ε submodel available in the KIVA-II code can be easily modified for the present study (see below). Whereas, a substantial amount of work would be involved in the implementation and verification of a more sophisticated model. Furthermore, the extra computational effort does not justify the expected improvement in accuracy, in the light of other approximations employed in the combustion and radiation submodels.

3. The k–ε model employed in the present study provides an appropriate basis from which to assess the performance of the more sophisticated turbulence submodels in a the further work.

3.2.5 Modification For Variable Density Flow

During the combustion phase, when the radiative heat transfer is dominant, significant nonhomogenities in density will result from the heat release. The standard k–ε model discussed in Section 3.2.3 is essentially concerned only with shear generated turbulence in uniform density non-reactive flow. In reactive flow, there is also the additional generation and depression of turbulence associated with the effect of density variations, velocity dilatation (volumetric effects) and pressure gradients caused by the flame evolution.

It is assumed that fluctuations in density are properly modelled in terms of the Favre averaged quantities, and that the model constants in Table 3.1, determined for density unweighted equations, are equally applicable to the density-weighted form. This assumption has been made by Jones and Whitelaw (1982) and other researchers, since its validity appears to be generally supported by present experimental evidence.

The effects due to dilatation or velocity divergence are already incorporated in the KIVA-II k–ε submodel by Amsden *et al.* (1989). This results in the appearance of an extra source term in the ε-equation, Eq. 3.31. The modified form accommodating compression and expansion effects is then:

$$\frac{\partial}{\partial t}(\bar{\rho}\varepsilon)+\frac{\partial}{\partial x_j}(\bar{\rho}\tilde{u}_j\varepsilon)=\frac{\partial}{\partial x_j}\left(\frac{\mu_{eff}}{\sigma_\varepsilon}\frac{\partial \varepsilon}{\partial x_j}\right)+\frac{\varepsilon}{k}(c_{\varepsilon 1}P_k-c_{\varepsilon 2}\bar{\rho}\varepsilon)-c_{\varepsilon 3}\bar{\rho}\varepsilon\frac{\partial \tilde{u}_k}{\partial x_k} \qquad (3.33)$$

where the model constant, $c_{\varepsilon 3}$, is taken as unity. This final form is identical to that derived by Grismo (1991, p.75) except that his model constant is taken as 1/3. However, all simulations in the present study use $c_{\varepsilon 3}=1.0$ as recommended by Amsden *et al.* (1989). The negative sign of the dilatation term can be reasoned from an understanding of the rotational nature of the turbulence: compression of the flow corresponds to an increase in vorticity and kinetic energy, and visa versa. Angular momentum is conserved, such that the product of the turbulence velocity scale, $k^{1/2}$, and length scale ($k^{3/2}/\varepsilon$) is constant: i.e. $k^2/\varepsilon=\text{constant}$. Hence, this constraint requires that the turbulent dissipation and kinetic energy both decrease during fluid compression, $\partial\tilde{u}_k/\partial x_k<0$, and increase in an expanding flow, $\partial\tilde{u}_k/\partial x_k>0$. These changes in eddy dissipation rate are thus correctly predicted by the negative source term in Eq. (3.33).

In the exact form of the turbulent kinetic energy equation, Eq. 3.27, arises a correlation between velocity fluctuation and pressure gradient. In variable density, reacting flow, significant inaccuracies may arise from neglecting this term, as is usually the case in the standard form of the $k-\varepsilon$ model for uniform density steady flow (see Section 3.2.3). It seems particularly inconsistent that dilatation effects have been included in the existing KIVA-II $k-\varepsilon$ submodel, but this pressure work term is neglected, even though its affect is of similar importance. Therefore, this deficiency has been corrected in the present study by introducing a modified production term, P_k^*, following the procedure outlined in Grismo (1991, p.76). The pressure correlation can be expanded as follows:

$$\overline{u_i''\frac{\partial p}{\partial x_i}} = \overline{u_i''}\frac{\partial \overline{p}}{\partial x_i} + \frac{\partial}{\partial x_i}(\overline{u_i''p'}) - \overline{p'\frac{\partial u_i''}{\partial x_i}} \tag{3.34}$$

The second term of the right-hand side describes a diffusive processes arising from pressure fluctuations (c.f. diffusion term Eq. (3.22)) and is thus considered to be accommodated by the gradient-diffusion approximation of Eq. (3.28). The third term is considered to have a negligible effect since the fluctuation velocity gradients are largest for the smallest eddies at the so-called Kolmogorov microscales. At these scales, production and dissipation are assumed to be in equilibrium, so the contribution of this term to the small scale turbulence motion is immediately dissipated by viscous action. Therefore, only the first term involving the mean pressure gradient requires attention. Applying an identity for the Favre velocity fluctuation, this term can be reexpressed as:

$$\overline{u_i''}\frac{\partial \overline{p}}{\partial x_i} = -\frac{1}{\overline{\rho}}\overline{\rho' u_i'}\frac{\partial \overline{p}}{\partial x_i} \tag{3.35}$$

then in a similar manner to the gradient-transport approximation of Eq. (3.25) for Favre-averaged quantities, the time-averaged fluctuating term in Eq. (3.35) is replaced by:

$$\overline{u_i''}\frac{\partial \overline{p}}{\partial x_i} = \frac{1}{\overline{\rho}^2}\frac{\mu_t}{\sigma_p}\frac{\partial \overline{\rho}}{\partial x_i}\frac{\partial \overline{p}}{\partial x_i} \tag{3.36}$$

where the turbulent Prantdl/Schmidt number, $\sigma_p = 0.8$, as in previous studies. The standard $k-\varepsilon$ model production term of Eq. (3.31) is then modified for variable density flow as:

$$P^* = P - \frac{1}{\overline{\rho}^2}\frac{\mu_t}{\sigma_p}\frac{\partial \overline{\rho}}{\partial x_i}\frac{\partial \overline{p}}{\partial x_i} \tag{3.37}$$

Note that in making this modification to the source term of k-equation, it is also assumed to be applicable to the source term of the modelled ε-equation. This is conveniently justified with the argument that the generation of ε by pressure-density-interactions is comparable to its generation by viscous stresses, and hence can be proportioned to the corresponding production of turbulent energy by the same factor, $c_{\varepsilon 1} = 1.44$.

3.2.6 Turbulence Closure

Turbulence closure of the Favre-averaged equations in Section 3.1 can now be obtained with the gradient-transport approximations for the Reynolds stresses and turbulent scalar fluxes in Eqs. (3.24) and (3.25) respectively. Then, the laminar transport coefficients (i.e. viscosity, species diffusivity and thermal conductivity) are simply replaced with effective turbulent values as follows:

$$\mu_{eff} = \mu_{air} + \mu_t = \frac{A_1 T^{\frac{3}{2}}}{A_2 + T} + c_\mu \bar{\rho} \frac{k^2}{\varepsilon} \tag{3.38}$$

$$D_{eff} = \frac{\mu_{eff}}{\bar{\rho} \mathrm{Sc}} \tag{3.39}$$

$$K_{eff} = \frac{\mu_{eff} c_P}{\mathrm{Pr}} \tag{3.40}$$

where the constants $A_1 = 1.457 \times 10^{-5}$ g / (cm s K$^{\frac{1}{2}}$), $A_2 = 110.33$ K and Pr = Sc = 0.9.

Note: Pr and Sc are the Prandtl and Schmidt numbers for the turbulent reacting mixture, respectively.

The additional contribution arising from the turbulent fluctuations in each of these expressions results in the effective transport coefficients being much larger than their laminar counterparts. Eq. (3.38) is the final form of Eq. (3.29), with Sutherland's formulae for air to calculate the laminar viscosity and Eq. (3.26) substituted for the turbulent viscosity. Replacing the laminar viscosity by this effective viscosity in the vector equation for momentum transport, Eq. (3.10) then incorporates the laminar-like part of the Reynolds stresses [Eq. (3.24)], but not the turbulent kinetic energy term.

Therefore, the k-term is accommodated by modifying the mean pressure in Eq. (3.10) as follows:

$$\overline{p}^{*} = \overline{p} - \tfrac{2}{3}\overline{\rho}k \tag{3.41}$$

The turbulent momentum equation is then closed.

The effective species diffusivity of Eq. (3.39) replaces the laminar diffusivity in both the species mass and internal energy conservation equations, Eqs. (3.8) and (3.14) respectively. This modified coefficient then includes the additional species transport arising from fluctuations in concentration gradients which, in turn, are associated with fluctuating heat flux gradients in the internal energy equation.

Finally, the internal energy flux arising from turbulent convection in Eq. (3.14) is modelled as part of the heat flux term using the effective thermal conductivity given by Eq. (3.40). A gradient-transport approximation [Eq. (3.25)] would ordinarily assume that the energy flux is proportional to the internal energy gradient, instead of the temperature gradient, as here. However, these two gradients are proportional for ideal gases, provided that gradients in specific heat are neglected (cf. Eq. 3.19). Ideal gas behaviour for the reacting mixture has already been assumed in the state relations of Section 3.1.6.

Thus, suitable approximations have been found for all of the unknown turbulence correlations. However, analysis of the internal energy and turbulent kinetic energy transport equations in their present form indicates that they both contain source contributions from turbulent viscous dissipation. This inconsistency is avoided by removing the viscous dissipation term, $\overline{\Phi}$, from the internal energy equation, Eq. (3.14), and replacing it by the rate of turbulent energy decay, $\rho\varepsilon$. Therefore, the turbulent viscous stresses are considered to create turbulent kinetic energy, which later decays to thermal energy, by the action of the decay term, $\rho\varepsilon$.

Summarised in Eqs. (3.42-51) are the final forms of the Favre-averaged Navier Stokes equations, together with the two transport equations of the k–ε model. Expressions for the state relations and effective transport coefficients have also been re-stated for completeness, together with the values used for all the model constants.

$$\frac{\partial}{\partial t}(\overline{\rho}\tilde{Y}_s)+\frac{\partial}{\partial x_i}(\overline{\rho}\tilde{u}_i\tilde{Y}_s)=\frac{\partial}{\partial x_i}\left(\overline{\rho}D_{eff}\frac{\partial\tilde{Y}_s}{\partial x_i}\right)+\dot{\overline{\rho}}_s, \qquad s=1,2,\ \ldots\ ,N \tag{3.42}$$

$$\frac{\partial\overline{\rho}}{\partial t}+\frac{\partial}{\partial x_i}(\overline{\rho}\tilde{u}_i)=0 \tag{3.43}$$

$$\frac{\partial}{\partial t}(\overline{\rho}\tilde{u}_i)+\frac{\partial}{\partial x_j}(\overline{\rho}\tilde{u}_i\tilde{u}_j)=-\frac{\partial\overline{p}}{\partial x_i}-\tfrac{2}{3}\frac{\partial}{\partial x_i}(\overline{\rho}k)+\frac{\partial\overline{\sigma}_{ij}}{\partial x_j}+\overline{\rho}\,\overline{g}_{ij} \tag{3.44}$$

$$\frac{\partial}{\partial t}(\overline{\rho}\tilde{I})+\frac{\partial}{\partial x_i}(\overline{\rho}\tilde{u}_i\tilde{I})=-\overline{p}\frac{\partial\tilde{u}_i}{\partial x_i}-\frac{\partial\overline{q}_i}{\partial x_i}-\overline{\rho}\varepsilon+\overline{\dot{Q}}_{chem} \tag{3.45}$$

$$\frac{\partial}{\partial t}(\overline{\rho}k)+\frac{\partial}{\partial x_j}(\overline{\rho}\,\tilde{u}_jk)=\frac{\partial}{\partial x_j}\left(\frac{\mu_{eff}}{\sigma_k}\frac{\partial k}{\partial x_j}\right)+P_k^*-\overline{\rho}\varepsilon \tag{3.46}$$

$$\frac{\partial}{\partial t}(\overline{\rho}\varepsilon)+\frac{\partial}{\partial x_j}(\overline{\rho}\,\tilde{u}_j\varepsilon)=\frac{\partial}{\partial x_j}\left(\frac{\mu_{eff}}{\sigma_\varepsilon}\frac{\partial\varepsilon}{\partial x_j}\right)+\frac{\varepsilon}{k}(c_{\varepsilon1}P_k^*-c_{\varepsilon2}\overline{\rho}\varepsilon)-c_{\varepsilon3}\overline{\rho}\varepsilon\frac{\partial\tilde{u}_k}{\partial x_k} \tag{3.47}$$

where:

$$\overline{\sigma}_{ij}=\mu_{eff}\left[\left(\frac{\partial\tilde{u}_i}{\partial x_j}+\frac{\partial\tilde{u}_j}{\partial x_i}\right)-\tfrac{2}{3}\delta_{ij}\frac{\partial\tilde{u}_k}{\partial x_k}\right] \tag{3.48}$$

$$\overline{q}_i=-K_{eff}\frac{\partial\tilde{T}}{\partial x_i}-\overline{\rho}D_{eff}\sum_s h_s(\tilde{T})\frac{\partial\tilde{Y}_s}{\partial x_i}+\overline{q}_{r,i} \tag{3.49}$$

$$P_k^*=\overline{\Phi}-\tfrac{2}{3}\overline{\rho}k\left(\frac{\partial\tilde{u}}{\partial x}+\frac{\partial\tilde{v}}{\partial y}+\frac{\partial\tilde{w}}{\partial z}\right)-\frac{1}{\overline{\rho}^2}\frac{\mu_t}{\sigma_p}\frac{\partial\overline{\rho}}{\partial x_i}\frac{\partial\overline{p}}{\partial x_i} \tag{3.50}$$

$$\begin{aligned}\overline{\Phi}=\mu_{eff}\Bigg[&2\left(\frac{\partial\tilde{u}}{\partial x}\right)^2+2\left(\frac{\partial\tilde{v}}{\partial y}\right)^2+2\left(\frac{\partial\tilde{w}}{\partial z}\right)^2+\left(\frac{\partial\tilde{u}}{\partial y}+\frac{\partial\tilde{v}}{\partial x}\right)^2+\left(\frac{\partial\tilde{v}}{\partial z}+\frac{\partial\tilde{w}}{\partial y}\right)^2\\&+\left(\frac{\partial\tilde{w}}{\partial x}+\frac{\partial\tilde{u}}{\partial z}\right)^2-\tfrac{2}{3}\left(\frac{\partial\tilde{u}}{\partial x}+\frac{\partial\tilde{v}}{\partial y}+\frac{\partial\tilde{w}}{\partial z}\right)^2\Bigg]\end{aligned} \tag{3.51}$$

with effective transport coefficients given by Eqs. (3.38-40):

$$\mu_{eff}=\frac{A_1T^{\frac{3}{2}}}{A_2+T}+c_\mu\overline{\rho}\frac{k^2}{\varepsilon}, \qquad D_{eff}=\frac{\mu_{eff}}{\overline{\rho}\mathrm{Sc}}, \qquad K_{eff}=\frac{\mu_{eff}c_P}{\mathrm{Pr}}$$

Table 3.1 Extended $k-\varepsilon$ turbulence model constants.

c_μ	$c_{\varepsilon1}$	$c_{\varepsilon2}$	$c_{\varepsilon3}$	σ_k	σ_ε	σ_p	Pr	Sc
0.09	1.44	1.92	1.0	1.0	1.3	0.8	0.9	0.9

3.3 Combustion and Ignition Models

Turbulent combustion in engines is characterised by a complex multi-step reaction process involving several hundred intermediate species. The exact nature of the coupling between the turbulence and chemistry is not well understood, and the problem is further compounded by uncertainties in relation to the fuel chemistry and reaction mechanisms of practical fuel hydrocarbon blends. Accordingly, a simplified reaction scheme is adopted in the KIVA-II code which uses a limited set of chemical reactions symbolised by:

$$\sum_s a_{s,r} x_s \rightleftharpoons \sum_s b_{s,r} x_s \tag{3.52}$$

where x_s represents one mole of species s and $a_{s,r}$ and $b_{s,r}$ are integral stoichiometric coefficients for species appearing as reactants and products respectively, for reaction r. The chemical species formation rates in the conservation equation for species mass fraction, Eq. (3.42), are then given by:

$$\overline{\dot{\rho}}_s = W_s \sum_r (b_{s,r} - a_{s,r}) \overline{\dot{\omega}}_r \tag{3.53}$$

and the chemical heat source in the internal energy equation, Eq. (3.45), by:

$$\overline{\dot{Q}}_{chem} = \sum_r Q_r \overline{\dot{\omega}}_r \tag{3.54}$$

where $\dot{\omega}_r$ is the reaction rate, Q_r is the negative heat of reaction at absolute zero,

$$Q_r = \sum_s (a_{s,r} - b_{s,r})(\Delta h_f^o)_s \tag{3.55}$$

and $(\Delta h_f^o)_s$ is the heat of formation of species s at absolute zero.

The problem is then reduced to finding appropriate expressions for the reaction rates, $\dot{\omega}_r$.

In KIVA-II the reactions are subdivided into two classes: those that proceed kinetically and those that are assumed to be in chemical equilibrium. The reactions used in the present study are classified as shown in Table 3.2. For each type of mechanism an appropriate procedure is used to evaluate the reaction rate. Sections 3.3.1 and 3.3.2 describe, respectively, the chemical equilibrium and kinetic submodels in KIVA-II.

In the discussion accompanying the kinetic model, important weaknesses are noted in the approach which question its ability to adequately simulate the complex turbulence-chemistry combustion interactions. Hence, subsequent sections focus on the development of a hybrid model based on the existing kinetic model and the eddy dissipation concept of Magnussen and Hjertager (1976). An empirical expression is then obtained for the mean reaction rate which includes the effects of both chemical kinetics *and* turbulent mixing. A discussion of alternative modelling approaches, including methods based on PDF formulations (i.e. Eq. (3.3)), can be found in Jones and Whitelaw (1982, 1984), Ramos (1989) and Warnatz *et al.* (1996). For brevity these have not been include here. Finally, details of the approach used to simulate spark ignition are given, together with a model for end-gas autoignition.

Table 3.2 Classification of chemical reactions

Fuel oxidation: kinetic/mixing-controlled model[a]

$$C_3H_8 + O_2 \longrightarrow 3CO_2 + 4H_2O \quad \text{(a)}$$

$$2C_8H_{18} + 25O_2 \longrightarrow 16CO_2 + 18H_2O \quad \text{(b)}$$

Extended Zeldovich mechanism: kinetic model

$$O_2 + 2N_2 \rightleftharpoons 2NO + 2N$$

$$N_2 + 2O_2 \rightleftharpoons 2NO + 2O$$

$$N_2 + 2OH \rightleftharpoons 2NO + 2H$$

Chemical equilibrium:

$$H_2 \rightleftharpoons 2H$$

$$O_2 \rightleftharpoons 2O$$

$$N_2 \rightleftharpoons 2N$$

$$2OH \rightleftharpoons O_2 + H_2$$

$$4OH \rightleftharpoons O_2 + 2H_2O$$

$$2CO_2 \rightleftharpoons O_2 + 2CO$$

[a]Fuel oxidation for: (a) propane and (b) iso-octane.

3.3.1 Equilibrium Reactions

The equilibrium rates are implicitly determined by the constraint conditions:

$$\prod_s \bar{c}_s^{\,b_{s,r}-a_{s,r}} = K_c^r(\tilde{T}) \tag{3.56}$$

where the mean molar concentration, $\bar{c}_s$, for each species, s, is given by:

$$\bar{c}_s = \bar{\rho}\frac{\tilde{Y}_s}{W_s} \tag{3.57}$$

and K_c^r is the concentration equilibrium constant for reaction r obtained from a curve fit to experimental data. These constraint conditions then constitute a coupled nonlinear system of equations which is solved by an iterative procedure. The details of this iteration scheme, which includes the effects of heat release from the equilibrium reactions on K_c^r, may be found in Appendix J of Amsden *et al.* (1989, pp. 129-134), together with additional references. A set of six independent equilibrium reactions for CO, CO_2, H_2O, H_2, O_2, N_2, H, O, N and OH are modelled in the present study as shown in Table 3.2. Convergence was quick and the scheme was stable for all the problems considered.

3.3.2 Kinetic Reactions

The progress rates for the kinetic chemical reactions are expressed in terms of instantaneous molar concentrations, c_s for each species s by:

$$\dot{\omega}_r = k_{f,r}\prod_s c_s^{a^*_{s,r}} - k_{b,r}\prod_s c_s^{b^*_{s,r}} \tag{3.58}$$

where $k_{f,r}$, $k_{b,r}$ are the forward and backward rate coefficients, respectively. These are assumed to be of a general Arrhenius form:

$$\begin{aligned} k_{f,r} &= A_{f,r}T^{\zeta_{f,r}}\exp(-E_{f,r}/R_uT) \\ k_{b,r} &= A_{b,r}T^{\zeta_{b,r}}\exp(-E_{b,r}/R_uT) \end{aligned} \tag{3.59}$$

where $A_{f,r}$, $A_{b,r}$ are the pre-exponential factors; $\zeta_{f,r}$, $\zeta_{b,r}$ are the temperature exponents, and $E_{f,r}$, $E_{b,r}$ are the activation energies, of the forward and backward reactions, respectively. Note that in Eq. (3.58) the reaction orders $a^*_{s,r}$ and $b^*_{s,r}$ are not necessarily equal to $a_{s,r}$ and $b_{s,r}$ in Eq. (3.52)

3.3.3 KIVA-II Kinetic Model

Substituting the Eqs. (3.58) into the turbulent Reynolds mass-averaged transport equations results in a mean rate with a series expansion for the exponential terms in Eq. (3.59). This introduces a rapidly expanding hierarchy of turbulent temperature-mass fraction-density correlations around the mean temperature (see Ahmadi-Befrui *et al.* 1981). Truncation of the high-order terms in this series is only valid if the fluctuations are small; a condition rarely satisfied in premixed turbulent chemically reacting flow. Furthermore, the task of determining the remaining terms is made even more formidable by the multiplicity of species and reaction mechanisms which characterise the combustion of practical hydrocarbon fuels. The reaction rates are in general stiff, that is, their time scales differ by many orders of magnitude from each other (Ramos 1989, p.47). Therefore, in KIVA-II, the fuel oxidation is characterised by simplified reaction mechanism involving a single irreversible one-step reaction of the form:

$$\{1\text{kg fuel } (F)\} + \{s \text{ oxidiser kg } (O)\} \xrightarrow{k_f} \{(1+s) \text{ kg product } (P)\} \qquad (3.60)$$

The global reaction rate is then expressed following Westbrook and Dryer (1981) as:

$$\overline{\dot{\omega}}_{kinetic} = -A\tilde{T}^n \exp(-E_a/R_u\tilde{T})\overline{c}_F^a\overline{c}_O^b \qquad (3.61)$$

where A is the forward pre-exponential factor, n is the temperature exponent, E_a is an effective activation energy and a, b are concentration exponents for the fuel and oxidiser, respectively. Setting $n = 0$, Westbrook and Dryer tuned the remaining modelling parameters to the rich and lean flammability limits, as well as the dependence of flame speed on pressure and equivalence ratio. Their values for the two fuels propane (C_3H_8) and iso-octane (C_8H_{18}) are shown in Table 3.3. These are used in the present study, but with moderate scaling of the pre-exponential factor A, by a factor C_A, to fit experimental data (see Secs. 6.3.2 and 6.4.3). This is not unreasonable since the model is derived for laminar conditions and requires case-by-case tuning of the reaction rate in different turbulent regimes. Diwakar (1984) showed that the pre-exponential factor correlates with the equivalence ratio and the residual mass fraction in combustion studies of a homogeneous-charge engine. Present calculations have found that the value of A is extremely sensitive to the mesh type and resolution in the numerical model. Too high a value results in an excessive heat release and abrupt rise in pressure, whereas with too low a value the combustion is not sustained.

Table 3.3 Single-step reaction rate parameters (Westbrook and Dryer 1987).

Fuel	A	E_a	a	b
C_3H_8	8.6×10^{11}	30.0	0.10	1.65
C_8H_{18}	4.6×10^{11}	30.0	0.25	1.50

Amsden (1993, p.38) suggests installing a turbulent mixing-controlled model which mitigates this sensitivity, such that the tabular values for A require less adjustment.

3.3.4 Eddy Break-Up Models: The Eddy Dissipation Concept

Spalding (1971, 1976) proposed that if the chemical kinetics is fast (i.e. a fast-chemistry assumption), then turbulent-mixing is the rate limiting process and, in particular, the rate of small-scale reactant mixing characterised by the turbulent kinetic energy, k, and its rate of dissipation, ε. i.e. Regions of unburned fluid are successively broken down by turbulence into smaller structures until the reactants are sufficiently mixed at a fine scale for heat conduction and chemical reaction. This concept resulted in the development of the so-called eddy-break-up (EBU) model for turbulent combustion, based on an intuitive argument that the combustion rate is proportional to the inverse of the turbulent time scale, k/ε. The mean fuel consumption rate is modelled as:

$$\bar{\dot{\rho}}_F = -C_{EBU}\left(\overline{Y_F'^2}\right)^{\frac{1}{2}}\bar{\rho}\frac{\varepsilon}{k} \tag{3.62}$$

where C_{EBU} is a model constant and $\overline{Y_F'^2}$ is the mean squared fluctuation of fuel mass fraction.

The eddy dissipation concept (EDC) proposed by Magnussen and Hjertager (1976), and later extended by Magnussen (1980, 1989), is closely related to the EBU model. EDC gives an empirical expression for the mean reaction rate based on the assumption that chemical reaction occurs in regions only where both fuel and oxidiser coexist, and mix at a sufficiently high temperature. Magnussen (1989) states that these regions consist of *fine structures*, which occupy only a small fraction of the flow. Kinetic energy is transferred from the mean flow to these fine structures through a cascade of turbulent interactions at intermediate scales. This is the basis of an analysis which enables expressions for the fine structure state to be developed.

EDC assumes that the fluid state is determined by the fine structure state, the surrounding state and the fraction of fine structures. For brevity only the final expressions given by Gran (1994) are presented here, since full details of their development can be found in the above references. In these expressions, superscripts * and $^\circ$ refer to the fine structures and surrounding fluid respectively. The turbulent fine structures are assumed to be concentrated in *fine-structure regions*, the mass fraction of the flow occupied by such regions is expressed as:

$$\gamma = \left(\frac{3C_{D2}}{4C_{D1}^2}\right)^{1/4}\left(\frac{\nu^*\varepsilon}{k^2}\right)^{1/4} \tag{3.63}$$

where $C_{D1} = 0.134$ and $C_{D2} = 0.5$ are model constants. Then the mass fraction occupied by the fine structures is modelled as γ^3. On the basis of simple geometrical considerations the time scale for the mass transfer rate between the fine structures and the surroundings is estimated as:

$$\tau^* = \left(\frac{C_{D2}}{3}\right)^{1/2}\left(\frac{\nu^*}{\varepsilon}\right)^{1/2} = \left(\frac{C_{D2}}{3}\right)^{1/2}\tau_\eta \tag{3.64}$$

where τ_η is the Kolmogorov time scale of the smallest scale motions. Hence, γ^3/τ^* would seem an appropriate expression for the rate of mass exchange between the fine structures and surroundings. However, Magnussen (1989) found that this tended to under predict the mass exchange rate, since it fails to consider the higher rate of entrainment of unreacted fluid concentrated in the fine structure regions enclosing the fine structures. Therefore, the mass exchange rate is modelled as:

$$\dot{m}^* = \frac{\gamma^2}{\tau^*} = \frac{3}{2C_{D1}}\cdot\frac{\varepsilon}{k} \tag{3.65}$$

Then the mean species reaction rate is given by:

$$\overline{\dot{\rho}}_s = \overline{\rho}\dot{m}^*\chi(Y_s^\circ - Y_s^*) \tag{3.66}$$

where χ is the fraction of fine structures where reaction occurs, defined later. The Favre-averaged mass fractions for each chemical species, *s*, are related to their fine structure and surroundings values by:

$$\tilde{Y}_s = \gamma^3\chi Y_s^* + (1-\gamma^3\chi)Y_s^\circ \tag{3.67}$$

An expression for the mean fuel consumption rate can now be developed from Eqs. (3.62-67). It is assumed that the fuel combustion is suitably represented by the same single irreversible one-step reaction as used for the KIVA-II kinetic model in Eq. (3.61). It is further assumed that this reaction progresses at an infinite-rate, such that the reacting fine structures achieve chemical equilibrium: i.e. the fast-chemistry limit. Then, the mass fraction of the reactant with the lowest availability in the fine structures is instantly consumed, such that the reaction rate is determined by its supply from the surroundings. Hence, the mass fraction of this reactant is expected to be very small in the fine structures (i.e. $Y_s^* \approx 0$), such that combination of Eqs. (3.66) and (3.67) enables the rate of fuel consumption to be described in terms of the Favre-averaged species mass fraction as:

$$\overline{\dot{\rho}}_F = \overline{\rho}\frac{\dot{m}^*\chi}{1-\gamma^3\chi}\hat{Y}_{\min} \tag{3.68}$$

where the following set of scaled mass fractions apply:

$$\hat{Y}_{\min} = \min[\hat{Y}_F, \hat{Y}_O], \qquad \hat{Y}_F = \frac{\tilde{Y}_F}{1}, \qquad \hat{Y}_O = \frac{\tilde{Y}_O}{s}, \qquad \hat{Y}_P = \frac{\tilde{Y}_P}{1+s} \tag{3.69}$$

Here $\tilde{Y}_F$, $\tilde{Y}_O$ and $\tilde{Y}_P$ are the local fuel, oxygen and products averaged mass fractions respectively, and s is the stoichiometric oxygen requirement to burn 1 kg of fuel. Magnussen (1989) suggests the following model for χ (also see Gran 1994, p.43):

$$\chi = \chi_1 \cdot \chi_2 \cdot \chi_3, \qquad 0 \le \chi \le 1 \tag{3.70}$$

where χ_1 is a correlation factor for non-premixedness of the reactants:

$$\chi_1 = \frac{(\hat{Y}_{\min} + \hat{Y}_P)^2}{(\hat{Y}_F + \hat{Y}_P)(\hat{Y}_O + \hat{Y}_P)} \tag{3.71}$$

χ_2 expresses the degree of heating from hot products, since not all the fine structures are sufficiently heated to react:

$$\chi_2 = \min[\alpha, 1], \qquad \alpha = \frac{\hat{Y}_P}{\gamma(\hat{Y}_P + \hat{Y}_{\min})} \tag{3.72}$$

and χ_3 limits the reaction rate due to lack of reactants:

$$\chi_3 = \min[\beta, 1] \qquad \beta = \frac{\gamma(\hat{Y}_P + \hat{Y}_{\min})}{\hat{Y}_{\min}} \tag{3.73}$$

Scenarios (for more details of this analysis, see Gran 1990, pp. 29-35):

1. Regions of high product concentration: $\chi_2 = 1$. Where reactants coexist equally $\chi_3 = \beta$, otherwise if one (or both) reactants are unavailable, $\chi_3 = 1$.

2. Regions of low product concentration: $\chi_2 = \alpha$. Always assumed that $\chi_3 = \beta$ such that fraction of hot products is rate limiting.

The mean fuel consumption rate, Eq. (3.65), can then be expressed in the compact form:

$$\overline{\dot{\rho}}_F = \overline{\rho} \frac{3}{2C_{D1}} \cdot \frac{\chi_1}{(1-\gamma^3\chi)} \cdot \frac{\varepsilon}{k} \min\left[\hat{Y}_{\min}, \hat{Y}_P, (\hat{Y}_{\min} + \hat{Y}_P)\gamma\right] \tag{3.74}$$

Note that the factor $1/(1-\gamma^3\chi)$ is generally very close to unity and has been omitted in some studies (e.g. Gran 1994). The strong appeal of the EDC model over the original eddy-breakup expression of Spalding is that it does not require prediction of the fluctuation in species mass fraction. Consequently, there is no need to solve additional equations for the concentration fluctuations as in a PDF approach. Gran (1994) demonstrated that EDC can give essentially similar results to those from a more complex, yet less general, laminar flamelet combustion model. Gran also concludes in this study that finite-rate kinetics should be incorporated into the EDC approach to ensure good agreement with experimental results.

3.3.5 Hybrid Kinetic/EDC Model

The KIVA-II kinetic combustion model has been adapted to account for both turbulent mixing and chemical kinetics. The new hybrid approach seeks to introduce the turbulent intermittency of the reacting species considered by the EDC model and retain the phenomena governed by chemical kinetics: ignition, pollutant formation, extinction, etc. First, a mean EDC progress rate, $\overline{\dot{\omega}}_{EDC}$, for the fuel combustion reaction is obtained by substituting Eq. (3.74) for the fuel consumption rate into Eq. (3.53) and rearranging. Then, its harmonic average is taken with the original kinetic reaction rate of Eq. (3.61), to give the combined expression:

$$\overline{\dot{\omega}}_{hybrid} = C_B \cdot \frac{\overline{\dot{\omega}}_{EDC} \cdot \overline{\dot{\omega}}_{kinetic}}{\overline{\dot{\omega}}_{EDC} + \overline{\dot{\omega}}_{kinetic}} \tag{3.75}$$

C_B is an adjustable constant for tuning the harmonic rate (see Secs. 6.3.2 and 6.4.3).

The original kinetic rate expression of Eq. (3.61) is then replaced directly by Eq. (3.75) in the KIVA-II numerical scheme. This integration method defines a constrained rate expression which prevents the density of any species from being driven negative regardless of the time step size (see Amsden *et al.* 1989, p.128). The form of Eq. (3.75) enables the mean reaction rate of the new hybrid combustion model to be incorporated into this scheme without further code modifications being required.

Finally, it is usual to assume that the turbulent mixing and chemical kinetic behaviour in spark-ignition combustion closely follows that of a premixed flame, as distinct from nonpremixed reaction. However, the present hybrid kinetic/EDC model is applicable to both regimes, such that simulations of Diesel engine combustion would also be viable in a subsequent study.

3.3.6 Spark Ignition

Ideally, an exact simulation of spark ignition requires that the processes present in the breakdown and arc phases of the ignition discharge are accurately resolved. See Heywood (1988, Sec. 9.5, p.427) for a detailed description of these. Notably, it is during the arc phase that the exothermic reactions which lead to a self-propagating flame kernel develop. However, the heat transfer characteristics and reactions mechanisms involved are so complex that a vastly simplified model must be adopted in a multidimensional code.

Therefore, ignition is simulated by adding internal energy at a uniform rate to computational cells in the spark plug region until the local temperature is raised to a cut-off input value (e.g. 1600 K). This rate is tuned to the minimum required for a self-propagating flame kernel to be established (see Amsden *et al.* 1989, p.81). Rather than supplying energy directly to the charge mixture, it can be provided indirectly as the exothermic heat of reaction in Eq. (3.60). Ignition is then modelled by converting the fuel to products in a few computational cells. However, this approach ignores processes such as evaporation and premixing that occur prior to mixing. Ramos (1989, p. 346) suggests a more sophisticated approach to simulating the heat addition rate, yet admits that this still represents a highly idealised approximation. Assessment of this and other methods requires further work.

3.3.7 Autoignition & Knock

A model to simulate end-gas autoignition in spark-ignition engines has been incorporated into the KIVA-II code according to Blunsdon (1994a), based on the popular Shell model (Halstead *et al.* 1975, 1977; Hirst and Kirsch 1980). This enabled several investigations to be conducted in the present study in which autoignition is induced in an iso-octane/air mixture.

Experimental studies of high pressure autoignition, using a wide variety of hydrocarbon fuels, have shown the following principal features (Halstead *et al.* 1975, 1977):

1. A sharp, well-defined two-stage ignition, i.e. slightly exothermic reactions in a *cool flame* leading to autoignition, followed by rapid high-temperature reactions in a *hot flame*.

2. Transition from two-stage ignition to single-stage ignition with increasing temperature.

3. A limited temperature rise ($< 200\,K$) in the cool flame period, due to reaction quenching, followed by a rapid rise in temperature after autoignition, typically about 10^7 K/s.

4. A pronounced region of 'negative temperature coefficient' in which the total ignition delay increases with increasing temperature (see Halstead *et al.* 1975, p524 for detail).

The Shell model was proposed as a generalised kinetic model capable of simulating this autoignition behaviour with only a very small number of characteristic reactions. Rather than pursuing the details of oxidation chemistry, this model is designed only to predict the overall ignition behaviour. Several more recent models have been proposed which attempt to provide more information concerning the preignition heat release and evolution of key chemical species (e.g. Li *et al.* 1996, Moses *et al.* 1995). These include the formation of the oxidation product carbon monoxide, CO and other species classes. As CO has a strong infrared radiative signature this would be a interesting model for a dedicated knock/radiation investigation. However, the more detailed kinetic schemes employed in these newer models are not as amenable to inclusion in the present numerical scheme. Accordingly, the reduced Shell model is preferred for the present study, which is

primarily concerned with the correct prediction of the ignition delay, prior to the onset of the hot flame reactions, in which the radiative combustion products are largely formed.

The following degenerate chain-branching reaction mechanism is employed in Shell model (Halstead *et al.* 1977):

$$\mathrm{RH} + \mathrm{O_2} \xrightarrow{k_q} 2\overline{\mathrm{R}} \qquad \text{primarily initiation} \qquad (3.76)$$

$$\overline{\mathrm{R}} \xrightarrow{k_p} \overline{\mathrm{R}} + \mathrm{P} + \text{heat} \qquad \text{propagation cycle} \qquad (3.77)$$

$$\overline{\mathrm{R}} \xrightarrow{f_1 k_p} \overline{\mathrm{R}} + \mathrm{B} \qquad \text{propagation forming B} \qquad (3.78)$$

$$\overline{\mathrm{R}} + \mathrm{Q} \xrightarrow{f_2 k_p} \overline{\mathrm{R}} + \mathrm{B} \qquad \text{propagation forming B} \qquad (3.79)$$

$$\overline{\mathrm{R}} \xrightarrow{f_3 k_p} \text{out} \qquad \text{linear termination} \qquad (3.80)$$

$$\overline{\mathrm{R}} \xrightarrow{f_4 k_p} \overline{\mathrm{R}} + \mathrm{Q} \qquad \text{propagation forming Q} \qquad (3.81)$$

$$2\overline{\mathrm{R}} \xrightarrow{k_t} \text{out} \qquad \text{quadratic termination} \qquad (3.82)$$

$$\mathrm{B} \xrightarrow{k_B} 2\overline{\mathrm{R}} \qquad \text{degenerate branching} \qquad (3.83)$$

This scheme involves the hydrocarbon fuel (RH), oxygen, radicals (R) formed from the fuel, products (P), degenerate-branching agent (B) and an autocatalytic product (Q), introduced to ensure a rapid chain acceleration at the second stage of ignition. R, B and Q are generic chemical entities, such that Eqs. (3.76-83) express a set of generalised reactions. In particular, species R represents the cumulative behaviour of all the propagation-chain radicals in local equilibrium (as signified by an overbar). For each reaction the rate parameters are fitted so that the measured ignition delays are correctly predicted. These all have an Arrhenius form, except for the global propagation rate, k_p, which is given by:

$$k_p = \frac{1}{1/k_{p_1}[\mathrm{O_2}] + 1/k_{p_2} + 1/k_{p_3}[\mathrm{RH}]} \qquad (3.84)$$

where $k_{p_i}\,(i = 1,2,3)$ are Arrhenius expressions describing the rate-determining propagation steps and the brackets [ ] denote the mean molar concentration of the enclosed chemical species (c.f. Eq. (3.57)).

The coefficients f_j introduce extra flexibility when fitting the rates and are given by:

$$f_j = f_j^{\circ}[\mathrm{O_2}]^{x_j}[\mathrm{RH}]^{y_j}, \qquad j = 1,2,3,4 \qquad (x_2 = y_2 = 0) \tag{3.85}$$

where f_j° are also expressed in Arrhenius form.

To implement the Shell model into a multidimensional code, several modifications to the reaction set in Eqs. (3.76-83) are required to ensure mass conservation is not violated. (Originally the model was developed for computations only up to the second stage of ignition.) Following the procedure of Schäpertöns and Lee (1985), the consumption of fuel and oxygen per propagation cycle is *increased* to balance the production of B and Q in Eqs. (3.78) and (3.81) which violate mass conservation. Assuming that the fuel structure is $\mathrm{C_nH_{2m}}$, and given that two hydrogen atoms are abstracted each propagation cycle, then Eq. (3.77) is replaced by:

$$\overline{\mathrm{R}} + (1+\alpha)\left[\frac{1}{m}\mathrm{RH} + \beta\mathrm{O_2}\right] \xrightarrow{k_p} \overline{\mathrm{R}} + \mathrm{P} + f_1\mathrm{B} + f_4\mathrm{Q} + \text{heat} \tag{3.86}$$

$$\mathrm{P} = \frac{n}{m}(\gamma - 1)\mathrm{CO_2} + \frac{n}{m}\gamma\,\mathrm{CO} + \mathrm{H_2O} \tag{3.87}$$

where the coefficients α, β and γ are given by:

$$\alpha = \frac{f_1 W_{\mathrm{B}} + f_4 W_{\mathrm{Q}}}{W_{\mathrm{RH}}/m + \beta W_{\mathrm{O_2}}}, \qquad \beta = \frac{n(2-\gamma)+m}{2m}, \qquad \gamma = \mathrm{CO/CO_2\ ratio} \tag{3.88}$$

The species R, B and Q molecular weights are related by: $W_{\mathrm{B}} = W_{\mathrm{Q}} = 2W_{\overline{\mathrm{R}}} = W_{\mathrm{RH}} + W_{\mathrm{O_2}}$

Finally, to ensure mass conservation throughout the system, Schäpertöns and Lee (1985) convert the radicals to inert nitrogen in the terminating reactions expressed by Eqs. (3.80) and (3.82).

$$\overline{\mathrm{R}} \xrightarrow{f_3 k_p} \delta\mathrm{N_2}, \qquad 2\overline{\mathrm{R}} \xrightarrow{k_t} 2\delta\mathrm{N_2} \qquad \text{where} \qquad \delta = \frac{W_{\mathrm{R}}}{W_{\mathrm{N_2}}} \tag{3.89}$$

An alternative (and perhaps more realistic scheme) is to covert the radicals to products, particularly in light of the fact that species R, B and Q are locally removed as products

when the hot flame reactions are established: this modification should be considered in a future work. From the present reaction scheme, nine rate equations for the concentration of each species are constructed as follows:

$$\frac{d[\mathrm{RH}]}{dt} = -k_q[\mathrm{RH}][\mathrm{O_2}] - \frac{\alpha+1}{m}k_p[\overline{\mathrm{R}}] \tag{3.90}$$

$$\frac{d[\mathrm{O_2}]}{dt} = -k_q[\mathrm{RH}][\mathrm{O_2}] - (a+1)\beta\, k_p[\overline{\mathrm{R}}] \tag{3.91}$$

$$\frac{d[\overline{\mathrm{R}}]}{dt} = 2k_q[\mathrm{RH}][\mathrm{O_2}] + 2k_B[\mathrm{B}] - 4k_t[\overline{\mathrm{R}}]^2 - f_3k_p[\overline{\mathrm{R}}] \tag{3.92}$$

$$\frac{d[\mathrm{B}]}{dt} = f_1k_p[\overline{\mathrm{R}}] + f_2k_p[\mathrm{Q}][\overline{\mathrm{R}}] - k_B[\mathrm{B}] \tag{3.93}$$

$$\frac{d[\mathrm{Q}]}{dt} = f_4k_p[\overline{\mathrm{R}}] - f_2k_p[\mathrm{Q}][\overline{\mathrm{R}}] \tag{3.94}$$

$$\frac{d[\mathrm{CO}]}{dt} = \frac{n}{m}\gamma\, k_p[\overline{\mathrm{R}}] \tag{3.95}$$

$$\frac{d[\mathrm{CO_2}]}{dt} = \frac{n}{m}(1-\gamma)k_p[\overline{\mathrm{R}}] \tag{3.96}$$

$$\frac{d[\mathrm{H_2O}]}{dt} = k_p[\overline{\mathrm{R}}] \tag{3.97}$$

$$\frac{d[\mathrm{N_2}]}{dt} = \delta f_3k_p[\overline{\mathrm{R}}] + 4\delta k_t[\overline{\mathrm{R}}]^2 \tag{3.98}$$

This system of coupled ordinary differential equations (ODEs) is then integrated to determine the time dependence of the species concentrations. These concentrations decay (or grow) from their initial values at widely varying rates such that the system exhibits *stiff* behaviour. Hence, a solver for systems of stiff ODEs is required. Kuo (1986, p.156) lists standard packages, but the present solver combines several short canned routines from Press *et al.* (1992). These employ a Kaps-Rentrop algorithm to implicitly integrate the eight ODEs with automatic adjustment of the time stepsize to ensure numerical stability.

The autoignition model is arranged to coexist alongside the high temperature reaction scheme in KIVA-II. Initial values for the chemical species concentrations are passed to the submodel, which then subcycles the ODE solver to integrate the rate equations over the time step imposed by the KIVA-II numerical scheme. The species concentrations are updated and heat source in Eq. (3.54) is incremented to account for the cool flame heat release by:

$$\Delta\overline{\dot{Q}}_{chem} = q\,(\alpha+1)\,k_p\left[\overline{\mathrm{R}}\right] \tag{3.99}$$

where q is the negative heat of reaction or exothermicity of the reaction in Eq. (3.86) when $1/m$ moles of fuel are abstracted per propagation cycle. The high temperature combustion model is then called to determine the progress of the hot flame reactions. If the low and high temperature reactions are allowed unrestricted competition, diffusion and convection of heat ahead of the flame front causes immediate autoignition in circumstances where normal flame propagation would be expected. To avoid this problem Schäpertöns and Lee (1985) suggest using the Q-concentration as an indicator to the progress of the cool flame reactions. Fig. 3.1 shows typical traces measured for the species concentrations of R, B and Q during two-stage autoignition. Maxima in the curves for R and B correspond to the development and subsequent quenching of the cool flame reactions, in which the Q-concentration rapidly builds to about 0.1 mol/m^3 and the temperature to 900 K. Thus, the autoignition model is skipped in computational cells above 900 K in which the Q-concentration is lower than 0.1 mol/m^3. Schäpertöns and Lee (1985) impose several other constraints to control the low temperature reactions and attain a smooth interface with the high temperature model. These have been largely adopted in the present implementation which operates according to Fig. 3.2. This procedure is repeated for each computational cell (i,j,k), since there is no direct chemical coupling between different cells. Then, the KIVA-II equilibrium solver is called to solve for the constraint conditions in Eq. (3.56) over the entire domain. A very similar scheme to that presented here has been shown to perform well in two spark-ignition engine studies (Blunsdon *et al.* 1993; 1994b) and also in Diesel engine combustion (Blunsdon *et al.* 1992; 1994c).

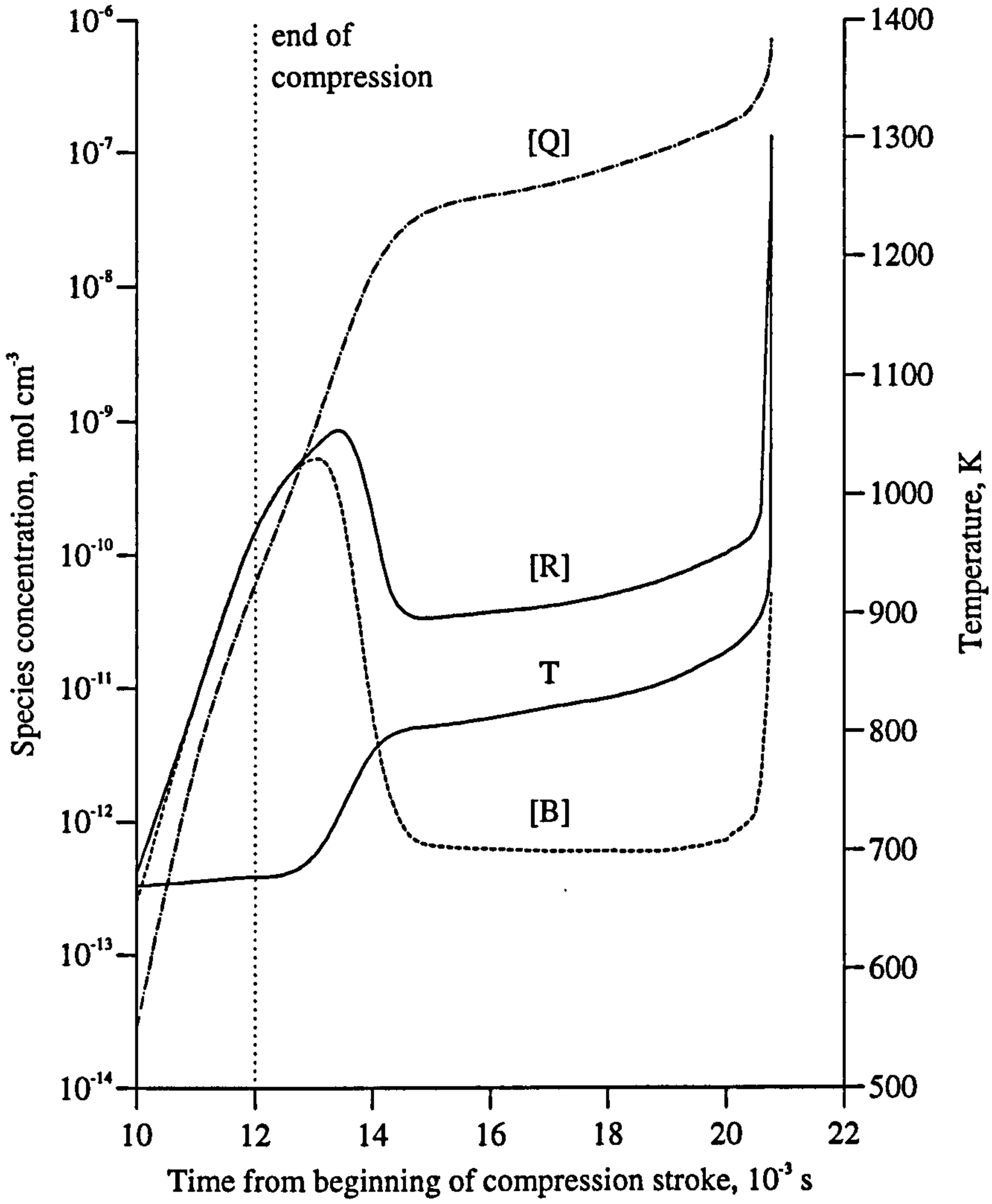

Figure 3.1 Experimental simulation of end-gas temperature and composition during two-stage autoignition in a spark-ignition engine. R, B and Q defined in the text. Reference: Halstead *et al.* (1977).

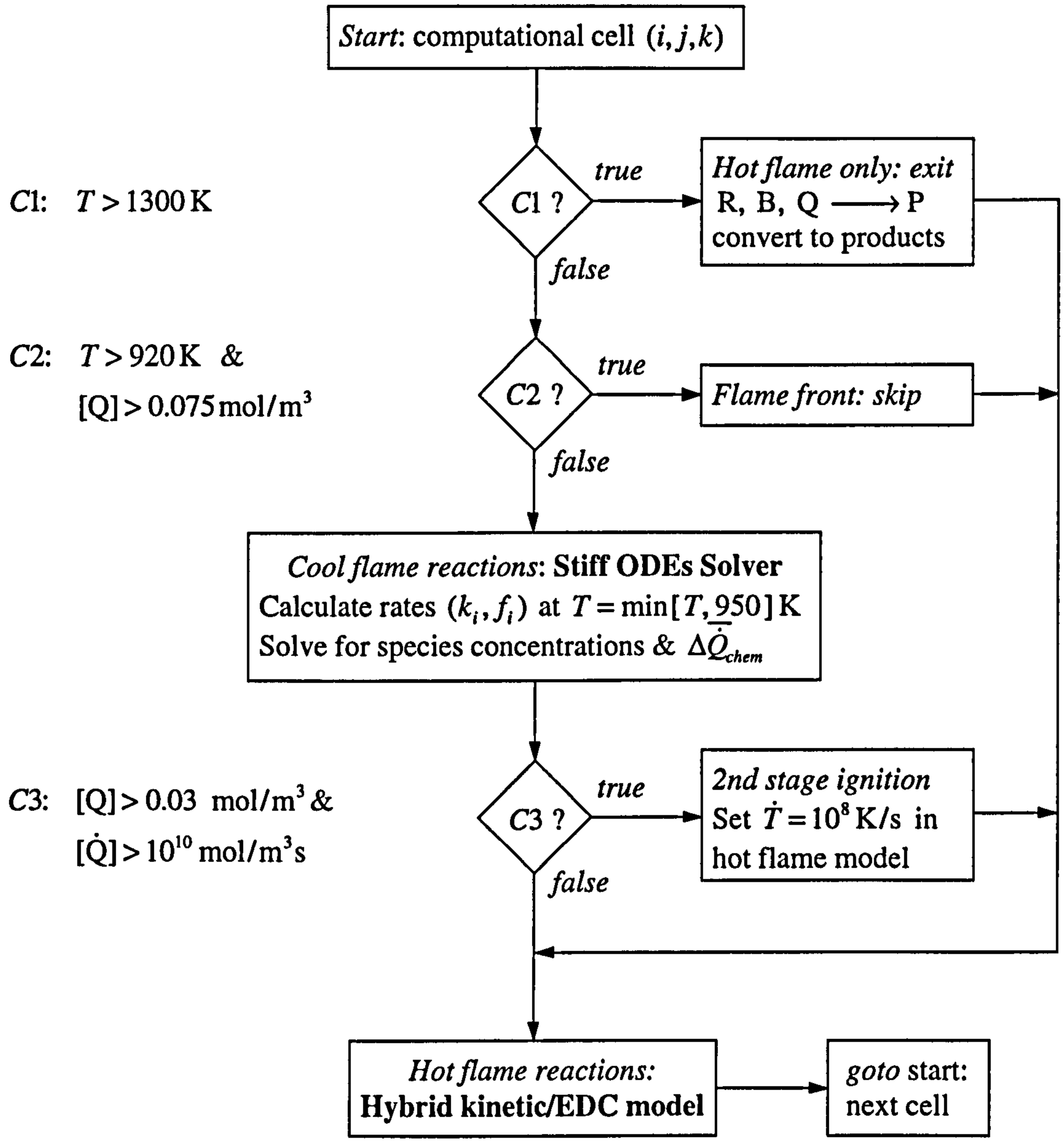

Figure 3.2 Control procedure in autoignition model for a representative computational cell (i, j, k).

3.4 Boundary Conditions

The following sections discuss several types of boundary condition for both two- and three-dimensional simulations of flow and combustion in spark-ignition engines. Specification of radiative properties at boundaries is discussed separately in Sec. 4.1.1.

3.4.1 Turbulent Wall Functions

Near-wall boundary layers are characterised by steep gradients in the flow properties for which numerical solution of the complete turbulent transport equations (see Sec. 3.2) is impractical due to massive spatial discretisation required to adequately resolve the detail. Therefore, for economy and convenience, conditions in the turbulent boundary layer are modelled with wall functions: one-dimensional analytic solutions to simplified forms of Eqs. (3.42-51). For brevity the analysis described by Amsden *et al.* (1989, pp. 98-106) is summarised here. The boundary layer flow is assumed to be a quasi-steady, one-dimensional Couette flow with constant shear stress and heat flux. Then, it is convenient to define a wall Reynolds number, ζ, at a perpendicular distance, y, from the surface as:

$$\zeta = \frac{\rho u^* y}{\mu} \tag{3.100}$$

where u^* is a characteristic velocity, called the shear speed and is related to the wall shear stress, σ_w by the expression:

$$\sigma_w = \rho (u^*)^2 \tag{3.101}$$

For notational convenience, the Favre-tildes and time-averaging overbars denoting mean-flow variables have been omitted in these equations. Unless otherwise stated, all state variables in the following expressions are for the mean flow.

The wall layer is modelled as two zones: the viscous sublayer, $\zeta < R_c$, and the inertial sublayer, $\zeta > R_c$, where the boundary between these two regions occurs at a critical Reynolds number, $R_c = 114$. For the zone adjacent to the wall, the flow is taken to be purely laminar, while in the outer zone it is assumed to be fully turbulent. Then the velocity component parallel to the wall, u, is determined by matching to the following logarithmic profile:

$$\frac{u}{u^*} = \begin{cases} \zeta^{1/2} & \zeta \le R_c \\ 1/\kappa \ln(c_{lw}\zeta^{7/8}) + B & \zeta > R_c \end{cases} \tag{3.102}$$

where the constants $\kappa = 0.4327$, $B = 5.5$ (for smooth walls) and $c_{lw} = 0.15$. The normal gas velocity is set equal to the normal wall velocity. An analogous temperature wall function is used to obtain the wall heat flux, J_w, for fixed temperature walls with the formula:

$$\frac{\rho u^* c_P (T - T_w)}{J_w} = \begin{cases} \mathrm{Pr}_l \dfrac{u}{u^*} & \zeta \le R_c \\ \mathrm{Pr}\left[\dfrac{u}{u^*} + R_c^{1/2}\left(\dfrac{\mathrm{Pr}_l}{\mathrm{Pr}} - 1\right)\right] & \zeta > R_c \end{cases} \tag{3.103}$$

where T_w is the specified wall temperature and Pr_l is the Prandtl number of the laminar fluid. Frictional dissipation at the wall by the shear stress, σ_w, causes fluid momentum to be converted to a heat. This is added to the internal energy of the wall layer, together with the source or sink associated with the wall heat flux, J_w.

Boundary conditions are also required for the $k-\varepsilon$ turbulence model. It is assumed that very close to the surface in the near-wall boundary layer that 'history' effects (i.e. convective and diffusive transport) can be neglected. Then the local rate of turbulence production is balanced by the viscous dissipation rate. In this local equilibrium, the wall functions for k and ε at a normal distance, y, are derived as:

$$k = c_\mu^{1/2} \frac{\sigma_w}{\rho} \tag{3.104}$$

$$\varepsilon = \frac{c_\mu^{3/4}}{\kappa} \frac{k^{3/2}}{y} \tag{3.105}$$

where the turbulence model constant, c_μ, is given in Table 3.1. The k–boundary condition of Eq. (3.104) is modified from original KIVA-II which satisfied $\nabla k \cdot \hat{\mathbf{n}} = 0$. It was found that a zero gradient boundary condition for k leads to short turbulent mixing times (i.e. k/ε) in the boundary layer and this gives rise to unrealistically fast (mixing-controlled) combustion along the chamber walls. This modification was suggested by Kuo and Reitz (1989). Grimsmo (1991, p. 108) also noted this problem, but chose instead to impose at limitation on the length scale y in the ε –boundary condition.

A key assumption in the numerical implementation of the wall functions in Eqs. (3.100-105) is that the finite difference mesh point nearest the wall falls within the two-zone boundary layer. Typically, this will be true if $\zeta^{1/2} < 400$ at the mesh point. Furthermore, the log-law relations are essentially based on the characteristics of a steady flow past a flat plate. However, the flow inside the engine combustion chamber is irregular, highly rotational and may have several moving stagnation points. Moreover, the chamber walls almost consist entirely of curves and corners. The apparent flatness of the wall can be increased by moving the near-wall mesh point closer to the boundary such that the radius y/r is smaller, where r is the radius of curvature, but in general the validity of the log-law wall functions is highly questionable. In particular, the boundary layer flow can be expected to show a significant departure from the flat plate model during combustion when wall quenching reactions are present. Another point to note is that, although the mixing-length formulation for ε given by Eq. (3.105) is used in both zones of the boundary layer, it is strictly only applicable in the inertial sublayer. Despite these problems, log-law wall functions are almost universally employed in multi-dimensional engine calculations for lack of a better alternative (Heywood 1988, p.803).

3.4.2 Open Boundaries: Intake and Exhaust Ports

In three-dimensional Cartesian geometries of the engine combustion chamber, annular orifices are opened and closed in the cylinder head according to the valve timing to simulate intake and exhaust ports. Existing code for the definition of inflow and outflow boundaries in KIVA-II has been extensively adapted for this purpose. The gas exchange process can then be modelled in which the exhaust products are expelled from the cylinder and replaced by the induction of fresh charge. A good description of the in-cylinder conditions prior to the combustion phase is obtained. This is a significant advantage over engine combustion studies in which computations are started at inlet valve closure, using assumed distributions for the flow variables within the combustion chamber (e.g. Kuo and Reitz 1989).

Since the intake and exhaust manifolds are not modelled, approximate conditions must be specified at the open port boundaries. In the present implementation, the treatment used at both intake and exhaust ports is identical. Each port is considered to be connected to a large plenum at a constant pressure, p_{amb}, which acts at a distance x outside the boundary.

The pressure *on* the boundary is then interpolated as (c.f. Amsden *et al.* 1989, p.86):

$$p_{boundary} = \frac{p_{amb} \cdot y + p \cdot x}{x + y} \tag{3.106}$$

where p is the pressure value in the first interior computational cell at a distance y inside. Setting $x = 0$ gives the true specified pressure condition, but is not advised since this results in the perfect reflection of acoustic waves and can affect the upstream flow in subsonic calculations with outflow boundaries. Taking x to be a characteristic dimension of the computational region is suggested to reduce this problem. Therefore, x is set equal to the engine cylinder radius and p_{amb} is adjusted to obtain a desired port mass flow.

In the present study, a *fixed* intake pressure was specified to simulate naturally aspirated charging of the engine cylinder, but the exhaust pressure was varied to include wave action effects in the exhaust. Following the procedure of Das (1996) the method of characteristics is used to calculate the response of a one-dimensional, unsteady, homentropic flow in the exhaust pipe. A wave action model by Benson (1982) was coupled to the KIVA-II for this purpose. The present implementation is relatively rudimentary, but it provides a good basis from which to develop more sophisticated analysis of gas flow in both the exhaust and intake manifolds. The simulation of exhaust blow down and displacement is demonstrated by the engine prediction in Sec. 6.4. (More discussion of the coupling between the wave action model and exhaust boundary is also given in Sec. 6.4.2.)

A non-homentropic analysis including effects such as temperature gradients, heat transfer, friction and chemical reaction should be considered in any future improvements. Pearson and Winterbone (1996) also discuss the recent popularity of finite-difference schemes over the method of characteristics.

In addition to the above pressure specification, the boundary flow velocities are arbitrarily set equal to those at corresponding mesh points on the first interior mesh plane. These two conditions are then sufficient for an outflow. However, for gas entering the cylinder through the intake ports, or when a backflow occurs through the exhaust ports, the chemical species densities, entropy, turbulent kinetic energy and turbulent length scale of the incoming fluid must also be specified. Reference incoming species densities, $\rho_{s,amb}$,

are given at pressure, p_{amb}. Then the values imposed at the inflow boundary are isentropically scaled with the relation (Amsden *et al.* 1989, p.85):

$$\rho_s = \rho_{s,amb} \cdot (p / p_{amb})^{1/\gamma_{amb}} \tag{3.107}$$

where p is the pressure calculated in the first interior computational cell and γ_{amb} is the ratio of specific heats of the inflow mixture. The inlet turbulence quantities are prescribed as:

$$k_{in} = 0.10\,\bar{u}_{in}^2 \tag{3.108}$$

$$y_{in} = \tfrac{1}{2} z'_{\max} \tag{3.109}$$

where $\bar{u}_{in}$ is the mean inflow velocity and $z'_{\max}$ is the maximum valve lift. The turbulent length scale, y_{in}, is then substituted into Eq. (3.105) to find the viscous dissipation rate. The turbulent kinetic energy, and its dissipation, are both assumed to be uniformly distributed at port boundaries. The sensitivity of the predicted combustion flow field to error in the estimated inlet turbulence is expected to be largely mitigated by the swamping effect of turbulence generation and dissipation during compression after inlet valve closure. However, this has not been assessed.

3.4.3 Moving Boundaries: Piston and Poppet Valve Simulation

Moving boundaries are used to simulate the piston motion, and in three-dimensional Cartesian geometries, the opening and closing of poppet valves in the cylinder head. In both cases, the boundary layer treatment is identical to that described for rigid walls above, and the only added complication is specification of the boundary position and velocity.

The instantaneous piston position and velocity are given by (Heywood 1988, Sec. 2.2):

$$z_p = a(1+\cos\theta) + (l^2 - a^2\sin^2\theta)^{1/2} - l \tag{3.110}$$

$$u_p = -a\omega\sin\theta\left[1 + \frac{a\cos\theta}{(l^2 - a^2\sin^2\theta)^{1/2}}\right] \tag{3.111}$$

where ω is the angular velocity of the crankshaft, θ is the crank angle and l and a are respectively the connecting rod length and crank radius as shown in Figure 3.3.

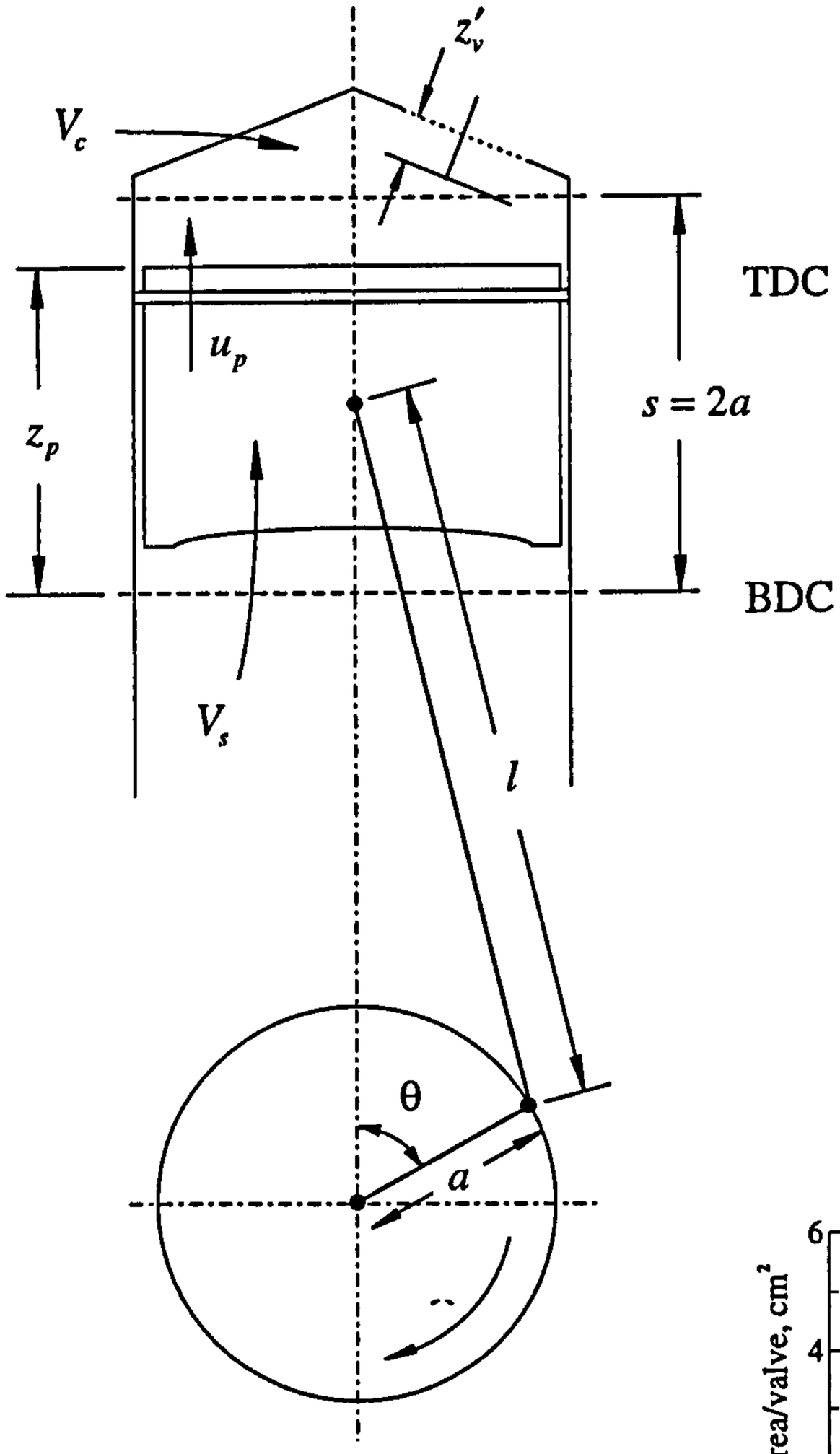

Figure 3.3

Parameters defining piston assembly and poppet valve geometry in pentroof combustion chamber.

s	stroke
a	crank radius
l	connecting rod length
θ	crank angle
V_c	clearance volume
V_s	swept volume
u_p	instantaneous piston velocity
z_p	height of piston top above BDC
z'_v	lift of canted poppet valve

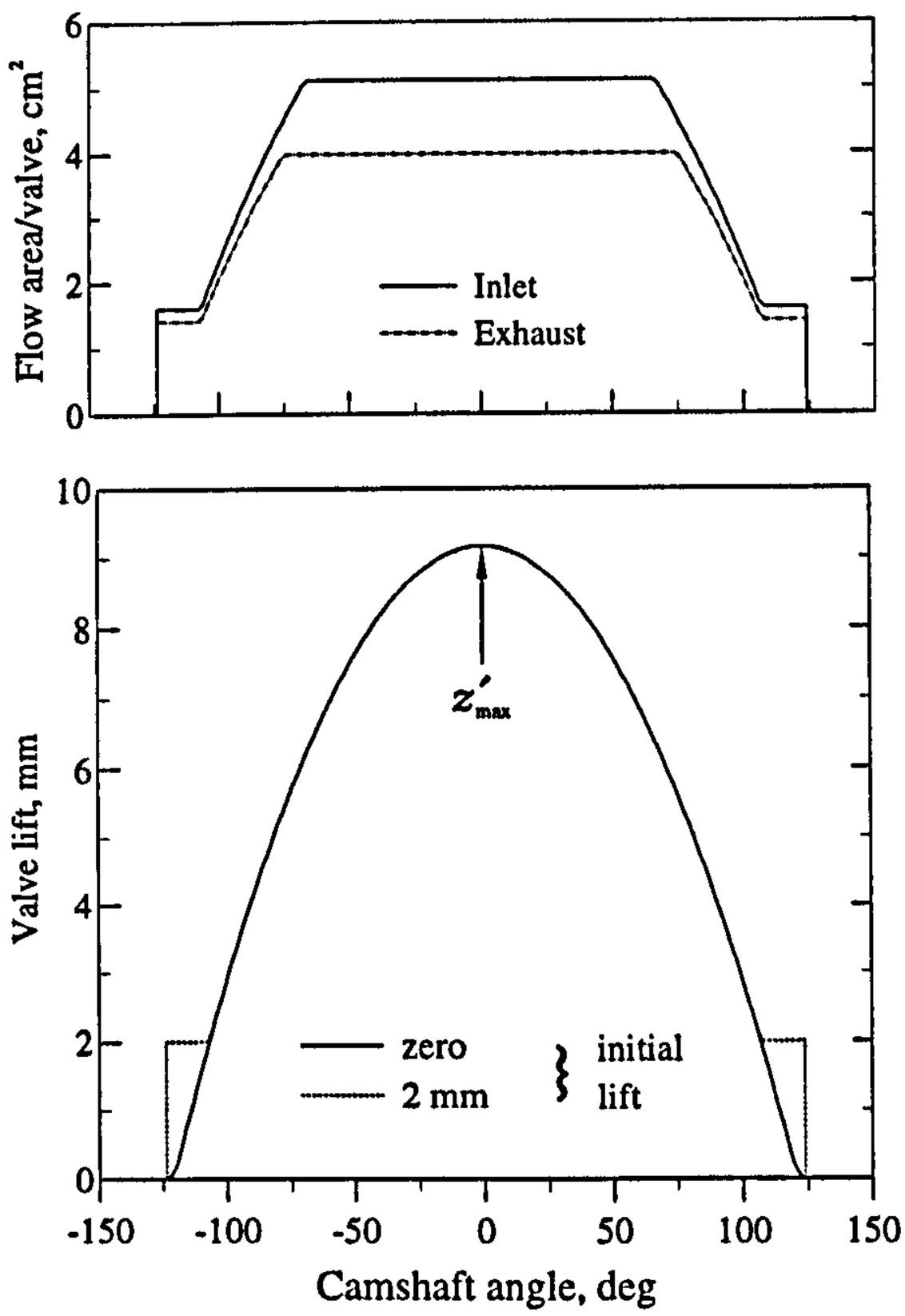

Figure 3.4

Poppet valve lift curve and corresponding intake and exhaust valve open areas as a function of camshaft angle (taken from the engine simulation in Sec. 6.4).

Numerically, Eq. (3.111) is implemented by specifying a velocity for all mesh points on the piston surface equal to the *mean* instantaneous piston velocity over each small timestep in the KIVA-II numerical scheme. Note that the piston velocity was inaccurately specified in the original code, but newer releases of KIVA (version 03/27/92 or later) use the same formulation as the present study.

Poppet valves are crudely modelled as an infinitesimally thin disk and stem as described in Sec. 2.4.5, thus avoiding the large computational requirement associated with an accurate description of the valve geometry (e.g. Chen *et al.* 1996). No valve cam data was available for the engines modelled in the present study, so the valve action was simulated from timing and maximum lift data, together with a specified acceleration ratio, $r_v = a_{\max}/a_{\min} = -20$. Then, the valve accelerates briefly at the start and end of its motion, with an extended period of constant deceleration in between. A typical lift curve is obtained as shown in Fig. 3.4 (c.f. Heywood 1988, p. 223), where $z'_{\max}$ is the maximum valve lift. This is described by the following equations of motion:

$$\begin{aligned} &\theta_{vo} \le \theta \le \theta_1: && z'_v = \tfrac{1}{2} a_{\max} (\theta - \theta_{vo})^2 \\ &\theta_1 < \theta < \theta_2: && z'_v = \tfrac{1}{2} a_{\min} (\theta - \theta_m)^2 + z'_{\max} \\ &\theta_2 \le \theta \le \theta_{vc}: && z'_v = \tfrac{1}{2} a_{\max} (\theta - \theta_{vc})^2 \end{aligned} \qquad (3.112)$$

where

$$\theta_m = \tfrac{1}{2}(\theta_{vo} + \theta_{vc}), \qquad \theta_1 = (\theta_m - r_v \theta_{vo})/(1 - r_v), \qquad \theta_2 = 2\theta_m - \theta_1 \qquad (3.113)$$

and θ_{vo} and θ_{vc} are the valve opening and closing crank angles. The corresponding open area profile is also shown in Fig. 3.4. Since the valve head and stem are assumed to be infinitesimally thin, the plateau region corresponds to the lift exceeding one quarter of the head diameter. (Note that a more realistic valve and seat geometry would give a much smoother variation in open area as shown by Heywood 1988, p.233.)

The poppet valve velocities are so small that for convenience, the valve heads are numerically implemented as stationary walls. Their position is then updated at each timestep of the KIVA-II numerical scheme according to the each valve's lift curve and orientation. To ensure numerical stability during computations a minimum initial valve lift of 2 mm was specified resulting in a truncated lift profile as shown by the dotted lines in Fig. 3.4.

3.4.4 Periodic Boundaries

Periodic boundaries have been used in the two-dimensional engine simulations. The flow field is assumed to have n-fold periodicity about the cylinder axis. A pseudo-polar computational mesh is defined in Cartesian co-ordinates such that the z-axis is aligned with the cylinder axis. Then the computational region is composed of points in the pie-shaped sector $0 \le \theta \le 2\pi/n$ such that the periodic boundaries are those for which $\theta = 0$ and $\theta = 2\pi/n$. The conditions imposed on these boundaries for scalar and vector quantities are, respectively,

$$\text{Scalars:} \qquad \phi(r, \theta + 2\pi/n, z) = \phi(r, \theta, z) \tag{3.114}$$

$$\text{Vectors:} \qquad \mathbf{u}(r, \theta + 2\pi/n, z) = \mathbf{R} \cdot \mathbf{u}(r, \theta, z) \tag{3.115}$$

where $r = (x^2 + y^2)^{1/2}$, $\theta = \tan^{-1}(x/y)$ and $\mathbf{R}$ is a rotation matrix about the z–axis for an angle of $2\pi/n$ degrees, i.e. the left-hand matrix in Eq. 4.31 with angle $\psi = 2\pi/n$.. Two-dimensional calculations are made in a single 0.5° slice assuming 720-fold periodicity in the above relations.

3.5 KIVA-II Numerical Scheme

The KIVA-II numerical scheme employees a finite-volume method to difference the governing transport equations presented in Sec. 3.2 in both space and time. The extensive historical development of this scheme has resulted in its documentation being spread over many articles. Five key references are the reports by Amsden *et al.* (1985a, 1985b, 1989) and O'Rourke *et al.* (1986, 1989) at the Los Alamos National Laboratory, New Mexico where the KIVA family of codes was written. Further references on particular aspects of the solution scheme can then be sourced from these.

Only a brief overview of the numerical scheme is given below: the detail is not repeated here in the interests of brevity. Several important methodology changes to the code are then discussed, together with troubleshooting techniques used to improve its numerical stability and efficiency.

3.5.1 Temporal and Spatial Differencing

Finite-differencing is based on a finite volume approach called the ALE (arbitrary Lagrangian-Eulerian) method which is largely a conservative and first order accurate scheme. Spatial differences are formed over a curvilinear mesh of hexahedral cells (see Sec. 2.4), whose vertex locations may be arbitrary specified as functions of time, such that the cells are arbitrary hexahedrons. This flexibility enables the computational mesh to follow changes in the combustion chamber geometry that arise from the piston and valve motion in spark ignition engines. The governing conservation equations are discretised in their integral form, with the volume of a typical mesh cell used as the control volume, and with gradient or divergence terms transformed to surface integrals by applying the divergence theorem. It is usually assumed that the integrands are uniform within cells or on cell faces when a volume or surface area integral is determined.

Temporal differencing is performed with respect to a sequence of discrete times t^n $(n = 0, 1, 2, \ldots)$ such that the solution is marched forwards in time through a series of finite time steps, $\Delta t^n = t^{n+1} - t^n$, where the integer n is the cycle number. Each computational cycle is divided into two stages: a Lagrangian phase followed by a rezone (or Eulerian) phase. In the Lagrangian phase the vertices of the computational mesh move with the fluid velocity, and the control volumes deform with the fluid such that there is no convection across cell boundaries. In the rezone phase, the flow field is frozen and the vertices are moved to new user-specified positions. The flow field is then remapped or rezoned onto the new computational mesh by convecting material across the cell boundaries, which are regarded as fixed in space in a Eulerian description of the fluid movement.

3.5.2 Solution Procedure

The Lagrangian calculation is subdivided into two phases, A and B, in the numerical scheme. Phase A calculates the mass and energy source terms due to chemical reactions (see Sec. 3.3). In the present implementation, the Phase A internal energy sources also includes changes due to radiative heat transfer from the combustion products (see Sec. 5.5). Phase B then solves for the diffusion terms in the governing equations, together with those associated with acoustic waves, namely the pressure gradient term and velocity dilatation terms. Previously, these terms have been solved explicitly with a time step satisfying the Courant sound speed restriction, $C_s = c\Delta t/\Delta x \leq 1/f$, where c is the

isentropic speed of sound and the factor $f \geq 1$. In low Mach number problems, this is inefficient because the flow features of interest usually vary on a time scale much longer than the Courant time step required to resolve the acoustic mode.

Therefore, to avoid this restriction, coupled implicit differencing of the diffusion and acoustic mode terms is used to stabilise the finite-difference approximations when the Courant condition is violated. These implicit equations are then solved together in Phase B using a modified SIMPLE algorithm (Patankar 1980), with individual equations being solved by the conjugate residual method (O'Rourke *et al.* 1986). The KIVA-II code authors selected the conjugate residual method for its rapid convergence properties, low storage requirements and its amenability to vectorisation for faster calculations (×5) with compilers offering that option. (Unfortunately, this last feature was not available on the HP and SUN machines used in the present study.) Despite these attractive properties, implicit solvers by their iterative nature can be very expensive. Therefore, to improve computational efficiency, a partially-implicit solution scheme is used where the amount of implicitness is varied to maintain numerical stability. A weighting factor, Φ_P, for the pressure terms is based on the sound speed Courant number, and an analogous parameter, Φ_D, is used to difference diffusion terms based on a local diffusion Courant number, $C_D = \nu \Delta t / \Delta x^2$, where ν is the diffusivity. The forms of these variable implicitness parameters are given in Appendix H by Amsden *et al.* (1989). A fully implicit solution is only used in the limit of an infinitely large time step. The remaining source terms in the $k-\varepsilon$ turbulence equations are also calculated in Phase B.

The convective transport terms are then determined in the rezone phase, or Phase C, such that each complete cycle in the KIVA-II numerical scheme is composed of three phases A, B and C. Two alternative convection schemes are available: quasi-second-order upwind (QSOU) differencing and partial donor cell (PDC) differencing. Amsden *et al.* (1989) fully describes these algorithms and presents the results of a comparison study with other convection schemes. Both QSOU and donor cell are monotone, explicit schemes. Monotonicity is a desired property to avoid computational oscillations in regions of steep gradients. However, their explicit formulation requires a calculation time step, Δt_c, that satisfies the Courant stability condition, $u_r \Delta t_c / \Delta x < 1$, based on the fluid velocity u_r relative to the computational mesh. In the discussion of the Lagrangian calculation above, the advantage of removing this limitation by using a implicit scheme were strongly advocated. However, although trial calculations with two implicit schemes

(i.e. QUICK and fully-implicit donor cell) where found to be unconditionally stable at time steps, $25 \times \Delta t_c$, they were much less accurate than those using explicit methods (O'Rourke *et al.* 1989, p.6). Therefore, the code authors considered it more favourable to choose an explicit scheme and subcycle the convection calculation $\Delta t / \Delta t_c$ times, where Δt is the overall computational time.

Subcycling the convection calculation and using implicit differencing for the remaining terms in the governing equations then removes any stability restrictions on the overall time step, Δt. Its size is then more loosely constrained by accuracy criteria associated with fluid accelerations and cell distortions during the Lagrangian phase, and with the turbulence-chemistry coupling (see Amsden *et al.* p.52-56).

Scalar variable are stored at cell centres, while the Cartesian velocity components are stored at cell vertices. The mesh vertex motion is then obtained directly from the velocity field during the Lagrangian phase of the ALE calculation, without the need for interpolation. However, this arrangement has a major drawback. Pressure waves are encouraged to propagate along cell diagonals, rather than via adjacent cells, creating a 'checkerboarding' effect in the numerical pressure field and associated irregularities in the velocity field. In KIVA-II, this difficulty is alleviated by introducing velocities centred on cell faces for temporary use during the acoustic subcycling and in the advective fluxing of cell-centred quantities. In addition, these parasitic velocity modes can be numerically damped using an alternate node coupler: this auxiliary procedure is fully described in Appendix L by Amsden *et al.* (1989). It is worth note that a scheme has been tested based on the exclusive use of face-centred velocities (Amsden *et al.* 1985b, p. 3). Dramatic improvements in the numerical behaviour were observed, but the method was judged too unwieldy due to the extra storage and indexing requirements.

3.5.3 Methodology Changes

The second release of KIVA-II (dated 05/31/90) was adapted for the present study. Several important methodology changes have been made to improve accuracy, remove inconsistencies and to accommodate the new submodels detailed in previous sections.

The centrifugal terms were rewritten to improve angular momentum conservation and the pressure gradient treatment at open boundaries and solid walls were modified to ensure numerical consistency with other parts of the code. Both of these changes are described by Amsden (1993, pp. 39-40), but were originally made on the basis of corrections provided with a later KIVA-II release (dated 03/27/92) and from a private communication with A. Amsden (Los Alamos National Laboratory).

New mesh generation software has been written to improve the meshing capabilities of the original code (Chapter 2). A more general routine was then required to setup the velocity boundary conditions on the arbitrary-shaped nonorthogonal computational meshes generated. Therefore, a new algorithm has been developed to handle the sharp, acute and obtuse edges and corners that arise on the boundary surfaces. The most complex section of the logic concerns zeroing normal velocity components on solid walls where the orientation of the surface normal must be calculated. This requires looking in all six logical directions from a vertex and selecting the neighbouring vertices (up to four) that lie on the same surface. Then, the cross-products of vectors, defined between the vertex and its neighbours, are averaged to find the required normal orientation. These vertex normals are calculated initially and stored. Recalculation is then only required when mesh planes are removed or replaced by the chopper (see Sec. 2.4.5).

The inclusion of pressure-density-interaction effects into the turbulence production term (see Sec. 3.2.4), has required modification of the original difference approximations given by Amsden *et al.* (1989, p.41). A new formulation has been successfully implemented in which new terms are differenced in an analogous manner to original ones. In particular, their prescription is chosen to avoid the appearance of negative computed values for k and ε. The differencing procedure is fully detailed in Appendix C using the notation of Amsden *et al.* (1989). The differencing methodology of Amsden should be studied beforehand, since it is too lengthy to be repeated here.

Finally, it was necessary to impose additional constraints on the overall computational time step, Δt, as follows:

- Spark ignition (Sec. 3.3.6): It was found necessary to cut the value of Δt at the time of ignition to prevent code failure due to the sudden heat release and obtain better temporal resolution of the initial flame propagation. A cut factor of 0.1 was used.

- Autoignition model (Sec. 3.3.7): When autoignition occurs in a computational cell, Δt is constrained such that the total chemical heat release does not exceed a specified fraction of the total internal energy in the cell. This is analogous with the constraint in Eq. (136) by Amsden *et al.* (1989).

- Opening of valve ports (Sec. 3.4.2): Engine simulations with valve ports require that Δt is cut when the ports open, due to the large fluid accelerations and strain rates that result, particularly at exhaust blowdown. A cut factor of 0.1 was used (c.f. Amsden 1993, p.30).

- Wave action submodel: The pressure wave oscillation in the exhaust is solved by the method of characteristics using a time step set by stability criteria . Δt is constrained by the submodel time step during exhaust open period, but usually accuracy criteria in the KIVA-II numerical scheme are more restrictive.

3.5.4 Program Structure

The entire solution procedure is represented in Fig. 3.5. Alongside each box in the flow diagram appears the primary and supporting subroutines called for the associated task. A comparison with the original KIVA-II program structure (Amsden *et al.* 1989, pp. 58-59) reveals extensive modifications. All routines concerned with spray modelling for Diesel engine combustion have been (temporarily) removed to reduce compilation time. New subroutines for the autoignition, wave action and radiation have been incorporated into the scheme, while preserving the highly modular nature of the original coding. Pre- and post-processing facilities in the original program have been largely replaced by dedicated and separate software.

Both original and new subroutines are almost exclusively programmed in FORTRAN 77 (and its extensions), with the exception of some C system routines. During development a library of linkable binaries was maintained to minimise compilation times. Numerous minor coding modifications have been made to improve accuracy, flexibility, robustness and portability. The original Cray code has been adapted to run on both HP and SUN workstations. Only four of the subroutines are platform dependent.

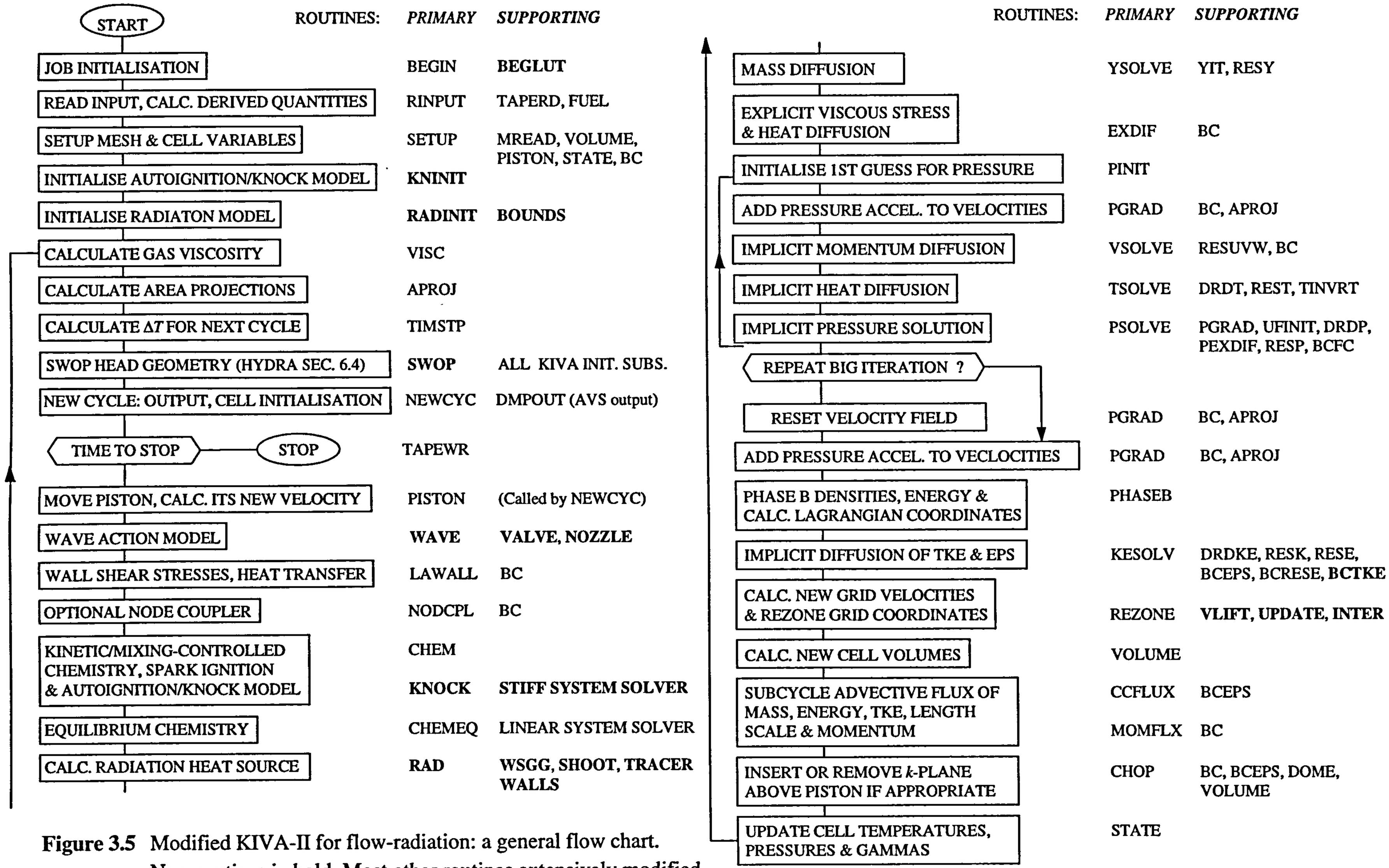

Figure 3.5 Modified KIVA-II for flow-radiation: a general flow chart. *New routines in bold. Most other routines extensively modified.*

3.5.5 Troubleshooting

In engine simulations of the gas exchange process it was found that the sudden changes in acceleration and strain rate when the valve ports first open, together with the large cell distortions arising from rezoning the valve motion, often caused the code to fail. Limiting the maximum time step to a small value (i.e. 0.1° crank angle) improved the solution stability, but convergence problems still arose at a few specific points in the calculation.

These problems were found to occur during the SIMPLE iteration in the Lagrangian phase of the numerical scheme. Essentially, this procedure involves predicting the pressure field and then implicitly solving for the diffusion terms in the velocity and temperature fields. These, in turn, are then used to solve for a corrected pressure field using equations that difference the pressure terms implicitly. This procedure is then repeated until the predicted and corrected pressures agree within a specified tolerance. Within this outer 'big' iteration, the implicit solution of each flow quantity (velocities, temperature and pressure) is also iterative. All these inner iteration loops in KIVA-II are terminated after 500 iterations, if convergence is not achieved. This has been modified, however, for the pressure iteration in the present study. After 50 pressure iterations control is returned to the outer loop, and the big iteration is then repeated up to 50 times. The velocity and temperature fields are thus updated more frequently in response to changes in the pressure solution, enhancing the robustness of the scheme.

To further improve the stability, a fully implicit Lagrangian (Phase B) calculation is used to bypass trouble spots. This has been achieved by overriding the automatic control of the variable implicitness parameter, Φ_p (Sec. 3.5.2), in the valve open period and globally setting it equal to unity. A moderate increase in the solution time must be forfeited.

Special treatment was also necessary when the combustion mesh was rezoned on to the mesh used during the valve open period in the engine prediction of Sec. 2.4. Unacceptably large changes in the shape and orientation of computational cells in the pentroof region of the combustion chamber would normally cause the convective transport calculation to fail. However, by enforcing a very small time step, Δt_c, for the explicit calculation it was possible to stabilise the scheme when the mesh was swopped. Then the convective time step was allowed gradually return to its original value, satisfying the Courant stability condition.

3.6 Summary

1. The turbulent combustion model solves the Favre-averaged Navier-Stokes equations for chemical species, mass, momentum and internal energy. The Favre-averaging results in unclosed terms, namely the Reynolds stresses, two turbulent scalar fluxes and the mean chemical reaction rate (and mean radiative heat flux).

2. Closure of the Reynolds stresses and scalar fluxes is by a first-order gradient-diffusion model based on a turbulent viscosity. The turbulent viscosity is evaluated from the k–ε turbulence model with extra terms to account for velocity dilatation and pressure-density effects. Higher-order models are also discussed.

3. Fuel oxidation is characterised by a simplified reaction mechanism involving a single irreversible one-step reaction. The mean reaction rate is found with a hybrid expression combining a kinetic model and the eddy dissipation concept (EDC) model for mixing-controlled combustion. Case-by-case tuning of this model is required. Other reactions are considered to proceed either kinetically or to be in chemical equilibrium.

4. Submodels are included for spark ignition, two-stage autoignition (i.e. the Shell model) and one-dimensional wave action in the exhaust pipe. Improvements are suggested.

5. A 'log-law' boundary layer model is used. The ability to model canted valves (as an infinitesimally thin disk and stem) for engine simulations has been added. The valve heads are treated in the numerical scheme as pseudo-stationary solid walls.

6. The numerical scheme is based on an ALE (arbitrary Lagrangian-Eulerian) calculation. Diffusion, pressure and dilatation terms are evaluated in a SIMPLE procedure: individual (implicit) equations are solved by the conjugate residual method. A subcycled, explicit calculation is used for convective terms.

7. There are concerns as to the validity of the numerical scheme for in-cylinder engine flows: Favre-averaged terms may not be appropriate; the k–ε turbulence model is unable to describe large anisotropy in the stress field associated with swirl and tumble; the general validity of the modelled ε–equation is suspect and several assumptions of the boundary-layer model are violated.

Chapter 4

Development of Radiative Heat Transfer Methods

The governing equations for radiation transport in complex media are stated and methods for their numerical solution are reviewed and classified. The Monte Carlo, YIX and discrete transfer methods are selected for implementation. An entire section is devoted to each method which fully detail their theory, coding, modifications and extensions.

An assumption used throughout this chapter is that the media under analysis are gray, that is, all optical properties are wavelength independent. However, the present methods are extended for nongray (spectrally dependent) media in Chapter 5.

4.1 Equations for Radiation Transport in Participating Media

The gaseous mixture in a spark-ignition engine combustion chamber at any instant in time may be considered as an enclosed participating medium absorbing, emitting and scattering radiative energy. The highly complex nature of the radiative heat transfer between the chamber walls and the medium requires that several assumptions are made to simplify the analysis to a manageable level. The system is assumed to be in local thermal equilibrium such that the time dependence of radiative intensity may be neglected and the Planck spectral distribution can be applied to describe the radiative emission. This is normal practice for most engineering problems. Furthermore, the medium refractive index n is taken as constant and equal to unity since for the radiating combustion products $n \approx 1$. As the bending of electromagnetic waves is caused by a varying refractive index, it follows from this later assumption that the radiant energy in the present system will travel along straight line paths or *rays*. Finally, the combustion chamber walls will be taken as opaque, gray surfaces which diffusely emit, absorb and reflect radiation, i.e. there is no transmission of radiation and the surface optical properties are independent of both the wavelength and the direction of the incident or outgoing radiation. In practice, this is a reasonable approximation for the radiative properties of the soot layer which tends to form on the combustion chamber walls.

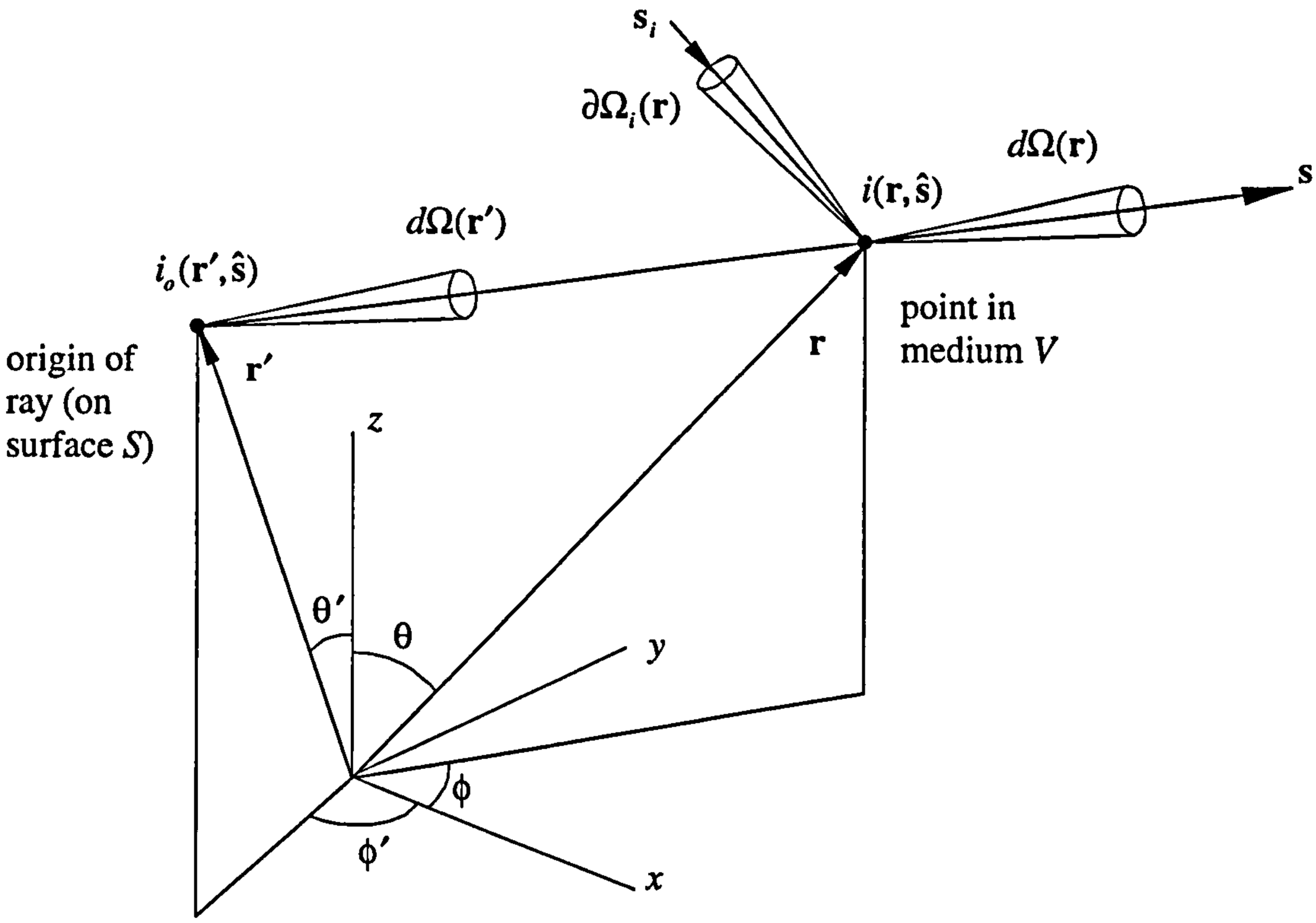

Figure 4.1 Geometry for the derivation of the equations for participating radiation.

4.1.1 Integro-Differential Formulation

The integro-differential equation of radiative transport is given by (Modest 1993, p. 304):

$$\frac{di(\mathbf{r},\hat{\mathbf{s}})}{ds} = \hat{\mathbf{s}}\cdot\nabla i(\mathbf{r},\hat{\mathbf{s}}) = -\beta i(\mathbf{r},\hat{\mathbf{s}}) + \kappa i_b(\mathbf{r}) + \frac{\sigma_s}{4\pi}\int_{4\pi} i(\hat{\mathbf{s}}_i)\Phi(\hat{\mathbf{s}}_i,\hat{\mathbf{s}})\, d\Omega_i(\mathbf{r}) \qquad (4.1)$$

where $i(\mathbf{r},\hat{\mathbf{s}})$ is the radiation intensity at a given location $\mathbf{r}$, in the direction $\hat{\mathbf{s}}$, within an infinitesimal beam of energy travelling through a participating medium.

The first term on the right-hand side describes the total attenuation of the radiative energy by absorption along the beam path and by scattering *away* from the direction of travel, i.e. *out*-scattering. Both phenomena are directly proportional to the magnitude of the incident energy and are written in terms of a absorption coefficient κ and a scattering coefficient σ_s, respectively. Absorbed energy is converted into internal energy, while scattered energy is redirected and appears as augmentation along another direction (see below).

The combined process is known as extinction and accordingly the combined constant of proportionality:

$$\beta = \kappa + \sigma_s \tag{4.2}$$

is called the extinction coefficient. Note that in a nonhomogeneous medium κ, σ_s and β are functions of the spatial location $\mathbf{r}$, but this has not been explicitly indicated in this and the following equations, to simply notation.

As the beam loses energy by extinction, it is also gains energy by emission from the medium and by scattering from other directions $\hat{\mathbf{s}}_i$ *into* the direction of travel $\hat{\mathbf{s}}$, i.e. *in-*scattering. At thermal equilibrium the emitted intensity in the medium is proportional to the local blackbody intensity $i_b(\mathbf{r})$ and the proportionality constant for emission equals that for absorption, namely κ. Hence, radiative emission along the beam path is described by the term κi_b. The integral term in Eq. (4.1) then represents the radiative energy contribution by in-scattering from the 4π solid angle $\Omega(\mathbf{r})$ surrounding the location $\mathbf{r}$ (including the direction $\hat{\mathbf{s}}$). $\Phi(\hat{\mathbf{s}}_i, \hat{\mathbf{s}})$ is the scattering phase function and describes the probability that a ray from one direction $\hat{\mathbf{s}}_i$ will be scattered into a certain other direction $\hat{\mathbf{s}}$. Mie theory will be used to model scattering in all particulate media considered in the present study (see Modest 1993, Chap. 10).

A common approximation for the Mie scattering phase function is then given by the series expansion (Chu and Churchill 1955):

$$\Phi(\hat{\mathbf{s}}_i, \hat{\mathbf{s}}) = \sum_{n=0}^{N} a_n P_n(\hat{\mathbf{s}}_i \cdot \hat{\mathbf{s}}) \tag{4.3}$$

where a_n $(n = 0, 1, \ldots, N)$ are constants and $P_n(\hat{\mathbf{s}}_i \cdot \hat{\mathbf{s}})$ are Legendre polynomials in terms of the cosine of the scattering angle, $\hat{\mathbf{s}}_i \cdot \hat{\mathbf{s}}$. The addition theorem for Legrendre functions (Yanovitskij 1997; Gradshteyn and Ryzhik 1994, p. 1033) is used to replace Eq. (4.3) by:

$$\Phi(\hat{\mathbf{s}}_i, \hat{\mathbf{s}}) = \sum_{k=0}^{M} c_k S_k(\hat{\mathbf{s}}) S_k(\hat{\mathbf{s}}_i) \qquad M = N(N+2) \tag{4.4}$$

c_k are constants and S_k are functions of the form $P_n^m(\cos\theta)\cos m\phi$ or $P_n^m(\cos\theta)\sin m\phi$. (Here θ and ϕ are the polar and azimuthal angles for the direction $\hat{\mathbf{s}}$, written in spherical coordinates, and P_n^m are spherical functions of the first kind.)

The phase function expressed in Eq. (4.4) is normally truncated after the fourth term (i.e. $M=3$), otherwise the analysis becomes too involved. This corresponds to a linear anisotropic scattering, i.e. $c_0=1,\ c_1=c_2=c_3=g$ and $S_0=1,\ (S_1,S_2,S_3)^T=\hat{\mathbf{s}}$ such that:

$$\Phi(\hat{\mathbf{s}}_i,\hat{\mathbf{s}})=1+g\,\hat{\mathbf{s}}\cdot\hat{\mathbf{s}}_i \tag{4.5}$$

where the asymmetry factor, g, describes the directional behaviour of the scattering. When $g=0$ equal amounts of energy are scattered into all directions and $\Phi=1$. This is isotropic scattering. Retaining Eq. (4.4) in its most general form for the present, substituting into (4.1) and dividing throughout by β yields:

$$\frac{di(\mathbf{r},\hat{\mathbf{s}})}{d\tau}=-i(\mathbf{r},\hat{\mathbf{s}})+(1-\omega)i_b(\mathbf{r})+\frac{\omega}{4\pi}\sum_{k=0}^{M}c_k\,S_k(\hat{\mathbf{s}})\,w_k(\mathbf{r}) \tag{4.6}$$

where the single scattering albedo, ω, the optical thickness, τ and the functions w_k are: defined as follows:

$$\omega=\sigma_s/\beta,\qquad 1-\omega=\kappa/\beta \tag{4.7}$$

$$\tau=\int\beta\,ds \tag{4.8}$$

$$w_k(\mathbf{r})=\int_{4\pi}S_k(\hat{\mathbf{s}})\,i(\mathbf{r},\hat{\mathbf{s}})\,d\Omega(\mathbf{r}) \tag{4.9}$$

These w_k's have an important physical significance. For example, w_0 is irradiation from all solid angles on a point $\mathbf{r}$ in the medium and w_1, w_2, w_3 are the three Cartesian components of the radiation flux vector, $\mathbf{q}_r$ at $\mathbf{r}$, i.e.

$$w_0=\int_{4\pi}i(\mathbf{r},\hat{\mathbf{s}})\,d\Omega(\mathbf{r}),\qquad (w_1,w_2,w_3)^T=\mathbf{q}_r(\mathbf{r})=\int_{4\pi}\hat{\mathbf{s}}\,i(\mathbf{r},\hat{\mathbf{s}})\,d\Omega(\mathbf{r}) \tag{4.10}$$

An important relation is obtained between these two quantities by integrating Eq. (4.6) over all solid angles from $0\rightarrow 4\pi$ giving (Modest 1993, pp. 313-314):

$$\nabla\cdot\mathbf{q}_r(\mathbf{r})=\kappa\left[4\pi i_b(\mathbf{r})-w_0(\mathbf{r})\right] \tag{4.11}$$

where $\nabla\cdot\mathbf{q}_r$ is the divergence of radiative heat flux at the point $\mathbf{r}$ in the medium, i.e. the net loss or gain in radiative energy per unit volume. Equation (4.11) is also written in terms of the gas blackbody emissive power, e_g, using the substitution $e_g=\pi i_b$.

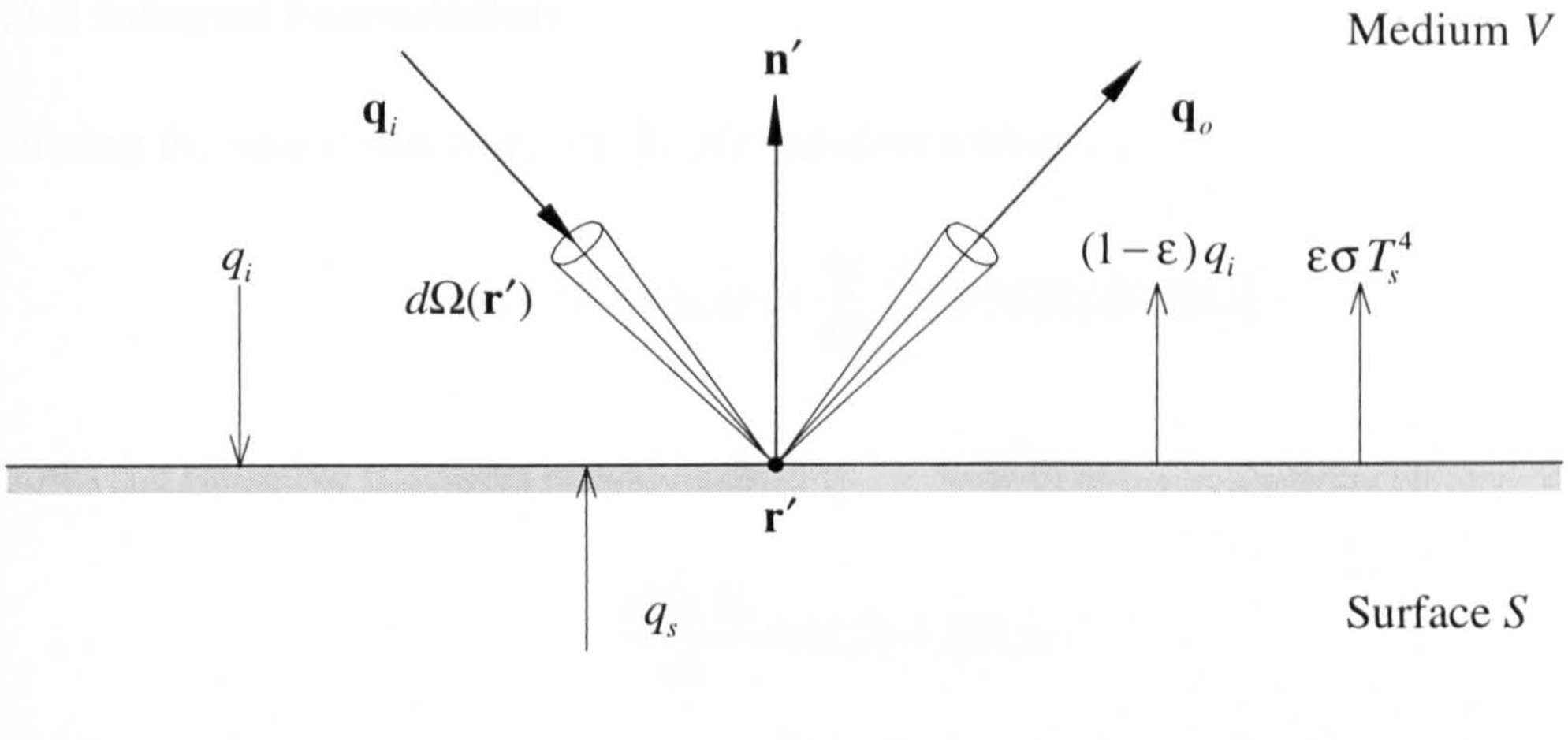

Figure 4.2 Radiative energy balance at the boundary surface.

A companion expression can be found for the radiative heat flux on the boundary surface. Consider a point $\mathbf{r}'$ as shown in Fig. 4.2. Integrating the incoming intensity over the entire 2π hemispherical solid angle above the surface, and dividing by the surface area, defines the incident heat flux as:

$$q_i(\mathbf{r}') = \mathbf{q}_i \cdot \hat{\mathbf{n}}' = \int_{2\pi} i(\mathbf{r}', \hat{\mathbf{s}})\hat{\mathbf{s}} \cdot \hat{\mathbf{n}}'\, d\Omega(\mathbf{r}') \tag{4.12}$$

where $\hat{\mathbf{n}}'$ is the unit normal to the surface at $\mathbf{r}'$. Since the boundary is taken as opaque, gray and diffuse, the emitted heat flux is given by:

$$q_o = \mathbf{q}_o \cdot \hat{\mathbf{n}}' = \pi\, i_o = (1-\varepsilon)\, q_i + \varepsilon\, e_s \tag{4.13}$$

where ε is the surface emissivity and e_s is the surface emissive power. All quantities are *only* functions of surface position $\mathbf{r}'$. (The outgoing intensity i_o is independent of the direction $\hat{\mathbf{s}}$ for a diffuse surface.) The net surface heat flux at $\mathbf{r}'$ is then:

$$q_s = \mathbf{q}_s \cdot \hat{\mathbf{n}}' = q_o - q_i \tag{4.14}$$

Finally, given a local temperature, T_s on the boundary surface, or T_g in the medium, the corresponding blackbody emissive powers are, respectively:

$$e_s = \sigma T_s^4\,, \qquad e_g = \sigma T_g^4 \tag{4.15}$$

where σ is the Stefan-Boltzmann constant.

4.1.2 Integral Formulation

Defining the source function, $S(\mathbf{r},\hat{\mathbf{s}})$, for radiative intensity as:

$$S(\mathbf{r},\hat{\mathbf{s}}) = (1-\omega) i_b(\mathbf{r}) + \frac{\omega}{4\pi} \int_{4\pi} i(\hat{\mathbf{s}}_i)\, \Phi(\hat{\mathbf{s}}_i,\hat{\mathbf{s}})\, d\Omega_i(\mathbf{r}) \tag{4.16}$$

allows the radiative transport equation (4.1) to be written as:

$$\frac{di(\mathbf{r},\hat{\mathbf{s}})}{d\tau} + i(\mathbf{r},\hat{\mathbf{s}}) = S(\mathbf{r},\hat{\mathbf{s}}) \tag{4.17}$$

Consider a small optical distance τ from the point $\mathbf{r}'$ to the point $\mathbf{r}$ along the ray path $\hat{\mathbf{s}}$ over which the extinction coefficient is assumed to be constant (for the present) such that Eq. (4.8) gives $\tau = \beta\, |\mathbf{r}-\mathbf{r}'|$. Then by integrating Eq. (4.17) over this path segment the equation of radiative heat transfer is expressed in its integral form as:

$$i(\mathbf{r},\hat{\mathbf{s}}) = i(\mathbf{r}',\hat{\mathbf{s}})\, e^{-\beta |\mathbf{r}-\mathbf{r}'|} + \int_0^{|\mathbf{r}-\mathbf{r}'|} S(\mathbf{r},,\hat{\mathbf{s}})\, e^{-\beta t} \beta\, dt \tag{4.18}$$

were it can be seen that the position vector $\mathbf{r}_t = \mathbf{r} - \hat{\mathbf{s}} t$ denotes all points between $\mathbf{r}'$ and $\mathbf{r}$ if it is noted that $\hat{\mathbf{s}} = (\mathbf{r}-\mathbf{r}')/|\mathbf{r}-\mathbf{r}'|$. The first term on the right-hand side of Eq. (4.18) describes the exponential decay of the initial intensity $i(\mathbf{r}',\hat{\mathbf{s}})$ due to extinction over the optical distance $\tau = \beta\, |\mathbf{r}-\mathbf{r}'|$ to the point $\mathbf{r}$. There, the local intensity $i(\mathbf{r},\hat{\mathbf{s}})$ is also augmented by emission from all points $\mathbf{r}_t$ along the path segment. This process is expressed by the second integral term, where the integrand represents the energy contribution from the local emission at $\mathbf{r}_t$, attenuated exponentially by self-extinction over the optical distance between $\mathbf{r}_t$ and $\mathbf{r}$.

Now expanding for the source function in Eq. (4.18) and replacing the solid angle integral by the series expansion in Eq. (4.6) gives:

$$i(\mathbf{r},\hat{\mathbf{s}}) = i(\mathbf{r}',\hat{\mathbf{s}})\, e^{-\beta |\mathbf{r}-\mathbf{r}'|} + \int_0^{|\mathbf{r}-\mathbf{r}'|} e^{-\beta t} \left[(1-\omega) i_b(\mathbf{r}_t) + \frac{\omega}{4\pi} \sum_{k=0}^{M} c_k\, S_k(\hat{\mathbf{s}})\, w_k(\mathbf{r}_t) \right] \beta\, dt \tag{4.19}$$

The point $\mathbf{r}'$ is taken to be on the boundary surface, which is diffuse, so the initial intensity $i(\mathbf{r}',\hat{\mathbf{s}})$ can be replaced by the outgoing intensity $i_o(\mathbf{r}')$. An expression for w_o,

w_1, w_2, etc. is then obtained by multiplying Eq. (4.19) by $S_i(\hat{\mathbf{s}})$ $(i=1,2,\ldots,M)$ and integrating over all solid angles from $0 \rightarrow 4\pi$ [c.f. Eq. (4.9)]. i.e.

$$\begin{aligned} w_i(\mathbf{r}) = & \iint_S \frac{e^{-\beta|\mathbf{r}-\mathbf{r}'|}}{|\mathbf{r}-\mathbf{r}'|^2} i_o(\mathbf{r}')\, S_i(\hat{\mathbf{s}})\, \hat{\mathbf{s}}\cdot\hat{\mathbf{n}}'\, dA(\mathbf{r}') \\ & + \iiint_V (1-\omega)\beta \frac{e^{-\beta|\mathbf{r}-\mathbf{r}_t|}}{|\mathbf{r}-\mathbf{r}_t|^2} i_b(\mathbf{r}_t)\, S_i(\hat{\mathbf{s}})\, dV(\mathbf{r}_t) \\ & + \frac{1}{4\pi}\sum_{k=0}^{M} c_k \iiint_V \omega\beta \frac{e^{-\beta|\mathbf{r}-\mathbf{r}_t|}}{|\mathbf{r}-\mathbf{r}_t|^2} S_i(\hat{\mathbf{s}})\, S_k(\hat{\mathbf{s}})\, w_k(\mathbf{r}_t)\, dV(\mathbf{r}_t) \qquad i=0,1,\ldots,M;\ \mathbf{r}\in V \end{aligned} \tag{4.20}$$

Similarly, an expression for q_i is found by taking $\mathbf{r}\in S$ in Eq. (4.19), multiplying it by $\hat{\mathbf{s}}\cdot\hat{\mathbf{n}}$, and integrating it over all solid angles from $0 \rightarrow 2\pi$ [c.f. Eq. (4.12)]. i.e.

$$\begin{aligned} q_i(\mathbf{r}) = & \iint_S \frac{e^{-\beta|\mathbf{r}-\mathbf{r}'|}}{|\mathbf{r}-\mathbf{r}'|^2} i_o(\mathbf{r}')\,(-\hat{\mathbf{s}}\cdot\hat{\mathbf{n}})\,\hat{\mathbf{s}}\cdot\hat{\mathbf{n}}'\, dA(\mathbf{r}') \\ & + \iiint_V (1-\omega)\beta \frac{e^{-\beta|\mathbf{r}-\mathbf{r}_t|}}{|\mathbf{r}-\mathbf{r}_t|^2} i_b(\mathbf{r}_t)\,(-\hat{\mathbf{s}}\cdot\hat{\mathbf{n}})\, dV(\mathbf{r}_t) \\ & + \frac{1}{4\pi}\sum_{k=0}^{M} c_k \iiint_V \omega\beta \frac{e^{-\beta|\mathbf{r}-\mathbf{r}_t|}}{|\mathbf{r}-\mathbf{r}_t|^2} w_k(\mathbf{r}_t)\, S_k(\hat{\mathbf{s}})\,(-\hat{\mathbf{s}}\cdot\hat{\mathbf{n}})\, dV(\mathbf{r}_t) \qquad \mathbf{r}\in S \end{aligned} \tag{4.21}$$

The subscript i here is for 'incident' heat flux and should not be confused with that of w in Eq. (4.20) which refers to the different values of $S_i(\hat{\mathbf{s}})$. Substituting Eqs. (4.11), (4.13) and (4.14) into Eqs. (4.20) and (4.21) and rearranging then gives the final form for the integral equations of radiative heat transfer as (c.f. Tan 1989):

$$\begin{aligned} f_g(\mathbf{r}) = & \iiint_V \beta\, K(\mathbf{r},\mathbf{r}_t)\,[F_g(\mathbf{r}_t) + F_w(\mathbf{r}_t)]\, dV(\mathbf{r}_t) \\ & + \iint_S K(\mathbf{r},\mathbf{r}')\, F_s(\mathbf{r}')\, \hat{\mathbf{s}}\cdot\hat{\mathbf{n}}'\, dA(\mathbf{r}') \end{aligned} \qquad \mathbf{r}\in V \tag{4.22}$$

$$\begin{aligned} f_w(\mathbf{r}) = & \iiint_V \beta\, K(\mathbf{r},\mathbf{r}_t)\,[F_g(\mathbf{r}_t) + F_w(\mathbf{r}_t)]\, S_i(\hat{\mathbf{s}})\, dV(\mathbf{r}_t) \\ & + \iint_S K(\mathbf{r},\mathbf{r}')\, F_s(\mathbf{r}')\, S_i(\hat{\mathbf{s}})\, \hat{\mathbf{s}}\cdot\hat{\mathbf{n}}'\, dA(\mathbf{r}') \end{aligned} \qquad \mathbf{r}\in V \tag{4.23}$$

$$\begin{aligned} f_s(\mathbf{r}) = & \iiint_V \beta\, K(\mathbf{r},\mathbf{r}_t)\,[F_g(\mathbf{r}_t) + F_w(\mathbf{r}_t)]\,(-\hat{\mathbf{s}}\cdot\hat{\mathbf{n}})\, dV(\mathbf{r}_t) \\ & + \iint_S K(\mathbf{r},\mathbf{r}')\, F_s(\mathbf{r}')\,(-\hat{\mathbf{s}}\cdot\hat{\mathbf{n}})\ \hat{\mathbf{s}}\cdot\hat{\mathbf{n}}'\, dA(\mathbf{r}') \end{aligned} \qquad \mathbf{r}\in S \tag{4.24}$$

where

$$f_g(\mathbf{r}) = 4e_g(\mathbf{r}) - \frac{1}{(1-\omega)\beta}\nabla\cdot\mathbf{q}_r(\mathbf{r}) \qquad F_g(\mathbf{r}) = e_g(\mathbf{r}) - \frac{\omega}{4(1-\omega)\beta}\nabla\cdot\mathbf{q}_r(\mathbf{r})$$

$$f_w(\mathbf{r}) = w_i(\mathbf{r}), \quad i = 1, 2, \ldots, M \qquad F_w(\mathbf{r}) = \frac{\omega}{4}\sum_{k=1}^{M} c_k\, S_k(\hat{\mathbf{s}})\, w_k(\mathbf{r}) \tag{4.25}$$

$$f_s(\mathbf{r}) = e_s(\mathbf{r}) - \frac{1}{\varepsilon}q_s(\mathbf{r}) \qquad F_s(\mathbf{r}) = e_s(\mathbf{r}) - \frac{1-\varepsilon}{\varepsilon}q_s(\mathbf{r})$$

and K denotes the exponential kernel function defined as:

$$K(\mathbf{r},\mathbf{r}') = \exp\left[-\int_0^{|\mathbf{r}-\mathbf{r}'|}\beta(\mathbf{r}-\hat{\mathbf{s}}t)dt\right] \Big/ \pi|\mathbf{r}-\mathbf{r}'|^2 \tag{4.26}$$

or with $\mathbf{r}_i$ replacing $\mathbf{r}'$ in $K(\mathbf{r},\mathbf{r}_i)$. Observe here that the integral term becomes $\beta|\mathbf{r}-\mathbf{r}'|$ if the extinction coefficient β is constant over the path segment $\mathbf{r}'$ to $\mathbf{r}$, as assumed previously in the derivation of Eqs. (4.20) and (4.21). However, with the kernel in its most general form, it is emphasised that Eqs. (4.22-26) are also applicable to media with spatially dependent optical properties such that $\beta = \beta(\mathbf{r})$, $\omega = \omega(\mathbf{r})$ and $\varepsilon = \varepsilon(\mathbf{r})$.

In later sections it is shown how several numerical methods are developed from these integral equations.

4.1.3 Closure Conditions: Surface Heat Flux & Divergence of Radiative Flux

For a general radiative problem there are two unknowns in the medium, i.e. e_g and $\nabla\cdot\mathbf{q}_r$, and two unknowns on the boundary, i.e. e_s and q_s, provided that all optical properties are known or specified as functions of these. One of each pair must be given in order to solve for the other. The most common closure conditions are as follows:

On the boundary:

(a) q_s is specified. This corresponds to a von Neumann boundary condition.

(b) e_s, or the equivalent surface temperature, T_s is specified – a Dirichlet condition.

(c) A mixed (Robin) boundary condition is applied.

In the medium:

(a) $\nabla \cdot \mathbf{q}_r$ is specified. A special case is radiative equilibrium, $\nabla \cdot \mathbf{q}_r = 0$. i.e. steady state conditions without significant heat conduction, convection, viscous dissipation, or internal heat sources.

(b) e_g, or the equivalent gas temperature, T_g is specified.

Condition (b) in the medium also includes combined mode heat transfer problems in which the gas temperature distribution is obtained by solving the conservation equations, Eqs. (3.42-51). The radiation transport equation is coupled to these equations primarily through the radiation flux vector $\mathbf{q}_r$ (written as $q_{r,i}$) in Eq. (3.49). Substituting back into the internal energy equation, Eq. (3.45) and expanding out the radiation term gives the divergence of radiative heat flux $\nabla \cdot \mathbf{q}_r$ as the unknown.

A combined mode solution then proceeds briefly as follows. An initial guess is made for the flux divergence $\nabla \cdot \mathbf{q}_r$ and the conservation equations are solved to obtain T_g. These temperatures are then fed back into the radiation calculation in order to update the flux divergence field. The entire process is repeated until a convergence criterion is met. A coupled flow-radiation solver is described later in Sec. 5.5.

4.2 Numerical Methods for Participating Media: A Review

The integro-differential nature of the radiation transport equation, which arises from the spatial *and* direction dependence of radiative intensity, makes the analysis of radiating participating media inherently complex. Exact analytical solution is only feasible for highly idealised situations, and as a result, a great diversity of approximate numerical methods have been proposed in the latter part of this century. Some methods have received much attention, while others that appeared promising in the past have now fallen out of favour. This is largely a result of: (*i*) the analyses of more difficult problems involving multidimensions, variable properties, scattering anisotropy and/or spectral effects, and (*ii*) the development of new computational hardware and software. Thus, the following discussion focuses only on the survivors, or new methods, that show the greatest promise for sustained development. The texts of Modest (1993), and Siegel and Howell (1992), together with two general review papers by Chan (1987) and Howell (1988) provide additional (albeit dated) information.

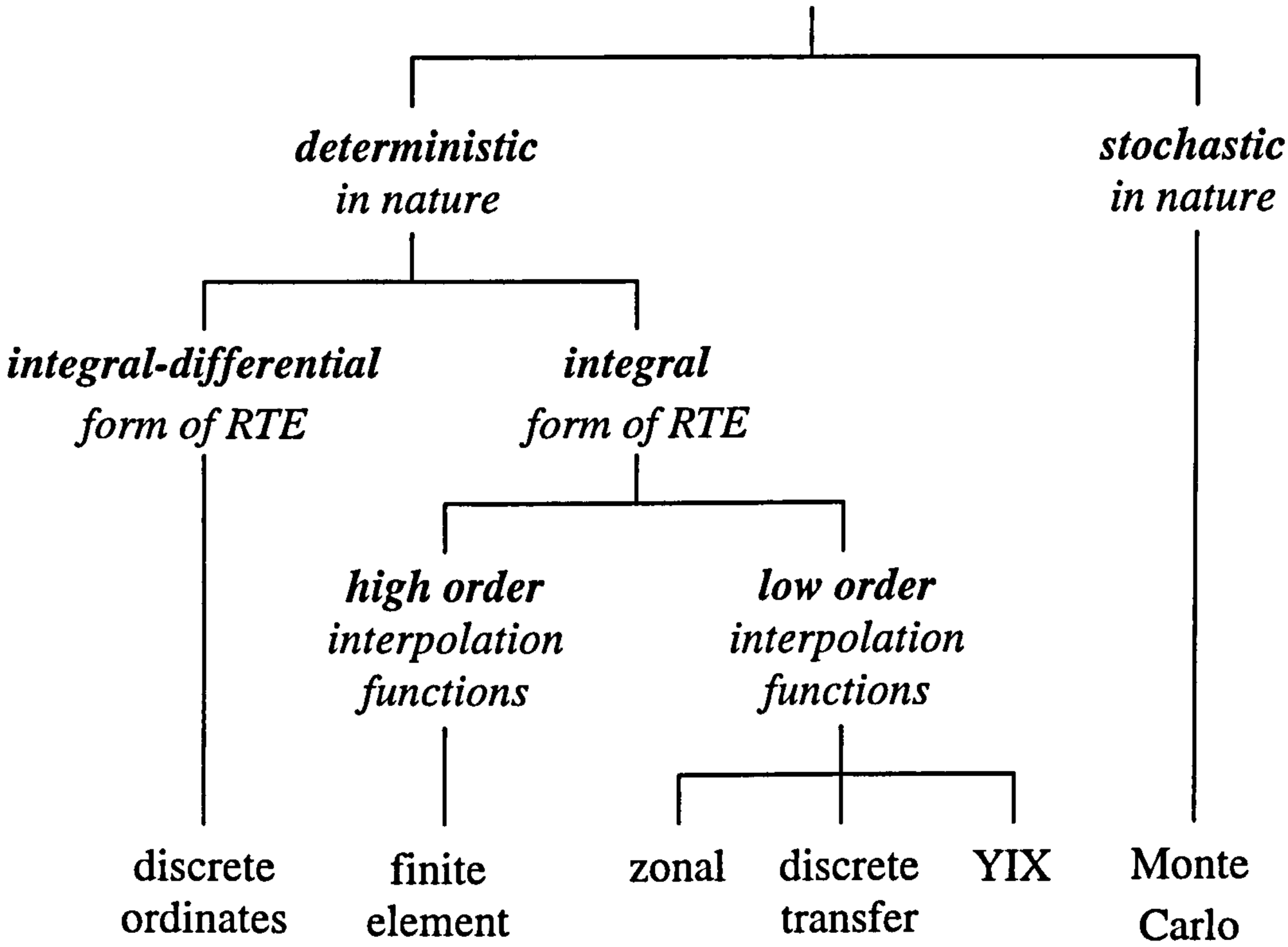

Figure 4.3 Classification of solution methods for the radiation transport equation (RTE).

To understand how different numerical methods relate to each other it is useful to develop a framework into which the techniques can be placed. Figure 4.3 shows a possible classification system where distinctions have been based on key aspects of methods' formulations. The stochastic nature of Monte Carlo methods immediately sets them apart from all other numerical techniques which use a deterministic approach. Subdivision of the deterministic methods is then possible depending on whether their formulation is based on the integro-differential or integral form of the radiation transport equation. Discrete ordinate methods are an example of the former while the zonal, discrete transfer, YIX and finite element methods are all developed from the exact integral form. Computationally, this distinction has important consequences. The integro-differential formulation generally leads to much sparser matrices than the integral form and thus solvers require much less computational effort for a given number of unknowns. However, the integro-differential equation is defined in a high-dimensional space $(\mathbf{r}, \hat{\mathbf{s}})$, so the number of unknowns is usually large. This is in contrast to the integral formulation, where only the three space coordinates appear resulting in fewer unknowns

when a numerical method is applied. Another advantage of the integral formulation is that the divergence of radiation flux in space is solved for directly. Tan (1991) argues that in cases of combined mode heat transfer the coupling is stronger between the radiation transport equation and the energy equation than when the integro-differential formulation is used. Hence, the convergence of iterative schemes is faster.

Monte Carlo Methods. A general solution method for participating radiative heat transfer, able in principle to exactly simulate all important physical processes, was presented as early as 1964: it is the Monte Carlo method of Howell and Perlmutter (1964a, b). In essence this method stochastically models the exchange of radiative energy by ray tracing a random sample of photons, or energy bundles, from their points of emission to their points of absorption. Ironically, it is the inherent modelling flexibility offered by this stochastic approach that is also responsible for the two principal shortcomings of all Monte Carlo methods. The first of these is the non-analytical, 'non-appealing' statistical nature of their results which always have some level of uncertainty. The second is the often extensive computational run times required to obtain an acceptable level of precision and accuracy in these results. Thus, historically, Monte Carlo methods have been used either as a means of verifying faster deterministic techniques, as in the present work, or where there is no other convenient method available. However, the competitive advantage of other methods is expected to shrink as problem complexity increases and computational hardware improves. A good, but dated, account of Monte Carlo methods for all modes of heat transfer is that of Haji-Sheikh (1988). Recently, the excellent doctoral thesis of Farmer (1995) reviews several Monte Carlo algorithms for radiative heat transfer and considers some of the more difficult aspects of realistic media. The 'pathlength' based Monte Carlo approach described in Sec. 4.4 is developed largely from this work.

Discrete Ordinate Methods. These techniques were first used to solve the neutron transport equation of integro-differential form (see Tan 1991, p.18). Since this equation is almost identical to that for radiation transport, discrete ordinate methods have also been optimised for radiative heat transfer problems (Fiveland 1984; 1988). Essentially, these methods transform the integro-differential formulation given by Eq. (4.1) into a set of n simultaneous partial differential equations, each describing the direction variation of radiative intensity, $i(\mathbf{r},\hat{\mathbf{s}}_i)$, $i=1,2,\ldots,N$. These N discrete directions are selected using S_n quadrature (Fiveland 1991) of the total solid angle of 4π, where $N=n(n+2)$.

Arbitrary anisotropic scattering phase functions can be treated using approximations similar to those shown in Eqs. (4.3-4.5). An efficient sparse matrix solver is then used to determine the intensity field, from which the radiative heat flux, on a surface or inside a medium, is readily calculated.

However, discrete ordinate methods are not without their shortcomings. Inaccuracies arise from ray effects and false scattering (Chai *et al.* 1993a). *Ray effect* refers to the error incurred by approximating the continuously varying angular nature of intensity into a finite set of discrete directions. It is a fundamental problem of all methodologies that use comparable angular discretisation schemes for the intensity. Chai *et al.* (1993a) refers to some possible remedies used by the neutron transport community. *False scattering*, on the other hand, is a problem associated specifically with discrete ordinate solvers, whereby an artificial scattering effect is introduced by the spatial differencing scheme. Consequently, genuine discontinuities in the intensity field appear smeared in solutions. (This phenomena can be considered analogous to numerical diffusion in fluid dynamics.) Negative intensities may also result from the spatial differencing, causing numerical oscillations and instabilities. Chai *et al.* (1993b) investigated the diamond, step (upwind), positive and variable-weight differencing schemes and found that only the step approximation is unconditionally stable. Finally, a major disadvantage of all conventional discrete ordinate schemes is that they lack sufficient generality to permit analysis of irregular, three-dimensional geometries.

Therefore, new angular and spatial discretisation practices are being developed. These employ sophisticated finite volume (Raithby and Chui 1990; Chui and Raithby 1992; 1993; Chai *et al.* 1993c) or finite element (Fiveland and Jessee 1993; 1994; Hoover *et al.* 1996) based discrete ordinate formulations. Testing of these methods for complex geometries and various element shapes is ongoing, but perhaps most encouraging of all is a new algorithm by Sakami *et al.* (1997). It uses an integral equation for radiation transport in place of classical spatial differencing schemes. In fact, the new approach could be considered as a discrete ordinate – discrete transfer hybrid, since the characteristic equation used is that which forms the basis of the latter method. This feature results in a general and accurate formulation with only a moderate increase in the level of complexity. The algorithm does not generate negative intensities and the authors believe that false scattering errors are minimal. At present the method is applicable to a tetrahedral mesh, but extension to arbitrary hexahedral element shapes is expected.

Zonal Methods. Hottel and Cohen (1958) pioneered the first analytical treatment of radiative heat transfer in participating media using a zoning approach. In their method a nonisothermal radiating system is subdivided into a finite number of isothermal volume and surface area zones. An energy balance is then written for the radiative heat exchange between any two zones. This leads to a set of simultaneous algebraic equations for the unknown temperatures or heat fluxes, the coefficients of which embody the opticogeometric properties of the system. These coefficients are referred to as the 'exchange areas' and must be computed. Larsen and Howell (1985) later expressed the energy balance in terms of 'exchange factors', which are physically measurable quantities and showed their mathematical relation to exchange areas. In a computational sense both methods are equivalent. More recently other zonal formulations have been proposed (e.g. Naraghi *et al.* 1988; Yuen *et al.* 1992) which improve accuracy or extend applicability to more difficult media. However, in spite of these efforts, zonal methods do not perform well in complex physical situations involving nonhomogeneous and nongray media. Furthermore, zonal methods are equivalent to a Galerkin finite element solution to the integral equations that uses a piecewise-constant interpolating function across elements (Tan 1991, p.22). Therefore, it is likely that more accurate finite element methods employing higher-order approximations will eventually supersede zonal calculations. Though, at present, zonal exchange area relations are useful in hybrid formulations with the Monte Carlo and YIX methods (see Secs. 4.4.4 and 4.5.3).

Discrete Transfer Method. This method (Shah 1979; Lockwood and Shah 1981) is a hybrid of Monte Carlo, zonal and discrete ordinate methods. It is particularly well suited for the analysis of complex geometries, since is combines the ray tracing basis of Monte Carlo algorithms with the faster deterministic nature of the later two methods. Other important attributes include: good economy, ease of application and a conceptually simple methodology which strongly retains in evidence the physics of the problem. This last quality should not be undervalued, and has certainly helped to maintain the method's appeal even as newer, more general, but also more complex, methods have been developed.

Discrete transfer calculations of combustors by Abbas *et al.* (1984), and of compartment fires by Lockwood and Malalasekera (1988), both demonstrate the method's general applicability to practical problems of combined mode heat transfer. However, it is not possible to resolve the error associated with the radiation treatment from that of the

turbulent combustion modelling in these studies. Hence, several more recent publications have focused on verifying the discrete transfer method in isolation. Carvalho *et al.* (1991) compared discrete transfer solutions with those from several other methods for absorbing, emitting and isotropically scattering media. Murthy and Choudhury (1992) and Meng *et al.* (1993) both verified calculations on irregular grids, the latter study using an unstructured triangular mesh. These studies were largely two-dimensional. Haidekker *et al.* (1994) compared Monte Carlo and discrete transfer solutions for absorbing and emitting media contained within three-dimensional arbitrary geometries discretised with a curvilinear mesh. Further cases have also been presented by Malalasekera and James (1995) with verification against exact solutions and those of other methods. An efficient ray tracing methodology, developed for the present study (Sec. 4.3.2), is also outlined in this latter paper. However, despite some criticism of the discrete transfer method in these studies (e.g. Meng *et al.* 1993), none significantly add to the original formulation of Lockwood and Shah (1981). In view of this, Cumber (1995) has suggested possible modifications to improve accuracy or computational performance. Notably, some new quadrature formulae are proposed, but the calculations to demonstrate the advantage of these are not particularly convincing. A discrete ordinate S_n quadrature has also been considered in the present study and its attributes are described later in Sec. 4.6.2. Cumber further modifies the original discrete transfer formulation to obtain a more accurate representation of the temperature field, though the improvement in accuracy does not seem to merit the added complexity, particularly in multi-dimensional problems. However, there is no discussion by Cumber or others of the method's restriction to diffuse boundaries and isotropically scattering media. Furthermore, there has been no formal verification of the method for several important aspects of realistic media that are relevant to this study, i.e. complex curvilinear geometries, nonhomogeneous and nongray properties. Therefore, these points need to be examined.

YIX Method. Tan (1989) perceived that a more efficient numerical method to solve the exact integral equations for radiative heat transfer might be obtained with specialised mathematical techniques. This work culminated in the development of the YIX method (Tan and Howell 1990a, b; Tan 1991). The integral equations are first transformed to a distance-angular form, then the distance integrals are constructed and pre-stored such that all subsequent integrations may be rapidly computed as simple sums. This approach eliminates the time consuming evaluation of the kernels (i.e. Eq. 4.26) of the distance

integrals. Tan (1991, p. 68) states that the computing time is proportional to the number of unknowns, N, whereas for analogous methods (e.g. zonal method, finite element method) it is proportional to N^2. Moreover, the formulation is very flexible: anisotropic scattering and nonhomogeneous, nongray media can be treated efficiently in three-dimensions (Hsu *et al.* 1993; Hsu and Farmer 1995; Hsu and Tan 1996). A benchmark conduction-radiation problem has also been solved (Hsu and Tan 1996) to demonstrate the method's application to combined mode heat transfer.

However, in spite of its success, the YIX method has not made as significant an impact on the heat transfer community as one might expect. Undoubtedly this is partly due to its novelty, but may also result from the fact that details of the three-dimensional formulation have as yet not been published and the complex mathematics is discouraging. The changes required to extend one- and two-dimensions schemes are not obvious since the form of the kernel function varies for each dimension, i.e. they are exponential functions in one-dimension and Bickley functions in two-dimensions (Tan and Howell 1990a). In addition, more work is required to develop an efficient ray tracing algorithm in order to treat irregular geometries.

Finite Element Methods. The widespread use of finite element methods for conductive and convective transport has stimulated interest in extending their application to radiative media. Most early works adopt a traditional Galerkin method of weighted residuals to solve for the integral equations of radiative heat transfer (Razzaque *et al.* 1983, 1984; Chung 1988). This approach is then directly compatible with established Galerkin methods for the other modes of heat transfer, and by choosing high-order interpolation or *shape* functions to describe radiative property variations across finite elements, it offers the possibility of high accuracy. However, usually linear or quadratic shape functions are specified since computation of higher-orders quickly becomes prohibitive. Furthermore, great complexity and computational expense is added to the traditional finite element method by the radiation terms involving fourth powers of temperature. This can be avoided by using the Swartz-Wendroff approximation in which the fourth power of temperature is expanded directly as a separate function, albeit one closely related to the temperature itself. Burns *et al.* (1994; 1985a) assessed its performance for sample conduction/radiation problems. Although there was a marginal loss of accuracy it was found that the Swartz-Wendroff approximation provided a significant speed-up and

improved numerical stability. Burns *et al.* (1995a, b) also analysed problems with nonhomogeneous and nongray radiative properties. Their formulation is restricted to diffusely reflecting boundaries and isotropically scattering media, but it is expected that these limitations can be removed with further work. Rather, it is the large computational requirements of finite element methods that remains their main disadvantage, even after the improvements of Burns and others.

Present Research Activity. The comment accompanying each of the methods reviewed above is based on the consensus of opinion in the heat transfer community at the time of writing. However, the situation was very different at the start of this research. The ray tracing methodology of discrete transfer and Monte Carlo methods seemed much more adaptable to complex geometries than the discretisation practices of contemporary finite element or discrete ordinate schemes. Hence, early work focused on the former methods: the discrete transfer formulation of Lockwood and Shah (1981) was implemented (with modifications to improve both generality and performance) together with several Monte Carlo algorithms from various sources in the literature. Shortly thereafter, the results of three-dimensional benchmark studies using the YIX method (Hsu *et al.* 1993) were so encouraging that it was also considered important to investigate this approach. Moreover, like the Monte Carlo and discrete transfer methods, the YIX formulation is built around a ray tracing methodology, such that all three methods may naturally be categorised as 'ray-tracing-based' techniques. A general three-dimensional YIX algorithm was developed on the basis of published one- and two-dimensional schemes (Tan 1991). Finally, the earlier Monte Carlo algorithms were updated to the present state-of-the-art from Farmer (1995).

Clearly, even in this short period there has been much activity in the field of participating radiative heat transfer and a continuous effort is required to stay abreast of new developments. In the formulation and coding of the present Monte Carlo, YIX and discrete transfer methods care has been taken to incorporate the best available knowledge from heat transfer, statistical and graphics literature. This work is detailed in following sections.

4.3 Geometric Modelling and Ray Tracing

A key feature of the radiation treatment in this study is that, irrespective of whether the user chooses to use a Monte Carlo, YIX or discrete transfer approach, all three methods embody the same geometric representation scheme and ray tracing procedures. This arrangement offered the following advantages:

1. *Easier coding and development*: a shared library of graphics routines could be used to code the geometric and ray tracing aspects in all three methods, such that only the unique part of each numerical scheme had to be implemented separately.

2. *Bias-free numerical comparisons*: variations in coding and optimisation strategies, particularly with respect to the graphics procedures, are minimal such that performance comparisons between the present methods will be more genuine than those compiled with data taken from independent studies (e.g. Tong and Skocypec 1992).

The efficiency of the procedures used in the graphics library is of critical importance to the overall performance of each method. For example, substantial speed-ups were obtained by careful optimisation of the ray tracing search strategy. Thus, considerable time and effort was invested in developing an efficient and robust geometric scheme, yet with sufficient generality to enable integration into existing finite volume or finite element software packages with only minor modification. Among its principal features are: the ability to accommodate irregular geometries, an efficient ray tracing algorithm which takes advantage of the element connectivity, the flexibility to describe nonhomogeneous property distributions, and direct data transfer, without interpolation, when the radiation transport is solved alongside other modes of heat transfer. These features are all discussed in the sections below.

4.3.1 Spatial Discretisation and Element Properties

In order that the radiation methods are compatible with the turbulent combustion model (Chapter 3), for a multi-moded heat transfer analysis of spark-ignition engines, they are specifically designed for the spatial discretisation described in Chapter 2. Here the radiation space is subdivided into hexahedral control volumes of arbitrary size and shape. Since finite element modellers use tetrahedral elements for greater flexibility, this would

appear to be a major limitation. However, for the purposes of the radiation analysis, hexahedral cells are effectively reduced into their tetrahedral primitives and cell faces are treated as two triangular elements. Consequently, only superficial changes are required to adapt the present geometric scheme to an unstructured tetrahedral mesh or one which has mixed element shapes. These changes are largely concerned with modifying the element indexing procedures.

For the structured hexahedral meshes considered in this study, two basic geometric properties must be determined: the cell face areas (coincident with boundaries) and the cell volumes. Consider the face ABCD of the arbitrary hexahedral volume in Fig. 4.4. Its area is obtained as the sum of the surface area vectors of the two triangles ABC and CDA, i.e.

$$\mathbf{A}_{ABCD} = \tfrac{1}{2}[(\mathbf{v}_{AB} \times \mathbf{v}_{BC}) + (\mathbf{v}_{CD} \times \mathbf{v}_{DA})] = \tfrac{1}{2}(\mathbf{v}_{AC} \times \mathbf{v}_{BD}) \tag{4.27}$$

which reduces to the vector product of the two diagonals AC and BD as shown. Here $\mathbf{v}_{AB}$ for example, represents the Cartesian vector from vertex A to B.

The cell volumes are obtained by subdividing each hexahedral element into tetrahedra and then summing the volumes of each tetrahedron. The volume of the tetrahedron ABDE, for example, is found from the vector expression:

$$V_{ABDE} = \tfrac{1}{6}\mathbf{v}_{AE} \cdot (\mathbf{v}_{AB} \times \mathbf{v}_{AD}) \tag{4.28}$$

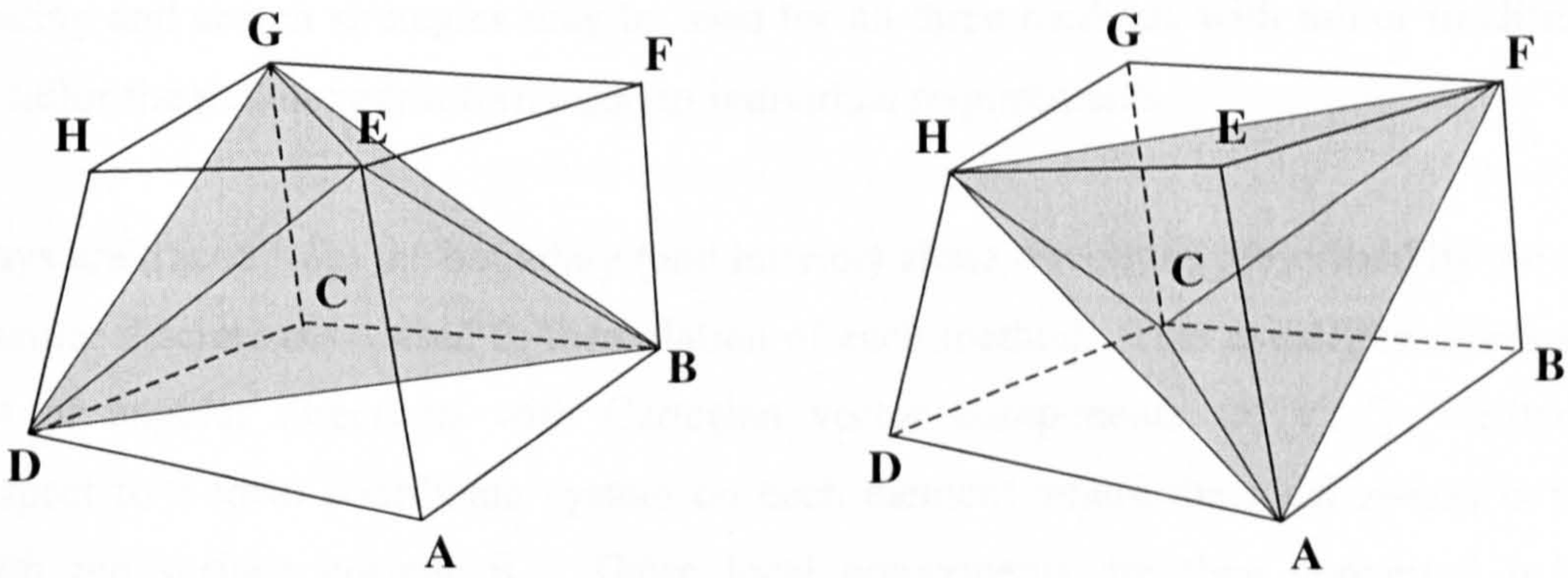

Figure 4.4 Two subdivisions of an arbitrary hexahedral element into five tetrahedra.

If the decomposition is made about a *single* vertex then six tetrahedra always result. However, only five tetrahedra are obtained using the arrangement shown in Fig. 4.4(a), i.e.

$$V_{HEX} = V_{EABD} + V_{EBFG} + V_{EDGH} + V_{EBGD} + V_{CBDG} \tag{4.29}$$

In this special decomposition four tetrahedra have E as their summit and one tetrahedron originates in point C, opposite to E. For the same two vertices C and E, there is a unique second decomposition into five tetrahedra as shown in Fig. 4.4(b), i.e.

$$V_{HEX} = V_{CAFB} + V_{CADH} + V_{CFHG} + V_{CAHF} + V_{EAFH} \tag{4.30}$$

Where the four corner points on any of the cell faces are not coplanar, Eqs. (4.29) and (4.30) do not give identical values for the volume, and thus the average is always taken. Hirsch (1988, p. 260) observes that the volumes of hexahedral cells can also be evaluated with a 2×2×2 Gaussian point integration formulae. However, this is found to give an equivalent result to the average of Eqs. (4.29) and (4.30).

4.3.2 Ray Tracing and Search Strategies

The major computational effort in all the present numerical methods is spent in tracing either the ray or bundle paths through the hexahedral volumes in the discretised radiation space. The information that must be returned by the ray tracing algorithm to the numerical routines differs slightly depending on the method: discrete transfer and Monte Carlo both require the path segment lengths in each cell cut by a ray, while YIX needs to know in which cells specific integration points along a ray path lie. However, the same tracing and search strategies may be used for all three methods with minor modifications to tailor the path length information to individual requirements.

Rays are traced from the boundary (and interior) along directions prescribed by the type of angular discretisation used in formulation of each method. This usually involves a fixed set of angular directions with Cartesian vector components (x', y', z'), written with respect to a local coordinate system on each element where the local z–axis is aligned with the surface normal $\hat{\mathbf{n}}$. These local components are then converted to global components by transforming from the local coordinate system to the global Cartesian system.

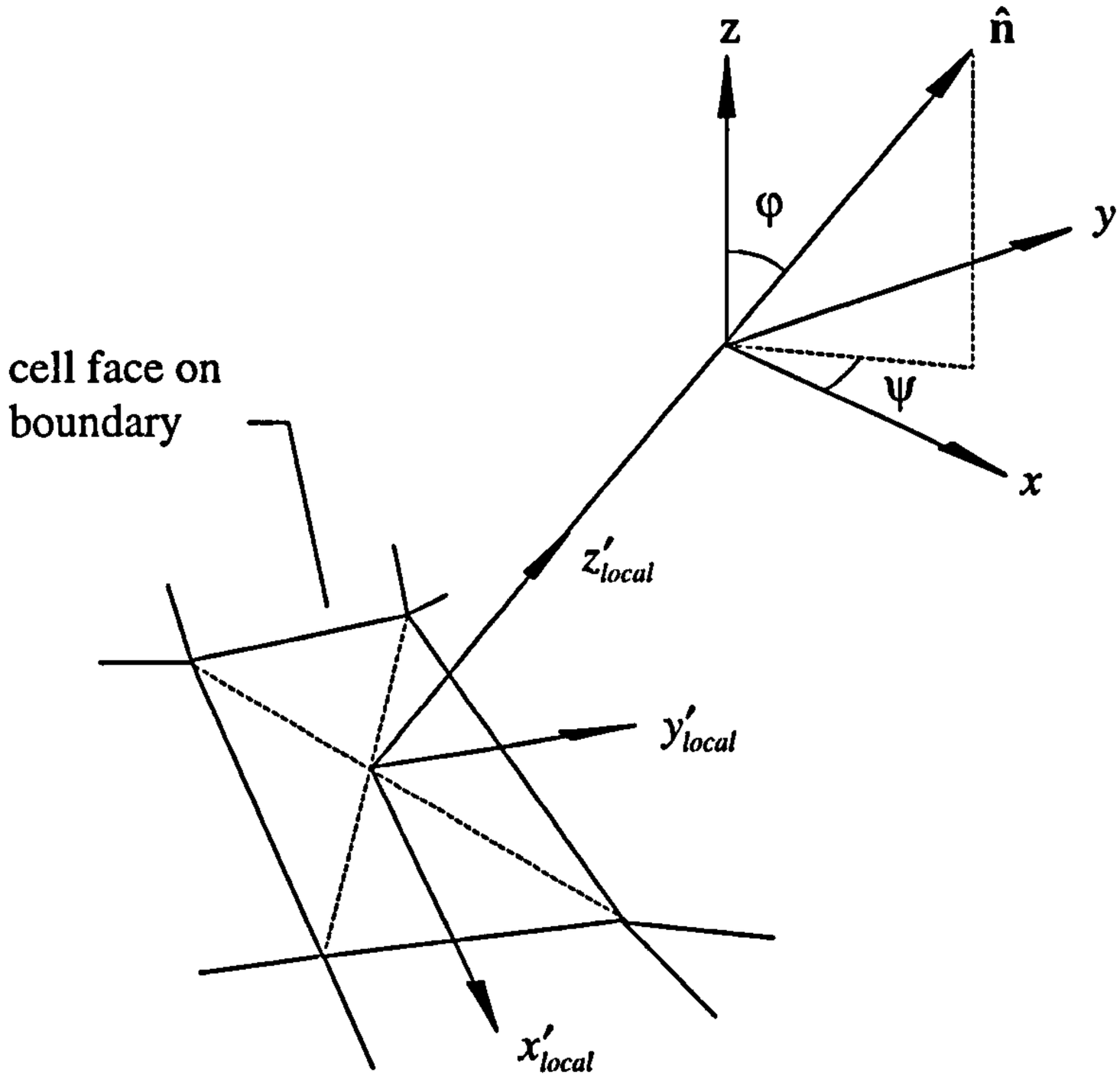

Figure 4.5 Definition of the polar and azimuthal angles φ and ψ for transforming from the global Cartesian coordinate system to a local system on the boundary surface.

Each local vector direction $(x', y', z')^T$ is rotated through an angle ψ about the z–axis, and an angle φ about the y–axis, such that its new direction $\hat{\mathbf{s}}$ becomes:

$$\hat{\mathbf{s}} = \begin{pmatrix} \cos\psi & -\sin\psi & 0 \\ \sin\psi & \cos\psi & 0 \\ 0 & 0 & 1 \end{pmatrix} \begin{pmatrix} \cos\varphi & 0 & \sin\varphi \\ 0 & 1 & 0 \\ -\sin\varphi & 0 & \cos\varphi \end{pmatrix} \begin{pmatrix} x' \\ y' \\ z' \end{pmatrix} \tag{4.31}$$

where φ and ψ are the polar and azimuthal angles with respect to the global axes when $\hat{\mathbf{n}}$ is written in spherical coordinates (see Fig. 4.5). The surface normals are conveniently calculated and pre-stored at the same time as the area calculation in Eq. (4.27), with the expression $\hat{\mathbf{n}} = \mathbf{A}/|\mathbf{A}|$.

If the position vector $\mathbf{r}'$ denotes the launch location or origin of the ray, travelling in the direction $\hat{\mathbf{s}}$, then its parametric representation is:

$$\mathbf{r}(t) = \mathbf{r}' + \hat{\mathbf{s}}\, t, \qquad (t = \text{scalar}) \tag{4.32}$$

The ray–cell boundary intersections must be found along this path. A robust approach is desired, able to handle both distortion in the hexahedral cell faces, and the precision problems (i.e., see Haines 1989) that can arise from floating-point errors, particularly when the ray strikes an edge. The first difficulty is overcome by pre-processing cell faces into two triangles prior to the intersection calculation. Thus, the six quadrilateral faces of each hexahedral volume are divided into twelve triangular elements. Care has to be taken to ensure that the same diagonal is chosen for a face common to two neighbouring cells, otherwise void spaces could result in the mesh. (This pre-processing stage would be skipped with tetrahedral spatial discretisation schemes.)

The problem is then reduced to recursively finding the nearest triangular element intersected by the ray, until a boundary surface is struck, or as in the case of the present Monte Carlo method (Sec. 4.4), when its associated radiative energy is fully depleted. Since millions of intersection calculations may be required for a complete radiation simulation, optimisation of the tracing algorithm is paramount.

Ray tracing methodology is an extensive area of research in computer graphics literature for the rendering of three-dimensional images. Some of the newest ideas are debated in Internet discussion groups and a special ray tracing FAQ (frequently asked questions) compiled by Haines (1992) provides excellent reviews of several ray-polygon intersection techniques.

A comparison of their speed for randomly generated n-sided polygons (n = 3, 4, etc.) found that an algorithm by Badouel (1990) is the fastest for ray-*triangle* intersections (i.e. $n = 3$). Run times were an order of magnitude smaller than for the least efficient method, namely an 'angle test' approach which is often found in older ray tracing literature. Furthermore, Badouel not only determines the global coordinates of the intersection point, but also the interpolation parameters (i.e. the barycentric coordinates), to localise this point with respect to the triangle's vertices. In the present implementation, these parameters are used in a novel way to simplify the tracing logic and eliminate problems from floating-point imprecision: the second difficulty noted above.

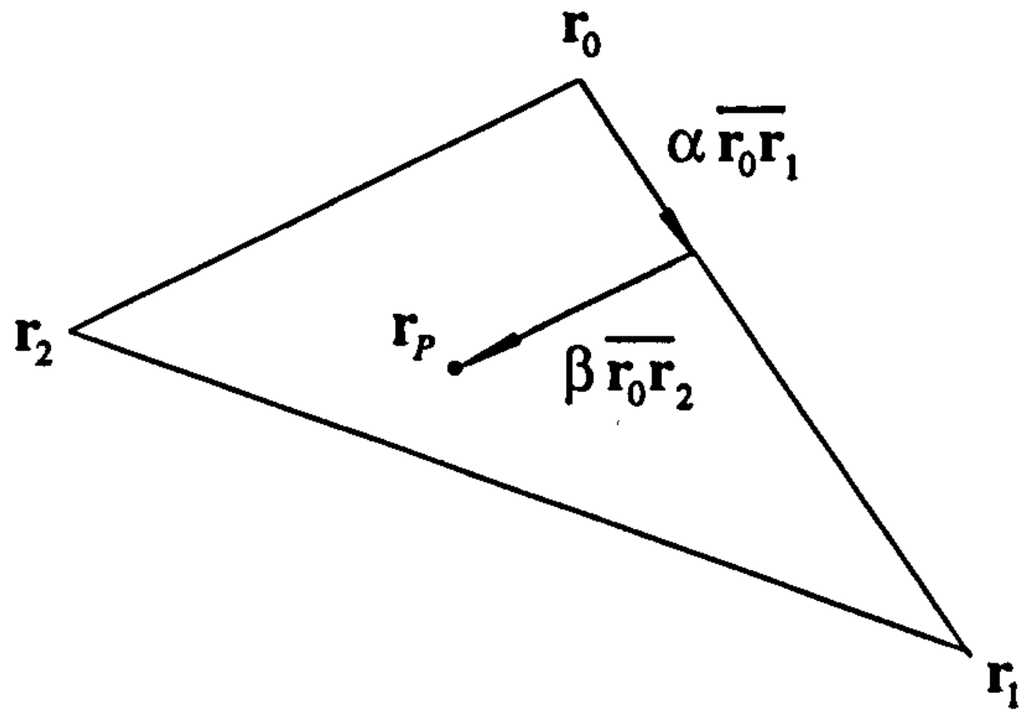

Figure 4.6 Parametric representation of the point intersection point $\mathbf{r}_P$.

Consider the triangle shown in Fig. 4.6 which has vertices, $\mathbf{r}_i$ $(i=0,1,2)$ with Cartesian coordinates (x_i, y_i, z_i). The algorithm first determines if the ray defined in Eq. (4.32) intersects the plane on which the triangle lies and then tests if this intersection point is inside the triangle.

Stage 1: Intersects Embedding Plane? The normal, **n**, of the plane containing the triangle is first calculated from the cross product:

$$\mathbf{n} = \overline{\mathbf{r}_0\mathbf{r}_1} \times \overline{\mathbf{r}_0\mathbf{r}_2} \tag{4.33}$$

where $\overline{\mathbf{r}_0\mathbf{r}_1} = \mathbf{r}_1 - \mathbf{r}_0$, etc. For each point $\mathbf{r}_P$ in the plane, the dot product $\mathbf{r}_P \cdot \mathbf{n}$ is a constant. This constant is equal and opposite to the value:

$$d = -\mathbf{r}_0 \cdot \mathbf{n} \tag{4.34}$$

since the triangle vertex $\mathbf{r}_0$ lies in the plane. Then the plane can be represented by the general vector expression:

$$\mathbf{r}_P \cdot \mathbf{n} + d = 0 \tag{4.35}$$

Substituting the parametric equation for the ray, Eq. (4.32) into (4.35), gives the value of the scalar parameter t corresponding to an intersection as:

$$t = -\frac{d + \mathbf{n} \cdot \mathbf{r}'}{\mathbf{n} \cdot \hat{\mathbf{s}}} \tag{4.36}$$

The intersection is rejected if the plane and ray are parallel (i.e. $\mathbf{n}\cdot\hat{\mathbf{s}}=0$), or the intersection is behind the ray origin (i.e. $t\leq 0$), otherwise the coordinates of the intersection point $\mathbf{r}_P$ are obtained by substituting t back into Eq. (4.32).

Stage 2: Intersects Triangle? The ray-*plane* intersection point $\mathbf{r}_P$ is expressed in terms of the barycentric coordinates (α, β, γ) of the triangle as follows:

$$\mathbf{r}_P = \gamma\, \mathbf{r}_0 + \alpha\, \mathbf{r}_1 + \beta\, \mathbf{r}_2 \tag{4.37}$$

If the point lies inside the triangle: $\alpha+\beta+\gamma=1$. Eliminating γ gives:

$$\overline{\mathbf{r}_0\,\mathbf{r}_P} = \alpha\ \overline{\mathbf{r}_0\,\mathbf{r}_1} + \beta\ \overline{\mathbf{r}_0\,\mathbf{r}_2} \tag{4.38}$$

where $\overline{\mathbf{r}_0\,\mathbf{r}_P} = \mathbf{r}_P - \mathbf{r}_0$, etc. and $\mathbf{r}_P$ is inside the triangle if:

$$\alpha \geq 0, \quad \beta \geq 0 \quad \text{and} \quad \alpha+\beta \leq 1. \tag{4.39}$$

Equation (4.38) is a system of three simultaneous linear equations for α and β, i.e.

$$\begin{aligned} x_P - x_0 &= \alpha(x_1 - x_0) + \beta(x_2 - x_0) \\ y_P - y_0 &= \alpha(y_1 - y_0) + \beta(y_2 - y_0) \\ z_P - z_0 &= \alpha(z_1 - z_0) + \beta(z_2 - z_0) \end{aligned} \tag{4.40}$$

A solution may be obtained by solving any two equations. This is equivalent to projecting the triangle onto one of the principal Cartesian planes, either *xy*, *xz* or *yz*. If the triangle is perpendicular to one of these planes, its projection onto the plane will be a line segment and a unique solution for α and β cannot be found. Hence, it is important to ensure that the chosen plane gives the largest projected area. This is taken as the plane perpendicular to the dominant axis of the normal vector, **n**, previously calculated in Stage 1. The following simple rule is used:

$$\text{Find MAX}[|\mathbf{n}_x|, |\mathbf{n}_y|, |\mathbf{n}_z|]: \begin{cases} \text{if } |\mathbf{n}_x| \text{ then solve with } y \text{ and } z \\ \text{if } |\mathbf{n}_y| \text{ then solve with } x \text{ and } z \\ \text{if } |\mathbf{n}_z| \text{ then solve with } x \text{ and } y \end{cases}$$

Then if α and β satisfy the conditions in Eq. (4.39), the ray intersects the triangle at $\mathbf{r}_P$.

The overall speedup obtained by optimising the ray intersection calculation is only fully realised if it is used in harmony with an effective search strategy that minimises the number of triangular elements that must be checked for an intersection. It is here that some of the most novel ideas have been implemented into the present tracing methodology. If a ray strikes the edge of a cell or a corner vertex, it may pass into one of three or seven possible neighbouring cells, respectively. Indexing and searching each of these cells for the next intersection is expensive and floating-point imprecision can cause the calculation to fail. However, the present strategy elegantly overcomes this problem by automatically detecting an edge/vertex strike, and repositioning the intersection point away from the boundary, such that the ray can only ever pass into *one* neighbouring cell. No loss of accuracy is incurred since the distance moved is a few magnitudes larger than the calculation precision. The parameters, α and β, a by-product of the intersection calculation, are used for both the detection and repositioning operations, such that the extra computation is minimal. A flow chart of the procedure is shown in Fig. 4.7.

As a ray traverses successive cells, its origin is updated to the position of the last intersection in the previous cell. For each hexahedral cell crossed, *all* twelve of its bounding triangular elements must be checked for an intersection, excluding that containing the new origin. This is because three intersections, rather than one, may be found in concave cells as illustrated in Fig. 4.8. Then the intersection closest to the ray origin is the true exit position. However, if the present tracing algorithm is adapted specifically for tetrahedral or orthogonal hexahedral structures, searching can be terminated as soon as the first intersection is found, since then there is always only one!

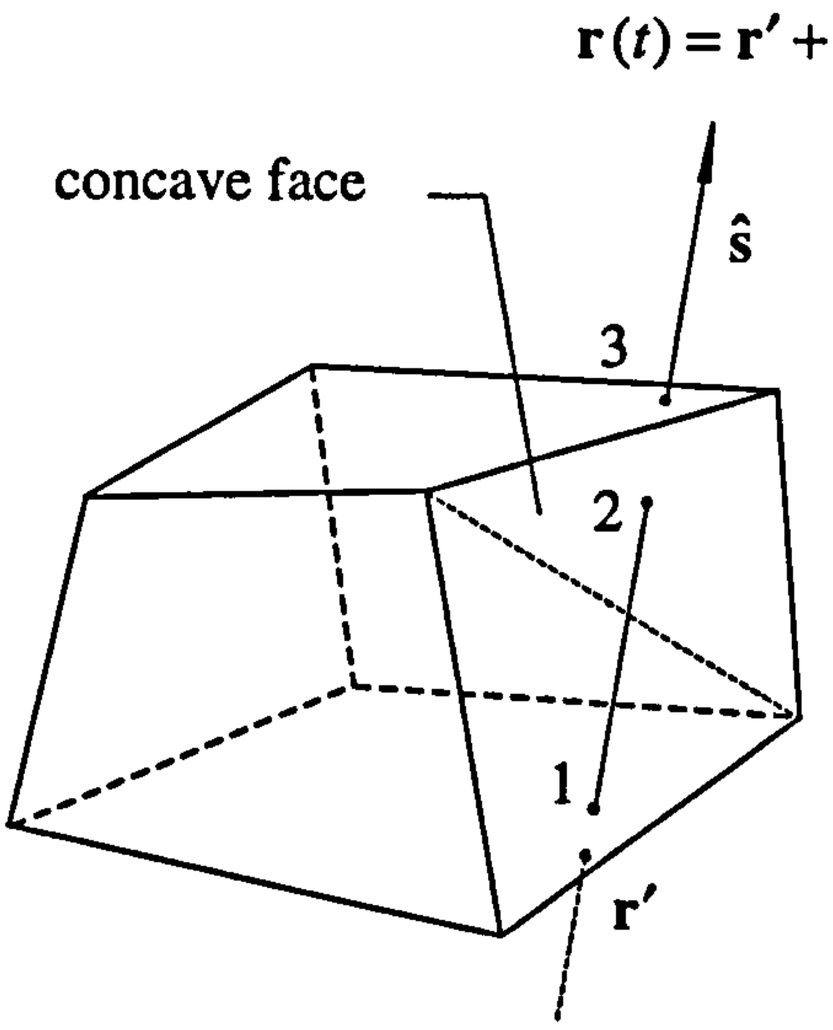

Figure 4.8

Concave face results in search algorithm finding three intersections with boundary faces for ray $\mathbf{r}(t)$: that closest to origin $\mathbf{r}'$ is accepted, i.e. (1).

Note: Fig. 4.7 on following page.

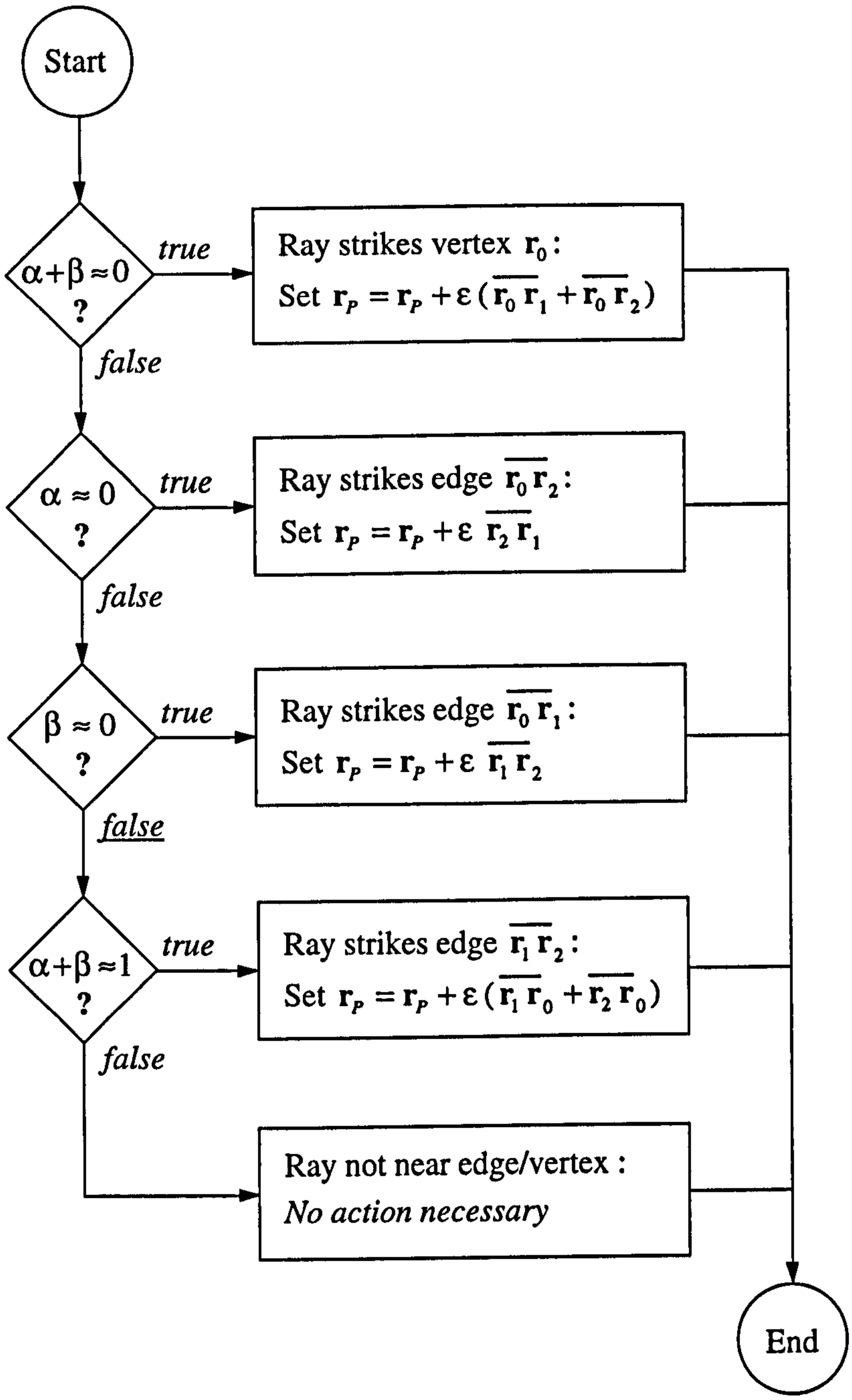

Figure 4.7 Ray repositioning logic in the event of a edge/vertex intersection.
ε = small tolerance a few magnitudes larger than machine precision.

4.3.3 Finite Element Parametric Mapping: Nonhomogeneous Properties

An important function of the geometric model is the mapping of the radiative properties onto the surface and volume elements of the discretised radiation space. Given that the elements are homogeneous (an assumption of the numerical methods in Secs. 4.4-4.6), the simplest and fastest approach, is to evaluate each property $\phi(\mathbf{r})$ at the element 'centre' $\mathbf{x}_c$ defined by:

$$\mathbf{x}_c = \frac{1}{N}\sum_{n=1}^{N}\mathbf{x}_n \tag{4.41}$$

where $\mathbf{x}_n$ refers to either the surface or volume nodal Cartesian coordinates (see $\mathbf{x}$ notation of Sec. 2.1). This single-point value $\phi(\mathbf{r}=\mathbf{x}_c)$ is then taken as constant over the entire element.

Table 4.1 Shape functions for quadrilateral and hexahedral element shapes.

Quadrilateral Element	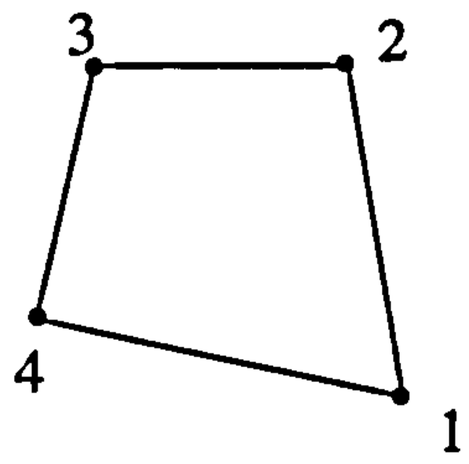	$\psi_1 = \xi(1-\eta)$ $\psi_2 = \xi\eta$ $\psi_3 = (1-\xi)\eta$ $\psi_4 = (1-\xi)(1-\eta)$ $0 \le (\xi,\eta) \le 1$
Hexahedral Element	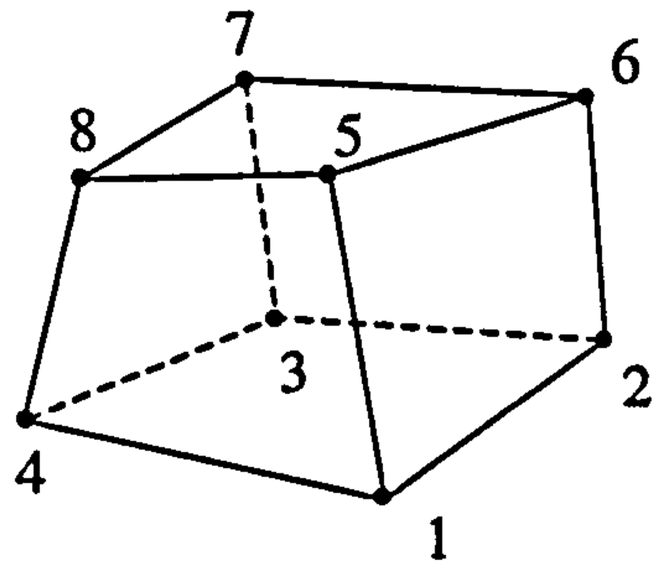	$\psi_1 = \xi(1-\eta)(1-\gamma)$ $\psi_2 = \xi\eta(1-\gamma)$ $\psi_3 = (1-\xi)\eta(1-\gamma)$ $\psi_4 = (1-\xi)(1-\eta)(1-\gamma)$ $\psi_5 = \xi(1-\eta)\gamma$ $\psi_6 = \xi\eta\gamma$ $\psi_7 = (1-\xi)\eta\gamma$ $\psi_8 = (1-\xi)(1-\eta)\gamma$ $0 \le (\xi,\eta,\gamma) \le 1$

However, a better approximation is obtained using a finite element parametric mapping technique to average the property distribution $\phi(\mathbf{r})$ over each element (Hirsch 1988, Sec. 5.4; Farmer 1995, Chap. 2). The value $\phi_i(\mathbf{r})$ at any location $\mathbf{r}$ *inside* the element is obtained from:

$$\phi_i(\mathbf{r}) = \sum_{n=1}^{N} \phi_n \psi_n(\xi,\eta,\zeta) \tag{4.42}$$

where $\phi_n(\mathbf{r}=\mathbf{x}_n)$ is the value of $\phi(\mathbf{r})$ at the node n and ψ_n is the shape or basis function corresponding to node n. The shape functions are locally defined polynomials within each element and zero outside the considered element. Suitable bilinear forms for quadrilateral and hexahedral elements are given in Table 4.1. (Similar expressions are available for triangular and tetrahedral elements.)

Equation (4.42) represents a mapping of the physical element in Cartesian (x,y,z) space onto a master element in a computational (ξ,η,ζ) space. This transformation is analogous to that described in Sec. 2.1, except that now the whole physical space is mapped on an element-by-element basis, rather than in a single global action. Computations are performed for the master element and then adjusted for the element in physical space according to:

$$\int_V dV = |J| \int_v dv \tag{4.43}$$

where V and v are the volumes (or areas) of the physical and master elements, respectively and $|J|$ is the determinant of the Jacobian matrix (i.e. the Jacobian) of the transformation (see below). Therefore, the volume average of $\phi(\mathbf{r})$ over the physical element may be found by numerically integrating $\phi_i(\mathbf{r})$ over the master element, transforming and dividing by V. Using Gaussian quadrature for the numerical integration this is:

$$\bar{\phi}(\mathbf{r}) = \frac{1}{V}\sum_{i=1}^{NI} \phi_i w_i |J|_i = \frac{1}{V}\sum_{i=1}^{NI}\sum_{n=1}^{N} \phi_n \psi_n w_i |J|_i, \qquad \mathbf{r} \in V \tag{4.44}$$

where there are NI integration points each with a weighting w_i. The volume (or area) averaged radiative property $\bar{\phi}(\mathbf{r})$ is then taken as constant over the entire element.

It is important to note that Eq. (4.44) also facilitates the transfer of data from the radiation schemes to finite element codes for other modes of heat transfer, since it links the averaged property value $\bar{\phi}(\mathbf{r} \in V)$ over each element to its nodal values $\phi_n(\mathbf{r} = \mathbf{x}_n)$. Furthermore, if ϕ represents a Cartesian coordinate (i.e. x, y or z), then Eq. (4.42) can be used to map a point (ξ,η,ζ) in the master element to its corresponding point (x,y,z) in the physical element. This feature is used by the present Monte Carlo algorithms to map the starting (emission) locations of energy bundles onto irregular physical elements and ensure the correct distribution of radiant energy (see Sec. 4.4.1.)

Evaluation of the Jacobian. The Jacobian, $|J|$, is required in the transformation of Eq. (4.43). The components of the Jacobian matrix are found directly via the parametric mapping function in Eq. (4.42) as follows:

$$J = \begin{bmatrix} \frac{\partial x}{\partial \xi} & \frac{\partial x}{\partial \eta} & \frac{\partial x}{\partial \zeta} \\ \frac{\partial y}{\partial \xi} & \frac{\partial y}{\partial \eta} & \frac{\partial y}{\partial \zeta} \\ \frac{\partial z}{\partial \xi} & \frac{\partial z}{\partial \eta} & \frac{\partial z}{\partial \zeta} \end{bmatrix} = \begin{bmatrix} \sum_N x_n \frac{\partial \psi_n}{\partial \xi} & \sum_N x_n \frac{\partial \psi_n}{\partial \eta} & \sum_N x_n \frac{\partial \psi_n}{\partial \zeta} \\ \sum_N y_n \frac{\partial \psi_n}{\partial \xi} & \sum_N y_n \frac{\partial \psi_n}{\partial \eta} & \sum_N y_n \frac{\partial \psi_n}{\partial \zeta} \\ \sum_N z_n \frac{\partial \psi_n}{\partial \xi} & \sum_N z_n \frac{\partial \psi_n}{\partial \eta} & \sum_N z_n \frac{\partial \psi_n}{\partial \zeta} \end{bmatrix} \tag{4.45}$$

e.g. For a hexahedral element, with the linear shape functions in Table 4.1, these are:

$$\frac{\partial \phi}{\partial \xi} = [(\phi_1 - \phi_4)(1-\eta) + (\phi_2 - \phi_3)\eta](1-\zeta) + [(\phi_5 - \phi_8)(1-\eta) + (\phi_6 - \phi_7)\eta]\zeta \tag{4.46}$$

$$\frac{\partial \phi}{\partial \eta} = [(\phi_3 - \phi_4)(1-\zeta) + (\phi_7 - \phi_8)\zeta](1-\xi) + [(\phi_2 - \phi_1)(1-\zeta) + (\phi_6 - \phi_5)\zeta]\xi \tag{4.47}$$

$$\frac{\partial \phi}{\partial \zeta} = [(\phi_8 - \phi_4)(1-\xi) + (\phi_5 - \phi_1)\xi](1-\eta) + [(\phi_7 - \phi_3)(1-\xi) + (\phi_6 - \phi_2)\xi]\eta \tag{4.48}$$

Hence, the Jacobian of the point (ξ,η,ζ) is obtained by substituting Eqs. (4.46-48) for ϕ equal to x, y and z for the matrix components of (4.45) and taking the determinant, i.e.

$$|J| = \frac{\partial x}{\partial \xi}\left(\frac{\partial y}{\partial \eta}\frac{\partial z}{\partial \zeta} - \frac{\partial y}{\partial \zeta}\frac{\partial z}{\partial \eta}\right) + \frac{\partial y}{\partial \xi}\left(\frac{\partial z}{\partial \eta}\frac{\partial x}{\partial \zeta} - \frac{\partial z}{\partial \zeta}\frac{\partial x}{\partial \eta}\right) + \frac{\partial z}{\partial \xi}\left(\frac{\partial x}{\partial \eta}\frac{\partial y}{\partial \zeta} - \frac{\partial x}{\partial \zeta}\frac{\partial y}{\partial \eta}\right) \tag{4.49}$$

(Note: the Jacobian $\equiv \sqrt{g}$ is also evaluated with metric tensor components in Chapter 2.)

4.4 Pathlength-Based Monte Carlo

Pathlength-based Monte Carlo is one of a generic family of Monte Carlo methods for radiative heat transfer that has proven to be particularly efficient for the type of participating media modelled in this study. The present algorithm was developed after several iterations and much of its final form is credited to Farmer (1995). However, some unique efficiency improvements have been added, including the ray tracing algorithm described in Sec. 4.3.2. The key features of its pathlength-based simulation methodology are described below, but for brevity, details of other Monte Carlo approaches have been omitted. For this the reader is referred to Farmer (1995), which also includes some interesting performance comparisons between methods.

4.4.1 Probability Distributions

The radiation transport in a participating medium is simulated by tracing a statistically large number of photons, or energy bundles, from their emission to their eventual absorption. What happens to each bundle is dependent on the radiative characteristics of the medium. These are described by a set of cumulative distribution functions (CDF's). Specifically, in the present pathlength-based Monte Carlo formulation, a CDF is used to determine direction and location of each bundle's emission, whether it is scattered and the direction of scatter in the medium or reflection at the boundary. For example, the derivation of a CDF for the scattering mean free path is as follows. Consider a purely scattering medium with a uniform scattering coefficient, σ_s. The number of energy bundles $N(s)$ travelling a distance s in a given direction before a scattering interaction can be approximated by:

$$N(s) = N(0)\exp(-\sigma_s s) \tag{4.50}$$

where $N(0)$ is the number of bundles travelling in the given direction at $s = 0$. Therefore, probability that a bundle travels a distance $s \pm \Delta s$ is given by the probability density function:

$$P(s) = N(s) \Big/ \int_0^{\infty} N(s)\,ds = \sigma_s \exp(-\sigma_s s) \tag{4.51}$$

The required CDF is then obtained by integrating from $s' = 0$ and $s' = s$, i.e.

$$R_\sigma(s) = \int_0^s P(s')\,ds' = 1 - \exp(-\sigma_s s), \qquad 0 \le R_\sigma \le 1 \tag{4.52}$$

This CDF is then used to map the probable distance s, that a energy bundle will travel before scattering, onto a uniform random number R_σ ranging from 0 to 1 (i.e. Eq. 4.57). Analogous procedures are used to construct CDF's for the other phenomena, e.g., see Modest (1993, Chap. 13). The resulting random number relations are summarised below. (All random numbers are uniformly distributed between 0 and 1.)

Emission Location. Special treatment is required to select the bundle emission points within the arbitrary hexahedral elements used to discretise the radiation space. The finite element parametric mapping technique described in Sec. 4.3.3 is used to map points selected in a square or cubic master element to the corresponding physical subregion. First, random numbers (R_x, R_y, R_z) are chosen for each coordinate direction corresponding to the localised curvilinear coordinates (ξ,η,ζ). Only two coordinates (ξ,η) are required for planar elements. These are then used to derive bilinear shape functions, $\psi_n(\xi,\eta,\zeta)$, appropriate for the master element shape (see Table 4.1). Finally, the coordinates $\mathbf{x}_e$ of the emission location are interpolated from the physical subregion's nodal coordinates $\mathbf{x}_n$, using Eq. 4.43, leading to:

$$\mathbf{x}_e = \sum_{n=1}^{N} \mathbf{x}_n \psi_n(\xi,\eta,\zeta) \tag{4.53}$$

Caution is required when Eq. (4.53) is used to map onto irregular physical regions since the emission locations are not uniformly distributed. Then the power associated with each energy bundle must be adjusted to compensate for the transformation. This is discussed later in Sec. 4.4.2.

Direction of Emission. Two random numbers (R_θ, R_ϕ) are chosen to find the polar and azimuthal angles, θ and ϕ respectively, of the emission direction $\hat{\mathbf{s}}$ relative to the global physical axes. For volume elements:

$$\phi = 2\pi R_\phi, \qquad \theta = \cos^{-1}(1 - 2R_\theta) \tag{4.54}$$

These angles are *global* angles and the direction cosines of $\hat{\mathbf{s}}$ are obtained immediately from:

$$\hat{\mathbf{s}} = \begin{pmatrix} \cos\phi \sin\theta \\ \sin\phi \sin\theta \\ \cos\theta \end{pmatrix} \tag{4.55}$$

For surface elements which are assumed to diffusely emit radiation:

$$\begin{aligned} \phi &= 2\pi R_\phi \\ \theta &= \sin^{-1}\sqrt{R_\theta} \end{aligned} \tag{4.56}$$

These angles now refer to a local Cartesian coordinate system on the element where the local z–coordinate axis is aligned with the surface normal $\hat{\mathbf{n}}$ (see Fig. 4.2). The direction cosines relative to the local element axes are first calculated from an expression similar to Eq. (4.55). The local direction cosines are then converted to the global direction cosines of $\hat{\mathbf{s}}$ via the transformation given by Eq. (4.31).

Scattering Mean Free Path. The probable distance s an energy bundle travels in a medium with uniform scattering coefficient σ_s before being scattered is found with a single random number R_σ as:

$$s = -\frac{1}{\sigma_s} \ln R_\sigma \tag{4.57}$$

The process of finding this expression has been outlined above: it is obtained directly from Eq. (4.52) by rearranging and replacing the difference $1 - R_\sigma$ by R_σ since this does not alter the distribution of the mapping. In nonhomogeneous media the scattering coefficient varies along the bundle path, though its value is presumed constant over each volume element. Therefore, a summation is taken over the pathlength segments δs_n for each cell n through which the bundle travels until Eq. (4.57) is satisfied at which time a scattering collision is considered to take place, i.e.

$$\sum_n \sigma_{sn} \delta s_n > -\ln R_\sigma \tag{4.58}$$

Direction of Scatter. Two random numbers (R_θ, R_ϕ) are chosen to find the polar and azimuthal scattering angles, θ_s and ϕ_s respectively, from the relations:

$$R_\theta = \int_0^{\theta_s} \Phi(\hat{\mathbf{s}}_i,\hat{\mathbf{s}})\sin\theta\, d\theta \Big/ \int_0^{\pi} \Phi(\hat{\mathbf{s}}_i,\hat{\mathbf{s}})\sin\theta\, d\theta \tag{4.59}$$

and

$$R_\phi = \int_0^{\phi_s}\int_0^{\pi} \Phi(\hat{\mathbf{s}}_i,\hat{\mathbf{s}})\sin\theta\, d\theta\, d\phi \Big/ \int_0^{2\pi}\int_0^{\pi} \Phi(\hat{\mathbf{s}}_i,\hat{\mathbf{s}})\sin\theta\, d\theta\, d\phi \tag{4.60}$$

where $\Phi(\mathbf{s}_i,\mathbf{s})$ is the scattering phase function describing the probability that an energy bundle travelling in the direction $\hat{\mathbf{s}}_i$ will be scattered into the direction $\hat{\mathbf{s}}$ (see Sec. 4.1.1). The polar angle θ_s is measured from an axis pointing in the $\hat{\mathbf{s}}_i$, and the azimuthal angle ϕ_s is measured in a plane normal to $\hat{\mathbf{s}}_i$ as shown in Fig. 4.9. For linear anisotropic scattering, from Eq. (4.5):

$$\Phi(\hat{\mathbf{s}}_i,\hat{\mathbf{s}}) = 1 + g\,\hat{\mathbf{s}}\cdot\hat{\mathbf{s}}_i = 1 + g\cos\theta_s \tag{4.61}$$

Hence substituting into Eqs. (4.59) and (4.60):

$$\phi_s = 2\pi R_\phi, \qquad R_\theta = \frac{1}{2}\left(1 - \cos\theta_s + \frac{g}{2}\sin^2\theta_s\right) \tag{4.62}$$

For isotropic scattering these relations reduce to those for emission, i.e. Eq. (4.54).

Once θ_s and ϕ_s have been computed, the scattered direction $\hat{\mathbf{s}}$ is found by introducing a local Cartesian coordinate system at the point of scattering (Fig. 4.9). The local z–axis is aligned with $\hat{\mathbf{s}}_i$ and the local x and y–directions are defined by the unit vectors $\hat{\mathbf{e}}_x$ and $\hat{\mathbf{e}}_y$:

$$\hat{\mathbf{e}}_x = \frac{\mathbf{v}\times\hat{\mathbf{s}}_i}{|\mathbf{v}\times\hat{\mathbf{s}}_i|}, \qquad \hat{\mathbf{e}}_y = \hat{\mathbf{s}}_i \times \hat{\mathbf{e}}_x \tag{4.63}$$

and $\mathbf{v}$ is any arbitrary vector (e.g. the unit vector aligned with the global x–axis). The first expression ensures that $\hat{\mathbf{e}}_x$ is perpendicular to $\hat{\mathbf{s}}_i$, and the second makes the local coordinate system right-handed. The scattered direction $\hat{\mathbf{s}}$ is then given by:

$$\hat{\mathbf{s}} = (\cos\phi_s\,\hat{\mathbf{e}}_x + \sin\phi_s\,\hat{\mathbf{e}}_y)\sin\theta_s + \cos\theta_s\,\mathbf{s}_i \tag{4.64}$$

If the scattering is isotropic then Eq. (4.55) may be used directly.

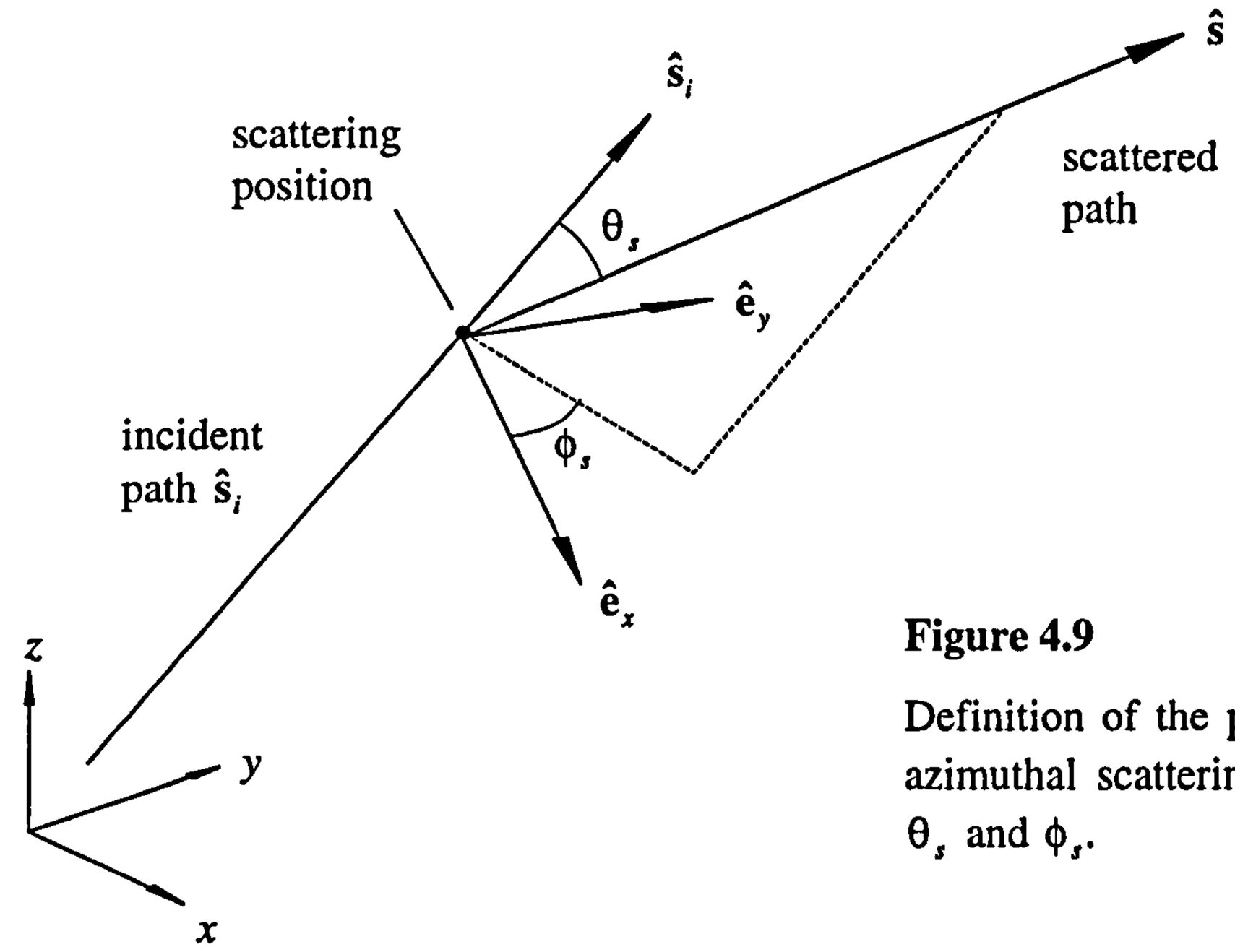

Figure 4.9

Definition of the polar and azimuthal scattering angles θ_s and ϕ_s.

Direction of Reflection. Given that it is assumed that the boundaries reflect diffusely, then the same random number relations are obtained as those for diffuse emission, i.e. Eq. (4.56). These are then used to find the global direction cosines of the reflected direction in an identical procedure to that for the direction of emission.

In some of the benchmark solutions presented later considerable computation was saved by simulating symmetry planes as specular mirrors. For a purely specular reflectors the polar and azimuthal angles of reflection, θ_r and ϕ_r respectively, follow from the laws of optics (without need for simulation) as:

$$\phi_r = \phi_i + \pi \,, \qquad \theta_r = \theta_i \tag{4.65}$$

where θ_i and ϕ_i are the corresponding polar and azimuthal incident angles with respect to a local coordinate system on the symmetry plane. If $\hat{\mathbf{n}}$ is the plane normal, then the direction of specular reflection, $\mathbf{s}_r$, of an energy bundle is determined from its incident direction, $\mathbf{s}_i$, via the vector expression:

$$\hat{\mathbf{s}}_r = \hat{\mathbf{s}}_i + 2|\hat{\mathbf{s}}_i \cdot \hat{\mathbf{n}}|\hat{\mathbf{n}} \tag{4.66}$$

(This approach is also used to 'reflect' ray paths at symmetry planes for problems solved with the present discrete transfer and YIX methods.)

4.4.2 Simulation Procedure

The radiation space is discretised into a mesh of homogeneous surface and volume elements as described in Sec. 4.3.1. With nonhomogeneous participating media the radiative properties are volume (or area) averaged over each element using appropriate expressions from Sec. 4.3.3. Then a large statistical sample of N energy bundles are traced one at a time from each element according to the procedure shown in Fig. 4.10. The following supplementary points should be noted.

Power/Energy Bundle. The radiative emission P_e from each volume element is $4\kappa e_g V$, and from each surface element, $\varepsilon e_s A$. (Here the notation of Sec. 4.1 is used.) Hence, if N energy bundles are launched from points *uniformly* distributed over each element, each bundle will carry an equal portion of the total emitted energy equal to P_e/N. However, a problem noted earlier is that the mapping of launch locations via Eq. (4.53) is *non*uniform when the physical region is irregular, as illustrated for a surface element in Fig. 4.8. This causes erroneous transport predictions if the energy bundles are assigned the same amount of power, since more energy is emitted from regions were the launch locations are concentrated compared with where they are dispersed by the mapping. Therefore, a correction is introduced to ensure that the emission is uniform. This requires the Jacobian associated with the transformation of each launch location from the master element to the corresponding physical element (see Sec. 4.3.3). First the volume v (or area a) of the master element is divided by the number of energy bundles to be launched, N. Then, for each energy bundle, the determinant of the Jacobian, $|J|$, is calculated for the localised coordinates (ξ,η,ζ) of its launch location in the master element via Eqs. (4.45-49). (Only two coordinates are required for surface elements). Finally, the emission per unit volume (or area) from the physical element is weighted by these factors to obtain the power carried by each bundle as:

$$\text{Volumes: } P = |J| \frac{P_e}{N} \frac{v}{V}, \qquad \text{Surfaces: } P = |J| \frac{P_e}{N} \frac{a}{A} \tag{4.67}$$

If the physical element is regular in shape, the determinant of the Jacobian is a constant and equal to the volume (or area) ratio of the physical and master elements. Then, as expected, each bundle carries the same amount of energy, P_e/N, irrespective of its launch location.

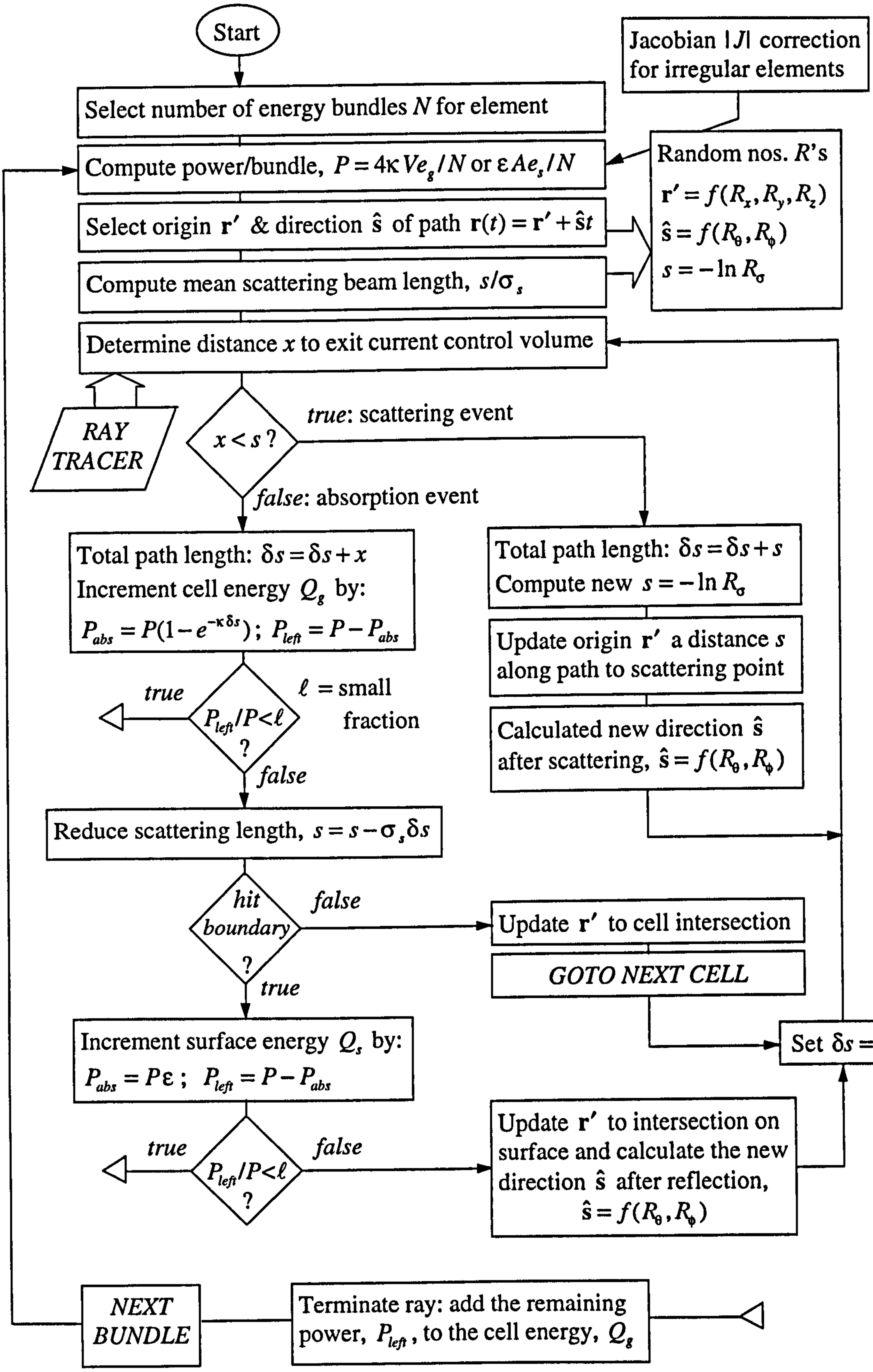

Figure 4.10 Pathlength-based Monte Carlo algorithm: repeated for every element.

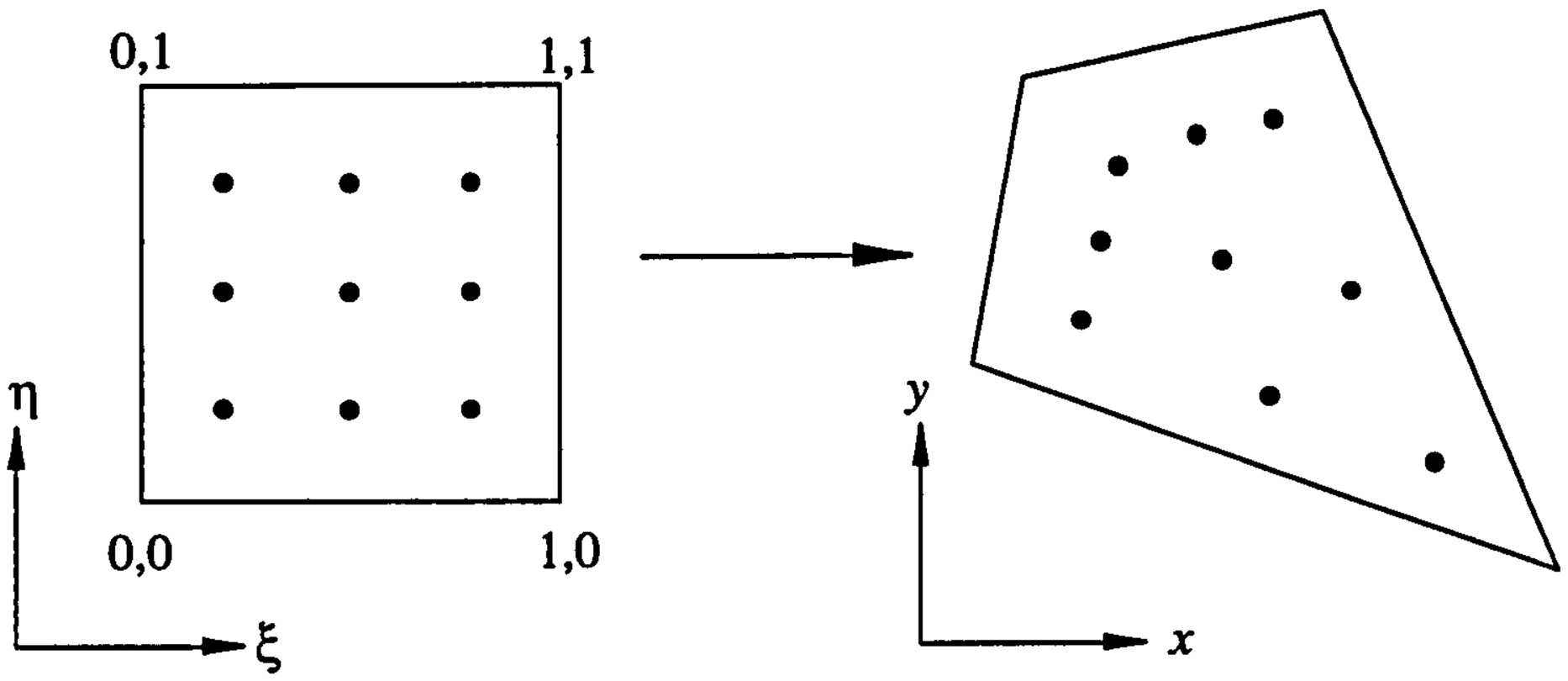

Master Element Physical Element

Figure 4.11 Nonuniform mapping of launch locations for surface.

Energy Partitioning. The power content of each energy bundle is continuously attenuated as it travels through the participating medium. It is envisaged that each energy bundle is equivalent to a large collection of photons emitted in roughly the same direction and from the same general location in the medium. Then as a bundle travels through the medium its initial photon population is continuously depleted by collisions with absorbing molecules or particles until its eventual extinction. The amount of power reduction depends directly on the optical pathlength travelled by the bundle: hence the approach being termed 'pathlength-based' Monte Carlo. Thus, if a bundle travels a distance δs_n across a homogeneous medium element with absorption coefficient κ_n the fraction of the initial bundle power absorbed by the volume is:

$$P_{abs} = 1 - \exp(-\kappa_n \delta s_n) \tag{4.68}$$

Therefore, the power content of each bundle is partitioned into successive volume elements along its path until the remaining energy falls below some preset cutoff level. This approach is in distinct contrast to the classical collision-based model of Howell and Perlmutter (1964a, b). Here each bundle travels undisturbed over a mean free path until its total absorption at a single location. The path length until absorption is determined from an additional random number in an analogous manner to that for the scattering mean free path in Eq. (4.58) except that the absorption coefficient κ_n is used in place of σ_n.

Consequently, a pathlength-based solution avoids this extra random number generation but requires the calculation of an exponential, at least once, for every cell along the path of the bundle. These extra exponentials are expensive and can be numerous in optically thin media. However, the statistical uncertainty is generally much lower in pathlength-based solutions for a fixed number of energy bundles resulting in a net advantage in accuracy versus run time over collision-based methods. See Farmer (1995) and (Modest 1993, p. 699) for numerical comparisons and more discussion.

Path Accumulation. If the scattering mean free path, s is shorter than the distance to exit the current volume element, x then a scattering collision occurs. In fact, multiple scattering events may take place within a single cell if the medium region is very optically thick. A significant speed-up results if the total path length is accumulated, such that the expensive exponential absorption calculation of Eq. (4.68) is performed only once, when $x < s$, rather than after each scattering collision. (This saving is embodied in the logic of the procedure in Fig. 4.10.)

Surface Absorption. Energy partitioning is used to model surface absorption in a similar manner to that for medium absorption. When a surface is struck by an energy bundle, its power is split into the fraction ε, which is absorbed, and the fraction $(1-\varepsilon)$, which is reflected, where ε is the gray surface emissivity. This generally gives improved performance over classical schemes (Howell and Perlmutter 1964a) which draw a random number to decide if an energy bundle is either fully absorbed or fully reflected.

Energy Bundle Termination. The tracking of each energy bundle continues until its power content falls below a 'cutoff' criterion set at the start of the simulation and then the remaining energy is considered absorbed by the last medium element crossed by the bundle. Farmer (1995, p. 67) considers cutoff values ranging from 10% to 0.01% of a bundle's initial power. Trial solutions suggest that a cutoff level of 0.1% or lower gives acceptable accuracy, but this criterion is problem dependent. Optically thick media generally require more stringent cutoff levels than thinner media. Intuitively, it might be expected that reducing the cutoff level to a very low value would result in the tracking process continuing indefinitely driving up the computation run time. However, some trial solutions performed in this study confirm earlier observations by Farmer and Howell (1994) that its value has only a moderate effect on the run time. This most likely results

from the optical depths of individual volume elements being too large to observe any major sensitivity: the extra power available in the 'long-life' bundles was being absorbed in distances comparable with the cell sizes. Consequently, the number of intersection calculations, and thus the problem run time, is not significantly increased. A cutoff level of 0.1% was used for all problems in this study.

If a bundle's power falls below the cutoff criterion at a surface absorption/reflection event, Farmer and Howell (1992) choose to add the remaining energy to that already absorbed by the surface element. However, in the present implementation the remaining energy is absorbed into the volume element with its face coincident with the surface. This modification may be reasoned if one considers an optically thick participating layer over a gray surface. The 'cutoff energy' from many histories would result in a sizeable non-physical heat flux to the surface if the former approach is adopted, whereas in reality this energy is reflected back into, and absorbed by, the medium layer.

4.4.3 Solution Values and Statistical Uncertainty

The total power absorbed by each volume and surface element, Q_{abs}, is tallied during the simulation procedure. When the simulation is complete, the net radiative heat flow Q_s on each of the N surface elements is given by the energy balance:

$$Q_{si} = \varepsilon_i A_i e_{si} - Q_{abs,i}, \qquad i = 1, 2, \ldots, N \tag{4.69}$$

and a similar energy balance over each of the K volume elements gives their net radiative heat source Q_g as:

$$Q_{gi} = 4\kappa_i V_i e_{gi} - Q_{abs,i}, \qquad i = 1, 2, \ldots, K \tag{4.70}$$

Then the required surface heat flux or divergence of radiative heat flux solution values are obtained directly for the surface and volume elements, respectively, from the expressions:

$$q_s = Q_s / A, \qquad \nabla \cdot \mathbf{q}_r = Q_g / V \tag{4.71}$$

Each radiative solution value is in fact an estimate of the exact result obtained after sampling infinitely many energy bundles. A second simulation can be expected to give a slightly different set of solution values. Hence, by performing several independent simulations, the size of the variability in the results can be quantified in terms of the

statistical uncertainty or variance. If each of n simulations gives an estimated result x (i.e. the surface heat flux or flux divergence), then the best estimate of the true or exact solution value is their arithmetic mean $\bar{x}$. The accuracy of this estimate, and hence the solution accuracy, is called the standard error. This in turn may also be estimated. Applying the central limit theorem, the estimated standard error, S_n is given by Barford (1985, Chap. 2) as:

$$S_n(\bar{x}) = \frac{s_n(x)}{\sqrt{n}} = \frac{1}{\sqrt{n(n-1)}} \sqrt{\sum_i (x_i - \bar{x})^2} \tag{4.72}$$

where s_n is the best estimate for the standard deviation of the sample distribution of x.

As would be expected, the solution uncertainty (measured by S_n) is reduced, eventually to zero, by increasing the number of simulations n, but the quantity s_n tends towards a fixed non-zero quantity which embodies the intrinsic accuracy of each sample result x. Consequently, since S_n decreases only as $1/\sqrt{n}$ (as seen in the intermediate expression), the extra computational effort is often better spent improving the intrinsic accuracy of each sample result, by using more energy bundles per simulation, rather than more simulations with a smaller number of histories. Furthermore it is important to use these bundles efficiently by releasing more in regions with a higher radiative emission. Hence, in the present Monte Carlo implementation the number of energy bundles launched from each element is directly proportional to its emission P_e, as defined in Sec. 4.4.2. A final point is that the independence of the Monte Carlo simulations relies on the randomness of the numerical sampling technique (Modest 1993, p. 673). Therefore, advantage was taken of a state-of-the-art random number generator algorithm by Marsaglia (1994), which can rapidly produce random 32-bit sequences with very large periods (i.e. 2^{250}).

The estimated standard error S_n is quoted with all Monte Carlo solutions in this study to allow confidence limits to be determined. For example, with 68% confidence the exact solution value should lie within the limits $\bar{x} \pm S_n$, or with 99% confidence within $\bar{x} \pm 2.58 S_n$. Typically $n = 10$ or 30 simulations were performed, and the number of bundle histories traced in each of these simulations was arbitrarily increased until the solution uncertainty fell to an acceptable level (or computational limitations were exceeded).

4.4.4 Hybrid Monte Carlo/Zonal Solution

The pathlength-based procedure discussed to this point cannot be applied to problems were the participating medium is subject to an applied source condition (e.g. radiative equilibrium). However, this limitation is easily removed and some other benefits are gained by adopting a hybrid Monte Carlo/zonal formulation. Here the simulation procedure is almost identical to that in Sec. 4.3.2, except that a record is kept of the element index releasing each energy bundle. Then as bundles are traced through the discretised radiation space, the total exchange areas between surface and volume elements are automatically determined and stored as follows:

$$\begin{aligned}
&\text{Surface-to-surface:} && \overline{S_i S_j} = \varepsilon_i A_i \phi_{ij} \\
&\text{Surface-to-volume:} && \overline{S_i G_j} = \varepsilon_i A_i \phi_{ij} \\
&\text{Volume-to-surface:} && \overline{G_i S_j} = 4\kappa_i V_i \phi_{ij} \\
&\text{Volume-to-volume:} && \overline{G_i G_j} = 4\kappa_i V_i \phi_{ij}
\end{aligned} \tag{4.73}$$

where ϕ_{ij} is the fraction of the total energy released by element i that is absorbed by element j, both directly and indirectly, after scattering interactions along the bundle paths and reflection at the surface elements. The Monte Carlo phase of the calculation is then complete and the analysis continues via a zonal matrix formulation. The total exchange areas are multiplied by either the surface or gas blackbody emissive powers, e_s and e_g, as appropriate to obtain the following energy balance for each of the N surface elements:

$$Q_{si} = \varepsilon_i A_i e_{si} - \sum_{j=1}^{N} \overline{S_i S_j} e_{sj} - \sum_{k=1}^{K} \overline{S_i G_k} e_{gk}\,, \qquad i = 1, 2, \ldots, N \tag{4.74}$$

where Q_s is the net radiative heat flow. Similarly, an energy balance for each of the K subvolumes gives their net radiative heat source Q_g as:

$$Q_{gi} = 4\kappa_i V_i e_{gi} - \sum_{j=1}^{N} \overline{G_i S_j} e_{sj} - \sum_{k=1}^{K} \overline{G_i G_k} e_{gk}\,, \qquad i = 1, 2, \ldots, K \tag{4.75}$$

A detailed derivation of these zonal relations is provided by Modest (1993, Chap. 18). A comparison with their counterparts, Eqs. (4.69) and (4.70), for a direct Monte Carlo solution, shows that the advantage gained from this zonal formulation is that the emissive powers are separated from the absorption terms. Consequently, for an applied source condition, the algebraic system resulting from Eqs. (4.74) and (4.75) may be solved using

an iterative scheme, matrix inversion, or some other matrix solution technique, to determine the gas emissive powers. The present implementation employs a successive overrelaxation (SOR) iterative solver (see Hirsch 1988, pp. 471-473) to speed-up computation, particularly when the exchange area matrices are large.

The storage of the exchange area matrices can require excessive amounts of memory and extra processing time is required to build and solve the matrix equations. Therefore, for media where it is required to evaluate the radiative fluxes from known emissive powers, direct Monte Carlo solution would seem more efficient. However, some special properties of the total exchange areas may be utilised in order to reduce the uncertainty in solutions, such that there is sometimes a net benefit in using a hybrid approach, even for temperature prescribed problems. Setting all the emissive powers equal in Eqs. (4.74) and (4.75) gives the relations:

$$\sum_{j=1}^{N} \overline{S_i S_j} + \sum_{k=1}^{K} \overline{S_i G_k} = \varepsilon_i A_i , \qquad i = 1, 2, \ldots, N \tag{4.76}$$

$$\sum_{j=1}^{N} \overline{G_i S_j} + \sum_{k=1}^{K} \overline{G_i G_k} = 4\kappa_i V_i , \qquad i = 1, 2, \ldots, K \tag{4.77}$$

since the heat fluxes are zero everywhere; and the reciprocity of total exchange areas (*except* in anisotropically scattering media) gives (Modest 1993, p. 649):

$$\overline{S_i S_j} = \overline{S_j S_i} , \qquad \overline{G_k S_j} = \overline{S_i G_k} , \qquad \overline{G_k G_i} = \overline{G_i G_k} \tag{4.78}$$

These relations can then be used in creative ways to first smooth the statistical scatter in the exchange area matrices prior to the matrix solution (e.g. Larsen and Howell 1986). Smoothing of trial benchmarking problems in this study did not always show a favourable adjustment so it was not used. After the total exchange areas have been determined by the Monte Carlo simulation, they can be used repeatedly to quickly calculate new solutions for various temperature or heat source conditions, depending on the problem type. The optical properties (i.e. gas extinction coefficient, surface emissivity) must be temperature independent, but there are no restrictions on the optical thickness or isotropy of scattering. This virtue proved particularly beneficial in this study for rapidly verifying discrete transfer and YIX solutions. A new Monte Carlo simulation is then only required when the geometry or optical properties are modified.

4.5 YIX Method

A three-dimensional YIX formulation has been developed to solve the exact integral equations of radiative heat transfer, i.e. Eqs. (4.22-26). It was derived and implemented on the basis of one and two-dimensional schemes by Tan and Howell (1990a), though several aspects of the present methodology are unique to three-dimensions. Moreover, greater flexibility in handling arbitrary complex geometries has been afforded by incorporating the geometric modelling and ray tracing approach described in Sec. 4.3, compared to the *ad hoc* searching procedures used by Hsu and Tan (1996).

4.5.1 Angular-Distance Form of the Integral Radiation Equations

The integral equations (4.22-26) were previously derived in their most general form for a Mie anisotropically scattering medium. This introduces many terms if a high order scattering phase function is to be modelled as a result of the Mie series summation in $F_w(\mathbf{r})$, Eq. (4.25). However, the linear phase function of Eq. (4.5) is adequate for the analysis of scattering media in this study. Introducing this approximation in Eq. (4.25) gives:

$$F_w(\mathbf{r}) = \frac{\omega}{4}\sum_{k=1}^{M} c_k\, S_k(\hat{\mathbf{s}})\, w_k(\mathbf{r}) = \frac{\omega\, g}{4}[S_1 w_1 + S_2 w_2 + S_3 w_3] = \frac{\omega\, g\, \hat{\mathbf{s}}^T w(\mathbf{r})}{4}, \quad M = 3 \tag{4.79}$$

where $g = c_1 = c_2 = c_3$, $\hat{\mathbf{s}} = (S_1, S_2, S_3)^T$ and $w(\mathbf{r}) = (w_1, w_2, w_3)^T$. Then Eqs. (4.22-26) may be rearranged into the compact matrix form:

$$\begin{bmatrix} f_g(\mathbf{r}) \\ f_w(\mathbf{r}) \\ f_s(\mathbf{r}) \end{bmatrix} = \begin{bmatrix} \overline{gg} & \overline{gw} & \overline{gs} \\ \overline{wg} & \overline{ww} & \overline{ws} \\ \overline{sg} & \overline{sw} & \overline{ss} \end{bmatrix} \begin{bmatrix} F_g(\mathbf{r}_t) \\ F_w(\mathbf{r}_t) \\ F_s(\mathbf{r}') \end{bmatrix} \tag{4.80}$$

where f_w and F_w in Eq. (4.25) are *redefined* as:

$$f_g(\mathbf{r}) = 4e_g(\mathbf{r}) - \frac{1}{(1-\omega)\beta}\nabla\cdot\mathbf{q}_r(\mathbf{r}) \qquad F_g(\mathbf{r}) = e_g(\mathbf{r}) - \frac{\omega}{4(1-\omega)\beta}\nabla\cdot\mathbf{q}_r(\mathbf{r})$$

$$f_w(\mathbf{r}) = w(\mathbf{r}) \qquad F_w(\mathbf{r}) = \frac{\omega\, g\, w(\mathbf{r})}{4} \tag{4.81}$$

$$f_s(\mathbf{r}) = e_s(\mathbf{r}) - \frac{1}{\varepsilon}q_s(\mathbf{r}) \qquad F_s(\mathbf{r}) = e_s(\mathbf{r}) - \frac{1-\varepsilon}{\varepsilon}q_s(\mathbf{r})$$

such that the matrix elements $\overline{gg}$, $\overline{gw}$, etc. are defined by:

$$\begin{bmatrix} \overline{gg} & \overline{gw} & \overline{gs} \\ \overline{wg} & \overline{ww} & \overline{ws} \\ \overline{sg} & \overline{sw} & \overline{ss} \end{bmatrix} = \begin{bmatrix} <1> & <\hat{\mathbf{s}}^T> & \{\hat{\mathbf{s}}\cdot\hat{\mathbf{n}}'\} \\ <\hat{\mathbf{s}}> & <\hat{\mathbf{s}}\,\hat{\mathbf{s}}^T> & \{\hat{\mathbf{s}}\;\hat{\mathbf{s}}\cdot\hat{\mathbf{n}}'\} \\ <-\hat{\mathbf{s}}\cdot\hat{\mathbf{n}}> & <-\hat{\mathbf{s}}\cdot\hat{\mathbf{n}}\,\hat{\mathbf{s}}^T> & \{-\hat{\mathbf{s}}\cdot\hat{\mathbf{n}}\;\hat{\mathbf{s}}\cdot\hat{\mathbf{n}}'\} \end{bmatrix} \tag{4.82}$$

Here $<*>F(\mathbf{r}_t)$ and $\{*\}F(\mathbf{r}')$ denote the volume and surface integrals:

$$<*>F(\mathbf{r}_t) \equiv \iiint_V \frac{F(\mathbf{r}_t)\,(*)}{\pi|\mathbf{r}-\mathbf{r}_t|^2}\,\beta \exp\left[-\int_0^{|\mathbf{r}-\mathbf{r}_t|}\beta(\mathbf{r}-\hat{\mathbf{s}}t)\,dt\right] dV(\mathbf{r}_t) \tag{4.83}$$

$$\{*\}F(\mathbf{r}') \equiv \iint_S \frac{F(\mathbf{r}')\,(*)}{\pi|\mathbf{r}-\mathbf{r}'|^2}\,\exp\left[-\int_0^{|\mathbf{r}-\mathbf{r}'|}\beta(\mathbf{r}-\hat{\mathbf{s}}t)\,dt\right] dA(\mathbf{r}') \tag{4.84}$$

after substitution of the exponential kernel function K from Eq. (4.26). In *angular-distance* form Eqs. (4.83) and (4.84) become:

$$<*>F(\mathbf{r}_t) \equiv \frac{1}{\pi}\int_{4\pi}\int_0^{|\mathbf{r}-\mathbf{r}'|}\beta \exp\left[-\int_0^{t}\beta(\mathbf{r}-\hat{\mathbf{s}}t')\,dt'\right]F(\mathbf{r}_t)\,(*)\,dt\,d\Omega \tag{4.85}$$

$$\{*\}F(\mathbf{r}') \equiv \frac{1}{\pi}\int_{2\pi}\exp\left[-\int_0^{|\mathbf{r}-\mathbf{r}'|}\beta(\mathbf{r}-\hat{\mathbf{s}}t)\,dt\right]F(\mathbf{r}')\,(*)\,d\Omega \tag{4.86}$$

where $\mathbf{r}_t = \mathbf{r}-\hat{\mathbf{s}}t$. To clarify the vector notation here: $\mathbf{r}$ is the origin of a ray travelling in the direction $-\hat{\mathbf{s}}$, through a solid angle Ω and striking the boundary at $\mathbf{r}'$; all points on this path are represented by $\mathbf{r}_t$ and the total ray path length is $|\mathbf{r}-\mathbf{r}'|$. These vectors are also shown in Fig. 4.1.

4.5.2 Angular and Distance Integration: YIX Quadrature

In order to demonstrate how the YIX method is formulated, consider an emitting, absorbing and nonscattering medium enclosed by a black boundary. The absorption coefficient of the medium may vary with position but no heat source or sink is present. Then from Eqs. (4.80-86), the radiation transport integral equation for the medium emissive power is reduced to:

$$4e_g(\mathbf{r}) = \frac{1}{\pi}\int_{4\pi}\int_{0}^{L} \beta \exp[-\int_{0}^{t}\beta(\mathbf{r}-\hat{\mathbf{s}}t')\,dt'\,]\,e_g(\mathbf{r}-\hat{\mathbf{s}}t)\,dt\,d\Omega$$
$$+\frac{1}{\pi}\int_{2\pi}\exp[-\int_{0}^{L}\beta(\mathbf{r}-\hat{\mathbf{s}}t)\,dt\,]\,e_s(\mathbf{r}-\hat{\mathbf{s}}L)\,\hat{\mathbf{s}}\cdot\hat{\mathbf{n}}'\,d\Omega \tag{4.87}$$

where the distance $L=|\mathbf{r}-\mathbf{r}'|$ is the length of the ray emitted from $\mathbf{r}$ in the direction $-\hat{\mathbf{s}}$ and striking the *nearest* boundary at $\mathbf{r}'$. Note that the substitutions $\mathbf{r}_t=\mathbf{r}-\hat{\mathbf{s}}t$ and $\mathbf{r}'=\mathbf{r}-\hat{\mathbf{s}}L$ have been made in Eq. (4.87).

Angular Quadrature. The angular integrations are approximated using S_n discrete ordinate quadrature (Lathrop and Carlson 1965), as follows:

$$4e_g(\mathbf{r}) = \frac{1}{\pi}\sum_{k=1}^{N_w} w_k \int_{0}^{L_k} \beta \exp[-\int_{0}^{t}\beta(\mathbf{r}-\hat{\mathbf{s}}_k t')\,dt'\,]\,e_g(\mathbf{r}-\hat{\mathbf{s}}_k t)\,dt$$
$$+\frac{1}{\pi}\sum_{k=1}^{N_w/2}\exp[-\int_{0}^{L_k}\beta(\mathbf{r}-\hat{\mathbf{s}}_k t)\,dt\,]\,e_s(\mathbf{r}-\hat{\mathbf{s}}_k L_k)\,\hat{\mathbf{s}}_k\cdot\hat{\mathbf{n}}_k'\,w_k \tag{4.88}$$

Here N_w is the number of ordinate directions, which depends on the order of the discrete ordinate set S_n, according to $N_w=n(n+2)$. These angular quadrature sets and weights were constructed so as to be fully symmetric (i.e. invariant after any rotation of 90°) and to also satisfy the zeroth, first and second moment integrations of intensity over a unit sphere:

$$\int_{4\pi} d\Omega = 4\pi = \sum_{k=1}^{N_w} w_k, \quad \int_{4\pi}\hat{\mathbf{s}}\,d\Omega = \mathbf{0} = \sum_{k=1}^{N_w} w_k\,\hat{\mathbf{s}}_k, \quad \int_{4\pi}\hat{\mathbf{s}}\hat{\mathbf{s}}\,d\Omega = \frac{4\pi}{3}\delta = \sum_{k=1}^{N_w} w_k\,\hat{\mathbf{s}}_k\,\hat{\mathbf{s}}_k \tag{4.89}$$

and the first moment over a unit hemisphere:

$$\int_{2\pi}\hat{\mathbf{s}}\cdot\hat{\mathbf{n}}\,d\Omega = \pi = \sum_{k=1}^{N_w/2}\hat{\mathbf{s}}_k\cdot\hat{\mathbf{n}}\,w_k \tag{4.90}$$

where δ is the unit tensor (c.f. Modest 1993, p. 512, 545). These moment conditions should be satisfied in order that the quadrature properly integrates, respectively, the incident energy, radiative heat flux and diffusion limit in the media and the heat flux at a surface. Discrete ordinate S_n sets satisfying these conditions for $n=6$ and 8 (plus special sets for $n=12$ and 16) are tabulated in Appendix D. (Note: Eq. (4.90) is only satisfied for orientations of the surface normal that are aligned with the principal Cartesian axes.)

Hsu *et al.* (1993) observe that a lower order S_n-approximation is justified at higher optical thicknesses, since in very thick media, the radiation is essentially an isotropic diffusion process. Therefore, only the distance variation is important. Conversely, at low optical thicknesses a high order discrete ordinate set, such as S_{12} or S_{16}, must be used to reduce ray effect (see discussion of this problem in Chai *et al.* 1993a). With nonhomogeneous media it is feasible to adjust the discrete ordinate set to suit the optical conditions at different locations, i.e. there is no requirement to use a consistent set over the entire problem domain as in conventional discrete ordinate methods. Incidentally, Tan (1991) named this method YIX for the rather ambiguous reason that the letters Y, I and X are formed by the integration point distributions with 3, 2 and 4 ordinate directions in a two-dimensional solution.

Distance Quadrature. The distance integral with respect to t in Eq. (4.88) is then evaluated with a nonuniform numerical quadrature as follows. Applying the substitutions:

$$\tau = \int_0^t \beta(\mathbf{r}-\hat{\mathbf{s}}t)\,dt, \qquad \Gamma = \int_0^L \beta(\mathbf{r}-\hat{\mathbf{s}}t)\,dt \tag{4.91}$$

the distance integral (in a certain ordinate direction) is reduced to the form:

$$I = \int_0^{t=L} e^{-\tau}\, e_g(\mathbf{r}-\hat{\mathbf{s}}t)\,d\tau \equiv \int_0^{\Gamma} e^{-\tau} f(\tau)\,d\tau \tag{4.92}$$

Here $\tau = \Gamma$ when $t = L$ (i.e. Γ is the optical distance corresponding to the ray length L). The integral is then subdivided as follows:

$$I = \sum_{i=1}^{n} \int_{\tau_{i-1}}^{\tau_i} e^{-\tau} f(\tau)\,d\tau + \int_{\tau_n}^{\Gamma} e^{-\tau} f(\tau)\,d\tau \tag{4.93}$$

where $0 = \tau_0 < \tau_1 < \ldots < \tau_n \le \Gamma$ and τ_i are optical abscissas to be decided.

Applying a two-point approximation to I in each subregion gives:

$$I_i = \int_{\tau_{i-1}}^{\tau_i} e^{-\tau} f(\tau)\,d\tau \approx a_i f(\tau_{i-1}) + b_i f(\tau_i) \tag{4.94}$$

Then the following conditions are used in order to find a_i and b_i in order that the integral I_i is approximated to first order accuracy:

$$\begin{aligned} f(\tau_{i-1}) = f(\tau_i) = 1 \quad &\rightarrow \quad a_i + b_i = \int_{\tau_{i-1}}^{\tau_i} e^{-\tau} d\tau = e^{-\tau_{i-1}} - e^{-\tau_i} \\ f(\tau_{i-1}) = f(\tau_i) = \tau \quad &\rightarrow \quad a_i\tau_{i-1} + b_i\tau_i = \int_{\tau_{i-1}}^{\tau_i} \tau\, e^{-\tau} d\tau = e^{-\tau_{i-1}}(\tau_{i-1}+1) - e^{-\tau_i}(\tau_i+1) \end{aligned} \tag{4.95}$$

Solving for a_i and b_i:

$$a_i = e^{-\tau_{i-1}} - D(\tau_i), \qquad b_i = D(\tau_i) - e^{-\tau_i} \quad \text{where} \quad D(\tau_i) = \frac{e^{-\tau_{i-1}} - e^{-\tau_i}}{\tau_i - \tau_{i-1}} \tag{4.96}$$

Substituting Eqs. (4.96) into Eq. (4.93) yields:

$$\begin{aligned} I \approx\ & [1 - D(\tau_1)] f(0) + \sum_{i=1}^{n-1} [D(\tau_i) - D(\tau_{i+1})] f(\tau_i) \\ & + [D(\tau_n) - D(\Gamma)] f(\tau_n) + [D(\Gamma) - e^{-\Gamma}] f(\Gamma) \end{aligned} \tag{4.97}$$

Setting:

$$2[1 - D(\tau_1)] = [D(\tau_i) - D(\tau_{i+1})] \equiv \lambda = \text{constant} \tag{4.98}$$

allows the contribution of $f(\tau_i)$ at each integration point $\tau_i > 0$ to the integral to be the same. This is desirable because it reduces the number of integrations as the distance increases because the contribution of further points decreases exponentially. The contribution of $f(0)$ is chosen to be $\lambda/2$ in Eq. (4.98), otherwise applying the approximation in opposite ordinate directions would result in $f(0)$ being counted twice. The value of τ_1 (or λ) is set by the user, then λ (or τ_1) and τ_i ($i = 2, 3, \ldots, N$) are computed recursively by solving Eq. (4.98) until τ_i is so large that $D(\tau_i) - D(\infty) < \lambda$, for which $\tau_i \equiv \tau_N$. Here Eq. (4.98) is written as:

$$F(\tau) = [D(\tau_i) - D(\tau_{i+1})] - \lambda = 0 \tag{4.99}$$

and the roots of $F(\tau)$, that is the required integration points τ_i, are found by a fast and robust false position method (Pearson 1986, pp. 4-8). In Table 4.1 values of N, τ_N and λ are listed for various orders of τ_1. The accuracy of the integration, but also the computation, increases as τ_1 (or λ) are decreased.

Table 4.2 Characteristic parameters of integration points for the three-dimensional exponential kernel function.

τ_1	N	τ_N	λ
.001	1000	7.70360	.00100
.002	500	7.01070	.00200
.005	200	6.09527	.00499
.01	100	5.40356	.00997
.02	50	4.71331	.01987
.05	20	3.80592	.04918
.1	10	3.12807	.09675
.2	5	2.45353	.18731

Substituting Eq. (4.98) into (4.97) then gives:

$$I \approx \lambda \left[\tfrac{1}{2} f(0) + \sum_{i=1}^{n-1} f(\tau_i)\right] + [D(\tau_n) - D(\Gamma)] f(\tau_n) + [D(\Gamma) - e^{-\Gamma}] f(\Gamma) \qquad (4.100)$$

Finally, to completely eliminate all exponential kernel evaluations during the ray tracing stage, the following first-order-accurate linear extrapolation is applied:

$$\begin{aligned} \int_{\tau_n}^{\Gamma} e^{-\tau} f(\tau)\, d\tau &= \frac{\Gamma - \tau_n}{\tau_{n+1} - \tau_n} \int_{\tau_n}^{\tau_{n+1}} e^{-\tau} f(\tau)\, d\tau \\ &\approx \frac{\Gamma - \tau_n}{\tau_{n+1} - \tau_n} [e^{-\tau_n} - e^{-\tau_{n+1}}] f(\tau_n), \qquad \tau_n \le \Gamma \le \tau_{n+1} \le \tau_N \end{aligned} \qquad (4.101)$$

In the case that τ_{n+1} does not exist, this integral is set to zero. Finally, substituting Eq. (4.101) into (4.100) gives:

$$I \approx \lambda \left[\tfrac{1}{2} f(0) + \sum_{i=1}^{n-1} f(\tau_i)\right] + [P_{n+1} + \Gamma Q_{n+1}] f(\tau_n) \qquad (4.102)$$

where

$$Q_i \equiv D(\tau_i) = \frac{e^{-\tau_{i-1}} - e^{-\tau_i}}{\tau_i - \tau_{i-1}} \qquad (4.103)$$

$$P_i \equiv D(\tau_{i-1}) - e^{-\tau_{i-1}} - \tau_{i-1} Q_i \qquad (4.104)$$

Hence, the distance integral in Eq. (4.92) is approximated as:

$$\int_0^{t=L} e^{-\tau}\, e_g(\mathbf{r}-\hat{\mathbf{s}}t)\,d\tau \approx \lambda\,[\tfrac{1}{2}e_g(\mathbf{r}) + \sum_{i=1}^{n-1} e_g(\mathbf{r}-\hat{\mathbf{s}}t_i)] + [P_{n+1}+\Gamma Q_{n+1}]\; e_g(\mathbf{r}-\hat{\mathbf{s}}t_n) \qquad (4.105)$$

Thus, for a specified value τ_1 (or λ), all of the constants $\lambda, \tau_i, Q_i, P_i$ are computed and stored in advance. Subsequently, in the computations of many integrals of the form of Eq. (4.105) the evaluation is replaced by a simple summation of $f(\tau_i)$.

This distance quadrature is then combined with the discrete ordinate angular quadrature to yield the fully discretised form of the integral transport equation (4.90) as:

$$\begin{aligned} 4e_g(\mathbf{r}) = &\frac{1}{\pi}\sum_{k=1}^{N_w} \{\lambda\,[\tfrac{1}{2}e_g(\mathbf{r}) + \sum_{i=1}^{n-1} e_g(\mathbf{r}-\hat{\mathbf{s}}_k t_i)] + [P_{n+1}-\Gamma_k Q_{n+1}]\; e_g(\mathbf{r}-\hat{\mathbf{s}}_k t_n)\}\, w_k \\ &+\frac{1}{\pi}\sum_{k=1}^{N_w/2} e^{-\Gamma_k}\, e_s(\mathbf{r}-\hat{\mathbf{s}}_k L_k)\,\hat{\mathbf{s}}_k\cdot\hat{\mathbf{n}}'_k\, w_k \end{aligned} \qquad (4.106)$$

where n satisfies $\tau_n \le \Gamma \le \tau_{n+1}$, and t_i are the geometric abscissas corresponding to the pre-calculated optical abscissas τ_i. These are found recursively from the relation:

$$t_{i+1} = t_i + \frac{\tau_{i+1}-\tau_i}{\beta(\mathbf{r}-\hat{\mathbf{s}}_k t_i)}, \qquad t_0 = \tau_0 = 0 \qquad (4.107)$$

Hence, the distribution of the integration points in space varies according to the extinction coefficient distribution along each discrete ordinate direction $\hat{\mathbf{s}}_k$. They are more concentrated in optically thicker regions as illustrated in Fig. 4.12. for representative ordinate directions on a coordinate plane. A schematic of the YIX double integration is also shown on Fig. 4.13.

The preceding example has demonstrated the YIX integration of the $\overline{gg}$ and $\overline{gs}$ matrix elements of Eq. (4.82). The other integral elements are calculated in an analogous manner. It is important to notice that elements on the second row are simply a multiple $\hat{\mathbf{s}}$ of those on the first row. i.e. $f_w(\mathbf{r}) = \hat{\mathbf{s}}\, f_g(\mathbf{r})$. Thus, the integrations in $\overline{wg}$, $\overline{ww}$ and $\overline{ws}$ can be avoided, saving considerable computation.

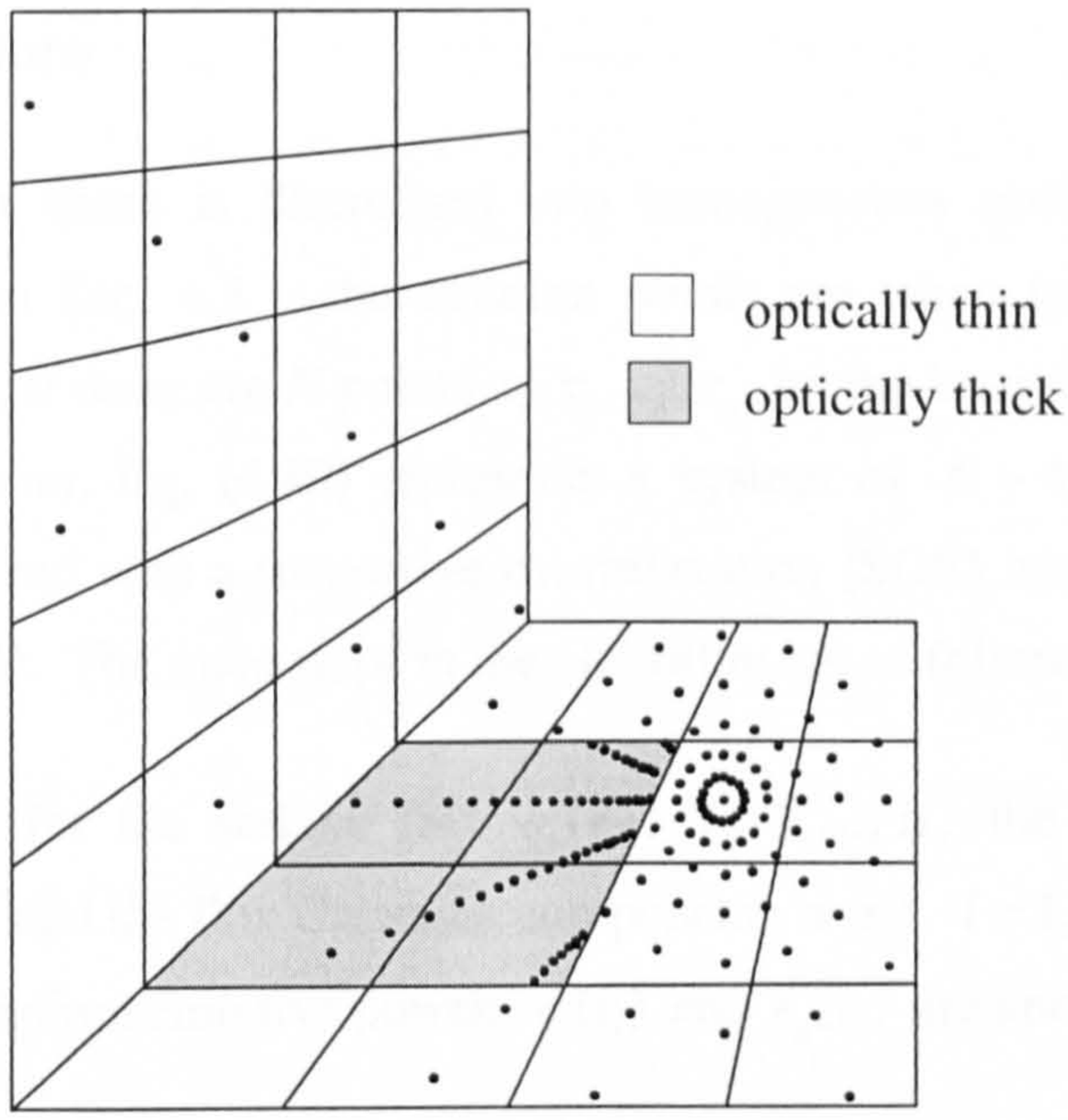

Figure 4.12 A typical distribution of integration points along ordinate directions in one coordinate plane. The YIX distance integration results in the points being more concentrated in optically thicker regions were the radiative emission is greater.

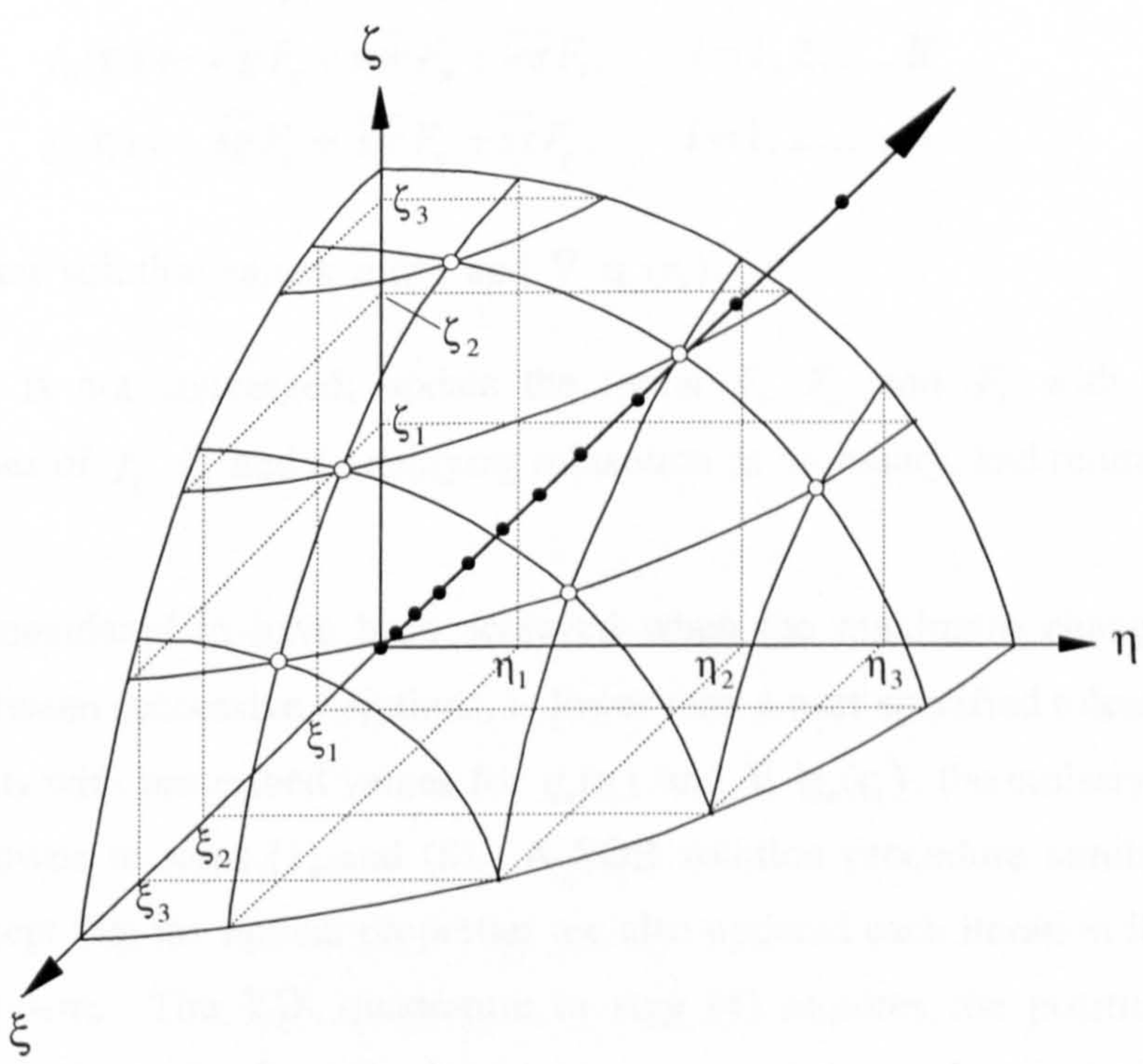

Figure 4.13 Schematic of YIX integration at a node. A level symmetric S_6 discrete ordinate quadrature is shown for one octant: total 48 rays, 6/octant. The distance integration points are also shown along one of the ordinates.

4.5.3 Solution Procedure

Given that the radiation space is discretised into homogeneous surface and volume elements, as described in Sec. 4.3.1, the solution points are taken to be the element geometric centres. Thus, if there are N points $\mathbf{r}_1, \mathbf{r}_2, \ldots, \mathbf{r}_N$ on the boundary and K points $\mathbf{r}_1, \mathbf{r}_2, \ldots, \mathbf{r}_K$ in the medium, Eq. (4.80) represents a system of $N+4K$ simultaneous equations. These are solved with a successive overrelaxation (SOR) iterative solver (see Hirsch 1988, pp. 471-473). The main steps in the algorithm are as follows:

1. Give an initial guess for the surface flux $q_s(\mathbf{r}_i)$, $i=1,\ldots,N$, the flux divergence $\nabla\cdot\mathbf{q}_r(\mathbf{r}_i)$, $i=1,\ldots,K$ and the flux Cartesian components $w(\mathbf{r}_i)$, $i=1,\ldots,K$, assuming that the surface and medium emissive powers $e_s(\mathbf{r}_i)$ and $e_g(\mathbf{r}_i)$ are known.

2. Calculate the optical properties β, ω and ε at the solution points.

3. Calculate the terms F_g, F_w and F_s of Eq. (4.81) at the solution points.

4. Calculate the integrals of Eq. (4.80) using YIX quadrature:

$$f_g(\mathbf{r}_i) \leftarrow \overline{gg}\,F_g + \overline{gw}\,F_w + \overline{gs}\,F_s, \qquad i=1,2,\ldots,K$$
$$f_w(\mathbf{r}_i) \leftarrow \overline{wg}\,F_g + \overline{ww}\,F_w + \overline{ws}\,F_s, \qquad i=1,2,\ldots,K$$
$$f_s(\mathbf{r}_i) \leftarrow \overline{sg}\,F_g + \overline{sw}\,F_w + \overline{ss}\,F_s, \qquad i=1,2,\ldots,N$$

5. Calculate the new solution values $q_s(\mathbf{r}_i)$ and $\nabla\cdot\mathbf{q}_r(\mathbf{r}_k)$.

6. If the solution is not converged; update the terms F_g, F_w and F_s with the most immediate values of f_g, f_w and f_s, applying relaxation as necessary, and return to (4).

Convergence is considered to have been achieved when the maximum change in any solution value, between successive iterations, is lower than a user specified tolerance (e.g. 10^{-6}). In problems with prescribed values for $q_s(\mathbf{r}_i)$ and $\nabla\cdot\mathbf{q}_r(\mathbf{r}_k)$, the emissive powers become the unknowns in steps (1) and (5). A SOR solution procedure similar to that above is used, except that the optical properties are also updated each iteration if they are temperature dependent. The YIX quadrature in step (4) requires the position of the integration points $\mathbf{r}-\hat{\mathbf{s}}t_i$ in the discretised radiation space and the total optical distance Γ corresponding to the length of each ray. Since constant properties are assumed in each volume elements, the first problem reduces to finding in which element each integration

point lies. Thus, for all the integration points along a given ordinate direction, the ray tracing procedure in Fig. 4.14 is used to determine the element indices in which they lie. The required value Γ is also accumulated during this tracing operation. These values are used to compute the matrix elements $\overline{gg}$, $\overline{gw}$, etc. of the integrals (4.83) and then stored for subsequent iterations of the solution procedure. Each volume element along a ray path may contain several integration points (see Fig. 4.12). Thus, the storage space is minimised by saving the element indices and the number of points in each (i.e. the point frequency), rather than by storing each point individually. Furthermore, as the distance quadrature is refined by reducing τ_1 (or λ), the point frequencies increase but the number of stored values remains about the same.

The matrix elements $\overline{gg}$, $\overline{gs}$, $\overline{sg}$ and $\overline{ss}$ in Eq. (4.80) have an important physical significance: they are the direct exchange factors between the surface and volume elements, i.e. the fraction of total radiative energy released by one element and *directly* absorbed by another, without scattering or reflection. They may be directly related to the total exchange areas defined by Eq. (4.73), and consequently, analogous relations to those of Eqs. (4.76) and (4.77) can be derived as follows:

$$\sum_{j=1}^{N}\overline{s_i s_j}+\sum_{k=1}^{K}\overline{s_i g_k}=1\,, \qquad i=1,2,\ldots,N \tag{4.108}$$

$$\sum_{j=1}^{N}\overline{g_i s_j}+\sum_{k=1}^{K}\overline{g_i g_k}=4\,, \qquad i=1,2,\ldots,K \tag{4.109}$$

An built-in check is used in the present solution procedure to test if the computed exchange factors satisfy these expressions. Failure to do so implies that the YIX quadrature is too coarse, and the user should choose a higher order discrete ordinate set S_n and/or reduce the distance to the first integration point, τ_1. If this is not practical, then the error can be used to introduce a 'correction' to the solution values. Note here that the YIX matrix equations resemble those of a zonal formulation because homogeneous elements are used in the spatial discretisation. A YIX formulation could also be developed for nonhomogeneous elements, using equations similar to Eq. (4.42) to describe variable property distributions across elements. Then the YIX equations would more closely resemble those of Galerkin finite element methods, though the improvement in accuracy may not merit the extra computation required by the more complex elements.

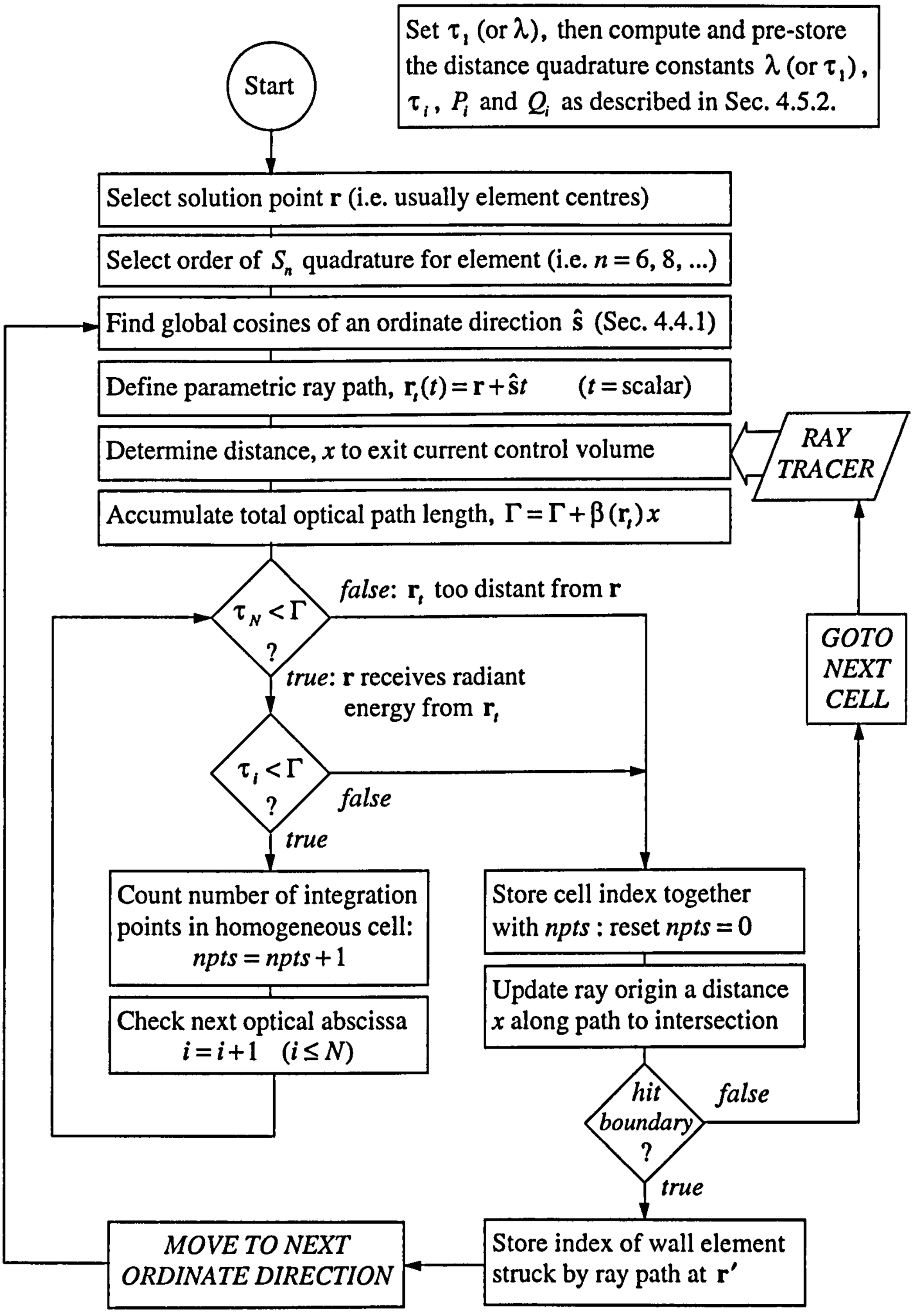

Figure 4.14 Procedure used to determine the ray path information in YIX quadrature: repeated for every solution point **r**.

4.6 Discrete Transfer Method

The discrete transfer method (Shah 1979; Lockwood and Shah 1981) has been revised and extended for the complex radiating media analysed in this study. The geometric modelling and ray tracing approach detailed in Sec. 4.3 have been incorporated into the original methodology, together with various other modifications to improve either generality or performance. These are discussed later below.

4.6.1 Original Formulation

First, the radiation space is subdivided into a collection of homogeneous surface and volume elements using the spatial discretisation described in Sec. 4.3.1. Next, the geometric centre of each surface element, say P, is determined and the 2π hemispherical solid angle above P is discretised into N_Ω finite solid angles $\delta\Omega$. Shah (1979) chose to divide the hemisphere into N_θ equal polar angles and N_ϕ equal azimuthal angles such that $N_\Omega = N_\theta \cdot N_\phi$ and:

$$\delta\theta = \frac{\pi}{2N_\theta}, \qquad \delta\phi = \frac{2\pi}{N_\phi} \tag{4.110}$$

An emission direction, $\hat{\mathbf{s}}$, is then defined by the polar and azimuthal angles, θ and ϕ, through the centre of each subdivision (Fig. 4.15). The local direction cosines of $\hat{\mathbf{s}}$ are first determined from Eq. (4.55) with respect to a local Cartesian coordinate system at P, where the local z–coordinate axis is aligned with the surface normal $\hat{\mathbf{n}}$, and then converted to global direction cosines via the transformation given by Eq. (4.31). A ray is traced in each direction $\hat{\mathbf{s}}$ through the radiation space until it strikes another surface, say at Q. Then, starting from Q, the ray is followed back to its origin (point P), while solving for the intensity distribution along its path with the recurrence relation:

$$i_{n+1}(\mathbf{r},\hat{\mathbf{s}}) = i_n(\mathbf{r}',\hat{\mathbf{s}})e^{-\beta|\mathbf{r}-\mathbf{r}'|} + S(1-e^{-\beta|\mathbf{r}-\mathbf{r}'|}) \tag{4.111}$$

where, n and $n+1$ designate successive cell face locations, separated by the distance $|\mathbf{r}-\mathbf{r}'|$, as the ray passes through each volume element from Q to P (Fig. 4.15). This expression is obtained directly from Eq. (4.18) by taking the extinction coefficient β and the radiative source function $S(\mathbf{r},\hat{\mathbf{s}})$ to be constant over the interval $|\mathbf{r}-\mathbf{r}'|$.

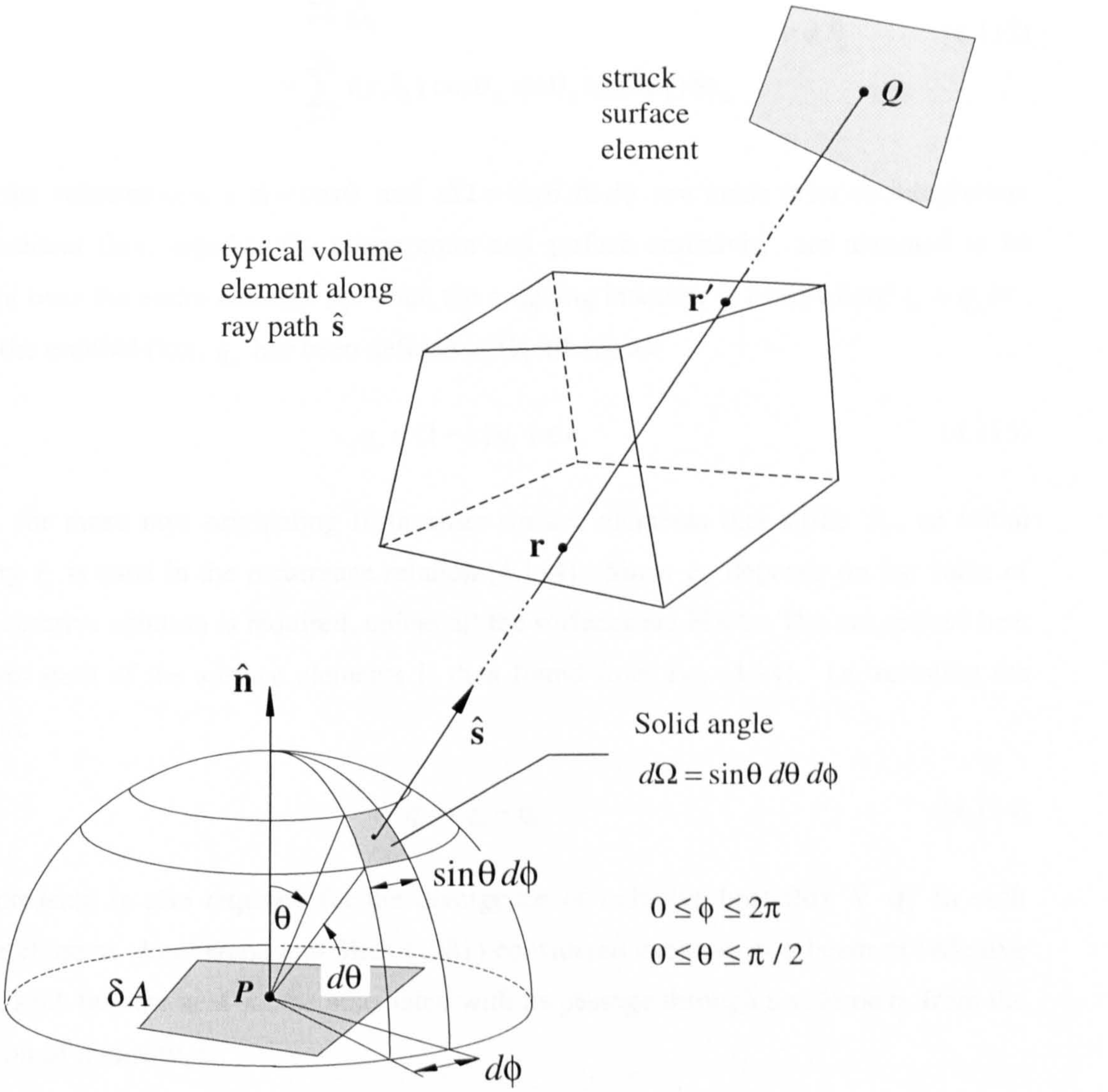

Figure 4.15 Definition of the solid angle $d\Omega$ through which the irradiation ray travelling in the direction $-\hat{\mathbf{s}}$ arrives at P. This ray is traced through the arbitrary volume elements of the discretised radiation space from P to Q.

The intensities calculated from Eq. (4.111) are assumed to be constant over each finite solid angle $\delta\Omega$, such that the incident radiative heat flux at P is obtained by substituting into Eq. (4.12) as:

$$\begin{aligned} q_i(\mathbf{r}) &= \sum_{k=1}^{N_\Omega} \int_{\delta\Omega_k} i(\mathbf{r},\hat{\mathbf{s}})\,\hat{\mathbf{s}}\cdot\hat{\mathbf{n}}\,d\Omega \\ &= \sum_{k=1}^{N_\Omega} i(\mathbf{r},\hat{\mathbf{s}}_k)\cos\theta_k \sin\theta_k \sin(\delta\theta_k)\delta\phi_k \end{aligned} \qquad \mathbf{r}\in S_e \qquad (4.112)$$

where the substitutions $\hat{\mathbf{s}}\cdot\hat{\mathbf{n}}=\cos\theta$ and $d\Omega=\sin\theta\,d\theta\,d\phi$ are made prior to integration. This incident flux, together the temperature and surface emissivity, are assumed to be constant over the entire element S_e. Then the outgoing intensity is everywhere $i_o = q_o/\pi$, where the emitted flux, q_o has been defined in Eq. (4.13) as:

$$q_o = (1-\varepsilon)q_i + \varepsilon e_s \qquad (4.113)$$

Hence, for those rays originating from other surface elements that strike S_e, an initial intensity i_o is used in the recurrence relation (4.114). Since q_o depends on the value of q_i, an iterative solution is required, unless all the surfaces are black. The net surface heat flux over each of the surface elements is then found from Eq. (4.14), i.e. restating the equation:

$$q_s = q_o - q_i \qquad (4.114)$$

An expression is also required for the divergence of radiative heat flux $\nabla\cdot\mathbf{q}_r$ in each volume element. Lockwood and Shah (1981) considered each ray as a beam of radiative energy, such that the heat source associated with its passage through a volume n, from the definition of intensity, is:

$$\begin{aligned} \delta Q_g &= \int_{\delta\Omega} (i_{n+1} - i_n)\,\delta A\,\hat{\mathbf{s}}\cdot\hat{\mathbf{n}}\,d\Omega \\ &= (i_{n+1} - i_n)\,\delta A \cos\theta \sin\theta \sin(\delta\theta)\delta\phi \end{aligned} \qquad (4.115)$$

where δA is the area of the surface element from which the ray was emitted and it is again assumed that the intensity is constant over the finite solid angle $\delta\Omega$. When the beam of energy associated with a ray only partially intersects a volume the actual source is a fraction of that in Eq. (4.115). However, complex source sharing calculations are

avoided by simply lumping all of the energy δQ_g into only those volume elements cut by the central ray path $\hat{\mathbf{s}}$, saving considerable computational effort, without a significant loss in accuracy. Summing the individual source contributions from all the N rays passing through a volume element, and then dividing this value by its volume, δV, gives the divergence of radiative heat flux as:

$$\nabla \cdot \mathbf{q}_r = \frac{1}{\delta V} \sum_{i=1}^{N} \delta Q_{g,i} \tag{4.116}$$

Note here that the flux divergence is assumed to be constant over each volume element as are the other radiative properties.

Finally, solution of equation (4.114) requires a value for the source function S defined by Eq. (4.16). Lockwood and Shah (1981) approximated the term as follows:

$$\begin{aligned} S &= (1-\omega)\, i_b + \frac{\omega}{4\pi} \int_{4\pi} i(\hat{\mathbf{s}}_i)\, \Phi(\hat{\mathbf{s}}_i, \hat{\mathbf{s}})\, d\Omega_i \\ &= (1-\omega)\, i_b + \frac{\omega}{4\pi} \sum_{i=1}^{N} i(\hat{\mathbf{s}}_i)_{avg}\, \Phi(\hat{\mathbf{s}}_i, \hat{\mathbf{s}})\, \delta\Omega_i \end{aligned} \tag{4.117}$$

where the averaged intensity is taken as the arithmetic mean of the entering i_n and leaving i_{n+1} radiant intensities for each ray passing through the subvolume within the finite solid angle $\delta\Omega_i$. This finite solid angle was evaluated for each $\delta\theta\, \delta\phi$ angular subdivision as (c.f. Siegel and Howell 1992, Sec. 2-5.5, p. 21):

$$\delta\Omega_i = \int_{\delta\phi} \int_{\delta\theta} \sin\theta\, d\theta\, d\phi = 2 \sin\theta\, \sin(\delta\theta/2)\, \delta\phi \tag{4.118}$$

The summation of Eq. (4.117) is then readily evaluated for an isotropically scattering medium by setting $\Phi(\hat{\mathbf{s}}_i, \hat{\mathbf{s}}) = 1$ (e.g. Meng *et al.* 1993). However, the author is not aware of any attempt to solve problems with anisotropically scattering media (see further discussion in next section).

The discrete transfer solution procedure is summarised in Fig. 4.16.

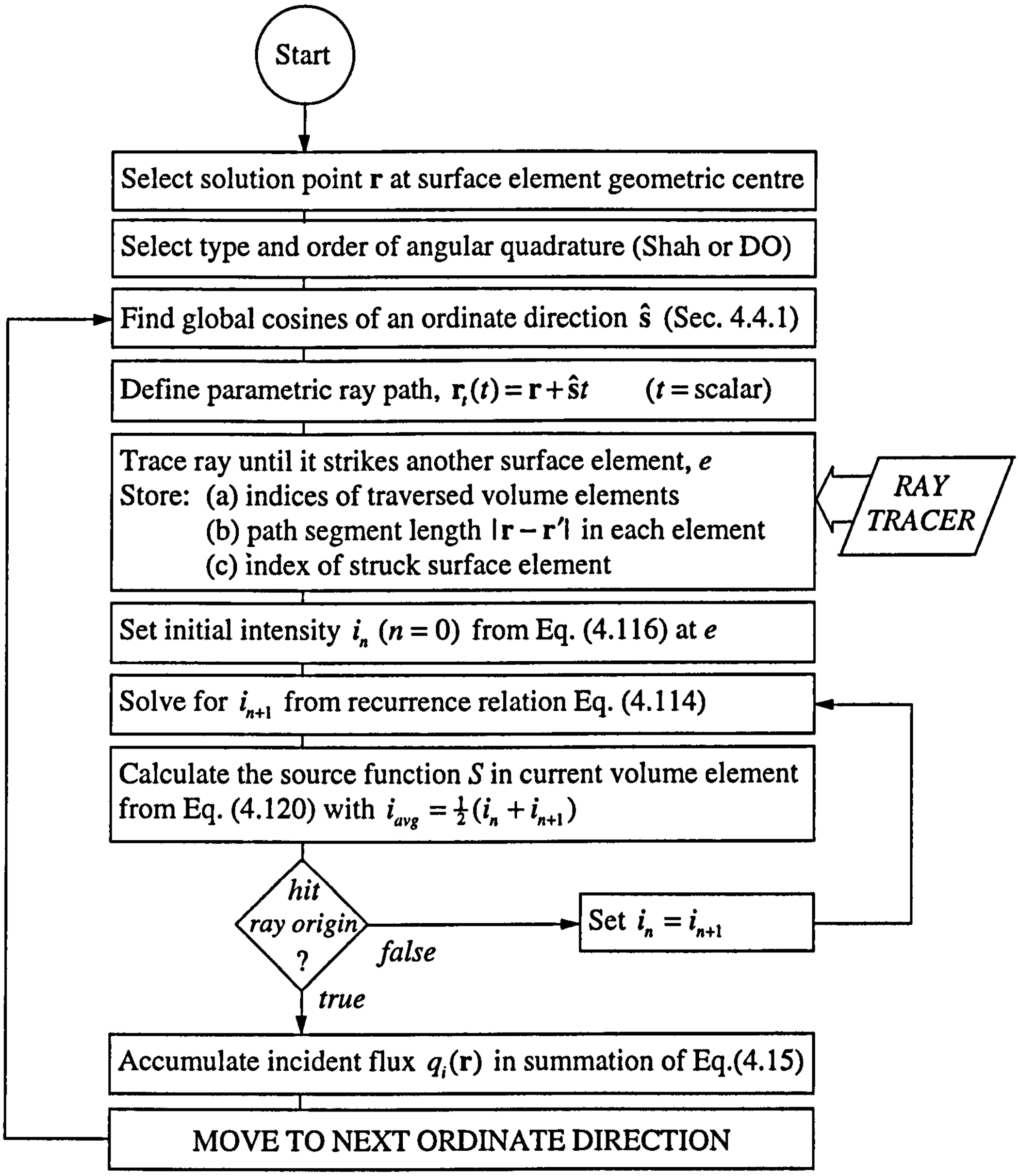

Figure 4.16 Discrete transfer solution procedure: repeated for each surface element and then globally until the radiative heat flux values are converged.

4.6.2 Modifications/Extensions

Several modifications or extensions to the original formulation have been considered. These are as follows:

Angular Quadrature. The discretisation of the hemispherical solid angle above each surface element by Shah (1979) uses a uniform distribution of rays in the spherical coordinates (θ, ϕ) and this practice has been adopted almost exclusively by others. A notable exception is the work of Cumber (1994) who suggests a new angular quadrature analogous to a Newton Cotes formula for numerical integration. This shows some improvement in solution accuracy over Shah's original quadrature, but the test problems are simplistic, and a rigorous analysis of the effect of arbitrary orientated surface elements is not shown. Interestingly, Cumber (1994) also considers a low-order Gaussian type quadrature, but later abandons it on practical grounds, because it is restricted to two directions in the polar plane and thus $\delta\theta$ can not be refined to reduce the discretisation error. However, this Gaussian quadrature is superior to the Newton Cotes quadrature for the same level of angular discretisation, and is in fact, an (nonsymmetric) S_4 type quadrature. Consequently, the discrete ordinate S_n quadrature sets constructed by Lanthrop and Carlson (1965) may offer a better alternative to Shah's original quadrature. As discussed in Sec. 4.5.2., these quadrature formulae satisfy certain order of moment integrations of intensity over a unit sphere and hemisphere. If Shah's quadrature weights are substituted into these expressions it is found that they are largely satisfied, except for the second moment when the angular discretisation is very coarse (e.g. 12 rays). Hence, if a low-order quadrature is used, an S_n set may be advantageous, but with finer discretisation both quadrature schemes are comparable in this respect. A second attribute of the S_n sets is that they are symmetric, preventing directional biases. In contrast, Shah's quadrature is non-symmetric, with more rays (ordinate directions) at smaller polar angles, θ. This may result in an accuracy loss from biasing problems, but there may also be an accuracy gain due to the $\cos\theta$ dependence of the incident intensity at a surface. Finally, it is noteworthy that Shah's quadrature weights can be easily generated up to any order. Therefore, taking all these points into consideration, Shah's original angular quadrature is the author's preferred choice.

In-scattered Radiation. A more conservative approximation for the in-scattering term of Eq. (4.117) is obtained if the summation is weighted by the solid angle as follows:

$$\int_{4\pi} i(\hat{\mathbf{s}}_i)\,\Phi(\hat{\mathbf{s}}_i,\hat{\mathbf{s}})\,d\Omega_i \approx \frac{4\pi\sum i(\hat{\mathbf{s}}_i)_{avg}\,\Phi(\hat{\mathbf{s}}_i,\hat{\mathbf{s}})\delta\Omega_i}{\sum\delta\Omega_i} \tag{4.119}$$

Here, for each volume element, the summation extends over all the crossing ray paths. In the special case of isotropic scattering, this approximation can be avoided altogether by recognising that the integral reduces to the irradiation, w_0 as defined by Eq. (4.10). Then, the irradiation is expressed directly in terms of the divergence of radiative flux by (c.f. Modest 1993, p. 314):

$$\int_{4\pi} i(\hat{\mathbf{s}}_i)\,d\Omega_i = w_0 = 4e_g - \nabla\cdot\mathbf{q}_r/\kappa \tag{4.120}$$

Thus, the source function S of Eq. (4.117) reduces to:

$$S = \frac{1}{\pi}\left(e_g - \frac{\omega}{4\kappa}\nabla\cdot\mathbf{q}_r\right) \tag{4.121}$$

for isotropically scattering media. Since the source function in each volume cell depends on the solution value $\nabla\cdot\mathbf{q}_r$, an iterative solution is required, unless the medium is nonscattering. Consideration of anisotropically scattering media with the discrete transfer approach is very problematic and the author is not aware of any successful strategies in the literature. However, for completeness, an effort was made in this study to extend the methodology for the linear anisotropic scattering (LAS) phase function of Eq. (4.5), i.e. $\Phi(\hat{\mathbf{s}}_i,\hat{\mathbf{s}}) = 1 + g\,\hat{\mathbf{s}}\cdot\hat{\mathbf{s}}_i$. The in-scattering contribution into the path $\hat{\mathbf{s}}$ of a ray, in every volume element, was accumulated by evaluating the dot product $\hat{\mathbf{s}}\cdot\hat{\mathbf{s}}_i$ with every other ray path $\hat{\mathbf{s}}_i$ passing through the volume. Using θ and ϕ to represent the global polar and azimuthal angles of each ray direction, respectively, this dot product is expressed as (Siegel and Howell 1992, p. 586):

$$\hat{\mathbf{s}}\cdot\hat{\mathbf{s}}_i = \cos\theta\cos\theta_i + \sin\theta\sin\theta_i\cos(\phi-\phi_i) \tag{4.122}$$

Trial calculations with this LAS formulation for gray, planar media between black parallel plates were found to agree with exact solutions by Dayan and Tien (1975). In these simple one-dimensional problems, the rays cross the volume elements (taken as

isothermal gas layers between the plates) in a conservative manner. However, in three-dimensional media, the distribution of rays crossing volume elements becomes highly asymmetric resulting in poor predictions with this approach. Perhaps this numerical asymmetry could be removed by fixing the ray ordinate directions relative to the global axes (irrespective of the surface element orientations) or by using some sort of averaging of the scattered energy over 'angular bins' in each volume element (e.g. see Drake 1996). Though, even if an accurate scheme can be developed, it is likely that the extra run-time and storage required to evaluate the phase function for each ray will rapidly become prohibitive, even for moderate problem sizes. Thus the present discrete transfer formulation is restricted to isotropic scattering media.

Media with a Prescribed Heat Source. For a uniform heat generation $\dot{Q}'''$ in each volume element, $\nabla \cdot \mathbf{q}_r$ is replaced by $\dot{Q}'''$ in Eq. (4.120) for the irradiation, w_0. An iterative discrete transfer solution is then required, where the medium emissive power in each volume element is updated every iteration according to:

$$(e_g)_{new} = (e_g)_{old} + \frac{1}{4\kappa}(\dot{Q}''' - \nabla \cdot \mathbf{q}_r) \tag{4.123}$$

This expression is obtained from Eq. (4.120).

Ensuring Energy Conservation. The total net surface heat flow through the boundary of an enclosed participating medium must equal the total volumetric heat source generated per unit time within the medium: a statement of the conservation of energy. For a purely radiating medium this condition requires that:

$$\sum_{i=1}^{N} \delta A_i \, q_{s,i} = \sum_{j=1}^{K} Q_{g,j} \tag{4.124}$$

where the summations are taken over all N surface elements and all K volume elements of the discretised radiation space. However, this overall radiant heat balance is *not* guaranteed in discrete transfer solutions unless the spatial and angular discretisation is sufficiently fine. For example, a situation where the energy imbalance is likely to be severe is shown in Fig. 4.17. The pronounced curvature of the convex surface, compounded here by the coarse spatial and angular discretisation, is such that the view factor of the outer concave surface to itself is not computed accurately. Given that *four*

rays are traced per surface element, it is found that only *three* rays strike the concave surface j from those emitted by all other surface zones. This results in a lack of strict reciprocity between the surfaces and the discrete transfer solution is nonconservative. A mathematical proof of this is provided by Coelho and Carvalho (1997). They also derive a global correction factor, C, such that an initial intensity $i_o = Cq_o/\pi$ is used in the recurrence relation (4.111) to ensure overall conservation. However, the value of this 'fix' is questionable: the solution accuracy is not necessarily improved and may even be reduced. Thus, it has not been used in the present discrete transfer implementation where it is felt better to tolerate a small (often tiny) energy imbalance, rather than to arbitrarily scale values.

Storage of Ray Path Information. The indices of the volume elements traversed, the distance travelled across each element, and the surface element struck by each ray, are traced and *stored* during the first iteration of the solution procedure. Then, for subsequent iterations this stored geometric information is used rather than recalculated. This results in a significant speed-up, especially if the data is read directly from memory or, when the memory capacity is exceeded, by using buffered input from a disk file.

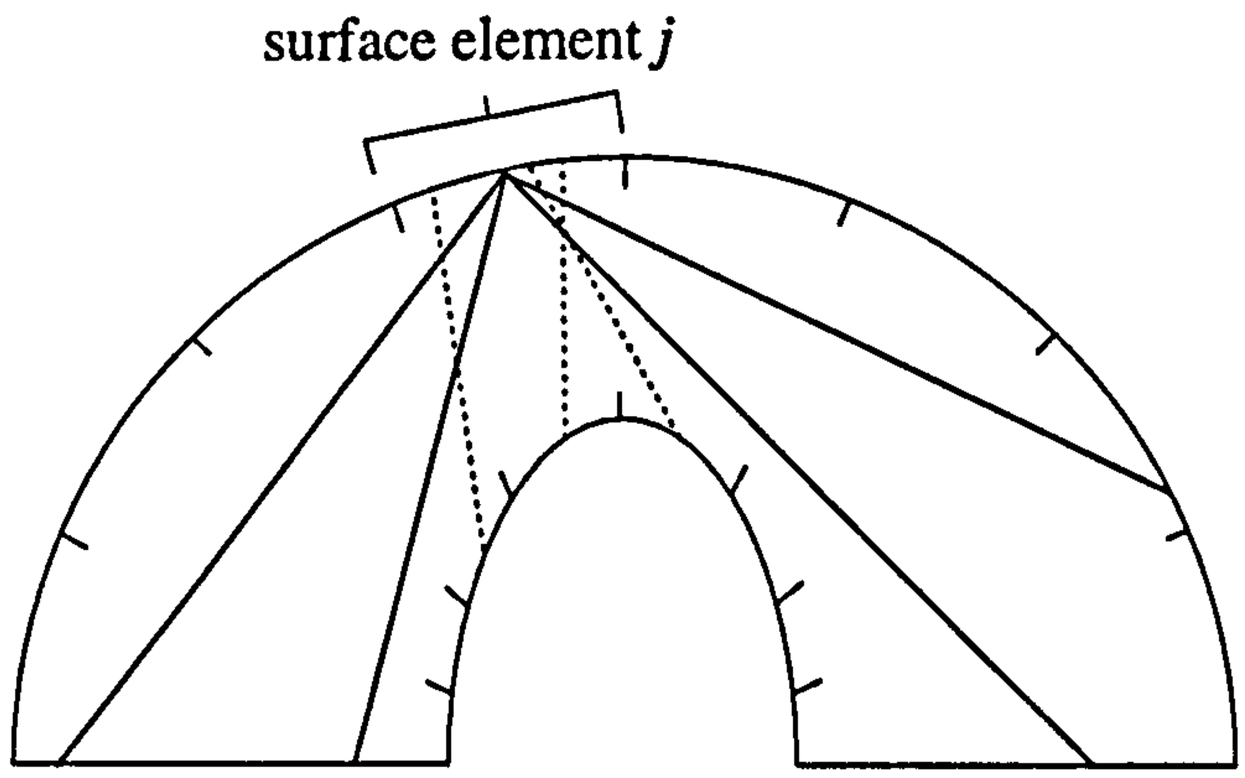

Figure 4.17 A two-dimensional geometry were care has to be taken to ensure an overall heat balance. The irradiation rays that arrive at (solid lines) or start from (dashed lines) the surface element j have been shown for a very coarse angular quadrature.

4.7 Summary

1. A governing equation for participating radiative heat transfer may be written in either integro-differential or integral form. Monte Carlo methods solve for the terms in the transport equation in a probabilistic manner; other methods are based on deterministic approximation.

2. Radiative heat flux and/or temperature conditions are specified in the medium and on the boundary. For combined mode problems only the divergence of radiative heat flux $\nabla \cdot \mathbf{q}_r$ appears in both the energy and radiation transport equations, so only $\nabla \cdot \mathbf{q}_r$ and not q_s (the radiative surface heat flux), needs to be treated as a primitive variable. This is obtained *directly* by methods that solve the transport equation in integral form.

3. Pathlength-based Monte Carlo algorithms offer superior performance over classical forms (for optically thin-to-moderately thick media) as statistical uncertainty is reduced. An efficient scheme is implemented with other speed-ups. A hybrid Monte Carlo/zonal formulation extends applicability of pathlength-based solvers to problems with an applied heat source condition and gains other benefits.

4. A YIX formulation for complex geometries is developed whereby the integral radiation equations are cast in angular-distance form. Angular integrations use discrete ordinate quadrature and distance integrals along ray paths use a nonuniform quadrature based on *optically* spaced coordinates (mapped onto the spatial discretisation).

5. The discrete transfer method is implemented largely in its original form. Alternative angular quadrature schemes are debated. The in-scattering analysis is restricted to an isotropic phase function: treatment of anisotropy is feasible but only at the expense of the conceptually simple methodology and computational efficiency. Likewise fixes to ensure energy conservation increase complexity and are of questionable benefit.

6. The Monte Carlo, YIX and discrete transfer methods all embody the same geometric representation scheme, tracing and search strategies for complex arbitrary geometries. The ray-tracer utilises an efficient ray-triangle intersection algorithm in a novel way to handle cell face distortion and edge intersections with minimum work. Finite element parametric mapping techniques are used to describe the properties of irregular elements.

Chapter 5

Generalised WSGG Model for Nonhomogeneous, Nongray Media

The radiative properties of gaseous participating media are a complex function of wavelength, temperature, pressure, composition and path length. Consequently, the grayness assumption of the previous chapter, where these dependencies were ignored, is unrealistic in all but a few limited situations (e.g. very sooty environments). However, orders of magnitude increases in the computation time are introduced by a nongray analysis; so it was a primary requirement of this study to develop an extremely efficient approach. This resulted in the development of a generalised weighted-sum-of-gray-gases (WSGG) model that can economically capture the spectral nature of an arbitrary gas mixture with good accuracy. Furthermore, the model can be incorporated directly into the Monte Carlo, YIX or discrete transfer gray solvers developed in the last chapter without any need for their reformulation. In fact, it is suitable for use with any gray solution method of the radiative transport equation, Eq. (4.1).

5.1 Gas Property Models: A Review

Gases emit and absorb electromagnetic radiation only at frequencies where the corresponding photon energies match the quantum changes in the energy of the gas molecules. This gives rise to many thousands of narrow lines in the absorption spectra, each of which cover a tiny but finite range of wavenumbers (i.e. no spectral line is truly monochromatic). A concise quantum mechanical explanation for this, together with a discussion of the phenomena which effect the shape and broadening of lines, is provided Modest (1993, Chap. 9). However, of more importance here is the fact that a hierarchy of gas property models of these absorption spectra have evolved corresponding to several wavenumber scales. Each scale represents a different trade-off between accuracy (i.e. the degree to which the line structure is resolved) and computational economy.

Line-By-Line Models. These offer the highest accuracy by using high-resolution spectroscopic data to generate integrated line intensities and spectral absorptivities. Typically the radiative heat transfer calculations are carried out at wavenumber intervals ranging from 0.0002 to 0.02 cm^{-1}: one-fifth the width of one broadened absorption line. Todate line-by-line methods have only be used to generate benchmark predictions for the simplest problems due to the intensive calculation required.

Band Models. At the next scales the absorption coefficient is spectrally averaged over either narrow bands of 5 to 50 cm^{-1} (Goody 1964; Ludwig *et al.* 1973), or over wider bands, typically ranging from 100 to 1000 cm^{-1} (Edwards 1976). This approach greatly reduces the amount of computation but results in another problem: Beer's law does not hold for an absorption coefficient spectrally averaged over many lines (see Edwards 1976, p. 132). Therefore, band models are based on a spectrally averaged band transmissivity (or absorptivity or emissivity) for a given path length. The radiation transport equation is then expressed in terms of a transmissivity differentiated with respect to distance along a line of sight. Forms based on the discrete transfer method (Docherty and Fairweather 1988; Bressloff *et al.* 1996) and on an S_n discrete ordinates formulation (Kim *et al.* 1990; 1991) have been developed for purely absorbing media and demonstrated in relatively simple geometries.

When seeking solutions to the radiative transport equation averaged over a wavenumber interval special attention must be paid to the spectral correlation between terms. Several studies (e.g. Taine 1983; Miranda and Sacadura 1996) have investigated the effect of solving for correlated and noncorrelated transmittance in nonhomogeneous media. Correlated transmittances are found by averaging values for the line/band parameters along the *entire* path length of the radiation. Narrow-band Curtis-Godson or wide-band scaling techniques are used, depending on the type of band model, to effectively replace a nonuniform gas along the line of sight by an 'equivalent' uniform gas (see Edwards 1976, Sec. V). In contrast, a nonhomogeneous path may be discretised into several shorter isothermal lengths and the combined transmittance obtained by multiplying together the transmittances of the separate segments: this is the noncorrelated transmittance. Though noncorrelated transmittances are cheaper to evaluate, Taine (1983) found significant errors in heat transfer calculations if a correlated value is not used. This seems to be contradicted by Miranda and Sacadura (1996) who report fair accuracy using a noncorrelated approach.

The term 'correlation' is also used to refer, rather confusingly, to the spectral averaging of the transmittance-intensity product that appears in the radiative transport equation (with narrow-band models). Although it is simpler to independently average the transmittance and intensity over each band, before finding their product, Kim *et al.* (1990; 1991) showed that large errors may result. Hence, to correctly account for the spectral correlation it is necessary to average the transmittance-intensity product as a unit, but only at the expense of much computation, i.e. see CPU times in Table 2 of Kim *et al.* (1990). Consequently, a fully correlated band model solution would require supercomputing facilities for the problems of interest to this study. Moreover, band models are incompatible with the numerical solution methods of Chapter 4 in which the absorption coefficient is specified locally as the fundamental radiative property.

Total Property Models. A number of gas property models employ curve fitting strategies to spectrally calculated total properties for the entire wavenumber range, thus avoiding the need to treat the spectral variation of absorptivity explicitly. Notable amongst these are the total emissivity-absorptivity models of Leckner (1972) and Modak (1978), the latter of which was used to generate property data for the total transmittance nonhomogeneous model (TTNH) of Grosshandler (1979). This TTNH has generated solutions within 10 percent of narrow-band calculations in a variety of combustion systems, yet it is at least two orders of magnitude faster (Grosshandler 1980; 1985). However, the model is not applicable to the general radiative heat transfer equation that assumes spatially independent absorption coefficients and does not cover the full range of temperature/pressure conditions in spark-ignition combustion systems.

Weighted-Sum-of-Gray-Gases (WSGG) Models. Classically, these comprised curve fits to total emissivity data, enabling a real gas to be modelled as a number of fictitious gray gases (e.g. Truelove 1976; Smith *et al.* 1982). Therefore, the distinct advantage of WSGG models over band property models is that they are directly compatible with the best available solution methods for radiative heat transfer in *gray* media. Furthermore, they are extremely economical and new variants of the WSGG approach allow the fitting of arbitrary spectra via the construction of a detailed histogram representation (Denison and Webb 1993; 1995).

5.2 Nongray Model Selection

A WSGG nongray analysis based largely on the approach of Denison and Webb (1993; 1995) was selected principally for its economy, generality and compatibility with gray gas solvers. Another advantage is that the number of gray gases used in an analysis can be scaled giving some freedom to choose a desired level of solution accuracy for a given level of computation.

An important point implicit in the discussion above is that WSGG solutions are essentially models of the other property models (used to generate the emissivity or absorptivity data). For example, the WSGG model of Denison and Webb (1993; 1995) is constructed with line-by-line spectral data from the high-resolution transmission molecular absorption (HITRAN) data base (Rothman *et al.* 1987; 1992; 1998). However, although HITRAN is extensive, all its data were assembled at room temperature such that application to high temperature and pressure problems requires extrapolation. The best available measurement of thermal radiation from nonhomogeneous masses of hot gases and flames are the data tables in the NASA Handbook of Infrared Radiation (Ludwig *et al.* 1973). The narrow-band code RADCAL (Grosshandler, 1979) uses this information in order to generate spectra for various mixtures of water vapour (H_2O), carbon dioxide (CO_2), carbon monoxide (CO), nitrogen (N_2) and oxygen (O_2) mixtures for a given path length. The path length dependence of this data must first be removed before it can be utilised in the WSGG approach. As discussed by Denison and Webb (1993) this involves finding a single absorption spectrum that brackets the range of path lengths for the required problem. They describe a rather complex optimisation procedure for this purpose, but there was insufficient time to implement this approach.

The next best alternative was to use a correlation by Li *et al.* (1995) for computing the spectral absorption coefficient of H_2O, CO_2, CO and other gases. In this model the spectral absorption coefficient is calculated solely as a function of the temperature, total pressure and partial pressure of the gases, i.e. the optimisation for path length has already been performed. Moreover, a number of important nongray benchmark problems have utilised absorption spectra generated by this model. Thus, a verification of the present nongray radiative analysis was possible (see Sec. 6.2). Li *et al.*'s (1995) model is described first and then the WSGG analysis is developed.

5.3 Computation of the Spectral Absorption Coefficient

Li *et al.* (1995) use a combined narrow- and wide-band formulation for computing the spectral variation in absorption coefficient. Individual spectral lines are considered to be of slowly varying intensity and to have nearly uniform spacing within narrow wavenumber bands: this is a good assumption for diatomic molecules and linear polyatomic molecules. Then the Elsasser narrow-band models gives the spectral absorption coefficient as (Siegel and Howell 1992, p. 555):

$$\kappa_\eta = \rho \frac{S}{\delta} \frac{\sinh(\pi\beta/2)}{\cosh(\pi\beta/2) - \cos[2\pi(\eta - \eta_c)/\delta]} \tag{5.1}$$

where η is the wavenumber for the band centred at η_c, ρ is the partial density of the radiating gas, δ is the line spacing, S is the mean line strength and β is a parameter to allow for the pressure broadening of the absorption lines. For large β at high pressures the lines are broad compared to their spacing and the line structure is lost as the lines strongly overlap. Thus, β is referred to as the line overlap parameter.

Li *et al.* (1985) argue that since the band shape prescribed by the Elsasser narrow-band model is arbitrary, there is no need to preserve it: only the integrated band absorptance is of importance. Therefore, they choose to take the mean strength-to-spacing ratio, S/δ, and the line overlap, β, as those specified in Edwards exponential wide-band model (Edwards 1976). The line spacing parameter, δ, is then adjusted in order to correlate experimental data for band absorptances, A, expressed as:

$$A = \int_{\eta_1}^{\eta_2} [1 - \exp(-\kappa_\eta L)]\, d\eta \tag{5.2}$$

where η_1 and η_2 are the lower and upper wavenumber limits for the absorption band under consideration, and L brackets the experimental range of path lengths. Any loss of accuracy from this approximation over an *entire* wide band, and certainly over the entire thermal radiation spectrum, is expected to be small. Here 'small' should be interpreted in light of the fact that Edwards wide-band model correlates experimental absorptance data with an average error of about ±20% and maximum errors as high as 80% (Modest 1993, p. 349).

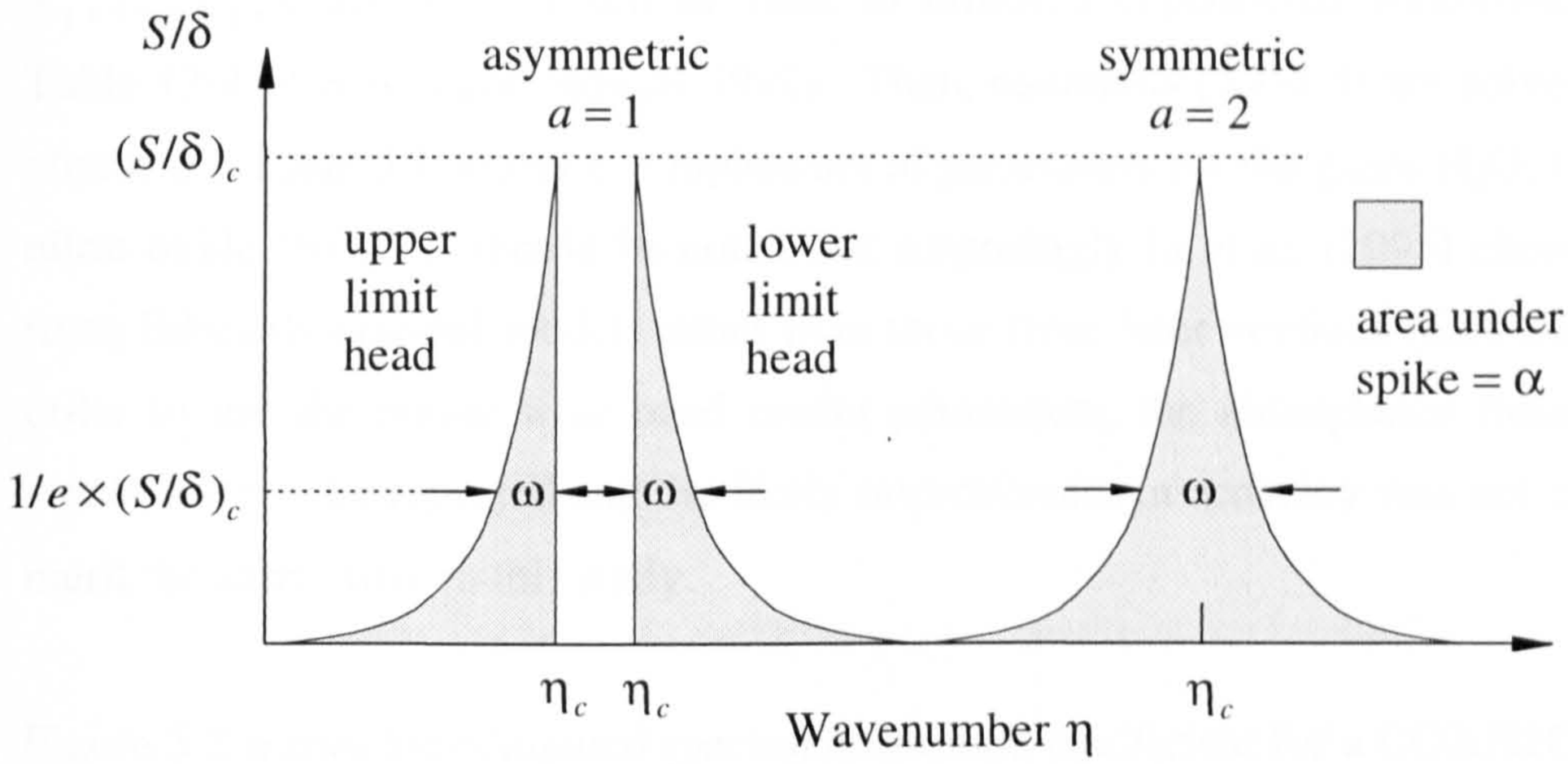

Figure 5.1 Band shapes for Edwards exponential wide-band model.

Quantum mechanics describes an exponential decrease in line intensity in the band wings far from the centre, so Edwards assumed that S/δ has the following profile:

$$\frac{S}{\delta}=\frac{\alpha}{\omega}\exp(-a|\eta-\eta_c|/\omega) \tag{5.3}$$

where $a=1$ for asymmetric bands and 2 for symmetric bands (Fig. 5.1); α and ω are wide band strength and width parameters. Referring to Fig. 5.1, α represents the area under the exponential spikes and ω the width at $1/e$ of the maximum. In the literature, α and ω have also been labelled as C_1 and C_3, respectively. Further, the line overlap parameter was specified as:

$$\beta = C_2^2 P_e/(4C_1C_3) \tag{5.4}$$

and

$$P_e=\left[p/p_0+(b-1)\,p_a/p_0\right]^n, \qquad p_0=1 \text{ atm} \tag{5.5}$$

where p_a is the partial pressure of the radiating gas, p is the total pressure of the gas mixture, and C_2, b and n are correlation parameters.

In summary, given a set of conditions (T, p and composition), the model parameters C_1, C_2, C_3, b and n are taken as those in Edwards exponential wide-band model (i.e. Table 12-4 of Siegel and Howell 1992). Then, equations (5.1-5.5) are solved in order to obtain δ. Table 5.1 shows a complete set of parameters for the gases H_2O, CO_2, CO and nitric oxide (NO). It should be noted that surprisingly Li *et al.* (1995) chose parameters from Edwards original model, rather than those from later versions (Edwards 1976). In order to use the newer wide-band model parameters, the absorptance fitting procedure would have to be repeated and the likely improvement in accuracy was not considered to merit the extra work in this study.

Figure 5.2 shows the computed spectral absorption coefficient for a CO2:H2O ratio of 8:9 (i.e. equal to the stoichiometric combustion of *n*-octane).

5.4 Weighted-Sum-of-Gray-Gases Model

The analysis of nongray media was initially performed using a 'bandwise' modelling approach similar to that described by Farmer (1995, Sec. 4.3.3, p. 126). Though not formally stated as such, his method is essentially a weighted-sum-of-gray-gases (WSGG) approximation, albeit an inefficient one. Subsequently, on the basis of work by Denison and Webb (1993; 1995), this bandwise model was revised in order to improve its performance and to extend its applicability to nonisothermal, nonhomogeneous media. The full development process is detailed below, since the initial bandwise model is a useful aid in understanding and verifying the final WSGG model.

5.4.1 Bandwise Solution

Consider, as an example, the absorption spectrum of Fig. 5.2. The essence of the bandwise approach is to construct its histogram representation. The actual spectrum is subdivided into many small wavenumber intervals, or bands, and the absorption coefficient is averaged across each interval as:

$$\kappa_j = \frac{1}{\eta_2 - \eta_1} \int_{\eta_1}^{\eta_2} \kappa_\eta \, d\eta \tag{5.6}$$

where η_1 and η_2 are the lower and upper wavenumber limits of the interval j.

Table 5.1 Correlation parameters for H_2O, CO_2, CO and NO (Li *et al.* 1995).

Gas	Band μm	Band centre η , cm^{-1}	Pressure parameter *b*	Pressure parameter *n*	C_1 $cm^{-1}/(g\,m^{-2})$	C_2[a] $cm^{-1}/[(gm^{-2})]^{1/2}$	C_3[a] cm^{-1}	δ cm^{-1}
H_2O[b]	6.3	1600	5.0	1.0	41.2	44	$52(T/T_0)^{0.5}$	250
	2.7	3750	5.0	1.0	23.3	39	$65(T/T0)^{0.5}$	100
	1.87	5350	5.0	1.0	$3.0\varphi_{011}(T)$	$6.0C_1^{0.5}$	$46(T/T_0)^{0.5}$	5
	1.38	7250	5.0	1.0	$2.5\varphi_{101}(T)$	$8.0C_1^{0.5}$	$46(T/T_0)^{0.5}$	200
CO_2[c]	15	667	1.3	0.7	19	$6.9(T/T_0)^{0.5}$	$12.9(T/T_0)^{0.5}$	100
	10.4	960	1.3	0.8	$0.76\varphi_1(T)$	$1.6(T/T_0)^{0.5}C_1^{0.5}$	$12.4(T/T_0)^{0.5}$	20
	9.4	1060	1.3	0.8	$0.76\varphi_1(T)$	$1.6(T/T_0)^{0.5}C_1^{0.5}$	$12.4(T/T_0)^{0.5}$	30
	4.3	2350	1.3	0.8	110	$31(T/T_0)^{0.5}$	$11.5(T/T_0)^{0.5}$	30
	2.7	3715	1.3	0.65	$4.0\varphi_2(T)$	$8.6\varphi_3(T)$	$24(T/T_0)^{0.5}$	1000
CO[d]	4.67	2143	1.1	0.8	20.9	$\varphi_5(T)$	$22(T/T_0)^{0.5}$	10
	2.35	4260	1.0	0.8	0.14	$0.08\varphi_5(T)$	$22(T/T_0)^{0.5}$	150
NO	5.35	1870	1.0	0.65	$125(273/T)$	$51.5–7.5(T/300)$	$45(T/300)^{0.5}$	1.7

[a] $T_0 = 100$ K

[b] For H_2O:

$$\varphi_{\nu_1\nu_2\nu_3} = \left[1-\exp\left(-\frac{hc}{kT}\right)\sum_{i=1}^{3}\nu_i\eta_i\right]\prod_{i=1}^{3}\left[1-\exp\left(-\frac{hc\eta_i}{kT}\right)\right]^{-1}$$

where $\eta_1 = 3652\ cm^{-1}$, $\eta_2 = 1595\ cm^{-1}$ and $\eta_3 = 3756\ cm^{-1}$.

[c] For CO_2:

$$\varphi_1 = \left\{1-\exp\left[-\frac{hc}{kT}(\eta_3-\eta_1)\right]\right\}\left[\exp\left(-\frac{hc\eta_1}{kT}\right)-\frac{1}{2}\exp\left(-\frac{2hc\eta_1}{kT}\right)\right]$$

$$\times\left[1-\exp\left(-\frac{hc\eta_1}{kT}\right)\right]^{-1}\left[1-\exp\left(-\frac{hc\eta_3}{kT}\right)\right]^{-1}$$

$$\varphi_2 = \left\{1-\exp\left[-\frac{hc}{kT}(\eta_1+\eta_3)\right]\right\}\left[1-\exp\left(-\frac{hc\eta_1}{kT}\right)\right]^{-1}\left[1-\exp\left(-\frac{hc\eta_3}{kT}\right)\right]^{-1}$$

$$\varphi_3 = \left[1+0.053\left(\frac{T}{T_0}\right)^{3/2}\right]$$

where $\eta_1 = 1351\ cm^{-1}$ and $\eta_3 = 2396\ cm^{-1}$.

[d] For CO:

$$\varphi_5 = \left[15.15+0.22\left(\frac{T}{T_0}\right)^{3/2}\right]\left[1-\exp\left(-\frac{hc\eta}{kT}\right)\right]$$

where $\eta = 2143\ cm^{-1}$.

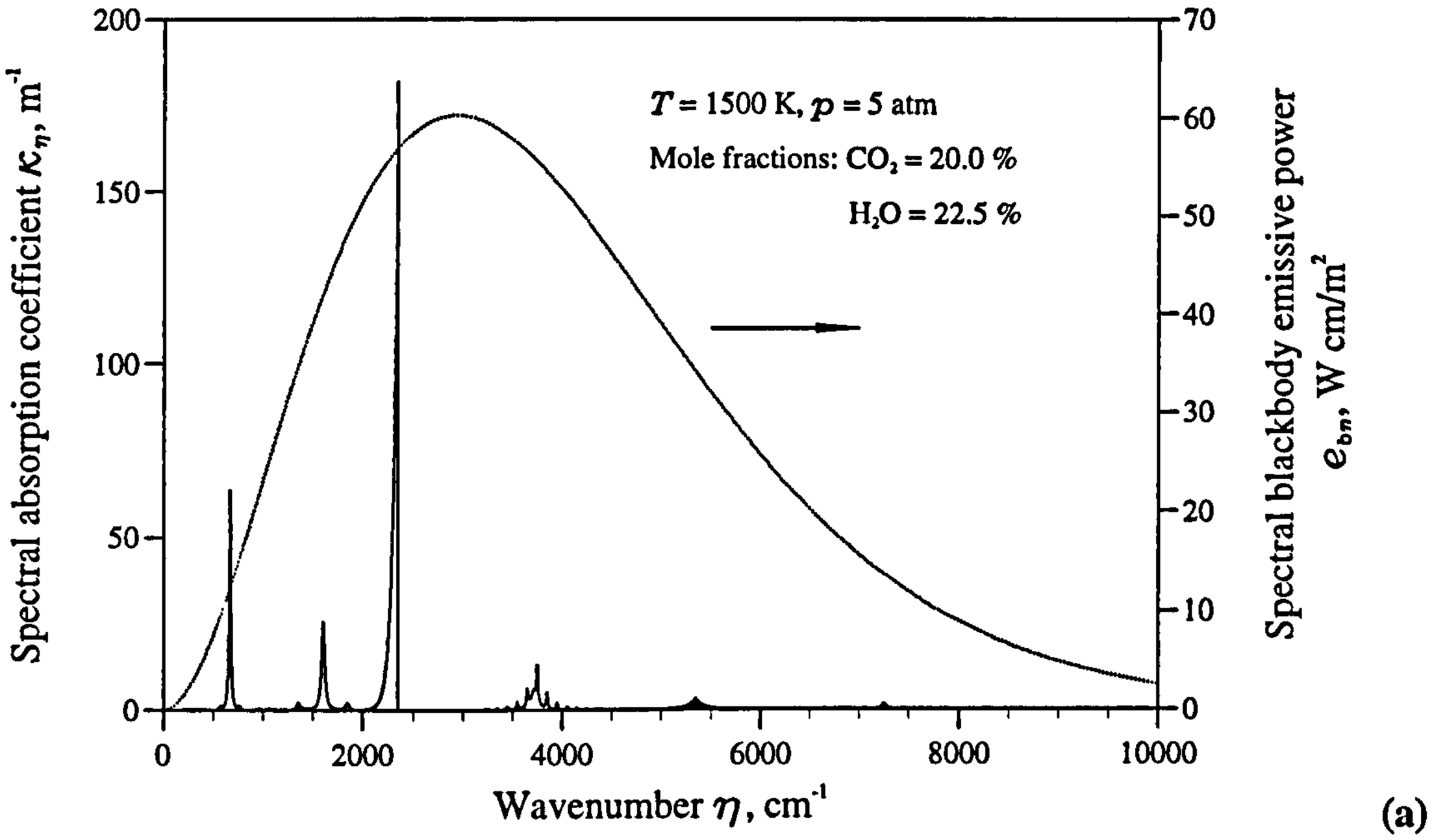

Figure 5.2 (a) Linear, and (b) logarithmic plots of the *model* absorption spectrum of a CO_2/H_2O mixture [conditions shown in (a)] computed via Eq. (5.1). The blackbody emissive power spectrum at the mixture temperature of 1500 K is also plotted in (a).

The spectral integration of Eq. (5.6) is evaluated using numerical quadrature. A value for the blackbody emissive power is found for each band interval j from the expression:

$$e_j = \int_{\eta_1}^{\eta_2} e_{b\eta}\, d\eta = [f(\eta_2/T) - f(\eta_1/T)]\sigma T^4 \tag{5.7}$$

where f is the fraction of the total blackbody emissive power, σT^4, between zero and η/T. Blackbody fractions are found from the series relationship (Chang and Rhee 1984):

$$f(\eta/T) = \frac{15}{\pi^4}\sum_{n=1}^{\infty}\left[\frac{\exp(-n\varsigma)}{n}\left(\varsigma^3 + \frac{3\varsigma^2}{n} + \frac{6\varsigma}{n^2} + \frac{6}{n^3}\right)\right], \quad \varsigma = C_2\eta/T \tag{5.8}$$

where $C_2 = 1.4388\ \text{cm}\cdot\text{K}$ is a constant in Planck's spectral power distribution. Here, the size of each successive term in the summation rapidly diminishes with increasing n such that only a small number of terms must be computed to determine f to a required accuracy. Then, the absorption and emissive power values from Eqs. (5.6) and (5.7) are used in a *gray* radiative transport analysis for each band. Subsequently, the band results are summed together in order to obtain the total transport results. (Here an isothermal, homogeneous medium is assumed such that the spectrum in Fig. 5.2 applies over the entire problem domain.)

It is noteworthy that since an independent analysis is performed for every band, any numerical procedure which solves the general radiative heat transfer equation may be applied, or even a combination of techniques. This flexibility is an important advantage when treating wavenumber intervals with a very large absorptivity, i.e. those at the centres of the CO_2 and H_2O exponential absorption spikes in Fig. 5.2. At these wavenumbers emitted radiation travels only a short distance before complete absorption (or scattering) such that the local intensity is a function of the local property gradients only. The radiative energy transfer can then be modelled as a simple diffusion process, i.e. the Rosseland diffusion approximation (Siegel and Howell 1992, Sec. 15-3.4). In practice, a numerical solution method for optically thin-to-moderate conditions is either coupled with the diffusion approximation (e.g. Farmer and Howell 1994; Burns *et al.* 1995) or its formulation is modified. A good example of the latter is the YIX method (Sec. 4.5) where a lower order S_n angular quadrature may be used for optically thick bands (Hsu *et al.* 1993). A cell optical thickness above 5 is the threshold condition often chosen for applying the diffusion approximation.

As each band requires a separate solution it is clearly essential to minimise their number, while retaining enough bands to resolve the spectral variation in absorption with sufficient fidelity: herein lies the most difficult aspect of the bandwise approach. As a general rule, more bands are required around the gas absorption spikes, with fewer, wider bands in the window regions between them. However, developing an automated procedure to optimally insert a given number of bands for an arbitrary absorption profile is a challenging problem. The following satisfactory, though imperfect, strategy was adopted in this study. A narrow band is first placed at the centre, η_c, of each gas absorption spike: this is only a few wavenumbers wide. The large wavenumber ranges in between are then recursively subdivided into bands until the specified number of bands has been inserted. Each new band is inserted by dividing an existing interval in two, though not necessarily symmetrically, but rather so as to minimise the error between the stepped and actual absorption profile. Additional complication arises from the fact that the absorption coefficient varies over several others of magnitude. A simple searching and fitting algorithm was devised in order to find at which wavenumber to make the division. Figure 5.3 shows the resulting spectral discretisation of the profile in Fig. 5.2.

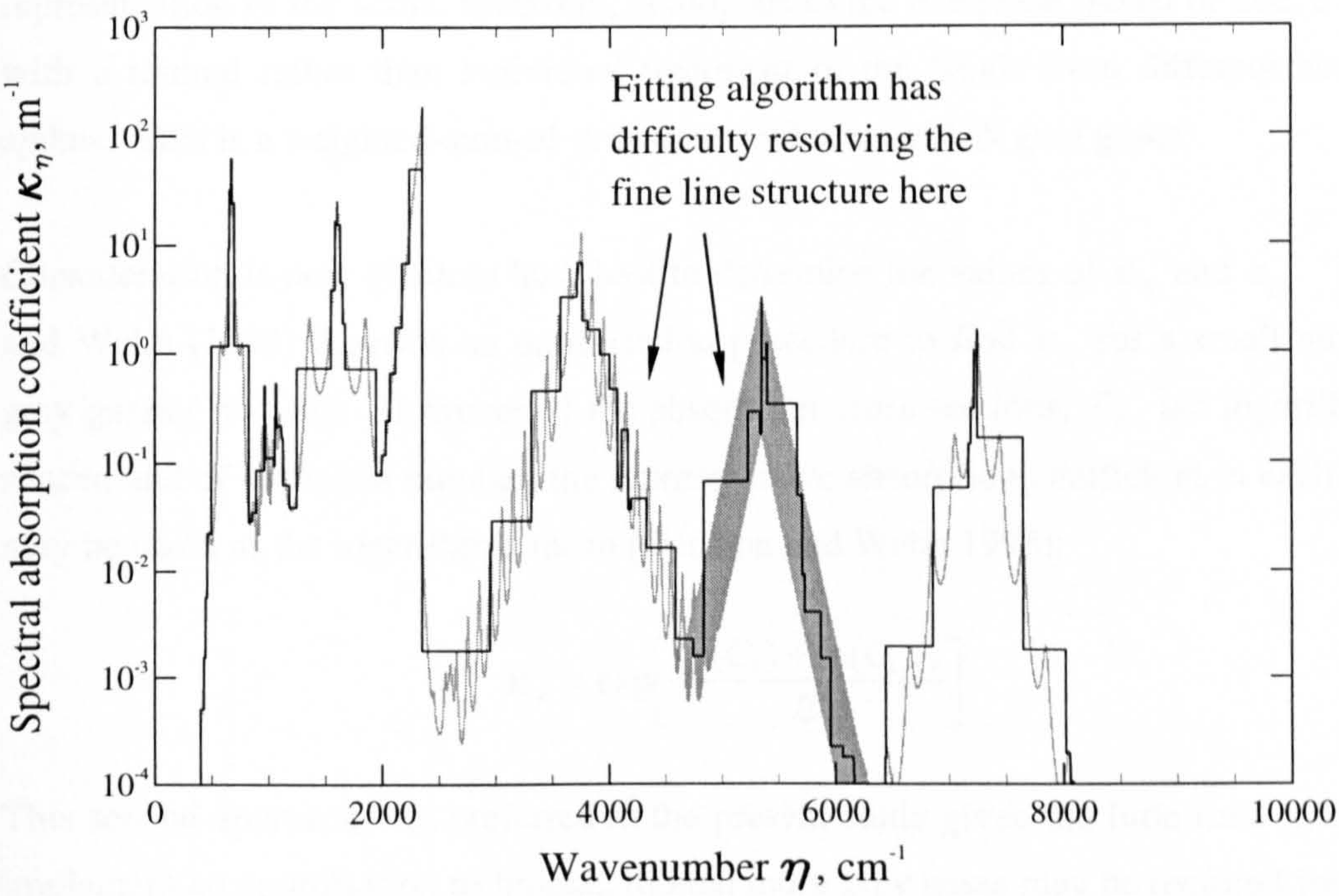

Figure 5.3 WSGG histogram model for the CO_2/H_2O spectrum of Fig. 5.2.

It can be seen that the algorithm had difficulty in capturing the fine line structure of the 1.87 μm H_2O band. Further, the number of bands required is large (80+) even after optimisation. The reason for this is that each absorption spike is resolved separately. It is observed that many bands have identical, or similar, levels of absorption such that conceptually they may be treated as a single unit, with a combined blackbody emissive power equal to the summation of their individual blackbody powers. This greatly reduces the level of computation and is the basis of a more efficient method using absorption cross-sections.

5.4.2 Banded Solution using Absorption Cross-Sections

An absorption cross-section, C_k, selects wavenumbers with absorption less than or equal to C_k from a complete spectrum (Fig. 5.4). Thus, a pair of absorption cross-sections C_k and C_{k+1} will segregate out all the wavenumber intervals, or bands, for which the spectral absorption coefficient is in the range $C_k \leq \kappa_\eta \leq C_{k+1}$. These bands are characterised as a single gray gas with a representative absorption coefficient, κ_k and combined blackbody emissive power e_{gk} (Fig. 5.5). Additional cross-sections are then added in order to discretise the entire absorption domain into N discrete levels of absorption, κ_k, with associated blackbody powers, e_{gk} $(k = 1, 2, \ldots, N)$. The result is a histogram representation of the actual spectrum, analogous to the bandwise model of Sec. 5.4.1, but with a mutual rather than individual treatment of the bands from different absorption spikes. This is a weighted-sum-of-gray-gases solution with N gray gases.

Consideration is now given to how best to determine the values of κ_k and e_{gk}. Denison and Webb (1993) describe an optimisation procedure to find κ_k for a small number of gray gases ($N < 10$). However, if the absorption cross-sections, C_k, are logarithmically spaced and of sufficient number, the representative absorption coefficient in each interval may be taken as the logarithmic mean (Dension and Webb 1995):

$$\kappa_k = \exp\left[\frac{\ln(C_k) + \ln(C_{k+1})}{2}\right] \tag{5.9}$$

This second approach was preferred in the present study given the little time available to implement an optimisation technique, though more gray gases may be required for a given level of accuracy.

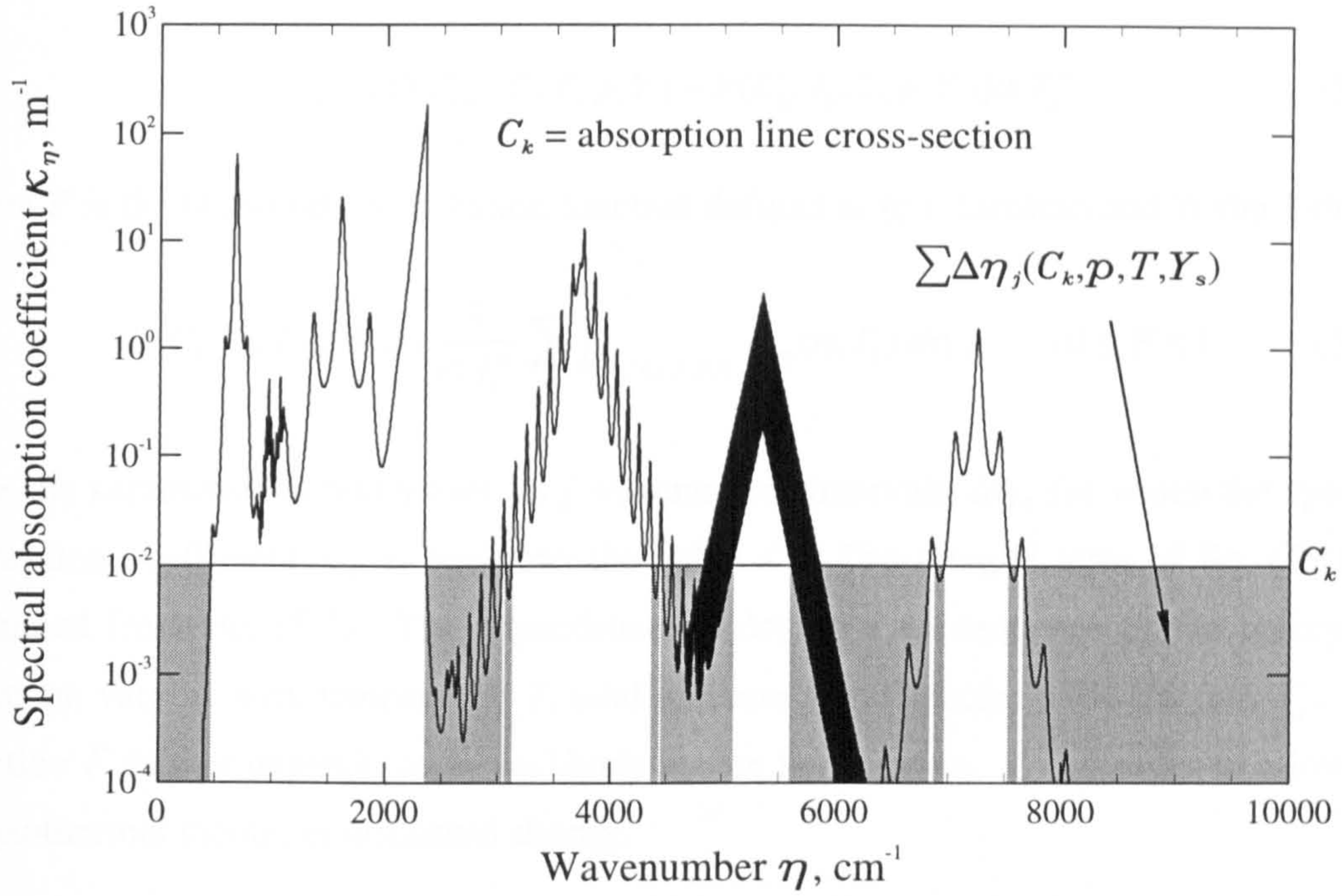

Figure 5.4 Geometrical interpretation of an absorption line cross-section. The blackbody energy is summed over the wavenumber intervals $\Delta\eta_j$ in order to calculate a blackbody distribution function F as defined by Eq. (5.11).

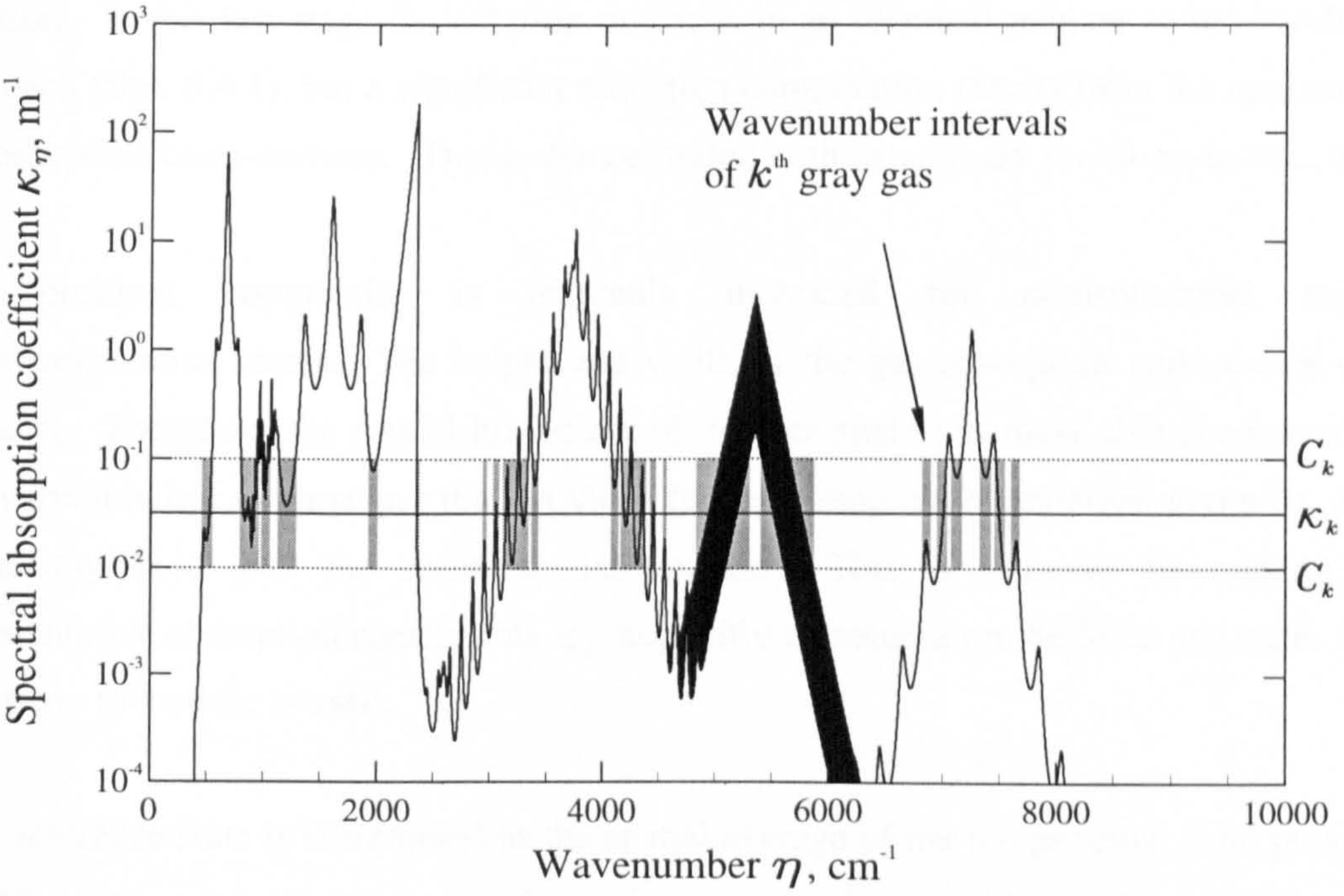

Figure 5.5 Representation of the k^{th} gray gas by a pair of absorption line cross-sections. Additional cross-sections are added to construct a complete WSGG model spectrum.

The blackbody power for the gray gas with absorption κ_k is:

$$e_{gk} = [F(C_{k+1}, T_b, T, p, Y_s) - F(C_k, T_b, T, p, Y_s)]\sigma T_b^4 \tag{5.10}$$

where F is the blackbody distribution function defined as (c.f. Denison and Webb 1995):

$$F(C_k, T_b, T, p, Y_s) = \frac{1}{\sigma T_b^4} \sum_j \int_{\Delta\eta_j(C_k, T, p, Y_s)} e_{g\eta}(\eta, T_b)\, d\eta\,, \qquad (0 \le F \le 1) \tag{5.11}$$

Here the summation is taken over all j wavenumber intervals $\Delta\eta_j$ for which the spectral absorption coefficient κ_η is less than the value C_k. The integral term of Eq. (5.11) is evaluated from Eq. (5.7). The dependence of $\Delta\eta_j$ is a consequence of the absorption spectrum varying with temperature T, total pressure p and species mole fraction Y_s. The function F further depends on a blackbody source temperature, T_b, in order to allow for nonisothermal media, as discussed shortly.

However, if the medium is isothermal and homogeneous, a single model spectrum will apply over the entire domain for the conditions T, p and Y_s ($T_b = T$). An independent analysis is performed for each of the k gray gases with the fitted values of κ_k and e_{gk}, after which the individual results are summed to obtain the total radiative heat transfer solution. In this last stage the solution proceeds in an identical manner to the bandwise approach (Sec. 5.4.1), but a significant reduction computation results from the application of absorption cross-sections. This is demonstrated with benchmark problems in Sec. 6.2.

The problem complexity is markedly increased for nonisothermal and/or nonhomogeneous media. The height and width of the gas absorption spikes vary with position. Therefore, the model histogram of the gas spectrum must also accommodate this variation, but in a manner that provides for the histogram boundaries, given by $\Delta\eta_j$, to remain fixed over the entire spatial domain. This is achieved by making the representative absorption coefficients κ_k implicitly dependent on the local gas state. The following procedure is used:

1. A reference state is determined as the spatial average of the temperature, total pressure and species mole fraction over the entire participating medium, and the variation in spectral absorption coefficient $\kappa_\eta(T_{ref}, p_{ref}, Y_{s,ref})$ is evaluated from Eq. (5.1).

2. The computed range of absorption coefficients is discretised into a number of increments by inserting absorption cross-sections, $C_{k,ref}$, and a reference absorption coefficient, $\kappa_{k,ref}$, is obtained for each increment from Eq. (5.9).

3. At each spatial location the local variation in absorption coefficient $\kappa_\eta(T_{loc}, p_{loc}, Y_{s,loc})$ is evaluated from Eq. (5.1).

4. The local gray gas absorption coefficients κ_k are found as those which satisfy the following condition:

$$\begin{aligned} F[C_k = \kappa_k; T_b = T_{ref}; T = T_{loc}; p = p_{loc}; Y_s = Y_{s,loc}] \\ = F[C_k = \kappa_{k,ref}; T_b = T_{ref}; T = T_{ref}; p = p_{ref}; Y_s = Y_{s,ref}] \end{aligned} \tag{5.12}$$

This arranges that the blackbody distribution functions are equivalent at the reference and the local states, i.e. it fixes the model histogram boundaries over the spatial domain as desired. The source temperature is set equal to the reference temperature for this purpose. Therefore, as discussed by Denison and Webb (1995), Eq. (5.12) is approximate in predicting the emission as a local phenomenon.

5. The gas blackbody weights are determined for each gray gas from Eq. (5.10) with the source temperature equal to the local temperature, i.e.

$$\begin{aligned} e_{gk} = [\, & F(C_{k+1}, T_b = T_{loc}, T = T_{ref}, p = p_{ref}, Y_s = Y_{s,ref}) \\ & - F(C_k, T_b = T_{loc}, T = T_{ref}, p = p_{ref}, Y_s = Y_{s,ref})] \, \sigma T_b^4 \end{aligned} \tag{5.13}$$

Setting T, p and Y_s equal to the reference condition here ensures that $\Delta\eta_j$ are fixed. A similar expression is used to evaluate the blackbody weights at a surface, i.e.

$$\begin{aligned} e_{sk} = [\, & F(C_{k+1}, T_b = T_{wall}, T = T_{ref}, p = p_{ref}, Y_s = Y_{s,ref}) \\ & - F(C_k, T_b = T_{wall}, T = T_{ref}, p = p_{ref}, Y_s = Y_{s,ref})] \, \sigma T_b^4 \end{aligned} \tag{5.14}$$

where the wall temperature T_{wall} is taken as the source temperature.

6. The surface heat flux and divergence of radiative heat flux are determined for each gray gas k with the fitted values κ_k, e_{gk} and e_{sk}. These results are summed to obtain the total heat transfer solution.

Some points should be noted regarding the implementation of this algorithm. The limits of the intervals $\Delta\eta_j$ lie at wavenumbers where the absorption line C_k intersects the graphic of κ_η, as detailed above. Thus each limit corresponds to a root of the function:

$$\kappa_\eta(\eta) - C_k = 0 \tag{5.15}$$

Numerous roots will exist if the spectral absorption coefficient has a fine line structure so it is important to choose an efficient root finding technique. This study uses a fast and robust false position method (Pearson 1986, pp. 4-8) and the convergence was assumed with a tolerance of 10^{-6} cm^{-1}. Furthermore, since Eq. (5.12) is implicit, a false position method is also used to determine the local κ_k, though the procedure is somewhat modified in order to allow for the logarithmic variation in absorption coefficient over the entire absorption domain. A solution to:

$$F[C_k = \kappa_k; T_b = T_{ref}; T = T_{loc}; p = p_{loc}; Y_s = Y_{s,loc}] - F_{ref} = 0 \tag{5.16}$$

is found where $F_{ref} = F[C_k = \kappa_{k,ref}; T_b = T_{ref}; T = T_{ref}; p = p_{ref}; Y_s = Y_{s,ref}]$. Here, each trial for κ_k requires that its blackbody distribution function F is determined, which in turn, requires that a full solution of Eq. (5.15). Consequently, in the gray gas fitting calculation the spectral absorption κ_η must be evaluated a vast number of times due to this hierarchical dependence and a significant speedup is achieved by generating lookup tables for κ_η (at step 3). Lookup tables for blackbody fractions may also be used to speed up evaluation of the gas blackbody weights. The complete fitting procedure is summarised in Fig. 5.6.

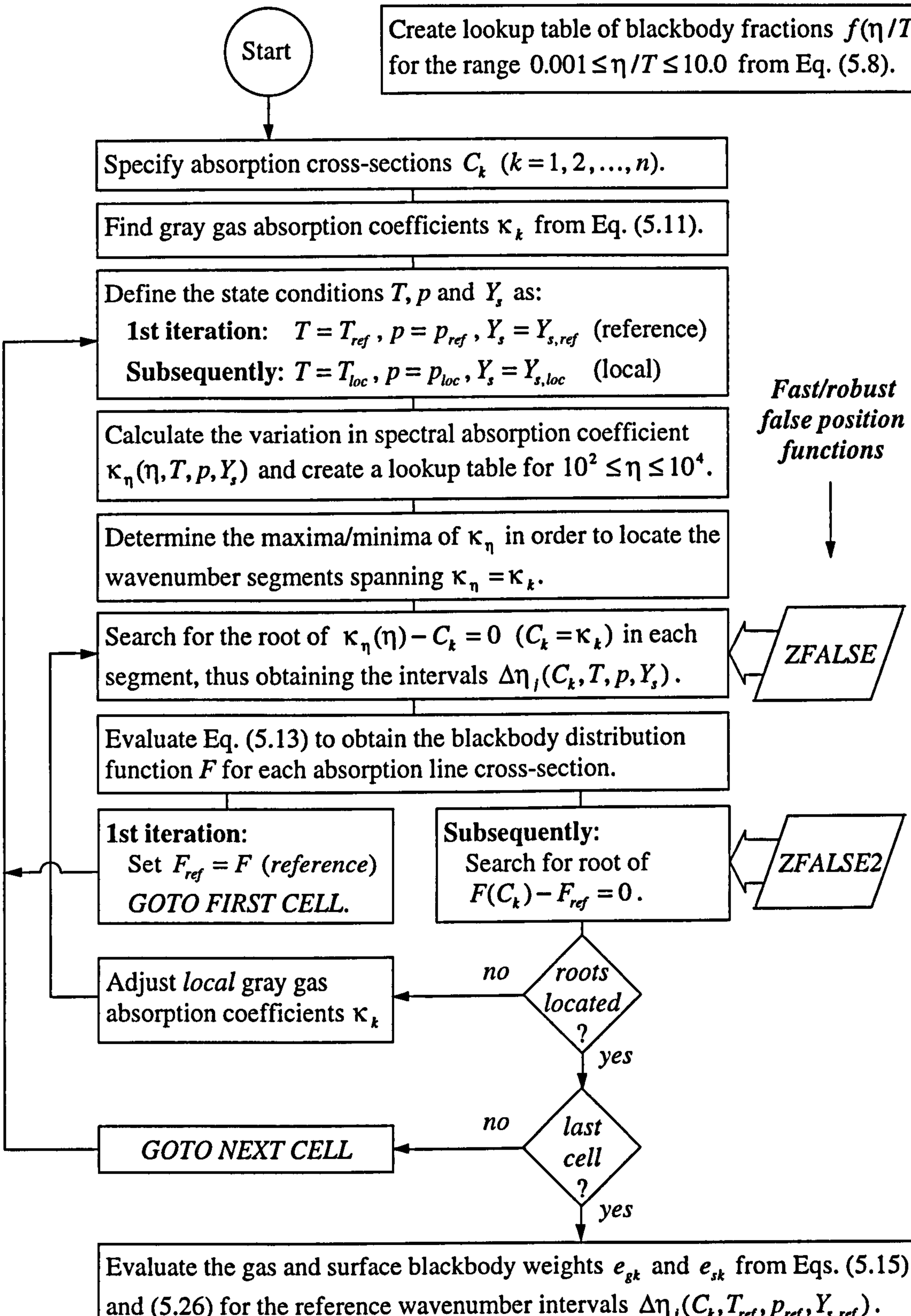

Figure 5.6 Procedure to determine a set of k gray gas absorption coefficients and blackbody weights in a WSGG model of a nonisothermal, nonhomogeneous medium.

5.5 Combined Mode Heat Transfer: Radiation Coupling

The theory detailed in preceding sections and chapters constitute all the essential elements for a radiative transport analysis of turbulent reacting flow. Figure 5.7 clarifies how the various models fit into an overall solution procedure. Bold type shows the relevant chapter or section of the thesis.

Models concerned with the radiation simulation are collected together in a separate program unit *RAD*. This is called from the main driver routine of the KIVA-II CFD code (Fig. 3.5) to determine the total radiative heat flux at surface elements, q_s, and the total divergence of radiative heat flux in volume elements, $\nabla \cdot \mathbf{q}_r$. For problems concerned solely with radiation, *RAD* doubles as a stand-alone code and a short input module is added to provide geometric and radiative property information.

Coupling of the radiation and flow fields is via the divergence of radiative heat flux term, $\nabla \cdot \mathbf{q}_r$, of the internal energy equation (see Sec. 4.1.3). In practice, the specific internal energy I of each computational cell is adjusted as follows:

$$I^* = I - (\nabla \cdot \mathbf{q}_r)\frac{\Delta t_n}{\overline{\rho}} \tag{5.17}$$

where the $\overline{\rho}$ is the total density within the cell and Δt_n is the n^{th} time step of the KIVA-II temporal differencing scheme (see Sec. 3.5.1). A negative sign is required in Eq. (5.17) since a positive value for the radiative source represents an energy sink. Furthermore, KIVA-II requires that all input is in CGS units such that the dimensions of $\nabla \cdot \mathbf{q}_r$ are ergs/(cm^3 s)$^{-1}$ [10^7 ergs = 1 Joule].

The radiation evaluation is much slower than the conduction/convection calculation, typically taking one-to-two orders of magnitude more time to compute, though this depends on many factors (i.e. mesh size, number of gray gases used in WSGG model, solution method, etc.). Thus in order to ease the computational overhead the radiation calculation is often performed on a coarser mesh than that used by the flow solver (e.g. Abbas *et al.* 1984). One possible technique is to merge several neighbouring fluid elements into a single radiation zone and pass volume averaged flame temperatures, pressures and species concentrations to the radiation model. Then on completion of the radiation simulation a reverse procedure is used to map the radiation sources back on to

the flow mesh. More specifically in regard to engine simulations, it is important to restrict the radiation calculation to those parts of the engine cycle where the cylinder gases are strongly radiating. Therefore, calculations are first carried out in the *absence* of radiation until the onset of combustion. Even then it is not always essential to update the radiative sources on every KIVA-II time step; the computation can be made less costly by updating them periodically.

Finally, it is noted that the KIVA-II numerical scheme uses Favre-averaged quantities (Sec. 3.1.1) and the affect of turbulent fluctuations on the predicted radiative fluxes is ignored. This will invariably cause underprediction of the emission from a hot medium, though the magnitude of this error is difficult to quantify as the interaction between radiation and turbulence is still poorly understood (Modest 1993, Sec. 20.7, p.743). This issue is discussed further in Sec. 7.2.2.

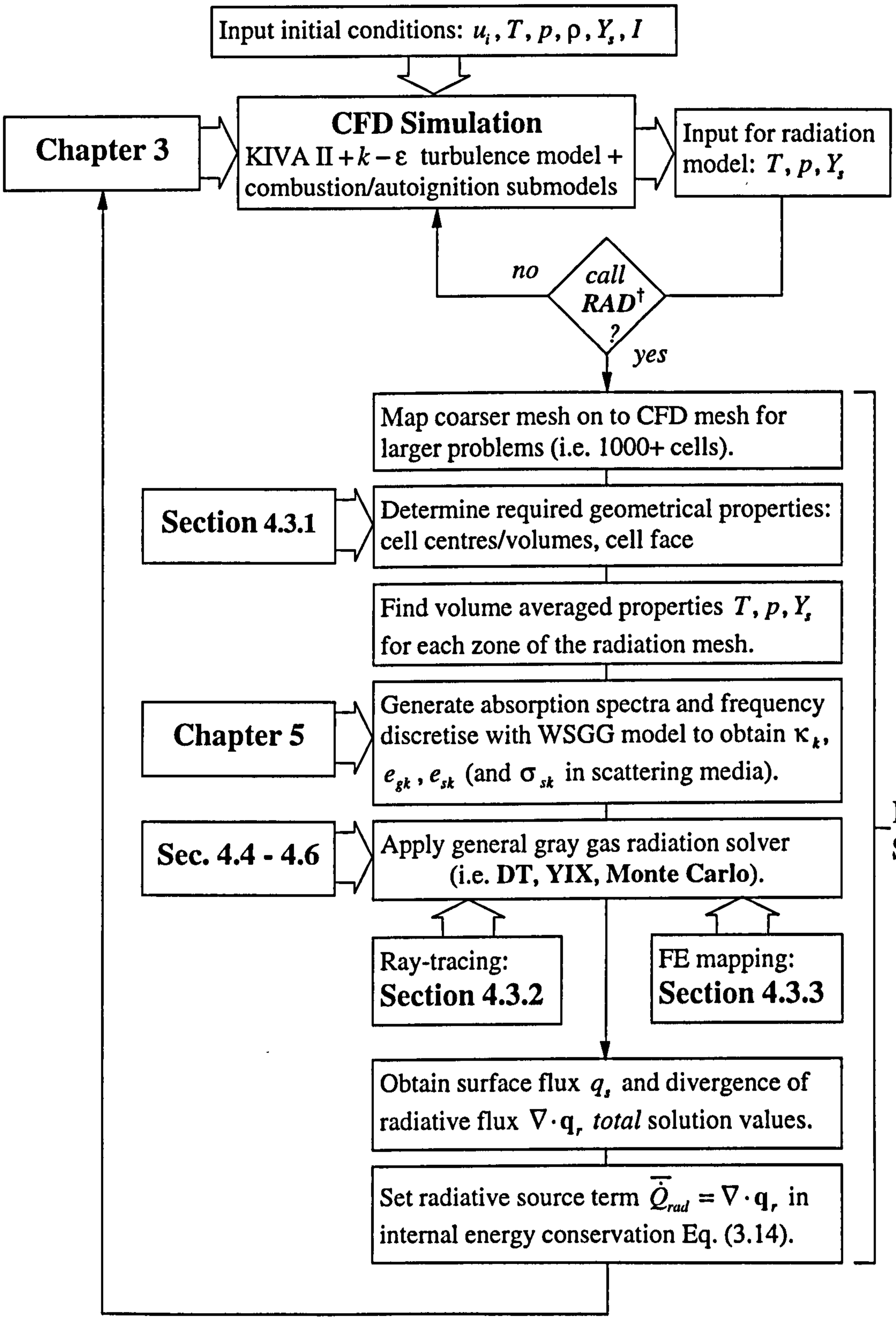

Figure 5.7 Coupling of the radiation and CFD codes via the radiative source term $\overline{\dot{Q}}_{rad}$ in the internal energy conservation equation. Relevant thesis chapters and sections are indicated. †Conditions to determine when radiation model is called are discussed in Sec. 5.5.

5.6 Summary

1. Radiative properties of realistic gaseous participating media are a complex function of wavelength, temperature, pressure, composition and radiation path length. A hierarchy of gas property models have evolved to describe this dependence for differing levels of spectral resolution and computation.

2. Classical (band) models return a spectrally averaged band transmissivity for a specified path length. The radiative transport equation must then be cast in a form in which the gas transmissivity is the fundamental radiative property.

3. A new generalised weighted-sum-of-gray-gases (WSGG) model is used in this work in which the local absorption coefficient is specified as the basic radiative property. Then an arbitrary solution method for radiation transport in complex participating media can be used *directly*.

4. The generalised WSGG model effectively replaces a spectral integration over wave-number with an integration over absorption coefficient. The entire absorption domain is discretised into N discrete levels of absorption coefficient, κ_k, with associated blackbody emissive powers, e_{gk} ($k = 1,2,\ldots,N$). These values vary spatially about a reference state according to local temperature, pressure and gas composition. A limitation of the model is that scattering properties must be taken as constant (gray) over the wavenumber range of interest.

5. A combined narrow- and wide-band model is used to compute the spectral variation in absorption coefficient as input to the WSGG model. (Line-by-line models of high-temperature, high-resolution spectral measurements may be used for greater accuracy.)

Thus, the simulation of radiation in combustion systems (i.e. engines) requires three levels of delineation to (a) compute the spectral absorption; (b) rationalise it into gray gases and (c) find a global coupled flow-radiation solution (with the radiation model combining the radiation transport from independent gray gas solutions).

Chapter 6

Results and Discussion

The radiative heat transfer models described in Chapters 4 and 5 are first verified in isolation from other modes of heat transfer. These studies are presented in Part A. Problems involving purely radiating media were chosen in order to identify strengths and weaknesses in each of the present methods. Subsequently, in Part B, the combined mode heat transfer in SI engine geometries is simulated by coupling the CFD solver described in Chapter 3 with the discrete transfer radiation model. Where possible past and present data is used to validate these engine predictions, but were no data was available, numerical results are presented for demonstration and comparison only.

PART A: PURE RADIATIVE HEAT TRANSFER STUDIES

The radiation models are applied to a series of benchmarks and new problems of increasing complexity. Here, the 'complexity' is measured by the number of difficult aspects (from a modelling perspective) present in a given problem. Table 6.1 demonstrates how several important benchmarks may be rationalised on this basis. The ability of a radiation method to handle each of these difficulties provides a good basis from which to assess its performance.

Twenty case studies are presented below (Cases A–E9). Performance data for each of these is summarised in Tables 6.2 and 6.14. The comparative performance of methods is of more importance here than the actual solution itself, and since solution differences are usually too small to be resolved graphically a tabular format is often used. The estimated error $S_n(\bar{x})$ is quoted with present Monte Carlo solutions as defined in Sec. 4.4.3. Discrete transfer calculations used 400 rays/subsurface, and YIX calculations used an S_{16} angular quadrature and first integration point of $\tau_1 = 0.001$, except where otherwise stated. Finally, the surface flux values q_s in all tables, except Tables 6.10–12, should strictly be *negative* (to indicate an *outgoing* net flux) but to simplify presentation positive numbers are shown.

Table 6.1 Important Benchmarking Studies Of Participating Media.

Reference:		1	2	3	4	5†	6†	7†	8†	9‡	10‡
Nonorthogonal geometry (or mesh)			✓	✓							✓
Nonuniform absorption:	$\kappa = f(x, y, z)$				✓	✓	✓	✓	✓	✓	✓
Nonuniform temperature:	$e_g = f(x, y, z)$	✓	✓	✓			✓	✓	✓	✓	✓
Isotropic scattering:	$\sigma_s \neq 0 \;\; g = 0$				✓	✓	✓	✓	✓	✓	✓
Anisotropic scattering:	$\sigma_s \neq 0 \;\; g \neq 0$				✓		✓	✓	✓	✓	✓
Hot boundaries:	$e_s \neq 0$	✓	✓	✓	✓						
Nonblack boundaries:	$\varepsilon < 1$						✓	✓	✓	✓	✓
Nongray properties:	$\kappa = f(\eta)$					✓	✓	✓	✓	✓	✓
Radiation combined with conduction										✓	✓

†Problems taken from 1992 ASME Symposium benchmarks.
‡New L-shaped problems proposed informally at 1996 ASME Symposium.

1. Selcuk, N. and Kayakol, N. (1997). Evaluation of Discrete Ordinates Method for Radiative Transfer in Rectangular Furnaces. *International Journal of Heat and Mass Transfer*, vol. 40, no. 2, pp. 213-222. (Includes discrete transfer solutions.)
2. Chui, E. H., Hughes, P. M. and Raithby (1993). Implementation of the Finite Volume Method for Calculating Radiative Transfer in a Pulverized Fuel Flame. *Combustion Science and Technology*, vol. 92, pp. 225-242.
3. Malalasekera, W. M. G. and James, E. H. (1995). Calculation of Radiative Heat Transfer in Three-Dimensional Complex Geometries. In *1995 National Heat Transfer Conference - Vol. 13*, HTD-vol. 315, ASME, pp. 53-61.
4. Hsu, P. and Farmer, J. T. (1995). Benchmark Solutions of Radiative Heat Transfer within Nonhomogeneous Participating Media using the Monte Carlo and YIX Methods. In *1995 National Heat Transfer Conference - Vol. 13*, HTD-vol. 315, ASME, pp. 29-36.
   Revised (condensed) version: *Journal of Heat Transfer*, vol. 119, pp. 185-188, 1997.
5. Burns, S. P., Howell, J. R. and Klein, D. E. (1995). Finite Element Solution for Radiative Heat Transfer with Nongray, Nonhomogeneous Radiative Properties. In *1995 National Heat Transfer Conference - Vol. 13*, HTD-vol. 315, ASME, pp. 3-10.
6. Hsu, P., Tan, Z. and Howell, J. R. (1993). Radiative Transfer by the YIX Method in Nonhomogeneous, Scattering and Nongray Media. *Journal of Thermophysics and Heat Transfer*, vol. 7, no. 3, pp. 487-495.
7. Farmer, J. T. and Howell, J. R. (1994). Monte Carlo Prediction of Radiative Heat Transfer in Inhomogeneous, Anisotropic, Nongray Media. *Journal of Thermophysics and Heat Transfer*, vol. 8, no. 1, pp. 133-139.
8. Maltby, J. D. (1994). Evaluation of Property-Induced Uncertainty in a Monte Carlo Simulation of Radiative Heat Transfer in a Participating Medium. In *Radiative Heat Transfer: Current Research*, HTD-vol. 276, ASME, pp. 161-170.
9. Hsu, P. and Tan, Z. (1996). The Radiative and Combined Mode Heat Transfer within the L-Shaped Nonhomogeneous and Nongray Participating Media. In *National Heat Transfer Conference - Vol. 3*, HTD-vol. 325, ASME, pp. 13-24.
10. Hoover, R. L., Li, W., Benmalek, A. and Tong, T. W. (1996). S_n Solutions for Radiative Heat Transfer in an L-Shaped Participating Medium. In *National Heat Transfer Conference, Vol. 3*, HTD-vol. 325, ASME, pp. 1-11. (Corrected solutions available.)

6.1 Nonhomogeneous Scattering Gray Media

6.1.1 Case A: Axially Fired Furnace of Rectangular Cross-Section

Problem Description. Selçuk (1985) proposed a benchmarking problem based on data taken in a large-scale experimental furnace. The physical situation was idealised as a rectangular box-shaped black walled enclosure filled with a nonscattering gray medium with uniform absorption/emission. However, some degree of realism was preserved by curve-fitting the actual experimental gas temperature distribution and by taking different surface temperatures for the refractory burner and back end walls, and the water-cooled side walls. The geometry and all necessary data for the problem is summarised in Fig. 6.1. The model parameters were chosen by normalising the experimental data with respect to a reference length of 0.48 m and a reference temperature of 1673 K. Given that there was no swirl in the experimental furnace Selçuk (1985) arranged that the gas temperature varied symmetrically about the burner axis and modelled 1/4 of the geometry with a 2×2×24 spatial discretisation. An analytical solution was then obtained with Gauss-Legendre numerical integration. Values were evaluated for both the volumetric heat source at the geometric centre of each cubic medium element and for the surface heat flux at the centre of each element face coincident with the furnace side walls. Recently, Selçuk and Kayakol (1997) published additional solutions using the discrete transfer method and an S_4 discrete ordinate approximation as part of an on going benchmarking exercise. Their S_4 approximation was found to require three orders of magnitude less computational time than a discrete transfer calculation with 64 rays per subsurface. Both methods showed inaccuracies but on the basis of computational efficiency it was concluded that the S_4 approximation is a better alternative.

Solution Comparisons. Discrete transfer, YIX and Monte Carlo solutions from the present methods are tabulated alongside the analytical solution of Selçuk (1985) in Tables 6.3 and 6.4. The discrete transfer and analytical results are also plotted in Fig. 6.2.

The variation in radiative heat flux, both in the medium and on the furnace side walls, is characterised by the nonuniform gas temperature distribution. As the axial gas temperature rises steeply from the burner wall (at z = -6), peaks, and then decreases smoothly towards the exhaust plane, so does the radiative flux. The only exception being in the corner regions where the gas temperature, and consequently the flux divergence, is almost uniform, i.e. the values at (0.75, 0.75, z) where $T_g^*(x,y,z) = T_e^*$.

A more interesting result is that the agreement between the discrete transfer and analytical solutions is much closer than that found by Selçuk and Kayakol (1997). An obvious explanation for this might be the finer angular discretisation used here, i.e. 400 rays per subsurface as opposed to 64. However, measures of deviation between the discrete transfer and analytical solutions did not significantly increase when a second calculation was made using only 64 angular divisions. Thus, it would seem that the poor performance demonstrated by Selçuk and Kayakol (1997) must be attributed to some other factor. It was noticed during the development of the present discrete transfer methodology that a biasing of the solution can arise if the rays traced in a particular (azimuthal) ordinate direction strike a boundary where the radiative properties are discontinuous (e.g. at a corner); essentially a severe case of ray effect. Ironically this situation tended only to manifest itself in benchmark problems where a regularly shaped geometry is specified with (unnaturally) discontinuous boundary conditions (e.g. hot/cold walls). Thus, a simple but effective remedy was introduced into the present code that re-orientates the solid angle hemisphere above a subsurface so that rays are never traced at azimuthal angles such as ±45° and ±135° which often result in corner intersections, particularly when the spatial discretisation results in cubic volume elements (as in the present case). Confirmation of this was obtained by removing this safeguard from the ray firing procedure: then the discrete transfer solution matched that found by Selçuk and Kayakol (1997).

Comparisons between the three present solution methods show good agreement: the average relative difference measures of the discrete transfer and YIX solutions with the Monte Carlo solution all falling within 2% (Table 6.2). It would be unrealistic to expect a closer level of agreement between the different formulations given the relatively coarse spatial discretisation. Though it is noteworthy that the discrete transfer and YIX methods give *identical* values for surface heat flux if the same angular quadrature scheme is used in both methods. This could be observed by interchanging the uniform angular discretisation of Shah (1979) with an S_n discrete ordinate set, or visa versa, in the appropriate method. However, the methodology used to evaluate the medium heat sources is fundamentally different such that the source values will always differ to some degree between the two deterministic methods for practical levels of discretisation. Consequently, in scattering media the surface heat flux values will also differ (even with identical angular quadrature schemes) due to their dependence on the medium heat sources.

Selçuk (1985) also evaluated the total rate of removal of radiative energy through the furnace walls and the total rate of generation of radiative energy within the enclosed medium using the analytical point values for the surface heat flux and medium heat source respectively. The rates of generation and removal correctly balanced at a normalised value of 1.424. Table 6.5 compares this analytical value against that obtained from the discrete transfer and S_4 solutions of Selçuk and Kayakol (1997) and the three present solutions. Encouragingly, the Monte Carlo result shows excellent agreement given that it is used to verify the deterministic methods in later benchmark problems. Small discrepancies between values for the discrete transfer and YIX results can be attributed to the coarse spatial discretisation used. This is confirmed by a reduction in both the energy imbalance, and deviation from the analytical result, for both methods after doubling the number of cells in each coordinate direction. However, the S_4 prediction would seem to provide the best performance of the three deterministic methods, though the formulation presented by Selçuk and Kayakol (1997) is limited to orthogonal geometries. In fact it is important to note that in spite of the rather elaborate expressions for calculation of the gas temperature distribution, this benchmark is very forgiving in all other respects, i.e. the problem geometry is nicely regular and a coarse spatial discretisation is used, the medium is gray and nonscattering and there are no other modes of heat transfer other than radiation. Thus, these more difficult aspects are examined in following benchmarks.

6.1.2 Case B: Nonorthogonal Cylindrical Geometry

Problem Description. A cylindrical benchmark by Chui *et al.* (1993) is used to verify the present methods in a nonorthogonal geometry. The geometry is 6 m long and 2 m in diameter with black walls at 500 K. The medium is absorbing, emitting and nonscattering with a nonuniform absorption coefficient, κ. The medium temperature varies axially along the enclosure as shown in Fig. 6.3. Thus in many respects this benchmark closely resembles that in Case A, but with two added complications: (1) a nonorthogonal curvilinear mesh is used to discretise the circular cross-section, and (2) optically thin to thick conditions are considered by solving for three values of absorption coefficient, namely $\kappa = 0.1$, 1 and 10 m^{-1} (Cases B1, B2 and B3). For each absorption level Chui *et al.* (1993, Fig. 3) solved for the radiative flux at discrete locations along the lateral wall of the cylinder by direct numerical integration. This analytical solution was then used to verify a new finite volume formulation. It also serves as a good benchmark here.

Solution Comparisons. Discrete transfer, YIX and Monte Carlo solutions for the net surface flux along the lateral wall of the cylinder are tabulated in Table 6.6. (These values and the analytical ones of Chui *et al.* (1993) are practically indistinguishable when plotted.) Fig. 6.4 also plots the axial variation in flux divergence for the present methods at a medium location near the cylinder wall. A 5×5×18 spatial discretisation was used: body-fitted to the cross-section (as shown in Fig. 6.4) and uniform in the axial direction.

The surface heat flux values calculated by each method are in close agreement for all three values of absorption coefficient. This is further confirmed by the relative difference measures listed in Table 6.2 where deviations are typically less than 2%. However, the flux divergence solutions are of more concern. Though the agreement is good for the optically thin and moderately thick problems (i.e. $\kappa = 0.1$ and 1 m^{-1}), large discrepancies are observed in the optically thick limit (i.e. $\kappa = 10$ m^{-1}). In fact the maximum deviations between the Monte Carlo and deterministic solutions are in excess of 70% (Table 6.2). Closer examination of the results found that this poor result was in part due to very small divergence values. These occur in the central region where the medium is so optically thick that it effectively acts as a good radiative insulation. Then the statistical uncertainty in the Monte Carlo result often exceeds the magnitude of the deterministic value such that the relative difference measures for flux divergence do not give a fair indication of the level of agreement which is generally much better. This problem is further compounded by the large statistical uncertainties that arise in Monte Carlo simulations of optically thick media where massive, and often prohibitive levels, of computation are required to drive down the uncertainty sufficiently for valid comparisons. However, the divergence of radiative flux is very large at the boundaries as a result of the temperature jump from the hot medium to the relatively cold cylinder walls. A point-to-point comparison of these values finds that the discrete transfer prediction always exceeds that of the YIX method, with the Monte Carlo solution tending to fall between the two. This result cannot be generalised as applying to all points in the medium, but what is important here is that the discrete transfer divergence solution is *consistently* higher than the YIX solution in the medium elements next to the boundary. This is indicative of fundamental differences in the source calculation of the two deterministic methods. Further evidence of this is provided by the overall heat balance, as tabulated for each method at the bottom of Table 6.6. This shows that while all three methods agree to within 1% for the net heat loss through the walls, the YIX methods predicts a markedly lower value for the total medium

heat source Q_g giving rise to a heat *im*balance of 57%. In contrast, the radiative heat balance is correct for the discrete transfer and Monte Carlo methods, so it would seem reasonable to suppose that the YIX source calculation is in error. However, the following example demonstrates that this is not necessarily true and explains the discrepancies observed above.

Consider the discrete transfer and YIX methods applied to a single cubic region enclosing a nonscattering optically thick participating medium with radiative properties $\kappa = 10$ and $e_g = 1.0$ (Fig. 6.5). The region has a side length of 1 m and it is arbitrary assumed to be enclosed by cold and black walls; though these could also be interfaces with other gas regions without significantly affecting the following argument. Simplification of the integral formulations in Sections 4.5 and 4.6 gives the incident (and net) surface heat flux at the centre of each face for both methods as:

$$q_s = \sum_{2\pi} \frac{1}{\pi}(1-e^{-\tau})\cos\theta \sin\theta \sin(\delta\theta)\delta\phi = 0.9983 \tag{6.1}$$

and the divergence of radiative heat flux at the centre of the region as:

DT:
$$\nabla \cdot \mathbf{q}_r = \iint_S q_s \, dA = 6 \times q_s = 5.9898 \tag{6.2}$$

YIX:
$$\nabla \cdot \mathbf{q}_r = 10\left[4 - \sum_{4\pi} \frac{1}{\pi}(1-e^{-\tau})\sin\theta \sin(\delta\theta)\delta\phi\right] = 0.1188 \tag{6.3}$$

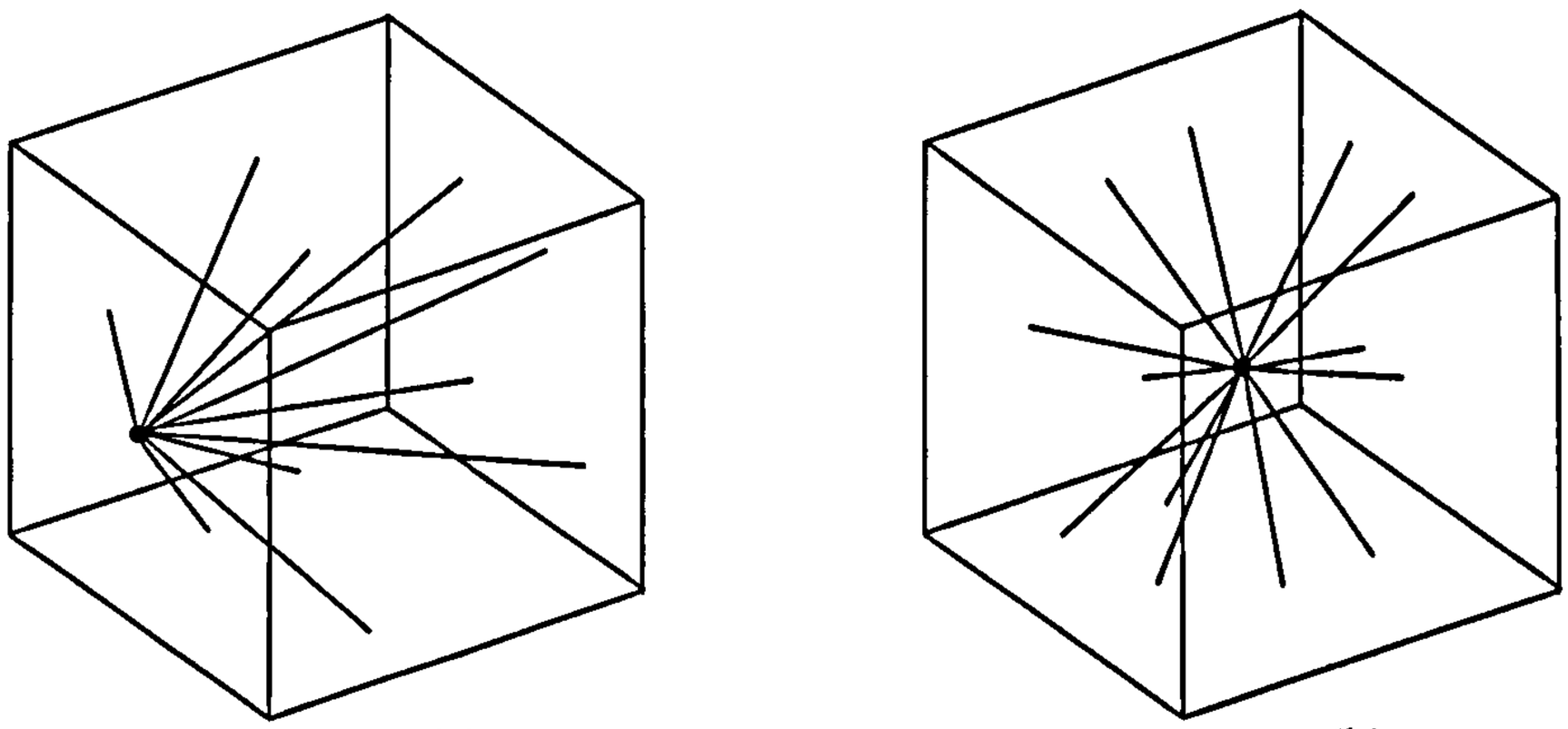

Figure 6.5 Representative ray paths in the discrete transfer and YIX solutions showing (a) integration at a face centre [Eq. (6.1)] and (b) integration at the region centre [Eq. (6.3)].

where an S_{16} discrete ordinate angular quadrature is used in both formulations. As observed with the optically thick cylindrical benchmark problem, the discrete transfer method gives a energy balance over the volume ($6 \times 0.9983 = 5.9898 \times 1$), but the net generation of radiative energy (= 0.1188) predicted by the YIX source calculation is much lower. However, solving Eq. (6.1) at locations other than the face centre gives:

Edge midpoint: $q_s(-0.5, 0, -0.4995) = 0.5090$

Corner: $q_s(-0.5, -0.4995, -0.4995) = 0.2622$

with the region centred on the coordinate origin. Thus, the value of 0.9983 at the face centre is in fact a maximum and a more representative value for the surface flux on each face lies somewhere between 0.9983 and the corner minimum of 0.2622. Integrating over a million surface elements gives this value as 0.9179. Similarly, solving Eq. (6.3) in the medium at various locations gives:

Near face centre: $\nabla \cdot \mathbf{q}_r(-0.4995, 0, 0) = 19.71$

Near edge midpoint: $\nabla \cdot \mathbf{q}_r(-0.4995, -0.4995, 0) = 29.59$

Near corner: $\nabla \cdot \mathbf{q}_r(-0.4995, -0.4995, -0.4995) = 34.59$

such that the YIX value at the region centre is in fact a minimum and a more representative value for the flux divergence over the entire region lies somewhere between 0.1188 and 34.59. Integrating over several million volume elements gives this value as 5.497. This gives a correct energy balances as $6 \times 0.9179 \approx 5.497 \times 1$. The following conclusions can drawn:

- The YIX method gives an accurate *point* solution for the divergence of radiative heat flux in the medium, but this value does *not* satisfy a total energy balance when applied over an element where the local radiative properties give rise to steep gradients in the divergence. In contrast, the discrete transfer method makes an energy balance over the medium element but the cell divergence value (found by back-calculation) may *differ* significantly from the point solution at the element centre.

- The discrete transfer and YIX methods both under- or over-predicted the surface heat flux through a boundary element by a margin that depends on the magnitude and direction of the local flux gradients across the surface.

Consequently, in the optically thick benchmark where the cell optical depths are as high as 4, neither method gives a truly accurate solution for the radiative heat flux (at the cylinder walls). The Monte Carlo method is the only method of the present three capable of this since it statistically averages conditions over the entire medium. Though it can be argued that the deterministic solutions should ultimately converge to that of the Monte Carlo method if the element size, and hence cell optical depths are reduced, it is often found that computational limitations do not allow this. Then some accuracy must be compromised. Given that the main objective here is to include the radiation method into a flow finite volume code, the discrete transfer method gives, on balance, a closer approximation. However, other aspects of complex media are still to be considered.

6.1.3 Case C: Cubic Benchmarking Media with Nonhomogeneous Extinction, a Hot Emitting Wall and Anisotropic Scattering

Problem Description. Hsu and Farmer (1995, 1997) posed and solved a series of benchmark problems using the Monte Carlo and YIX methods. Further numerical comparisons with a finite element formulation have also been published by Burns *et al.* (1995). The geometry in all problems is a unit cube with black and diffuse walls. This encloses various participating media for which the extinction coefficient varies according to the relation:

$$\beta(x, y, z) = a(1-2|x|)(1-2|y|)(1-2|z|)+b \qquad [1/\mathrm{m}] \tag{6.4}$$

where the coordinate origin lies at the cube centre and $-0.5 \le (x, y, z) \le 0.5$ is the domain of computation. The optical thickness distribution is varied with parameters a and b, such that the extinction decreases linearly from a to b between the centre and the walls. Nonscattering and scattering media are considered: the latter including the effects of anisotropy. These problems are fully specified in Fig. 6.6. In cases C1 and C2 the medium has unity blackbody emissive power and results are sought for the surface heat flux and divergence of radiative heat flux. Whereas, cases C3, C4 and C5 are solved for radiative equilibrium (i.e. zero flux divergence) such that the medium emissive power distribution is then the unknown, together with the surface flux. Case C1 is primarily intended to assess the accuracy in modelling the nonhomogeneous radiative property distribution: the medium is purely absorbing. The problem complexity is then incrementally increased by introducing first isotropic (case C2) and then linear anisotropically scattering conditions. In the latter cases both forward ($g = 1$) and

backward ($g=-1$) scattering phase functions are considered, and an asymmetry in the boundary conditions (one hot wall) is used to enhance their effect. For all scattering media a large single scattering albedo of $\omega=0.9$ is chosen. Finally, the optical thickness is increased in case C5, via the extinction parameters a and b, in order to assess its effect on performance.

Solutions were obtained by discretising the geometry into a 9×9×9 orthogonal mesh of cubic volume elements, each with a side length of 1/9. The element centres are located symmetrically about the coordinate axes at $(x, y, z)=(0,\pm 1/9,\pm 2/9,\pm 3/9,\pm 4/9)$. The only exception is case C5 where the YIX computation uses a finer 27×27×27 cubic mesh and a first integration point of 0.01 (as opposed to 0.001) in the distance quadrature. These changes were made to ensure compatibility with the E7 YIX solution obtained by Hsu and Farmer (1995). Finally, additional discrete transfer and YIX solutions were obtained for case C1 using the 27×27×27 mesh in order to assess grid dependency effects. For each problem the extinction coefficient was evaluated from Eq. (6.4) at the centre of each medium element and presumed constant over the surrounding volume.

Solution Comparisons. Tables 6.7 to 6.12 compare results from the three present methods with published solutions (Hsu and Farmer 1995; Burns *et al.* 1995). The zonal Monte Carlo algorithm was used for all problems. There are no discrete transfer solutions for cases C3, C4 and C5 since the method is unable to handle scattering anisotropy.

The present results for cases C1 and C2 are in excellent agreement with each other – average deviations are less than 1% in both surface flux and flux divergence (Table 6.2) – and with the published YIX and Monte Carlo solutions. Deviations between the finite element results and those from the three other methods (present and published) are slightly larger. In contrast to the discrete transfer, YIX and Monte Carlo methods which all approximate the extinction distribution in a stepwise manner, shape functions in the finite element method afford a much better description. Therefore, solutions from the present methods would be expected to converge towards the finite element result with a finer spatial discretisation. This was verified by computing a second set of discrete transfer and YIX solutions over a 27×27×27 mesh. The new surface heat flux and flux divergence solutions showed, on the whole, much closer agreement to the finite element result. Table 6.8 records the improvement in surface flux.

The present YIX and Monte Carlo solutions to cases C3, C4 and C5 are in good agreement with the benchmark values obtained by Hsu and Farmer (1995). Moreover, their finding that average differences for both surface heat flux and emissive power are around 6% in cases C3 and C4, but smaller in case C5, is also observed here (Table 6.2). This is perhaps of more importance than the solutions themselves, since it confirms that the coding complexities associated with the scattering anisotropy and asymmetric boundary conditions are working correctly. Nevertheless, it is important to establish why deviations between the YIX and Monte Carlo solutions are larger here as compared with cases C1 and C2. A contour plot of the emissive power distribution reveals irregularities in the YIX solution in medium elements distant from the hot wall at $x = -0.5$ (Figs. 6.7 and 6.8). These occur irrespective of the scattering direction. When the medium extinction is increased in case C5 a smoother emissive power distribution results (Fig. 6.9). Hsu and Farmer (1995) concluded, as here, that this can be attributed to ray effect in the YIX method arising from the asymmetric hot/cold boundary conditions. Accuracy can only be improved by using a higher order S_n angular quadrature. The increased medium extinction in case C5 prevents radiation from the hot wall propagating deep into the interior and as a result the ray effect is mitigated.

6.1.4 Case D: Nonorthogonal, Nonhomogeneous L-shaped Geometry

Problem Description. Two new benchmarking media are considered which seek to combine several aspects studied so far in isolation: a nonorthogonal mesh, a nonhomogeneous property distribution and particle scattering. An L-shaped geometry was chosen as shown in Fig. 6.10. The regular grid on the side walls enables surface flux comparisons without interpolation and the shadowing effect of the bend poses a more interesting problem. The extinction coefficient varies according to:

$$x \le -y: \quad \beta(x,y,z) = 0.9(1.5+x)(1-2|y|)(1-2|z|)/(1.5-y)+0.1 \quad [1/\mathrm{m}]$$

$$x > -y: \quad \beta(x,y,z) = 0.9(1-2|x|)(2.5-y)(1-2|z|)/(2.5+x)+0.1 \quad [1/\mathrm{m}] \quad (6.5)$$

where the coordinate origin lies at the centre of the corner diagonal. The walls are black and diffuse. Case D1 has a blackbody emissive power of 0.25 on the surface and unity in the medium. Results are sought for the surface heat flux and divergence of radiative heat flux when the scattering albedo is $\omega = 0.9$. In contrast, case D2 has a prescribed volumetric heat source such that the variation in medium emissive power and surface flux

is required. The L-shape is divided into two volumes by a z–plane through the corner diagonal (i.e. at $x = -y$). There is a uniform radiative heat source (divergence) of 1 W/m^3 in the smaller volume and 0.5 W/m^3 in the larger volume. The walls are cold and the scattering albedo is arbitrary chosen as $\omega = 0.5$. It is worth noting that this choice affects only the emissive power distribution, since the surface heat flux is independent of the albedo value in isotropically scattering media. Half the geometry is discretised with a 20×7×4 body-fitted mesh: a symmetry plane is at $z = 0$. The extinction coefficient was evaluated from Eq. (6.5) at the centre of each medium element and presumed constant over the surrounding volume.

Solution Comparisons. Table 6.13 compares sample surface heat flux values for each of the three present methods along the face centrelines (-1.5, y, 0) and (-0.5, y, 0). Contours at $z = 0$ for the flux divergence in D1 and the emissive power in D2 are also plotted in Fig. 6.11. Only one set of plots is reproduced from the three methods since differences between values are indistinguishable when displayed graphically. Typically deviations of only 0.5% occur in the media (Table 6.2). The contour plots clearly reveal the strong influence of the extinction distribution. Fig. 6.11(a) has a high radiative source in the optically thick central region which then decreases towards the walls as the medium becomes thinner. The gradients are reversed in Fig. 6.11(b) with a cold dense central region surrounded by hotter gas near the walls. In addition, the contours are strongly asymmetric as a result of the abrupt discontinuity in source values across the corner diagonal. All the methods capture this feature reasonably well in spite of the rather coarse spatial discretisation. Finally, note that the wiggles in the contours arise from the graphical interpolation and are *not* present in the numerical solutions.

6.1.5 Run Times and Memory Requirements

The preceding discussion has largely focused on solution accuracy but greater disparity is seen between the methods when assessed in terms of their computational economy. A trade-off invariably exists between the computing time and memory requirements: here 'memory' is taken to include both information held in RAM and any temporary data files stored on disk. The discrete transfer, YIX and (zonal) Monte Carlo methods can store path length/exchange area data so as to avoid re-tracing a geometry when an iterative solution is required. Disk storage must be used if a machine does not have sufficient capacity to hold all of this information in RAM, for a given method and problem size.

Then the additional overhead resulting from the disk writing/reading operations may considerably extend the total solution time = processor time + communication time. Disk swapping operations associated with virtual RAM can also greatly increase total solution times, though usually to a lesser degree.

The problem run times are reported in Table 6.2. The discrete transfer, YIX and Monte Carlo methods were all executed on HP9000/750 workstations running HP-UX 9.01. Identical FORTRAN/9000 compiler options (f77 +O3) were used. With these options the HP9000/750 has a LINPACK benchmark rating of 22 Mflops in double-precision operations on 100×100 matrices. (The LINPACK benchmarks are a standard suite of programs devised to determine a computer's numerical computing capacity, measured in millions of floating-point operations per second (Mflops), see Dongarra (1998) for more information.) Each workstations had 64 Mbytes of RAM. This was sufficient for all the problems, except for the YIX solution of case C5 which required 470 Mbytes of space. Though disk storage could have been used on the HP9000/750, it was more convenient for timing purposes to solve the entire problem in memory on a Sun Ultra Enterprise II workstation with 512 Mbytes of RAM. The Sun time was then factored by 1/1.5 to obtain the equivalent HP 750 processing time in Table 6.2, i.e. the Sun was approximately 1.5 times faster. It should also be noted that the Monte Carlo times in Table 6.2 represent the *total* solution time required to obtain the quoted uncertainties in the results. Therefore, the time of each independent simulation is $1/N$ of this value, where N is the number of simulations.

The times reported for each solution arise from a combination of factors. These are:

- **Discretisation Level.** Consideration is first given to the two deterministic methods. It is of note that while the discrete transfer and YIX times for cases A and B1 are comparable, the YIX method takes 1.6 times longer for case C1, despite all three media having similar radiative properties and the solutions being non-iterative. Evaluating the number of rays that must be traced for each solution finds that this arises from the effect of the spatial (and angular) discretisation on the tracing times in each method. The discrete transfer solutions use 400 rays/surface hemi-spherical solid angle (and none from volume elements), whereas the S_{16} YIX angular quadrature gives 144 rays/surface and 288 rays/volume. Case A has 104 active surface elements (i.e. excluding those on symmetry boundaries) and 96 volume elements. Therefore, the

discrete transfer and YIX methods trace 41600 and 42624 rays, respectively. This ratio is close to unity, as is the problem time ratio (i.e. 6:7), given that the times are scaled to the nearest second. A similar result follows for case B1. However, the cubic geometry of C1 has 486 surface elements and 729 volume elements. Consequently, 194400 rays are traced in the discrete transfer solution compared with 279936 rays in the YIX solution and the run times scale accordingly. Thus, in general it is found that YIX run times increase at a significantly greater rate than those of the discrete transfer method with increased mesh size. This rate depends on the efficiency of the ray tracing algorithm, and varies as the ratio of volume elements to surface elements.

The Monte Carlo run times vary in direct proportion to the total number of bundles traced. This value is analogous to the number of rays in deterministic solutions; i.e. it embodies both the spatial and angular discretisation. Though, it is worth emphasising that the times depend only indirectly on the level of spatial discretisation for a given problem. This is because the number of bundles launched from each element is determined from its surface or energy density and is thus independent of its physical size (Sec. 4.4.2). However, the solution uncertainty increases when the mesh is refined because fewer bundles contribute to each solution result. Consequently, more bundles must be launched per unit of radiative energy density in order to maintain the same level of precision.

- **Optical Thickness.** Cases B1, B2 and B3 demonstrate the influence of increasing optical thickness (in nonscattering media). The discrete transfer run times are largely unaffected since the methodology is based on a spatial, rather than an optical, approximation. In contrast, the YIX solution times increase with optical thickness, as more integration points are required in the numerical evaluation of each distance integral (Sec 4.5.2). However, a coarser angular discretisation, particularly at the YIX medium points, might have sufficed in the optically thicker media, though this was not assessed.

The performance of the Monte Carlo method deteriorates rapidly with optical thickness. As the medium absorption increases the energy bundles travel over shorter distances and contribute to fewer results. Therefore, almost 10 times as many bundles had to be traced for case B3 compared to that of B1 in order to drive down the solution

uncertainties, though the corresponding increase in run time is somewhat less (i.e. about 5.5 times longer) due to the shorter life of each bundle. Farmer (1995, Sec. 5.1.1) discusses two possible hybrids of the present approach to improve performance in optically thick media.

- **Isotropic Scattering**. Case C1 is a purely absorbing and emitting medium. The effect of imposing a non-zero scattering albedo in C2 is to increase both the discrete transfer and YIX solution times since then several iterations are required to establish the incident radiation w_0 from in-scattering. However, it is noticed that the discrete transfer method takes significantly longer than the YIX method to converge after the initial tracing period. This is largely attributed to economies afforded by the YIX distance quadrature which not only eliminates the numerous exponential kernel evaluations on each iteration but also has a much smaller memory requirement. All the path information is stored entirely in 2 byte integer form for the YIX quadrature, whereas that of the discrete transfer method uses an 8 byte real representation. The end result of this is that the present YIX solutions take about half the storage space of discrete transfer solutions, e.g. for C2 the requirements were 10.98 Mbytes and 22.07 Mbytes respectively. This is likely to be a critical factor when the problem size exceeds the machine capacity. Then the read/write time associated with the path information is expected to give the YIX method a significant performance advantage. In addition, more time is likely to be spent in the iterative phase than in the initial tracing phase, as larger problems generally take more iterations to converge.

In marked contrast, Monte Carlo solution times decrease with increased scattering albedo because scattering tends to spread out the bundle paths improving uniformity and reducing the statistical uncertainty. Another effect of setting the scattering albedo equal to 0.9 in C2 is to lower the medium absorption coefficients by an order of magnitude from that in C1, as both media have the same extinction distribution. This in turn extends the life and distance travelled by the energy bundles such that they pass through more volume elements and contribute to more results, again reducing the uncertainty. Consequently, an order of magnitude less bundles are required in C2 compared with C1, though the drop in run time is not quite as great due to the extended bundle life.

- **Anisotropic Scattering**. Cases C3 and C4 have the same medium extinction distribution and scattering albedo as C2, but with strong forward and backward linear anisotropically scattering phase functions, respectively. However, this additional complexity adds only 14% to the YIX run time: the extra integrals associated with the anisotropy are obtained directly from those for the irradiation (Sec. 4.5.2). Conversely, the Monte Carlo run time is increased dramatically as more bundles are required to capture the scattering anisotropy. However, two factors complicate the time comparison with C2. First, the solution in case C2 was found directly for the prescribed emissive power without iteration, whereas C3 and C4 are solved for radiative equilibrium. Hence, it was necessary to use a hybrid Monte Carlo/zonal approach (Sec. 4.4.4) to iteratively satisfy this condition, though the iterative phase represented only a small part of the total solution time. Second, energy bundles were launched from *all* the walls during the exchange area computation, despite surface flux values being compared for only the hot wall.

- **Symmetry**. All three methods simulate planes of symmetry as adiabatic specularly mirrored surfaces. Advantage is taken of the symmetry in cases A and D to reduce the solution times by a quarter and a half, respectively. (N.B. This option was unavailable at the time cases B and C were solved though these also contain symmetry planes.)

Particular care should be exercised with the YIX method for anisotropically scattering media. The surface flux and flux divergence solutions for cases C3, C4 and C5 have symmetry about the planes $y = 0$ and $z = 0$ so it would seem viable to simulate them as mirrored surfaces. However, the linear anisotropic scattering phase function requires the calculation of the flux components w_i [see Eq. 4.23] and it is found that one component differs in sign across each plane, i.e. w_2 across $y = 0$ and w_3 across $z = 0$. Therefore, symmetry cannot be used unless some means is devised to record the sign of w_i each time a ray is reflected.

In light of the above comments it is possible to predict the run time and storage requirements of most problems by allowing for the different factors involved.

Table 6.2 Comparison of CPU run-times and relative differences for gray benchmark problems A – D
The number of simulations and total number energy bundles are also given for each Monte Carlo (MC) solution.

	Mesh size	CPU run time on HP-9000/750 [s]			Monte Carlo simulations		Average relative difference[b] [%]				Maximum relative difference[b] [%]			
							q_s		$\nabla \cdot \mathbf{q}_r$ or e_{bg}		q_s		$\nabla \cdot \mathbf{q}_r$ or e_{bg}	
Case	[cells]	DT	YIX	MC	bundles[a]	N	DT	YIX	DT	YIX	DT	YIX	DT	YIX
A	96	6	7	1317	7.00×10^6	10	1.42	2.04	1.38	0.72	6.15	7.77	6.78	1.82
B1	450	23	22	6471	3.00×10^7	10	0.92	1.02	1.39	0.31	6.11	11.43	4.75	1.84
B2	450	23	33	14768	7.80×10^7	10	0.98	0.72	1.50	3.81	3.20	4.93	7.63	8.59
B3	450	23	34	35447	2.83×10^8	10	1.14	1.04	4.48	63.13	8.00	7.92	71.89	86.63
C1	729	50	80	24621	9.95×10^7	30	0.64	0.78	0.66	0.09	2.33	3.07	1.45	1.02
C2	729	79	91	2943	1.06×10^7	30	0.51	0.87	0.08	0.01	2.02	2.81	0.18	0.11
C3	729	-	104	58973	1.93×10^8	10	-	6.18	-	5.73	-	37.96	-	37.46
C4	729	-	104	58973	1.93×10^8	10	-	5.94	-	5.94	-	15.01	-	43.11
C5	19683	-	8109[c]	681059[d]	1.12×10^9	10	-	2.52	-	1.72	-	10.62	-	6.80
D1	560	60	58	1246	8.67×10^6	10	1.04	1.68	0.13	0.04	8.59	8.86	0.52	0.19
D2	560	60	58	11480	8.61×10^7	10	1.14	1.37	0.50	0.09	8.98	7.68	3.56	0.46

[a]Monte Carlo *total* number of energy bundles = bundles/simulation × number of simulations (N).

[b]Average relative difference: $\text{ARD} = 1/n \sum |(\text{X} - \text{MC})/\text{MC}|$: Maximum relative difference: $\text{MRD} = MAX\,|(\text{X} - \text{MC})/\text{MC}|$
where X = DT (discrete transfer) or YIX for n values (i.e. N surfaces fluxes or K volumetric quantities).

[c]Estimated equivalent time on HP9000/750: YIX C5 run on a Sun workstation (in 5406 s) for its large 512 MB RAM capacity.

[d]Monte Carlo mesh size = 729 cells [9×9×9].

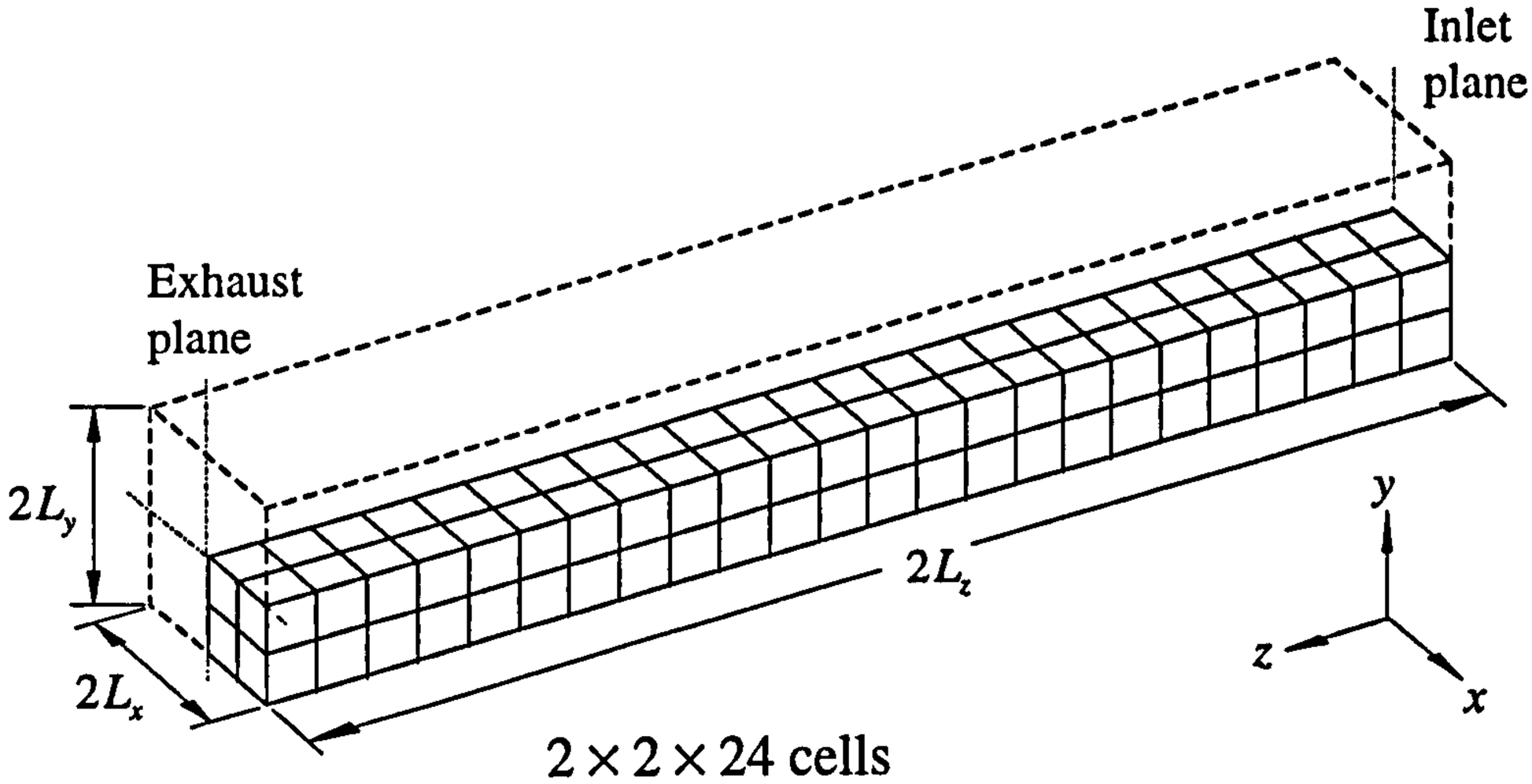

Gas temperature distribution: $T_g^*(x, y, z) = [a(z') - T_e^*] f(r/R) + T_e^*$

where the axial variation for $z' = z / L_z$ is:

$$a(z') = 1 + (1 - T_i^*)\left(\frac{z' + z'_{\max}}{1 - z'_{\max}}\right)^3, \qquad -1 \le z' \le -z'_{\max}$$

$$a(z') = 1 - [d_e(1 + z'_{\max}) + 3(1 - T_e^*)]\left(\frac{z' + z'_{\max}}{1 + z'_{\max}}\right)^2 + [d_e(1 + z'_{\max}) + 2(1 - T_e^*)]\left(\frac{z' + z'_{\max}}{1 + z'_{\max}}\right)^3, \qquad -z'_{\max} \le z' \le 1$$

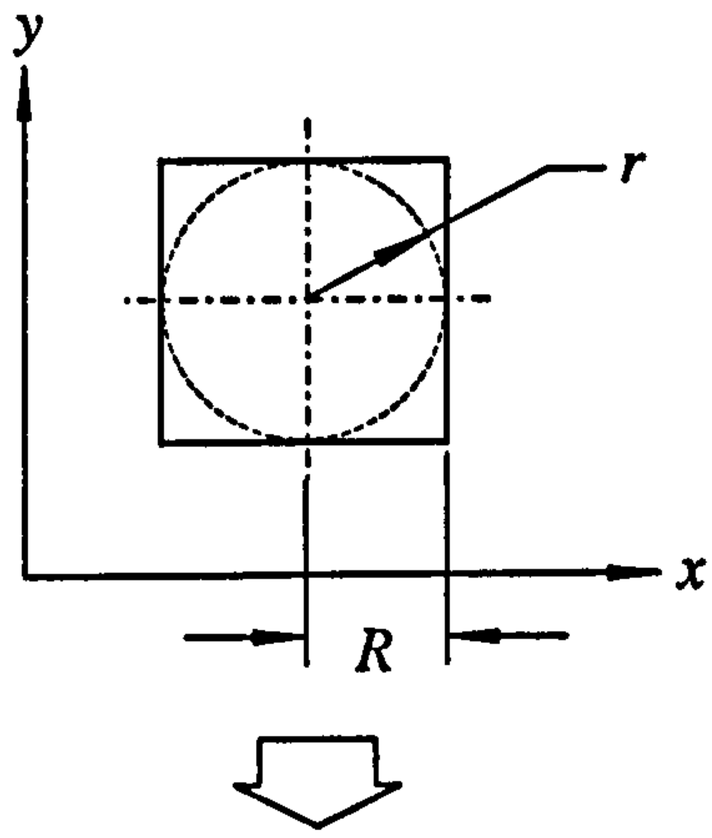

and the cross-sectional variation is:

$$f(r/R) = 1 - 3(r/R)^2 + 2(r/R)^3 \qquad r = (x^2 + y^2)^{1/2} \le R, \quad R = L_x = L_y$$

Dimensions of the furnace	$L_x^* = L_y^* = 1, L_z^* = 6$	* = dimensionless
Optical thickness	$\tau^* = 1/6$	
Wall black-body intensities	$i_{b,\text{burner}}^* = 0.0574$; $i_{b,\text{side}}^* = 0.0020$; $i_{b,\text{exit}}^* = 0.0167$	
Gas temperatures	$T_i^* = 0.1775$; $T_e^* = 0.6222$; $T_{\max}^* = 1$	
Position of peak temperature	$z'_{\max} = 0.8$	
Slope of gas temperature at exit	$d_e = -0.220$	

Reference values used to make the experimental data dimensionless:
$L_0 = 0.48$ m, $T_0 = 1673$ K, $i_{b0} = 1.4139 \times 10^5$ W m^{-2} sr^{-1}.

Figure 6.1 Case A: Axially fired furnace of square cross-section (Selçuk 1985).

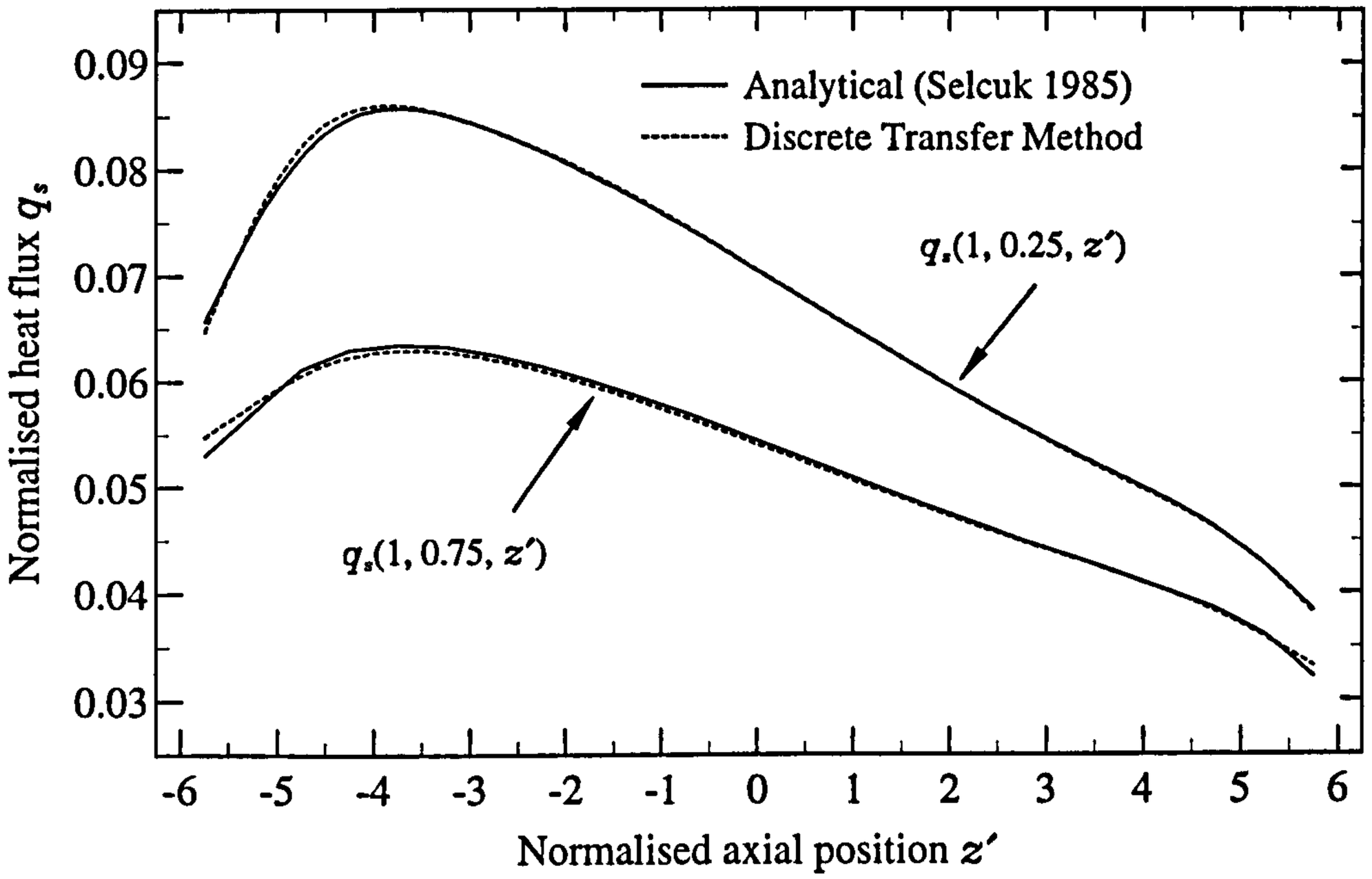

(a)

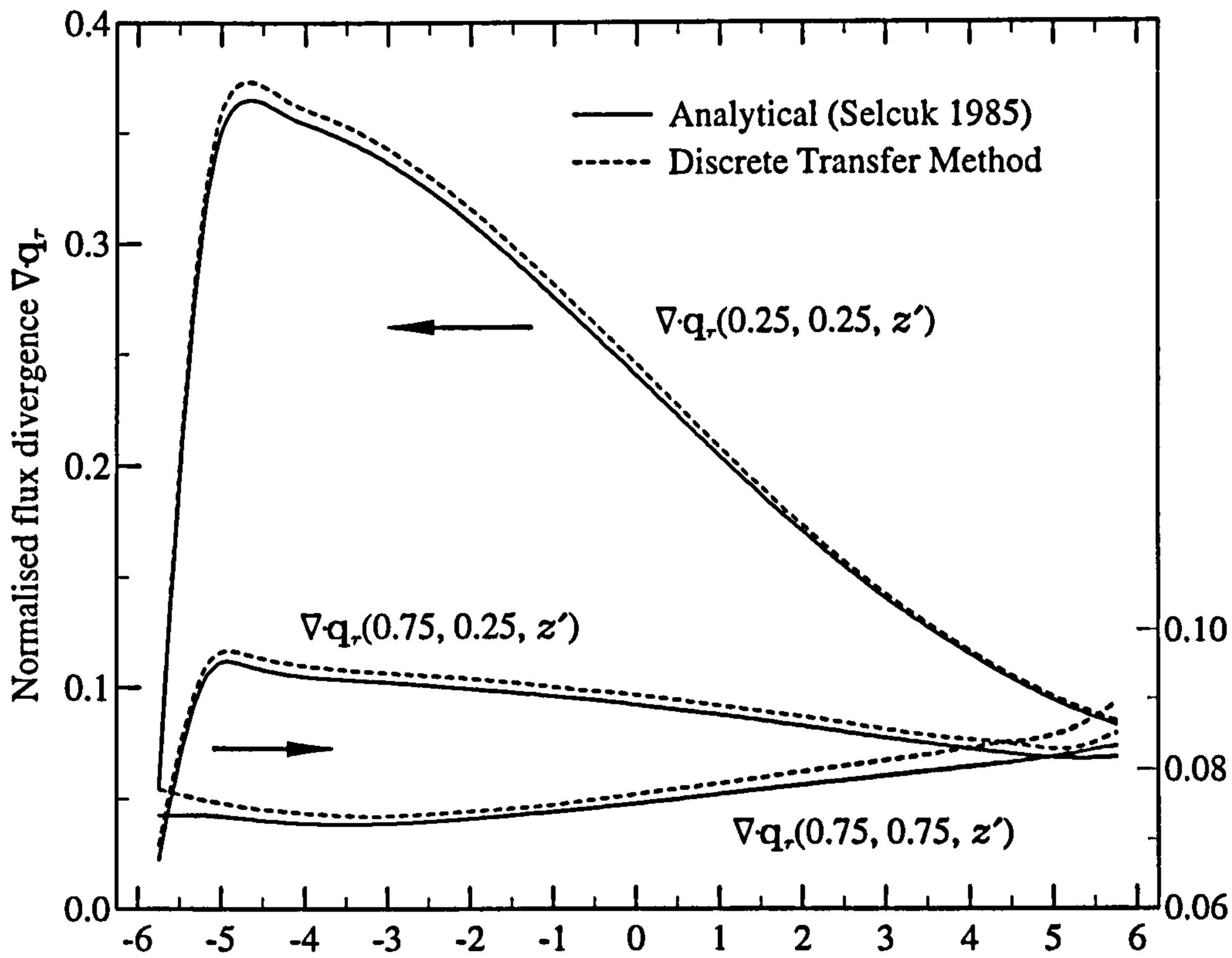

(b)

Figure 6.2 Case A: Comparison of the present discrete transfer prediction with an analytical solution by Selçuk (1985) for (a) the net radiative heat flux along the furnace side wall and (b) the radiative heat source distribution in the medium. (All values are normalised with respect to $L_0 = 0.48$ m, $e_{b0} = 4.4419 \times 10^5$ W/m^2).

Table 6.3 Surface heat flux for Case A: Axially fired rectangular furnace (Selcuk 1985).

	$q_s(1, 0.25, z)$					$q_s(1, 0.75, z)$				
z'	Analytical[a]	DT	YIX	MC	$S_n(\bar{x})$	Analytical[a]	DT	YIX	MC	$S_n(\bar{x})$
–5.75	0.0642	0.0634	0.0646	0.0641	0.0004	0.0530	0.0546	0.0545	0.0522	0.0004
–5.25	0.0753	0.0759	0.0780	0.0748	0.0002	0.0571	0.0571	0.0575	0.0563	0.0006
–4.75	0.0824	0.0834	0.0842	0.0810	0.0005	0.0611	0.0615	0.0607	0.0602	0.0004
–4.25	0.0850	0.0850	0.0862	0.0848	0.0005	0.0630	0.0627	0.0611	0.0628	0.0004
–3.75	0.0855	0.0860	0.0876	0.0849	0.0006	0.0635	0.0627	0.0617	0.0628	0.0004
–3.25	0.0848	0.0848	0.0864	0.0837	0.0003	0.0633	0.0627	0.0615	0.0623	0.0004
–2.75	0.0834	0.0835	0.0847	0.0828	0.0007	0.0625	0.0621	0.0608	0.0614	0.0005
–2.25	0.0816	0.0817	0.0830	0.0810	0.0005	0.0614	0.0609	0.0598	0.0606	0.0003
–1.75	0.0795	0.0798	0.0809	0.0785	0.0004	0.0601	0.0596	0.0586	0.0594	0.0005
–1.25	0.0771	0.0772	0.0782	0.0769	0.0003	0.0586	0.0582	0.0571	0.0576	0.0005
–0.75	0.0746	0.0747	0.0756	0.0732	0.0006	0.0570	0.0566	0.0556	0.0562	0.0005
–0.25	0.0719	0.0719	0.0727	0.0712	0.0003	0.0553	0.0549	0.0541	0.0538	0.0006
0.25	0.0691	0.0692	0.0699	0.0687	0.0006	0.0536	0.0532	0.0525	0.0527	0.0004
0.75	0.0663	0.0664	0.0671	0.0654	0.0006	0.0518	0.0515	0.0509	0.0500	0.0004
1.25	0.0636	0.0636	0.0642	0.0631	0.0004	0.0500	0.0498	0.0493	0.0490	0.0003
1.75	0.0609	0.0610	0.0614	0.0604	0.0003	0.0483	0.0481	0.0478	0.0473	0.0002
2.25	0.0583	0.0582	0.0587	0.0585	0.0004	0.0466	0.0464	0.0463	0.0460	0.0003
2.75	0.0557	0.0557	0.0560	0.0550	0.0004	0.0450	0.0449	0.0448	0.0440	0.0006
3.25	0.0533	0.0532	0.0535	0.0531	0.0004	0.0434	0.0433	0.0434	0.0427	0.0005
3.75	0.0510	0.0509	0.0511	0.0513	0.0003	0.0418	0.0417	0.0420	0.0409	0.0003
4.25	0.0487	0.0485	0.0485	0.0485	0.0003	0.0402	0.0401	0.0405	0.0391	0.0003
4.75	0.0463	0.0461	0.0462	0.0466	0.0005	0.0385	0.0386	0.0391	0.0379	0.0004
5.25	0.0433	0.0433	0.0434	0.0435	0.0004	0.0362	0.0362	0.0367	0.0349	0.0002
5.75	0.0378	0.0376	0.0385	0.0369	0.0002	0.0322	0.0328	0.0333	0.0309	0.0005

[a]Analytical benchmark result by Selcuk (1985). (All values normalised w.r.t. $e_{b0} = 4.4419 \times 10^5$ W/m^2.)

Table 6.4 Divergence of radiative heat flux for Case A: Axially fired rectangular furnace (Selcuk 1985).

	$\nabla \cdot \mathbf{q}_r(0.25, 0.25, z)$					$\nabla \cdot \mathbf{q}_r(0.75, 0.25, z)$					$\nabla \cdot \mathbf{q}_r(0.75, 0.75, z)$				
z'	Analytical[a]	DT	YIX	MC	$S_n(\bar{x})$	Analytical[a]	DT	YIX	MC	$S_n(\bar{x})$	Analytical[a]	DT	YIX	MC	$S_n(\bar{x})$
−5.75	0.0493	0.0505	0.0499	0.0492	0.0001	0.0667	0.0688	0.0668	0.0670	0.0001	0.0734	0.0775	0.0731	0.0740	0.0001
−5.25	0.3115	0.3193	0.3118	0.3147	0.0002	0.0930	0.0945	0.0925	0.0934	0.0001	0.0741	0.0760	0.0736	0.0745	0.0001
−4.75	0.3602	0.3686	0.3614	0.3641	0.0002	0.0948	0.0963	0.0944	0.0950	0.0001	0.0731	0.0748	0.0723	0.0734	0.0001
−4.25	0.3567	0.3636	0.3579	0.3608	0.0001	0.0939	0.0955	0.0937	0.0938	0.0001	0.0725	0.0743	0.0722	0.0727	0.0001
−3.75	0.3506	0.3573	0.3512	0.3543	0.0001	0.0933	0.0947	0.0935	0.0936	0.0001	0.0724	0.0737	0.0727	0.0727	0.0001
−3.25	0.3417	0.3481	0.3420	0.3453	0.0002	0.0929	0.0942	0.0931	0.0930	0.0001	0.0724	0.0734	0.0728	0.0726	0.0001
−2.75	0.3302	0.3362	0.3308	0.3335	0.0001	0.0925	0.0938	0.0926	0.0926	0.0001	0.0726	0.0737	0.0728	0.0729	0.0001
−2.25	0.3166	0.3227	0.3170	0.3198	0.0001	0.0920	0.0934	0.0920	0.0923	0.0001	0.0730	0.0740	0.0730	0.0732	0.0001
−1.75	0.3012	0.3071	0.3015	0.3044	0.0002	0.0915	0.0929	0.0916	0.0919	0.0001	0.0734	0.0745	0.0735	0.0737	0.0001
−1.25	0.2846	0.2903	0.2846	0.2875	0.0002	0.0910	0.0923	0.0910	0.0914	0.0001	0.0739	0.0748	0.0740	0.0742	0.0001
−0.75	0.2670	0.2724	0.2669	0.2698	0.0001	0.0904	0.0916	0.0903	0.0909	0.0001	0.0745	0.0755	0.0745	0.0748	0.0001
−0.25	0.2490	0.2543	0.2490	0.2515	0.0001	0.0898	0.0911	0.0897	0.0902	0.0001	0.0750	0.0763	0.0750	0.0756	0.0001
0.25	0.2308	0.2356	0.2308	0.2328	0.0002	0.0890	0.0904	0.0890	0.0895	0.0001	0.0757	0.0770	0.0756	0.0762	0.0001
0.75	0.2128	0.2168	0.2126	0.2146	0.0002	0.0883	0.0896	0.0882	0.0887	0.0001	0.0763	0.0777	0.0761	0.0767	0.0001
1.25	0.1952	0.1987	0.1951	0.1967	0.0001	0.0876	0.0888	0.0874	0.0880	0.0001	0.0769	0.0784	0.0767	0.0775	0.0001
1.75	0.1783	0.1813	0.1782	0.1799	0.0001	0.0867	0.0880	0.0866	0.0871	0.0001	0.0776	0.0794	0.0773	0.0781	0.0001
2.25	0.1622	0.1647	0.1621	0.1636	0.0001	0.0859	0.0872	0.0858	0.0864	0.0001	0.0782	0.0801	0.0778	0.0788	0.0001
2.75	0.1471	0.1491	0.1470	0.1484	0.0001	0.0850	0.0862	0.0849	0.0856	0.0001	0.0788	0.0810	0.0784	0.0794	0.0001
3.25	0.1331	0.1350	0.1330	0.1342	0.0001	0.0842	0.0853	0.0841	0.0846	0.0001	0.0795	0.0817	0.0790	0.0801	0.0001
3.75	0.1203	0.1219	0.1203	0.1210	0.0001	0.0834	0.0845	0.0833	0.0838	0.0001	0.0801	0.0826	0.0795	0.0806	0.0001
4.25	0.1087	0.1101	0.1087	0.1094	0.0001	0.0826	0.0840	0.0825	0.0831	0.0001	0.0807	0.0838	0.0800	0.0813	0.0001
4.75	0.0983	0.0999	0.0982	0.0988	0.0001	0.0820	0.0833	0.0818	0.0824	0.0001	0.0814	0.0843	0.0807	0.0822	0.0001
5.25	0.0893	0.0911	0.0891	0.0896	0.0000	0.0816	0.0829	0.0814	0.0820	0.0001	0.0823	0.0853	0.0817	0.0831	0.0001
5.75	0.0824	0.0841	0.0824	0.0828	0.0001	0.0818	0.0852	0.0816	0.0824	0.0001	0.0834	0.0898	0.0827	0.0841	0.0001

[a]Analytical benchmark result by Selcuk (1985). (All values normalised w.r.t. $e_{b0}/L_0 = 9.2540 \times 10^5$ W/m^3.)

Table 6.5 Case A: Comparison of global radiative energy generation/removal.

Method	Total energy generation Q_g	Total energy removal Q_s	% error in Q_g	% error in Q_s	% energy imbalance
Analytical[a]	1.424	1.424	0	0	0
DT (64)[b]	1.361	1.394	-2.34	-2.12	2.37
DOM (S_4)[b]	1.428	1.428	0.29	0.29	0
DT (400)	1.441	1.442	1.19	1.26	0.07
YIX	1.413	1.448	-0.77	1.69	2.48
MC	1.423	1.423	-0.07	-0.07	0

[a]Analytical benchmark result by Selçuk (1985).

[b]Discrete transfer and S_4 solutions of Selçuk and Kayakol (1997).

(Energy values are normalised w.r.t. $e_{b0} \cdot L_0^2 = 1.0234 \times 10^5$ W for 1/4 of the geometry.)

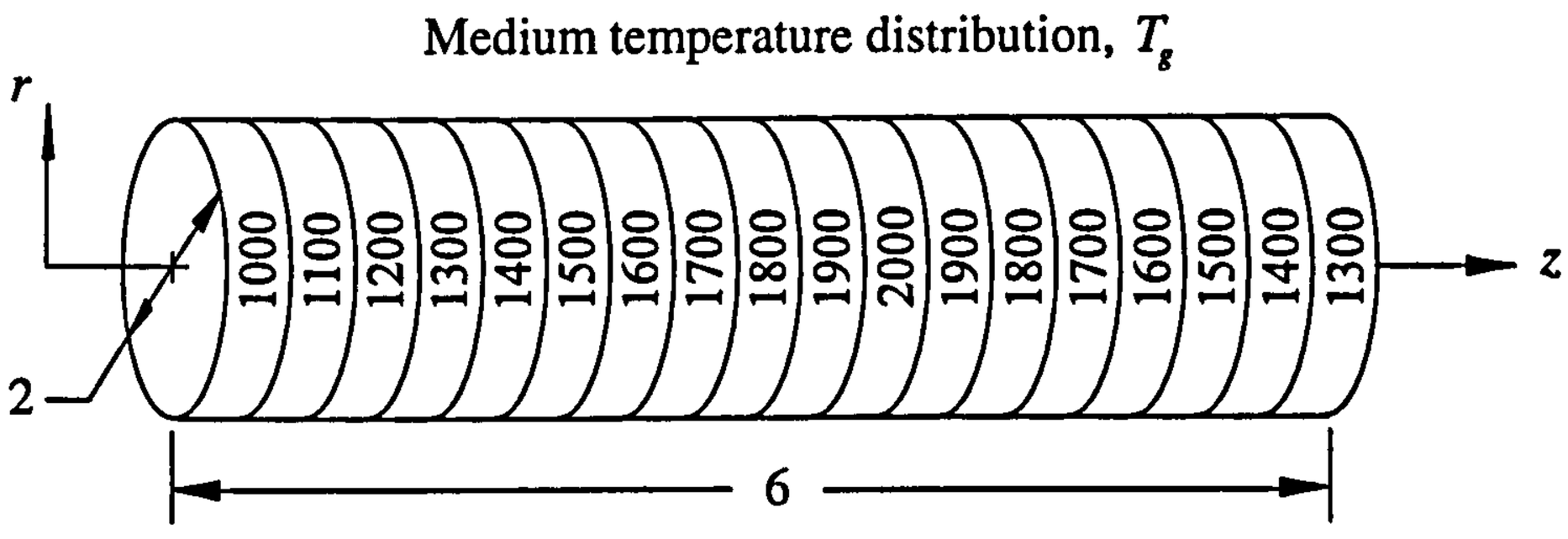

- Medium: nonscattering ($\omega = 0$) with uniform absorption coefficient, κ.
- Surface: black ($\varepsilon = 1$) at a constant temperature of 500 K.

Figure 6.3 Case B: Nonorthogonal cylindrical enclosure (Chui *et al.* 1993).

Table 6.6 Surface heat flux for Case B: Nonorthogonal cylindrical enclosure (Chui *et al.* 1993).

	Case B1: $\kappa = 0.1$				Case B2: $\kappa = 1.0$				Case B3: $\kappa = 10.0$			
z	DT	YIX	MC	$S_n(\bar{x})$	DT	YIX	MC	$S_n(\bar{x})$	DT	YIX	MC	$S_n(\bar{x})$
1/6	12.89	12.91	12.48	0.11	44.84	44.76	43.89	0.33	52.56	52.47	50.3'	0.42
3/6	18.36	18.31	18.10	0.14	70.62	70.19	70.06	0.25	79.56	79.43	79.2'	0.50
5/6	24.78	24.76	24.63	0.24	100.98	100.45	100.80	0.49	114.12	113.94	113.75	0.51
7/6	32.53	32.47	32.70	0.22	138.56	137.81	137.87	0.31	158.48	158.23	157.29	0.75
9/6	41.87	41.78	41.84	0.17	184.98	183.96	185.49	0.45	214.34	214.01	215.26	0.65
11/6	52.94	52.69	52.15	0.29	241.51	240.05	239.30	0.66	283.53	283.10	282.25	0.77
13/6	65.55	65.20	65.46	0.30	308.79	306.97	307.76	1.02	368.04	367.48	367.98	1.29
15/6	79.48	79.10	79.06	0.37	386.85	384.71	385.25	0.86	469.95	469.24	468.06	0.79
17/6	94.15	93.75	93.78	0.25	473.90	471.36	470.80	0.96	591.53	590.63	589.46	0.98
19/6	107.94	107.26	107.23	0.30	562.54	559.00	557.76	0.83	735.04	733.97	734.34	1.89
21/6	116.70	115.93	114.40	0.43	626.38	623.90	614.71	1.12	895.72	894.45	875.41	1.30
23/6	107.85	107.16	106.50	0.38	562.42	558.87	555.72	0.59	735.04	733.97	733.03	1.45
25/6	93.94	93.52	92.99	0.44	473.60	471.03	468.76	0.67	591.53	590.63	588.23	1.55
27/6	79.04	78.68	78.06	0.43	386.12	384.01	384.79	0.82	469.95	469.24	466.74	1.10
29/6	64.79	64.47	64.70	0.18	307.27	305.51	305.81	0.53	368.04	367.48	366.72	1.04
31/6	51.69	51.46	51.35	0.28	238.38	236.96	237.18	0.80	283.53	283.10	282.73	0.91
33/6	39.73	39.57	39.60	0.14	177.96	176.79	176.79	0.50	214.31	213.99	212.78	1.14
35/6	28.45	28.40	28.35	0.22	120.25	120.09	117.64	0.26	156.14	155.91	151.70	0.51
Total Q_s	2509	2502	2488	-	11863	11806	11750	-	14753	14731	14633	-
Total Q_g	2509	2481	2488	-	11863	11329	11750	-	14753	6059	14633	-
HI (%)	0.0	0.8	0.0		0	4.0	0	-	0	56.5	0	-

HI = % Heat imbalance w.r.t. MC value. Units: surface heat flux, kW/m^2 ; heat sources Q_s and Q_g, kW.

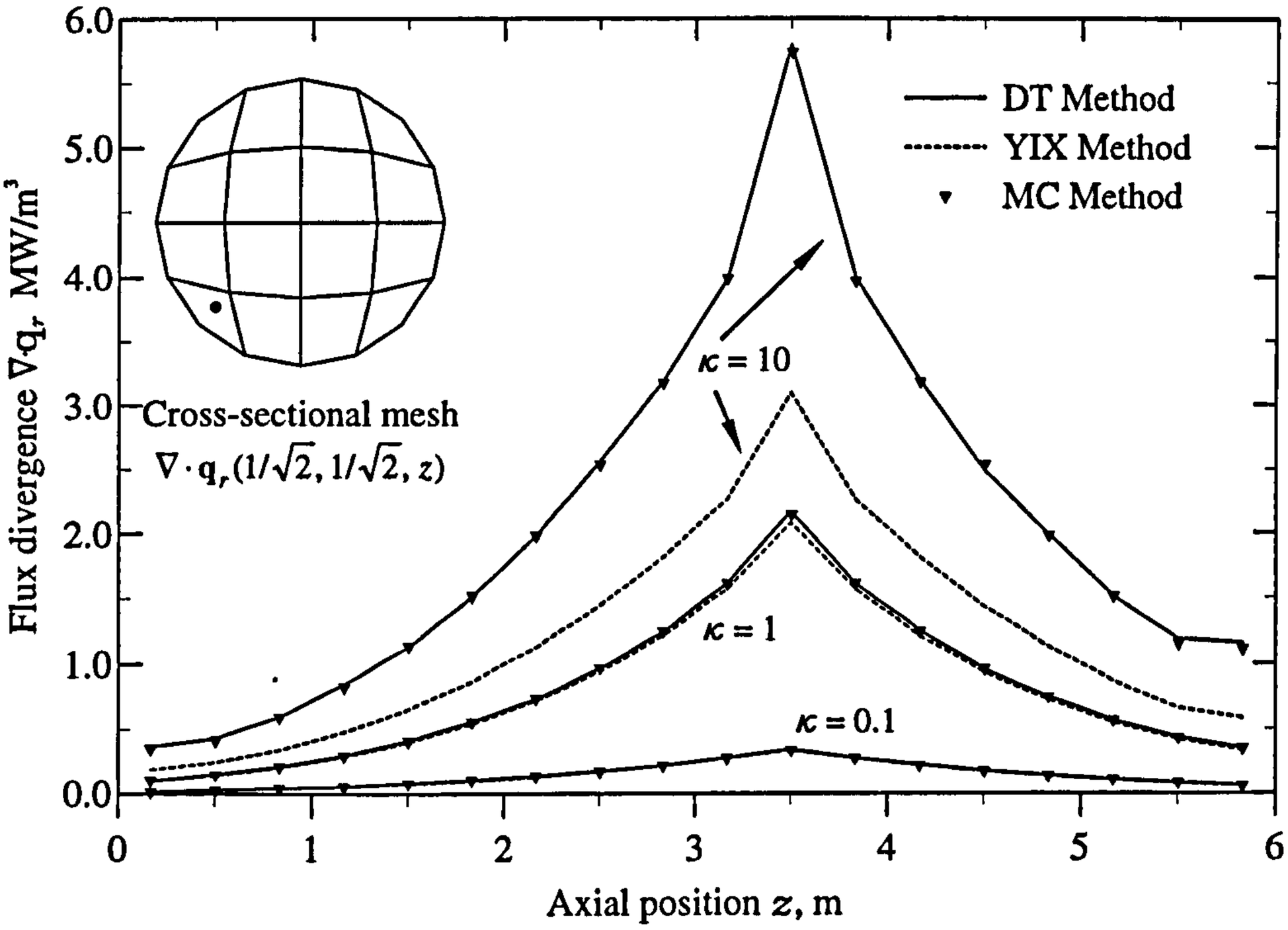

Figure 6.4 Case B: Axial variation in flux divergence near boundary.

(Note: Figure 6.5 is in main body of text.)

- Unit cube centred at coordinate origin.

  $-0.5 \le (x, y, z) \le 0.5$

- All surfaces are diffuse and black ($\varepsilon = 1$).

- Medium scattering phase function :

  $\Phi(\hat{\mathbf{s}}_i, \hat{\mathbf{s}}) = 1 + g\, \hat{\mathbf{s}} \cdot \hat{\mathbf{s}}_i$

  and nonhomogeneous extinction coefficient:

  $\beta(x, y, z) = a(1-2|x|)(1-2|y|)(1-2|z|) + b$

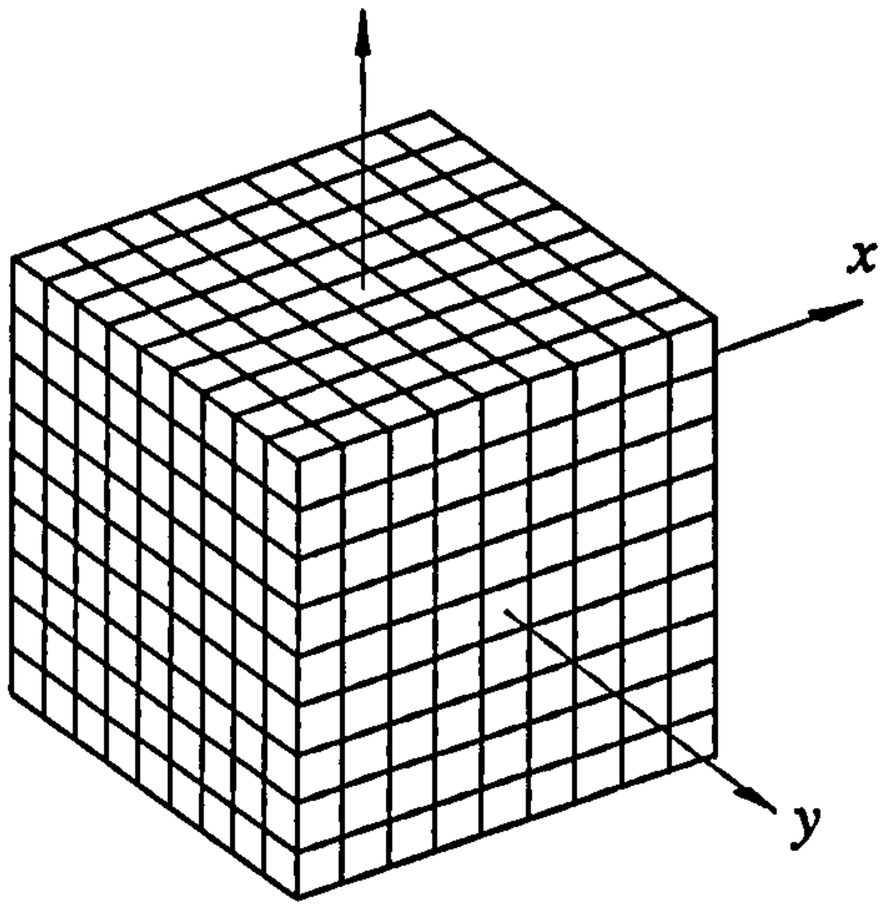

Case	Scattering albedo ω	LAS coeff. g in $\Phi(\hat{\mathbf{s}}_i, \hat{\mathbf{s}})$	In $\beta(x,y,z)$ a	b	Medium e_g	$\nabla \cdot \mathbf{q}_r$	Boundary conditions†
C1	0.	n/a	0.9	0.1	1.	?	6 cold walls
C2	0.9	0.	0.9	0.1	1.	?	6 cold walls
C3	0.9	1.	0.9	0.1	?	0.	1 hot/5 cold
C4	0.9	-1.	0.9	0.1	?	0.	1 hot/5 cold
C5	0.9	1.	0.5	0.5	?	0.	1 hot/5 cold

†Cold walls: $e_s = 0$, hot walls: $e_s = 1$. Radiative surface heat flux and ? is unknown.

Figure 6.6 Case C: Cubic benchmarking media with nonhomogeneous extinction, a hot emitting wall and anisotropic scattering.

Table 6.7 Results for Case C1: Nonscattering ($\omega = 0$).

	$q_s(-0.5, 0, z)$ W/m^2					
z	MC[a]	YIX	DT	MC[c]	YIX[c]	FE[d]
±4/9	0.10857	0.10795	0.10967	0.10959	0.10872	0.10743
±3/9	0.14012	0.14094	0.14107	0.14125	0.14171	0.13759
±2/9	0.16566	0.16545	0.16645	0.16729	0.16619	0.16255
±1/9	0.18468	0.18492	0.18543	0.18552	0.18569	0.18049
0	0.19239	0.19220	0.19286	0.19260	0.19291	0.18760
	$\nabla \cdot \mathbf{q}_r(x, 0, 0)$ W/m^3					
x	MC[b]	YIX	DT	MC[c]	YIX[c]	FE[d]
±4/9	0.72336	0.72302	0.72860	0.72910	0.72219	0.72502
±3/9	1.37701	1.37419	1.38099	1.38739	1.37209	1.38007
±2/9	1.96893	1.95985	1.96458	1.98360	1.95658	1.97318
±1/9	2.51700	2.50114	2.52182	2.53635	2.49628	2.52438
0	3.07462	3.04339	3.08144	3.09813	3.03664	3.08571

[a]Standard error $S_n(\bar{x}) < 0.00008$ for all MC values on surface.

[b]Standard error $S_n(\bar{x}) < 0.00001$ for all MC values on plane.

[c]Hsu and Farmer (1995). [d]Burns *et al.* (1995).

Table 6.8 Surface heat fluxes $q_s(-0.5, 0, z)$ for Case C1 with discrete transfer and YIX methods for a finer spatial discretisation.

	9×9×9			27×27×27	
z	FE[a]	YIX	DT	YIX	DT
±4/9	0.10743	0.10795	0.10967	0.10594	0.10798
		(0.48%)[b]	(2.09%)	(-1.39%)	(0.51%)
±3/9	0.13759	0.14094	0.14107	0.13945	0.13821
		(2.43%)	(2.53%)	(1.35%)	(0.45%)
±2/9	0.16255	0.16545	0.16645	0.16299	0.16327
		(1.78%)	(2.40%)	(0.27%)	(0.44%)
±1/9	0.18049	0.18492	0.18543	0.18169	0.18136
		(2.45%)	(2.74%)	(0.66%)	(0.48%)
0	0.18760	0.19220	0.19286	0.18862	0.18848
		(2.45%)	(2.80%)	(0.54%)	(0.47%)

[a]Burns *et al.* (1995). Units: W/m^2

[b]Deviation of value as % of FE value.

Table 6.9 Results for Case C2: Isotropic scattering ($\omega = 0.9$, $g = 0$).

	$q_r(-0.5, 0, z)$ W/m^2					
z	MC[a]	YIX	DT	MC[c]	YIX[c]	FE[d]
±4/9	0.01213	0.01205	0.01217	0.01219	0.01214	0.01193
±3/9	0.01573	0.01579	0.01574	0.01564	0.01589	0.01536
±2/9	0.01867	0.01867	0.01870	0.01892	0.01877	0.01826
±1/9	0.02104	0.02097	0.02094	0.02103	0.02107	0.02037
0	0.02176	0.02182	0.02182	0.02202	0.02192	0.02120

	$\nabla \cdot \mathbf{q}_r(x, 0, 0)$ W/m^3					
x	MC[b]	YIX	DT	MC[c]	YIX[c]	FE[d]
±4/9	0.07914	0.07913	0.07921	0.07974	0.07912	0.07916
±3/9	0.15748	0.15742	0.15751	0.15866	0.15739	0.15750
±2/9	0.23496	0.23487	0.23495	0.23673	0.23482	0.23506
±1/9	0.31191	0.31170	0.31202	0.31433	0.31163	0.31205
0	0.38894	0.38852	0.38911	0.39192	0.38842	0.38916

[a]Standard error $S_n(\bar{x}) < 0.00008$ for all MC values on surface.

[b]Standard error $S_n(\bar{x}) < 0.00001$ for all MC values on plane.

[c]Hsu and Farmer (1995). [d]Burns *et al.* (1995).

Table 6.10 Results for Case C3: Forward scattering ($\omega = 0.9$, $g = 1$).

	$q_r(-0.5, 0, z)$ W/m^2					
z	YIX	MC	$S_n(\bar{x})$	YIX[a]	MC[a]	$S_n(\bar{x})$[a]
±4/9	0.98597	0.98543	0.00024	0.98586	0.98490	0.00016
±3/9	0.98120	0.98116	0.00027	0.98112	0.98010	0.00024
±2/9	0.97715	0.97742	0.00025	0.97706	0.97620	0.00025
±1/9	0.97373	0.97416	0.00038	0.97360	0.97310	0.00036
0	0.97180	0.97305	0.00029	0.97170	0.97170	0.00027

	$e_g(x, 0, 0)$ W/m^2					
x	YIX	MC	$S_n(\bar{x})$	YIX[a]	MC[a]	$S_n(\bar{x})$[a]
–4/9	0.50694	0.46372	0.00269	0.50679	0.46100	0.00053
–3/9	0.36277	0.36549	0.00075	0.36282	0.36640	0.00038
–2/9	0.28163	0.28371	0.00075	0.28177	0.28420	0.00042
–1/9	0.22108	0.21861	0.00071	0.22135	0.21830	0.00047
0	0.16661	0.16611	0.00108	0.17049	0.16650	0.00042
1/9	0.11934	0.12638	0.00095	0.11959	0.12580	0.00024
2/9	0.09529	0.09532	0.00081	0.09547	0.09642	0.00027
3/9	0.06816	0.07490	0.00084	0.06832	0.07516	0.00020
4/9	0.06405	0.06105	0.00150	0.06417	0.05986	0.00020

[a]Hsu and Farmer (1995). Hot wall at $x = -0.5$.

Table 6.11 Results for Case C4: Backward scattering ($\omega = 0.9$, $g = -1$).

	$q_s(-0.5, 0, z)$ W/m^2					
z	YIX	MC	$S_n(\bar{x})$	YIX[a]	MC[a]	$S_n(\bar{x})$[a]
±4/9	0.96702	0.96669	0.00025	0.96680	0.96560	0.00039
±3/9	0.95235	0.95137	0.00060	0.95218	0.95100	0.00037
±2/9	0.93963	0.94005	0.00024	0.93944	0.93870	0.00043
±1/9	0.92974	0.93045	0.00051	0.92947	0.92950	0.00038
0	0.92489	0.92653	0.00045	0.92465	0.92530	0.00058
	$e_g(x, 0, 0)$ W/m^2					
x	YIX	MC	$S_n(\bar{x})$	YIX[a]	MC[a]	$S_n(\bar{x})$[a]
–4/9	0.52310	0.47480	0.00378	0.52294	0.47660	0.00045
–3/9	0.37704	0.38089	0.00125	0.37710	0.37990	0.00051
–2/9	0.29248	0.29663	0.00085	0.29267	0.29450	0.00060
–1/9	0.22703	0.22395	0.00090	0.22730	0.22430	0.00046
0	0.16661	0.16630	0.00067	0.17050	0.16640	0.00029
1/9	0.11485	0.12154	0.00074	0.11505	0.12120	0.00026
2/9	0.08901	0.09026	0.00094	0.08914	0.08987	0.00023
3/9	0.06147	0.06832	0.00069	0.06159	0.06820	0.00021
4/9	0.05786	0.05228	0.00091	0.05795	0.05326	0.00021

[a]Hsu and Farmer (1995). Hot wall at $x = -0.5$.

Table 6.12 Results for Case C5: Forward scattering in an optically thick medium ($a = 5.0$, $b = 5.0$). YIX solutions on 27×27×27 mesh.

	$q_s(-0.5, 0, z)$ W/m^2					
z	YIX	MC	$S_n(\bar{x})$	YIX[a]	MC[a]	$S_n(\bar{x})$[a]
±4/9	0.72737	0.73347	0.00044	0.72862	0.73260	0.00076
±3/9	0.62298	0.62625	0.00042	0.62774	0.62550	0.00071
±2/9	0.56706	0.56772	0.00025	0.57357	0.56670	0.00101
±1/9	0.53538	0.53513	0.00032	0.54266	0.53450	0.00063
0	0.52370	0.52355	0.00027	0.53151	0.52340	0.00110
	$e_g(x, 0, 0)$ W/m^2					
x	YIX	MC	$S_n(\bar{x})$	YIX[a]	MC[a]	$S_n(\bar{x})$[a]
–4/9	0.64629	0.64485	0.00036	0.64099	0.64420	0.00047
–3/9	0.48180	0.48266	0.00034	0.47755	0.48220	0.00060
–2/9	0.35127	0.35149	0.00029	0.34883	0.35100	0.00042
–1/9	0.24775	0.24759	0.00022	0.24702	0.24700	0.00030
0	0.16616	0.16656	0.00020	0.16740	0.16640	0.00021
1/9	0.10549	0.10774	0.00011	0.10854	0.10760	0.00015
2/9	0.06682	0.06876	0.00009	0.06940	0.06878	0.00014
3/9	0.04146	0.04312	0.00014	0.04358	0.04310	0.00010
4/9	0.02391	0.02477	0.00009	0.02548	0.02484	0.00006

[a]Hsu and Farmer (1995). Hot wall at $x = -0.5$.

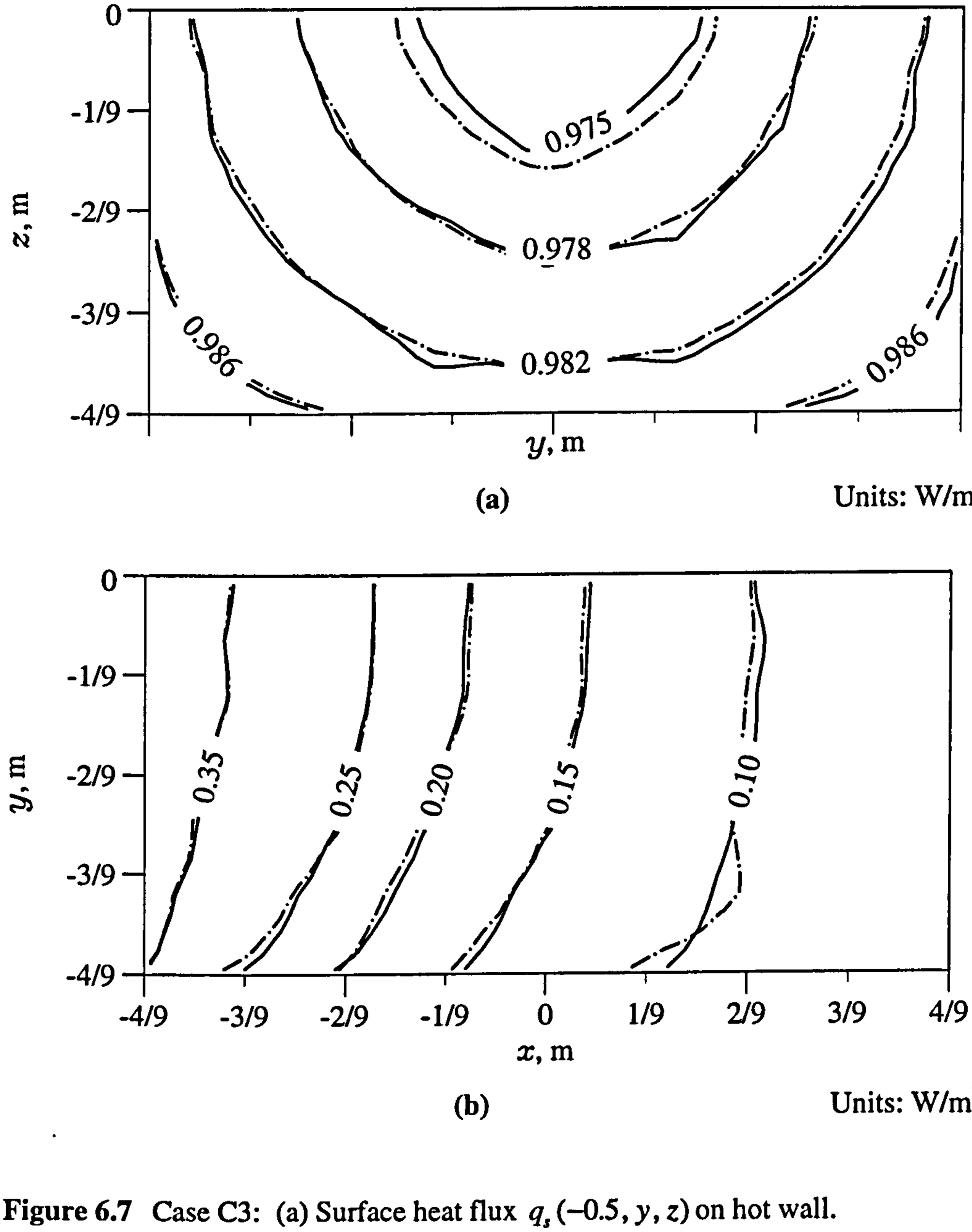

(a) Units: W/m^2

(b) Units: W/m^2

Figure 6.7 Case C3: (a) Surface heat flux $q_s(-0.5, y, z)$ on hot wall.
(b) Blackbody emissive power $e_s(x, y, 0)$.

Solid line = Monte Carlo solution.
Dot-dash line = YIX solution.

Compare with Fig. 3 by Hsu and Farmer (1995).

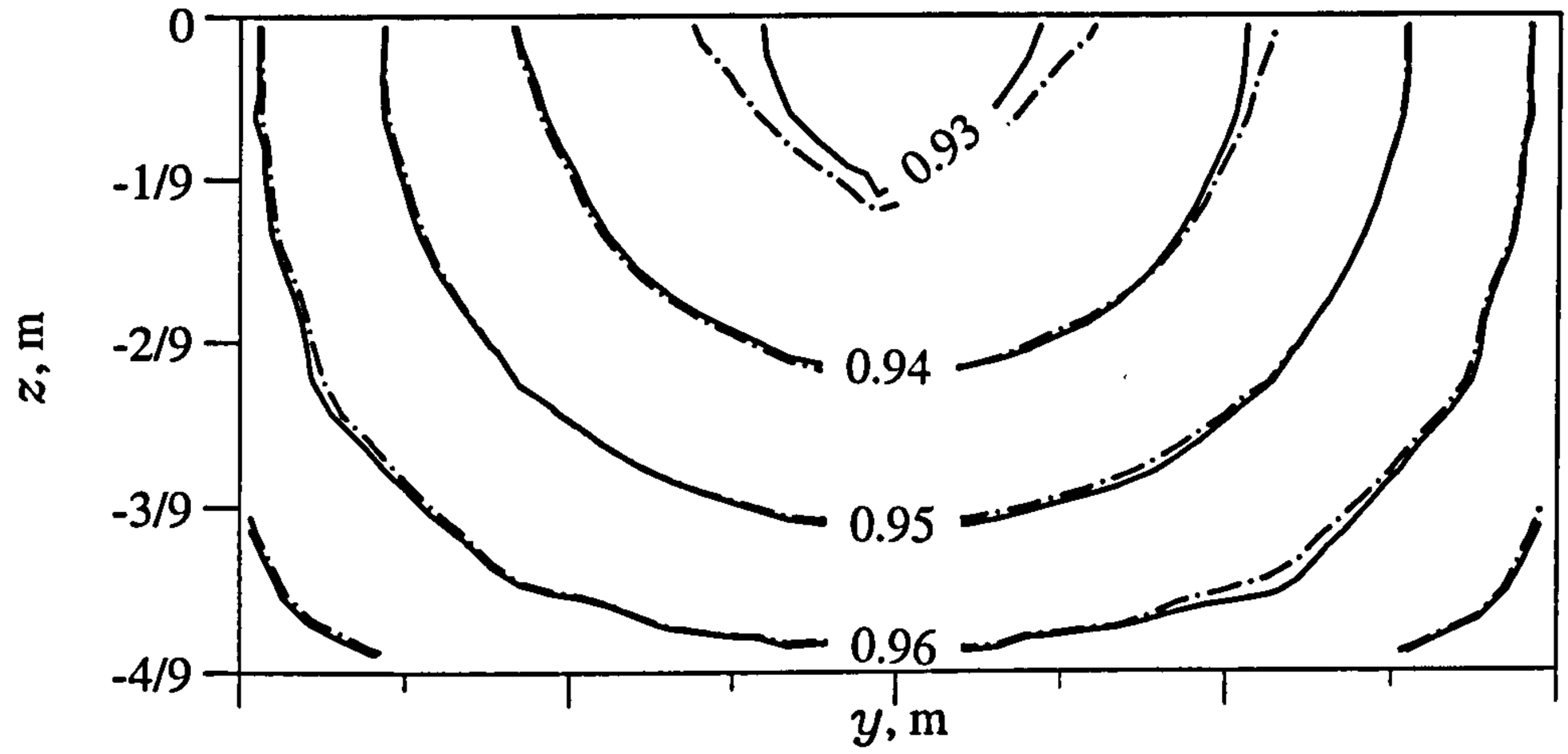

(a) Units: W/m^2

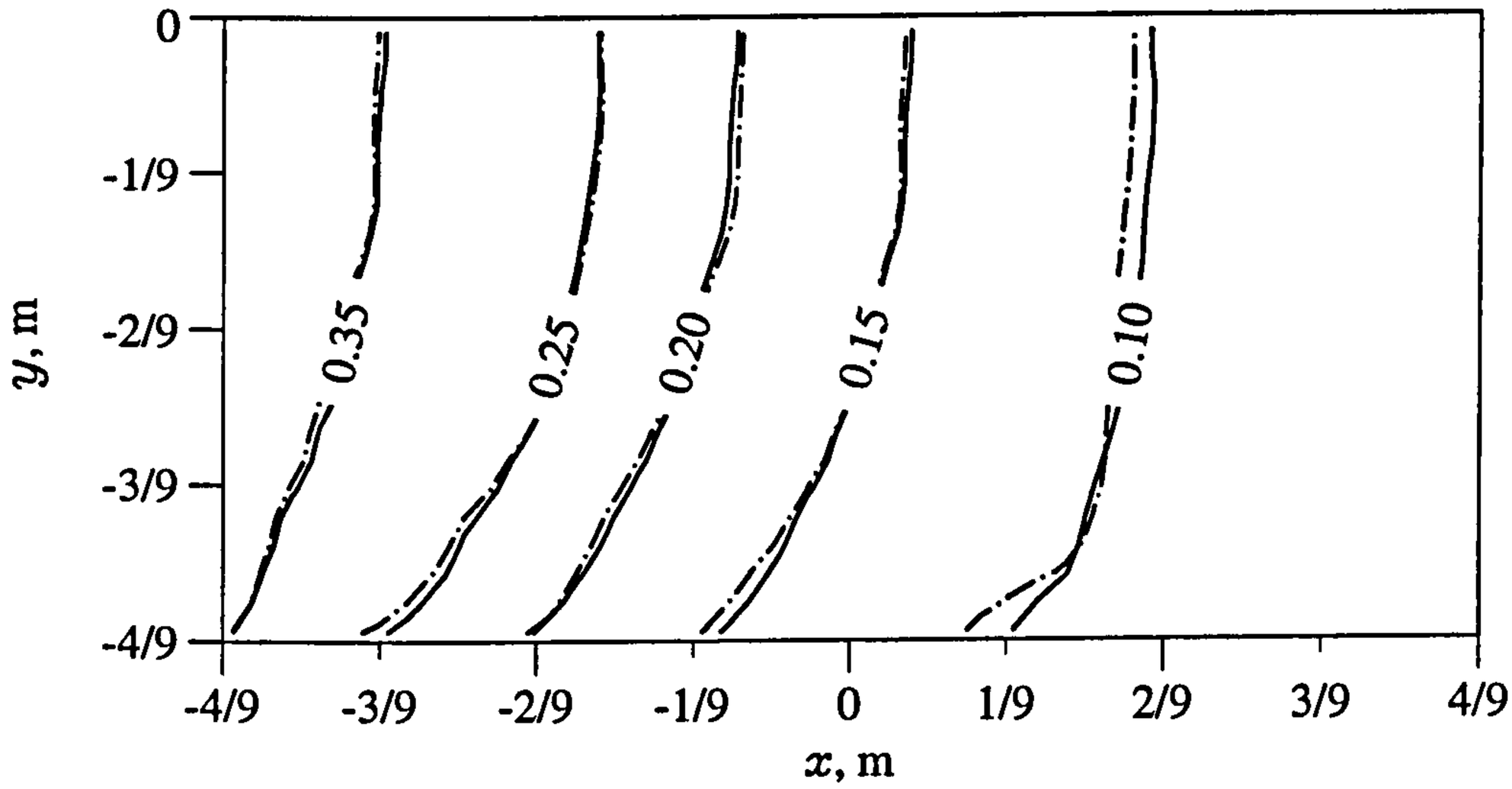

(b) Units: W/m^2

Figure 6.8 Case C4: (a) Surface heat flux $q_s(-0.5, y, z)$ on hot wall.
(b) Blackbody emissive power $e_g(x, y, 0)$.

Solid line = Monte Carlo solution.
Dot-dash line = YIX solution.

Compare with Fig. 4 by Hsu and Farmer (1995).

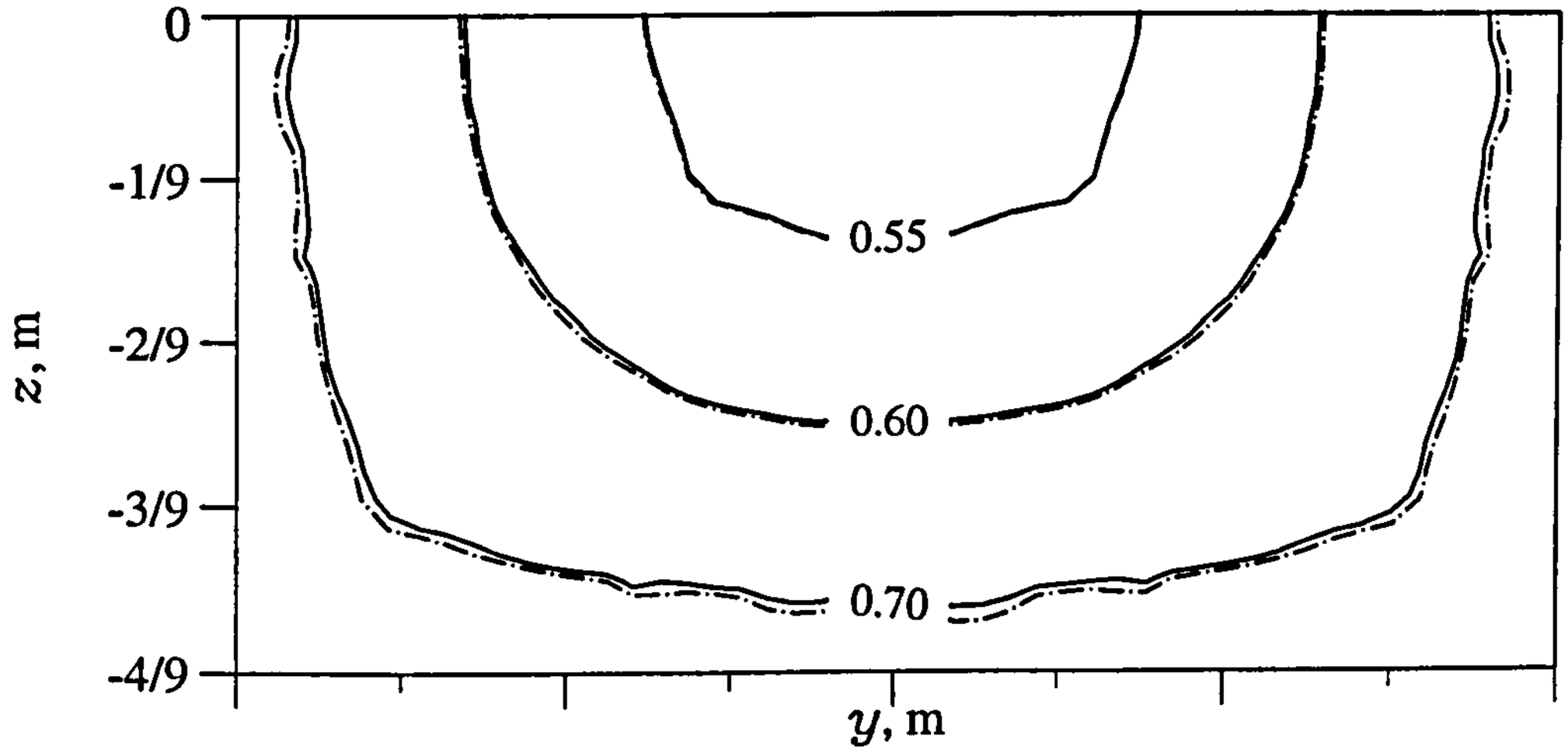

(a) Units: W/m^2

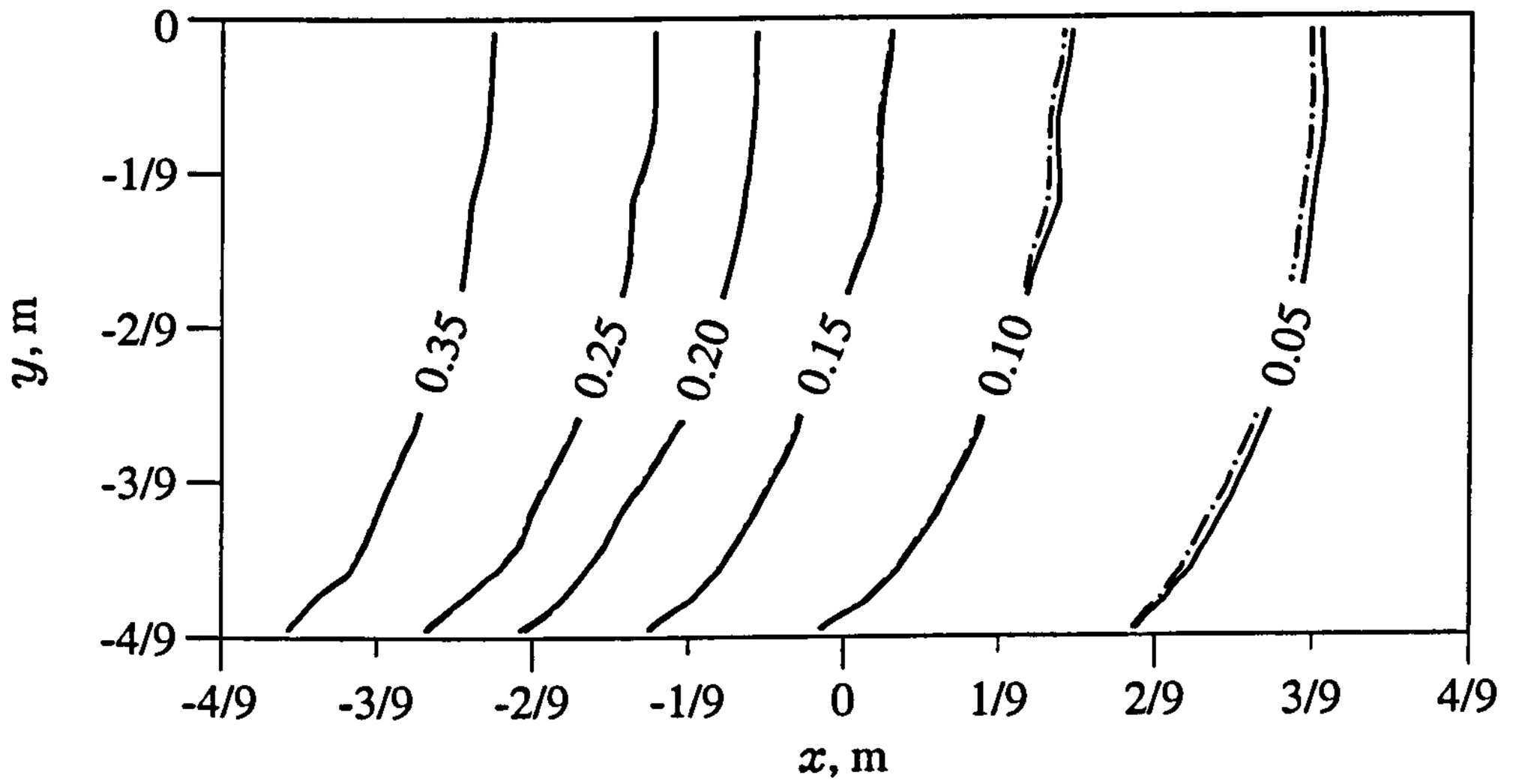

(b) Units: W/m^2

Figure 6.9 Case C5: (a) Surface heat flux $q_s(-0.5, y, z)$ on hot wall.
(b) Blackbody emissive power $e_g(x, y, 0)$.

Solid line = Monte Carlo solution.
Dot-dash line = YIX solution.

Compare with Fig. 5 by Hsu and Farmer (1995).

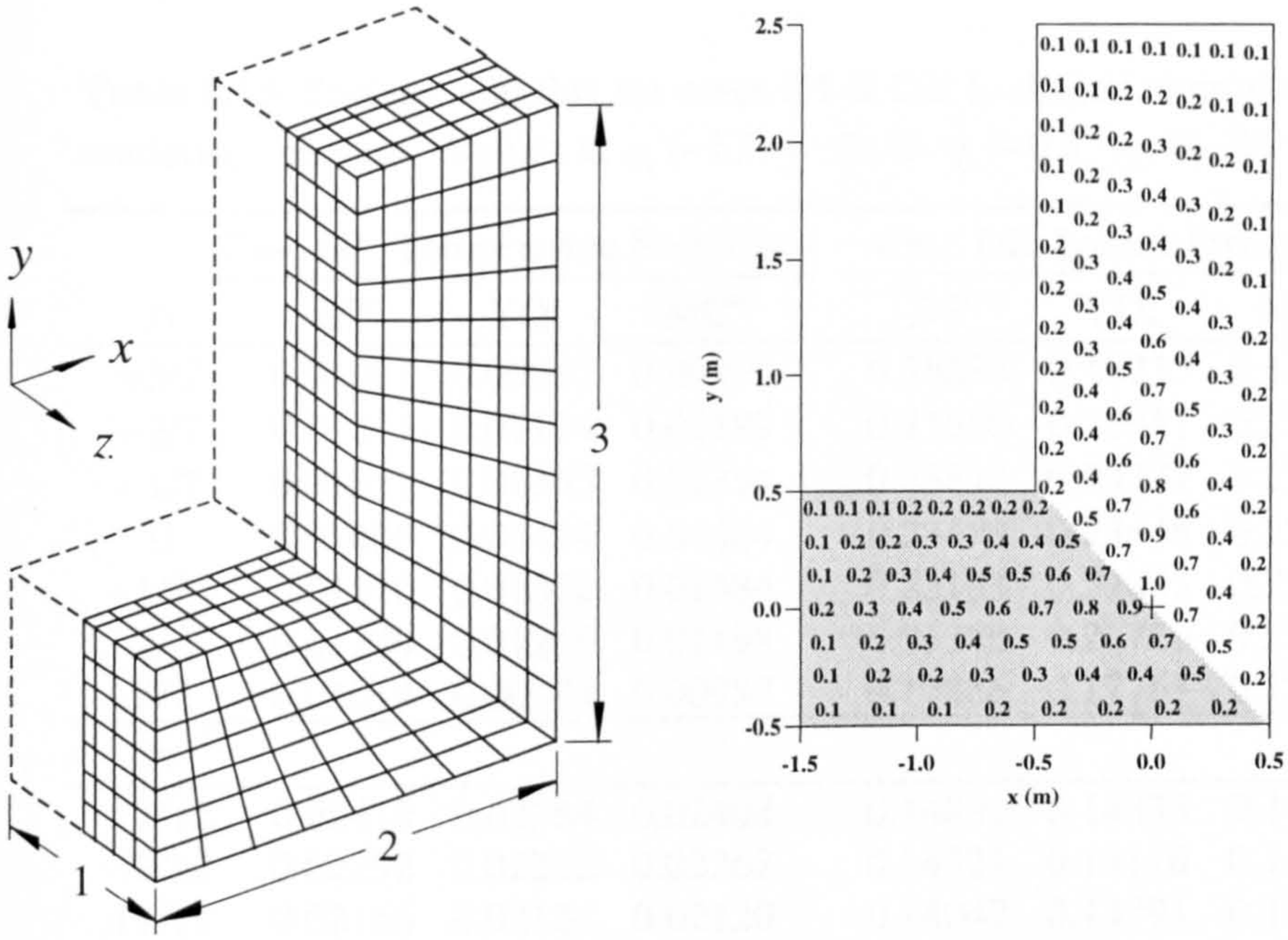

- L-shape composing 4 unit cubes with the coordinate origin at the centre of the corner diagonal.
- All surfaces are diffuse and black ($\varepsilon = 1$).
- Medium is isotropically scattering with nonhomogeneous extinction coefficient:

$$\beta\,(x \le -y) = \frac{0.9(1.5+x)(1-2|y|)(1-2|z|)}{(1.5-y)} + 0.1 \qquad \mathrm{m}^{-1}$$

$$\beta\,(x > -y) = \frac{0.9(1-2|x|)(2.5-y)(1-2|z|)}{(2.5+x)} + 0.1 \qquad \mathrm{m}^{-1}$$

Sample values are shown at $(x, y, 0)$ above.

Case	Scattering albedo ω	Medium e_g	Medium $\nabla \cdot \mathbf{q}_r$	Boundary e_s	Boundary q_s	Type of problem
D1	0.9	1.0	?	0.25.	?	Temperature prescribed.
D2	0.5	?	$x^{\dagger}$	0.	?	Source prescribed.

$^{\dagger}\nabla \cdot \mathbf{q}_r(x \le -y) = 1, \quad \nabla \cdot \mathbf{q}_r(x > -y) = 0.5.$? = unknown.

Figure 6.10 Case D: Nonorthogonal, nonhomogeneous, L-shaped geometry.

Table 6.13 Surface heat flux for cases D1 & D2: L-shaped isotropically scattering medium. Values at $q_s(-1.5, y_1, 0)$ & $q_s(-0.5, y_2, 0)$ W/m^2.

	Case D1: Temperature Prescribed			Case D2: Source Prescribed		
y_1	DT	YIX	MC[a]	DT	YIX	MC[b]
–3/7	0.01001	0.00985	0.00996	0.18298	0.18215	0.18368
–2/7	0.01201	0.01194	0.01199	0.21650	0.21951	0.21637
–1/7	0.01351	0.01353	0.01354	0.23312	0.23277	0.23138
0	0.01406	0.01434	0.01404	0.23453	0.23648	0.23492
1/7	0.01370	0.01372	0.01384	0.23153	0.22885	0.22913
2/7	0.01230	0.01266	0.01198	0.21388	0.21720	0.21329
3/7	0.01014	0.00974	0.00987	0.17886	0.17765	0.17754
y_2						
7/12	0.02419	0.02384	0.02408	0.14891	0.14835	0.14914
9/12	0.02292	0.02252	0.02262	0.14321	0.14116	0.14118
11/12	0.02166	0.02124	0.02120	0.14047	0.13791	0.13819
13/12	0.02031	0.01988	0.01976	0.13830	0.13547	0.13610
15/12	0.01888	0.01852	0.01866	0.13580	0.13382	0.13404
17/12	0.01742	0.01710	0.01732	0.13334	0.13222	0.13252
19/12	0.01592	0.01562	0.01573	0.13069	0.13019	0.13019
21/12	0.01440	0.01413	0.01423	0.12773	0.12742	0.12665
23/12	0.01280	0.01262	0.01269	0.12309	0.12336	0.12290
25/12	0.01114	0.01097	0.01100	0.11656	0.11719	0.11627
27/12	0.00932	0.00913	0.00940	0.10585	0.10679	0.10632
29/12	0.00714	0.00699	0.00719	0.08650	0.08815	0.08637

[a]Standard error $S_n(\bar{x}) < 0.00020$ for all MC values on surface (Case D1).

[b]Standard error $S_n(\bar{x}) < 0.00060$ for all MC values on surface (Case D2).

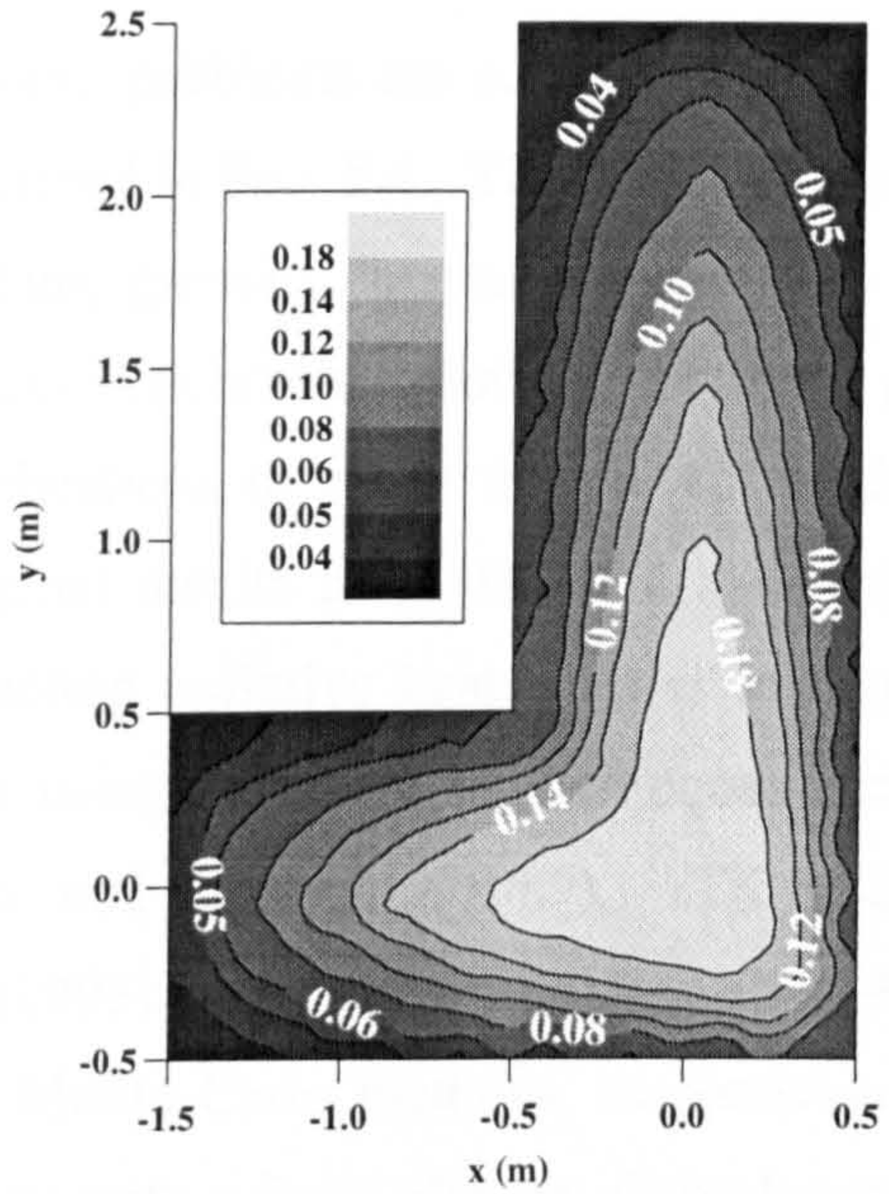

(a)

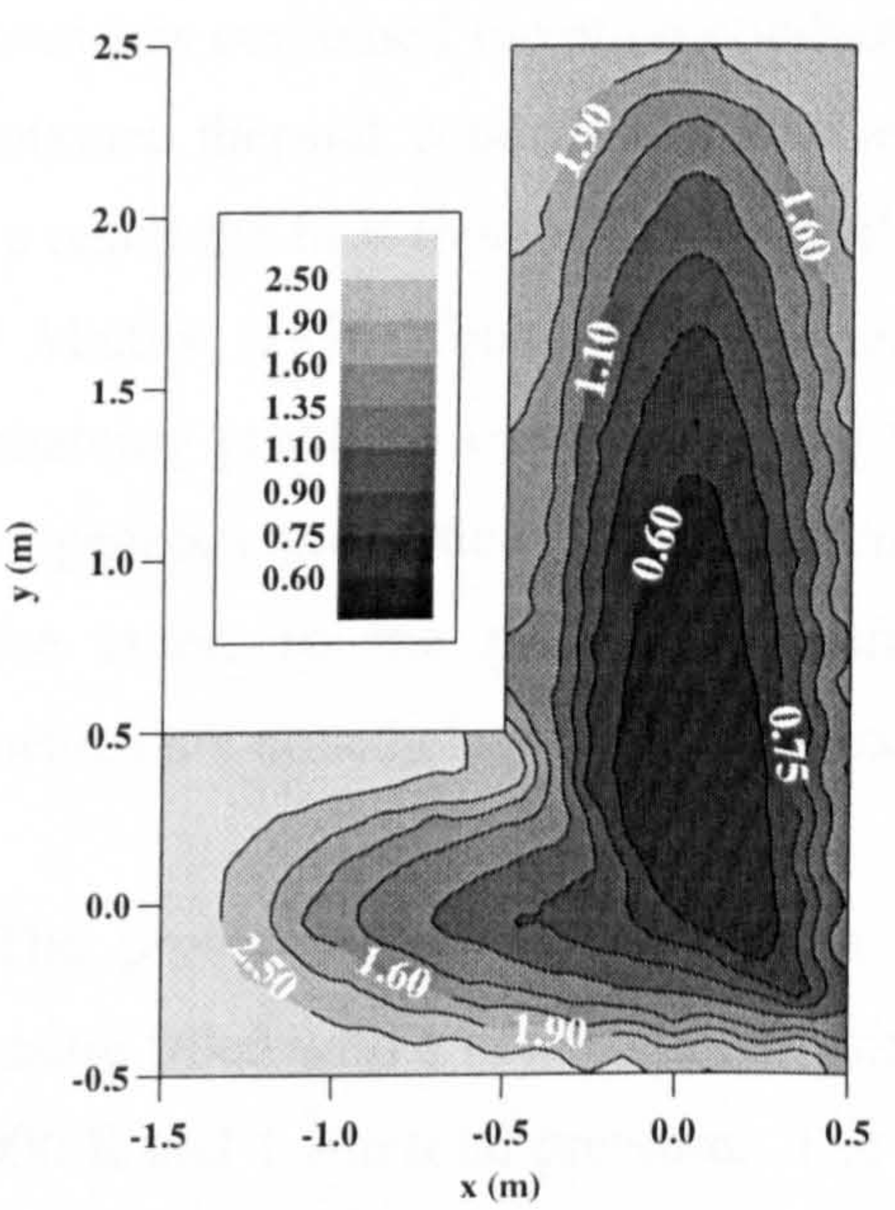

(b)

Figure 6.11 (a) Case D1: Divergence of radiative heat flux $\nabla \cdot \mathbf{q}_r(x, y, 0)$.
(b) Case D2: Blackbody emissive power $e_g(x, y, 0)$.
Units: W/m^2.

6.2 Homogeneous Scattering NonGray Media

Several wavelength dependent problems are solved to verify the weighted-sum-of-gray-gases (WSGG) model described in Sec. 5.4. These require the prediction of the radiative heat transfer in an absorbing gaseous mixture seeded with various concentrations of carbon particles. Numerical benchmark solutions for these problems have been taken from several principal publications to verify the present methods. Tong and Skocypec (1992) summarise the original results presented at a symposium on the comparison of solution methods for predicting radiative heat transfer in complex media. These were contributed by researchers using a variety of techniques including the zonal, discrete exchange factor (Naraghi and Litkouhi, 1989), YIX and Monte Carlo methods. Subsequently, Hsu *et al.* (1993) and Farmer and Howell (1994) updated their original solutions for the YIX and Monte Carlo methods, respectively. Burns *et al.* (1995) has also made some comparisons with a finite element formulation. Recently, new solutions have been determined by Hoover *et al.* (1996) with the discrete ordinates (S_n) method and by Hsu and Tan (1996) with the YIX method for an extended set of problems. The most ambitious of these considers combined radiation-conduction in a nonhomogeneous medium. However, the mixture thermal conductivity was assigned an extremely low value of 0.06 W/m K. As a result the heat transfer is so heavily radiation dominated that Hsu and Tan (1996) and Maltby (1996) found it impossible to obtain a converged temperature field. The remaining problems comprise purely radiative media with both homogeneous and nonhomogeneous properties. Poor agreement is observed between published solutions for the latter, so the present comparisons are limited to the homogeneous benchmarks which are nonetheless quite complex.

Problem Description. The problem geometry as shown in Fig. 6.12 is a three-dimensional L-shaped enclosure filled with a homogeneous mixture of suspended carbon particles, CO_2 and N_2 at 1000 K and 1 atm total pressure. The walls of the enclosure are cold and black and there is no emission or reflection from the boundaries. The enclosure width, W, height, H, and length, L, are 2 m, 3 m and 5 m respectively. The extension depth, b, is 2 m and the geometry is modelled with three extension heights, a, of 0, 1 and 2 m. The case of zero extension height serves as a baseline as it corresponds to a simple rectangular box geometry. The spectral variation in absorption coefficient of the CO_2 gas is found from the combined Elsasser narrow-band/ Edwards wide-band model described in Sec. 5.3.

All parameters are as stated previously with the single exception of the line spacing, δ, which is found from the relation:

$$\delta = 30\,C_3 \tag{6.6}$$

where the model parameter C_3 is evaluated at a temperature of 100 K. The partial gas density, ρ required in Eq. (5.1) is determined from the ideal gas equation using a specified CO_2 mole fraction of 21%. Spherical carbon particles with a diameter $d = 30$ μm are selected for the analysis. Their spectral scattering and extinction efficiencies, Q_{sca} and Q_{ext}, are found from applying Mie theory to soot data reported by Foster and Howarth (1968). These are listed in Table 6.15 (Tong and Skocypec 1992). Then for N_s particles per unit volume the soot absorption and scattering coefficients are (Modest 1993, p. 393):

$$\kappa_s = \frac{\pi d^2 N_s}{4}(Q_{ext} - Q_{sca}) \tag{6.7}$$

$$\sigma_s = \frac{\pi d^2 N_s}{4} Q_{sca} \tag{6.8}$$

Three carbon particle concentrations are considered: 2×10^7, 2×10^8 and 2×10^9 particles/m^3 to assess the effect of optical thickness on the solution. Fig. 6.13 shows the variation in total absorption coefficient with wavelength for the particle/gas mixture, where the total absorption is equal to the sum of the absorption due to the gaseous CO_2 and that due to the carbon particles. The carbon particle concentration in this case is 2×10^9 particles/m^3. The carbon particles have a scattering phase function approximated by a gray δ–Eddington formulation given as (Tong and Skocypec 1992):

$$\Phi(\Theta) = 2f\delta(1-\cos\Theta) + (1-f)(1+3g'\cos\Theta) \tag{6.9}$$

Here $\Theta = \cos^{-1}(\hat{\mathbf{s}}\cdot\hat{\mathbf{s}}_i)$ represents the scatter angle and the specified parameters $f = 0.111$ and $g' = 0.215$ customise the biased shape of the phase function to closely approximate its exact form. The δ is the Dirac-delta function defined by:

$$\delta(x) = \lim_{\varepsilon\to 0}\begin{cases} 0, & |x| > \varepsilon \\ 1/\varepsilon, & |x| < \varepsilon \end{cases} \tag{6.10}$$

such that it adds a forward 'spike' to the phase function for zero scattering angles.

The combination of three extension heights and three soot concentrations totals nine cases (E1–E9), as summarised in Table 6.14. For each problem the heat flux through the enclosure walls and the divergence of radiative flux within the media are sought at specific locations.

Solution Strategies. The above problem statement requires special consideration of how best to model: (a) the δ–Eddington scattering phase function, and (b) the spectral dependence of absorption *and* scattering, in each of the present methodologies. In regard to the first issue, it is common practice to model the Dirac-delta portion of the phase function as unscattered radiation by scaling the scattering coefficient, σ_s with a factor $(1-f)=0.889$. The reduced phase function (i.e. the last bracketed term) is then in the linear anisotropic form of Eq. (4.5), where the asymmetry parameter, g is replaced by $3g'$, i.e. g is set equal to 0.645 in the Monte Carlo random number relation Eq. (4.62) and in the YIX expression Eq. (4.79). However, an isotropic approximation must be used with the discrete transfer method by setting $g'=0$, since linear anisotropic scattering cannot be simulated, though σ_s is scaled as before to account for the Dirac-delta forward scattering 'spike'. (The affect of this approximation is discussed later.)

Sec. 5.4 presented two methods for representing the absorption spectrum: a bandwise solution and a more efficient variation using the concept of absorption cross-sections. Either method will discretise the *total* absorption spectrum of the particle/gas mixture into a number of gray gases, but the latter requires far fewer gases to characterise the absorption (i.e. the advantage gained from using absorption cross-sections is that wavenumber intervals with similar levels of absorption are combined and solved simultaneously.) However, an added difficulty here is that a scattering coefficient must be found for each gray gas representative of the scattering in its constituent wavenumber intervals. If these intervals are widely dispersed over the entire spectrum, such that σ_s varies significantly from interval-to-interval, taking some mean value is likely to be extremely erroneous. In contrast, the bandwise approach suffers no such disadvantage because the solutions for different wavenumber intervals are independent of each other and, in principle at least, the interval widths can be progressively reduced in order to capture localised spectral variations in both the absorption and scattering coefficient. Therefore, the bandwise method is a better choice here if accuracy is the main concern: it is also the method used in all the previous studies cited above. Though having said this, it

is found that the spectral variation in scattering coefficient is in fact very small, such that absorption cross-sections should still give a good approximation for much less computation. Thus, solutions using both methods for the spectral discretisation are presented below.

Bandwise Solutions. A complete set of nongray solutions was generated for the discrete transfer, YIX and Monte Carlo methods with the bandwise WSGG model. These are tabulated in Tables 6.16 to 6.21. Measures of relative difference and run times for each of the deterministic solutions are given in Table 6.14. Monte Carlo times were typically an $O(10^2)$ times longer than those of the deterministic solutions. For each of the cases E1–E9 choices had to be made regarding the spatial, angular and spectral discretisation.

The box geometry is modelled with a 9×9×9 and the L-shaped geometry with a 9×11×14 mesh (see Fig. 6.12). An orthogonal mesh structure is used for both enclosures in order that the results are found at the solution points without interpolation. The L-shape is described by deactivating a 6×5 block of cells. The discrete transfer and Monte Carlo solution times may be dramatically reduced by taking advantage of the problem symmetry. Then, only one-eighth of the box geometry (x, y, z all ≥ 0) and one-half of the L-shaped geometry ($x \geq 0$) need to be considered. However, symmetry cannot be used with the present YIX method where there is scattering anisotropy (see last section). Discrete transfer solutions used 400 rays per surface element. YIX solutions were obtained with S_{16} angular quadrature and a first integration point of $\tau_1 = 0.001$. Pilot studies indicates that these results are unlikely to change by more 0.5% with finer spatial or angular discretisation, particularly given the nicely homogeneous radiative properties and cold boundary conditions. However, the solution accuracy is highly sensitive to the fidelity of the gray gas approximation. Since this stems from the bandwise WSGG model, the effect on the discrete transfer, YIX or Monte Carlo solutions is the same. It is found that with too few wavenumber intervals the strong CO_2 absorption spikes are not accurately resolved and large errors result. Moreover, it is important to fit a given number of intervals efficiently so as to resolve the most detail (see Sec. 5.4.1). Figure 6.14 shows how the *total* surface flux for case E4 converges as the number of intervals is increased. The flux is within 0.1% of its converged value with 80 intervals and so this number was taken for all the present solutions.

Trends observed in the surface heat flux and divergence of radiative heat flux solutions are explained as follows. The positive values of flux divergence correspond to the heat source required to maintain the homogeneous media at 1000 K by balancing heat losses at the boundaries. As would be expected the maximum divergence in all cases is predicted in the corner regions where the gas is in close proximity with three cold walls. As the particle concentration is increased from 2×10^7 to 2×10^9 particles/m^3, the surface heat flux and divergence also increase as a result of increased radiative heat transfer from the particles. It is also observed that the flux gradients in the media become more pronounced. At the highest particle concentration the medium is so optically thick that it behaves as a good radiative insulation and consequently, the flux divergence in the central region falls. However, heat losses through the boundaries are greater such that the divergence there rises. The net effect is a greater disparity between flux divergence values at the centre and those at the boundaries as the particle concentration is increased.

Varying the extension height a has much less influence on the heat transfer characteristics of the media compared to the particle concentration. Increasing a tends to reduce the flux divergence, particularly at locations which become more removed from the new extension boundaries. This is most noticeable in the optically thick media (i.e. E7, E8 and E9) due to the insulating effect of the intervening media. However, the surface heat flux increases slightly with a since the surface-to-volume ratio is lowered and a larger volume is radiating to a smaller surface area. Analysis of the surface heat flux values in the z–direction at $x = 0$, $y = L/2$ also reveal the shading effects that arise in the L-shape geometries when $a > 0$. The flux remains relatively constant from the centre of the surface towards the edge until 0.25 to 0.5 m from the top of the extension when it decreases rapidly as the view factor to the main body of hot gas is reduced. This shading effect is most pronounced in the optically thinner media (i.e. E1, E2 and E3).

A second set of Monte Carlo solutions were found for a scattering asymmetry factor $g' = 0$ in order to assess the effect of this approximation in the discrete transfer solutions. In all cases removing the forward scattering bias reduces both the surface heat flux and flux divergence. The solutions change typically by less than 1% for cases E1–E6, but for the optically thick media (i.e. E7, E8 and E9) the effect is more pronounced: the surface heat flux falls on average by about 6% corresponding to a 10% drop in flux divergence. This error is excluded from the difference measures in Table 6.14 by comparing solutions

on a like-with-like basis, i.e. the discrete transfer results are compared with Monte Carlo values found with $g'=0$ and YIX results with the exact Monte Carlo values for which $g'=0.215$. Thus, any deviation arises from differences between the methods rather than the problem description.

Each nongray bandwise solution is essentially a combination of 80 individual gray solutions spanning a wide optical range. Those solutions in optically thin (or thinner) intervals between the CO_2 absorption spikes show the closest agreement, but for several intervals at and around the spike centres the absorption is very large, and this tends to exaggerate differences in the way each method resolves the radiative property gradients in an manner similar to case B3 in Sec. 6.1. In particular, for reasons stated previously, the YIX and Monte Carlo flux divergence values at medium points may differ by several tens of per cent in these thick intervals such that overall maximum deviations are as large as 50%. Moreover, it is observed that the solution disparity is noticeably larger for cases E7, E8 and E9, where the minimum spectral absorption exceeds 1 m^{-1} due to the high carbon particle concentration. Better agreement could be achieved by coupling each method with a diffusion solver for the thick intervals (see p. 163). However, the solution disparity is expected to be far less severe in the engine combustion studies (Part B) where the characteristic dimensions (and therefore optical lengths) of the combustion chambers are much smaller than those here.

Table 6.22 compares surface heat flux and flux divergence values from the present solutions with results from several other methods (or implementations). For brevity, sample results are only shown for the box enclosure with 2×10^8 particles/m^3 (case E4) and a more extensive comparison can be made by referring directly to the indicated publications. (The discrete transfer and finite element solutions both include errors associated with the scattering phase function approximation.) Relatively poor agreement is observed with solutions from the discrete exchange factor and discrete ordinate (S_n) methods, particularly between divergence values. However, the other results agree to within 5% of the present Monte Carlo value.

Performance comparisons for the gray problems in Sec. 6.1 found that discrete transfer run times were shorter than those of the YIX method where the majority of the time is taken in tracing the geometry, but the faster convergence of YIX solutions helped to

somewhat re-address the balance. One effect of the nongray analysis here is to shift the emphasis further from tracing to iterating in the overall solution procedure. Both deterministic methods trace the geometry only once and the path length information is stored. This data is then used recursively to solve for each gray gas in the spectral discretisation. These individual solutions take typically between 3 to 15 iterations so that an entire problem involves several hundred iterations and only *one* tracing step. Therefore, the discrete transfer and YIX run times are comparable for cases E1, E2 and E3 (if the problem symmetry is not exploited) – see Table 6.14. However, there is another more overriding factor impairing the YIX performance, which only becomes evident as the particle concentration is increased. Between reading the pathlength data and building the matrix equations the YIX solver must re-locate and store a new set of optical integration points. This procedure takes more time for spectral intervals with high absorptivity since more points must be found. At any given spectral position the absorptivity increases with the number of carbon particles such that the YIX solution of the problems with the highest concentration take twice the time of a discrete transfer solution. The YIX solver also requires more storage space, about 1.5 times that of the discrete transfer method, since in a nongray calculation both optical *and* spatial pathlength information must be retained. Thus, the discrete transfer method is faster and has a lower memory requirement.

Solutions using Absorption Cross-Sections. A WSGG model based on absorption cross-sections was initially verified against solutions presented by Denison and Webb (1993, 1995) that had accompanied their original model development. These considered a broad range of one-dimensional nonisothermal and/or nonhomogeneous purely gaseous media in which H_2O vapour is the radiating gas. It was found that the present model generally predicted the correct variations in one-dimensional flux, but values deviated by up to 20% in magnitude. This was attributed in part to the lack of a formal optimisation technique for fitting the gray gases, but mostly due to the underlying method used to compute the spectral absorption coefficient (*prior* to the spectral subdivision). The present correlation is based on wide-band absorptance measurements, whereas Denison and Webb use high-resolution line-by-line H_2O spectra (see Secs. 5.2 & 5.3). It is therefore not unreasonable to expect some discrepancies. Additional one-dimensional comparisons were made with RADCAL (Grosshandler 1979) solutions for total incident flux. Agreement with the narrow-band results was good for CO_2 media, but poorer when H_2O was the radiating gas.

The model was incorporated into the three-dimensional discrete transfer solver and applied to cases E1-E9. Table 6.23 compares performance with the corresponding bandwise solutions. Here any errors arise solely from the spectral subdivision. Impressively, the present model is 6 – 8 times faster and its surface flux and flux divergence solutions differ, on average, by less than 2% with the bandwise results in Tables 6.16 and 6.17. With optimisation of the model even better agreement is expected. A logarithmic subdivision of the absorption domain was used as described in Sec. 5.4.2. Additional cross-sections were used to resolve the variation in particle absorption, since by its continuous nature even small errors in the discretisation are significant, shifting the total flux solution up or down by a few percent. Seven, nine and eight-gray-gases are solved for the media with 2×10^7, 2×10^8 and 2×10^9 carbon particles/m^3, respectively. In each case, three or four represented the particle absorption.

Since E1-E9 are all homogeneous media only one set of conditions needed to be considered. Typically, to generate the model spectrum and fit the gray gases took 0.5 s which is less than 1% of the total run time in each case.

For nonisothermal/nonhomogeneous media the pre-processing time scales linearly with the level of spatial discretisation such that for large meshes it may become a sizeable overhead. Then further approximations may be necessary. Solutions have been found for nonisothermal/nonhomogeneous media with good results by Denison and Webb (1995) and also in this study with the discrete transfer-WSGG solver. These trials are incomplete (and omitted here), but sufficiently encouraging, that some preliminary studies of spark ignition engine combustion seems justified.

Table 6.14 Comparison of CPU run-times and relative differences for nongray benchmark problems E1 – E9.

	Extension height (a)	Particle density	Mesh size	CPU run time on HP-9000/750 [s]		Average relative difference[a] [%] q_s		Average relative difference[a] [%] $\nabla \cdot \mathbf{q}_r$		Maximum relative difference[a] [%] q_s		Maximum relative difference[a] [%] $\nabla \cdot \mathbf{q}_r$	
Case	[m]	[m^{-3}]	[cells][b]	DT[c]	YIX	DT	YIX	DT	YIX	DT	YIX	DT	YIX
E1	0	2×10^7	729	2082	2139	1.28	1.18	1.48	22.83	4.99	4.96	6.84	50.85
E2	1	2×10^7	1386	3312	3230	1.31	1.22	2.10	22.83	5.30	4.20	19.10	51.13
E3	2	2×10^7	1386	3256	3240	1.31	1.24	2.14	22.97	5.67	4.43	20.54	51.43
E4	0	2×10^8	729	2111	3127	1.21	0.88	1.17	13.20	4.13	2.46	4.19	38.97
E5	1	2×10^8	1386	3360	4715	1.21	1.02	1.58	13.47	6.70	3.63	9.49	39.38
E6	2	2×10^8	1386	3350	4720	1.20	1.06	1.62	13.39	4.19	3.44	9.10	39.02
E7	0	2×10^9	729	2959	6332	3.67	2.31	4.16	19.26	10.62	6.40	15.37	31.97
E8	1	2×10^9	1386	4707	7359	3.63	2.14	4.11	16.31	9.67	8.51	15.33	26.39
E9	2	2×10^9	1386	4696	7339	3.74	2.27	4.34	16.64	10.32	9.18	16.74	26.57

[a]Average relative difference: $\mathrm{ARD} = 1/n \sum |(\mathrm{X} - \mathrm{MC})/\mathrm{MC}|$: Maximum relative difference: $\mathrm{MRD} = MAX\,|(\mathrm{X} - \mathrm{MC})/\mathrm{MC}|$
where X = DT (discrete transfer) or YIX for n values (i.e. N surfaces fluxes or K volumetric quantities).

[b]30 cells in cases E2, E3, E5, E6, E8 and E9 are deactivated, so that active mesh size = 1356 cells.

[c]Discrete transfer times are for full geometry in each case. Symmetry may be used to reduce the times to:
E1: 298 s, E2: 1718 s, E3: 1709 s, E4: 286 s, E5: 1740 s, E6: 1711 s, E7: 399 s, E8: 2404 s and E9: 2364 s.

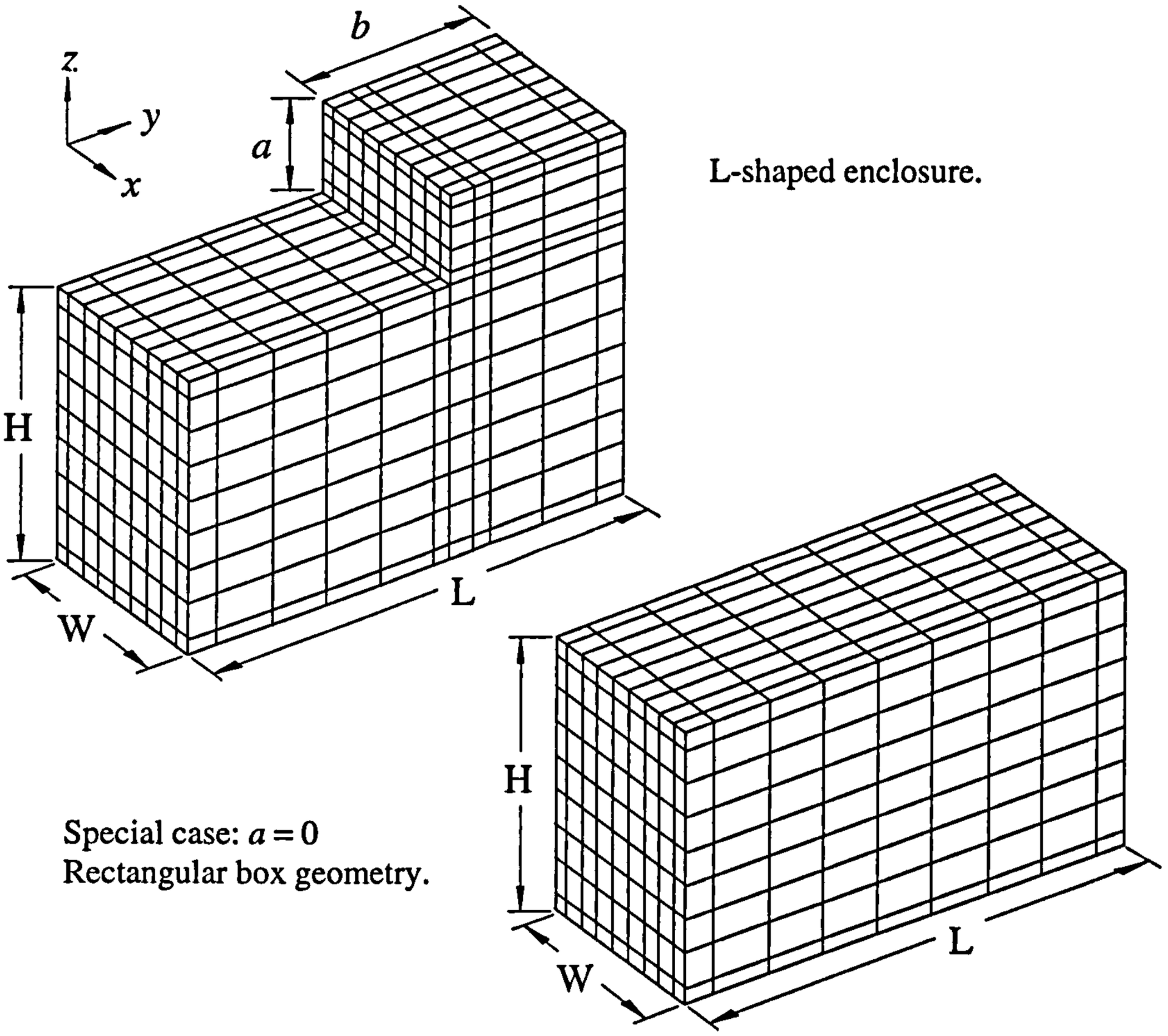

L-shaped enclosure.

Special case: $a = 0$
Rectangular box geometry.

Figure 6.12 L-shaped enclosure. W, H and L and b are fixed lengths: a is a variable extension height in the problem statement. Note: A different y–spacing is used for box mesh when $a = 0$.

Table 6.15 Radiative properties of 30 μm diameter carbon particles.

λ (μm)	Scattering efficiency	Extinction efficiency	λ (μm)	Scattering efficiency	Extinction efficiency
2.0	1.17680	2.14549	7.5	1.23875	2.34059
2.5	1.18157	2.16843	8.0	1.23015	2.35180
3.0	1.18368	2.18941	8.5	1.27949	2.37534
3.5	1.18698	2.20853	9.0	1.30680	2.39128
4.0	1.18751	2.22588	9.5	1.31753	2.40501
4.5	1.19100	2.24290	10.0	1.32398	2.42856
5.0	1.18874	2.26063	10.5	1.32844	2.43151
5.5	1.18296	2.28103	11.0	1.33279	2.44393
6.0	1.18687	2.29533	11.5	1.33577	2.45601
6.5	1.21067	2.30932	12.0	1.33871	2.46775
7.0	1.21895	2.32287			

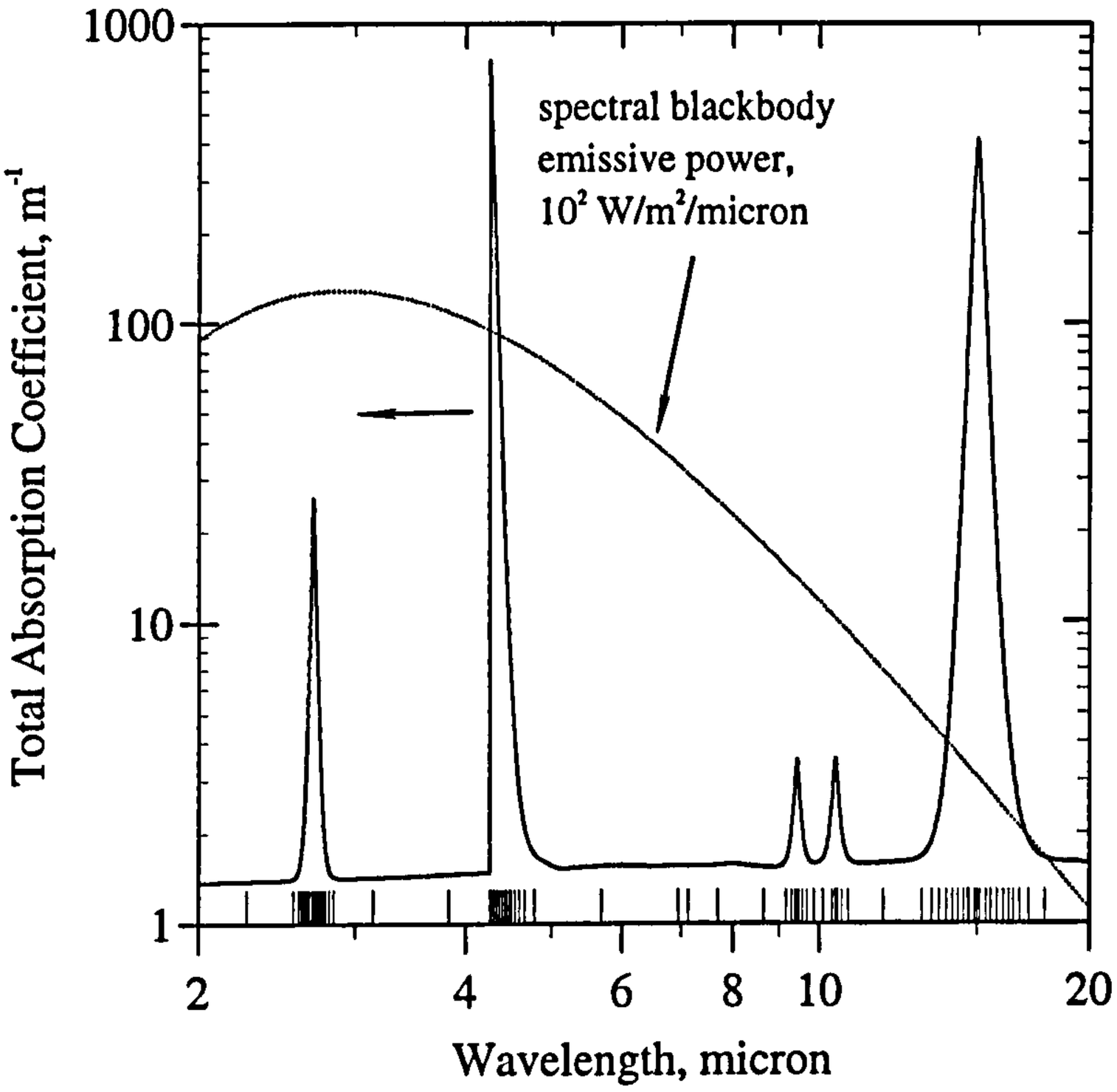

Figure 6.13 Total spectral absorption coefficient for mixture with $2 \cdot 10^9$ particles/m^3. The dotted curve shows the spectral blackbody emissive power variation over the same wavelength interval and the short vertical lines indicate the (80) band centres used in the spectral integration.

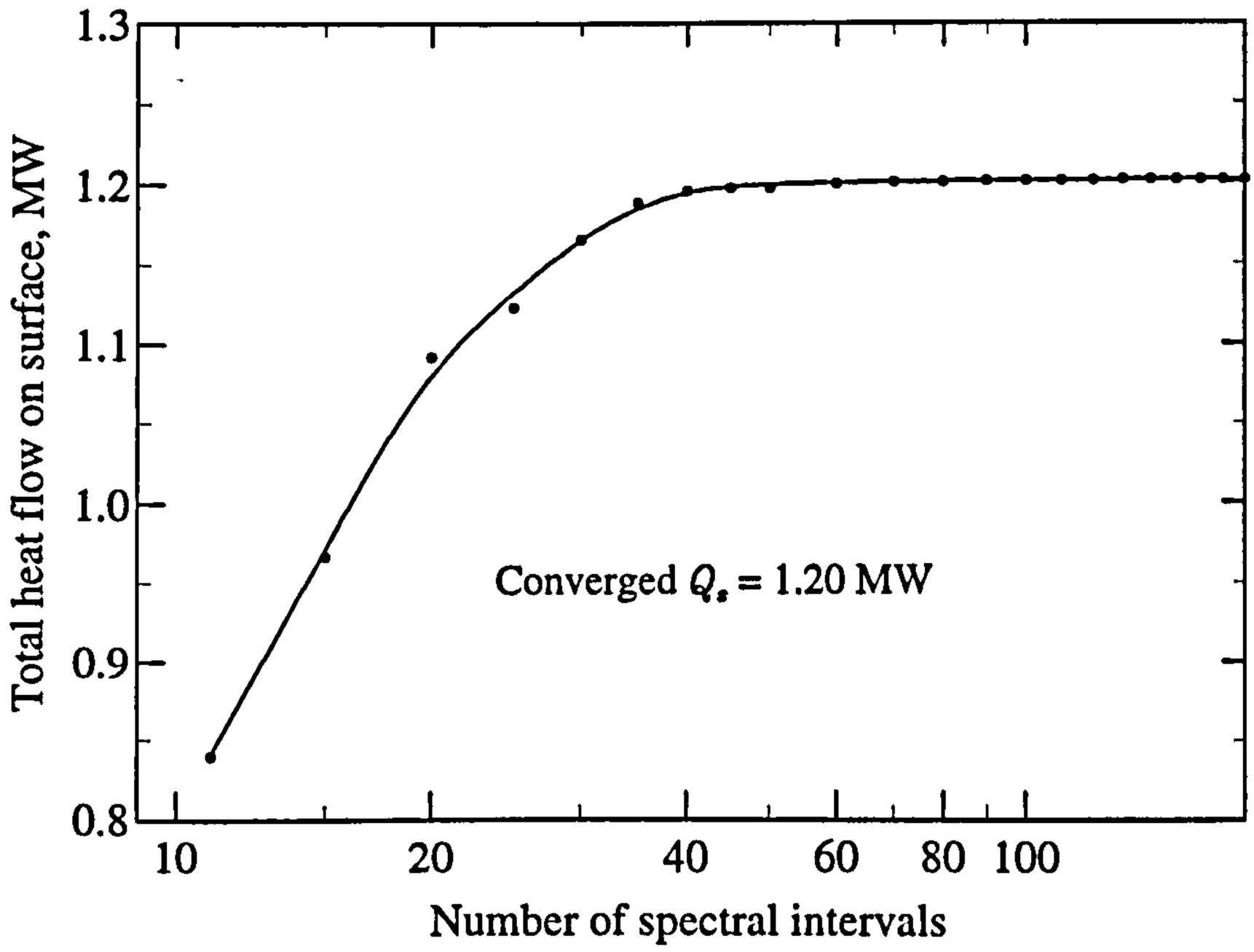

Figure 6.14 Convergence of total surface heat flux for case E4 as the number of intervals is increased in spectral integration.

Table 6.16 Nongray discrete transfer solutions for surface heat flux (W/m^2).

			2×10^7 particles/m^3			2×10^8 particles/m^3			2×10^9 particles/m^3		
			E1	E2	E3	E4	E5	E6	E7	E8	E9
x	y	z	$a=0$	$a=1$	$a=2$	$a=0$	$a=1$	$a=2$	$a=0$	$a=1$	$a=2$
0			10535	10536	10539	22618	22693	22729	48658	48860	48867
W/8	0	H/2	10463	10463	10466	22356	22426	22460	48236	48419	48426
W/4			10191	10190	10192	21455	21541	21544	46720	46866	46877
3W/8			9552	9550	9552	19546	19589	19613	42628	42708	42718
		0	10389	10532	10575	21897	22435	22592	48926	49032	49040
		H/8	10352	10595	10652	21742	22653	22868	48830	49204	49218
		H/4	10100	10538	10636	20891	22456	22828	48106	49134	49214
0	L/2	3H/8	9523	10409	10582	19068	21996	22651	45148	49008	49294
		H/2+a/4	-	9968	10293	-	20473	21611	-	48075	48983
		H/2+a/2	-	9633	9992	-	19380	20573	-	46615	48568
		H/2+3a/4	-	8955	9460	-	17371	18795	-	42410	46356
		0	10652	10728	10748	23197	23471	23549	49116	49116	49120
W/2	0	H/8	10578	10699	10735	22929	23364	23494	48944	48995	49020
		H/4	10313	10440	10465	21991	22459	22558	48119	48256	48264
		3H/8	9729	9853	9856	20057	20510	20550	44975	45153	45174
	0		10652	10728	10748	23197	23471	23549	49116	49116	49120
W/2	L/8	0	10608	10722	10763	23019	23477	23617	49057	49197	49179
	L/4		10431	10564	10608	22350	22848	23007	48819	48890	48881
	3L/8		9929	10065	10114	20581	21084	21253	47232	47317	47314
		0	10431	10564	10608	22350	22848	23007	48819	48890	48881
		H/8	10365	10594	10662	22106	22953	23207	48620	48890	48972
		H/4	10125	10534	10638	21261	22717	23104	47837	48780	48858
W/2	L/4	3H/8	9531	10398	10558	19339	22211	22804	44760	48594	48658
		H/2+a/4	-	9846	10081	-	20252	21064	-	47182	47800
		H/2+a/2	-	9410	9781	-	18807	19995	-	45487	47369
		H/2+3a/4	-	8847	9243	-	17116	18192	-	41467	45240

Table 6.17 Nongray discrete transfer solutions for flux divergence (W/m^3).

			2×10^7 particles/m^3			2×10^8 particles/m^3			2×10^9 particles/m^3		
			E1	E2	E3	E4	E5	E6	E7	E8	E9
x	y	z	$a=0$	$a=1$	$a=2$	$a=0$	$a=1$	$a=2$	$a=0$	$a=1$	$a=2$
0			7565	7519	7498	25219	25057	24983	13605	13444	13432
W/8	0	0	7843	7816	7806	25734	25619	25569	17218	17093	17093
W/4			8688	8703	8685	27073	27051	26983	30720	30690	30698
3W/8			11637	11712	11700	31022	31107	31053	67379	67498	67510
		0	7565	7519	7498	25219	25057	24983	13605	13444	13432
0	0	H/8	7736	7625	7602	25585	25276	25192	15273	14735	14713
		H/4	8227	8085	8063	26493	26144	26061	22862	21589	21534
		3H/8	10279	10144	10081	29619	29319	29154	51051	48716	48645
	0		7565	7519	7498	25219	25057	24983	13605	13444	13432
0	L/8	0	7615	7531	7506	25352	25089	24994	13912	13312	13194
	L/4		7853	7738	7674	25920	25588	25393	16295	15645	15568
	3L/8		8969	8846	8796	27933	27594	27436	32013	31357	31321
	0		9244	9162	9142	28127	27906	27831	38670	37709	37618
W/4	L/8	H/4	9289	8671	8597	28245	26905	26686	38962	33400	33128
	L/4		9488	8911	8812	28717	27555	27271	40913	33132	32788
	3L/8		10557	9929	9830	30644	29375	29094	54407	46808	46463
		0	8688	8703	8685	27073	27051	26983	30720	30690	30698
W/4	0	H/8	8782	8747	8718	27264	27133	27036	32071	31709	31651
		H/4	9244	9162	9142	28127	27906	27831	38670	37709	37618
		3H/8	11202	11138	11082	31091	30928	30790	64533	62734	62517
		0	7853	7738	7674	25920	25588	25393	16295	15645	15568
		H/8	8034	7756	7685	26305	25631	25413	17994	15493	15374
		H/4	8516	7845	7729	27189	25833	25502	25384	16404	16093
0	L/4	3H/8	10540	8063	7889	30235	26297	25843	53127	18936	17960
		H/2+a/4	-	9083	8632	-	28281	27412	-	32121	26416
		H/2+a/2	-	9965	9062	-	29725	28368	-	45594	31047
		H/2+3a/4	-	13035	10449	-	34024	30670	-	79962	50287
		0	8969	8846	8796	27933	27594	27436	32013	31357	31321
		H/8	9134	8908	8827	28264	27716	27478	33743	31480	31287
		H/4	9595	8932	8809	29114	27785	27449	40254	31595	31196
0	3L/8	3H/8	11506	9008	8857	31951	27975	27569	65519	32296	31474
		H/2+a/4	-	9595	9088	-	29136	28167	-	40231	33476
		H/2+a/2	-	10526	9411	-	30712	28910	-	52600	36962
		H/2+3a/4	-	13456	10787	-	34638	31161	-	85888	55826

Table 6.18 Nongray YIX solutions for surface heat flux (W/m^2).

			2×10^7 particles/m^3			2×10^8 particles/m^3			2×10^9 particles/m^3		
			E1	E2	E3	E4	E5	E6	E7	E8	E9
x	y	z	$a=0$	$a=1$	$a=2$	$a=0$	$a=1$	$a=2$	$a=0$	$a=1$	$a=2$
0			10505	10507	10508	22607	22687	22701	50283	50513	50516
W/8	0	H/2	10459	10461	10462	22428	22506	22520	49891	50113	50116
W/4			10276	10278	10279	21797	21870	21883	48363	48560	48563
3W/8			9539	9541	9542	19619	19682	19694	44182	44337	44340
		0	10411	10547	10591	22071	22582	22744	50870	50960	50962
		H/8	10362	10600	10662	21873	22743	22978	50707	51015	51026
		H/4	10176	10611	10705	21178	22714	23070	49914	50997	51035
0	L/2	3H/8	9579	10440	10600	19353	22191	22786	46875	50895	51025
		H/2+a/4	-	10107	10289	-	20916	21684	-	49856	50891
		H/2+a/2	-	9608	10013	-	19385	20721	-	48262	50497
		H/2+3a/4	-	9110	9469	-	17894	18934	-	44111	48409
		0	10635	10706	10728	23174	23441	23520	50651	50672	50672
W/2	0	H/8	10563	10671	10700	22911	23309	23415	50470	50529	50531
		H/4	10296	10440	10466	21983	22509	22606	49636	49776	49779
		3H/8	9777	9896	9901	20288	20736	20776	46560	46808	46811
	0		10635	10706	10728	23174	23441	23520	50651	50672	50672
W/2	L/8	0	10598	10705	10741	23024	23426	23559	50627	50680	50681
	L/4		10423	10560	10607	22378	22895	23063	50424	50510	50512
	3L/8		9913	10053	10103	20621	21136	21313	48983	49065	49067
		0	10423	10560	10607	22378	22895	23063	50424	50510	50512
		H/8	10351	10580	10651	22122	22971	23225	50249	50544	50554
		H/4	10110	10529	10629	21286	22770	23142	49438	50453	50488
W/2	L/4	3H/8	9579	10413	10574	19580	22329	22923	46399	50194	50316
		H/2+a/4	-	9810	10089	-	20228	21196	-	48718	49544
		H/2+a/2	-	9428	9794	-	18968	20142	-	47097	49074
		H/2+3a/4	-	8860	9276	-	17277	18421	-	43047	47110

Table 6.19 Nongray YIX solutions for flux divergence (W/m^3).

			2×10^7 particles/m^3			2×10^8 particles/m^3			2×10^9 particles/m^3		
			E1	E2	E3	E4	E5	E6	E7	E8	E9
x	y	z	$a=0$	$a=1$	$a=2$	$a=0$	$a=1$	$a=2$	$a=0$	$a=1$	$a=2$
0			8398	8333	8317	26213	26013	25948	15153	14966	14961
W/8	0	0	8609	8543	8527	26572	26369	26303	18529	18350	18345
W/4			9399	9330	9313	27798	27587	27523	31198	31037	31033
3W/8			11907	11857	11845	31230	31071	31021	64159	64034	64031
		0	8398	8333	8317	26213	26013	25948	15153	14966	14961
0	0	H/8	8517	8415	8402	26455	26172	26116	16643	16155	16143
		H/4	9007	8851	8837	27365	26976	26919	23488	22361	22337
		3H/8	10725	10528	10524	29987	29555	29530	47961	45904	45872
	0		8398	8333	8317	26213	26013	25948	15153	37478	14961
0	L/8	0	8446	8344	8320	26342	26050	25955	15367	33998	14900
	L/4		8655	8520	8488	26834	26457	26341	17066	32598	16310
	3L/8		9589	9455	9422	28555	28185	28064	28794	42355	28078
	0		9934	9787	9768	28807	28438	28369	38450	31037	37458
W/4	L/8	H/4	9970	9555	9483	28903	28027	27809	38609	32058	33846
	L/4		10144	9536	9446	29312	28078	27809	39893	37478	32332
	3L/8		10925	10339	10245	30751	29559	29284	49345	58666	42096
		0	9399	9329	9312	27798	27588	27523	31198	16333	31033
W/4	0	H/8	9497	9400	9382	27998	27725	27655	32472	16044	32049
		H/4	9934	9787	9768	28807	28438	28369	38450	16788	37458
		3H/8	11494	11319	11313	31156	30768	30739	60444	18963	58639
		0	8655	8520	8488	26833	26457	26341	17066	16333	16310
		H/8	8770	8488	8438	27064	26389	26222	18500	16044	15961
		H/4	9236	8560	8473	27913	26547	26285	25164	16788	16480
0	L/4	3H/8	10944	8757	8584	30513	26972	26521	49308	18963	17935
		H/2+a/4	-	9716	9257	-	28851	27990	-	31002	24313
		H/2+a/2	-	10653	9646	-	30437	28852	-	44143	28162
		H/2+3a/4	-	13169	10801	-	33885	30795	-	75559	43975
		0	9589	9455	9422	28555	28185	28064	28794	28100	28078
		H/8	9688	9414	9363	28752	28093	27922	30041	27695	27614
		H/4	10092	9441	9350	29476	28160	27890	35912	27887	27587
0	3L/8	3H/8	11666	9536	9368	31835	28392	27951	58091	28771	27773
		H/2+a/4	-	10200	9594	-	29731	28534	-	36770	29149
		H/2+a/2	-	10953	9917	-	30919	29264	-	48407	32206
		H/2+3a/4	-	13392	11024	-	94236	31110	-	78653	47399

Table 6.20 Nongray Monte Carlo solutions for surface heat flux (W/m^2).

			2×10^7 particles/m^3			2×10^8 particles/m^3			2×10^9 particles/m^3		
			E1	E2	E3	E4	E5	E6	E7	E8	E9
x	y	z	$a=0$	$a=1$	$a=2$	$a=0$	$a=1$	$a=2$	$a=0$	$a=1$	$a=2$
0			10477	10527	10526	22515	22665	22700	50942	51357	
W/8	0	H/2	10411	10435	10470	22411	22338	22344	50544	50789	
W/4			10084	10177	10134	21436	21549	21520	48929	49039	
3W/8			9530	9539	9488	19562	19585	19654	44051	44350	
		0	10452	10561	10577	21945	22539	22696	50533	50955	
		H/8	10382	10499	10568	21708	22627	22924	50328	50993	
		H/4	10049	10494	10590	20984	22468	22813	49612	51092	
0	L/2	3H/8	9441	10392	10502	19101	21948	22706	45749	50824	
		H/2+a/4	-	9962	10193	-	20623	21563	-	49523	
		H/2+a/2	-	9480	9944	-	19401	20581	-	47983	
		H/2+3a/4	-	8879	9359	-	17469	18625	-	43342	
		0	10627	10732	10680	23050	23281	23394	52135	52092	
W/2	0	H/8	10569	10587	10697	22807	23175	23242	51867	51954	
		H/4	10275	10401	10420	21857	22410	22475	50717	50983	
		3H/8	9602	9807	9817	19952	20471	20458	46866	47320	
	0		10627	10732	10680	23050	23281	23394	52135	52092	
W/2	L/8	0	10536	10653	10749	22855	23249	23414	52041	52082	
	L/4		10409	10492	10550	22185	22690	22908	51616	51852	
	3L/8		9917	10017	10053	20454	20917	21052	49426	49635	
		0	10409	10492	10550	22185	22690	22908	51616	51852	
		H/8	10323	10538	10636	21974	22760	23009	51432	51860	
		H/4	10078	10480	10579	21131	22544	22968	50354	51688	
W/2	L/4	3H/8	9484	10335	10499	19253	22119	22653	46515	51348	
		H/2+a/4	-	9765	10020	-	20113	21041	-	49339	
		H/2+a/2	-	9359	9728	-	18751	19889	-	47405	
		H/2+3a/4	-	8726	9179	-	16827	18162	-	42849	

Table 6.21 Nongray Monte Carlo solutions for flux divergence (W/m^3).

			2×10^7 particles/m^3			2×10^8 particles/m^3			2×10^9 particles/m^3		
			E1	E2	E3	E4	E5	E6	E7	E8	E9
x	y	z	$a=0$	$a=1$	$a=2$	$a=0$	$a=1$	$a=2$	$a=0$	$a=1$	$a=2$
0			7869	7401	7434	25654	25279	25506	19436	19130	
W/8	0	0	7859	7722	7709	26042	25664	25559	22863	22591	
W/4			8668	8463	8496	26929	27064	26961	36222	35907	
3W/8			11666	11560	11578	31104	30927	30755	70697	70529	
		0	7869	7401	7434	25654	25279	25506	19436	19130	
0	0	H/8	7418	7573	7519	26030	25507	25312	21079	20386	
		H/4	8037	7975	8032	26642	26397	26227	28726	27557	
		3H/8	10378	10007	9985	29554	29136	28992	57140	53472	
	0		7869	7401	7434	25654	25279	25506	19436	19130	
0	L/8	0	7467	7234	7410	25819	25276	25203	19437	18520	
	L/4		7725	7658	7644	26233	25832	25615	22007	21231	
	3L/8		8963	8845	8829	27965	27754	27601	38216	38044	
	0		9147	8946	8912	28185	27746	27823	44899	43276	
W/4	L/8	H/4	9312	8652	8729	28273	27523	27109	45367	39438	
	L/4		9488	8719	8770	28621	27460	27161	47119	38425	
	3L/8		10333	9614	9593	30451	29087	28771	60686	52170	
		0	8668	8463	8496	26929	27064	26961	36222	35907	
W/4	0	H/8	8752	8659	8544	27445	27127	27012	37867	37086	
		H/4	9147	8946	8912	28185	27746	27823	44899	43276	
		3H/8	10995	10787	10741	30804	30385	40336	70118	67313	
		0	7725	7658	7644	26233	25832	25615	22007	21231	
		H/8	7912	7701	7660	26346	25796	25559	23946	20610	
		H/4	8518	7646	7720	27256	25937	25706	31675	22134	
0	L/4	3H/8	10469	8063	7825	30118	26222	25960	58274	24896	
		H/2+a/4	-	8875	8515	-	28381	27389	-	39857	
		H/2+a/2	-	9907	9097	-	29844	28425	-	53746	
		H/2+3a/4	-	12709	10223	-	33853	30532	-	86226	
		0	8963	8845	8829	27965	27754	27601	38216	38044	
		H/8	9113	8876	8758	28374	27721	27528	40268	37246	
		H/4	9566	8780	8715	29036	27612	27529	47094	37729	
0	3L/8	3H/8	11480	8925	8718	31593	28039	27543	71299	39085	
		H/2+a/4	-	9510	8977	-	29294	28067	-	47655	
		H/2+a/2	-	10288	9316	-	30533	28854	-	60143	
		H/2+3a/4	-	13264	10531	-	34125	30983	-	90757	

Table 6.22 Case E4 solution comparisons for surface radiative heat flux (kW/m^2) and flux divergence (W/m^3) at sample point locations.

	$q_s(x, 0, H/2)$							
x	MC	YIX	DT	S_n [a]	YIX[b]	FE[c]	DEF[d]	MC[e]
0	22.5	22.6 (0.4%)[f]	22.6 (0.4%)	25.0 (0.1%)	23.5 (4.4%)	22.3 (-0.9%)	22.6 (0.4%)	23.0 (2.2%)
W/8	22.4	22.4 (0.0%)	22.4 (0.0%)	24.5 (9.4%)	23.3 (4.0%)	22.0 (-1.8%)	21.5 (-4.0%)	22.4 (0.0%)
W/4	21.4	21.8 (1.9%)	21.5 (0.5%)	23.0 (7.5%)	22.5 (5.1%)	21.0 (-1.9%)	20.3 (-5.1%)	21.5 (0.5%)
3W/8	19.6	19.6 (0.0%)	19.5 (-0.5%)	19.7 (0.5%)	20.1 (2.6%)	19.1 (-2.6%)	18.6 (-5.1%)	19.8 (1.0%)

	$\nabla \cdot \mathbf{q}_r(x, 0, 0)$							
x	MC	YIX	DT	S_n [a]	YIX[b]	FE[c]	DEF[d]	MC[e]
0	25.7	26.0 (1.2%)[f]	25.2 (-1.9%)	26.3 (2.3%)	26.0 (1.2%)	26.4 (2.7%)	26.8 (4.3%)	25.1 (-2.3%)
W/8	26.0	26.4 (1.5%)	25.7 (-1.2%)	27.1 (4.2%)	26.3 (1.2%)	26.7 (2.7%)	29.6 (13.8%)	26.1 (0.4%)
W/4	26.9	27.7 (3.0%)	27.0 (0.4%)	30.5 (13.4%)	27.5 (2.2%)	28.0 (4.1%)	32.4 (20.4%)	26.1 (-3.0%)
3W/8	31.1	31.1 (0.0%)	31.0 (-0.3%)	37.7 (21.2%)	32.5 (4.5%)	31.3 (0.6%)	35.0 (12.5%)	31.6 (1.6%)

[a]Hoover *et al.* (1996).

[b]Hsu *et al.* (1994).

[c]Burns *et al.* (1995).

[d]Naraghi and Litkouhi (1989).

[e]Farmer and Howell (1994).

[f]Deviation of value as % of present MC value.

N.B. $g' = 0$ in DT & FE solutions (see Sec. 6.2).

Table 6.23 Comparison of weighted-sum-of-gray-gases (WSGG) models.
M1 = Bandwise (80 intervals). M2 = Banded solution using absorption cross-sections.
(N.B. Gray gases in the spectral subdivision solved via the discrete transfer method.)

	Gray gases	CPU run time on HP-9000/750 [s]		Speed-up[a]	Average relative difference[b] [%]		Max. relative difference[c] [%]	
Case	M2	M1	M2	×	q_s	$\nabla \cdot \mathbf{q}_r$	q_s	$\nabla \cdot \mathbf{q}_r$
E1	7	2082	252	8.3	0.48	1.29	1.73	4.41
E2	7	3312	395	8.4	0.49	1.24	1.84	5.06
E3	7	3256	385	8.5	0.50	1.22	1.87	5.69
E4	9	2111	350	6.0	0.29	1.34	0.85	2.71
E5	9	3360	550	6.1	0.32	1.33	1.00	2.71
E6	9	3350	544	6.2	0.29	1.32	0.89	2.71
E7	8	2959	410	7.2	0.21	0.51	0.71	1.17
E8	8	4707	580	8.1	0.30	0.58	0.94	2.01
E9	8	4696	571	8.2	0.29	0.56	0.91	1.99

[a]Speed-up = CPU time M1/CPUtime M2.

[b]Average relative difference: $\mathrm{ARD} = 1/n \sum |(\mathrm{M2} - \mathrm{M1})/\mathrm{M1}|$ for all n values.

[c]Maximum relative difference: $\mathrm{MRD} = MAX\,|(\mathrm{M2} - \mathrm{M1})/\mathrm{M1}|$

Part A: Summary

1. The present Monte Carlo, YIX and discrete transfer solutions very closely agree with benchmark results for radiatively participating media. Difficulties considered include nonorthogonal geometries, nonhomogeneous properties, optically thin and thick limits, scattering anisotropy, hot/cold boundary conditions and nongray behaviour.

2. Solutions are in excellent agreement for optically thin-to-moderately thick (gray) media (i.e. $\tau < 1$), but discrepancies arise in thicker media. Pathlength-based Monte Carlo solutions suffer increasing statistical uncertainty for a given level of computation since the energy bundles travel short distances and contribute to fewer results. The YIX and discrete transfer methods fail to capture radiative property gradients adequately and differences in their methodologies for the calculation of medium heat sources are exacerbated. On balance, discrete transfer values are more representative of the *volume averaged* heat sources in optically thick elements, but errors can be high.

3. Ray effect leads to irregularities or biasing in discrete transfer and YIX solutions: a finer angular discretisation can lessen this problem.

4. The discrete transfer method is restricted to isotropic scattering. YIX can handle linear anisotropic scattering with little additional effort.

5. Monte Carlo run times are of the order 10^2 times those of the deterministic methods. YIX calculations are more expensive than discrete transfer ones due to time required to (i) trace additional rays in the medium integration and to (ii) post-process path length information into optical coordinates. Here, the first factor scales with mesh size and the second with optical thickness. This time disadvantage is mitigated somewhat in iterative solutions where the YIX distance integration avoids the expensive exponential calculations of the discrete transfer method.

6. Nongray solutions are highly sensitive to the fidelity of the gray gas approximation in a WSGG analysis. These solutions are essentially a combination of independent gray gas solutions for optically thick wavenumber intervals at gas band centres and for thin (or thinner) intervals in between. Therefore, discrepancies found between the methods for optically thick gray problems are also evident in their nongray solutions.

PART B: SI ENGINE SIMULATIONS

6.3 Parametric Studies and Comparisons: Ricardo E6 Engine

Radiative heat flux predictions from a parametric study of a Ricardo E6 engine by Blunsdon *et al.* (1993) were found to corroborate several experimentally measured trends. The effect of variations in engine speed, ignition timing, air/fuel ratio and percent exhaust gas recirculation (EGR) were simulated with the mixed gray gas model of Truelove (1976). However, peak heat fluxes due to the gas radiation of 0.4–0.5 MW/m^2 were predicted, whereas measurements are of the order 0.2–0.3 MW/m^2 (e.g. Baker and Laserson 1951). The Truelove correlation also has limited applicability, motivating the development of the present generalised weighted-sum-of-gray-gases (WSGG) model. In order to assess the expected improvements in its predictive ability the study of Blunsdon *et al.* (1993) is repeated here with the new model.

6.3.1 Experimental Observations

The experimental trends modelled by Blunsdon *et al.* (1993) are largely based on those reported by Remboski *et al.* (1989). Radiation measurements were made in the near-infrared at 927.7 ± 20 nm: a H_2O absorption band. This wavelength was chosen since it almost coincided with the peak spectral response of an inexpensive silicon photodiode and was not prone to strong blackbody emission from the combustion chamber walls. For brevity the reader is referred to the reference for details of the instrumentation and data acquisition system. (Also see Nutton and Pinnock 1990.) Key observations made by Remboski *et al.* (1989) are as follows:

1. The luminosity signal L (i.e. intensity) in the near-infrared is negligible during compression until the mass-burn fraction is 1%, except for a weak impulse at the start of ignition. The intensity peaks about 10° after the peak heat-release rate dQ_{max} and about 2° after the peak cylinder pressure P_{max} at the baseline engine operating condition (Fig. 6.15).

2. Retarding the ignition timing or the addition of EGR both reduces the peak pressure and intensity (Fig. 6.16). The former event is also accompanied by an increase in the lag between the pressure and intensity maxima from about 2 – 4° as the timing is retarded.

3. Maximum intensities coincide with maximum IMEP and peak cylinder pressure at a mixture strength slightly rich of stoichiometric (i.e. $\phi \approx 1.1$). The intensity decreases with the peak pressure in richer mixtures, due to poorer combustion efficiency, and in leaner mixtures due to the diluent effect of excess air (Fig 6.17).

These findings are supported by several other studies and, in addition, it is noted that:

4. The principal emitters are CO_2 and H_2O, but CO emission is also important in fuel rich conditions. The continuous radiation from soot (i.e. carbon aggregates) is negligible under normal operating conditions and nearly all the radiant energy is emitted in the infrared spectrum between 1–10 μm (Marvin *et al.* 1934). See Fig. 6.18: here the banded emission of a spark ignition engine contrasts markedly with that of combusting diesel where there is the added presence of a radiative continuum from incandescent soot.

5. For a given engine/optical sensor setup a certain mass-burn fraction (in the order of 90%) can be correlated with the position of the peak intensity. Its actual value depends upon the view angle of the sensor and the geometry of the combustion chamber (Nutton and Pinnock 1990).

6. Knocking combustion is characterised by an abrupt increase in the radiative intensity and coincident phasing with the average pressure rise (c.f. no. 2). Moreover, a sudden change in the intensity signal (due to changes in the combustion chemistry) can indicate that knock is on the threshold of occurring (i.e. borderline knock) when there is no oscillation in the pressure waveform (Nutton and Pinnock 1990). Knock results in a shorter reaction period and lower intensities at the point of exhaust valve opening (evo) compared with normal operation (McComiskey *et al.* 1993).

6.3.2 Present Predictions

Details of the Ricardo E6 engine studied by Blunsdon *et al.* (1993) are given in Table 6.24. To reduce the amount of computation the pancake combustion chamber was modelled as a two-dimensional axisymmetric 0.5° slice with central-ignition as for the original study (Fig. 6.19). Fortunately, strongly non-axisymmetric charge motions cannot be generated by the engine's simple port/ head design. Calculations were started during compression (-144°) with uniform distributions of the state variables within the combustion chamber. The initial gas temperature, pressure and species densities were

determined from the ideal gas equation using experimental pressure data and air/fuel flow rates. The burnt gas composition was estimated from the mole fractions defined in Table 4.3 of Heywood (1988) for a 3% residual gas fraction. The initial turbulent kinetic energy, k was set equal to 3% of the kinetic energy based on the mean piston speed. The dissipation rate was then evaluated from k via Eq. (3.105) with a length scale, y equal to the distance to the nearest solid boundary. Finally, the flow field was initialised with zero radial u and tangential v velocity components and an axial w component varying linearly with z from between u_p at the piston face and zero at the cylinder head. Here u_p is the piston velocity as defined by Eq. (3.111). The wall temperature was fixed at 450 K. A maximum calculation timestep of 0.5° crank angle was specified.

Sensitivity to Model Parameters. The sensitivity of predictions to variations in model parameters (e.g. mesh size, model constants, etc.) was assessed in order to gain some feel for how these factors affect the solution and where attention should be focused in future studies.

Mesh Size. Several analysts have tried to assess the effects of the grid resolution and type on the properties of KIVA numerical schemes (e.g. Amato and Petrillo 1992), but the inherent complexity of in-cylinder fluid dynamics, even in grossly simplified engine models, limits their ability to define any general guidelines. Attention was focused on the combustion phase in the present study since this showed a marked sensitivity to the grid resolution. For example, with a radial and axial grid spacing at TDC of 2.54 and 2.40 mm, respectively (i.e. comparable to that of the original study), the peak pressure was about 10% lower than with spacings of 1.27 and 1.44 mm, respectively (Fig. 6.20). One possible explanation is that small differences in the modelled heat release at ignition affect the flame kernel development and its subsequent propagation. This problem is unavoidable since the calculation timestep, chopper action and dimensions of the spark region all differ to some extent as the mesh size is altered. It was also evident from other predictions that the mesh size may modify the combustion calculation via the boundary layer treatment; i.e. the kinetic rate via the wall heat transfer model, and the mixing-controlled rate via the wall $k-\varepsilon$ model. Further analysis of this is required. Fortunately, it was found that further refinement of the grid had a diminished effect. Consequently, the present predictions used the 1.27 × 1.44 mm grid corresponding to 30 cells in the radial direction and a minimum of 10 cells in the axial direction, at or near TDC, increasing to 23 cells as the piston descends. (The axisymmetric slice is 1 cell thick.)

Combustion Model Constants. Following the recommendations of previous studies the turbulence model constants were assigned the values given in Sec. 3.2.5. The combustion model constants C_A and C_B, which scale the kinetic and overall reaction rates, respectively, were then adjusted to obtain reasonable agreement with measured pressure data. It was found that conditions at the start of ignition, particularly the gas temperature, strongly affected the choice of C_A and C_B. In addition, it was possible to reoptimise the constants for a different set of conditions and still obtain good agreement with measured data. For example, a ± 25 K (i.e. about 7%) variation in the absolute gas temperature at ignition is easily accommodated. However, put another way, this means that specific quantities can be predicted with sizeable error even when the overall level of agreement is 'good'.

Initially, some predictions were made without radiation. C_A and C_B were assigned values of 3.0 and 2.8, respectively. The effect of radiation is to enhance heat losses to the combustion chamber walls leading to lower gas temperatures, slower combustion, and ultimately, a slight underprediction of the peak pressure. This was compensated for by increasing C_B from 2.8 to 3.0 (Fig. 6.21). It is noteworthy that the values of C_A and C_B are somewhat interdependent such that C_A might have been increased instead. In hindsight, this would have made better sense from a theoretical standpoint, since only the kinetic reaction rate is affected by the gas temperature, but in practice it makes little difference which constant is modified. With further work the combined rate expression (i.e. Eq. 3.75) could be better formulated.

Wall Boundary Conditions. Two important parameters in the wall boundary layer model are the laminar Prandtl number, Pr_l and surface emissivity, ε. The Prandtl number appears in the temperature wall function, Eq. (3.103), for the convective wall heat flux and is set to 0.74 (the standard value for air) by default. However, in previous studies it has been used more as an arbitrary constant in order to improve agreement with measured heat flux. For example, Kuo and Reitz (1989) note better predictions using a Prandtl number of 0.6 but at specific locations their model still underpredicted experimental data by as much as 40%. Measurements by Alkidas (1979) indicate peak heat fluxes ranging from $1.5 - 3$ MW/m^2 on the cylinder head. With $Pr_l = 0.74$, peak heat flux values computed in the present study were under 1 MW/m^2 supporting the previous findings that suggest using a laminar Prandtl number of 0.6, or lower. Though one

obvious limitation of both the past and present numerical models is their reliance on a fixed wall temperature. A more realistic description which allows for both temporal and spatial variation should form the basis of future work.

Fortunately, the radiative heat flux prediction is much less sensitive to inaccuracies in the wall temperature description as most emission is from the high temperature burned gases (due to the T^4 dependence). It is very sensitive, however, to the estimated surface emissivity (via Eq. 4.13). Measurements of emissivity range widely and depend on the material type, surface temperature, surface finish, the presence of deposits, radiation wavelength, etc. For example, the total emissivity of polished aluminium alloy is about 0.1 but with carbon deposits the surface becomes almost black (i.e. $\varepsilon = 1$). Given the numerous factors involved it is doubtful whether the limited emissivity data presently available is applicable. Rather it is proposed that a representative value is taken for the emissivity and this is modified within limits in order that predictions match experimental measurements of radiative flux in much the same way that a modified Prandtl number has been used with the (convective) heat flux model. Empirical calculations for radiative flux in diesel engines have used values ranging from 0.75 to 0.9 (Williams 1976). Accordingly, the gray surface emissivity in the present model was nominally taken as $\varepsilon = 0.8$.

Numerical Results. A baseline operating condition was modelled with a spark timing of 20° BTDC, an engine speed of 1500 rpm and near stoichiometric air-fuel ratio of 15.5. Around 500 timesteps where required and nearly 0.5 Mbytes of data is generated on each, all of which cannot be presented here, so the following discussion attempts to highlight the most salient features. Typically, the CFD portion of each timestep required only a few seconds while the radiation calculation took between 1 and 4 minutes. Computations were performed on the Sun workstation discussed in Sec. 6.1.

The calculated pressure and fuel mass fraction burned curves at the baseline condition are plotted in Fig. 6.22, and the sequence of vector/contour plots in Fig. 6.23 shows the gas motion and temperature from 2° crank angle after the spark. Initially the enflamed region is hemispherical and grows in volume uniformly. Compression between the piston and the flame front induces a resultant charge motion upwards and radially outwards. This structure tends to preferentially convect the flame along the cylinder head somewhat distorting its hemispherical shape.

At 5° BTDC the enflamed region impinges on the piston and its axial growth is constrained. The remaining radial front sweeps towards the cylinder walls inducing a clockwise vortex ahead of the flame and an anticlockwise vortex behind. Eventually, the former disappears, as the unburnt charge is totally engulfed, and the later develops into a bulk downwards movement during expansion (i.e. from about 13.5° ATDC). Experimental comparisons may be made with schlieren images of an engine flame by Gatowski *et al.* (1984) – Fig. 6.24. It is seen that the growth of the enflamed region closely resembles that of the present simulation, though the initial flame 'ball' is more spherical and it retains its shape for much longer close to the cylinder head. This points to deficiencies in the present ignition and boundary layer models which do not adequately describe the detailed physics (i.e. laminar kinetics, wall quenching, etc.). The modelled temporal and spatial variation in heat release shows more evidence of this problem. Burning is more fierce in regions of the flame front closest to the cylinder head but this is not observed experimentally. It is also noteworthy that with the original KIVA-II zero-gradient boundary condition for k (see Sec. 3.4.1) combustion along the wall is so severe as to result in a concave (forwards-facing) edge to the modelled flame front. Thus, the present k boundary condition is an improvement, though as noted earlier, further work is still required.

It is also interesting to compare mass fraction burned curves (c.f. Figs. 6.22 and 6.24). The overall burning angle (i.e. 0 to 90% burnt) for the engine in the schlieren study is about 65° crank angle whereas it is only 38° in the present prediction. This is in fact a good result. The field of view in the schlieren images covers the entire width of the combustion chamber such that the spark plug is close to the cylinder wall. Therefore, the centrally located plug in the present geometry would be expected to give approximately twice the flame area of a side plug geometry for a given flame radius and consequently burn about twice as fast, as is the case.

Figure 6.25 shows the variation of net radiative surface heat flux with pressure and heat release. Flux values are for the cylinder wall location shown in Fig. 6.19. Predictions from the present WSGG model are compared with those of the Truelove (1976) mixed gray gas model. (The present numerical scheme allows either gas submodel to be called as desired by the user.) It is observed that the radiative flux computed with the Truelove correlation is comparable to that of Blunsdon *et al.* (1993) and peaks at 0.48 MW/m^2. However, predictions with the present WSGG model are 50% (or more) smaller, and in

much better agreement with measurements, peaking at around 0.23 MW/m^2. This is very encouraging but the wide disparity between the two results is at first surprising, since in its present form, the WSGG model embodies data with comparable levels of error to the wide band correlation data used by Truelove. A likely explanation is that this disparity arises from model extrapolation error, since the Truelove correlation is empirical and primarily for conditions encountered in oil or gas fired combustors. Specifically, an average CO_2/H_2O partial pressure ratio of 1:1 (or 1:2) and a total pressure of 1 atm. This is not to say that the present WSGG prediction is free from extrapolation error, undoubtedly there is some, but its severity is much reduced as, in effect, a separate correlation is made for every condition (of T, p and composition) in the flow field. Accordingly the model is able to accommodate much more detail concerning the localised property variations across the flame front. For example, the CO_2/H_2O molar concentration ratio increases from about 1:1.15 in the coolest flame regions ($\approx$ 800 K) to about 1:1.65 in the hottest flame regions ($\approx$ 2800 K).

Though the radiation models show poor agreement with regard to the strength of the flux, the predicted growth and decline of the flux throughout the combustion is remarkably similar and indicates that, for this aspect at least, the detail of the combustion model has a much greater influence than that of the radiation model. The relative timing of the flux history with the heat release and pressure follows experimental trends: the radiative flux is negligible until the fuel mass-burn fraction is about 1-2% (c.f. Fig. 6.22 with Fig. 6.25) and then it rises to a peak value some 6° after the peak in heat release rate and 2° after the peak pressure. This point corresponds to a time at the tail end of combustion, when the gas temperature is just starting to fall and the product mass fraction is nearing its maximum (Fig. 6.26). The fuel mass-burn fraction is about 95%. Subsequently, the radiative flux falls away during the expansion stroke mainly due to its T^4 dependence on the gas temperature.

The relative importance of emission from the CO_2 and H_2O combustion products is shown in Fig. 6.27. (This information was obtained by performing an auxiliary radiation calculation with only *one* radiating product in the WSGG analyses, prior to a full calculation to ensure that the radiative source terms were unaltered.) Radiation from the water vapour amounts to about 2/3 of the total combined CO_2/H_2O radiative heat transfer. This result is explained by referring back to the model absorption spectrum of Fig. 5.2. It is seen that the four H_2O bands cover a much wider range of wavenumbers than the four

CO_2 bands and have comparable levels of absorption. Some preliminary calculations were also made with the 4.67 and 2.35 μm CO bands and 5.35 μm NO band included in the WSGG analysis. The results indicated that these products contribute only a few percent of the total radiative heat transfer at the baseline operating condition. However, a more thorough analysis with CO and NO, including testing of their correlation parameters in Table 5.1, is left for a future work.

The optical investigations referenced in Sec. 6.3.1 all used a single sensor at a fixed location. An important advantage of the numerical model is that it is able to map the radiative heat flux over the entire chamber surface. For the present axisymmetric geometry this may be shown on two-dimensional plots – Fig. 6.28. Radial flux profiles on the cylinder head and piston top, and axial profiles along the cylinder wall, are plotted in 5° crank angle steps upto the time of (or near) maximum flux. As the flame propagates across the combustion chamber it radiates more strongly to *all* surfaces such that there is no significant difference in the phasing of the peak radiative flux at different wall locations. However, in the early stages of combustion, the flux magnitude does vary strongly with position, most notably on the cylinder head. Ahead of the flame front it falls away sharply with increasing radius since emission from the flame volume strikes the surface more obliquely. At the end of combustion the burnt gas radiates more uniformly to the walls, but the peak flux is still some 10% lower on the cylinder wall compared with that on the cylinder head. This result is of practical importance if optoelectronics are used as an engine diagnostic and/or control signal. For maximum signal output it would seem best to site an optical sensor as close as possible to the spark plug, or even integrate it into the plug itself, avoiding the need for additional access holes (see Nutton and Pinnock 1990). Deposit build-up is also discouraged if the probe tip extends well beyond the combustion chamber wall into the combustion space.

Figure 6.29 shows two more predictions with the spark timing retarded and advanced, but all other parameters, including the model parameters, unchanged. As before the Truelove (1976) correlation is believed to substantially overpredict the radiative heat flux and more confidence is placed with the present WSGG model result. (See discussion above.) With the spark at 14° BTDC the combustion extends later into the expansion stroke and the peak pressure (and temperature) are delayed and reduced in magnitude. Consequently, the peak radiative flux is also delayed, and about 12% lower (than the baseline value), but it does not fall-off so rapidly.

Advancing the spark timing has a reverse effect. With the spark at 26° BTDC the engine is knocking and this behaviour is captured well by the autoignition model. Rapid burning of the end-gas results in an abrupt rise in the (averaged and localised) pressure, temperature and product concentration. Consequently, the peak radiative flux is greater (by about 16%) and almost coincident with the peak average cylinder pressure. These trends are confirmed by experimental observations.

Further calculations were made with a parametric variation of the spark timing ($14° \leq \theta \leq 26°$ BTDC) and of the air-fuel ratio ($0.8 \leq \phi \leq 1.1$) in an attempt to reproduce the experimental correlations found by Remoboski *et al.* (1989) in Figs. 6.16 and 6.17. The present results are plotted in Fig. 6.30. The peak radiative flux at each condition is normalised by the peak flux at the baseline condition. The expected correlation is obtained between the modelled peak flux and peak cylinder pressure for the variation in spark timing, and arguably, for the variation in air-fuel ratio in spite of differences in the position of the 'rich' mixture point. Here, it must be remembered that the latter study is based on a *fixed* spark timing (i.e. 20° BTDC), whereas the experimental results are at MBT timing. Thus, maximum quantities are predicted (correctly) at the baseline operating condition ($\phi \approx 1$) where the fixed timing coincides most closely with MBT. At richer and leaner conditions the MBT spark advance increases.

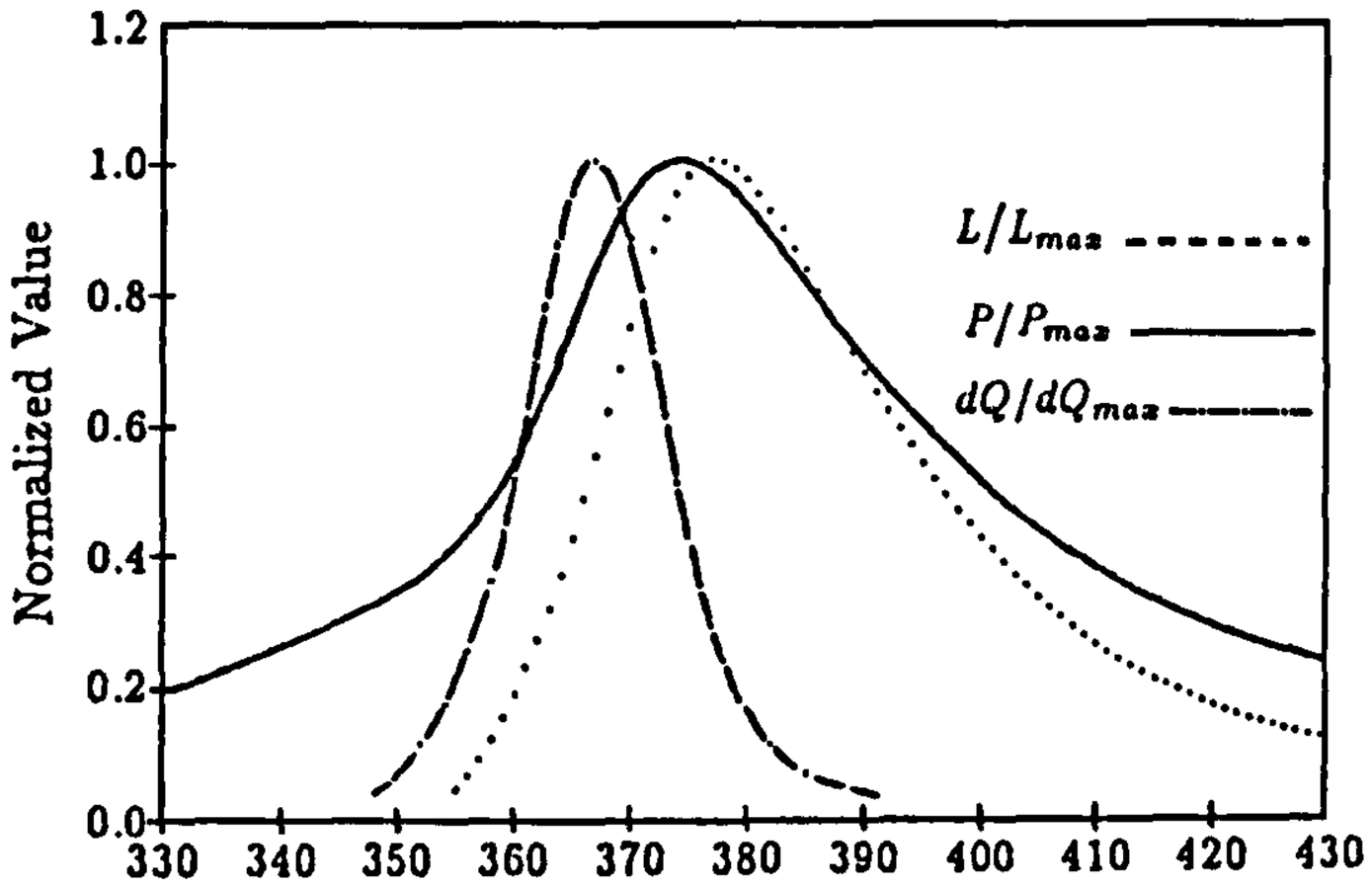

Figure 6.15

Comparison of pressure, heat release rate and luminosity for a baseline operating condition (i.e. 2400 rpm, WOT, MBT & an air-fuel ratio of 14.6).

Reference:
Remboski *et al.* (1989).

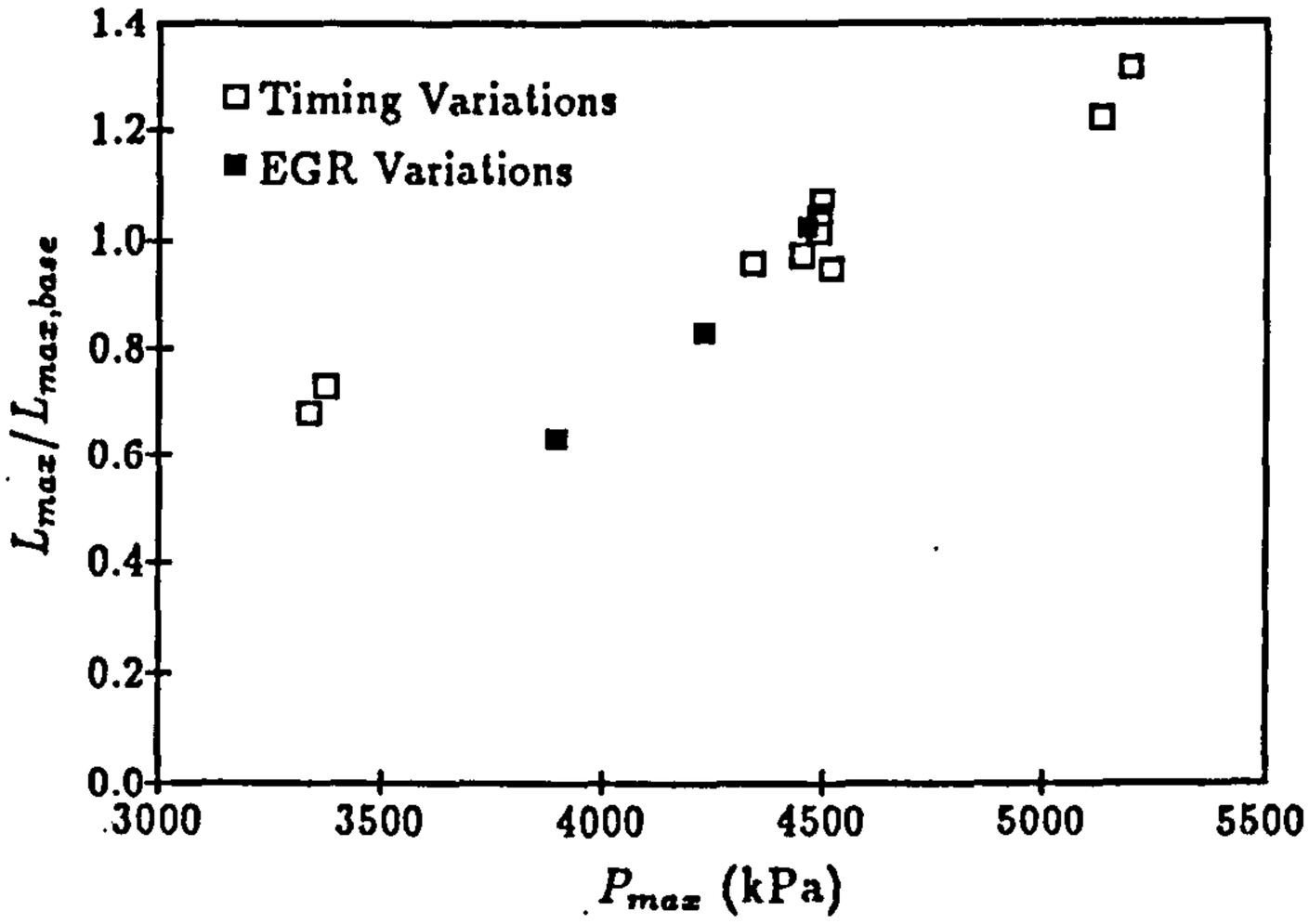

Figure 6.16

Correlation of normalised peak luminosity with peak pressure for speed and air-fuel ratio variations at WOT.

Reference:
Remboski *et al.* (1989).

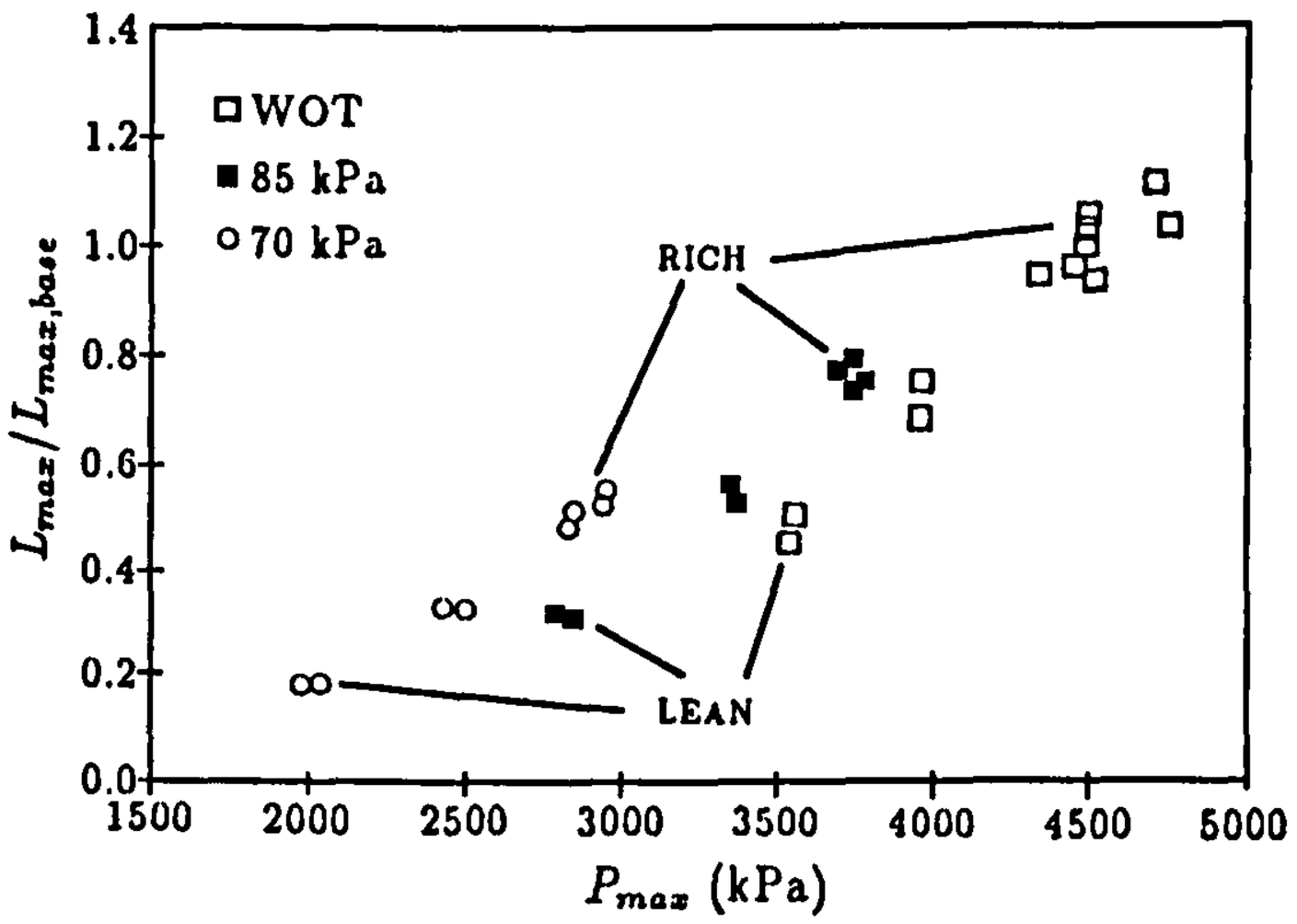

Figure 6.17

Correlation of normalised peak luminosity and peak pressure for intake manifold pressure and air-fuel ratio variations at 2400 rpm.

Reference:
Remboski *et al.* (1989).

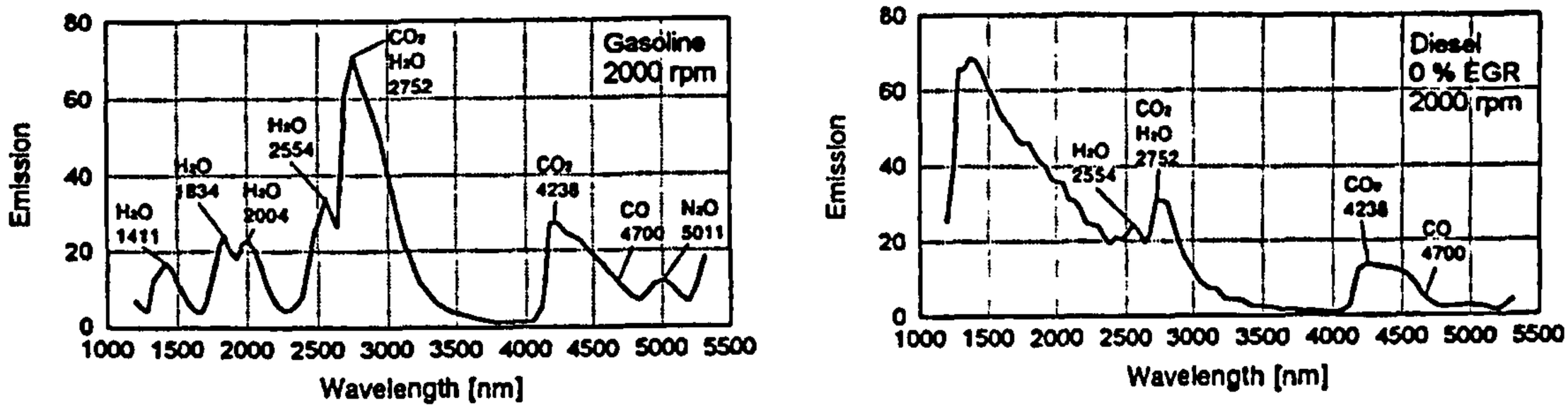

(a) (b)

Figure 6.18 Sample infrared spectrometer recordings of combusting (a) gasoline and (b) diesel. Reference: Ohmstede and Hentschel (1995).

Table 6.24 Design and operating parameters for engines studied.

	Ricardo E6[a]	**Ricardo Hydra**
Bore	76.20 mm	80.065 mm
Stroke	111.1 mm	79.35 mm
Connecting rod length	241.3 mm	132.0 mm
Swept volume	506.7 cc	399.5 cc
Compression ratio (geometric)	8.70	9.22
Inlet valves (poppet type)	1	2 (identical)
Exhaust valves (poppet type)	1	2 (identical)
Inlet valve diameter/maximum lift	-	25.5/8.53 mm
Exhaust valve diameter/maximum lift	-	22.5/9.79 mm
Inlet valve opens	-	-372° ATDC[b]
Inlet valve closes	-	-124° ATDC
Exhaust valve opens	-	-596° ATDC
Exhaust valve closes	-	-348° ATDC
Engine speed	1500 rpm	1500 rpm
Fuel	iso-octane C_8H_{18}	propane C_3H_{18}
Equivalence ratio (air/fuel ratio)	0.97 (15.5)	0.88 (17.8)
Ignition timing(s) BTDC	14°, 20°, 26°	15°

[a]See Blunsdon *et al.* (1993).

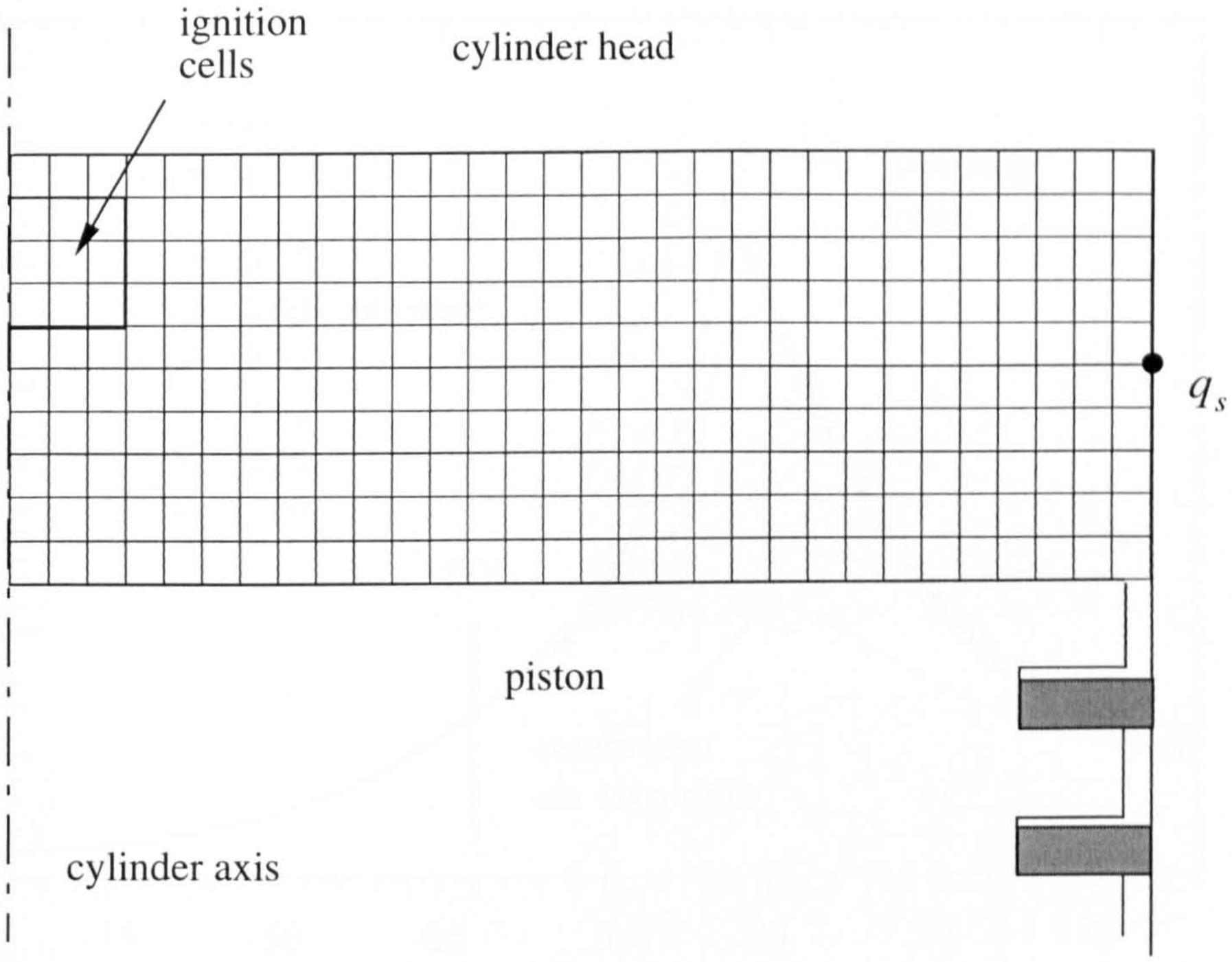

Figure 6.19 Ricardo E6: Computational mesh at TDC (30×1×10 cells). Radiative flux predictions in Figs. 6.25-29 are at the wall location marked by q_s.

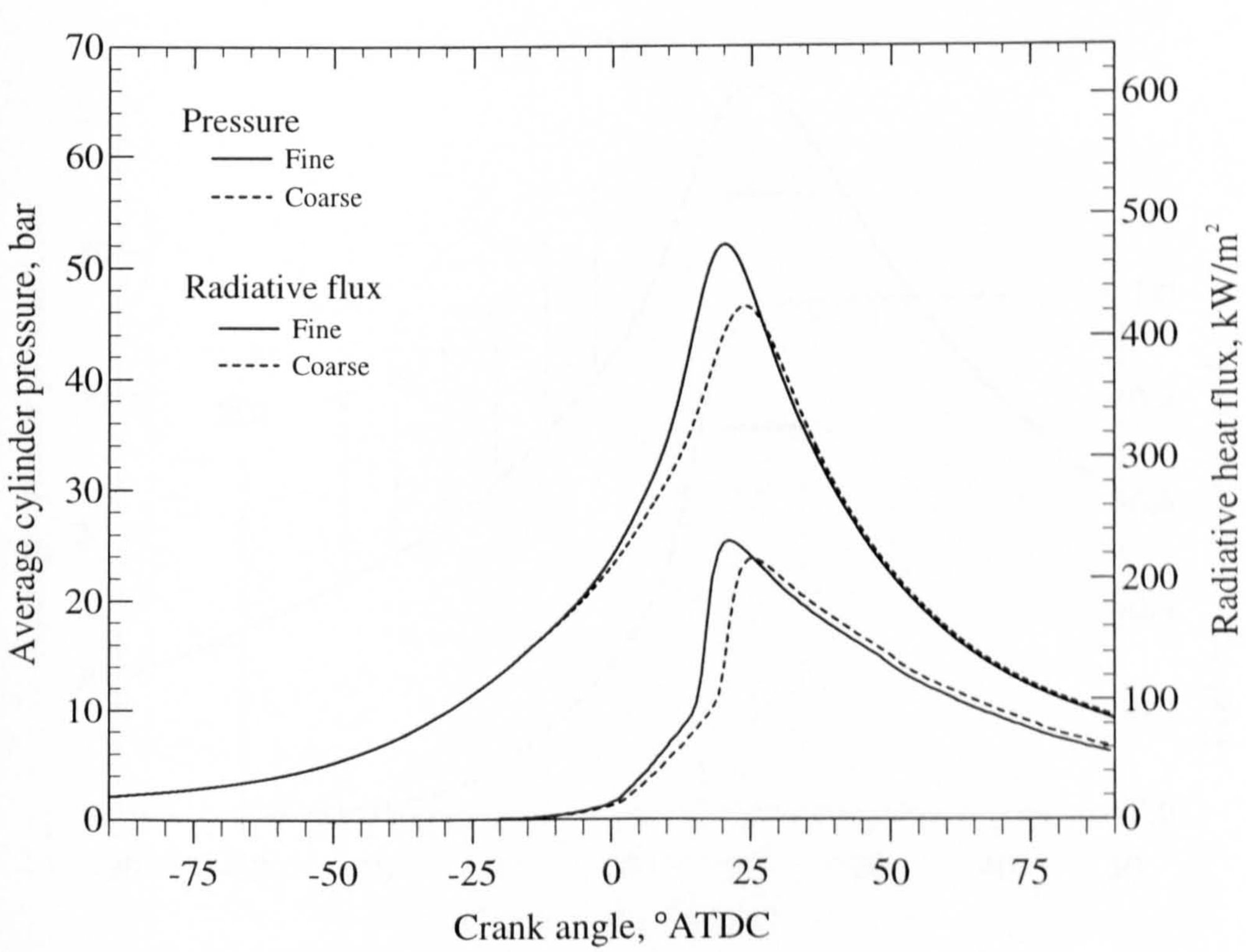

Figure 6.20 Grid dependency study for Ricardo E6 axisymmetric geometry. Coarse mesh has 15×1×6 cells and fine mesh has 30×1×10 cells at TDC.

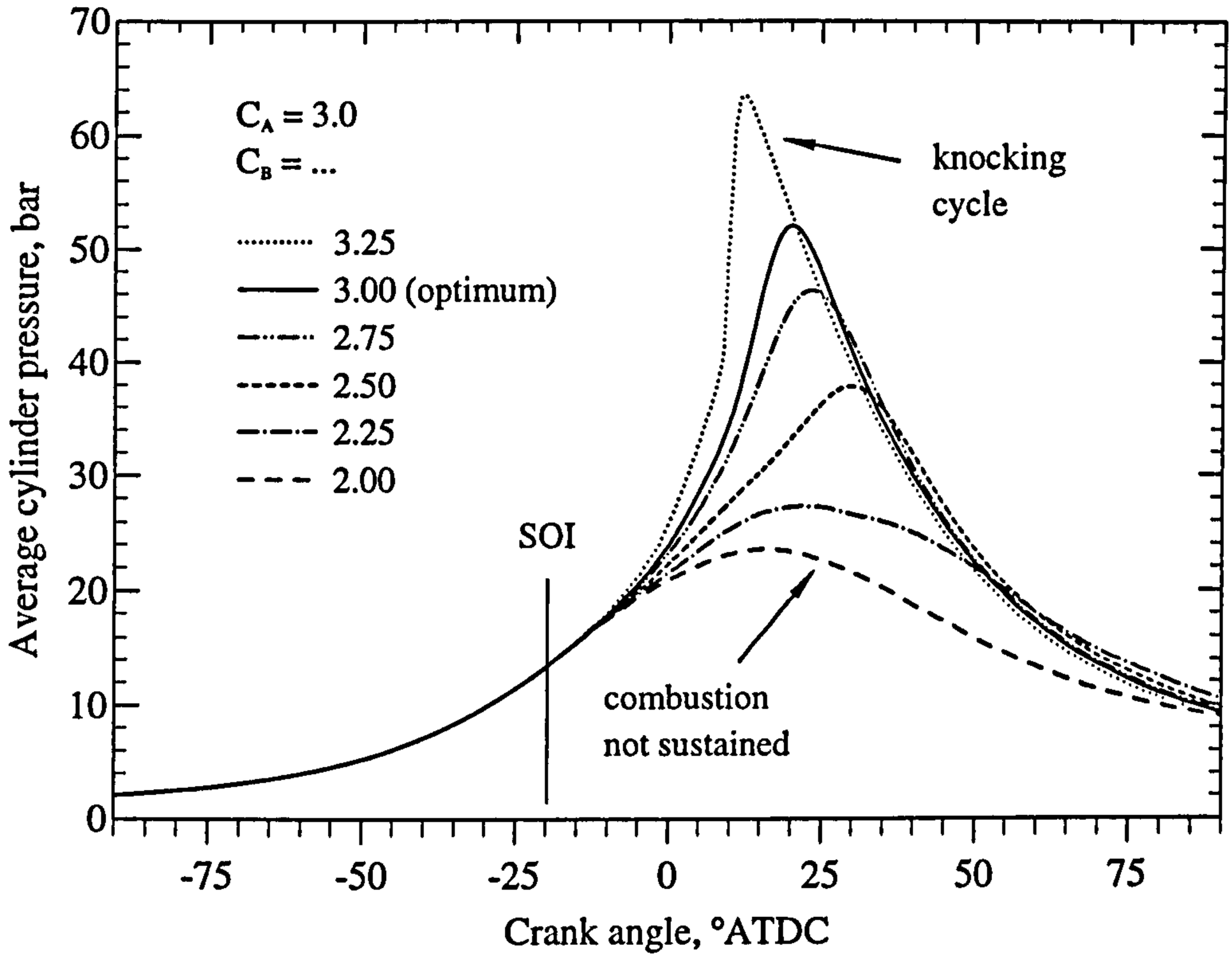

Figure 6.21 The scaling of the overall combustion rate with the model constant C_B.

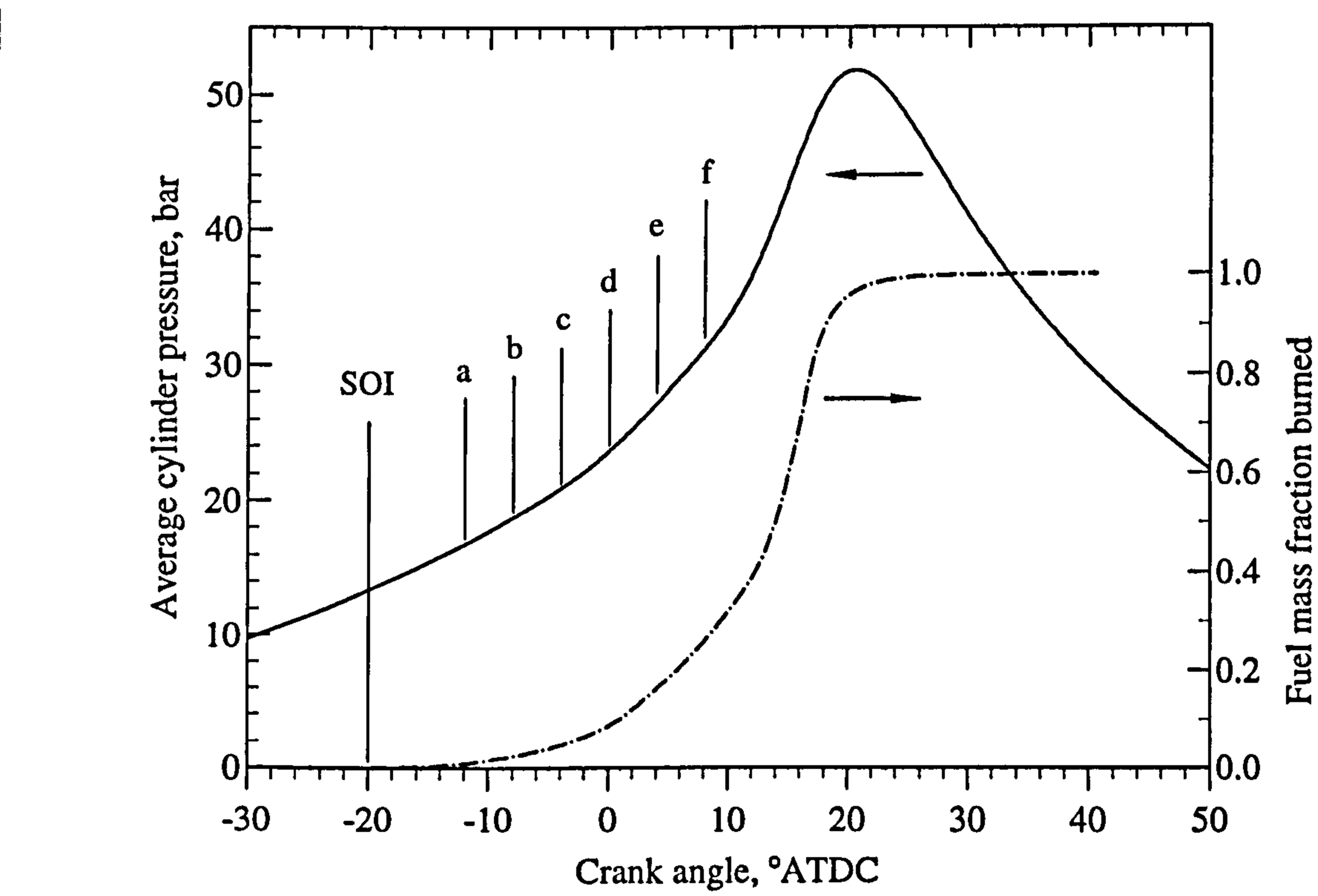

Figure 6.22 Ricardo E6: Crank positions of vector/contour plots in Fig. 6.23 with pressure and fuel mass fraction burned curves (baseline condition).

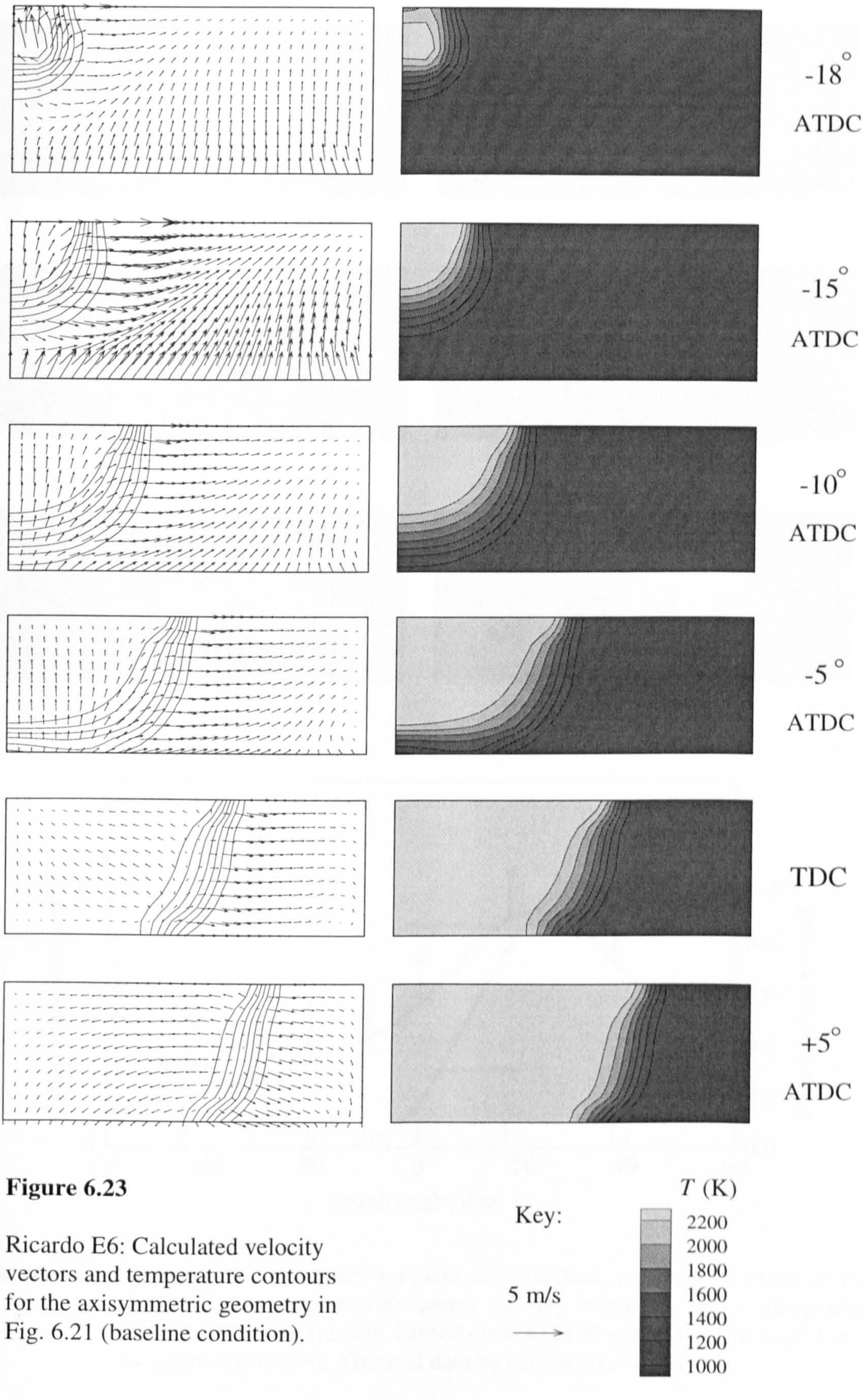

Figure 6.23

Ricardo E6: Calculated velocity vectors and temperature contours for the axisymmetric geometry in Fig. 6.21 (baseline condition).

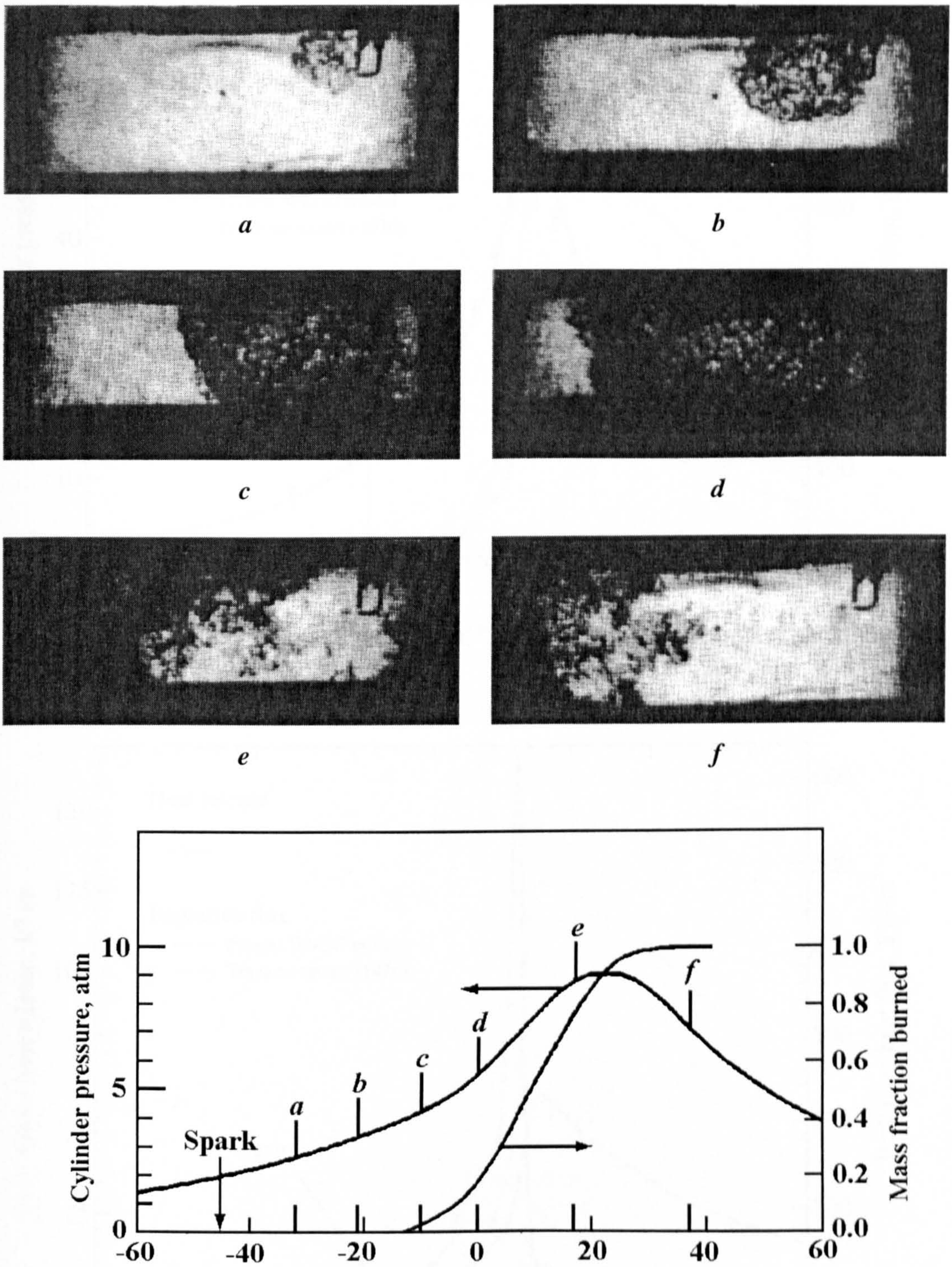

Figure 6.24 Sequence of stills from a square cross-section combustion chamber of a single-cylinder engine with quartz viewing windows, and corresponding pressure and mass fraction burned curves (1400 rpm). Copied from Fig. 9-14, Heywood (1988). Original data by Gatowski *et al.* (1984).

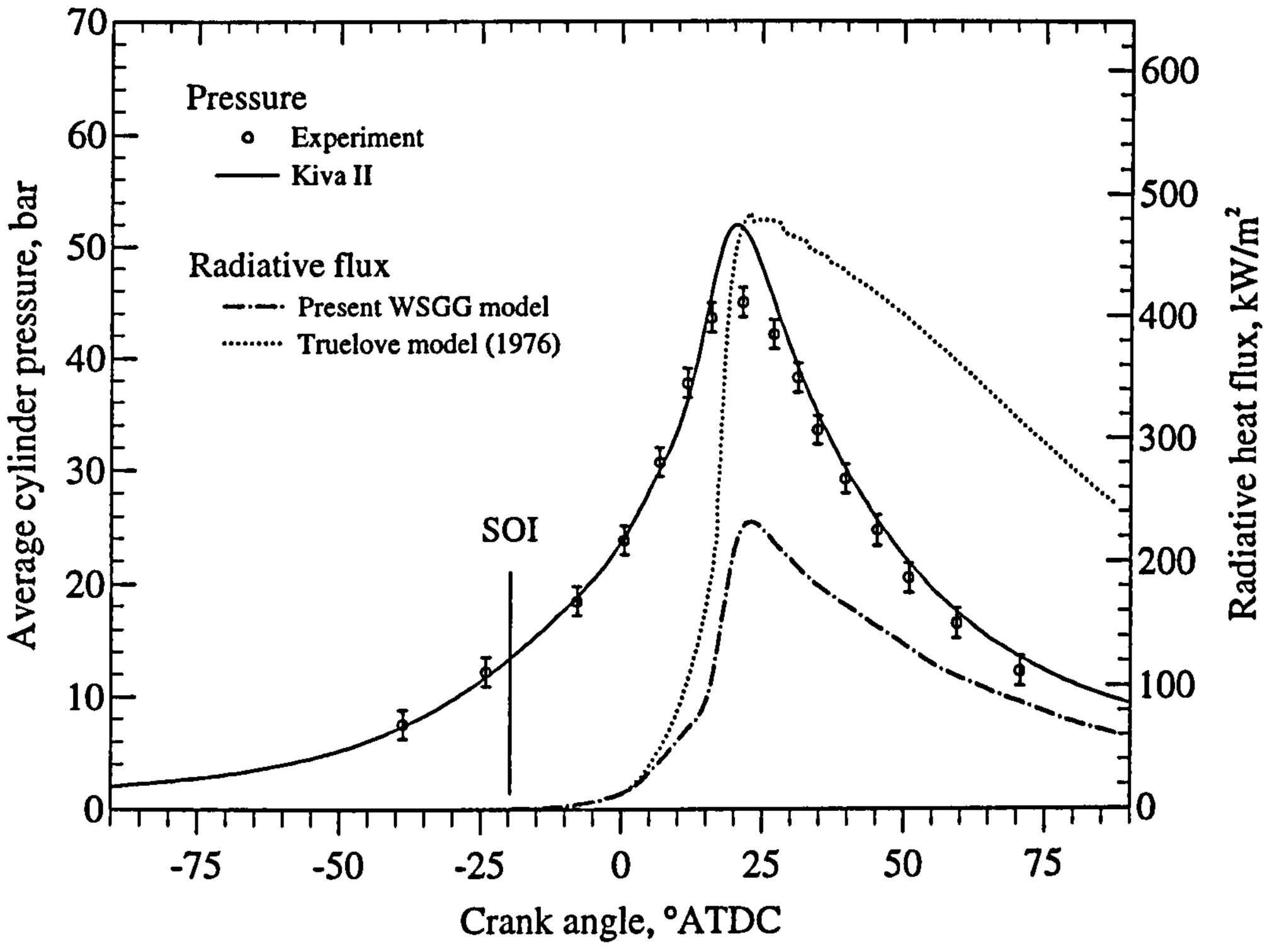

(a)

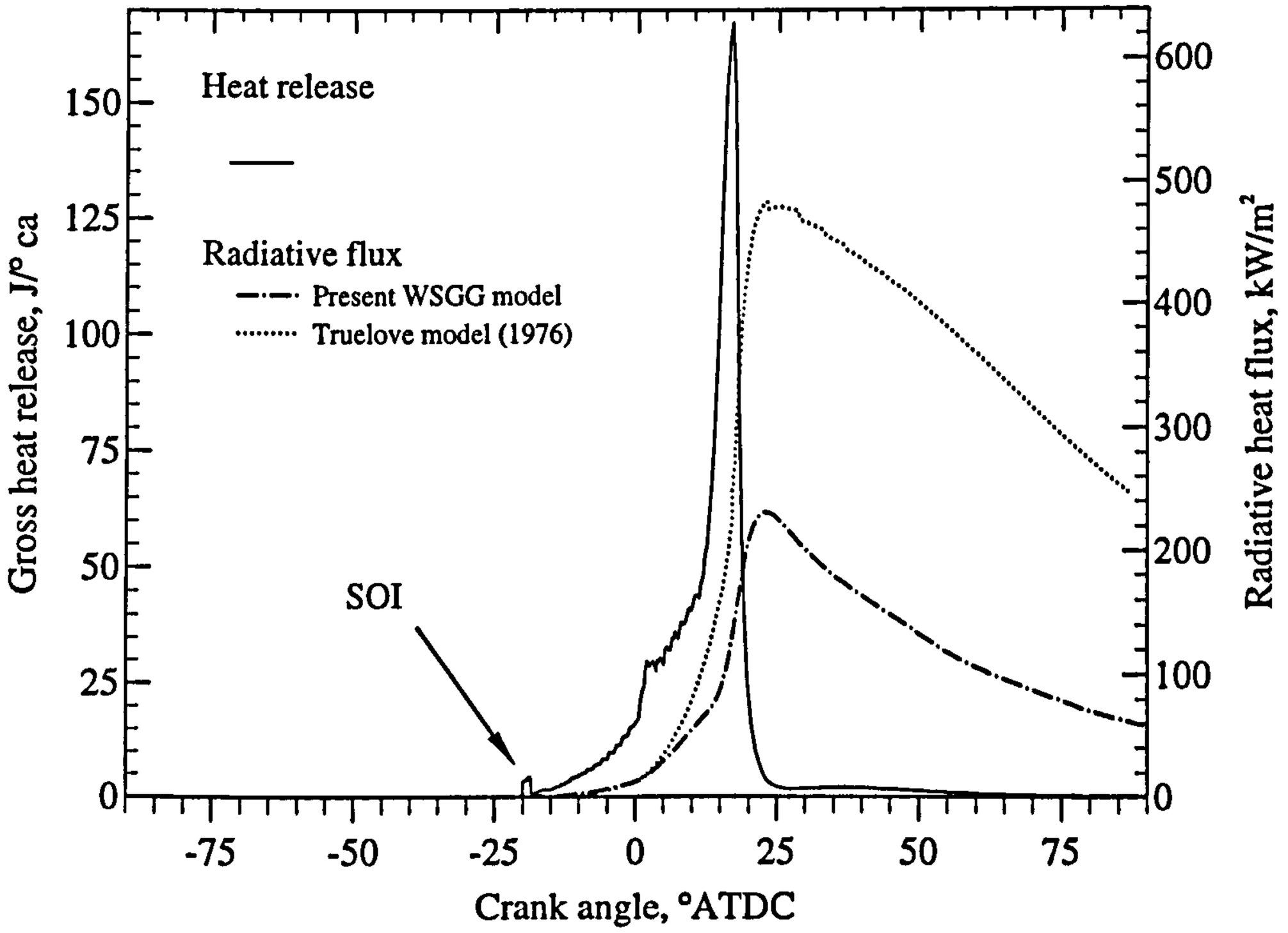

(b)

Figure 6.25 Ricardo E6: (a) Calculated cylinder pressure, radiative heat flux and (b) heat release rate for baseline operating condition (spark timing 20° BTDC, 1500 rpm and 0.97 equivalence ratio).

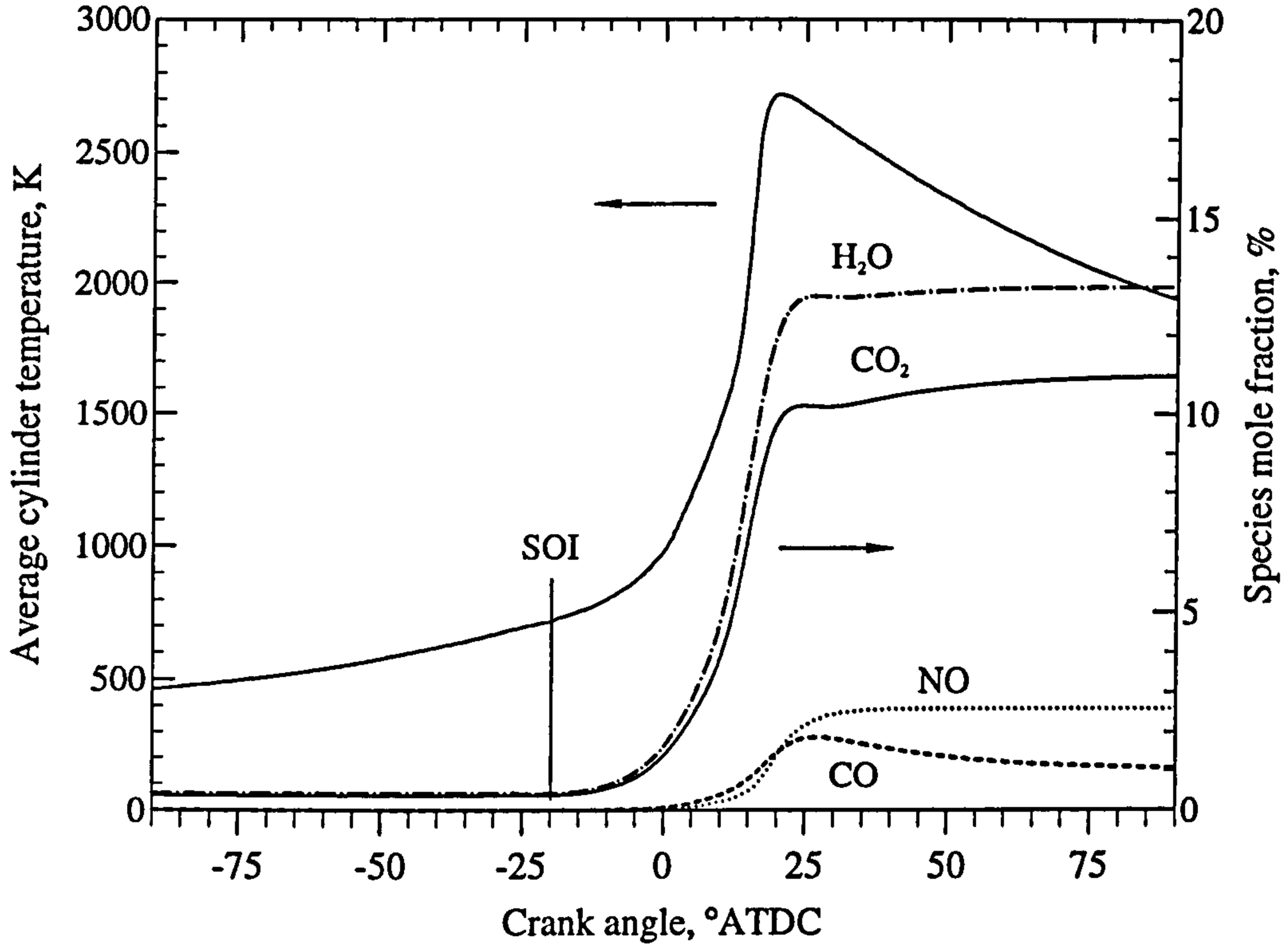

Figure 6.26 Ricardo E6: Computed variation in temperature & combustion products (baseline condition). NB: NO and CO *not* included in radiation analysis.

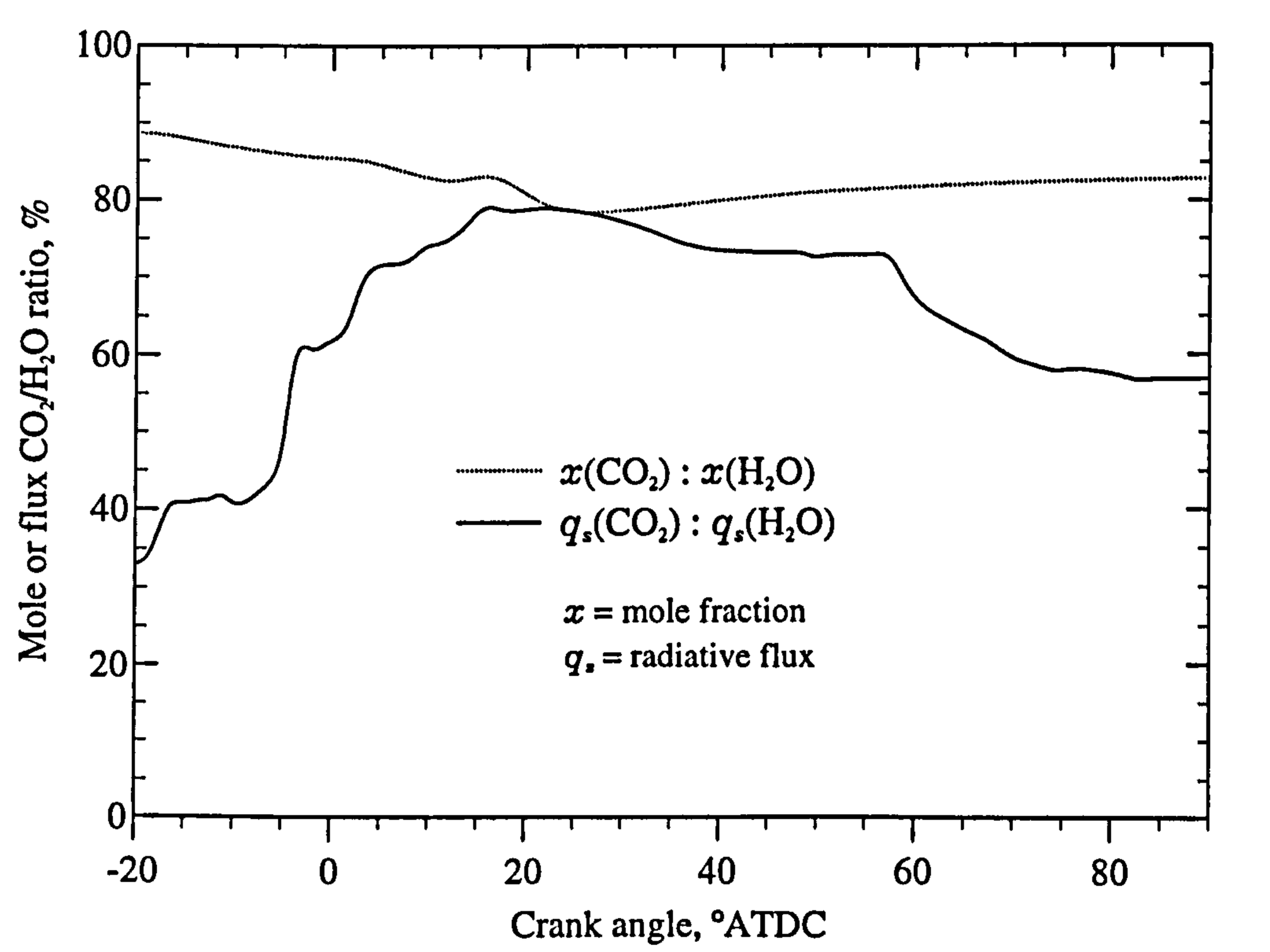

Figure 6.27 Ricardo E6: (a) Portion of total radiative flux (i.e. CO_2+H_2O) that is from the water, and (b) CO_2:H_2O mole fraction ratio. (N.B. For the stoichiometric combustion of iso-octane the latter quantity equals 89%.)

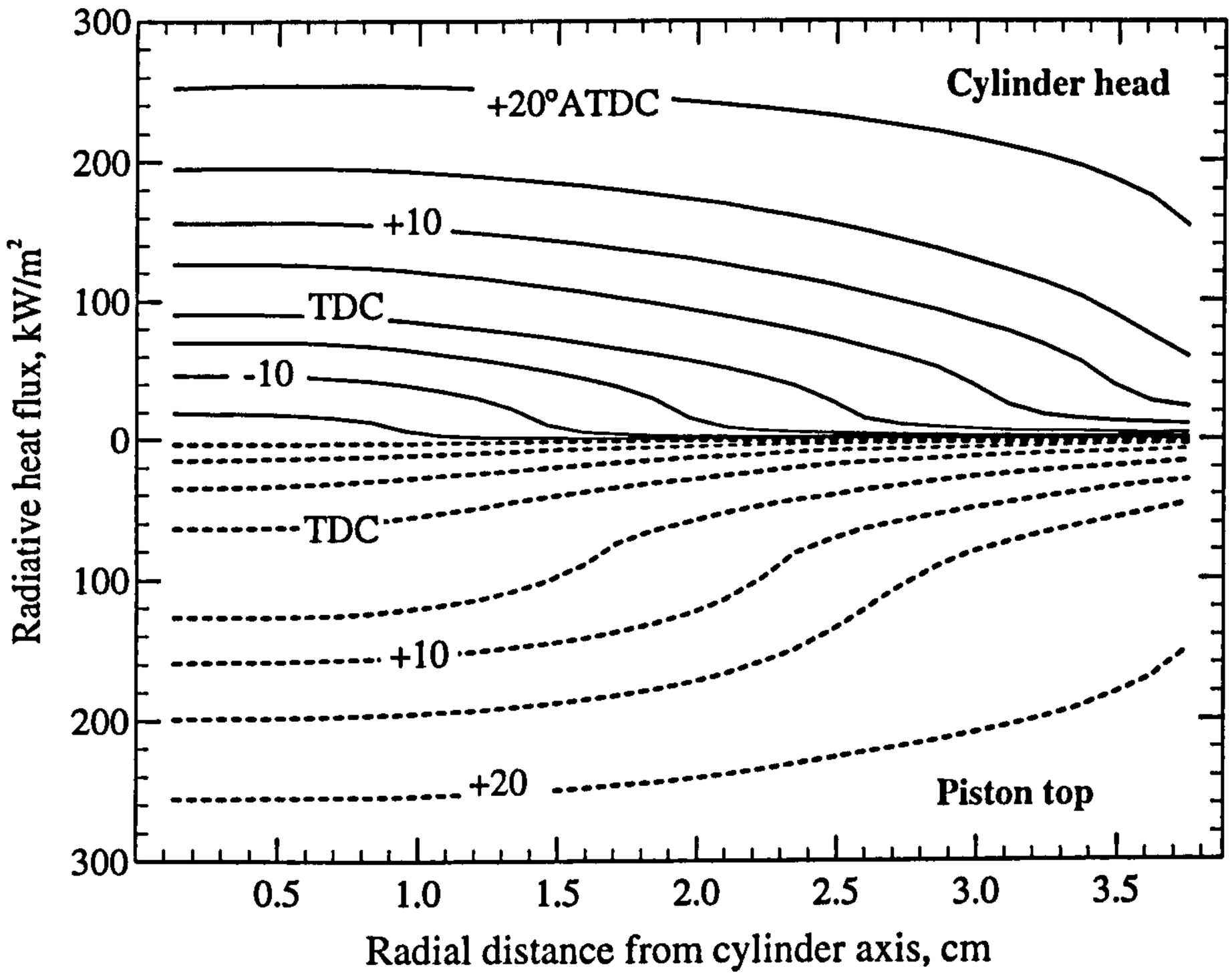

(a)

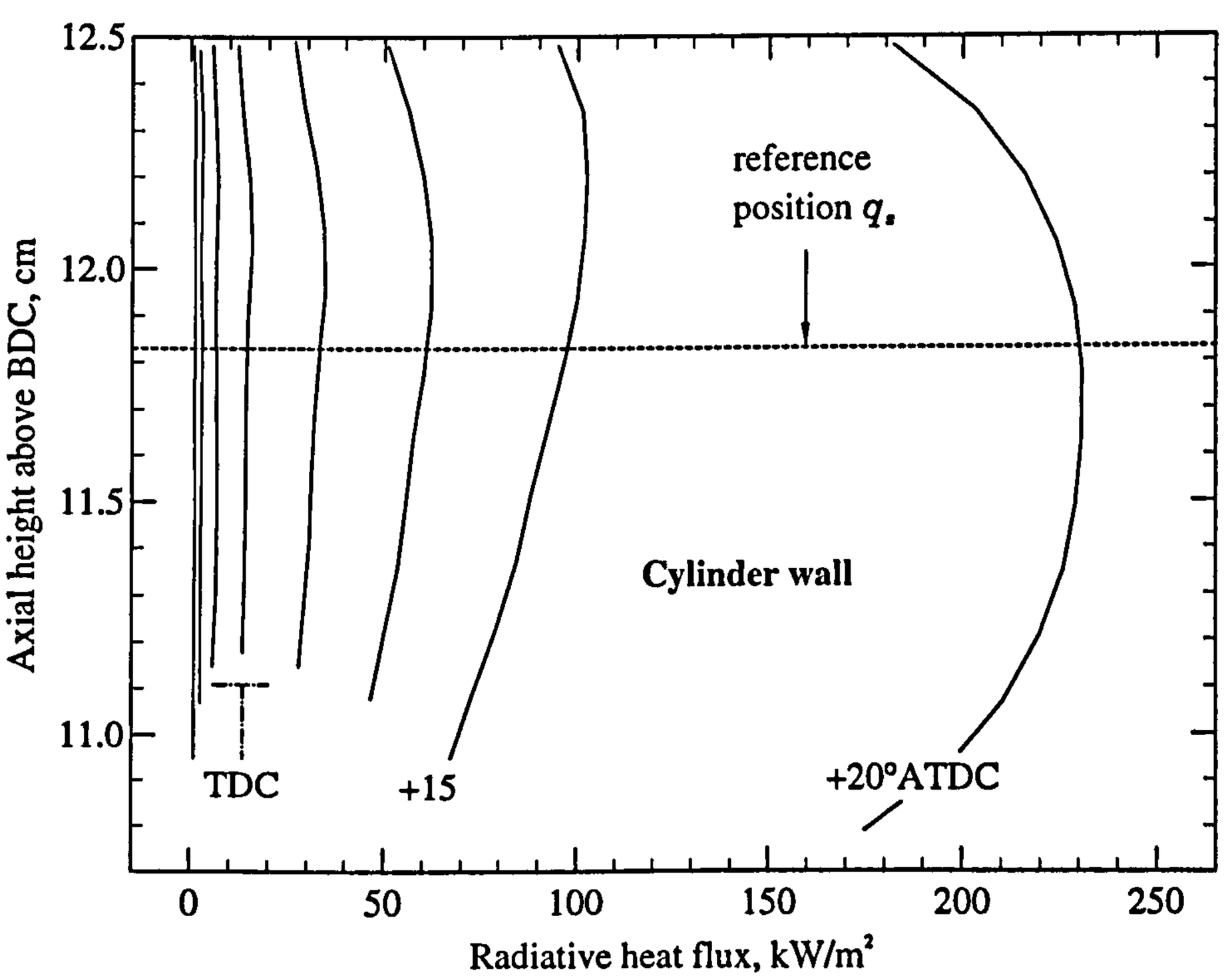

(b)

Figure 6.28 Ricardo E6: Calculated temporal and spatial variation in radiative surface heat flux on (a) the cylinder head and piston top, and (b) the cylinder wall (at the baseline condition.)

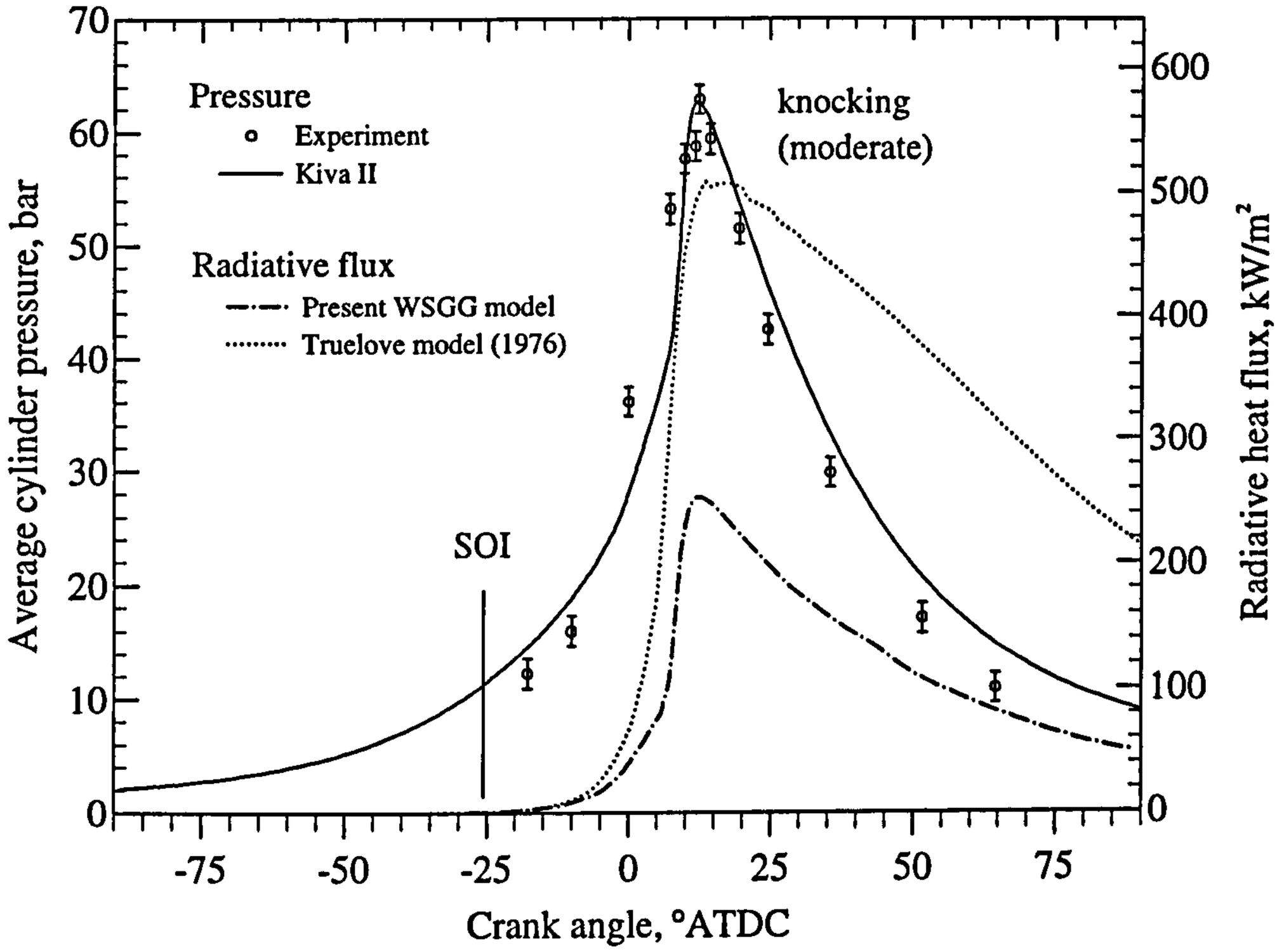

(a)

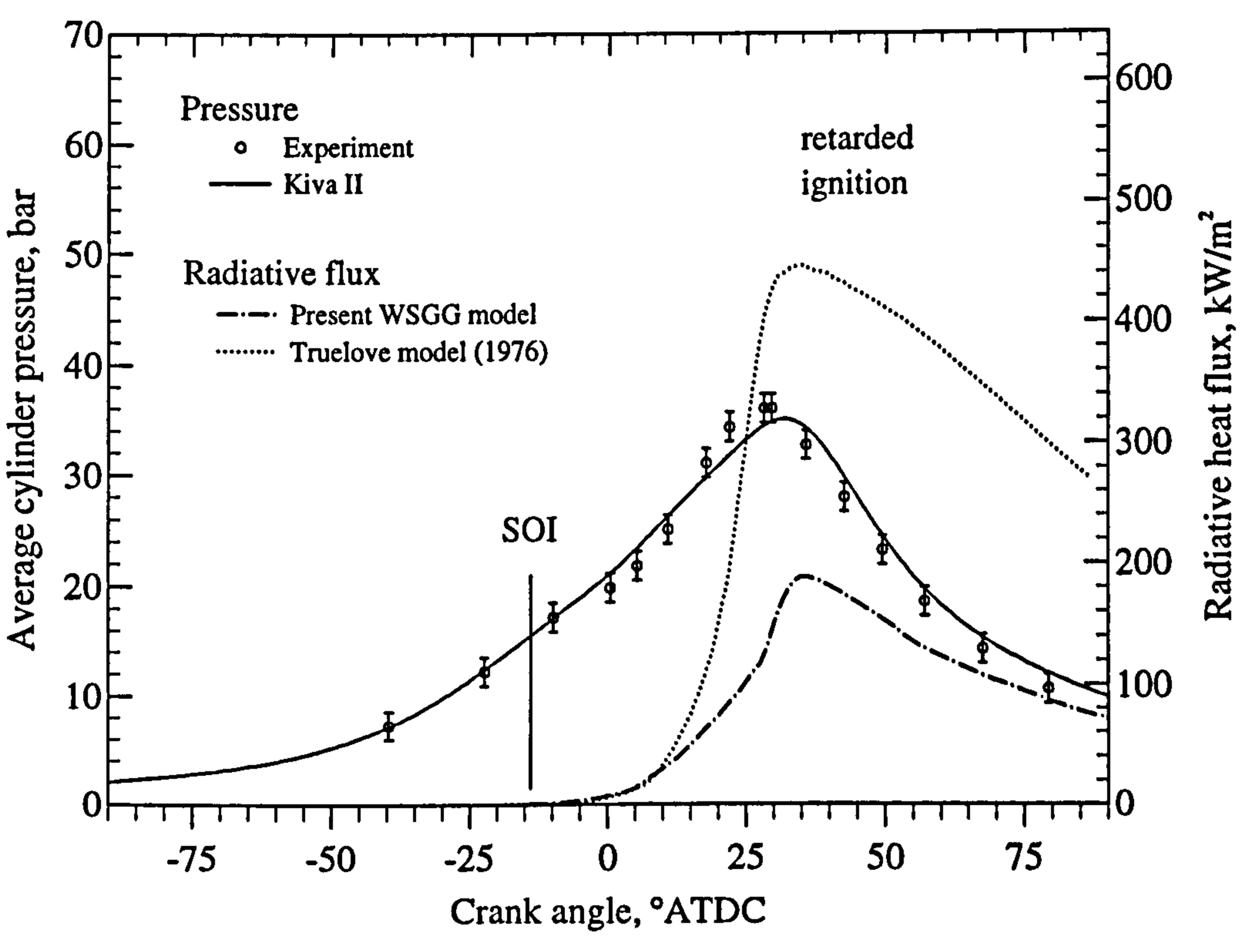

(b)

Figure 6.29 Ricardo E6: Computed cylinder pressure and radiative heat flux for (a) advanced 26° BTDC and (b) retarded 14° BTDC spark timings (speed 1500 rpm and 0.97 equivalence ratio).

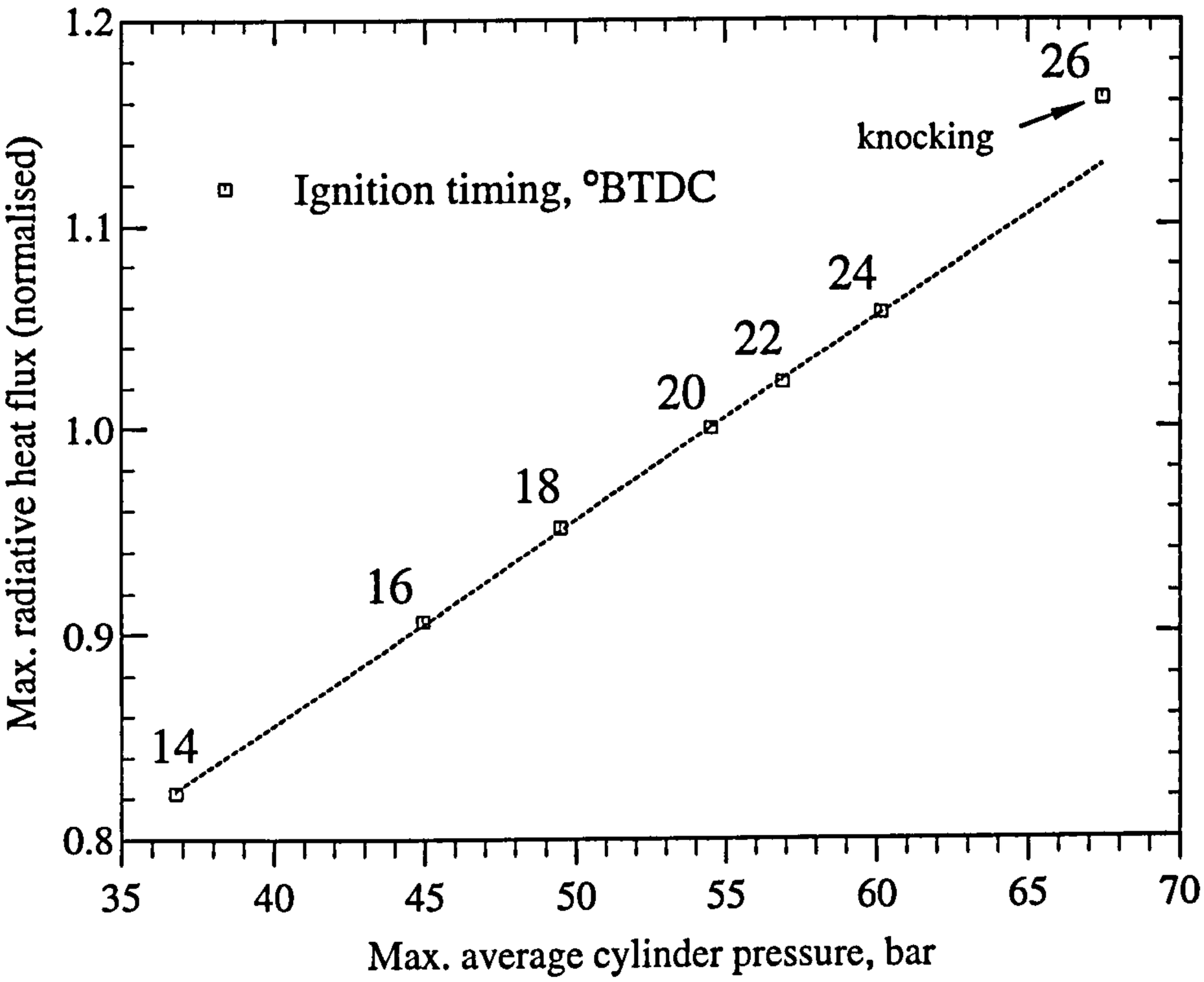

(a)

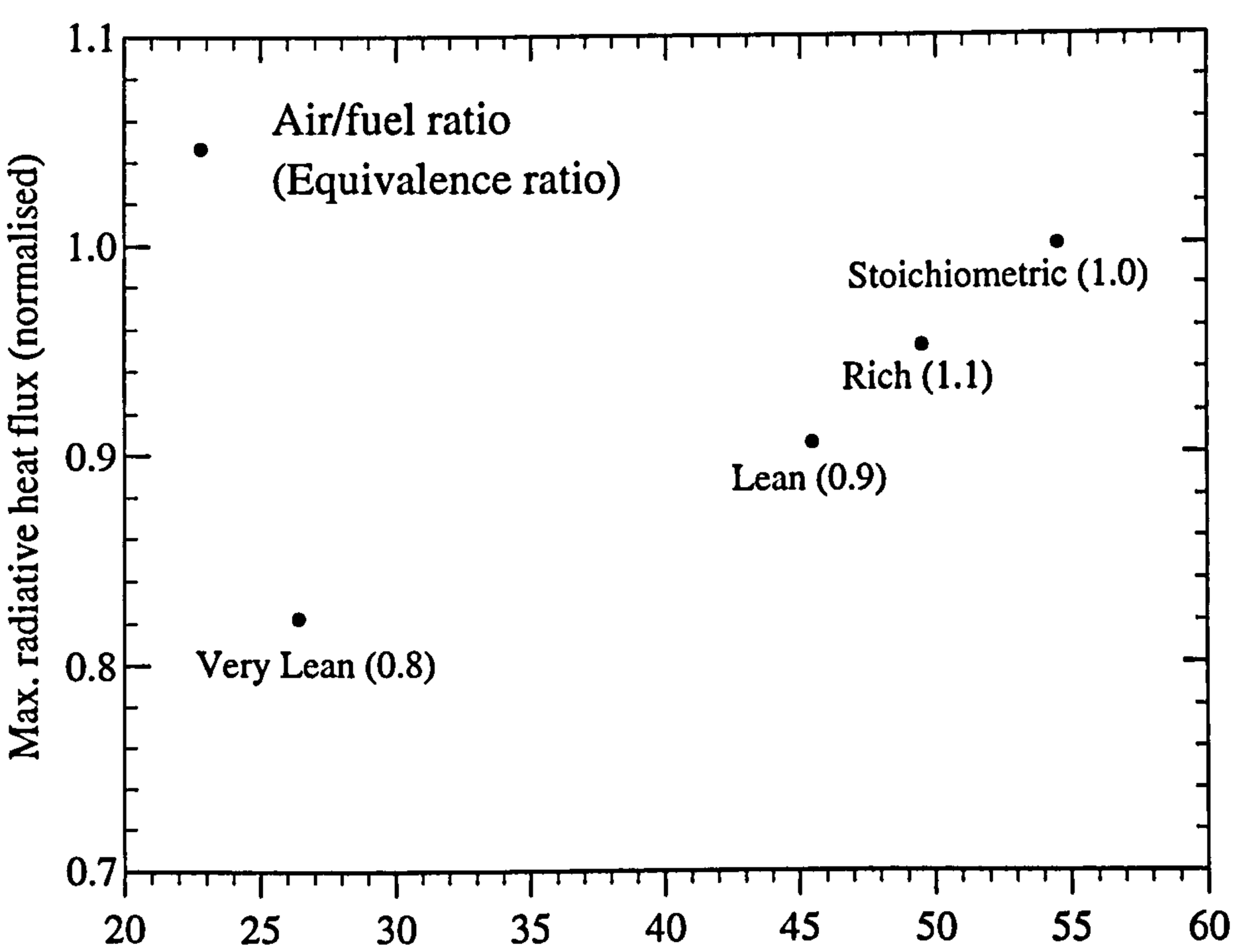

(b)

Figure 6.30 Ricardo E6: Correlation of normalised peak radiative heat flux with peak cylinder pressure for variations in (a) ignition timing and (b) air-fuel ratio (and other parameters fixed at baseline condition).

6.4 Full Cycle Simulation of a Four Valve Pentroof Combustion Chamber: Ricardo Hydra Engine

An ultimate goal of the automotive community is to be able to predict the turbulent reacting flow field in modern multi-valve engine geometries over a full cycle. Most predictions to date considered the combustion phase in isolation, by starting computations from inlet valve closure (ivc) with an assumed flow field (e.g. Kuo and Reitz 1989). However, for motored conditions, several authors have been able to obtain reasonable predictions of the flow field over a full cycle (e.g. Le Coz *et al.* 1990; Jones and Junday 1995, Das and Dent 1995) and experimental verification was obtained with laser doppler or particle image velocimetry techniques. A natural next step is the visualisation and numerical modelling for *firing* cycles.

Therefore, to demonstrate the feasibility of the present numerical methods for this purpose the multidimensional premixed combustion in a Ricardo Hydra pentroof spark ignition engine is simulated for a full 720° four-stroke cycle. Moreover, at selected crank angle positions the radiation from the combustion products CO_2 and H_2O is calculated with the present generalised weighted-sum-of-gray-gases model. Cylinder pressure data was used to tune the combustion model but at present there are no measurements of the flow field and radiative heat flux. Thus, the following analysis is largely qualitative, but nevertheless demonstrates the possibility to include detailed nongray radiation calculations in complex combustors.

6.4.1 Engine Test Conditions and Cylinder Pressure Measurement

The engine is a single-cylinder, water cooled, four-stroke Ricardo Hydra fitted with a four-valve pentroof head and twin overhead cams (Fig. 6.31). A single spark-plug is located centrally between the valve ports on the cylinder head and the piston is flat-topped. Geometric and operating details are summarised in Table 6.24. (It is believed that the bore and stroke are non-standard as a result of earlier modifications.) The fuel system was adapted to accommodate a basic venturi gas carburettor for fuelling with propane gas. Manual adjustment of the fuel line pressure was necessary in order to obtain specific operating points.

The cylinder pressure variation was measured with an air cooled Kistler series 600A pressure transducer integrated with an in-house modified spark plug. Consequently,

modifications to the cylinder head could be avoided. However, this arrangement has some limitations, notably the problem of datum referencing due to thermal drift, and the damping effect of the connecting passage of the spark plug adapter (see Randolph 1990a, b). A Kistler 5007 charge amplifier was used to interface the sensor to the data acquisition system. It was initially found that spark noise and earth currents severely affected the pressure signal. The earth current problem was particularly severe as a result of a poor test bed design with power cables looping around the engine block. Earth leads and additional insulation were used to suppress this interference to an acceptable level.

The pressure signal was sampled at 2° crank angle intervals with a Data Translations DT2805 analogue-to-digital data acquisition card. A slotted disc encoder on the engine crankshaft provided the required sampling and reference trigger signals to synchronise digital scanning of the pressure signal with crank angle. Pressure signals were averaged over 50 consecutive cycles and scaled such that the absolute pressure at bottom-dead-centre (BDC) after the intake stroke equalled the mean intake manifold absolute pressure. It was found that the expansion line on pressure-volume (p-V) plots curved sharply near BDC and the gas exchange process showed a crossover in pressures: commonly called the 'bow tie effect' – Fig. 6.32(b). This thermal effect could not be complete avoided and is even observed in pressure measurements made by Ricardo for a similar engine (Jackson and Stokes 1984).

6.4.2 Computational Model: Mesh Definition and Boundary Conditions

Details of the approach used to mesh the pentroof combustion chamber are given in Sec. 2.4. An unusual feature is the use of different meshes for the valve open and combustion periods as shown in Fig. 2.15: the valve motion and complex boundary surface detail could not be described with a single structure (see Sec. 2.4.5). The grid resolution is also quite coarse, but is considered sufficient for demonstrating the coupling of the radiation and chemical-kinetics.

Calculations were started at -600° ATDC (i.e. just before exhaust valve opens). Treatment of the gas exchange processes and valve action is largely as detailed in Secs. 3.4.2 and 3.4.3. i.e. A constant pressure condition was used at both the intake and exhaust port open boundaries, specified as a plenum pressure, p_{amb}, acting at a distance x outside the boundary. However, in practice the calculated boundary fluxes were often

quite different from those expected due to the interpolation (via Eq. 3.106) used to calculate the actual boundary pressure. Notably, at the exhaust port boundary this resulted in a mis-match between the mass flux calculated in KIVA with that calculated by the one-dimensional wave action analyses of the exhaust pipe (see Sec. 3.4.2), when both codes are coupled through the pressure condition at the cylinder boundary. Moreover, the mass flux varied strongly with the value chosen for x. Therefore, a modified approach was developed whereby the value of p_{amb} (for an arbitrary fixed value of x) is factored on each timestep so that the computed KIVA exhaust port mass flux follows that of the wave action code. A simple control algorithm was written for this purpose using the difference in mass flux on the previous timestep as an input error signal. This refinement resulted in much better agreement between simulated and measured cylinder pressures during exhaust blowdown. At the intake boundary p_{amb} was initially set equal to the measured averaged inlet manifold pressure and then adjusted iteratively until the inducted air/ fuel mass closely matched experimental measurements. The reference incoming species densities for propane, oxygen and nitrogen (i.e. taking zero EGR) were determined for the specified air/fuel ratio at the pressure p_{amb}. The corresponding values imposed at the intake boundary were then scaled according to Eq. (3.107). The turbulent kinetic energy, k, was taken as 10% of the averaged inflow velocity squared, and its dissipation rate, ε, was evaluated from a length scale equal to half the maximum lift of the intake valve, i.e. refer to Eqs. (3.108) and (3.109), respectively.

Mean temperatures on the combustion chamber surfaces were estimated on the basis of thermal maps obtained by Zhao *et al.* (1991, 1994) for a similar sized engine and compression ratio. The cylinder walls were assumed to be coolest at 450 K, with the piston surface somewhat hotter at 490 K and the highest temperatures on the cylinder head. Here, the temperature was varied smoothly over the head from 450 K at the cylinder wall boundary to 480 K near the central spark plug. Local maxima of 505 K and 585 K were also introduced at surface elements coinciding with the centres of the intake and exhaust valve faces. Given that the temperatures depend on many factors (i.e. materials, cooling design, engine speed, spark timing, etc.) actual values may differ by 20% or more. However, as noted in Sec. 6.3.2 this error has only a minor effect on the radiative heat flux prediction which depends largely on the quality of the burned gas temperature prediction. The surface emissivity was assumed to be gray and equal to $\varepsilon = 0.8$.

Initially, the calculation was started using assumed distributions of the flow variables within the combustion chamber. These initial conditions were used only as a first guess. The calculation was then run until there was a 1% difference in global values between consecutive cycles. This required three 720° cycles. A maximum calculation timestep of 1 degree crank angle was used. Several thousand timesteps were required for a full cycle taking some 120 hours, with an additional 1.75 to 7 hours per instantaneous radiation calculation (at a specific crank position). Computations were performed on the Sun workstation described in Sec. 6.1.

6.4.3 Flow Characteristics over a Full Cycle

The calculated full cycle pressure-time and pressure-volume curves are plotted with measured pressure data in Fig. 6.32. Firing TDC is at 0° crank angle. The combustion model constants $C_A = 2.0$ and $C_B = 1.9$ were optimised to reproduce the measured peak cylinder pressure of 47 bar, but the close agreement observed elsewhere can be attributed solely to the predictive ability of the model. The largest discrepancies are observed in the later stages of the expansion stroke where computed pressures are 1 bar (i.e. 20%) higher than measurements at exhaust blowdown. This in turn results in some over-prediction in the amplitude of the pressure oscillations during the exhaust stroke, but even so the blowdown/displacement simulation is remarkably good given that there are numerous uncertainties in the exhaust manifold boundary conditions and the large pressure gradients across the open ports.

The computed instantaneous mass flow rates through the exhaust and intake ports are shown in Fig. 6.33. (Negative values represent outflow from the cylinder.) The intake mass flow is relatively smooth in comparison to the large oscillation observed during exhaust blowdown and displacement. This merely results from the different boundary models: in reality small oscillations in the intake mass flow would also be expected, but the present constant pressure boundary condition cannot capture this. A wave action analysis of the intake manifold could be used if this feature is considered important. It should also be noted that the 'spikes' observed in the exhaust mass flow and step changes in the intake mass flow arise erroneously from numerical instabilities in the solution at moments when rezoning shifts a valve head to a new k-plane (see Sec. 2.4.5). They have no physical significance. A finer spatial discretisation or smoothing algorithm should be employed in a future study to correct this problem.

Consider Figs. 6.34–38. Velocity vector plots of planes $i = 12$ and 24, and $j = 12$ give some insight into how the flow field develops during the gas exchange strokes (-540° to -90° ATDC). These planes were chosen since they intersect the valve centres where the largest flow gradients occur. Further plots of the central planes at $i = 18$ and $j = 18$ then show a cross-section of the motion during the compression and combustion (-45° to 67.5° ATDC). Unfortunately, the strongly three-dimensional nature of the flow can only be fully appreciated with a dynamic multi-plane visualisation, but the most important features are highlighted in the discussion below.

At -540° (BDC) the exhaust blowdown is nearly complete and the exhaust mass flow is starting to fall from its peak value of 65 g/s. Note the velocity gradient from almost zero at the (instantaneously stationary) piston face to a maximum of 260 m/s at the exhaust ports. Back pressure in the exhaust pipe then results in a backflow wave into the cylinder. By -450° the pressure gradient has reversed again and an outflow has re-established. However, now there is a bulk upwards gas motion quite different from that observed during blowdown. This is characteristic of the displacement phase of the exhaust stroke. The streamline curvature also nicely demonstrates the blocking effect of the valve heads.

The intake valves open at -372° ATDC and there then follows a period of valve overlap until the exhaust valves close at -348° ATDC. The slant of the pentroof results in the upper edges of the ports being in close proximity and consequently there is a significant amount of short circuiting of the intake flow directly into the exhaust (e.g. see *j*-plane at 360°). Otherwise the inflow is deflected by the curvature of the cylinder walls and circulates below the valve heads to the exhaust. This structure efficiently removes the remaining burnt gas as the calculated residual gas fraction is only 5.6%.

During induction the most complex flow patterns arise within the cylinder volume. Gas issues from each intake valve opening as a conical jet at about 40 m/s, i.e. 10 times the mean piston speed. Separation of the jet from the valve seat and lip produces shear layers around each intake valve periphery with large velocity gradients. These interact with the cylinder walls and the moving piston to set up several tumbling regions of recirculation. Consider the *j*-plane at -315°. Two centres of rotation may be discerned, immediately below, and to the left and right of the intake valve lip. What is seen is in fact a cross-sectional view of an inclined torus-like vortex extending all around the valve head. The

character and movement of this vortex varies greatly with circumferential position. The right centre of rotation (as viewed) remains stationary throughout the intake stroke while the left follows the piston's descent. A second vortex extends around the other intake valve such that *four* centres of rotation are visible in the *i*-plane passing through both intake valves. Figure 6.39 plots the velocities in selected *k*-planes at BDC. This reveals strong swirling rotations, particularly close to the piston top. A three-dimensional interpretation of this combined tumbling-swirling motion is also sketched alongside.

At -124° ATDC the intake valves close removing the energy source driving the vortex field. Then shearing forces quickly deplete the vortex energy and the whole flow structure breaks down to be replaced by a more ordered upwards movement during compression. As the piston moves towards TDC it tends to 'roll-up' the boundary layer and new regions of recirculation form. These convect the gas towards the cylinder axis following the curvature of the side walls and the ridge of the pentroof (e.g. see the central *i*-plane at -45° ATDC). This motion is further enhanced by the burnt gases expanding away from the central spark plug after ignition at -15° ATDC. Unburnt gas ahead of the flame front is squeezed into the squish regions where it swirls around the cylinder wall to join the fluid recirculating along the pentroof ridge. Eventually it develops into an ordered downwards movement some way into the expansion stroke.

To conclude, the flow description presented here is quite plausible but supporting evidence is difficult to find. Previous studies have often involved special porting or shrouded valves in order to enhance tumble during induction and compression. Consequently, comparisons can not be made as the flow patterns are profoundly different. One exception is a basic four valve pentroof geometry (labelled 'A') investigated by Le Coz *et al.* (1990). Here, a computational analysis predicted two inclined counter-rotating tumbling motions during induction similar to the present simulation.

6.4.4 Flame Development and Radiative Heat Flux

The flame front may be characterised by a rapid transition in local temperature from typically 800 K at the leading edge to in excess of 2200 K at the trailing edge (e.g. Fig. 6.23). Thus, by plotting iso-surfaces through all points at some intermediate temperature, it is possible to visualise the flame front shape and how it develops in time. Figure 6.40 shows a sequence of iso-surfaces at 2000 K from -5° to 20° ATDC. The turbulent flow

field has a marked influence on the flame geometry. Initially, the burned gas volume is quite spherical except where it impinges on the cylinder head and piston top. However, its shape then becomes increasingly distorted. Consider first the flame development close to the cylinder head. In the symmetry plane, the flame expands freely down the inclined sides of the pentroof, but fluid recirculating along the ridge of the pentroof impedes its growth in a perpendicular direction. Consequently, the flame front intersects the cylinder head with an hourglass-shaped profile.

Now consider the flame propagation on the piston surface. Initially it expands uniformly in all radial directions. However, unburnt gas ahead of the flame is compressed into the squish region such that an opposing pressure gradient is set up. This gradually shapes the flame front to the inner profile of the squish region as it sweeps towards the cylinder wall. An extremely contorted flame surface results from these quite different profiles on the cylinder head and piston top. The squish and the corner regions at either end of the pentroof ridge are the last volumes of gas to be engulfed by the flame. Thereafter, all combustion is of unburnt gas entrained into the enflamed region. The cylinder pressure peaks at 18.5° ATDC when the flame front makes contact with the cylinder wall.

Figures 6.41 and 6.42 plot the variation in radiative heat flux on the cylinder head and walls from -5 to 115° ATDC (shortly after which the exhaust valves open). At the centre of the head, in close proximity to the spark plug, the flux rises to a local peak of 207 kW/m^2 at 20° ATDC before falling away later in the expansion stroke. Locations furthest from the spark, or with no direct line of sight to the enflamed region receive the least radiation. For example, on the surfaces immediately above the squish regions the radiative flux never exceeds 80 kW/m^2.

However, the most remarkable aspect of these results is just how closely the radiative heat flux contours follow the flame front, recording both its shape and passage in time (c.f. Fig. 6.40). Consider the plot at 15° ATDC when almost the entire gas volume is enflamed. Here the hottest contour traces an early profile of the flame front and then each cooler contour corresponds to a progressively more recent position of the front. After this time mixing in the postflame gases gradually evens out thermal and species concentration gradients, and a more uniform radiative emission to the surface results, i.e. by 115° ATDC there is only a 30 kW/m^2 difference between the flux minima and maxima.

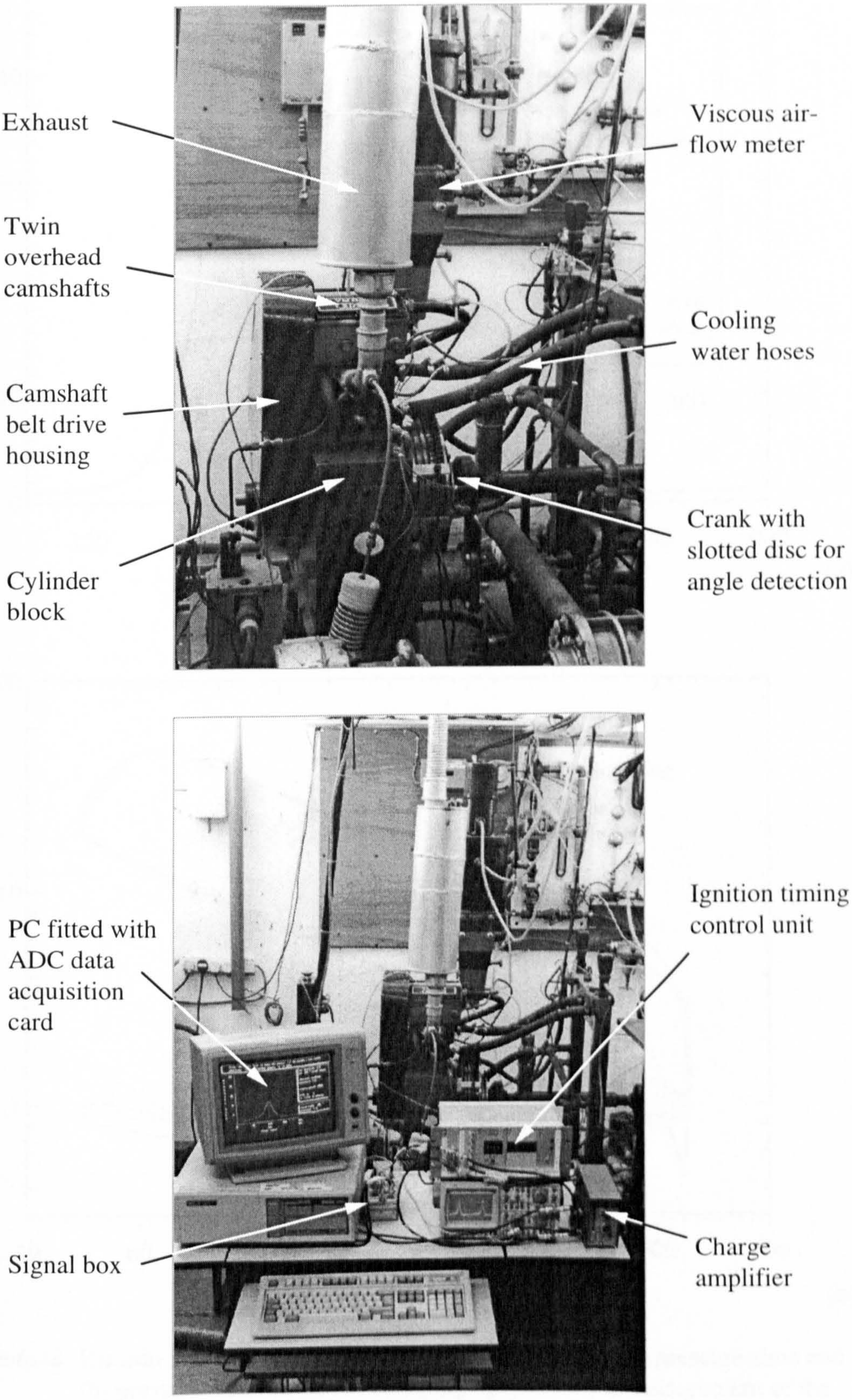

Figure 6.31 Ricardo Hydra: Experimental engine and instrumentation.

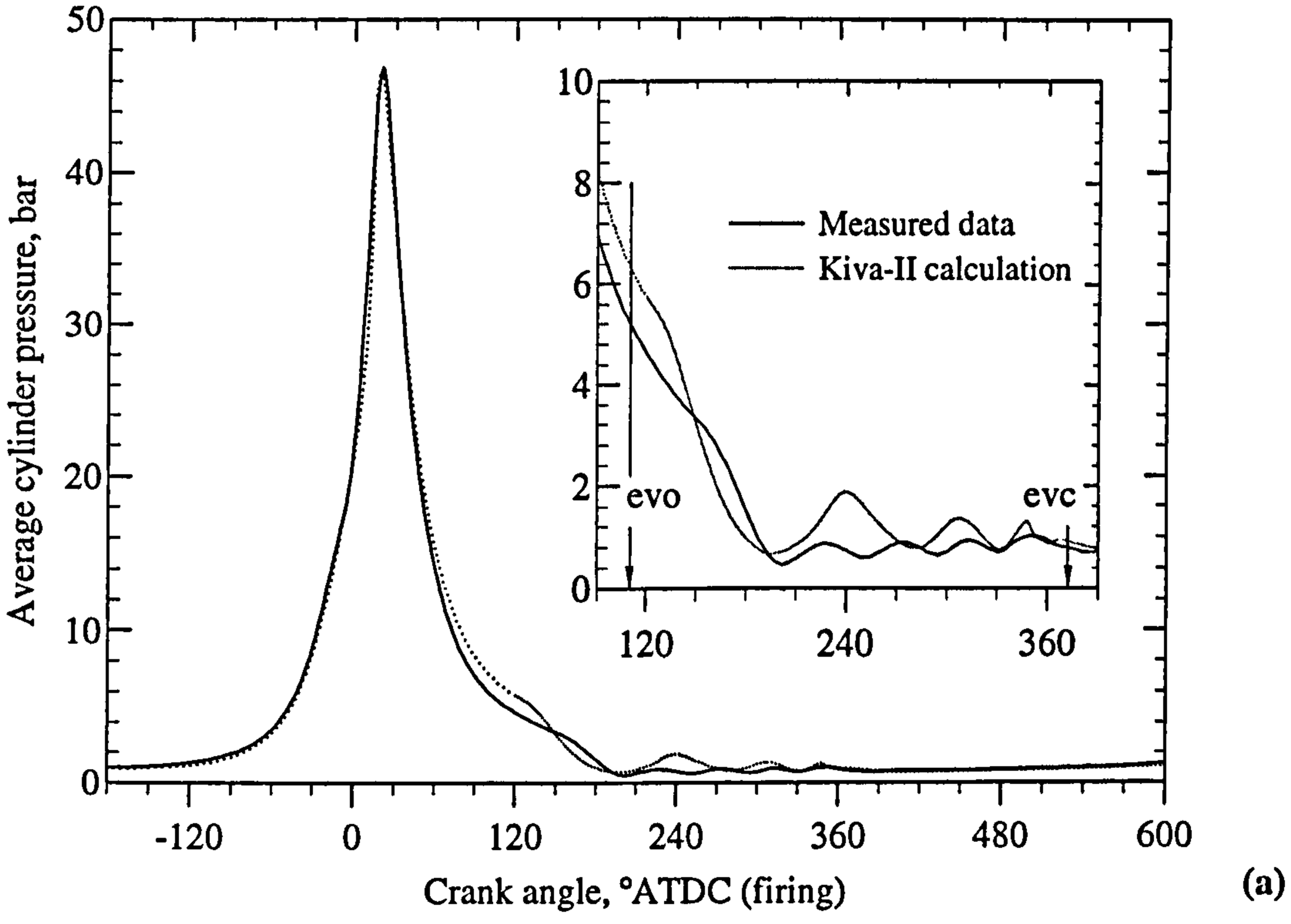

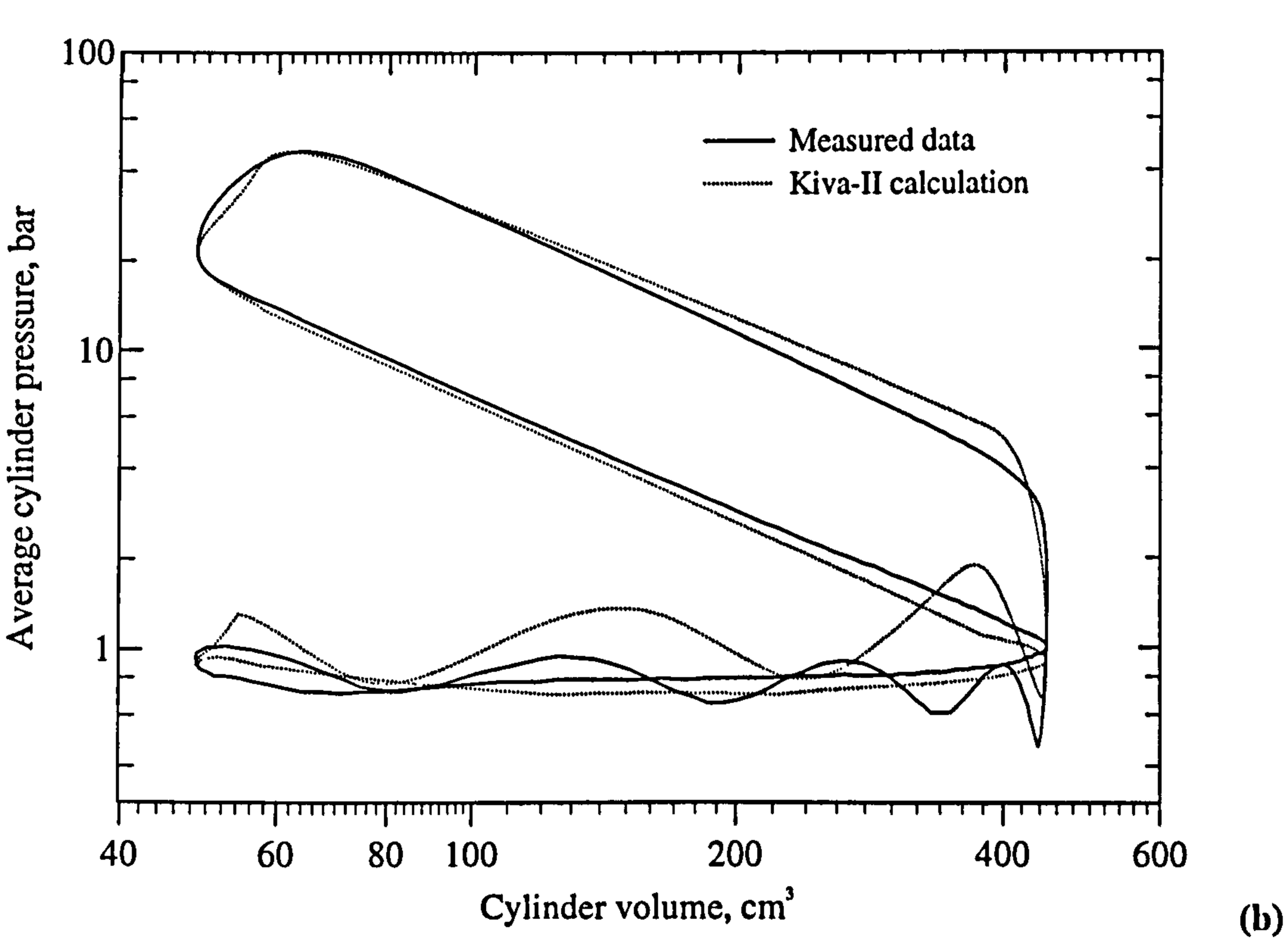

Figure 6.32 Ricardo Hydra: Measured and calculated full cycle (a) pressure-time and (b) pressure-volume curves for firing operation. An enlargement of the exhaust blowdown and displacement is also shown in (a).

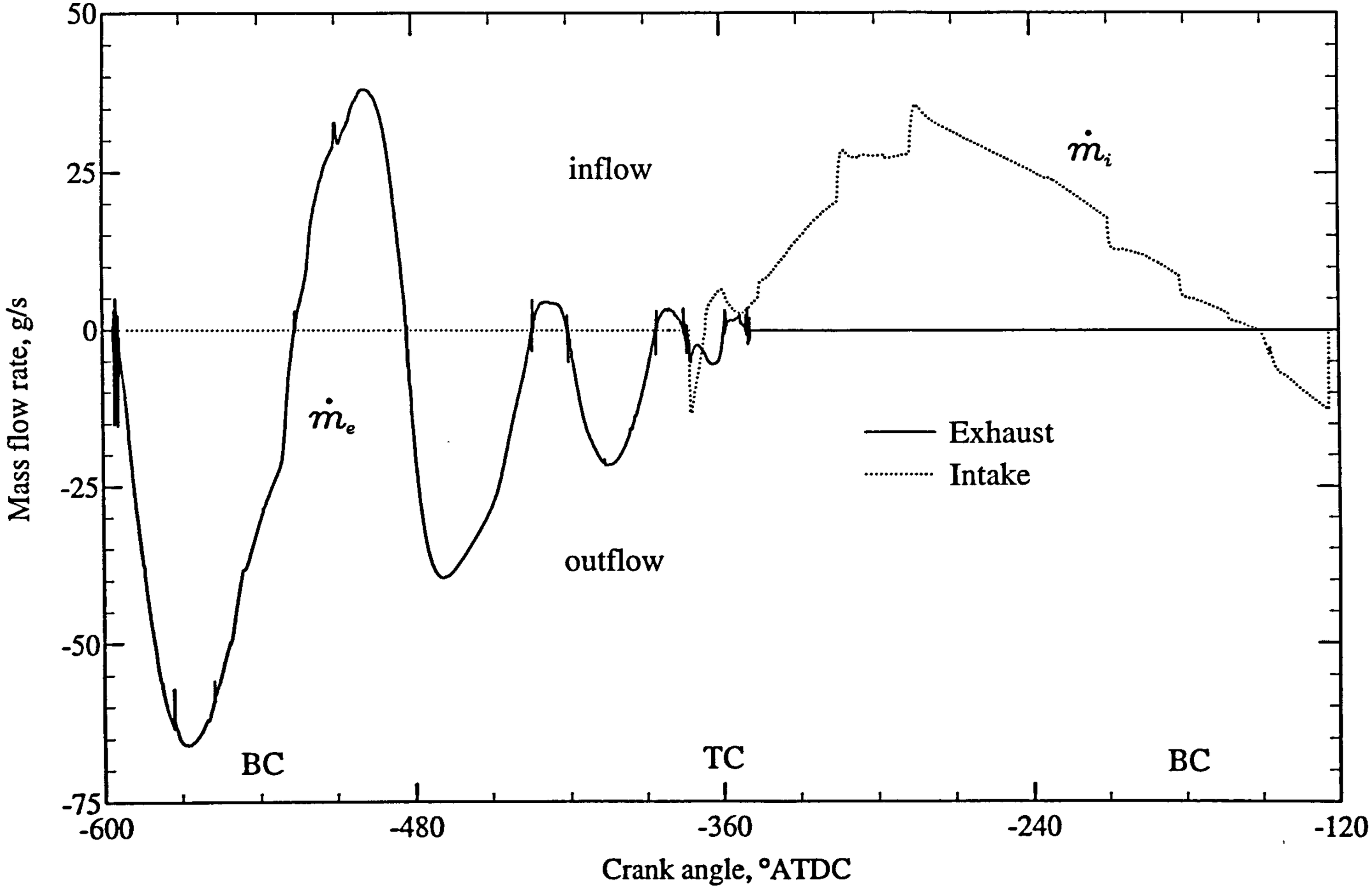

Figure 6.33 Ricardo Hydra: Computed mass flow rates through the exhaust and intake ports versus crank angle.

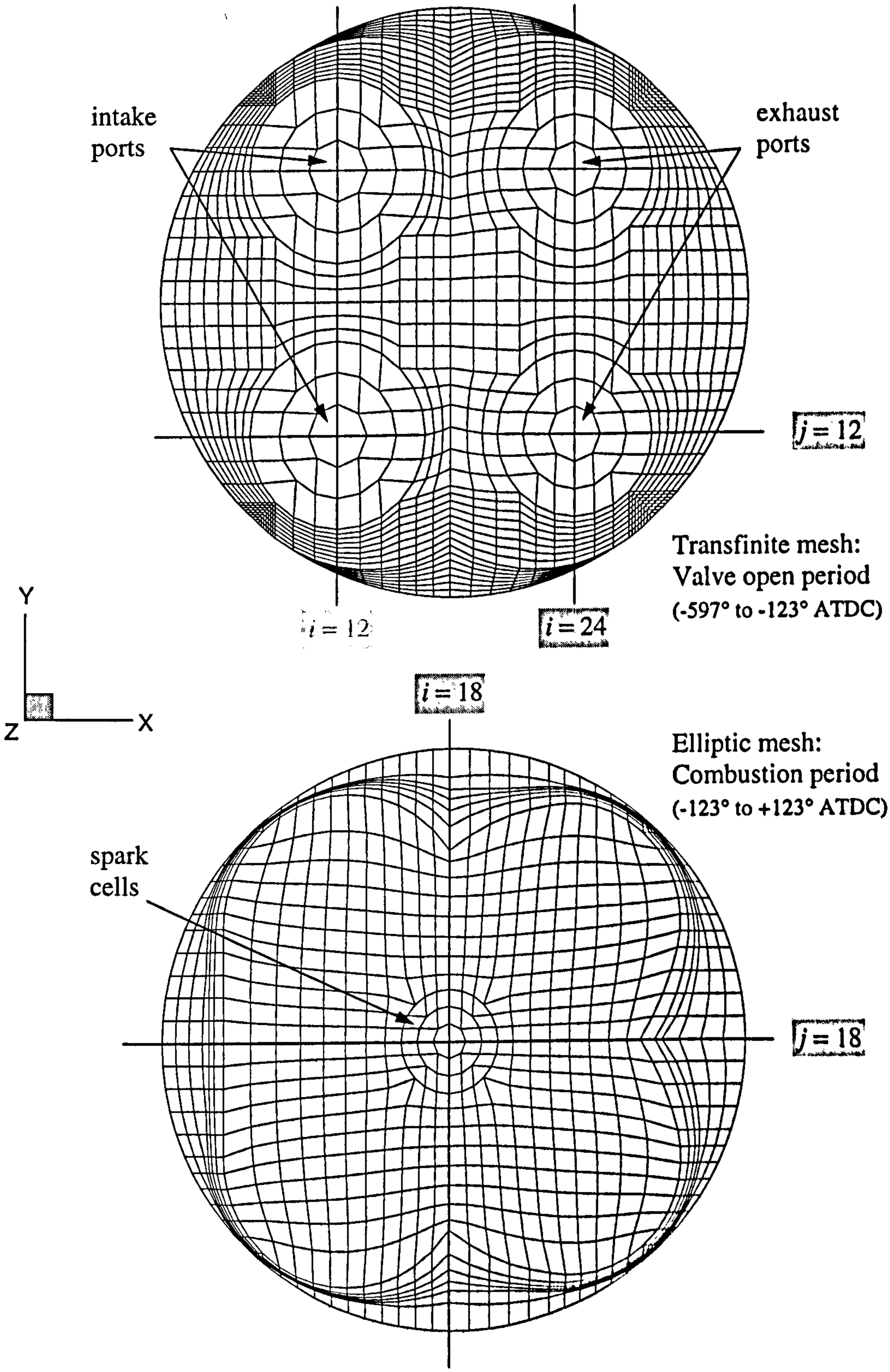

Figure 6.34 Ricardo Hydra: Location of *i* and *j* vertical planes on which vector field data is plotted in Figs. 6.35-38. (More mesh detail is shown in Fig. 2.15.)

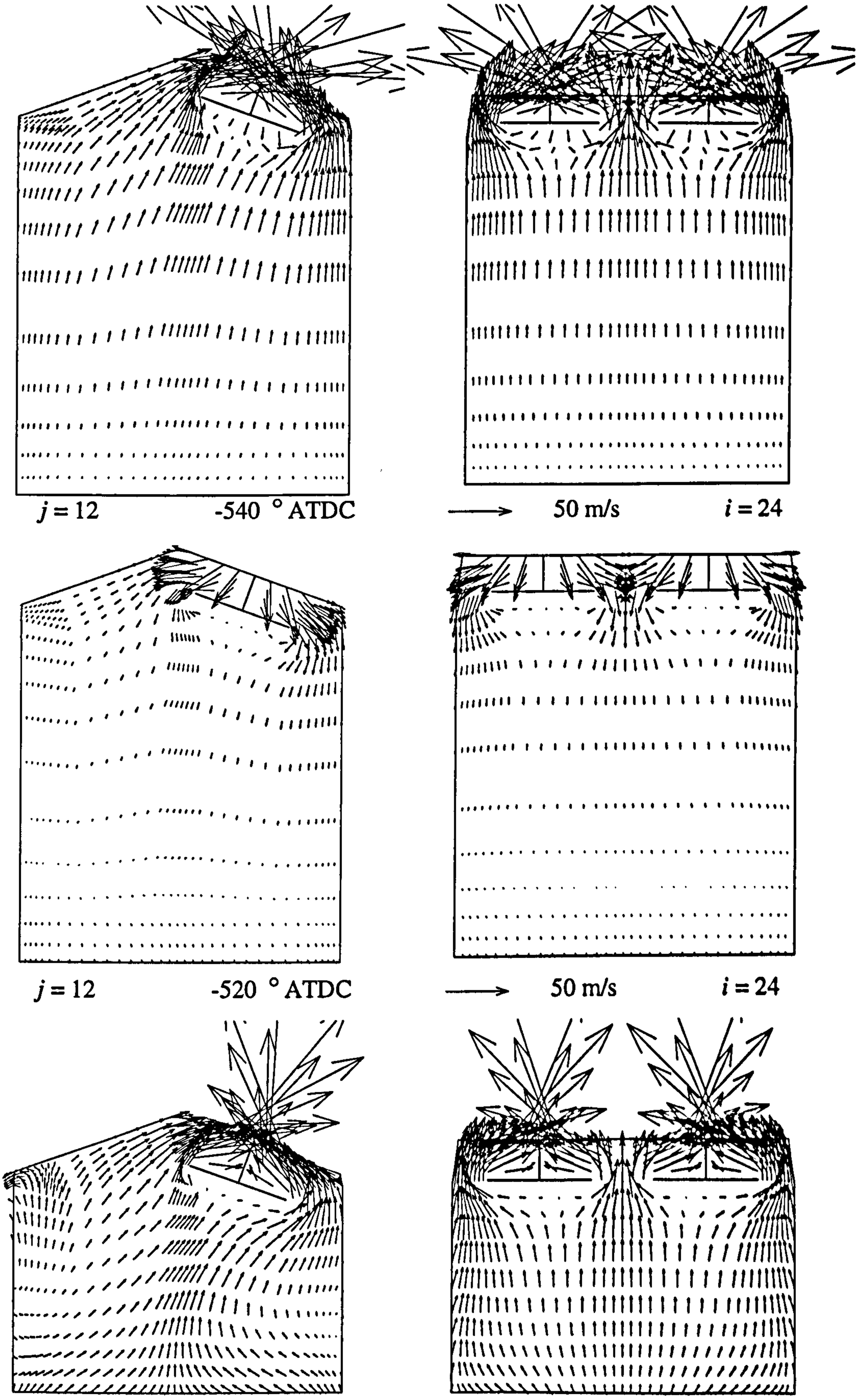

Figure 6.35 Ricardo Hydra: Computed velocities – exhaust blowdown and displacement.

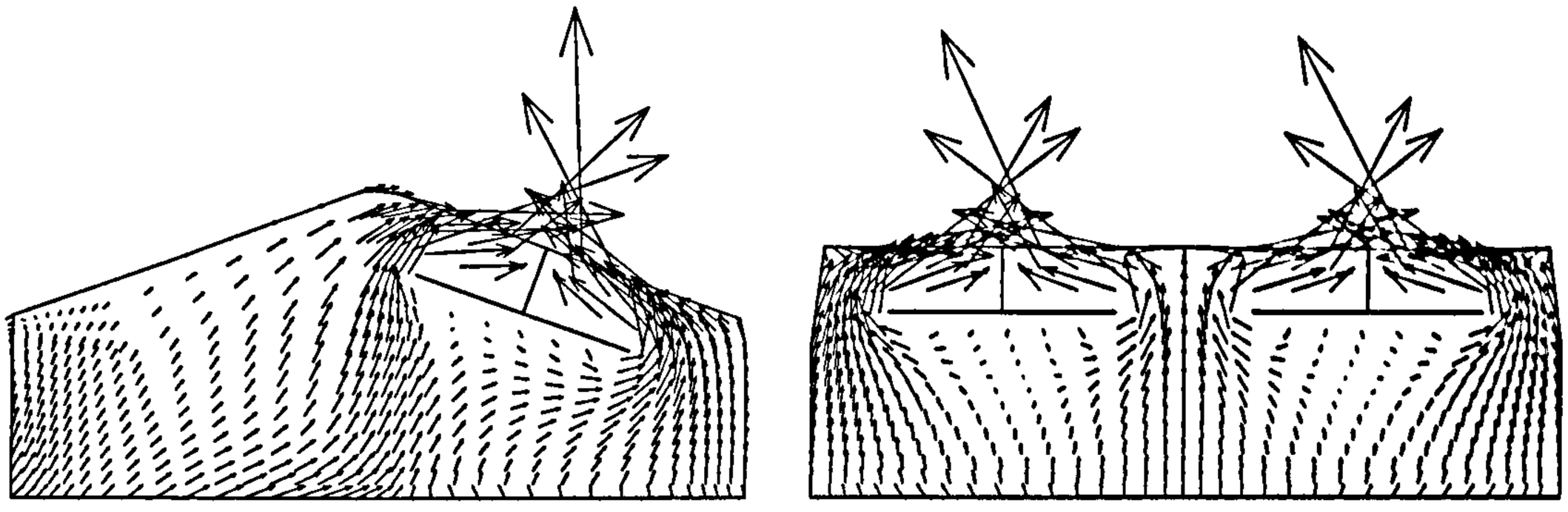

Figure 6.36 Ricardo Hydra: Computed velocities – exhaust, valve overlap and intake.

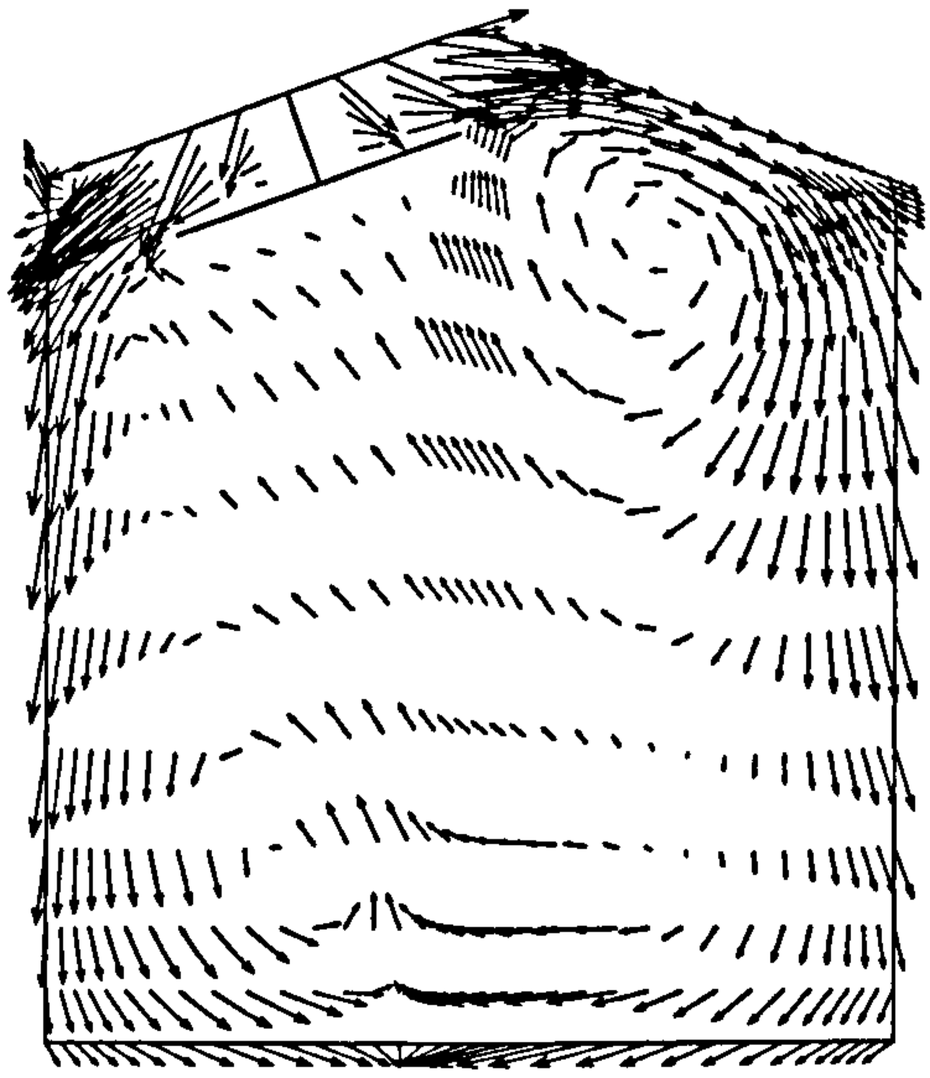

$j = 12$ -225 ° ATDC

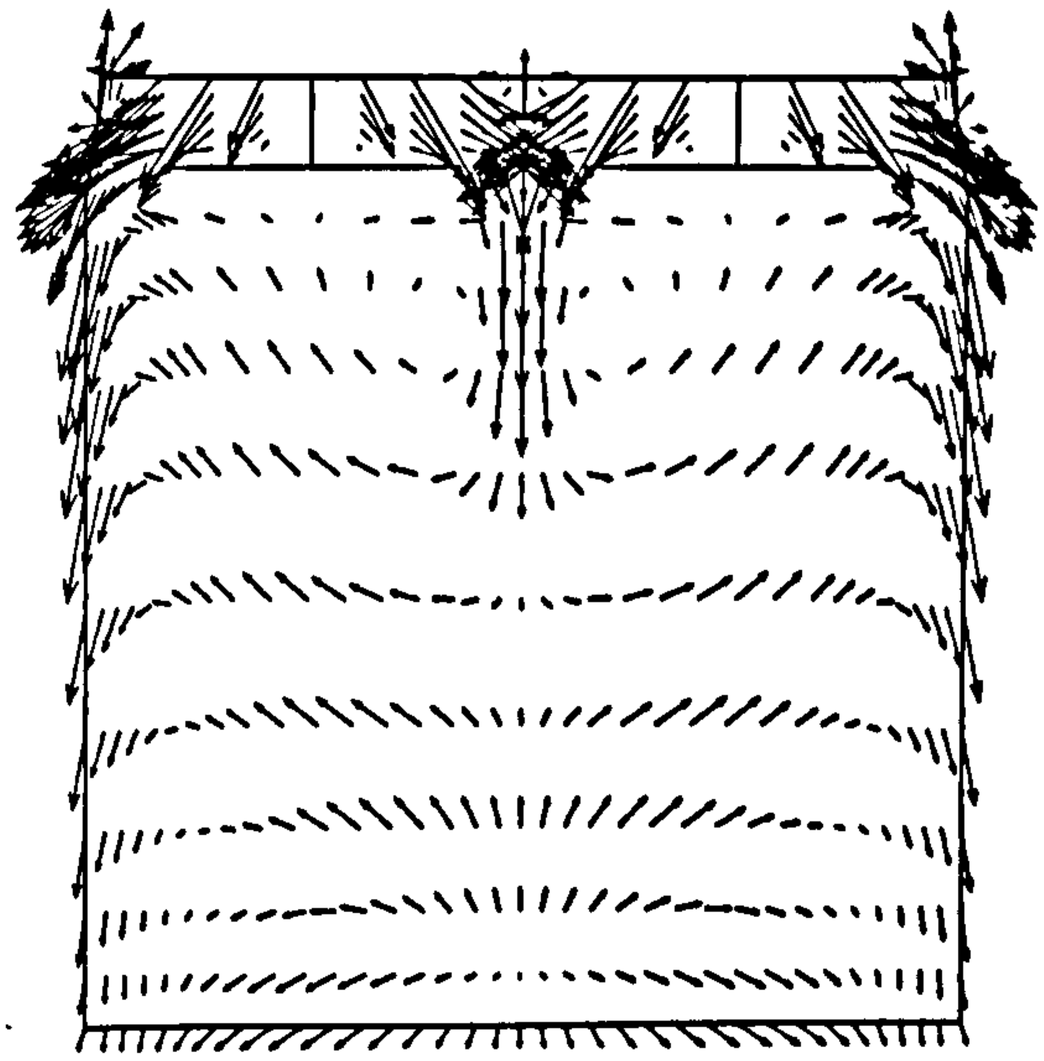

⟶ 25 m/s $i = 12$

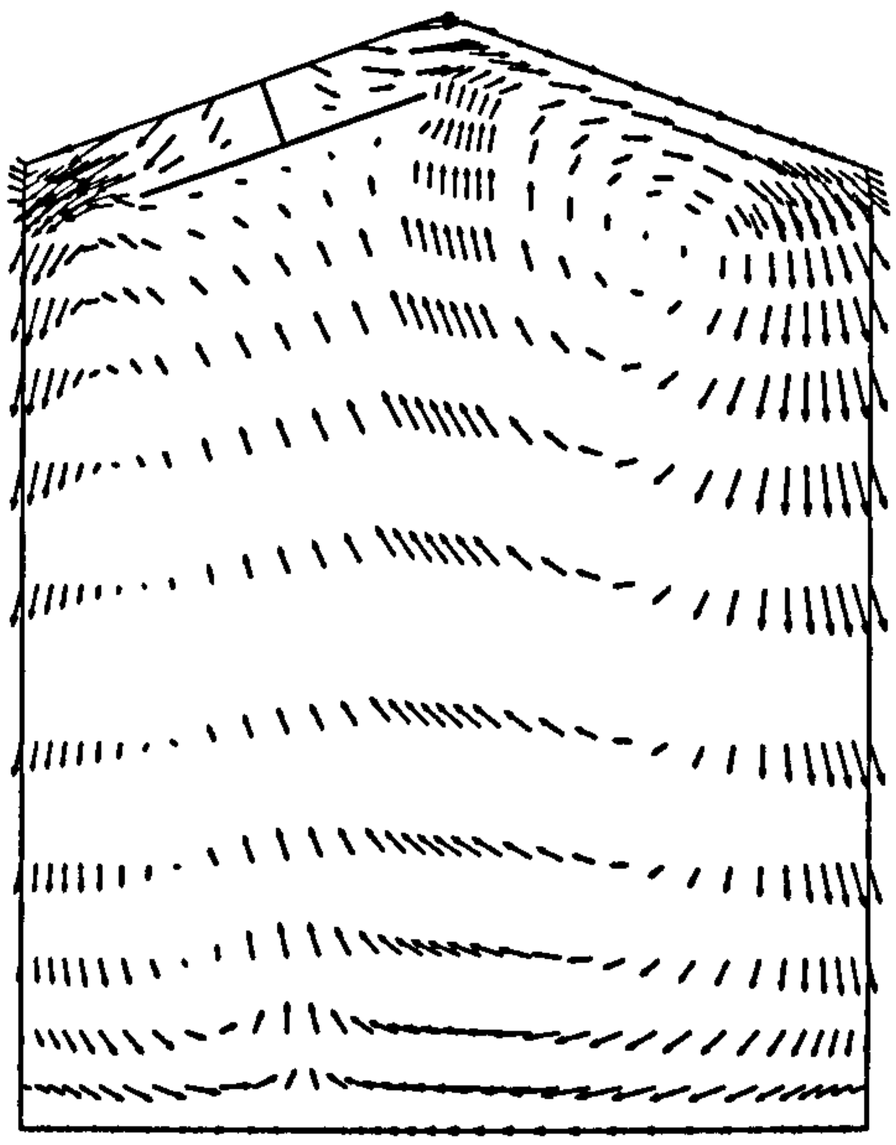

$j = 12$ -180 ° ATDC

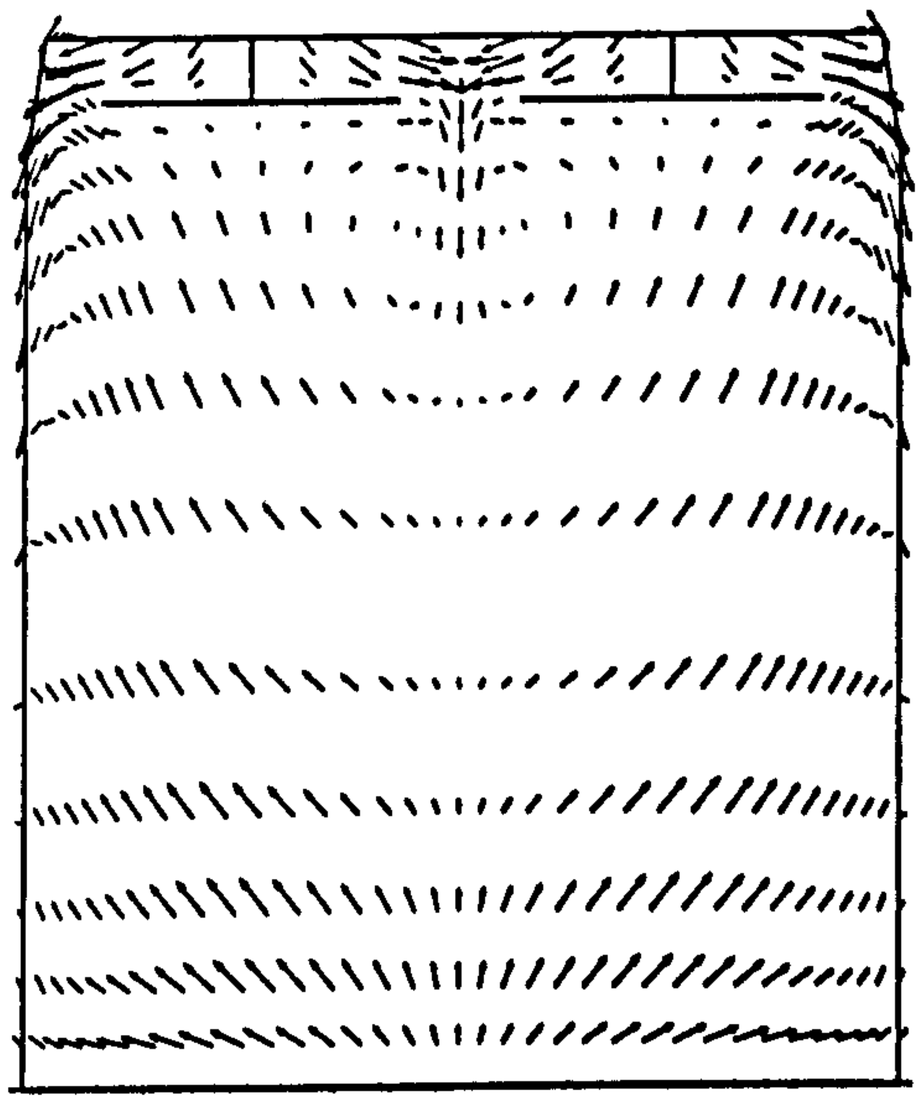

⟶ 25 m/s $i = 12$

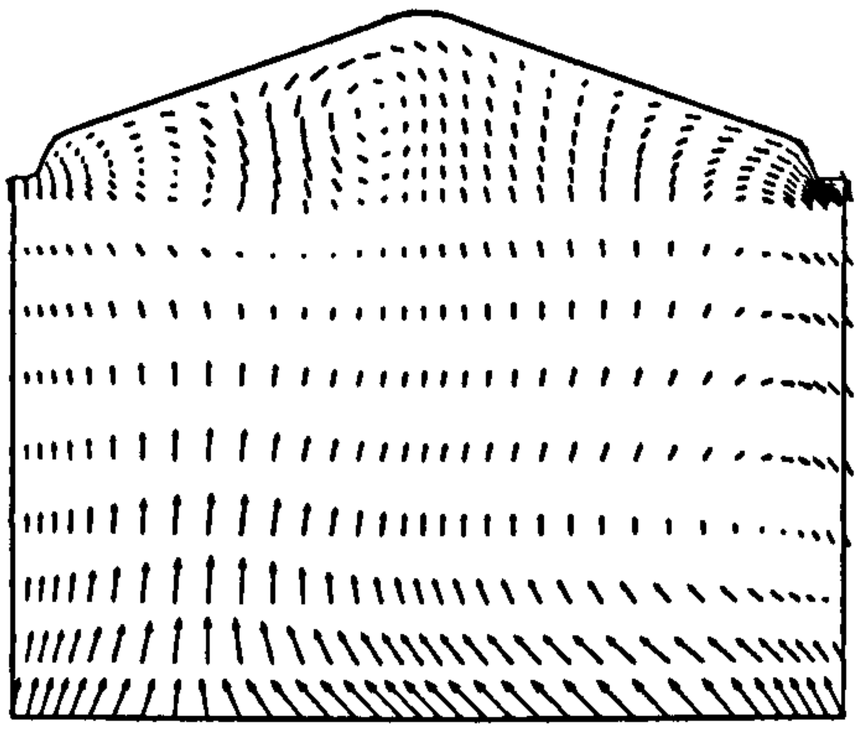

$j = 12$ -90 ° ATDC

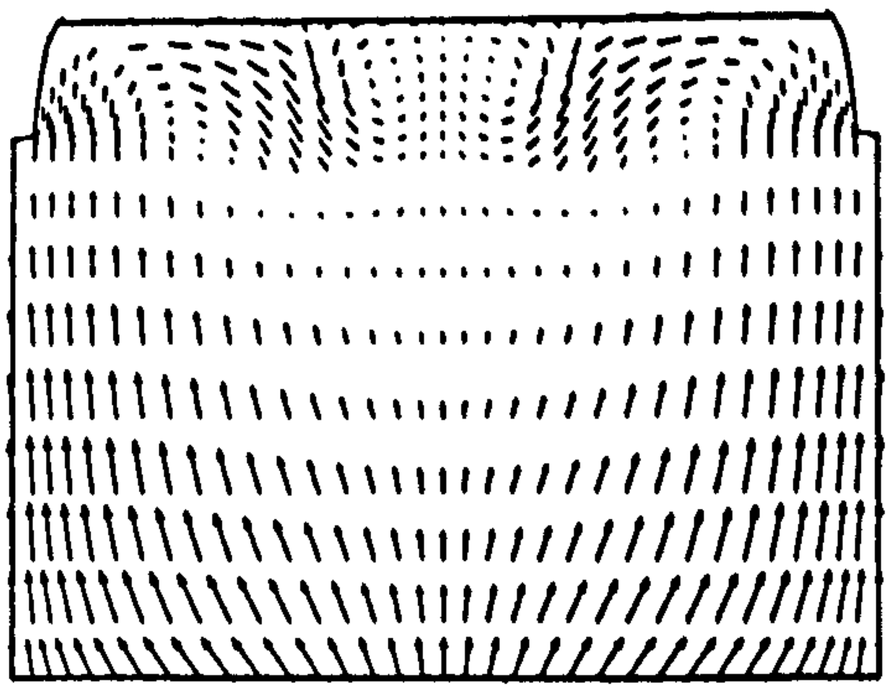

⟶ 25 m/s $i = 12$

Figure 6.37 Ricardo Hydra: Computed velocities – intake and compression.

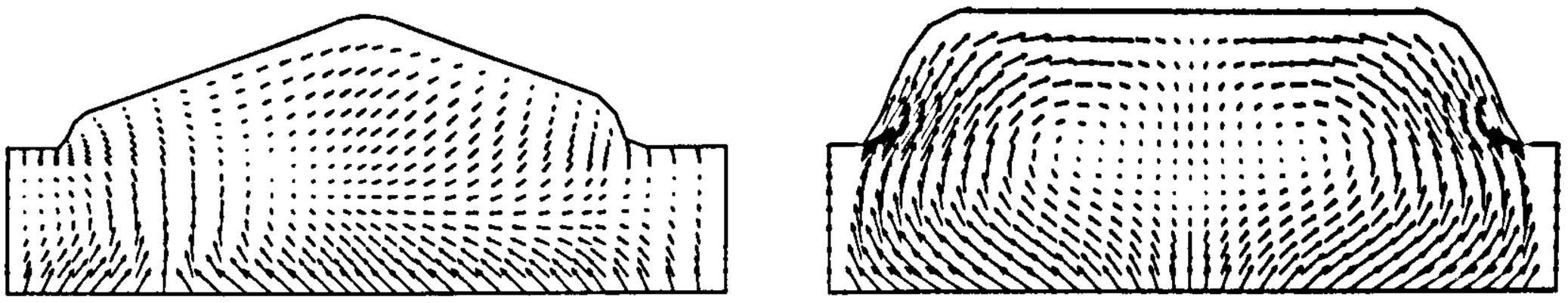

$j = 18$ -45° ATDC → 25 m/s $i = 18$

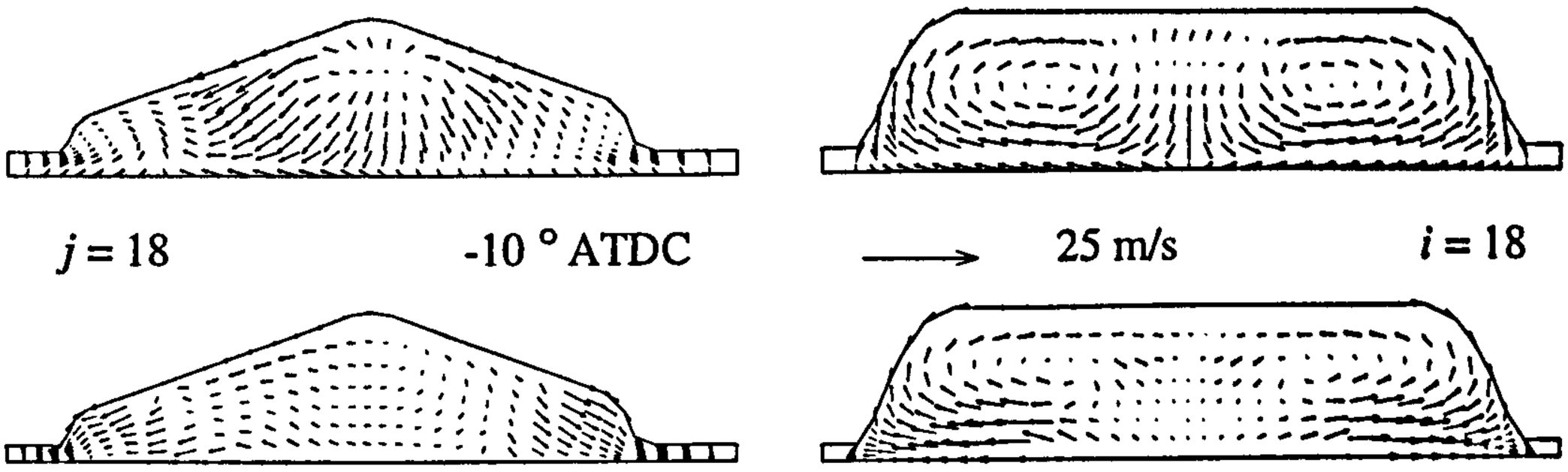

$j = 18$ -10 ° ATDC → 25 m/s $i = 18$

$j = 18$ Firing TDC → 25 m/s $i = 18$

$j = 18$ 10 ° ATDC → 25 m/s $i = 18$

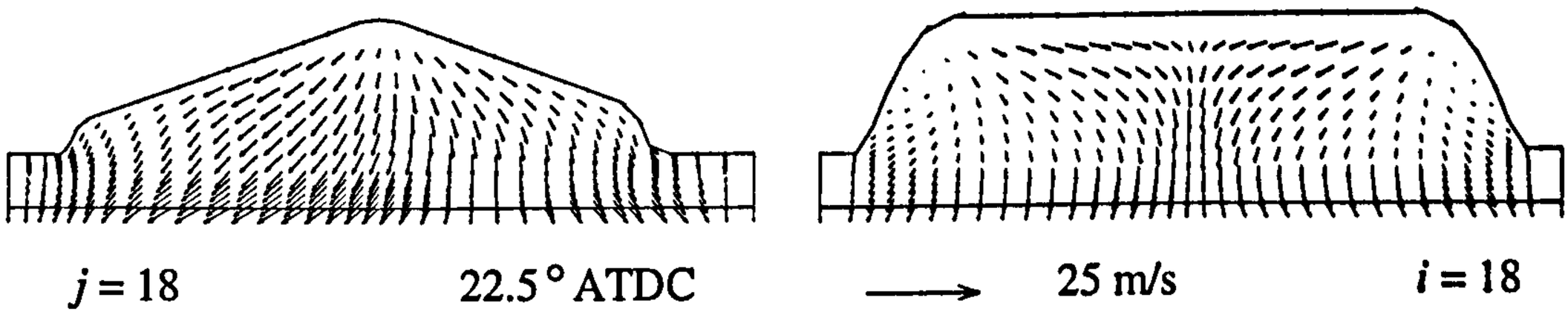

$j = 18$ 22.5 ° ATDC → 25 m/s $i = 18$

$j = 18$ 45 ° ATDC → 25 m/s $i = 18$

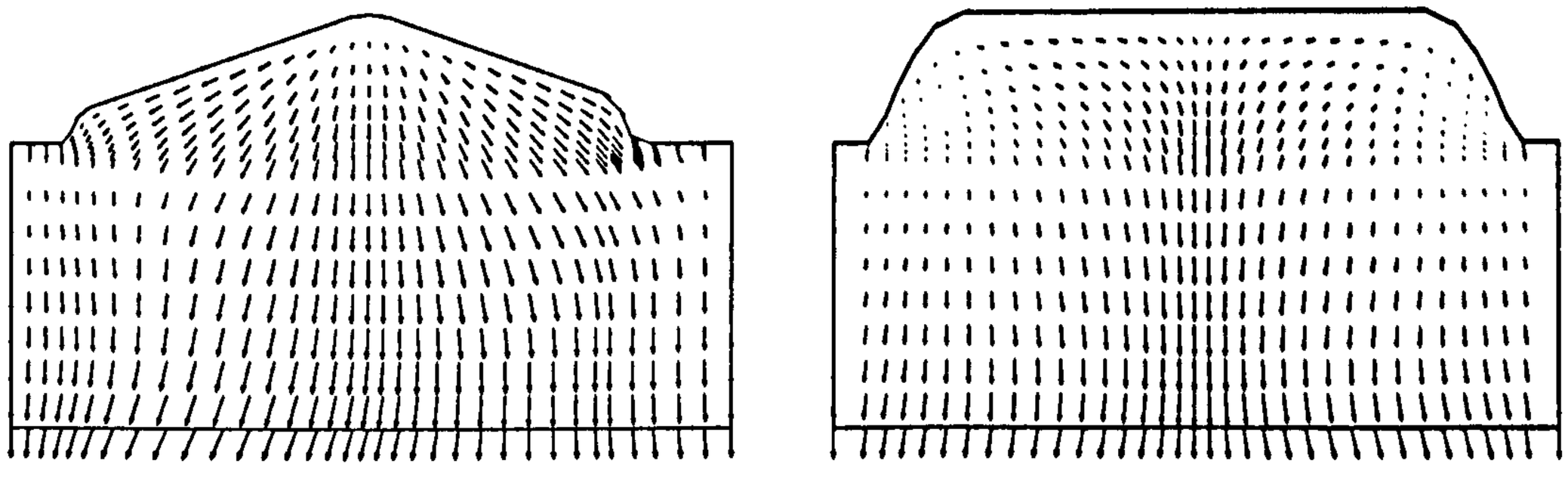

$j = 18$ 67.5 ° ATDC → 25 m/s $i = 18$

Figure 6.38 Ricardo Hydra: Computed velocities – compression, firing and expansion.

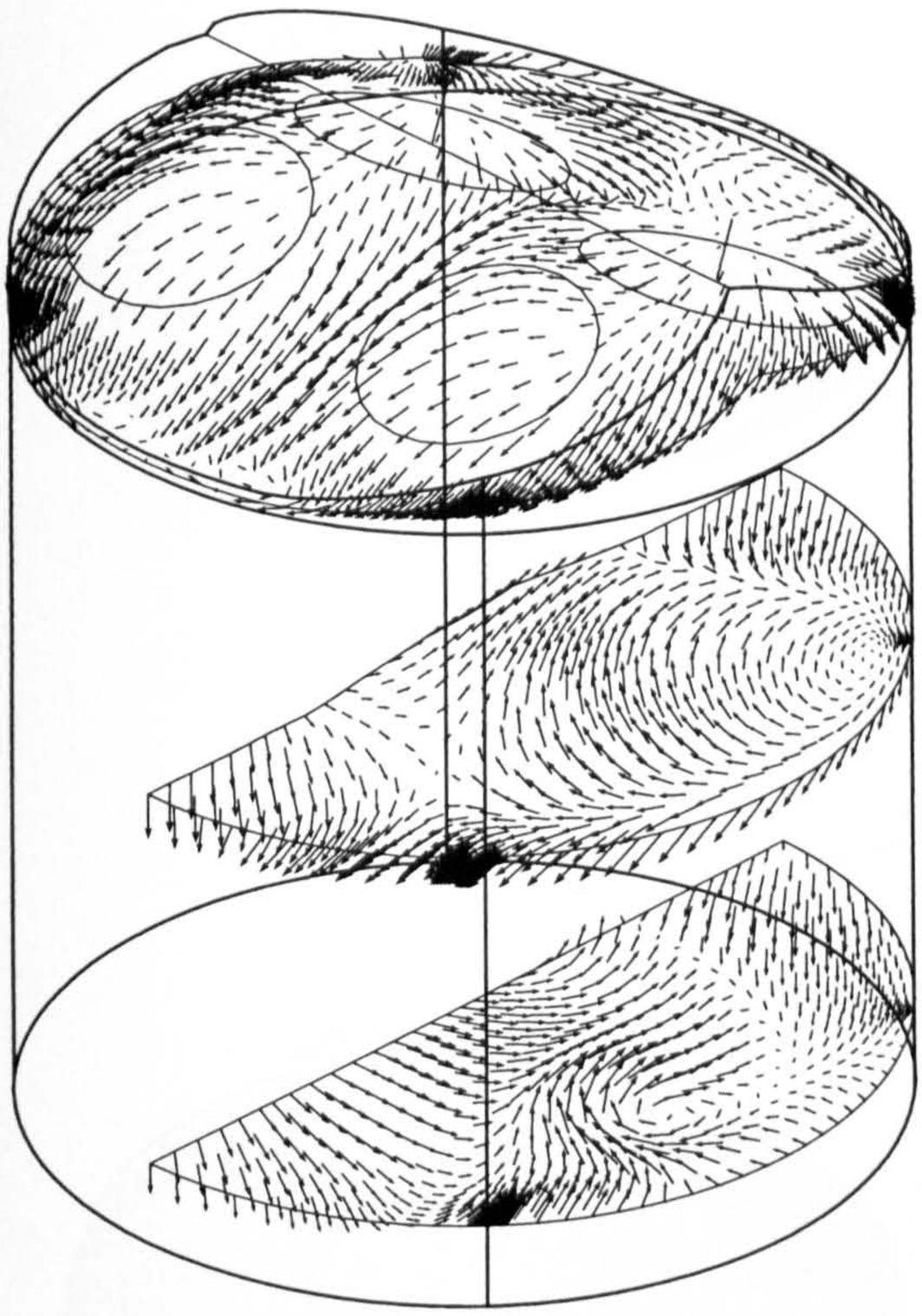

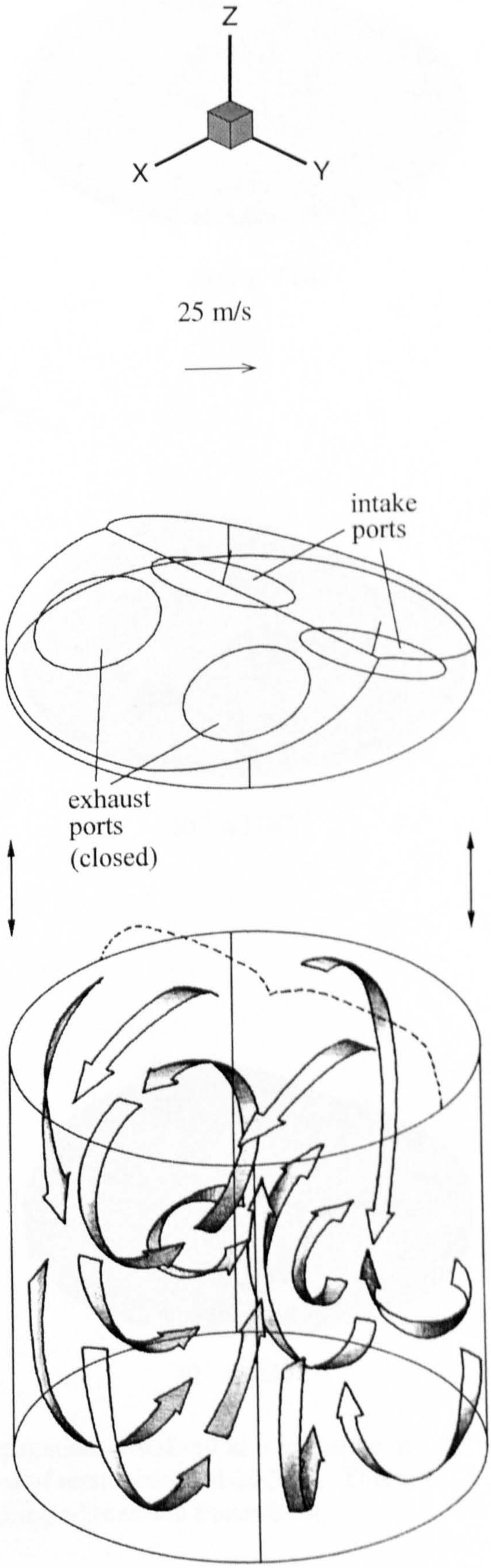

Figure 6.39

Computed velocities (above) and their interpretation (right) showing the three-dimensional flow structure at intake BDC (-180° ATDC).

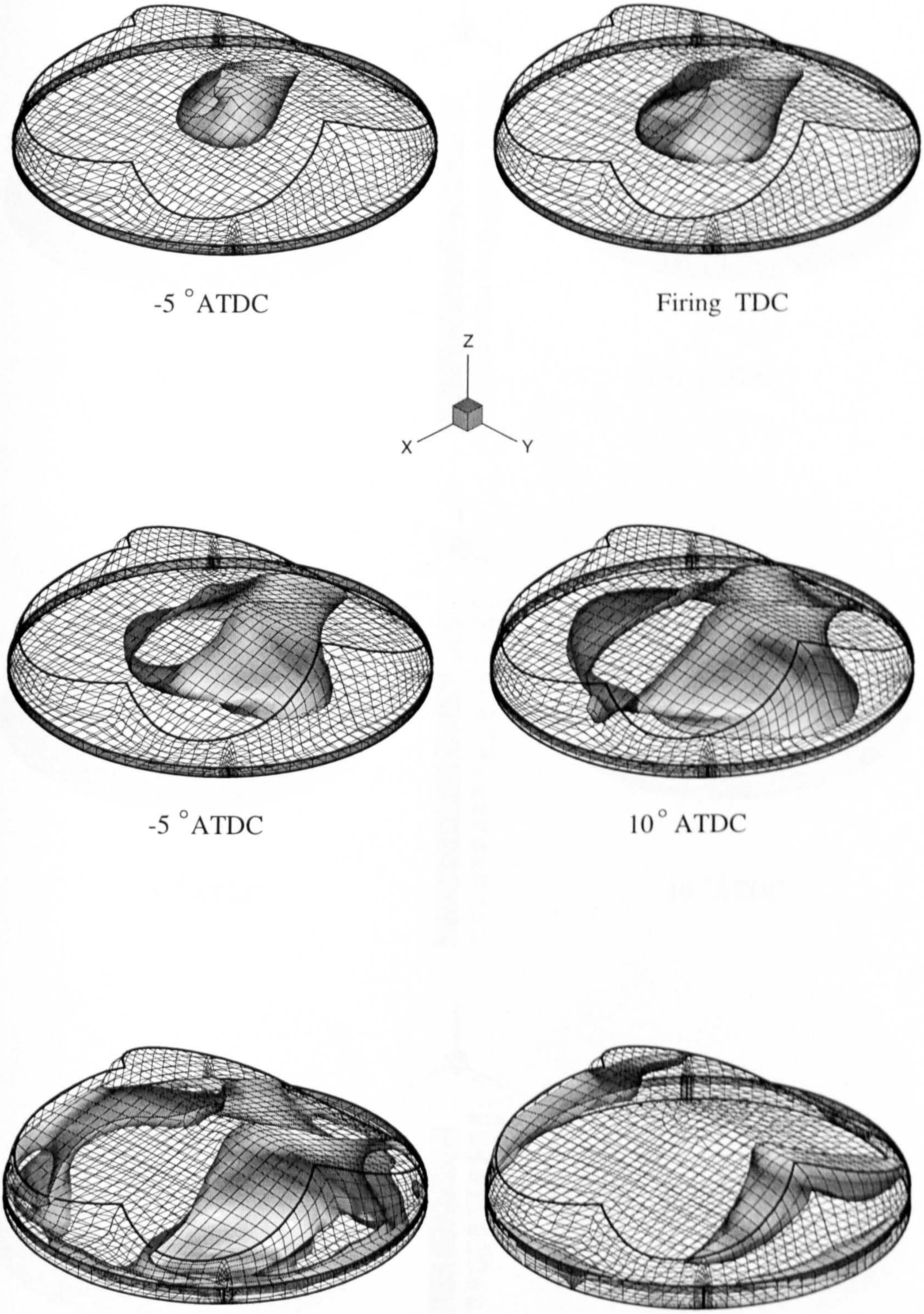

Figure 6.40 Ricardo Hydra: Flame front propagation visualised as a sequence of iso-surfaces (i.e. contour surfaces of equal value) at 2000 K. This is the temperature of gas in the trailing edge of the flame front.

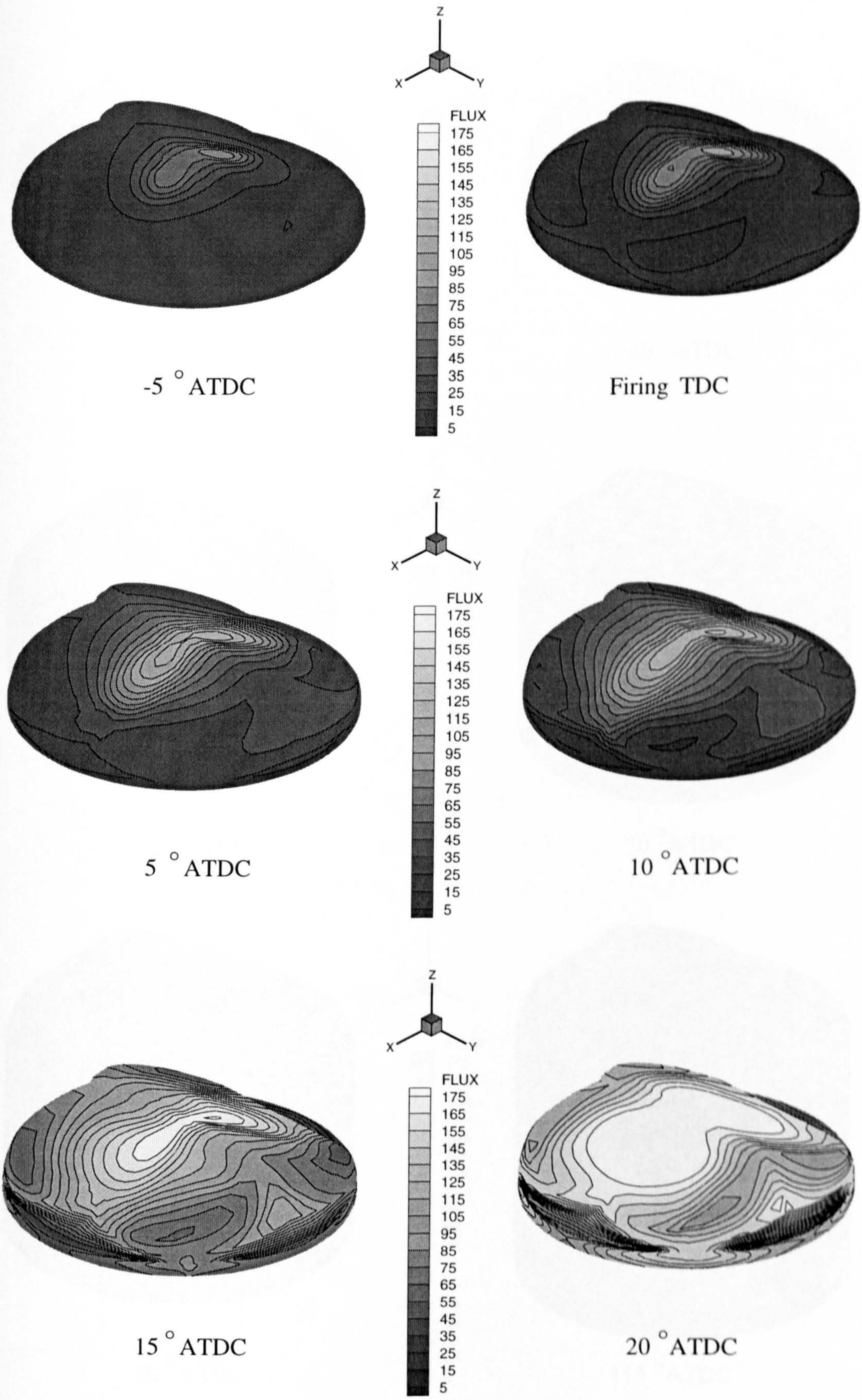

Figure 6.41 Ricardo Hydra: Computed contours of radiative surface heat flux, kW/m^2.

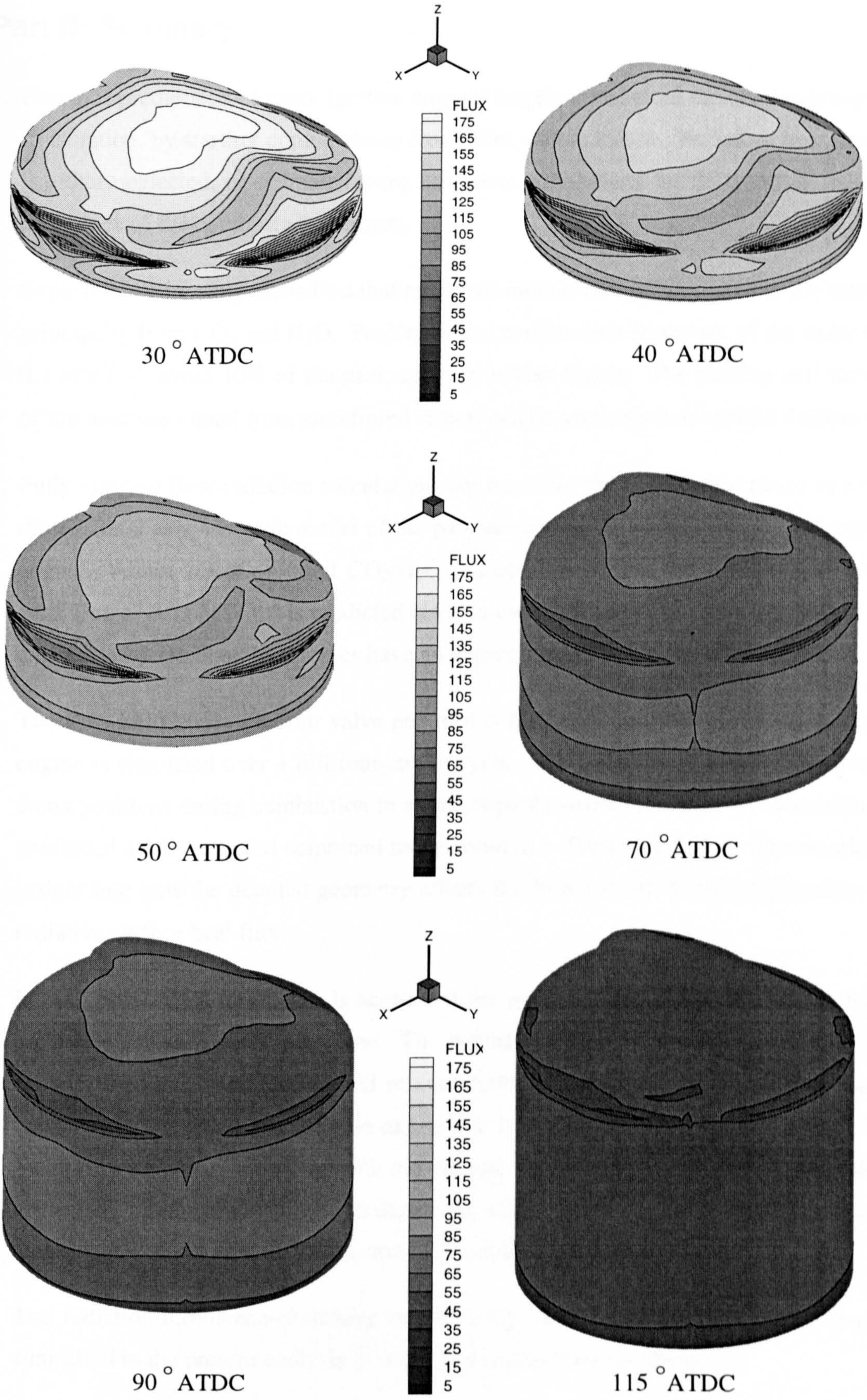

Figure 6.42 Ricardo Hydra: Computed contours of radiative surface heat flux, kW/m^2.

Part B: Summary

1. Previous predictions of spark ignition engines largely considered the combustion phase in isolation, by starting computations from inlet valve closure. Radiative heat transfer is either neglected, or estimated using empirical correlations for the nongray radiative properties of the combustion products.

2. Experimental investigations find that nearly all radiant energy is emitted in the infrared principally from CO_2 and H_2O. Peak radiative surface heat fluxes are of the order 0.2–0.3 MW/m^2: about 10% of the peak convective heat fluxes. The phasing and strength of the intensity signal from an infrared sensor can be used as a combustion diagnostic.

3. Fully-coupled flow-radiation calculations are made for the combustion phase in a two-dimensional axisymmetric model of the pancake combustion chamber of a Ricardo E6 engine. About 2/3 of the total CO_2/H_2O radiant flux is from the water vapour and a peak flux of 0.23 MW/m^2 is predicted close to the spark where products are hottest and concentrated. Radiant heat losses have an appreciable effect on the reaction rate.

4. The flow field inside the four valve pentroof combustion chamber of a Ricardo Hydra engine is simulated over a full four-stroke cycle. The radiant flux is found at specific crank positions during combustion in an uncoupled calculation. (Computational limits precluded a fully-coupled combined mode solution.) These results provide remarkable insight into how the detailed geometry effects the flow motion, flame propagation and radiative surface heat flux.

5. In both predictions turbulence is accounted for with the k–ε model: additional terms are added for variable density flow. The hybrid kinetic/EDC combustion model is to account for kinetics-controlled and mixing-controlled combustion. Tuning of model constants in the mean reaction rate expression is via experimental pressure data. The radiation transport is simulated with the discrete transfer–WSGG model. Calculations are largely demonstrational due to numerous uncertainties in boundary conditions for temperature, emissivity, etc. and unavoidable discretisation errors.

6. The radiation-turbulence-chemistry is intimately linked, but this relation is grossly simplified in the present analysis in order that calculations are tractable.

Chapter 7

Conclusions and Recommendations

A numerical scheme for the coupled solution of turbulent combustion with participating radiative heat transfer has been developed and applied in studies of spark ignition engines. Here, the ability to handle complex geometry, nonhomogeneous properties (spatial and temporal) and the strong spectral dependence of the radiation transport in a tractable, yet accurate, manner has been the principal achievement of this work.

Section 7.1 lists the present contribution. The concluding remarks of Sec. 7.2 then follow the general outline of the thesis highlighting the main aspects or findings pertaining to the objectives of the research (Sec. 1.3). Limitations are identified in the present approach and this forms the basis of suggestions for further work in Sec. 7.3.

7.1 Present Contribution

The following achievements comprise the main contribution of this research.

- Numerical mesh generation techniques for the body-fitted representation of complex geometries with arbitrary hexahedral elements have been developed and implemented.

- The KIVA-II engine-specific CFD code has been extensively modified to enable the simulation of open ports and moving valves, and one-dimensional wave action effects in the exhaust. Furthermore, new k–ε turbulence terms for variable density flows; the EDC model for mixing-controlled combustion and the Shell model for end-gas autoignition have also been added to improve predictions, in addition to provision for coupled flow-radiation calculations.

- The Monte Carlo, YIX and discrete transfer radiation models for complex participating media have been implemented from the best available knowledge. A systematic assessment of their performance is shown for a variety of benchmark problems.

- A general WSGG model has been implemented to provide a gray-gas approximation of nongray, nonisothermal radiating combustion products. A hybrid narrow- and wide-band model is used to compute the spectral variation in absorption coefficient as input to the WSGG model. It is shown that predictions from the overall procedure are in good agreement with nongray benchmark solutions for CO_2 radiating media.

- Two-dimensional axisymmetric flow-radiation predictions of combustion in a pancake engine have reproduced experimental correlations of peak radiative intensity with peak cylinder pressure. Calculations reveal temporal/spatial variations in the instantaneous radiative flux at the cylinder walls, the effect of changing engine operating parameters, and the relative importance of emission from different combustion products.

- A three-dimensional simulation has demonstrated how the complex geometry of a pentroof combustion chamber affects the flow structure, the flame front evolution and the radiation over a four-stroke engine cycle.

7.2 Concluding Remarks

There is a need for models able to describe participating radiative heat transfer in coupled CFD heat transfer calculations. Engine combustion is a particularly demanding problem being characterised by complex geometry, transient conditions, property discontinuities and spectral effects: methods versatile enough to handle all these difficulties should also be generally applicable to a wide variety of fire and combustion systems

7.2.1 Spatial Discretisation

The first effort in this research was concerned with developing flexible numerical mesh generation tools to enable the body-fitted description of complex geometries with a single block of arbitrary hexahedral elements suitable for the finite-volume CFD code KIVA-II.

Transfinite interpolation is fast, inexpensive and conceptually simple in that a multi-directional interpolation of boundary surfaces is built-up by effectively interpolating in each coordinate direction and combining the results. However, boundary discontinuities propagate into the interior since there is no inherent smoothing mechanism. A transfinite mesh may be smoothed by solving an elliptic system of partial differential equations for

the mesh coordinates. Then, constraints on the mesh line distribution may also be introduced via control functions and by fixing interior nodes. The elliptic mesh generation of the complex pentroof engine geometry in Sec. 2.4 required all of these techniques and would not have been possible with simpler algebraic methods.

To achieve the greatest modelling flexibility it was desired that the radiation model should incorporate a geometric scheme for arbitrary hexahedral and/or tetrahedral elements. This capability is realised by preprocessing elements into triangles, prior to ray-tracing, and by representing property distributions with finite element parametric mapping techniques. At present the scheme is designed for direct incorporation into KIVA-II and search strategies take advantage of the structured *ijk* cell indexing of the CFD code. However, application to unstructured meshes simply requires modification of the search algorithms to utilise their nodal connectivity. Then it should be compatible with most commercial mesh generators. From a numerical point of view this geometric representation avoids errors associated with interpolating radiation sources in coupled flow-radiation calculations and elements can be arbitrarily defined so as to resolve the strong gradients in reactive flows.

7.2.2 Description of Turbulence and Combustion

Considerable time was invested in an effort to improve the original KIVA-II CFD models of turbulence and combustion: these are the foundation on which the flow-radiation solver is developed.

The computation of multi-species turbulent flow involving chemical reaction is based on a finite-volume scheme which solves the Favre-averaged momentum and scalar equations in an arbitrary Lagrangian-Eulerian (ALE) calculation. Closure for the Reynolds stresses and scalar fluxes is obtained via the k–ε turbulence model using a linear eddy viscosity gradient-diffusion approximation. Extra source terms were added to the standard k and ε–equations to account for volumetric and pressure-density effects in variable density flow. Unclosed terms in the scalar equations due to chemical reaction are calculated by making assumptions about the time-scale of reaction and the nature of the reaction. In the original KIVA-II scheme all reactions were assumed to proceed either kinetically or be in chemical equilibrium: no allowance was made for reactant mixing (and heating) times.

Thus, the eddy dissipation concept (EDC) was introduced into the existing scheme to attempt to account for both kinetics- and mixing-controlled processes: here mean reaction rates from each mechanism are combined by taking their harmonic average. Case-by-case tuning of the reaction rate with experimental data is required. Additional submodels are used for ignition, and autoignition during knocking combustion. The reduced Shell model has been incorporated into the code for the latter purpose. This model simulates the cool flame reactions leading to autoignition with a simplified reaction mechanism. Classical 'log-law' relations are used to model conditions in near-wall boundary layers: the original KIVA-II treatment for turbulence kinetic energy had to be modified in order to avoid unrealistically fast mixing-controlled combustion along walls when the EDC model is active. Finally, wave action effects at the exhaust boundary are simulated with a one-dimensional gas dynamics model based on the method of characteristics.

Calculations of the in-cylinder combustion in two- and three-dimensional studies of spark ignition engines demonstrate good flow and heat release predictions. The complex flow motions during induction, particularly the vortex field at intake BDC, and the flame front evolution in the three-dimensional Ricardo Hydra study are notable results. Visualisation data was not available, but previous experimental (and computational) studies for similar engine geometries are cited to support the present predictions. Here, it is observed that as the flow complexity increases experimental measurements involve more uncertainty and visualisation data is open to more interpretation. Consequently, the quality of predictions, including those in the present study, becomes more difficult to justify.

Strengths and weaknesses with regard to the different models used in the present scheme have been discussed, but taking precedence over all of these is a general feeling of dissatisfaction with the combustion treatment. The introduction of the EDC approach certainly provides for a greater degree of control, reducing stability problems suffered with the original kinetic scheme, but the prediction of reaction rate still depends crucially on the specified initial conditions and choice of model constants. Optimising the model for any given engine operating condition can be extremely time consuming and is moving the emphasis away from prediction and more towards correlation. In the presence of radiation, another shortcoming of the turbulence-combustion treatment is its inability to provide the fluctuation in temperature and species concentration to enable an accurate assessment of the turbulence-radiation interaction (TRI). Lower flame temperatures can

be expected when TRI is included but by how much is still a matter of conjecture. This has focused interest in probability density function (PDF) methods. These represent the mean reaction rate term exactly, such that the empirical EDC-like models are avoided, and in addition, they allow the accurate determination of scalar fluctuations. At present there is interest in developing PDF schemes for the calculation of the reactive sources and the turbulence-radiation interactions, which are then fed into a finite volume solver for the transport of momentum and averaged scalars. Modest and Collins (1989) details difficulties that must first be overcome.

7.2.3 Radiation Model

The review, selection and development of radiation methods suitable for the analysis of complex participating media has been the main focus of this study.

The integro-differential and integral forms of the governing equation for participating radiation transport are first presented. These provide an interesting basis from which to review and classify solution methods, e.g. discrete ordinate techniques solve the primitive integro-differential form in $(\mathbf{r},\hat{\mathbf{s}})$ space, in contrast to integral-based formulations such as YIX and discrete transfer in which only the three space coordinates appear. These latter two methods also seemed more conducive to the analysis of nonorthogonal geometries, when this research was started, and consequently, were selected for further study. Much work was required in order to develop a three-dimensional YIX solver. In addition, an efficient pathlength-based Monte Carlo algorithm was implemented: here 'efficient' refers to a speed-up compared with classical Monte Carlo. Calculations are longer by two orders of magnitude (or more) compared with deterministic methods; but advantage is taken of the ability of the stochastic approach to provide accurate solutions, together with a measure of their uncertainty for verifying other methods.

Additional models are required in order to treat the nongray (spectrally dependent) nature of radiative transfer in high temperature gases. A weighted-sum-of-gray-gases (WSGG) model has been implemented from a very new scheme reported in the literature. This approach is conceptually quite different from classical WSGG correlations in that it provides for a numerical treatment of nonisothermal and nonhomogeneous arbitrary gas mixtures. The model parameters may be generated from line-by-line or band model data. The former option provides for high accuracy but presupposes that line-by-line spectral

data for radiating species at high temperature and pressure is readily available. As yet this is not the case and given limited time a more approximate narrow- and wide-band model is used to generate the required input data for the WSGG model. The end result of this nongray treatment is a set of local gray absorption coefficients that can be used directly in the present Monte Carlo, YIX or discrete transfer methods, or for that matter any solution method where the absorption coefficient is specified as the basic radiative property (as opposed to transmissivity).

The solution of both gray and nongray benchmarking media demonstrate that the present Monte Carlo, YIX and discrete transfer methods yield almost identical solutions when cell optical thicknesses $\tau < 1$. However, if this limit is exceeded solution discrepancies are noticeable due to the different manner in which each method approximates property gradients across medium elements. This is of concern in the WSGG analysis of nongray media due to the disproportionate error that arises from the solution of optically thick gray gas intervals at gas band centres compared to optically thin intervals in the discretised absorption spectrum. It is envisaged that the present techniques could be combined with specialised methods which solve separately for the radiative transport in the optically thick intervals in order to improve accuracy. Another consequence of the strong variation in spectral absorption is that small differences in the gray gas approximation significantly effect the total radiative heat transfer solution: a problem noted in efforts to benchmark nongray media.

The discrete transfer method is found to be fast, economic and reasonably accurate: on balance it provides a better approximation for radiation sources in optically thick medium elements than YIX. Scattering anisotropy and non-diffuse boundaries cannot be solved. It is felt that attempts to make the method more flexible or accurate (i.e. 'conservative' schemes) may be misguided since these always add computation and complexity, and the YIX method or another technique provides in all respects a better alternative. At first sight the YIX methodology appears quite different from that of discrete transfer being mathematically rigorous. However, in application it shares many similarities, particularly with regard to the integration of the incident radiative flux at surface points. In fact, it is arguably an extension of the discrete transfer approach with improved modelling fidelity in medium elements, although it has never been acknowledged as such in the literature. It differs in two important respects.

First, YIX integrates the intensities along rays traced from points both within the medium and on the enclosing boundaries, whereas discrete transfer traces rays solely from the boundary. This facilitates the treatment of scattering anisotropy and gives accurate *point* values for the irradiation at points within the medium, but a downside is that substantially more computation is required. Here, it is not difficult to conceive an analogous discrete transfer scheme. Then discrete transfer solutions for scattering anisotropy would be feasible and the level of accuracy should be comparable for both methods. However, YIX would still be superior because of its other chief distinction, i.e. the distance quadrature. A performance advantage is attained by YIX via the elimination of exponential kernel evaluations. Therefore, the 'extended' discrete transfer scheme would always be less efficient; but in simpler problems (i.e. without scattering anisotropy) the classical discrete transfer method is much faster as the advantage of tracing far fewer rays more than offsets the penalty associated with the exponential calculation. Consequently, it is recommended that YIX is reserved for more complex anisotropic media where discrete transfer fails.

Monte Carlo methods offer unprecedented flexibility and coding simplicity. They have proved an invaluable tool for verification purposes in the present study, but their massive computational requirement precluded their application for coupled, transient calculations of engine combustion. However, it is possible to foresee a scenario where these methods may be the preferred choice even for these problems. If PDF methods based on a Monte Carlo simulation of turbulent reacting flow become popular (for the reasons noted above) then all modes of heat transfer, including radiation, are based on a stochastic scheme. The benefits of this are likely to be fully realised in parallel computations, were inefficiencies resulting from discord between different schemes for heat and mass transport are avoided, and were the inherent parallelism of Monte Carlo may be exploited.

The discrete transfer–WSGG radiation calculations in the engine combustion studies are an excellent demonstration of the ability to cope with complex geometry and very strong property gradients. Radiant losses to the cylinder walls result in a small, but appreciable lowering of flame temperatures during combustion. The predictions reproduce important experimental trends and provide additional insight into how the flame front propagation influences the instantaneous radiative heat flux on the cylinder walls. The ability to perform accurate quantitative calculations requires experimental measurement of surface emissivities and high temperature spectra in order to validate the model parameters.

7.3 Recommendations for Further Work

Several areas that would benefit from further work were noted in the preceding chapters. The recommendations here focus on the most interesting emerging developments.

1. A Reynolds stress model should be implemented in place of the k–ε turbulence model following the approach of Lebrère and Dillies (1996), or as a cheaper alternative, the cubic eddy-viscosity model of Craft et al. (1996) could be investigated. This provides for the description of turbulence anisotropy in complex engine flows.

2. The kinetic/EDC combustion model should be improved by eliminating redundancy in the model constants and by considering a better representation of the chemical kinetics, e.g. see comparisons of detailed and reduced ILDM schemes with EDC by Gran (1994). Premixed laminar flamelet (e.g. Bray, Libby and Moss 1985) or PDF transport models (Mazumder and Modest (1997a, b) in place of EDC should be assessed. A new wrinkled-flame (Weller) combustion model is also worth consideration: its application to SI engine simulation is demonstrated by Heel *et al.* (1998). In addition, this work includes reference to a detailed ignition model.

3. New discrete ordinate schemes for nonorthogonal geometries should be evaluated: the algorithm by Sakami *et al.* (1997) (see discussion of Sec. 4.2) is a notable example. In parallel computations the efficiency of algorithms for frequency, angular and critically, spatial domain-based decomposition is important (see Burns and Christon 1996): these additional criteria should be included in the assessment of radiation methodologies.

4. An optimisation technique should be implemented to minimise discretisation errors in the WSGG model spectrum (Sec. 5.4.2): a conjugate gradient method is employed by Dension and Webb (1993). Advantage should also be taken of high temperature line-by-line spectral data under compilation in the HITEMP database (Rothman 1998).

5. Further tests of the present models against experimental data are required. Engine flow visualisations need to be combined with detailed in-cylinder measurements of pressure, temperature, velocity and radiation intensity at multiple sites and over a wide range of operating conditions in order to achieve the greatest benefit for model validation.

Appendix A

Transformation Relations

A.1 Basic Relations

A physical domain is represented by Cartesian coordinates $x_i \,(\equiv x, y, z)$, $i = 1, 2, 3$ and its transformation in the computational domain by curvilinear coordinates $\xi_i \,(\equiv \xi, \eta, \zeta)$, $i = 1, 2, 3$. Then the one-to-one mapping between the two may be expressed as:

$$x = x(\xi,\eta,\zeta), \qquad y = y(\xi,\eta,\zeta) \qquad \text{and} \qquad z = z(\xi,\eta,\zeta) \tag{A.1}$$

and by implication $\xi = \xi(z, y, z)$, etc. Given these relationships first derivatives w.r.t. ξ, η and ζ for a function A are given by:

$$A_{x_i} = \sum_{j=1}^{3} A_{\xi^j} \left(\xi^j\right)_{x_i} \qquad i = 1, 2, 3 \tag{A.2}$$

or, equivalently,

$$A_{\xi^i} = \sum_{j=1}^{3} A_{x_i} \left(x_j\right)_{\xi^i} \qquad i = 1, 2, 3 \tag{A.3}$$

where the subscripts denote partial differentiation, i.e. expanding Eq. (A.2)::

$$i = 1, \qquad \frac{\partial A}{\partial x} = \left(\frac{\partial A}{\partial \xi}\right)\left(\frac{\partial \xi}{\partial x}\right) + \left(\frac{\partial A}{\partial \eta}\right)\left(\frac{\partial \eta}{\partial x}\right) + \left(\frac{\partial A}{\partial \zeta}\right)\left(\frac{\partial \zeta}{\partial x}\right) \tag{A.4}$$

$$i = 2, \qquad \frac{\partial A}{\partial y} = \left(\frac{\partial A}{\partial \xi}\right)\left(\frac{\partial \xi}{\partial y}\right) + \left(\frac{\partial A}{\partial \eta}\right)\left(\frac{\partial \eta}{\partial y}\right) + \left(\frac{\partial A}{\partial \zeta}\right)\left(\frac{\partial \zeta}{\partial y}\right) \tag{A.5}$$

$$i = 3, \qquad \frac{\partial A}{\partial z} = \left(\frac{\partial A}{\partial \xi}\right)\left(\frac{\partial \xi}{\partial z}\right) + \left(\frac{\partial A}{\partial \eta}\right)\left(\frac{\partial \eta}{\partial z}\right) + \left(\frac{\partial A}{\partial \zeta}\right)\left(\frac{\partial \zeta}{\partial z}\right) \tag{A.6}$$

The *coefficients* of the derivatives w.r.t. ξ, η and ζ are the **metrics**, i.e. $\xi_x, \eta_x, \zeta_x, \xi_y$, etc. Either formulation may be used to relate the Cartesian derivatives to the curvilinear derivatives for function A. However, different transformation derivatives must be found

in each case, i.e. the vectors $\nabla\xi^i$ $(i=1,2,3)$ are required for Eq. (A.2) and the vectors $\mathbf{r}_{\xi^i}$ $(i=1,2,3)$ are required for Eq. (A.3). e.g.

$$\nabla\xi = \frac{\partial\xi}{\partial x}\hat{\mathbf{i}} + \frac{\partial\xi}{\partial y}\hat{\mathbf{j}} + \frac{\partial\xi}{\partial z}\hat{\mathbf{k}} \tag{A.7}$$

$$\mathbf{r}_\xi = \frac{\partial x}{\partial\xi}i + \frac{\partial y}{\partial\xi}j + \frac{\partial z}{\partial\xi}k \tag{A.8}$$

and similarly for η and ζ in place of ξ in Eqs. (A.7) and (A.8).

A.2 Covariant and Contravariant Base Vectors

Consider a co-ordinate line along which only the coordinate ξ varies. A tangent vector to this line is given by $\mathbf{r}_\xi$, Eq. (A.8): the set of tangent vectors to the ξ, η and ζ –coordinate lines are the three **covariant base vectors**, namely,

$$\mathbf{a}_i = \mathbf{r}_{\xi^i} \qquad i=1,2,3 \tag{A.9}$$

A normal vector to the co-ordinate surface on which the coordinate ξ is constant is given by $\nabla\xi$, Eq. (A.7): the set of normal vectors to the three coordinate surfaces on which ξ, η and ζ are constant are the three **contravariant base vectors**, namely,

$$\mathbf{a}^i = \nabla\xi^i \qquad i=1,2,3 \tag{A.10}$$

Both sets of vectors are shown in Fig. A.1. It should be noted that in orthogonal systems the covariant and contravariant base vectors are parallel and the three base vectors of each type are mutually perpendicular.

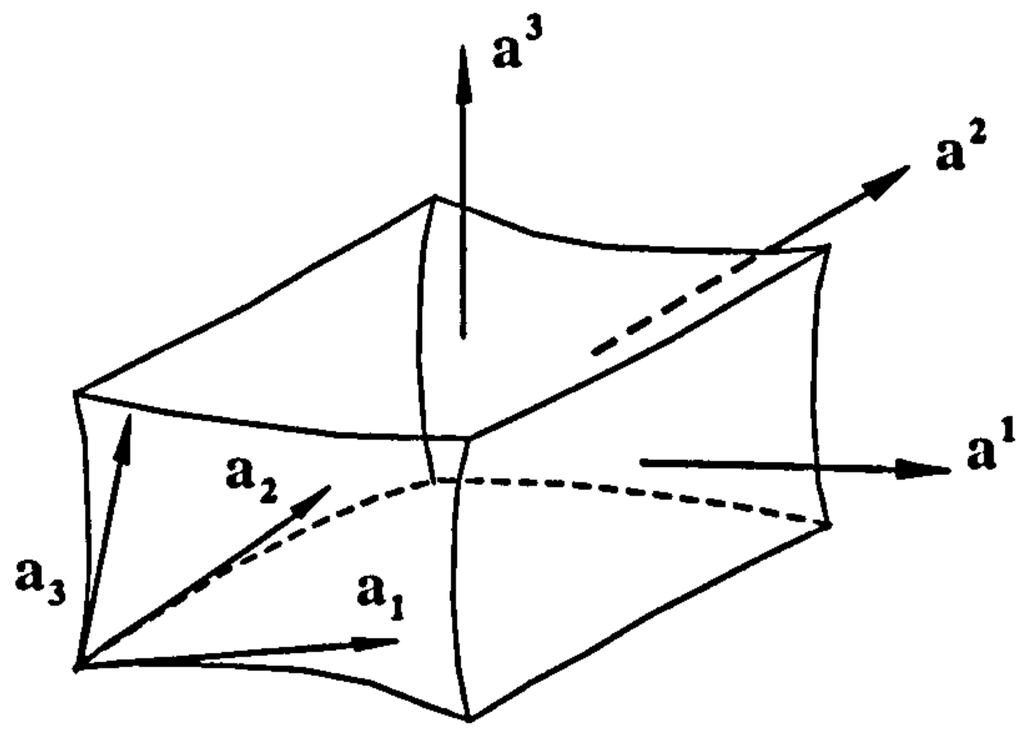

Figure A.1 Covariant and contravariant base vectors w.r.t. curvilinear element.

A.3 Covariant and Contravariant Metric Tensors

The covariant metric tensor (Table A.1) has nine components formed from dot products of the covariant base vectors. i.e.

$$g_{ij} = \mathbf{a}_i \cdot \mathbf{a}_j = g_{ji} \qquad i = 1,2,3 \text{ and } j = 1,2,3 \tag{A.11}$$

Similarly, the components of the contravariant metric tensor (Table A.1) are dot products of the contravariant base vectors. i.e.

$$g^{ij} = \mathbf{a}^i \cdot \mathbf{a}^j = g^{ji} \qquad i = 1,2,3 \text{ and } j = 1,2,3 \tag{A.12}$$

A.4 Tensor Relations for the Jacobian

The Jacobian defined in Eq. (4.49) may be written in terms of the covariant base vectors:

$$|J| = \mathbf{a}_1 \cdot (\mathbf{a}_2 \times \mathbf{a}_3) \tag{A.13}$$

Expanding for $|J|^2$ using vector identities gives:

$$\begin{aligned}[\mathbf{a}_1 \cdot (\mathbf{a}_2 \times \mathbf{a}_3)]^2 &= (\mathbf{a}_1 \cdot \mathbf{a}_1)[(\mathbf{a}_2 \times \mathbf{a}_3) \cdot (\mathbf{a}_2 \times \mathbf{a}_3)] - [\mathbf{a}_1 \times (\mathbf{a}_2 \times \mathbf{a}_3)]^2 \\ &= (\mathbf{a}_1 \cdot \mathbf{a}_1)[(\mathbf{a}_2 \cdot \mathbf{a}_2)(\mathbf{a}_3 \cdot \mathbf{a}_3) - (\mathbf{a}_2 \cdot \mathbf{a}_3)^2] - [(\mathbf{a}_1 \cdot \mathbf{a}_3)\mathbf{a}_2 - (\mathbf{a}_1 \cdot \mathbf{a}_2)\mathbf{a}_3]^2\end{aligned} \tag{A.14}$$

Here the last term may be expanded as:

$$\begin{aligned}[(\mathbf{a}_1 \cdot \mathbf{a}_3)\mathbf{a}_2 - (\mathbf{a}_1 \cdot \mathbf{a}_2)\mathbf{a}_3]^2 = (\mathbf{a}_1 \cdot \mathbf{a}_3)^2(\mathbf{a}_2 \cdot \mathbf{a}_2) + (\mathbf{a}_1 \cdot \mathbf{a}_2)^2(\mathbf{a}_3 \cdot \mathbf{a}_3) \\ - 2(\mathbf{a}_1 \cdot \mathbf{a}_3)(\mathbf{a}_1 \cdot \mathbf{a}_2)(\mathbf{a}_2 \cdot \mathbf{a}_3)\end{aligned}$$

Then replacing the dot products according to Eq. (A.11) gives:

$$\begin{aligned}[\mathbf{a}_1 \cdot (\mathbf{a}_2 \times \mathbf{a}_3)]^2 &= g_{11}(g_{22}g_{33} - g_{23}^2) - g_{13}^2 g_{22} - g_{12}^2 g_{33} - 2g_{13}g_{12}g_{23} \\ &= g_{11}(g_{22}g_{33} - g_{23}^2) - g_{12}(g_{12}g_{33} - g_{13}g_{23}) + g_{13}(g_{12}g_{23} - g_{13}g_{22}) \\ &= \det|g_{ij}| = g\end{aligned} \tag{A.15}$$

i.e. the Jacobian of the transformation is equal to the square root of the determinant of the covariant metric tensor, $\sqrt{g}$.

A.5 The Laplacian

For brevity relations presented here are quoted from Thompson *et al.* (1985, Sec. III). All expressions for derivative operators (i.e. gradient, divergence, curl and Laplacian) may be derived by applying the Divergence Theorem to a volume element bounded by coordinate surfaces (e.g.. Fig. A.1). i.e.,

$$\iiint_V \nabla \cdot \mathbf{A} \sqrt{g}\, d\xi\, d\eta\, d\zeta = \sum_{i=1}^{3} \iint_{S^i} \mathbf{A} \cdot (\mathbf{a}_j \times \mathbf{a}_k)\, d\xi^j\, d\xi^k \tag{A.16}$$

where $dV = \sqrt{g}\, d\xi\, d\eta\, d\zeta$ and $\hat{\mathbf{n}}\, dS = (\mathbf{a}_j \times \mathbf{a}_k)\, d\xi^j\, d\xi^k$ are made. Replacing **A** with the scalar A and taking the limit as the element volume shrinks to zero gives the gradient as:

$$\nabla A = \underbrace{\frac{1}{\sqrt{g}} \sum_{i=1}^{3} [(\mathbf{a}_j \times \mathbf{a}_k) A]_{\xi^i}}_{\text{conservative form}} = \underbrace{\frac{1}{\sqrt{g}} \sum_{i=1}^{3} (\mathbf{a}_j \times \mathbf{a}_k) A_{\xi^i}}_{\text{nonconservative form}} \tag{A.17}$$

where the identity $\sum_{i=1}^{3} (\mathbf{a}_j \times \mathbf{a}_k)_{\xi^i} = 0$ has been used. Then substituting $A = \xi^l$:

$$\nabla \xi^l = \mathbf{a}^l = \frac{1}{\sqrt{g}} \sum_{i=1}^{3} (\mathbf{a}_j \times \mathbf{a}_k)\, \delta_i^l = \frac{1}{\sqrt{g}} (\mathbf{a}_m \times \mathbf{a}_n) \tag{A.18}$$

Here the summation disappears as $l = i$ is the only nonzero term. Eq. (A.18) enables the contravariant and covariant metric tensor components to be related, i.e.

$$g^{il} = \mathbf{a}^i \times \mathbf{a}^l = \frac{1}{\sqrt{g}} (\mathbf{a}_j \times \mathbf{a}_k) \cdot \frac{1}{\sqrt{g}} (\mathbf{a}_m \times \mathbf{a}_n) = \frac{1}{g} (g_{jm} g_{kn} - g_{jn} g_{km}) \tag{A.19}$$

$i = 1, 2, 3$ $\qquad$ $l = 1, 2, 3$

(i, j, k) cyclic $\qquad$ (l, m, n) cyclic

Finally, the Laplacian operator is obtained by replacing **A** with $\nabla \mathbf{A}$ in Eq. (A.17) as:

Laplacian:
$$\nabla^2 A = \sum_{i=1}^{3} \sum_{j=1}^{3} g^{ij} A_{\xi^i \xi^j} + \sum_{k=1}^{3} (\nabla^2 \xi^k) A_{\xi^k} \tag{A.20}$$

where
$$\nabla^2 \xi^l = -\sum_{i=1}^{3} \sum_{j=1}^{3} g^{ij} \mathbf{a}^l \cdot \mathbf{r}_{\xi^i \xi^j} \qquad l = 1, 2, 3 \tag{A.21}$$

Covariant Metric Tensor (g_{ij})

$$g_{11}=\left(\frac{\partial x}{\partial \xi}\right)^2+\left(\frac{\partial y}{\partial \xi}\right)^2+\left(\frac{\partial z}{\partial \xi}\right)^2$$

$$g_{12}=\left(\frac{\partial x}{\partial \xi}\right)\left(\frac{\partial x}{\partial \eta}\right)+\left(\frac{\partial y}{\partial \xi}\right)\left(\frac{\partial y}{\partial \eta}\right)+\left(\frac{\partial z}{\partial \xi}\right)\left(\frac{\partial z}{\partial \eta}\right)$$

$$g_{13}=\left(\frac{\partial x}{\partial \xi}\right)\left(\frac{\partial x}{\partial \zeta}\right)+\left(\frac{\partial y}{\partial \xi}\right)\left(\frac{\partial y}{\partial \zeta}\right)+\left(\frac{\partial z}{\partial \xi}\right)\left(\frac{\partial z}{\partial \zeta}\right)$$

$$g_{21}=\left(\frac{\partial x}{\partial \xi}\right)\left(\frac{\partial x}{\partial \eta}\right)+\left(\frac{\partial y}{\partial \xi}\right)\left(\frac{\partial y}{\partial \eta}\right)+\left(\frac{\partial z}{\partial \xi}\right)\left(\frac{\partial z}{\partial \eta}\right)$$

$$g_{22}=\left(\frac{\partial x}{\partial \eta}\right)^2+\left(\frac{\partial y}{\partial \eta}\right)^2+\left(\frac{\partial z}{\partial \eta}\right)^2$$

$$g_{23}=\left(\frac{\partial x}{\partial \eta}\right)\left(\frac{\partial x}{\partial \zeta}\right)+\left(\frac{\partial y}{\partial \eta}\right)\left(\frac{\partial y}{\partial \zeta}\right)+\left(\frac{\partial z}{\partial \eta}\right)\left(\frac{\partial z}{\partial \zeta}\right)$$

$$g_{31}=\left(\frac{\partial x}{\partial \xi}\right)\left(\frac{\partial x}{\partial \zeta}\right)+\left(\frac{\partial y}{\partial \xi}\right)\left(\frac{\partial y}{\partial \zeta}\right)+\left(\frac{\partial z}{\partial \xi}\right)\left(\frac{\partial z}{\partial \zeta}\right)$$

$$g_{32}=\left(\frac{\partial x}{\partial \eta}\right)\left(\frac{\partial x}{\partial \zeta}\right)+\left(\frac{\partial y}{\partial \eta}\right)\left(\frac{\partial y}{\partial \zeta}\right)+\left(\frac{\partial z}{\partial \eta}\right)\left(\frac{\partial z}{\partial \zeta}\right)$$

$$g_{33}=\left(\frac{\partial x}{\partial \zeta}\right)^2+\left(\frac{\partial y}{\partial \zeta}\right)^2+\left(\frac{\partial z}{\partial \zeta}\right)^2$$

Contravariant Metric Tensor (g^{ij})

$$g^{11}=\left(\frac{\partial \xi}{\partial x}\right)^2+\left(\frac{\partial \xi}{\partial y}\right)^2+\left(\frac{\partial \xi}{\partial z}\right)^2$$

$$g^{12}=\left(\frac{\partial \xi}{\partial x}\right)\left(\frac{\partial \eta}{\partial x}\right)+\left(\frac{\partial \xi}{\partial y}\right)\left(\frac{\partial \eta}{\partial y}\right)+\left(\frac{\partial \xi}{\partial z}\right)\left(\frac{\partial \eta}{\partial z}\right)$$

$$g^{13}=\left(\frac{\partial \xi}{\partial x}\right)\left(\frac{\partial \zeta}{\partial x}\right)+\left(\frac{\partial \xi}{\partial y}\right)\left(\frac{\partial \zeta}{\partial y}\right)+\left(\frac{\partial \xi}{\partial z}\right)\left(\frac{\partial \zeta}{\partial z}\right)$$

$$g^{21}=\left(\frac{\partial \xi}{\partial x}\right)\left(\frac{\partial \eta}{\partial x}\right)+\left(\frac{\partial \xi}{\partial y}\right)\left(\frac{\partial \eta}{\partial y}\right)+\left(\frac{\partial \xi}{\partial z}\right)\left(\frac{\partial \eta}{\partial z}\right)$$

$$g^{22}=\left(\frac{\partial \eta}{\partial x}\right)^2+\left(\frac{\partial \eta}{\partial y}\right)^2+\left(\frac{\partial \eta}{\partial z}\right)^2$$

$$g^{23}=\left(\frac{\partial \eta}{\partial x}\right)\left(\frac{\partial \zeta}{\partial x}\right)+\left(\frac{\partial \eta}{\partial y}\right)\left(\frac{\partial \zeta}{\partial y}\right)+\left(\frac{\partial \eta}{\partial z}\right)\left(\frac{\partial \zeta}{\partial z}\right)$$

$$g^{31}=\left(\frac{\partial \xi}{\partial x}\right)\left(\frac{\partial \zeta}{\partial x}\right)+\left(\frac{\partial \xi}{\partial y}\right)\left(\frac{\partial \zeta}{\partial y}\right)+\left(\frac{\partial \xi}{\partial z}\right)\left(\frac{\partial \zeta}{\partial z}\right)$$

$$g^{32}=\left(\frac{\partial \eta}{\partial x}\right)\left(\frac{\partial \zeta}{\partial x}\right)+\left(\frac{\partial \eta}{\partial y}\right)\left(\frac{\partial \zeta}{\partial y}\right)+\left(\frac{\partial \eta}{\partial z}\right)\left(\frac{\partial \zeta}{\partial z}\right)$$

$$g^{33}=\left(\frac{\partial \zeta}{\partial x}\right)^2+\left(\frac{\partial \zeta}{\partial y}\right)^2+\left(\frac{\partial \zeta}{\partial z}\right)^2$$

Table A.1 Covariant and contravariant metric tensors.

Appendix B

FORTRAN Mesh Generation Routines

Three FORTRAN routines are presented in this Appendix to supplement the numerical mesh generation theory in Chapter 2. These apply to a mesh with NI×NJ×NK vertices in the Cartesian directions x, y and z respectively.

B.1 Subroutine *Trans*

Transfinite interpolation of the boundary surfaces of a three-dimensional region.

B.2 Subroutine *Metric*

Calculated the metrics (e.g. $\xi_x, \xi_y, \xi_z, \eta_x$, etc.) to build the coefficients and source term in the discretised equation for ϕ ($\equiv x$, y or z), Eq. (2.29).

B.3 Subroutine *Lisolv*

Line-by-line Tri-Diagonal Matrix Algorithm (TDMA) with alternate direction implicit (ADI) sweeping to solve the general discretised equation for ϕ, Eq. (2.29).

B.1 Subroutine *Trans*

region in which interpolation is made

```
      subroutine trans(x,y,z,imin,jmin,kmin,imax,jmax,kmax)
C     ------------------------------------------------------------
C     Desc: 3-dimensional transfinite interpolation.
C     ------------------------------------------------------------
      integer i,j,k,imin,jmin,kmin,imax,jmax,kmax

      parameter(nn=50)
      real*8  x(nn,nn,nn),y(nn,nn,nn),z(nn,nn,nn),
     .        x1(nn,nn,nn),x2(nn,nn,nn),x3(nn,nn,nn),
     .        y1(nn,nn,nn),y2(nn,nn,nn),y3(nn,nn,nn),
     .        z1(nn,nn,nn),z2(nn,nn,nn),z3(nn,nn,nn),
     .        f,g,h
```

Sec. 2.2.2, p. 12

```
      do i=imin,imax
        do j=jmin,jmax
          do k=kmin,kmax
            f=dble(imax-i)/dble(imax-imin)
            x1(i,j,k)=f*x(imin,j,k)+(1.d0-f)*x(imax,j,k)
            y1(i,j,k)=f*y(imin,j,k)+(1.d0-f)*y(imax,j,k)
            z1(i,j,k)=f*z(imin,j,k)+(1.d0-f)*z(imax,j,k)
          enddo
        enddo
      enddo
```

Stage 1:

1D Lagrangian interpolation in the i–direction, Eq. (2.7)

```
      do i=imin,imax
        do j=jmin,jmax
          do k=kmin,kmax
            g=dble(jmax-j)/dble(jmax-jmin)
            x2(i,j,k)=       g *(x(i,jmin,k)-x1(i,jmin,k))+
     .           (1.d0-g)*(x(i,jmax,k)-x1(i,jmax,k))
            y2(i,j,k)=       g *(y(i,jmin,k)-y1(i,jmin,k))+
     .           (1.d0-g)*(y(i,jmax,k)-y1(i,jmax,k))
            z2(i,j,k)=       g *(z(i,jmin,k)-z1(i,jmin,k))+
     .           (1.d0-g)*(z(i,jmax,k)-z1(i,jmax,k))
          enddo
        enddo
      enddo
```

Stage 2:

1D Lagrangian interpolation in the j–direction.

```
      do i=imin,imax
        do j=jmin,jmax
          do k=kmin,kmax
            h=dble(kmax-k)/dble(kmax-kmin)
            x3(i,j,k)=       h *(x(i,j,kmin)-x1(i,j,kmin)-x2(i,j,kmin))+
     .           (1.d0-h)*(x(i,j,kmax)-x1(i,j,kmax)-x2(i,j,kmax))
            y3(i,j,k)=       h *(y(i,j,kmin)-y1(i,j,kmin)-y2(i,j,kmin))+
     .           (1.d0-h)*(y(i,j,kmax)-y1(i,j,kmax)-y2(i,j,kmax))
            z3(i,j,k)=       h *(z(i,j,kmin)-z1(i,j,kmin)-z2(i,j,kmin))+
     .           (1.d0-h)*(z(i,j,kmax)-z1(i,j,kmax)-z2(i,j,kmax))
          enddo
        enddo
      enddo
```

Stage 3:

1D Lagrangian interpolation in the k–direction.

```
      do i=imin,imax
       do j=jmin,jmax
         do k=kmin,kmax
           x(i,j,k)=x1(i,j,k)+x2(i,j,k)+x3(i,j,k)
           y(i,j,k)=y1(i,j,k)+y2(i,j,k)+y3(i,j,k)
           z(i,j,k)=z1(i,j,k)+z2(i,j,k)+z3(i,j,k)
         enddo
       enddo
      enddo
      return
      end
```

Stage 4:

Δx, Δy, Δz are combined from all three stages, Eq. (2.11)

x, y and z are replaced with new interpolated values.

B.2 Subroutine *Metric*

mesh spacings defined in Fig. 2.2, p. 17

```
      subroutine metric(ni,nj,nk,x,y,z,dae,daw,dbn,dbs,dct,dcb,
     .                  p1,p2,p3,nvar,phi)
c     ------------------------------------------------------------
c     Desc: Calculates metrics to form coefficients and source
c           term in discretised equation for phi.
c     ------------------------------------------------------------
      integer i,j,k,ni,nj,nk,nn

      parameter(nn=50)
      real*8  x(nn,nn,nn),y(nn,nn,nn),z(nn,nn,nn),p1(nn),p2(nn),p3(nn),
     .        dae(nn),daw(nn),dbn(nn),dbs(nn),dct(nn),dcb(nn),
     .        ae(nn,nn,nn),aw(nn,nn,nn),an(nn,nn,nn),as(nn,nn,nn),
     .        at(nn,nn,nn),ab(nn,nn,nn),su(nn,nn,nn),phi(nn,nn,nn),
     .        dxda,dxdb,dxdc,dyda,dydb,dydc,dzda,dzdb,dzdc,dab,dac,dba,
     .        dbc,dca,dcb1,g,gn11,gn12,gn13,gn22,gn23,gn33,gv11,gv12,
     .        gv13,gv22,gv23,gv33,sf1,sf2,sf3,wfew,wfns,wftb

c --- calculate coefficients
```

Sec. 2.3.2, p. 16

```
      do i=2,ni-1
        do j=2,nj-1
          do k=2,nk-1

            wfew=dae(i)/daw(i)
            wfns=dbn(j)/dbs(j)
            wftb=dct(k)/dcb(k)

            dxda=((x(i+1,j,k)-x(i,j,k))/wfew
     .           -(x(i-1,j,k)-x(i,j,k))*wfew)/(dae(i)+daw(i))
            dxdb=((x(i,j+1,k)-x(i,j,k))/wfns
     .           -(x(i,j-1,k)-x(i,j,k))*wfns)/(dbn(j)+dbs(j))
            dxdc=((x(i,j,k+1)-x(i,j,k))/wftb
     .           -(x(i,j,k-1)-x(i,j,k))*wftb)/(dct(k)+dcb(k))

            dyda=((y(i+1,j,k)-y(i,j,k))/wfew
     .           -(y(i-1,j,k)-y(i,j,k))*wfew)/(dae(i)+daw(i))
            dydb=((y(i,j+1,k)-y(i,j,k))/wfns
     .           -(y(i,j-1,k)-y(i,j,k))*wfns)/(dbn(j)+dbs(j))
            dydc=((y(i,j,k+1)-y(i,j,k))/wftb
     .           -(y(i,j,k-1)-y(i,j,k))*wftb)/(dct(k)+dcb(k))

            dzda=((z(i+1,j,k)-z(i,j,k))/wfew
     .           -(z(i-1,j,k)-z(i,j,k))*wfew)/(dae(i)+daw(i))
            dzdb=((z(i,j+1,k)-z(i,j,k))/wfns
     .           -(z(i,j-1,k)-z(i,j,k))*wfns)/(dbn(j)+dbs(j))
            dzdc=((z(i,j,k+1)-z(i,j,k))/wftb
     .           -(z(i,j,k-1)-z(i,j,k))*wftb)/(dct(k)+dcb(k))

c ---       calculate mixed derivatives for phi

            dab=((phi(i+1,j+1,k)-phi(i+1,j,k)
     .           -phi(i-1,j+1,k)+phi(i-1,j,k))/wfns
     .          -(phi(i+1,j-1,k)-phi(i+1,j,k)
     .           -phi(i-1,j-1,k)+phi(i-1,j,k))*wfns)*dc(k)/2.d0

            dac=((phi(i+1,j,k+1)-phi(i+1,j,k )
     .           -phi(i-1,j,k+1)+phi(i-1,j,k))/wftb
     .          -(phi(i+1,j,k-1)-phi(i+1,j,k)
     .           -phi(i-1,j,k-1)+phi(i-1,j,k))*wftb)*db(j)/2.d0

            dba=((phi(i+1,j+1,k)-phi(i,j+1,k)
     .           -phi(i+1,j-1,k)+phi(i,j-1,k))/wfew
     .          -(phi(i-1,j+1,k)-phi(i,j+1,k)
     .           -phi(i-1,j-1,k)+phi(i,j-1,k))*wfew)*dc(k)/2.d0
```

$\Delta\xi_e/\Delta\xi_w$, $\Delta\eta_n/\Delta\eta_s$, $\Delta\zeta_t/\Delta\zeta_b$

$\frac{\partial x}{\partial\xi}, \frac{\partial x}{\partial\eta}, \frac{\partial x}{\partial\zeta}$

$\frac{\partial y}{\partial\xi}, \frac{\partial y}{\partial\eta}, \frac{\partial y}{\partial\zeta}$

$\frac{\partial z}{\partial\xi}, \frac{\partial z}{\partial\eta}, \frac{\partial z}{\partial\zeta}$

Approximating Eq. (2.28):

$\Delta V \frac{\partial\phi^2}{\partial\xi\partial\eta}$

$\Delta V \frac{\partial\phi^2}{\partial\xi\partial\zeta}$

$\Delta V \frac{\partial\phi^2}{\partial\eta\partial\xi}$

continues on next page

```
      dbc=((phi(i,j+1,k+1)-phi(i,j+1,k)
     .     -phi(i,j-1,k+1)+phi(i,j-1,k))/wftb
     .    -(phi(i,j+1,k-1)-phi(i,j+1,k )
     .     -phi(i,j-1,k-1)+phi(i,j-1,k))*wftb)*da(i)/2.d0

      dca=((phi(i+1,j,k+1)-phi(i,j,k+1)
     .     -phi(i+1,j,k-1)+phi(i,j,k-1))/wfew
     .    -(phi(i-1,j,k+1)-phi(i,j,k+1 )
     .     -phi(i-1,j,k-1)+phi(i,j,k-1))*wfew)*db(j)/2.d0

      dcb1=((phi(i,j+1,k+1)-phi(i,j,k+1 )
     .     -phi(i,j+1,k-1)+phi(i,j,k-1))/wfns
     .    -(phi(i,j-1,k+1)-phi(i,j,k+1)
     .     -phi(i,j-1,k-1)+phi(i,j,k-1))*wfns)*da(i)/2.d0
```

$\Delta V \frac{\partial \phi^2}{\partial \eta \partial \zeta}$

$\Delta V \frac{\partial \phi^2}{\partial \zeta \partial \xi}$

$\Delta V \frac{\partial \phi^2}{\partial \zeta \partial \eta}$

```
c ---       components of covariant metric tensor

            gv11=dxda*dxda+dyda*dyda+dzda*dzda
            gv12=dxda*dxdb+dyda*dydb+dzda*dzdb
            gv13=dxda*dxdc+dyda*dydc+dzda*dzdc
            gv22=dxdb*dxdb+dydb*dydb+dzdb*dzdb
            gv23=dxdb*dxdc+dydb*dydc+dzdb*dzdc
            gv33=dxdc*dxdc+dydc*dydc+dzdc*dzdc
```

g_{ij}

Note: $g_{ij} = g_{ji}$

```
c ---       components of contravariant metric tensor and g
            note: sqrt(g) = Jacobian of transformation

            gn11=gv22*gv33-gv23*gv23
            gn12=gv23*gv13-gv12*gv33
            gn13=gv12*gv23-gv22*gv13

            g=gv11*gn11+gv12*gn12+gv13*gn13
```

g, Eq. (2.20)

```
            gn11=gn11/g
            gn12=gn12/g
            gn13=gn13/g
            gn22=(gv33*gv11-gv13*gv13)/g
            gn23=(gv13*gv12-gv23*gv11)/g
            gn33=(gv11*gv22-gv12*gv12)/g
```

g^{ij}, Eq. (2.19)

Note: $g^{ij} = g^{ji}$

```
c ---       assemble coefficients

            an(i,j,k)=gn22*da(i)*dc(k)/dbn(j)
            as(i,j,k)=gn22*da(i)*dc(k)/dbs(j)
            ae(i,j,k)=gn11*db(j)*dc(k)/dae(i)
            aw(i,j,k)=gn11*db(j)*dc(k)/daw(i)
            at(i,j,k)=gn33*da(i)*db(j)/dct(k)
            ab(i,j,k)=gn33*da(i)*db(j)/dcb(k)
```

a_N

a_S

a_E

a_W, Eq. (2.31)

a_T

a_B

```
c ---       calculate stretching terms

            sf1=gn11*db(j)*dc(k)*p1(i)
            sf2=gn22*da(i)*dc(k)*p2(j)
            sf3=gn33*da(i)*db(j)*p3(k)

            if(nvar.eq.1) su(i,j,k)=sf1*dxda+sf2*dxdb+sf3*dxdc
            if(nvar.eq.2) su(i,j,k)=sf1*dyda+sf2*dydb+sf3*dydc
            if(nvar.eq.3) su(i,j,k)=sf1*dzda+sf2*dzdb+sf3*dzdc

            su(i,j,k)=su(i,j,k)+gn12*(dab+dba)+gn13*(dac+dca)
           .                    +gn23*(dbc+dcb1)
         enddo
      enddo
   enddo
   return
   end
```

phi	nvar
x	1
y	2
z	3

Source term $S \cdot \Delta V$ with the control functions P_i

S is defined in Eq. (2.24).

B.3 Subroutine *Lisolv*

coefficients of the discretised equation for phi

```
      subroutine lisolv(ni,nj,nk,ae,aw,an,as,at,ab,su,ap,phi,nsw)
C     ------------------------------------------------------------
CC    Desc: Applies a Line-by-Line Tri-Diagonal Matrix Algorithm (TDMA)
CC          using an alternating direction implicit (ADI) sweeping
CC          strategy to solve the general discretised equation for phi.
C     ------------------------------------------------------------

      integer i,j,k,ii,jj,kk,istart,jstart,kstart,istm1,jstm1,kstm1,
     .        itsw,nn,nsw
      parameter(nn=50)
      real*8  ae(nn,nn,nn),aw(nn,nn,nn),an(nn,nn,nn),as(nn,nn,nn),
     .        at(nn,nn,nn),ab(nn,nn,nn),su(nn,nn,nn),ap(nn,nn,nn),
     .        aa(nn),bb(nn),cc(nn),dd(nn),phi(nn,nn,nn),term

      istart=2
      jstart=2
      kstart=2
      istm1=istart - 1
      jstm1=jstart - 1
      kstm1=kstart - 1

      do itsw=1,nsw

c ---    commence W-E traverse

        aa(istm1)=0.0d0
        do k=kstart,nk
          do j=jstart,nj
            cc(istm1)=phi(istm1,j,k)
            do i=istart,ni

c ---         assemble TDMA coefficients

              aa(i)=ae(i,j,k)
              bb(i)=aw(i,j,k)
              cc(i)=an(i,j,k)*phi(i,j+1,k)+as(i,j,k)*phi(i,j-1,k)
     .             +at(i,j,k)*phi(i,j,k+1)+ab(i,j,k)*phi(i,j,k-1)
     .             +su(i,j,k)
              dd(i)=ap(i,j,k)

c ---         calculate coefficients of recurrence formula

              term=1.d0/(dd(i)-bb(i)*aa(i-1))
              aa(i)=aa(i)*term
              cc(i)=(cc(i)+bb(i)*cc(i-1))*term
            enddo

c ---       obtain new phi

            do ii=istart,ni
              i=ni+istart-ii
              phi(i,j,k)=aa(i)*phi(i+1,j,k)+cc(i)
            enddo
          enddo
        enddo
```

Sec. 2.3.3, p. 20 (Note: notation differs here from that in theory.)

number of global sweeps of solver

Sweep ξ–lines

$\alpha_1 = 0$

$\beta_1 = \phi_1$

α_i

β_i

$\phi_i = \alpha_i \phi_{i+1} + \beta_i$

continues on next page

```
c ---    commence S-N traverse                                    Sweep η–lines

         aa(jstm1)=0.0d0                                          α1 = 0
         do k=kstart,nk
           do i=istart,ni
             cc(jstm1)=phi(i,jstm1,k)                             β1 = φ1
             do j=jstart,nj
c ---          assemble TDMA coefficients
               aa(j)=an(i,j,k)
               bb(j)=as(i,j,k)
               cc(j)=ae(i,j,k)*phi(i+1,j,k)+aw(i,j,k)*phi(i-1,j,k)
     .               +at(i,j,k)*phi(i,j,k+1)+ab(i,j,k)*phi(i,j,k-1)
     .               +su(i,j,k)
               dd(j)=ap(i,j,k)
c ---          calculate coefficients of recurrence formula
               term=1.d0/(dd(j)-bb(j)*aa(j-1))                    αj
               aa(j)=aa(j)*term
               cc(j)=(cc(j)+bb(j)*cc(j-1))*term                   βj
             enddo
c ---        obtain new phi's
             do jj=jstart,nj                                      φj = αjφj+1 + βj
               j=nj+jstart-jj
               phi(i,j,k)=aa(j)*phi(i,j+1,k)+cc(j)
             enddo
           enddo
         enddo


c ---    commence B-T traverse                                    Sweep ζ–lines

         aa(kstm1)=0.0d0                                          α1 = 0
         do j=jstart,nj
           do i=istart,ni
             cc(kstm1)=phi(i,j,kstm1)                             β1 = φ1
             do k=kstart,nk
c ---          assemble tdma coefficients
               aa(k)=at(i,j,k)
               bb(k)=ab(i,j,k)
               cc(k)=ae(i,j,k)*phi(i+1,j,k)+aw(i,j,k)*phi(i-1,j,k)
     .               +an(i,j,k)*phi(i,j+1,k)+as(i,j,k)*phi(i,j-1,k)
     .               +su(i,j,k)
               dd(k)=ap(i,j,k)
c ---          calculate coefficients of recurrence formula
               term=1.d0/(dd(k)-bb(k)*aa(k-1))                    αk
               aa(k)=aa(k)*term
               cc(k)=(cc(k)+bb(k)*cc(k-1))*term                   βk,   Eq. (2.36)
             enddo
c ---        obtain new phi
             do kk=kstart,nk
               k=nk+kstart-kk                                     φk = αkφk+1 + βk
               phi(i,j,k)=aa(k)*phi(i,j,k+1)+cc(k)
             enddo                                                Eq. (2.35)
           enddo
         enddo

         enddo                                                    Loop back and
         return                                                   re-sweep ξ–lines
         end
```

Appendix C

Differencing of Pressure-density Term in KIVA-II Numerical Scheme

The following model expression results in the closure of the velocity fluctuation–pressure gradient correlation in the k–ε equations for variable density flow (see Sec. 3.2.5):

$$-\frac{1}{\overline{\rho}^2}\frac{\mu_t}{\sigma_t}\frac{\partial\overline{\rho}}{\partial x_i}\frac{\partial\overline{p}}{\partial x_i}, \qquad i=1,2,3 \tag{B.1}$$

This term is differenced in an analogous manner to other terms in the Lagrangian phase of the KIVA-II numerical scheme, i.e. Amsden *et al.* (1989, pp. 34-43 & Appendix K). First the density and pressure gradients are written as the following identity :

$$\frac{\partial\phi}{\partial x_i} = \nabla\cdot(\phi\,\hat{\mathbf{e}}_i) \tag{B.2}$$

where $\phi = \{\overline{\rho}, \overline{p}\}$ is the mean density or pressure and $\hat{\mathbf{e}}_i$ is the unit vector in the ith Cartesian coordinate direction. Then, integrating Eq. (B.2) over a computational cell and applying the Divergence Theorem to the right-hand side gives:

$$\int_V \frac{\partial\phi}{\partial x_i}dV = \int_S \phi\,\hat{\mathbf{e}}_i\cdot d\mathbf{A} \tag{B.3}$$

where V is the cell volume and S the cell surface area. Finally, the area integral over the cell surface is approximated by a summation over the six cell faces such that a differenced form for Eq. (B.3) is obtained as:

$$\frac{\partial\phi}{\partial x_i}V = \sum_a \phi_a\,\hat{\mathbf{e}}_i\cdot\mathbf{A}_a \tag{B.4}$$

where ϕ_a is the interpolated density or pressure on face a, and $\mathbf{A}_a$ is the outward area projection vector of face a. Eq. (B.1) is therefore differenced over a cell ijk as:

$$-\frac{1}{\overline{\rho}^2}\frac{\mu_t}{\sigma_t}\frac{\partial\overline{\rho}}{\partial x_i}\frac{\partial\overline{p}}{\partial x_i}\bigg|_{ijk} = \frac{1}{\sigma_t}\left(\frac{\mu_t}{\overline{\rho}^2V^2}\right)_{ijk}\sum_{i=1}^{3}\left[\sum_a(\overline{\rho}_a\,\hat{\mathbf{e}}_i\cdot\mathbf{A}_a)\sum_a(\overline{p}_a\,\hat{\mathbf{e}}_i\cdot\mathbf{A}_a)\right] \tag{B.5}$$

Here, it is stressed that the notation of Eq. (B.5) represents the summation of three terms, one for each Cartesian direction $\hat{\mathbf{e}}_i$ when $i = 1, 2, 3$. Each term contains the product of the density and pressure gradients in the associated direction.

This differenced expression for pressure-density interactions is now incorporated into the original difference approximations to the turbulent kinetic energy, k and eddy dissipation, ε equations, i.e. see Amsden *et al.* (1989, p.41).

***k*–equation.** The differenced turbulent kinetic energy equation is modified to:

$$\frac{M_{ijk}^B k_{ijk}^B - M_{ijk}^n k_{ijk}^n}{\Delta t} = -\tfrac{2}{3}\rho_{ijk}^B \frac{V_{ijk}^B - V_{ijk}^n}{\Delta t}[(1-f_{ijk})k_{ijk}^n + f_{ijk}k_{ijk}^B] + (VD)_{ijk}$$
$$-\frac{\Delta t}{\sigma_t}\frac{\mu_{ijk}^n}{(\rho_{ijk}^n V_{ijk}^n)^2}\sum_{i=1}^{3}\left[\sum_a(\rho_a^n\hat{\mathbf{e}}_i\cdot\mathbf{A}_a)\sum_a(p_a^n\hat{\mathbf{e}}_i\cdot\mathbf{A}_a)\right][(1-f_{2,ijk})+f_{2,ijk}\frac{k_{ijk}^B}{k_{ijk}^n}]$$
$$+\sum_a\frac{\mu_a^n}{\mathrm{Pr}_k}\nabla[\Phi^D k^B+(1-\Phi^D)k^A]_a\cdot\mathbf{A}_a - M_{ijk}^B\frac{\varepsilon_{ijk}^n}{k_{ijk}^n}k_{ijk}^B \qquad \text{(B.6)}$$

where the new term is the second line on the right-hand side. The quantity $f_{2,ijk}$ is zero or unity depending on the sign of the pressure-density term, say denoted by Ψ, such that:

$$f_{2,ijk} = \begin{cases} 1 & \text{if } \Psi < 0 \quad \textit{implicit solution} \\ 0 & \text{otherwise} \quad \textit{explicit solution} \end{cases} \qquad \text{(B.7)}$$

ε–equation. Similarly, the differenced dissipation rate equation is modified to:

$$\frac{M_{ijk}^B \varepsilon_{ijk}^B - M_{ijk}^n \varepsilon_{ijk}^n}{\Delta t} = -(\tfrac{2}{3}c_{\varepsilon_1} - c_{\varepsilon_3})\rho_{ijk}^B \frac{V_{ijk}^B - V_{ijk}^n}{\Delta t}[(1-f_{ijk})\varepsilon_{ijk}^n + f_{ijk}\varepsilon_{ijk}^B] + c_{\varepsilon_1}\frac{\varepsilon_{ijk}^n}{k_{ijk}^n}(VD)_{ijk}$$
$$-\frac{\Delta t}{\sigma_t}\frac{\mu_{ijk}^n}{(\rho_{ijk}^n V_{ijk}^n)^2}\sum_{i=1}^{3}\left[\sum_a(\rho_a^n\hat{\mathbf{e}}_i\cdot\mathbf{A}_a)\sum_a(p_a^n\hat{\mathbf{e}}_i\cdot\mathbf{A}_a)\right]\frac{c_{\varepsilon_1}}{k_{ijk}^n}[(1-f_{2,ijk})\varepsilon_{ijk}^n + f_{2,ijk}\varepsilon_{ijk}^B]$$
$$+\sum_a\frac{\mu_a^n}{\mathrm{Pr}_\varepsilon}\nabla[\Phi^D\varepsilon^B+(1-\Phi^D)\varepsilon^A]_a\cdot\mathbf{A}_a - c_{\varepsilon_2}M_{ijk}^B\frac{\varepsilon_{ijk}^n}{k_{ijk}^n}\varepsilon_{ijk}^B \qquad \text{(B.8)}$$

Note: This prescription for $f_{2,ijk}$ is chosen to prevent negative computed values of k and ε. The form is analogous to the prescription of f_{ijk} in the velocity dilation terms of Eqs. (B.7) and (B.8), c.f. Amsden *et al.* (1989, p.41, Eq. (98)).

Appendix D

Discrete Ordinate Sets

Table D.1 Discrete ordinates sets S_n for angular integrations in YIX method (p. 135).

	Direction cosines of $\hat{\mathbf{s}}$			Weights
	ξ	η	ζ	w
S_4	0.2958759	0.2958759	0.9082483	0.5235989
	0.2958759	0.9082483	0.2958759	0.5235989
	0.9082483	0.2958759	0.2958759	0.5235989
S_6	0.1838670	0.1838670	0.9656013	0.1609516
	0.1838670	0.6950514	0.6950514	0.3626469
	0.1838670	0.9656013	0.1838670	0.1609516
	0.6950514	0.1838670	0.6950514	0.3626469
	0.6950514	0.6950514	0.1838670	0.3626469
	0.9656013	0.1838670	0.1838670	0.1609516
S_8	0.1422555	0.1422555	0.9795543	0.1712360
	0.1422555	0.5773503	0.8040087	0.0992285
	0.1422555	0.8040087	0.5773503	0.0992285
	0.1422555	0.9795543	0.1422555	0.1712360
	0.5773503	0.1422555	0.8040087	0.0992285
	0.5773503	0.5773503	0.5773503	0.4617180
	0.5773503	0.8040087	0.1422555	0.0992285
	0.8040087	0.1422555	0.5773503	0.0992285
	0.8040087	0.5773503	0.1422555	0.0992285
	0.9795543	0.1422555	0.1422555	0.1712360
S_{12}	0.1596536	0.1596536	0.9741773	0.1227207
	0.1596536	0.4584710	0.8742511	0.0811106
	0.1596536	0.6284124	0.7613202	0.0674176
	0.1596536	0.7613202	0.6284124	0.0674176
	0.1596536	0.8742511	0.4584710	0.0811106
	0.1596536	0.9741773	0.1596536	0.1227207
	0.4584710	0.1596536	0.8742511	0.0811106
	0.4584710	0.4584710	0.7613203	0.0552766
	0.4584710	0.6284124	0.6284124	0.0485448
	0.4584710	0.7613203	0.4584710	0.0552766
	0.4584710	0.8742511	0.1596536	0.0811106
	0.6284124	0.1596536	0.7613203	0.0674176
	0.6284124	0.4584710	0.6284124	0.0485448
	0.6284124	0.6284124	0.4584710	0.0485448
	0.6284124	0.7613203	0.1596536	0.0674176
	0.7613203	0.1596536	0.6284124	0.0674176
	0.7613203	0.4584710	0.4584710	0.0552766
	0.7613203	0.6284124	0.1596536	0.0674176
	0.8742511	0.1596536	0.4584710	0.0811106
	0.8742511	0.4584710	0.1596536	0.0811106
	0.9741773	0.1596536	0.1596536	0.1227207
S_{16}	0.1364305	0.1364305	0.9812102	0.0888367
	0.1364305	0.3917822	0.9098865	0.0567956
	0.1364305	0.5370040	0.8324742	0.0448868
	0.1364305	0.6505792	0.7470832	0.0412208
	0.1364305	0.7470832	0.6505792	0.0412208
	0.1364305	0.8324742	0.5370040	0.0448868
	0.1364305	0.9098865	0.3817822	0.0567956
	0.1364305	0.9812102	0.1364305	0.0888367
	0.3917822	0.1364305	0.9098865	0.0567956
	0.3917822	0.3917822	0.8324742	0.0368034
	0.3917822	0.5370040	0.7470832	0.0296818
	0.3917822	0.6505792	0.6505792	0.0281066
	0.3917822	0.7470832	0.5370040	0.0296818
	0.3917822	0.8324742	0.3917822	0.0368034
	0.3917822	0.9098865	0.1364305	0.0567956
	0.5370040	0.1364305	0.8324742	0.0448868
	0.5370040	0.3917822	0.7470832	0.0296818
	0.5370040	0.5370040	0.6505792	0.0246508
	0.5370040	0.6505792	0.5370040	0.0246508
	0.5370040	0.7470832	0.3917822	0.0296818
	0.5370040	0.8324742	0.1364305	0.0448868
	0.6505792	0.1364305	0.7470832	0.0412208
	0.6505792	0.3917822	0.6505792	0.0281066
	0.6505792	0.5370040	0.5370040	0.0246508
	0.6505792	0.6505792	0.3917822	0.0281066
	0.6505792	0.7470832	0.1364305	0.0412208
	0.7470832	0.1364305	0.6505792	0.0412208
	0.7470832	0.3917822	0.5370040	0.0296818
	0.7470832	0.5370040	0.3917822	0.0296818
	0.7470832	0.6505792	0.1364305	0.0412208
	0.8324742	0.1364305	0.5370040	0.0448868
	0.8324742	0.3917822	0.3917822	0.0368034
	0.8324742	0.5370040	0.1364305	0.0448868
	0.9098865	0.1364305	0.3917822	0.0567956
	0.9098865	0.3917822	0.1364305	0.0567956
	0.9812102	0.1364305	0.1364305	0.0888367

Reference: Hsu *et al.* (1992).

Nomenclature

Latin letters

A	area (or physical surface element) [m^2]
a	area of master surface element
a	band symmetry factor in Edwards wide band model = 1 or 2
a	extension height of L-shaped enclosure in Case E benchmarks (Fig. 6.12) [m]
A, A_f, A_b	pre-exponential factors in Arrhenius Eqs. (3.59) and (3.61)
A_1, A_2	model constants in Sutherland formula for μ_{air}, see Eq. (3.38)
$\mathbf{A}$	area vector (pointing inwards) [m^2]
a	crank radius in Eqs. (3.109) and (3.110) [m]
a	acceleration in Eq. (3.111) [m/s^2]
a_n	coefficients of discretised equation, Eq. (2.29)
a_n	scattering phase function coefficients, Eq. (4.3)
B	constant for smooth walls in log-law wall function, Eq. (3.101)
b	pressure correlation parameter in Edwards wide band model (Table 5.1)
C_{D1}, C_{D2}	model constants in eddy-dissipation concept (EDC), Eq. (3.63)
C_{EBU}	constant in eddy-break-up (EBU) combustion model, Eq. (3.62)
C_A	adjustable factor to scale kinetic reaction rate
C_B	adjustable factor to scale harmonic reaction rate, Eq. (3.75)
C_k	absorption cross-section [cm^{-1}]
C_1, C_2, C_3	correlation parameters in Edwards wide band model (Table 5.1)
c	molar concentration, Eq. (3.57) [mol/m^3]
c_k	scattering phase function coefficients, Eq. (4.4)
c_P	specific heat at constant pressure [J/kg K]
c_V	specific heat at constant volume [J/kg K]
$c_{\varepsilon 1}$, $c_{\varepsilon 2}$, $c_{\varepsilon 3}$	model constants in the ε-equation, Eq. (3.47)
c_μ	model constant in definition of turbulent viscosity, Eq. (3.26)
c_{lw}	model constant in log-law wall function, Eq. (3.101)
D	function in YIX distance quadrature, Eq. (4.96)
D	species mass diffusivity [m^2/s]
d	spherical carbon particle diameter [μm]
E_a	effective activation energy, Eq. (3.61) [J/mol]
E_f, E_b	activation energies in forward and backward reactions, Eq. (3.59)

e_s, e_g	surface, gas blackbody emissive power, Eq. (4.15) [W/m^2]
$\hat{\mathbf{e}}_x, \hat{\mathbf{e}}_y, \hat{\mathbf{e}}_z$	local Cartesian unit vectors, Eq. (4.63)
F	blackbody distribution function in WSGG model, Eq. (5.13)
F_g, F_w, F_s	terms on left-hand side of integral radiation equations, Eq. (4.25)
f	blackbody fraction, Eq. (5.8)
f	constant parameter in δ–Eddington scattering phase function, Eq. (6.9)
f	(also g, h) stretching (blending) function, Eqs. (2.5) and (2.6)
f_1, f_2, f_3, f_4	Arrhenius rate coefficients in Shell autoignition model [s^{-1}]
f_i	blending function in ξ–coordinate direction (index i), Eq. (2.7)
f_g, f_w, f_s	terms on right-hand side of integral radiation equations, Eq. (4.25)
$\overline{G_iS_j}, \overline{G_iG_j}$	total exchange areas, Eq. (4.73) [m^3]
$\overline{gs}, \overline{gg}$	direct exchange factors, Eq. (4.82)
g	determinant of covariant tensor ≡ Jacobian^2, Eq. (2.20)
g	asymmetry factor ≡ average cosine of scattering angle
g'	constant parameter in δ–Eddington scattering phase function, Eq. (6.9)
g_{ij}	covariant metric tensor elements
g^{ij}	contravariant metric tensor elements
g_i	blending function in η–coordinate direction (index j), Eq. (2.10)
H	height of L-shaped enclosure in Case E benchmark problem (Fig. 6.12) [m]
h	specific enthalpy [J/kg]
h_i	blending function in ζ–coordinate direction (index k), Eq. (2.12)
I	distance integral (YIX distance quadrature), Eq. (4.92)
I	specific internal energy [J/kg]
i	radiation intensity [W/m^2 sr]
i_b	blackbody intensity [W/m^2 sr]
i, j, k	curvilinear indices
J	Jacobian matrix, Eq. (4.45)
J_w	convective wall heat flux in log-law function, Eq. (3.102) [W/m^2]
K	exponential kernel function in integral radiation equations, Eq. (4.26)
K	thermal conductivity [W/m K]
K_c	equilibrium constant, Eq. (3.56)
k	turbulent kinetic energy [m^2/s^2]
k_p, k_q, k_B, k_t	Arrhenius rate coefficients in Shell autoignition model [s^{-1}]
k_f, k_b	Arrhenius forward and backward rate coefficients, Eq. (3.59) [s^{-1}]

L	length of ray path $\hat{\mathbf{s}}$ from $\mathbf{r}$ to $\mathbf{r}'$ on boundary surface [m]
L	length of L-shaped enclosure in Case E benchmark problem (Fig. 6.12) [m]
l	connecting rod length [m]
m	moles of H_2 in fuel RH: Shell autoignition model
N	number of energy bundles, sample population size (Monte Carlo methods)
N_s	carbon particles per unit volume in gas/particulate mixture [m^{-3}]
n	pressure correlation parameter in Edwards wide band model (Table 5.1)
n	moles of C in fuel RH: Shell autoignition model
$\hat{\mathbf{n}}, \hat{\mathbf{n}}'$	unit surface normal (pointing into the medium)
P	power [W]
P	probability density function
$P^{(i)}; P^{(j)}; P^{(k)}$	projectors in ξ, η and ζ –coordinate directions, respectively.
$P^i; P_i$	control functions in elliptic mesh generation systems, $i = 1, 2$ or 3
P_i	function in YIX distance quadrature, Eq. (4.104)
P_k	production rate of turbulent kinetic energy [W]
P_n	Legrendre functions
P_n^m	spherical functions of the first kind
Pr	Prandtl number, Eq. (3.40)
p	pressure [N/m^2]
R	uniformly distributed random number from 0 to 1
R_u	universal gas constant = 8.3143 [J/mol K]
Q	heat rate [W]
$\dot{Q}'''$	heat production per unit volume [W/m^3]
Q_i	function in YIX distance quadrature, Eq. (4.103)
$\dot{Q}_{chem}$	chemical heat source [W/m^3]
Q_{ext}	extinction efficiency
Q_{sca}	scattering efficiency
q	exothermicity from oxidising $1/m$ moles of fuel RH: Shell model [J/mol^2]
q_t	total heat flux vector, unclosed: Eq. (3.15); closed: Eq. (3.49) [W/m^2]
q_s	net radiative surface heat flux, Eq. (4.14) [W/m^2]
$q_r, \mathbf{q}_r$	radiative heat flux, radiative heat flux vector [W/m^2]
R_c	critical Reynolds number = 114 in boundary layer model
r_v	ratio of maximum to minimum accelerations of valve
$\mathbf{r}, \mathbf{r}'$	position vector in medium, position vector at point (usually) on surface

$\mathbf{r}_t$	position vector of all points on path $\hat{\mathbf{s}}$ between $\mathbf{r}'$ and $\mathbf{r}$
S	source term of discretised equation, Eq. (2.24)
S	radiative source function, Eq. (4.16) [W/m^2 sr]
S	line strength ≡ line-integrated absorption coefficient [cm^{-1}/(kg m^{-2})]
S_i	functions of form $P_n^m(\cos\theta)\cos m\phi$ or $P_n^m(\cos\theta)\sin m\phi$, $i = 1, 2$ or 3
$\overline{S_iS_j}$, $\overline{S_iG_j}$	total exchange areas, Eq. (4.73) [m^2]
S_n	best estimate of standard error, Eq. (4.72)
Sc	Schmidt number, Eq. (3.39)
s	distance in direction $\hat{\mathbf{s}}$ [m]
s	normalised coordinate, Eq. (2.2)
s_n	best estimate of standard deviation (precision), Eq. (4.72)
$\overline{ss}$, $\overline{sg}$	direct exchange factors, Eq. (4.82)
$\hat{\mathbf{s}}$	unit vector in a given direction
$\hat{\mathbf{s}}_i$	unit vector in direction of in-scattered radiation
T	temperature [K]
t	constant parameter *or* time [s]
u_i	Cartesian velocity components: u, v, w
x_i	Cartesian coordinates: x, y, z
$\bar{x}$	mean of sample values x
$\mathbf{x}$	Cartesian position vector
V	volume (of physical element) [m^3]
v	volume of master element
W	width of L-shaped enclosure in Case E benchmark problem (Fig. 6.12) [m]
W_s	molecular weight of species s [kg/mol]
w_0	incident radiation (or irradiation) ≡ direction-integrated intensity [W/m^2]
w_i	Cartesian components of radiative heat flux vector: w_1, w_2, w_3 [W/m^2]
w_i	quadrature weights
$\mathbf{w}$	$(w_1, w_2, w_3)^T$
Y_s	mass fraction of chemical species s
y	perpendicular distance from wall in boundary layer model [m]

Greek symbols

α	band strength parameter ≡ band-integrated absorption coeff. [$cm^{-1}/(kg\ m^{-2})$]
α, β, γ	barycentric coordinates, Eq. (4.37)
β	extinction coefficient, Eq. (4.2) [m^{-1}]
β	pressure broadening (or line overlap) parameter in band model, Eq. (5.4)
γ	ratio of specific heats, Eq. (3.21)
γ	mass fraction of turbulent fine-structure regions: EDC model, Eq. (3.63)
Δt	overall computational timestep [s]
$\Delta\xi, \Delta\eta, \Delta\zeta$	spacings between ξ, η and ζ –coordinate lines, respectively, Eq. (2.22)
δ	absorption line spacing in band model [cm^{-1}]
δ	Dirac-delta function (in δ–Eddington scattering phase function), Eq. (6.10)
δs	pathlength segment on ray path [m]
δ_{ij}	Kronecker delta function
ε	surface emissivity
ε	rate of turbulence kinetic energy (or eddy) dissipation [m^2/s^3]
ζ	wall Reynolds number in boundary layer model, Eq. (3.99)
ζ_f, ζ_b	temperature exponents of forward and backward reactions, Eq. (3.59)
η	wavenumber [cm^{-1}]
Θ	scatter angle in δ–Eddington scattering phase function, Eq. (6.9)
θ	(and φ) polar angle in spherical coordinate system [rad]
θ	crank angle [rad or deg]
κ	absorption coefficient [m^{-1}]
κ	bulk viscosity, Eq. (3.12) [kg/m s]
κ	derived von Karman constant in log-law wall function = 0.4327
λ	constant in YIX distance quadrature, Eq. (4.98)
λ	second coefficient of dynamic viscosity [kg/m s]
μ	first coefficient of dynamic viscosity [kg/m s]
ξ^i; ξ, η, ζ	curvilinear coordinates, $i = 1, 2$ or 3.
ρ	density [kg/m^3]
σ	Stefan-Boltzmann constant $= 5.6696 \times 10^{-8}$ $W/m^2\ K^4$
σ	Prandtl/Schmidt number
σ_s	scattering coefficient [m^{-1}]
σ_w	wall shear stress in boundary layer model, Eq. (3.100) [N/m^2]
σ_{ij}	viscous stress tensor, unclosed: Eq. (3.11); closed: Eq. (3.46) [N/m^2]
Γ	equivalent optical distance (or thickness) of path length L

τ	optical coordinate, optical thickness, Eq. (4.8)
τ	characteristic time scale in EDC model [s]
τ_η	Kolmogorov time scale of smallest motions [s]
ν	kinematic viscosity [m^2/s]
Φ	scattering phase function, Eq. (4.3) [sr^{-1}]
Φ	viscous dissipation term, unclosed: Eq. (3.16); closed: Eq. (3.51) [W/m^3]
ϕ	(and ψ) azimuthal angle in spherical coordinate system [rad]
ϕ	dependent variable
ϕ	polynomials, Eq. (2.3)
χ	fraction of fine structures reacting: EDC model, Eq. (3.70)
χ_1, χ_2, χ_3	correlation factors in EDC model, Eqs. (3.71-73)
ψ	bilinear shape (or basis) functions in FE parametric mapping
Ω	solid angle [sr]
ω	relaxation factor, Eq. (2.37)
ω	single scattering albedo, Eq. (4.7)
ω	bandwidth parameter in band model, Eq. (4.7) [cm^{-1}]
ω	chemical reaction rate [mol/m^3 s]
ω	angular velocity of crank shaft [rad/s]

Subscripts and Superscripts

b	blackbody
e	element
eff	effective ≡ laminar + turbulent
F	fuel
g	gas
i	incident *or* incoming
O	oxidiser
o	outgoing
P	product
p	piston
l	laminar
r	reaction *or* reflection
s	chemical species *or* surface
t	turbulent
w	wall

Diacritical marks

$\overline{\phi}$	time-averaged mean quantity ϕ, Eq. (3.4)
$\tilde{\phi}$	Favre-averaged mean quantity ϕ, Eq. (3.6)
ϕ'	turbulent fluctuation of ϕ after time-averaging, Eq. (3.5)
ϕ''	turbulent fluctuation of ϕ after Favre-averaging, Eq. (3.7)
ϕ^*	modified, characteristic *or* EDC model fine structure quantity ϕ
ϕ°	quantity ϕ in fluid surrounding fine structures in EDC model
$[\phi]$	mean molar concentration of ϕ [mol/m^3]

Abbreviations

ADI	alternate direction implicit
ASM	algebraic stress model
ATDC	after top-dead-centre
BDC	bottom-dead-centre
BTDC	before top-dead-centre
CDF	cumulative distribution function
CFD	computational fluid dynamics
DEF	discrete exchange factor
DOM	discrete ordinates method
DT	discrete transfer
EDC	eddy dissipation concept
EVO	exhaust valve opens
EVC	exhaust valve closes
FE	finite element
ILDM	intrinsic low-dimensional manifold
IVC	inlet valve closes
IVO	inlet valve opens
MBT	maximum brake torque
MC	Monte Carlo
NURBS	nonuniform rational B-splines
ODE	ordinary differential equation
PDC	partial donar cell
PDF	probability density function
QSOU	quasi-second-order upwind
RSM	*Reynolds stress model*
SI	spark ignition
SIMPLE	semi-implicit pressure linked eqs.
SLOR	successive line overrelaxation
SOR	successive overrelaxation
TDC	top-dead-centre
TDMA	tri-diagonal matrix algorithm
TRI	turbulence-radiation interactions
WSGG	weighted-sum-of-gray-gases

Note: (a) YIX is not an abbreviation (see p. 136).

(b) 'divergence of radiative heat flux' is often abbreviated as 'flux divergence'.

References

Chapter 1

Amsden, A. A., O'Rourke, P. J. and Butler, T. D. (1989). KIVA-II: A Computer Program for Chemically Reactive Flows with Sprays. Report no. LA-11560-MS. Los Alamos National Laboratory, New Mexico.

Bensler, H. and Oppermann, R. (1996). CFD optimization of powertrain components. Paper no. C499/057/96 in *Computers in Reciprocating Engines and Gas Turbines*, IMechE Conference Transaction 1996-1, pp. 249-268.

Buchou, C. (1994). Towards The 3D Modelling Of Intake Flow In Spark Ignition Engines Using the Kiva 2 Code. Abstracts of the Fourth International KIVA Users Meeting at the SAE Congress, Feb. 27, Detroit.

Chan, S. H. (1998). The Role of Radiative Transfer in Combustion. In *Radiative Transfer - II*, Proceedings of 2nd International Symposium on Radiative Transfer, ed., Mengüç, M. P., Begell House, New York, pp. 463-474.

Gritzo, L. A., Skocypec, R. D. and Tong, T. W. (1995). The Use of High-Performance Computing to Solve Participating Media Radiative Heat Transfer Problems - Results of an NSF Workshop. Report no. SAND95-0225. Sandia National Laboratories, New Mexico.

Heywood, J. B. (1988). *Internal Combustion Engine Fundamentals*. McGraw-Hill, New York.

Taghavi, R. and Dupont, A. (1989). Multidimensional Flow Simulation in an Inlet Port/ Combustion Chamber Assembly featuring a Moving Valve. In *Basic Processes In Internal Combustion Engines 1989*, ed., T. Uzkan, ICE-Vol. 6, ASME, pp. 9-15.

Tatschl, R., Fuchs, H. and Branstatter, W. (1996). Experimentally validated multi-dimensional simulation of mixture formation and combustion in gasoline engines. Paper no. C499/050/96 in *Computers in Reciprocating Engines and Gas Turbines*, IMechE Conference Transaction 1996-1, pp. 11-23.

Tong, T. W. and Skocypec, R. D. (1992). Summary on Comparison of Radiative Heat Transfer Solutions for a Specified Problem. In *Developments in Radiative Heat Transfer*, HTD-vol. 203, ASME, pp. 253-264.

Chapter 2

Amsden, A. A., O'Rourke, P. J. and Butler, T. D. (1989). KIVA-II: A Computer Program for Chemically Reactive Flows with Sprays. Report no. LA-11560-MS. Los Alamos National Laboratory, New Mexico..

Dierckx, P. (1993). *Curves And Surface Fitting With Splines Vol. 1*. Clarendon Press, Oxford.

Fletcher, C. A. J. (1991). *Computational Techniques For Fluid Dynamics Vol. 2: Specific Techniques for Different Flow Categories*. 2nd ed., Springer-Verlag, Berlin.

Hirsch, C. (1988). *Numerical Computation of Internal and External Flows. Vol. 1 Fundamentals of Numerical Discretization.* Wiley, New York.

Pletcher, R. H., Minkowycz, W. J., Sparrow, E. M. and Schneider, G. E. (1988). Overview of Basic Numerical Methods. In *Handbook Of Numerical Heat Transfer*, eds., Minkowycz, W. J., Sparrow, E. M., Schneider, G. E. and Pletcher, R. H., Wiley, New York, p. 55.

Rogers, D. F. and Adams, J. A. (1990). *Mathematical Elements For Computer Graphics.* 2nd ed., McGrawHill, Singapore.

Shieh, C. F. (1984). Three-Dimensional Grid Generation Using Elliptic Equations with Direct Grid Distribution Control. *AIAA Journal*, vol. 22, no. 3, pp. 361-364.

Taghavi, R. and Dupont, A. (1989). Multidimensional Flow Simulation in an Inlet Port/ Combustion Chamber Assembly featuring a Moving Valve. In *Basic Processes In Internal Combustion Engines 1989*, ed., T. Uzkan, ICE-vol. 6, ASME, pp. 9-15.

Thompson, J. F. (1984). Grid Generation Techniques in Computational Fluid Dynamics. *AIAA Journal*, vol. 22, no. 11, pp. 1505-1523.

Thompson, J. F. (1988). Grid Generation. In *Handbook Of Numerical Heat Transfer*, eds., Minkowycz, W. J., Sparrow, E. M., Schneider, G. E. and Pletcher, R. H., Wiley, New York, Chapter 21.

Thompson, J. F., Warsi, Z. U. A. and Mastin, C. W. (1985). *Numerical Grid Generation: Foundations and Applications.* North-Holland, New York.

Vinokur, M. (1983). *Journal of Computational Physics*, vol. 50, pp. 215-234.

Chapter 3

Ahmadi-Befrui, B., Gosman, A. D., Lockwood, F. C. and Watkins, A. P. (1981). Multidimensional Calculation of Combustion in an Idealised Homogeneous Charge Engine: a Progress Report. SAE paper no. 810151.

Amsden, A. A. (1997). KIVA-3V: A Block-Structured KIVA Program for Engines with Vertical or Canted Valves. Report no. LA-13313-MS. Los Alamos National Laboratory New Mexico.

Amsden, A. A. (1993). KIVA-3: A KIVA Program with Block-Structured Mesh for Complex Geometries. Report no. LA-12503-MS. Los Alamos National Laboratory, New Mexico.

Amsden, A. A., Ramshaw, J. D., O'Rourke, P. J. and Dukowicz, J. K. (1985a). KIVA: A Computer Program for Two- and Three-Dimensional Fluid Flows with Chemical Reactions and Fuel Sprays. Report no. LA-10245-MS. Los Alamos Alamos National Laboratory, New Mexico.

Amsden, A. A., Ramshaw, J. D., Cloutman, L. D. and O'Rourke, P. J. (1985b). Improvements and Extensions to the KIVA Computer Program. Report no. LA-10534-MS. . Los Alamos National Laboratory, New Mexico.

Amsden, A. A., O'Rourke, P. J. and Butler, T. D. (1989). KIVA-II: A Computer Program for Chemically Reactive Flows with Sprays. Report no. LA-11560-MS. Los Alamos National Laboratory, New Mexico.

Anderson, A. D., Tannehill, J. C. and Pletcher, R. H. (1984). *Computational Fluid Mechanics and Heat Transfer.* Hemisphere, New York.

Benson, R. S. (1982). *The Thermodynamics and Gas Dynamics of Internal Combustin Engines. Vol. 1.* Clarendon Press, Oxford.

Blunsdon, C. A. (1994a). Personal communication.

Blunsdon, C. A. and Dent, J.C. (1994b). The Simulation of Autoignition and Knock in a Spark Ignition Engine with Disk Geometry. SAE paper no. 940524.

Blunsdon, C. A. and Dent, J.C. (1994c). Modelling the Source of Combustion Noise in a Direct Injection Diesel Engine using CFD. SAE paper no. 941898.

Blunsdon, C. A., Malalasekera, W. M. G. and Dent, J. C. (1993). Modelling Infrared Radiation from the Combustion Products in a Spark Ignition Engine. SAE paper no. 932699.

Blunsdon, C. A., Malalaskera, W. M. G. and Dent J. C. (1992). Application of the Discrete Transfer Model of Thermal Radiation in a CFD Simulation of Diesel Combustion and Heat Transfer. SAE paper no. 922305.

Chen, A., Mahmood, Z., Yianneskis, M. and Ganti, G. (1996). Three-dimensional Simulation of the Flow through a Twin-Intake Port Engine. Paper no. C499/055/96. In *Computers in Reciprocating Engines and Gas Turbines*, pp. 239-248. IMechE Conference Trans. 1996 - 1.

Das, S. (1996). Computational Fluid Dynamic Modelling Of Flow And Combustion In Spark Ignition Engines. Ph. D. Thesis. Department of Mechanical Engineering, Loughborough University, UK.

Diwakar, R. (1984). Assessment of the Ability of a Multidimensional Computer Code to Model Combustion in a Homogeneous-Charge Engine. SAE paper no. 840230.

Fletcher, C. A. J. (1991). *Computational Techniques for Fluid Dynamics. Vol. 1.* 2nd ed., Springer-Verlag, Berlin.

Gran, I. R. (1994). Mathematical Modeling And Numerical Simulation Of Chemical Kinetics in Turbulent Combustion. Dr. Ing. Thesis. University of Trondheim, Norway.

Gran, I. R. (1990). Numerical Simulation of Fluid Flow and Combustion in Gas Turbine Combustors. Diploma Thesis. University of Trondheim, Norway.

Grimsmo, B. (1991). Numerical Simulation of Turbulent Flow and Combustion in a Four Stroke Homogeneous Charge Internal Combustion Engine. Dr. Ing. Thesis. University of Trondheim, Norway.

Halstead, M. P., Kirsch, L. J. and Quinn, C. P. (1977). The autoignition of Hydrocarbon Fuels at High Temperatures and Pressures–Fitting of a Mathematical Model. *Combustion and Flame,* vol. 30, pp. 45-60.

Halstead, M. P., Kirsch, L. J., Prothero, A. and Quinn, C. P. (1975). A mathematical model for hydrocarbon autoignition at high pressures. *Proceedings of the Royal Society of London, Series A*, vol. 346, pp. 515-538.

Heywood, J. B. (1988). *Internal Combustion Engine Fundamentals*. McGraw-Hill, New York.

Hirst, S. L. and Kirsch, L. J. (1980). The Application of a Hydrocarbon Autoignition Model in Simulating Knock and Other Engine Combustion Phenomena. In *Combustion Modelling in Reciprocating Engines*, eds. Mattavi, J. N. and Aman, C. A., Plenum Press, New York, pp. 193-229.

Jones, W. P. (1982). Modelling of Combustion Chambers and Furnaces. Lecture notes. Department of Chemical and Mechanical Engineering, Imperial College, London.

Jones, W. P. and Launder, B. E. (1972). The Prediction of Laminarisation with a Two Equation Turbulence Model. *International Journal of Heat and Mass Transfer*, vol. 15, p. 301.

Jones, W. P. and Whitelaw, J. H. (1984). Modelling and Measurements in Turbulent Combustion. In *Twentieth Symposium (International) on Combustion*. The Combustion Institute, Pittsburgh, pp. 233-249.

Jones, W. P. and Whitelaw, J. H. (1982). Calculation Methods for Reacting Turbulent Flows: A Review. *Combustion and Flame*, vol. 48, pp. 1-26.

Kuo, K. K. (1986). *Principles of Combustion*. Wiley, New York.

Kuo, T. and Reitz, R.D. (1989). Computation of Premixed-Charge Combustion in Pancake and Pent-Roof Engines. SAE paper no. 890670.

Launder, B. E. (1983). Second-Moment Closure: Methodology and Practice. Report no. TFD/82/4 (Corrected Version). For participants in NMHFF-II, University of Manchester.

Li, H., Miller, D. L. and Cernansky, N. P. (1996). Development of a Reduced Chemical Kinetic Model for Prediction of Preignition Reactivity and Autoignition of Primary Reference Fuels. SAE paper no. 960498.

Magnussen, B. F. (1989). Modeling of Pollutant Formation in Gas Turbine Combustors Based on the Eddy Dissipation Concept. In *Eighteenth International Congress on Combustion Engines*, Tianjin, China. International Council on Combustion Engines.

Magnussen, B. F. (1980). Modeling of Reaction Processes in Turbulent Flames with Special Emphasis On Soot Formation and Combustion. Report sourced with private communication. (Also available in *Particulate Carbon Formation During Combustion*, Plenum 1981).

Magnussen, B. F. and Hjertager, B. H. (1976). On Mathematical Modeling of Turbulent Combustion with Special Emphasis On Soot Formation and Combustion. In *Sixteenth Symposium (International) on Combustion*. The Combustion Institute, Pittsburgh, pp. 719-729.

Modest, M. F. (1993). *Radiative Heat Transfer*. McGraw-Hill, New York.

Moses, E., Yarin, A. L. and Bar-Yoseph, P. (1995). On Knocking Prediction in Spark Ignition Engines. *Combustion and Flame*, vol. 101, pp. 239-261.

O'Rourke, P. J., Amsden, A. A., Butler, T. D. and McKinley, T. L. (1989). Improvements of the KIVA-II Computer Program for Numerical Combustion. Los Alamos National Laboratory report LA-UR-89. Los Alamos, New Mexico 87545.

O'Rourke, P. J. and Amsden, A. A. (1986). Implementation of a Conjugate Residual Iteration in the KIVA Computer Program. Los Alamos National Laboratory report LA-10849-MS. Los Alamos, New Mexico 87545.

Patankar, S. V. (1980). *Numerical Heat Transfer and Fluid Flow*. Hemisphere, New York.

Pearson, R. J. and Winterbone, D. E. (1996). Calculation of one-dimensional unsteady flow in internal combustion engines - how long should it take? Paper no. C499/012/96. In *Computers in Reciprocating Engines and Gas Turbines*, pp. 193-202. IMechE Conference Transaction 1996-1.

Press, W. H., Teukolsky, S. A., Vetterling, W. T. and Flannery, B. P. (1992). *Numerical Recipes in Fortran 77: The Art of Scientific Computing*. 2nd ed. Cambridge University Press.

Ramos, J. I. (1989). Internal Combustion Engine Modeling. Hemisphere Pub. Corp., New York.

Schäpertöns, H., and Lee, W. (1985). Multidimensional Modelling of Knocking Combustion in SI Engines. SAE International Congress and Exposition, Detroit, Mich., SAE paper no. 850502.

Smirnoff, A. (1995). Evaluation of Different Turbulence Models Used in Simulations of Confined Swirl Flows. Internal report posted on WWW. Department of Thermo and Fluid Dynamics, Chalmers University of Technology, Göteborg, Sweden, pp. 15-19.

Spalding, D. B. (1976). Development of the Eddy-Break-Up Model of Turbulent Combustion. In *Sixteenth Symposium (International) on Combustion*. The Combustion Institute, Pittsburgh, pp. 1657-1663.

Spalding, D. B. (1971). Mixing and Chemical Reaction in Steady Confined Turbulent Flames. In *Thirteenth Symposium (International) on Combustion*. The Combustion Institute, Pittsburgh, pp. 649-657.

Stull, D. R. and Prophet, H. (1974). JANAF Thermochemical Tables. 2nd ed. (U.S. Department of Commerce/National Bureau of Standards, NSRDS-NBS 37, June 1971). *Journal of Physical and Chemical Reference Data*, vol. 3, p. 311

Warnatz, J., Maas, U. and Dibble, R. W. (1996). Combustion: physical and chemical fundamentals, modelling and simulation, experiments, pollutant formation. Springer-Verlag, Berlin.

Westbrook, C. K. and Dryer, F. L. (1981). Simplified Reaction Mechanisms for the Oxidation of Hydrocarbon Fuels in Flames. *Combustion Science and Technology*, vol. 27, pp. 31-43.

Chapter 4

Abbas, A. S., Lockwood, F. C. and Salooja, A. P. (1984). The Prediction of the Combustion and Heat Transfer Performance of a Refinery Heater. *Combustion and Flame*, vol. 58, pp. 91-101.

Badouel, D. (1990). An Efficient Ray-Polygon Intersection. In *Graphics Gems*, ed. Glassner, A. S., Academic Press, New York.

Barford, N. C. (1985). *Experimental Measurements: Precision, Error and Truth*, 2nd ed., Wiley, Chichester.

Burns, S. P. (1995a). Finite Element Solution of Combined Mode Heat Transfer with Nonhomogeneous, Nongray Radiative Properties. Ph.D. Thesis. The University of Texas at Austin, Texas, USA.

Burns, S. P., Howell, J. R. and Klein, D. E. (1995b). Finite Element Solution for Radiative Heat Transfer with Nongray, Nonhomogeneous Radiative Properties. In *1995 National Heat Transfer Conference - Vol. 13*, HTD-vol. 315, ASME, pp. 3-10.

Burns, S. P., Howell, J. R. and Klein, D. E. (1994). Assessment of the Swartz-Wendroff Finte Element Formulation for Combined Mode Heat Transfer. In *Radiative Heat Transfer: Current Research*, HTD-vol. 276, ASME, pp. 1-7.

Carvalho, M. G., Farias, T. and Fontes, P. (1991). Predicting Radiative Heat Transfer in Absorbing, Emitting, and Scattering Media Using the Discrete Transfer Method. In *Fundamentals of Radiation Heat Transfer*, HTD-vol. 160, ASME, pp. 17-26.

Chai, J. C., Lee, H. S. and Patankar, S. V. (1993a). Ray Effect and False Scattering in the Discrete Ordinates Method. University of Minnesota Supercomputer Institute Research Report UMSI 93/106, 1200 Washington Avenue South, Minneapolis, Minnesota..

Chai, J. C., Lee, H. S. and Patankar, S. V. (1993b). An Evaluation of Spatial Differencing Practices for the Discrete-Ordinates Method. University of Minnesota Supercomputer Institute Research Report UMSI 93/105, 1200 Washington Avenue South, Minneapolis, Minnesota..

Chai, J. C., Lee, H. S. and Patankar, S. V. (1993c). Radiation Heat Transfer Calculations using a Control-Angle, Control-Volume-Based Discrete Ordinates Method. University of Minnesota Supercomputer Institute Research Report UMSI 93/103, 1200 Washington Avenue South, Minneapolis, Minnesota. (Also *AIAA* paper no. 93-2731.)

Chan, S. H. (1987). Numerical Methods for Multidimensional Radiative Transfer Analysis in Participating Media. In *Annual Review of Numerical Fluid Mechanics and Heat Transfer*, vol. 1, pp. 305-350.

Chu, C. M. and Churchill, S. W. (1955). Representation of an Angular Distribution of Radiation Scattered by a Spherical Particle. *Journal of the Optical Society of America*, vol. 45, pp. 958-962.

Chui, E. H. and Raithby, G. D. (1992). Prediction of Radiative Transfer in Cylindrical Enclosures with the Finite Volume Method. *Journal of Thermophysics and Heat Transfer*, vol. 6, no. 4, pp. 605-611.

Chui, E. H. and Raithby, G. D. (1993). Computation of Radiant Heat Transfer on a Nonorthogonal Mesh Using the Finite-Volume Method. *Numerical Heat Transfer*, Part B, vol. 23, pp. 269-288.

Chung, T. J. (1988). Integral and Integro-Differential Systems. In *Handbook of Numerical Heat Transfer*, eds., Minkowycz, W. J., Sparrow, E. M., Schneider, G. E. and Pletcher, R. H., Wiley, New York, Chapter 14.

Cumber, P. S. (1995). Improvements to the Discrete Transfer Method of Calculating Radiative Heat Transfer. *International Journal of Heat and Mass Transfer*, vol. 38, no. 12, pp. 2251-2258.

Coelho, P. J. and Carvalho, M. G. (1997). A Conservative Formulation of the Discrete Transfer Method. *Journal of Heat Transfer*, vol. 119, pp. 118-128.

Dayan, A. and Tien, C.L. (1975). Heat Transfer in a Gray Planar Medium with Linear Anisotropic Scattering, *ASME Journal of Heat Transfer*, vol. 97, no. 3, pp. 391-396.

Drake, D. (1996). A Beam Tracking Method for 3D Radiation Transport in Participating Media. Open Forum paper at 1996 ASME National Heat Transfer Conference, Houston, Texas.

Farmer, J. T. (1995). Improved Algorithms for Monte Carlo Analysis of Radiative Heat Transfer in Complex Participating Media. Ph.D. Thesis. The University of Texas at Austin, Texas, USA.

Farmer, J. T. and Howell, J. R. (1992). Monte Carlo Solution of Radiative Heat Transfer in a Three-Dimensional Enclosure with an Anisotropically Scattering, Spectrally Dependent, Inhomogeneous Medium. In *Developments in Radiative Heat Transfer*, HTD-vol. 203, ASME, pp. 301-309.

Farmer, J. T. and Howell, J. R. (1994). Monte Carlo Prediction of Radiative Heat Transfer in Inhomogeneous, Anisotropic, Nongray Media. *Journal of Thermophysics and Heat Transfer*, vol. 8, no. 1, pp. 133-139.

Fiveland, W. A. (1984). Discrete-Ordinate Solutions of the Radiative Transport Equation for Rectangular Enclosures. *Journal of Heat Transfer,* vol. 106, pp. 699-706.

Fiveland, W. A. (1988). Three-Dimensional Radiative Heat Transfer Solutions by the Discrete-Ordinates Method. *Journal of Thermophysics and Heat Transfer*, vol. 2, no. 4, pp. 309-316.

Fiveland, W. A. (1991). The Selection of Discrete Ordinate Quadrature Sets for Anisotropic Scattering. In *Fundamentals of Radiation Transport*, HTD-vol. 160, ASME, pp. 89-96.

Fiveland, W. A. and Jessee, J. P. (1993). A Finite Element Formulation of the Discrete-Ordinates Method for Multidimensional Geometries. In *Radiative Heat Transfer: Theory and Applications*, HTD-vol. 244, ASME, pp. 41-48.

Fiveland, W. A. and Jessee, J. P. (1994). Comparisons Of Discrete Ordinate Formulations For Radiative Heat Transfer In Multidimensional Geometries. In *Radiative Heat Transfer: Current Research*, HTD-vol. 276, ASME, pp. 49-57.

Gradshteyn, I. S. and Ryzhik, I. M. (1994). *Table of Integrals, Series, and Products.* 5th ed. Academic Press, New York.

Haidekker, A., Charette, A. and Kocaefe, Y. S. (1994). Application of the Hybrid Zone/ Monte Carlo Method to 3-D Curvilinear Grids in Radiative Heat Transfer. *International Journal for Numerical Methods in Engineering*, vol. 37, pp. 203-216.

Haines, E. (1989). Essential Ray Tracing Algorithms. In *An Introduction To Ray Tracing*, ed. Glassner, A. S., Academic Press, New York.

Haines, E. (1992). Light Makes Right. In *Ray Tracing News*, vol. 5, no. 3. Posted on Internet anonymous FTP site 'pinceton.edu:/pub/Graphics/RTNews' or e-mail: erich@eye.com.

Haji-Sheikh. (1988). Monte Carlo Methods. In *Handbook Of Numerical Heat Transfer*, eds., Minkowycz, W. J., Sparrow, E. M., Schneider, G. E. and Pletcher, R. H., Wiley, New York, Chapter 16.

Hirsch, C. (1988). *Numerical Computation of Internal and External Flows. Vol. 1. Fundamentals of Numerical Discretization.* Wiley, New York.

Hoover, R. L., Li, W., Benmalek, A. and Tong, T. W. (1996). *Sn* Solutions for Radiative Heat Transfer in an L-Shaped Participating Medium. In *National Heat Transfer Conference, Vol. 3*, HTD-vol. 325, ASME, pp. 1-11.

Hottel, H. C. and Cohen, E. S. (1958). Radiant Heat Exchange in a Gas-Filled Enclosure: Allowance for Nonuniformity of Gas Temperature. *AIChE Journal*, vol. 4, pp. 3-14.

Howell, J. R. (1988). Thermal Radiation in Participating Media: The Past, the Present, and Some Possible Futures. *Journal of Heat Transfer*, vol. 110, pp. 1220-1229.

Howell, J. R. and Perlmutter, M. (1964a). Monte Carlo Solution of Thermal Transfer through Radiant Media between Gray Walls. *Journal of Heat Transfer*, vol. 86, no. 1, pp. 116-122.

Howell, J. R. and Perlmutter, M. (1964b). Monte Carlo Solution of Radiant Heat Transfer in a Nongrey Nonisothermal Gas with Temperature Dependent Properties. *AIChE Journal*, vol. 10, no. 4, pp. 562-567.

Hsu, P. and Farmer, J. T. (1995). Benchmark Solutions of Radiative Heat Transfer within Nonhomogeneous Participating Media using the Monte Carlo and YIX Methods. In *1995 National Heat Transfer Conference - Vol. 13*, HTD-vol. 315, ASME, pp. 29-36.

Hsu, P. and Tan, Z. (1996). The Radiative and Combined Mode Heat Transfer within the L-Shaped Nonhomogeneous and Nongray Participating Media. In *National Heat Transfer Conference - Vol. 3*, HTD-vol. 325, ASME, pp. 13-24.

Hsu, P., Tan, Z. and Howell, J. R. (1993). Radiative Transfer by the YIX Method in Nonhomogeneous, Scattering, and Nongray Media. *Journal of Thermophysics and Heat Transfer*, vol. 7, no. 3, pp. 487-495.

Larsen, M. E. and Howell, J. R. (1985). The Exchange Factor Method: An Alternative Basis for Zonal Analysis of Radiating Enclosures. *Transactions of the ASME, Journal of Heat Transfer*, vol. 107, pp. 936-942.

Larsen, M. E. and Howell, J. R. (1986). Least-Squares Smoothing of Direct-Exchange Areas in Zonal Analysis. *Journal of Heat Transfer*, vol. 108 pp. 239-242.

Lathrop, K. D. and Carlson, B. G. (1965). Discrete-Ordinates Angular Quadrature of the Neutron Transport Equation. Technical Information Series Report LASL-3186. Los Alamos National Laboratory.

Lockwood, F. C. and Shah, N. G. (1981). A New Radiation Solution Method for Incorporation in General Combustion Prediction Procedures. In *Eighteenth Symposium (International) on Combustion*. The Combustion Institute, Pittsburgh, pp. 1405-1414.

Lockwood, F. C. and Malalasekera, W. M. G. (1988). Fire Computation: The 'Flashover' Phenomenon. In *Twenty-Second Symposium (International) on Combustion*. The Combustion Institute, Pittsburgh, pp. 1319-1328.

Malalasekera, W. M. G. and James, E. H. (1995). Calculation of Radiative Heat Transfer in Three-Dimensional Complex Geometries. In *1995 National Heat Transfer Conference - Vol. 13*, HTD-vol. 315, ASME, pp. 53-61.

Marsaglia, G. (1994). Dept. of Statistics, Florida State University, e-mail: geo@stat.fsu.edu (Posted on internet newsgroup: sci.math.num-analysis).

Meng, F. L., McKenty, F. and Camarero, R. (1993). Radiative Heat Transfer by the Discrete Transfer Method using an Unstructured Mesh. In *Radiative Heat Transfer: Theory and Applications*, HTD-vol. 244, ASME, pp. 55-66.

Modest, M. F. (1993). *Radiative Heat Transfer*. McGraw-Hill, New York.

Murthy, J. Y. and Choudhury, D. (1992). Computation of Participating Radiation in Complex Geometries. In *Developments in Radiative Heat Transfer*, HTD-vol. 203, pp. 153-160.

Naraghi, M. N. H., Chung, B. T. F. and Litkouhi, B. (1988). A Continuous Exchange Factor Method for Radiative Exchange in Enclosures with Participating Media. *Journal of Heat Transfer*, vol. 110, no. 2, pp. 456-462.

Pearson, C. E. (1986). *Numerical Methods in Engineering and Science.* Van Nostrand Reinhold Company. New York.

Raithby, G. D. and Chui, E. H. (1990). A Finite-Volume Method for Predicting a Radiant Heat Transfer in Enclosures With Participating Media. *Journal of Heat Transfer*, vol. 112, pp. 415-423.

Razzaque, M. M., Klein, D. E. and Howell, J. R. (1983). Finite Element Solution of Radiative Heat Transfer in a Two-Dimensional Rectangular Enclosure With Gray Participating Media. *Journal of Heat Transfer*, vol. 105, no. 4, pp. 933-934.

Razzaque, M. M., Klein, D. E. and Howell, J. R. (1984). Coupled Radiative and Conductive Heat Transfer in a Two-Dimensional Rectangular Enclosure With Gray Participating Media Using Finite Elements. *Journal of Heat Transfer*, vol. 106, no. 3, pp. 613-619.

Sakami, M., Charette, A. and Le Dez, V. (1997). Radiative Heat Transfer in Three-Dimensional Enclosures of Complex Geometry by using the Discrete Ordinates Method. *Journal of Quantitative Spectroscopy and Radiative Transfer*, vol. 59, no. 1-2, pp. 117-136.

Shah, N. G. (1979). New Method of Computation of Radiant Heat Transfer in Combustion Chambers. Ph.D. Thesis. Imperial College of Science and Technology, London, UK.

Siegel R. and Howell, J. R. (1992). *Thermal Radiation Heat Transfer*. 3rd ed., Hemisphere, Washington.

Tan, Z. (1989). Radiative Heat Transfer in Multidimensional Emitting, Absorbing, and Anisotropic Scattering Media - Mathematical Formulation and Numerical Method. *Journal of Heat Transfer*, vol. 111, pp. 141-147.

Tan, Z. (1991). New Numerical Methods for Radiation Heat Transfer and Rarefied Gas Dynamics. Ph.D. Thesis. Mechanical Engineering Department, The University of Texas at Austin, Texas, USA.

Tan, Z. and Howell, J. R. (1990a). New Numerical Method for Radiation Heat Transfer in Nonhomogeneous Participating Media. *Journal of Thermophysics and Heat Transfer*, vol. 4, no. 4, pp. 419-424.

Tan, Z. and Howell, J. R. (1990b). Two-Dimensional Radiative Heat Transfer in an Absorbing, Emitting, and Linearly Anisotropically Scattering Medium Exposed to a Collimated Source. In *Radiation Heat Transfer: Fundamentals and Applications*. HTD-vol. 137, ASME, pp. 101-106.

Tong, T. W. and Skocypec, R. D. (1992). Summary on Comparison of Radiative Heat Transfer Solutions for a Specified Problem. In *Developments in Radiative Heat Transfer*, HTD-vol. 203, ASME, pp. 253-264.

Yanovitskij, E. G. (1997). A Recurrence Formula for Computing Fourier Components of the Henyey-Greenstein Phase Function. *Journal of Quantitative Spectroscopy and Radiative Transfer*, vol. 57, no. 1, pp. 141-144.

Yuen, W. W., Ma, A. K. and Takara, E. E. (1992). Evaluation of Radiative Heat Transfer using the Generalized Zonal Method and the Absorption Mean Beam Length Concept. In *Developments in Radiative Heat Transfer*, HTD-vol. 203, ASME, pp. 265-273.

Chapter 5

Abbas, A. S., Lockwood, F. C. and Salooja, A. P. (1984). The Prediction of the Combustion and Heat Transfer Performance of a Refinery Heater. *Combustion and Flame*, vol. 58, pp. 91-101.

Bressloff, N. W., Moss, J. B. and Rubini, P. A. (1996). Assessment of a Differential Total Absorptivity Solution to the Radiative Transfer Equation as applied in the Discrete Transfer Radiation Model. *Numerical Heat Transfer: Part B*, vol. 29, no. 3, pp. 381-397.

Burns, S. P., Howell, J. R. and Klein, D. E. (1995). Finite Element Solution for Radiative Heat Transfer with Nongray, Nonhomogeneous Radiative Properties. In *1995 National Heat Transfer Conference - Vol. 13*, HTD-vol. 315, ASME, pp. 3-10.

Chang, S. L. and Rhee, K. T. (1984). Blackbody Radiation Functions, *International Communication in Heat and Mass Transfer*, vol. 11, pp. 451-455, 1984.

Denison, M. K. and Webb, B. W. (1993). A Spectral Line-Based Weighted-Sum-of-Gray-Gases Model for Arbitrary RTE Solvers. *Journal of Heat Transfer*, vol. 115, pp. 1004-1012.

Denison, M. K. and Webb, B. W. (1995). The Spectral Line-Based Weighted-Sum-of-Gray-Gases Model in Nonisothermal Nonhomogeneous Media. *Journal of Heat Transfer*, vol. 117, pp. 359-365.

Docherty, P. and Fairweather, M. (1988). Predictions of Radiative Transfer from Nonhomogeneous Combustion Products Using the Discrete Transfer Method. *Combustion and Flame*, vol. 71, pp. 79-87.

Edwards, D. K. (1976). Molecular Gas Band Radiation. In *Advances in Heat Transfer*, vol. 12, pp. 115-193.

Farmer, J. T. (1995). Improved Algorithms for Monte Carlo Analysis of Radiative Heat Transfer in Complex Participating Media. Ph.D. Thesis. The University of Texas at Austin, Texas, USA.

Farmer, J. T. and Howell, J. R. (1994). Hybrid Monte Carlo/Diffusion Methods for Enhanced Solution of Radiative Transfer in Optically Thick Nongray Media. In *Radiative Heat Transfer: Current Research*, HTD-vol. 276, ASME, pp. 203-212.

Goody, R. M. (1964). *Atmospheric Radiation*. Clarendon Press, Oxford.

Grosshandler, W. L. (1979). *Radiation from Nonhomogeneous Fires*. Technical Report FMRC J. I. OAOE6.BU-4, Factory Mutual Research Corp., Factory Mutual System, Norwood, Massachusetts.

Grosshandler, W. L. (1980). Radiative Heat Transfer in Nonhomogeneous Gases: A Simplified Approach. *International Journal of Heat and Mass Transfer*, vol. 23, pp. 1447-1459.

Grosshandler, W. L. (1985). Transmittance Nonhomogeneous Radiation Model to Methane Combustion. *Journal of Heat Transfer*, vol. 107, pp. 445-450.

Hsu, P., Tan, Z. and Howell, J. R. (1993). Radiative Transfer by the YIX Method in Nonhomogeneous, Scattering, and Nongray Media. *Journal of Thermophysics and Heat Transfer*, vol. 7, no. 3, pp. 487-495.

Kim, T. K., Menart, J. A. and Lee, H. S. (1990). Nongray Radiative Gas Analyses Using the Multilayer and S-N Techniques. In *Radiation Heat Transfer: Fundamentals and Applications*. HTD-vol. 137, ASME, pp. 149-156.

Kim, T. K., Menart, J. A. and Lee, H. S. (1991). Nongray Radiative Gas Analyses Using the S-N Discrete Ordinates Method. *Journal of Heat Transfer*, vol. 113, pp. 946-952.

Leckner, B. (1972). Spectral and Total Emissivity of Water Vapor and Carbon Dioxide. *Combustion and Flame*, vol. 19, pp. 33-48.

Li, W., Tong, T. W., Dobranich, D. and Gritzo, L. A. (1995). A Combined Narrow- and Wide-Band Model for Computing the Spectral Absorption Coefficient of CO2 , CO, H2O, CH4 , C2H2 and NO. *Journal of Quantitative Spectroscopy and Radiative Transfer*, vol. 54, no. 6, pp. 961-970.

Ludwig, C. B., Malkmus, W., Rcardon, J. E. and Thomson, J. A. L. (1973). *Handbook of Infrared Radiation from Combustion Gases*. Technical Report SP-3080, NASA.

Miranda, A. B. D. and Sacadura (1996). An Alternative Formulation of the S-N Discrete Ordinates for Predicting Radiative Transfer in Nongray Gases. *Journal of Heat Transfer*, vol. 118, pp. 650-653.

Modak, A. T. (1978). Radiation from Products of Combustion. *Fire Research*, vol. 1, pp. 339-361.

Modest, M. F. (1993). *Radiative Heat Transfer*. McGraw-Hill, New York.

Pearson, C. E. (1986). *Numerical Methods in Engineering and Science.* Van Nostrand Reinhold Company. New York.

Rothman, L. S., Gamache, R. R., Goldman, A., Brown, L. R., Toth, R. A., Pickett, H. M., Poynter, R. L., Flaud, J. M., Camy-Peyret, C., Barbe, A., Husson, N., Rinsland, C. P. and Smith, M. A. H. (1987). The HITRAN database: 1986 edition. *Applied Optics*, vol. 26, no. 19, pp. 4058-4095.

Rothman, L. S., Gamache, R. R., Tipping, R. H., Rinsland, C. P., Smith, M. A. H., Benner, D. C., Devi, V. M., Flaud, J-M., Camy-Peyret, C., Perrin, A., Goldman, A., Massie, S., Brown, L. R. and Toth, R. A. (1992). The HITRAN Molecular Database: Editions of 1991 and 1992. *Journal of Quantitative Spectroscopy and Radiative Transfer*, vol. 48, pp. 469-507.

Rothman, L. S. (1998). The HITRAN Database. Available at WWW at: http://www.hitran.com/

Siegel R. and Howell, J. R. (1992). *Thermal Radiation Heat Transfer*. 3rd ed., Hemisphere, Washington.

Smith, T. F., Shen, Z. F. and Friedman, J. N. (1982). Evaluation of Coefficients for the Weighted Sum of Gray Gases Model. *Journal of Heat Transfer*, vol. 104, pp. 602-608.

Taine, J. (1983). A Line-By-Line Calculation of Low-Resolution Radiative Properties of CO2-CO-Transparent Nonisothermal Gases Mixtures upto 3000 K. *Journal of Quantitative Spectroscopy and Radiative Transfer*, vol. 30, no. 4, pp. 371-379.

Truelove, J. S. (1976). *A Mixed Grey Gas Model for Flame Radiation.* Technical Report AERE - R8494, Thermodynamics Division, AERE, Harwell.

Chapter 6: Part A

Burns, S. P., Howell, J. R. and Klein, D. E. (1995). Finite Element Solution for Radiative Heat Transfer with Nongray, Nonhomogeneous Radiative Properties. In *1995 National Heat Transfer Conference - Vol. 13*, HTD-vol. 315, ASME, pp. 3-10.

Chui, E. H., Hughes, P. M. and Raithby (1993). Implementation of the Finite Volume Method for Calculating Radiative Transfer in a Pulverized Fuel Flame. *Combustion Science and Technology*, vol. 92, pp. 225-242.

Denison, M. K. and Webb, B. W. (1993). A Spectral Line-Based Weighted-Sum-of-Gray-Gases Model for Arbitrary RTE Solvers. *Journal of Heat Transfer*, vol. 115, pp. 1004-1012.

Denison, M. K. and Webb, B. W. (1995). The Spectral Line-Based Weighted-Sum-of-Gray-Gases Model in Nonisothermal Nonhomogeneous Media. *Journal of Heat Transfer*, vol. 117, pp. 359-365.

Dongarra, J. J. (1998). Performance of Various Computers Using Standard Linear Equations Software. Report no. CS-89-85, Computer Science Department, University of Tennessee. Available on the WWW at: http://www.netlib.org/benchmark/performance.ps

Farmer, J. T. and Howell, J. R. (1994). Monte Carlo Prediction of Radiative Heat Transfer in Inhomogeneous, Anisotropic, Nongray Media, *AIAA Journal of Thermophysics and Heat Transfer*, Vol. 8, No. 1, pp. 133-139.

Foster, P. J. and Howarth, C. R. (1968). Optical Constants of Carbons and Coals in the Infrared, *Carbon*, Vol. 6, pp. 719-729.

Grosshandler, W. L. (1979). *Radiation from Nonhomogeneous Fires*. Technical Report FMRC J. I. OAOE6.BU-4, Factory Mutual Research Corporation, Norwood, Massachusetts.

Hoover, R. L., Li, W., Benmalek, A. and Tong, T. W. (1996). *Sn* Solutions for Radiative Heat Transfer in an L-Shaped Participating Medium. In *National Heat Transfer Conference, Vol. 3*, HTD-vol. 325, ASME, pp. 1-11. (Solutions corrected later.)

Hsu, P. and Farmer, J. T. (1995, 1997). Benchmark Solutions of Radiative Heat Transfer within Nonhomogeneous Participating Media using the Monte Carlo and YIX Methods. In *1995 National Heat Transfer Conference - Vol. 13*, HTD-vol. 315, ASME, pp. 29-36. Revised (condensed) version: *Journal of Heat Transfer*, vol. 119, pp. 185-188, 1997.

Hsu, P. and Tan, Z. (1996). The Radiative and Combined Mode Heat Transfer within the L-Shaped Nonhomogeneous and Nongray Participating Media. In *National Heat Transfer Conference - Vol. 3*, HTD-vol. 325, ASME, pp. 13-24.

Hsu, P., Tan, Z. and Howell, J. R. (1993). Radiative Transfer by the YIX Method in Nonhomogeneous, Scattering and Nongray Media, *Journal of Thermophysics and Heat Transfer*, vol. 7, no. 3, pp. 487-495.

Maltby, J. D. (1996). Coupled Monte Carlo / Finite Element Solution of Radiation - Conduction Problems in a Shaded Geometry. Open Forum Paper: Radiative Heat Transfer Theory and Applications, ASME National Heat Transfer Conference, Houston, Texas, 6th August, 1996.

Modest, M. F. (1993). *Radiative Heat Transfer*. McGraw-Hill, New York.

Naraghi, M. H. N. and Litkouhi, B. (1989). Discrete Exchange Factor Solution of Radiative Heat Transfer in Three-Dimensional Enclosures, ASME HTD-Vol. 106, pp. 221-229.

Selçuk, N. (1985). Exact Solutions for Radiative Heat Transfer in Box-Shaped Furnaces. *Transactions of the ASME, Journal of Heat Transfer*, vol. 107, pp. 648-655.

Selcuk, N. and Kayakol, N. (1997). Evaluation of Discrete Ordinates Method for Radiative Transfer in Rectangular Furnaces. *International Journal of Heat and Mass Transfer*, vol. 40, no. 2, pp. 213-222.

Shah, N. G. (1979). New Method of Computation of Radiant Heat Transfer in Combustion Chambers. Ph.D. Thesis. Imperial College of Science and Technology, London, UK.

Tong, T. W. and Skocypec, R. D. (1992). Summary on Comparison of Radiative Heat Transfer Solutions for a Specified Problem. In *Developments in Radiative Heat Transfer*, HTD-vol. 203, ASME, pp. 253-264.

Chapter 6: Part B

Alkidas, A. C. (1979). Heat Transfer Characteristics of a Spark-Ignition Engine. General Motors Research Publication no. GMR-2914 R. (Presented at the 18th ASME/AIChE National Heat Transfer Conference, San Diego, California, August 5-8, 1979.)

Amato, U. and Petrillo, F. (1992). On Some Properties of KIVA Numerical Schemes. *Math. Mech.*, vol. 72, pp. 175-188.

Baker, H. D. and Laserson, G. L. (1951). An Investigation into the Importance of Chemi-luminescent Radiation in Internal Combustion Engines, IMechE/ASME Proceedings General Discussion on Heat Transfer, London, pp. 334-340..

Blunsdon, C. A., Dent, J.C. and Malalasekera, W. M. G. (1993). Modelling Infrared Radiation from the Combustion Products in a Spark Ignition Engine. SAE paper no. 932699.

Das, S. and Dent, J. C. (1995). Simulation of the Mean Flow in the Cylinder of a Motored 4-valved Spark Ignition Engine. SAE paper no. 952384.

Gatowski, J. A., Heywood, J. B. and Deleplace, C. (1984). Flame Photographs in a Spark-Ignition Engine. *Combustion and Flame*, vol. 56, pp. 71-81.

Heywood, J. B. (1988). *Internal Combustion Engine Fundamentals*. McGraw-Hill, New York.

Jackson, N. S. and Stokes, J. (1984). Combustion Study on the Ford 2.0 Litre OHC Bowl in Piston Gasoline Engine: A Compilation of Test Results Oct. 1983 - Apr. 1984. DP 84/1468 Restricted. Ricardo Consulting Engineers.

Jones, P. and Junday, J. S. (1995). Full Cycle Computational Fluid Dynamics Calculations in a Motored Four Valve Pent Roof Combustion Chamber and Comparison with Experiment. SAE paper no. 950286.

Kuo, T. W. and Reitz, R. D. (1989). Computation of Premixed-Charge Combustion in Pancake and Pent-Roof Engines. SAE paper no. 890670.

Le Coz, J. F., Henriot, S. and Pinchon, P. (1990). An Experimental and Computational Analysis of the Flow Field in a Four-Valve Spark Ignition Engine–Focus on Cycle-Resolved Turbulence. SAE paper no. 900056.

Marvin, C. F., Caldwell, F. R. and Steele S. (1934). Infrared Radiation from Explosions in a Spark-Ignition Engine. NACA report no. 486.

McComiskey, T., Jiang, H., Qian, Y., Rhee, K. T. and Kent, J. C. (1993). High-Speed Spectral Infrared Imaging of Spark Ignition Engine Combustion. SAE paper no. 930865.

Nutton, D. and Pinnock, R. A. (1990). Closed Loop Ignition and Fueling Control Using Optical Combustion Sensors. SAE paper no. 900486.

Ohmstede, G. and Hentschel, W. (1995). Time-Resolved Infrared Spectroscopy: Evaluation of Temperature for Various EGR Rates in a DI-Diesel Engine. SAE paper no. 952516.

Randolph, A. L. (1990a). Cylinder Pressure Mounting Techniques to Maximise Data Accuracy. SAE paper no. 900171.

Randolph, A. L. (1990b). Methods of Processing Cylinder Pressure Transducer Signals to Maximise Data Accuracy. SAE paper no. 900170..

Remboski, D. J., Plee, Jr. and S. L., and Martin, J. K. (1989). An Optical Sensor for Spark-Ignition Combustion Analysis and Control. SAE paper no. 890159.

Truelove, J. S. (1976). *A Mixed Grey Gas Model for Flame Radiation.* Technical Report AERE - R8494, Thermodynamics Division, AERE, Harwell.

Williams, H. S. (1976). A Preliminary Study of the Magnitudes of Radiative and Convective Heat Transfer in a Diesel Engine. Masters Thesis. Loughborough University, UK.

Zhao, H., Collings, N. and Ma, T. (1991). The Cylinder Head Temperature Measurement by Thermal Imaging Technique. SAE paper no. 912404.

Zhao, H., Collings, N. and Ma, T. (1994). Two-dimensional Temperature Distributions of Combustion Chamber Surfaces in a Firing Spark Ignition Engine. Proceedings of IMechE, Part D: Journal of Automobile Engineering, Vol. 208, No. , pp. 99-1994.

Chapter 7

Bray, K. N. C., Libby, P. A. and Moss, J. B. (1983). Unified Modelling Approach for Premixed Turbulent Combustion - Part 1: General Formulation. *Combustion and Flame*, vol. 61, no. 1, pp. 87-102.

Burns, S. P. and Christon, M. A. (1996). Spatial Domain-Based Parallelism in Large Scale, Participating-Media, Radiative Transport Applications. Open Forum paper at 1996 ASME National Heat Transfer Conference, Houston, Texas.

Craft, T. J., Launder, B. E. and Suga, K. (1996). Development and application of a cubic eddy-viscosity model of turbulence. *International Journal of Heat and Fluid Flow*, vol. 17, pp. 108-115.

Denison, M. K. and Webb, B. W. (1993). A Spectral Line-Based Weighted-Sum-of-Gray-Gases Model for Arbitrary RTE Solvers. *Journal of Heat Transfer*, vol. 115, pp. 1004-1012.

Gran, I. R. (1994). Mathematical Modeling And Numerical Simulation Of Chemical Kinetics in Turbulent Combustion. Dr. Ing. Thesis. University of Trondheim, Norway.

Heel, B., Maly, R., Weller, H. G. and Gosman, A. D. (1998). Validation of SI Combustion Model over range of Speed, Load, Equivalence Ratio and Spark Timing. Submitted to COMODIA98. Posted at WWW site: http:/monet.me.ic.uk/publications/combustion.html

Lebrère, L. and Dillies, B. (1996). Engine Flow Calculations Using a Reynolds Stress Model in the KIVA-II Code. SAE paper no. 960636.

Mazumder, S. and Modest, M. F. (1997a). Boundary Treatment and Efficient Pressure Algorithm for Internal Trubulent Flows Using the PDF Method. *International Journal for Numerical Methods in Fluids,* vol. 24, pp. 215-232.

Mazumder, S. and Modest, M. F. (1997b). A Stochastic Lagrangian Model for Near-Wall Turbulent Heat Transfer. *Journal of Heat Transfer*, vol. 119, no. 1, pp. 46-52.

Modest, J. F. and Collins, L. R. (1998). Numerical Study of Turbulence-Radiation Interactions in Reactive Flows. A project outline for collaborative research between Pennsylvania State University and Sandia National Laboratories Fire Science and Technology Program. Posted at WWW site: http://michelle.me.psu.edu/~mfm/research/nsfsnl/nsfsnl.html

Rothman, L. S. (1998). The HITEMP Database: a high temperature analogue of the HITRAN database. Available at WWW at: http://www.hitran.com/

Sakami, M., Charette, A. and Le Dez, V. (1997). Radiative Heat Transfer in Three-Dimensional Enclosures of Complex Geometry by using the Discrete Ordinates Method. *Journal of Quantitative Spectroscopy and Radiative Transfer*, vol. 59, no. 1-2, pp. 117-136.

Appendices

Amsden, A. A., O'Rourke, P. J. and Butler, T. D. (1989). KIVA-II: A Computer Program for Chemically Reactive Flows with Sprays. Report no. LA-11560-MS. Los Alamos National Laboratory, New Mexico.

Hsu, P., Tan, Z. and Howell, J. R. (1992). Application of the YIX Method to Radiative Heat Transfer within a Mixture of Highly Anisotropic Scattering Particles and Nongray Gas. In *Developments in Radiative Heat Transfer*, HTD-vol. 203, ASME, pp. 285-299.